



The
University
Of
Sheffield.

Department
Of
Mechanical
Engineering.

EFFECT OF COMPRESSION, IMPACT AND SLIPPING ON ROLLING CONTACT FATIGUE AND SUBSURFACE MICROSTRUCTURAL DAMAGE

**A thesis submitted in partial fulfillment of the
requirements for the degree of**

Doctor of Philosophy

Author:

Jasim Hasan Ilik AL-Bedhany

Registration No: 140249307

February 2020

ABSTRACT

Rolling Contact Fatigue (RCF) manifests itself in different engineering applications such as bearings, gears, railway tracks, and cams. In Wind Turbine Gearboxes (WTGs), which are designed to be in service for 20 to 25 years, the service life of their bearings is often below their design life despite depending on advanced technologies and standards in the gearbox design. This premature bearing failure occurs by flaking, mainly in the bearing inner races. Furthermore, bearing service life cannot be precisely predicted despite many life prediction models and using advanced analyses for the gearbox design. This premature bearing failure increases the wind energy cost due to unplanned maintenance and early replacement. In addition to that the main causes and mechanisms of this premature failure have not been completely understood. This has motivated an increasing investigation in this field due to the scientific and economic impacts.

There are a considerable number of factors affecting premature bearing failure. Three parameters which are widely reported as the main causes were investigated in this study which are contact pressure, slipping and impact loading. Two failed planetary bearings from a multi-megawatt wind turbine gearbox were investigated first to evaluate their surface and subsurface damage features and to estimate the parameter testing levels. A new test rig that can apply impact loading in combination with compression and slipping was designed. Two contact discs made from bearing material (AISI 52100 steel) were used in this test rig. Sixteen tests are designed using Minitab software for design of experiments using a line contact with flat test discs with stress concentration at the contact edges because stress concentration cannot be avoided in roller bearings, which is the type usually used in the turbine gearboxes. The effect of the key parameters on the test disc life in terms of the number of cycles to failure and subsurface damage features distribution at the microscale level were analyzed. These distributions were correlated with the subsurface stress distribution within the contact region of the bearings and the test discs to predict which stress type was responsible for each damage type. Further tests were also designed and conducted to avoid the stress concentration using fully crowned disc profiles to investigate the effect of the key parameters on disc life. The investigation led to the suggestion of a new simple damage estimation model depending on the contact stress levels and the number of cycles under each level.

The results of the qualitative and quantitative investigation confirm the considerable role of contact stress followed by slipping and then impact loading. Despite impact-loading affecting damage as contact pressure, it reveals two different effects on the subsurface damage features. The first was observed in shallow regions as internally cracked inclusions within the disc material while, the second by introducing damaged inclusions in deeper regions. The individual and interactive effects of impact loading with the other two parameters were found to be different from the compression loading effects. The correlation of damage distribution with the subsurface stress distributions confirms the postulation of Von-Mises and maximum shear stresses as being the main contributors to damage initiation and propagation. The suggested life prediction model was tested by using the test results and real wind turbine operating data of SCADA for two years in addition to using the average annual wind speed distribution. The results of this model were very close to the reported wind turbine gearbox bearing life. More testing is still required to confirm the reliability of this simple and applicable model. The metallographic investigations confirmed that the subsurface microcracks were often not associated with non-metallic inclusions, but may be started from the voids associated with the material carbides is a significant damage initiation source in addition to that of non-metallic inclusions which have been widely reported in the previous studies. Furthermore, Slipping Ratio (SR) is found to have more effect under low contact loading levels. A considerable role of impact loading in the butterfly wing damage feature is postulated. Moreover, the Intrusion/Extrusion and dislocation damage mechanism theories may be more suitable for describing overloading fatigue damage.

The novelty of this study is that it is the first study of the rolling contact fatigue life and the behaviour of the bearing steel under impact-loading in combination with compression and sliding to investigate the individual and interactive effects of these parameters on the trend of fatigue life variation by developing a new test rig. A new bearing life prediction methodology is proposed, and the results showed a lower percentage of errors in the turbine bearing predicted life compared with the standards currently use. More tests and metallographic investigations are recommended to investigate the effect of lower and higher contact stress levels and impact loading to understand the effect of these parameters on the initiation and propagation of the subsurface damage features.

PUBLICATIONS AND PRESENTATIONS

Publications

- ❖ Jasim H Al-Bedhany and Hui Long, “Microscopic investigation of subsurface initiated damage of wind turbine gearbox bearings,” J. Phys.: Conf. Ser. 1106 012029, 2018.
- ❖ Tahseen Ali Mankhi, Stanisław Legutko, Jasim H AL-Bedhany and Abdulmuttalib A Muhsen, “Selecting the Most Efficient Bearing of Wind Turbine Gearbox Using (Analytical Hierarchy Process) Method “AHP”, International Conference on Sustainable Engineering Techniques, Iraq, March 2019.

Presentations

- ❖ “Investigation of premature failure of wind turbine gearbox bearings,” Energy 2050, Energy Research Symposium (ERS), Grantham Centre, the University of Sheffield, UK, 2017.
- ❖ “Microscopic investigation of subsurface initiated damage of wind turbine gearbox bearings”, MPSVA conference, Clare College, University of Cambridge, Cambridge, UK, 2018.

Poster presentations

- ❖ “BEARING WHITE ETCHING CRACK DAMAGE AND LIFE PREDICTION METHOD,” a poster presented in the Ph.D. poster Event at the University of Sheffield 2017.

DEDICATION

To my homeland (IRAQ) the dearest than all. To every drop of blood spilled by the Iraqi martyrs and any others injured during the battle against ISIS (Terrorism State). To my university (Misan), its Engineering college and everybody who supported me during the study.

To the spirit of my father, to my mother and my brother Ahmed.

To my wife and my children Hasan, Aya, Retaj, Zahraa, and Ahmed.

To my friends who care about me and hope me to succeed.

I hope I will be as you expect, and I promise you that, I shall continue doing my best to serve humanity.

Jasim H. AL-Bedhany

ACKNOWLEDGMENTS

The author sincerely thanks the Iraqi Ministry of Higher Education and Scientific Research (MOHESR), The Iraqi Cultural Attaché in London, UK, Misan University and Engineering College for sponsoring my Ph.D. scholarship. Special thanks to my supervisor Professor R. Lewis for his support, guidance, and monitoring of this study and for Professor Bill Nimmo and the head of the department Professor Neil Sims. Thanks to Vestas Wind System A/S for supplying the two failed planetary bearings.

A special thanks to many others have provided a fruitful input to this project, including:

- * Terry Hattersley, Harthill© Development Ltd. company for his support and help in the manufacturing of the test rig.
- * Phillip C. Pickstock, the Departmental Technical Manager, for his support in installing the electrical controls of the test rig.
- * Jamie Booth, the department research technician, for his support in manufacturing some components for the test rig.
- * Karl Rotchell, the electrical workshop team leader for his support in completing urgent mechanical works required.
- * Ashley KW Ng, MEng student for working together on MATLAB software to analyze the bearing contact stresses.
- * Dr. Alistair John, The University of Sheffield for his support and fruitful recommendations.

Jasim Hasan AL-Bedhany

NOMENCLATURES

Unless otherwise stated, all units used through this thesis are SI.

σ	Stress (Pa)
P_o	Maximum contact pressure (Pa)
a and b	Half of the contact width (m)
τ , τ_{xy} , τ_{max}	Shear, orthogonal and unidirectional shear stresses (Pa)
$\sigma_1, \sigma_2, \sigma_3$	Principal stresses (Pa)
σ_y	Yield stress (Pa)
z	Depth beneath the contact surface (m)
Z_{rol}	Number of bearing roller
L_{10}	Rated bearing life with 90% reliability in million cycles (Cycle)
c	Dynamic load capacity (N)
p_{eq}	Equivalent radial load (Pa)
n	Number of cycles
N, N_f	Number of cycles to failure
e	Life estimation empirical exponent
D	Damage
x_k	Variable depends on loading level
r	Cyclic ratio (number of rotating cycles to number of cycles to failure)
A and B	Constants
w	Exponent depend on fatigue stress amplitude
α	The fraction for crack initiation
β	The fraction of crack propagation
N_b, N_{II}	Number of cycles for crack initiation and propagation respectively
m and n	Contact parameters

s	Bearing raceway survival probability (%)
L_f	Fatigue life (Cycle)
a_o and a_f	Initial and final crack lengths (m).
E	Modulus of elasticity (GPa)
ν	Poisson's ratio
G	The gear ratio of the turbine gearbox
P_{gen}	Power of turbine generator (W)
H	Number of rows in planetary bearings
ω_{gen}	Rotating speed of the turbine generator (rad/s)
η	Overall drivetrain efficiency
R_D	Ring gear diameter in planetary stage (m)
S_D	Sun gear diameter in planetary stage (m)
T	Torque (N.m)
R_a	Arithmetic surface roughness
HV	Vickers hardness
HRC	Rockwell Hardness
U_{ud}, U_{ld}	The linear velocities of the upper and lower test disc respectively (m/s)
SR	Slipping ratio
AR	Aspect ratio
T_1, T_2	Upper and lower test disc thickness respectively (m)
R_1, R_2	Upper and lower test disc radii respectively
ρ	Density (kg/m ³)
φ	Dynamic viscosity (cSt)
h_f	Lubricant film thickness (μm)
\mathcal{K}	kinematic viscosity (cP)
ϑ	Pressure-viscosity coefficient
μ	Friction coefficient

V_{cam}	Tip cam velocity (m/s)
N_{cam}	Cam rotational speed (rpm)
R_c	Cam tip radius (m)
ω_{il}	Impact lever rotational speed (rad/s)
V_{imp}	Impact velocity (m/s)
M_{eff}	Effective impact mass (kg)
d_g	The distance between the radius of gyration and impact lever center (m)
I	Angular mass moment of inertia (kg.m ²)
L	Length (m)
k_s	Stiffness parameter (N/m)
E_{imp}	Impact energy (J)
F_i	Impact force (N)
p_{oi}	Maximum contact pressure due to impact (Pa)
μ_{mean}	Mean value of the output
β_{input}	Effect of the input factor
ε_{noise}	Error due to noise
SD	Standard deviation
β	Scale Parameter
\aleph	Shape Parameter
$F_{(pr)}$	probability fraction
t_n	Test number
N_T	Total number of tests
t	Time (s)

ABBREVIATIONS

RCF	Rolling Contact Fatigue
WTGs	Wind Turbine Gearboxes
O&M	Operating and Maintenance
WT	Wind Turbine
WE	Wind Energy
RE	Renewable Energy
LSS	Low-Speed Shaft
PP	Planetary Pin
HSS	High-Speed Shaft
MSS	Medium Speed Shaft
UW	UpWind
DW	Down Wind
WSF	White Structure Flaking
DEAs	Dark Etching Areas
WTGBs	Wind Turbine Gearbox Bearings
WEAs	White Etching Areas
WEBs	White Etching Bands
WECs	White Etching Cracks
SR	Slipping Ratio
R/S	Rolling/Sliding
SCADA	Supervisory Control And Data Acquisition
WTs	Wind Turbines
LRM	Light Reflection Microscope
OD	Over-rolling Direction
WL	White Layer
DZ	Deformed Zone

LEDS	Low Energy Dislocation Structure
FHA	Frictional Heat Accumulation
LEAs	Light Etching Areas
LAB	Low Angle Band
HAB	High Angle Band
FE	Finite Element
EHL	Elastohydrodynamic Lubrication
NREL	National Renewable Energy Laboratory
SRCR	Single-Row Cylindrical Roller bearing
DRCR	Double-Row Cylindrical Roller bearing
SEM	Scanning Electron Microscope
EDX	Energy Dispersive X-ray analysis
WD	Working Distance
HV	Vickers Hardness
AISI	American Iron and Steel Institute
HRC	Rockwell Hardness
SRACBs	Single Row Angular Contact Ball Bearings
DOE	Design Of Experiment
SD	Standard Deviation
PDF	Probability Density Function
EFDA	Energy Fraction of Damage Accumulation
P-M	Palmgren-Miner theory
CTE	Coefficient of Thermal Expansion
DLDR	Double Linear Damage Rule
TF	Transfer Function
LEFM	Linear Elastic Fracture Mechanics
AR	Aspect Ratio

PS	Probability of Survival
COD	Crack Opening Distance

CONTENTS

ABSTRACT	i
PUBLICATIONS AND PRESENTATIONS	i
DEDICATION	ii
ACKNOWLEDGMENTS	iii
NOMENCLATURES	iv
ABBREVIATIONS	ix
CONTENTS	xi
LIST OF FIGURES	xvii
LIST OF TABLES	xxviii
1 INTRODUCTION	1
1.1 Justification of the research	2
1.2 Research aims and objectives.....	8
1.3 Thesis layout	10
1.4 Main novelty key contributions	11
2 LITERATURE REVIEW	13
2.1 Introduction	13
2.2 Wind turbine gearbox design and Bearings loading.....	17
2.3 Wind turbine gearbox operating and monitoring	19
2.4 Factors affecting the premature failure of WTG bearings	20
2.4.1 Effect of impact and transient loadings	24
2.4.2 Compressive contact loading of WTGBs	25
2.4.3 Slipping of contact surfaces.....	28
2.4.4 Inclusions of bearing steels	30

2.5	Phenomena associated with WTGB premature failure	32
2.6	Bearing damage features.....	33
2.6.1	Surface and subsurface microcracks	33
2.6.2	Microstructural alterations	35
2.6.3	Theories and mechanisms of microstructural alterations	37
2.7	Rolling Contact Fatigue (RCF)	44
2.8	Theories and mechanisms of fatigue damage.....	47
2.9	Test rigs used to investigate RCF	51
2.10	Fatigue life prediction theories.....	54
2.11	Summary and research gap	60
3	DAMAGE INVESTIGATION OF FAILED PLANETARY BEARINGS.....	62
3.1	Investigation of failed planetary bearings	63
3.2	Stresses induced in the investigated bearings	66
3.3	Investigation procedure.....	72
3.4	Surface investigations.....	74
3.4.1	Contact surface hardness.....	75
3.4.2	Surface roughness	76
3.5	Subsurface investigations.....	80
3.5.1	Sample sectioning and mounting.....	80
3.5.2	Sample preparation.....	80
3.6	Subsurface microstructural observations.....	82
3.6.1	Butterfly wings	88
3.6.2	Subsurface microcracks.....	98
3.6.3	Other observations.....	101

3.7	Bearing failure causes and mechanisms.....	103
3.8	Discussion	104
3.9	Conclusions.....	106
3.10	Key findings forward to rig design and testing	107
4	TEST RIG DESIGN FACILITATING COMBINED ROLLING, SLIDING AND IMPACT LOADING	108
4.1	Design concept development	108
4.1.1	Compression mechanism	113
4.1.2	Slipping mechanism.....	116
4.1.3	Impact mechanism	117
4.2	Test disc design.....	120
4.2.1	Material and dimensions.....	121
4.2.2	Test disc design to avoid the edge stress concentration	123
4.2.3	Heat treatment.....	124
4.2.4	Surface finishing	125
4.3	Design calculations	125
4.3.1	Compressive pressure and stress calculations.....	126
4.3.2	Slip Ratio and traction force calculations.....	131
4.3.3	Assumptions of impact stress calculations	133
4.3.4	Static and dynamic response of test disc material.....	134
4.3.5	Theoretical calculations of impact forces and stresses.....	136
4.4	Lubrication and lubricant specifications.....	140
4.5	Test rig capabilities	141

5	EFFECT OF TESTING PARAMETERS ON THE TEST DISC FATIGUE LIFE	143
5.1	Introduction	143
5.2	Test parameters and variation ranges.....	146
5.3	The experimental results and analyses	148
5.3.1	Individual effects of the study parameters	152
5.3.1.1	Effect of compression	153
5.3.1.2	Effect of impact.....	156
5.3.1.3	Effect of slipping ratio.....	160
5.3.1.4	Analysis of fully crowned discs	162
5.3.2	Interactive effect of the study parameters on disc life	164
5.3.3	Effect of slipping and impact under different contact levels	168
5.3.4	Effect of surface roughness.....	170
5.4	Quantitative analysis of the study parameters on test disc life	170
5.4.1	Individual effects	170
5.4.2	Combined and interactive effects	171
5.5	S-N curve of the disc material and disc life prediction	174
5.6	Discussion	175
5.7	Key findings.....	176
6	A NEW FATIGUE LIFE PREDICTION METHOD	178
6.1	Introduction	178
6.2	Stress-based fatigue damage theories and their issues	179
6.3	New damage estimation method	182
6.4	Assumptions and limitations of the model.....	187
6.5	Applying the new method on the conducted tests	188

6.6	Testing the new method using SCADA data	190
6.6.1	Fatigue life prediction results.....	192
6.6.2	Effect of operating events on damage estimation.....	197
6.7	Discussion	199
6.8	Key findings.....	199
7	MICROSTRUCTURAL DAMAGE ANALYSIS OF TEST DISCS	202
7.1	Test disc damage investigation.....	203
7.1.1	Surface hardness	207
7.1.2	Surface roughness	208
7.1.3	Effect of impact loading on damage propagation.....	210
7.2	Preparing for subsurface investigations	211
7.3	Damaged inclusions and microcracks.....	215
7.3.1	Inclusion damage by separation.....	218
7.3.1.1	Effect of compressive loading.....	219
7.3.1.2	Effect of the impact stress.....	223
7.3.1.3	Effect of Slipping Ratio (SR)	224
7.3.2	Subsurface cracking damage.....	226
7.3.2.1	Effect of compressive loading.....	227
7.3.2.2	Effect of impact loading.....	231
7.3.2.3	Effect of Slipping Ratio (SR)	235
7.4	Investigation of the test without impact loading	240
7.5	Investigation of fully crowned test discs	242
7.5.1	Surface analyses	242
7.5.2	Subsurface analyses	244

7.6	Justification of not producing microstructural alterations.....	246
7.7	Comparison of test disc and bearing materials	246
7.7.1	Surface and subsurface microcracks as damage initiation sites	249
7.7.2	Testing of accumulative frictional energy hypothesis.....	251
7.8	Key findings.....	252
8	CONCLUSIONS AND FUTURE WORK	254
8.1	Conclusions.....	254
8.1.1	Investigation of the failed planetary bearings	255
8.1.2	Investigated parameters and test discs	257
8.1.3	The new bearing damage estimation and life prediction method (EFDA).....	259
8.2	Recommendations for future work.....	259
8.2.1	Future testing	259
8.2.2	Improving the test rig.....	261
8.2.3	Improving the WTG design.....	262
	REFERENCES.....	264
	Appendix A.....	282
	Appendix B	287
	Appendix C	288
	Appendix D.....	293
	Appendix E	294
	Appendix F.....	297
	Appendix G.....	301

LIST OF FIGURES

Figure 1-1: (a) Growth of global renewable electricity generation [1]; (b) the top 10 countries and their production of wind energy in GW in 2016 (reproduced from [1]).	2
Figure 1-2: Wind turbine components showing the details of the gearbox (top) [15]; planetary stage components and their rotations and forces (down) [16].....	4
Figure 1-3: Rotor torque and speed variations with time during three operating events, start-up (upper), speed up (middle) and normal shutdown [32]......	7
Figure 1-4: Flowchart of the study progress.....	9
Figure 2-1: Examples of failed inner races of wind turbine gearbox bearings by flaking... 14	
Figure 2-2: Microstructural alterations with their depth and orientations (a) WEC [46]; (b) Dark Etching Region (DER), High Angle Band (HAB) and Low Angle Band (LAB) [34]; (c) butterfly wings.....	15
Figure 2-3: Factors affecting wind turbine premature failure.....	16
Figure 2-4: (a) Typical gearbox consists of one planetary stage showing the bearings locations (b) torque variation during grid loss and braking events [16].....	18
Figure 2-5: Contact stress distribution under different roller types and contact stresses [20].	23
Figure 2-6: Shear stress distribution under rolling-sliding conditions [111].....	27
Figure 2-7: Positive and negative slipping ratio.....	29
Figure 2-8: Examples of damaged inclusions (a) side separation damage; (b) crack initiated from an inclusion; (c) internally cracked inclusion; (d) inclusion associated with butterfly wing damage feature.....	31
Figure 2-9: Contact stress and the number of cycles for the formation of microstructural alterations [164].	36
Figure 2-10: Zwirlien and Schlicht diagram of microstructural change correlation with contact pressure and the number of rotating cycles [167]......	36
Figure 2-11: Butterfly wings feature and their types (a) double wings; (b) upper wing; (c) lower wing.....	42
Figure 2-12: Characterization of butterfly wings with depth [25].	44

Figure 2-13: Examples of bearing inner race failures [147]. (a) Spalling in early-stage; (b) Spalling in advanced stage; (c) micro-spalls; (d) Smearing; (e) contact corrosion; (f) surface-initiated micro-spalls; (g) surface-initiated spalling; (h) fretting; (i) smearing and skidding.....	45
Figure 2-14: Pressure distribution and maximum stresses in the contact region under Hertzian contact pressure of 2.4 GPa on a typical 2 MW planetary bearing.....	46
Figure 2-15: Theories of white structure flaking initiation.	49
Figure 2-16: Stages of rolling contact fatigue and microstructural damage associated (adapted from [109],[200] and [191]).	50
Figure 2-17: Typical test rigs used to investigate RCF failure. (a) MPR test rig [115]); (b) real bearing tester; (c) twin disc test rig; (d) thrust loading rig [121]; (e) ball against rod tester [189]; (f) thrust bearing test rig [97],[212].....	52
Figure 3-1: Investigated failed inner races and specimen locations (upwind on the left-hand side and downwind on the right).....	64
Figure 3-2: Spalling damage locations due to misalignment.....	64
Figure 3-3: Hertzian contact of two parallel cylinders.	66
Figure 3-4: Effect of increasing contact pressure on stresses (a) contact pressure distribution and locations of maximum shear stresses; (b) stresses under 1.8 GPa contact pressure and friction ($\mu=0.05$); (c) stresses under 2.15 GPa contact pressure and friction ($\mu=0.05$).....	68
Figure 3-5: Variation of subsurface stresses von-Mises (top), maximum shear (middle) and orthogonal shear (down), with increasing friction coefficient under compression of 1.8 GPa.	69
Figure 3-6: Maximum subsurface stresses distribution beneath the contact region under a compressive stress of 1.8 GPa and coefficient of friction ($\mu=0.05$ and 0.15); von-Mises (top); maximum shear (middle) and orthogonal shear (bottom).....	70
Figure 3-7: Investigation stages of the bearing inner races.....	72
Figure 3-8: Surface damaged regions in the investigated up-wind bearing.....	73
Figure 3-9: Microscopes used (a) Optical Nikon Eclipse LV 150 microscope; (b) FEI-inspect F Scanning Electron Microscope (SEM); (c) TM3030Plus SEM.....	74

Figure 3-10: Hardness measurements of the regions within and outside the loading zone.	76
Figure 3-11: Bearing surface roughness variations before and after used in service.	77
Figure 3-12: Surface roughness using non-contact contour GT: (left) out of the contact region and (right) inside the contact region.	78
Figure 3-13: Example of analysis of a dent observed on the UW bearing inner race surface.	79
Figure 3-14: A butterfly wing observed beneath the dent in the circumferential section...	79
Figure 3-15: Cutting and numbering of zone 1 specimens.....	80
Figure 3-16: Distribution of damaged inclusions with their depth.....	83
Figure 3-17: Distribution of the investigated inclusions according to inclusion aspect ratio (a) axial direction; (b) circumferential direction.	84
Figure 3-18: Inclination angle of damaged inclusions, (a) distribution with depth; (b) percentages (c) schematic representation of inclusion orientation inside the bearing material bulk.	85
Figure 3-19: Damaged inclusions by separation, (a) in relation to subsurface depth; (b) numbers and percentages of separated inclusions.	86
Figure 3-20: Damaged inclusions by cracking, (a) in relation to subsurface depth; (b) numbers and percentages of cracked inclusions.	87
Figure 3-21: Types of investigated butterfly wings (rolling surface in the top).	88
Figure 3-22: Examples of butterfly wings showing the associated cracked inclusions (rolling surface in the top and the rolling direction from left to right).	89
Figure 3-23: Distribution of observed butterfly wings with depth.	89
Figure 3-24: Investigated butterflies (a) distribution according to wing length and depth showing the average length and depth; (b) approximate wing angle and percentage; (c) distribution of wing frequency and length.	91
Figure 3-25: Upper and lower butterfly wing types (a) two butterfly types located at the same depth; (b) two butterfly types located at different depths (from the circumferential specimen 4 UW bearing).	92

Figure 3-26: Double and single butterfly wings (a) double and upper butterfly wings depth ~220µm; (b) double and upper butterfly wings depth ~230 µm (from the circumferential specimen 6 UW bearing).	93
Figure 3-27: Two stages of butterfly wings (a) initiation of a baby butterfly; (b) small wing.	93
Figure 3-28: Analysis of butterfly inclusion (a) Optical image of the largest investigated butterfly; (b) SEM image of one wing; (c) EDX analysis of the central inclusion.....	94
Figure 3-29: Two butterfly wings close to cracks, but not connecting with the crack network (from the circumferential specimen No. 2 UW bearing).	95
Figure 3-30: Butterfly wing and associated damage and changes (from the circumferential specimen No. 3 DW bearing).	95
Figure 3-31: EDX analysis of the most dominant inclusion type associated with butterfly wings (from the circumferential specimen No. 4 UW bearing).....	96
Figure 3-32: (a) butterfly wings not connected to the crack network causing flaking; (b) and (c) two features with double wings on each side; (d) and (e) two butterfly wings without central inclusion.....	97
Figure 3-33: Over etched specimens showing microcracks (a) and (b) circumferential sections; (c) axial section.	98
Figure 3-34: SEM images showing microcracks initiated in the subsurface region without inclusion.	99
Figure 3-35: Large inclusion unconnected to the crack network in the axial direction. ...	100
Figure 3-36: Crack orientation in axial and circumferential sections (a) and (b) axial sections; (c) and (d) circumferential sections.	101
Figure 3-37: Microstructural alteration features; (a), (b) and (c) WEAs in axial section; (d) WECs in circumferential direction; (e) and (f) WEB in the axial direction.	102
Figure 3-38: Surface and subsurface cracks' role in spalling failure initiation.....	103
Figure 3-39: Crack direction changed towards the weak points such as voids and inclusions.	103
Figure 4-1: Main components of rolling/sliding and impact test rig.	110
Figure 4-2: Control panel of the test rig.	110

Figure 4-3: Details of the test rig gears.....	111
Figure 4-4: Details of the belt drive mechanism used to rotate the camshaft, without cover (left) and with cover (right).....	112
Figure 4-5: Impact releasing mechanism and extensometer.	112
Figure 4-6: Schematic diagram showing the main parts of the designed test rig.....	113
Figure 4-7: Main components of the compression mechanism.....	114
Figure 4-8: Configuration of test discs and impact head with loading shaft supporting bearing.	115
Figure 4-9: Calibration curve of the test rig load cell.	116
Figure 4-10: Test discs contact showing compression force and pressure distribution (left) and, velocity and traction force (right).....	117
Figure 4-11: Main components of the impact mechanism.	118
Figure 4-12: Camshaft details (left) and cam dimensions (right).....	119
Figure 4-13: Characteristic curves of the cam, displacement curve (top) and impact roller velocity curve at the contact region (down).	119
Figure 4-14: Impact lever components.	120
Figure 4-15: Flat test discs dimensions (a) Upper disc; (b) lower disc.....	122
Figure 4-16: Full section and dimensions of crowned and flat test disc (a) upper test disc (b) lower test disc.....	124
Figure 4-17: Variation of contact stresses beneath the test disc contact region (a) Hertzian contact stress of 2.40 GPa; (b) Hertzian contact stress of 2.64 GPa.	127
Figure 4-18: Distribution of σ_x under uniform traction load [195].	128
Figure 4-19: Variation of shear stress distribution with increasing load and slipping.....	129
Figure 4-20: Variation of Von-Mises stress distribution with increasing load and slipping.	130
Figure 4-21: Variation of orthogonal shear stress distribution with increasing load and friction.....	130
Figure 4-22: Variation of contact stress with SR under different compressive force levels.	131

Figure 4-23: Variation of traction coefficient with the slipping ratio [83].	132
Figure 4-24: Experimental measurement of the test disc response.	135
Figure 4-25: Adding of extensometer to measure the deformation due to impact.	136
Figure 4-26: Impact mechanism details (a) cam-impact lever velocities relation (b) impact lever schematic diagram with mass, velocities and mass moment of inertia.	137
Figure 4-27: Variation of impact force and impact energy with test rig rotational speed.	139
Figure 4-28: Variation of combined compressive contact stress during one test rig cycle.	140
Figure 4-29: Fill in and emptying the test rig oil (a) the fill-in plug; (b) the drain plug; (c) the oil level mark.	141
Figure 4-30: Drain holes to empty the test rig lubricant.	141
Figure 5-1: Number of cycles to failure (N) under different test parameter levels.	150
Figure 5-2: Normality test curve of the test results.	151
Figure 5-3: Box and whisker plot for assessing the response normality of cycles to failure.	152
Figure 5-4: Probability distribution of the test results.	152
Figure 5-5: Individual mean effect of the tested factors on the line contact tests.	153
Figure 5-6: Mean effect of compressive loading without stress concentration using, (a) linear and exponential fitting curves extended out of the test range; (b) linear mean plot; (c) exponential mean and variation ranges.	155
Figure 5-7: Mean effect of compressive stresses on test disc life due to combined compression of impact and compressive loading with stress concentration.	156
Figure 5-8: Individual mean effect of impact force on test disc life (a) impact force only without stress concentration; (b) combined force corresponding to impact with stress concentration.	157
Figure 5-9: Effect of impact (a) variation trends of S-N curves under four impact levels; (b) variation range of the number of cycles to failure.	159
Figure 5-10: Individual effect of impact on the test disc life using flat discs.	160
Figure 5-11: Mean effect of slipping ratio on the number of cycles to failure.	161

Figure 5-12: Effect of slipping (a) variation trends of S-N curves under four levels of slipping ratios; (b) variation range of the number of cycles to failure.	162
Figure 5-13: Effect of the study parameters on crowned test disc life.....	163
Figure 5-14: Interaction effect of slipping ratio and compressive loading on the number of cycles to failure.....	165
Figure 5-15: Interaction effect of impact stress and compressive loading on the number of cycles to failure.....	166
Figure 5-16: Interaction effect of slipping ratio and impact stress on the number of cycles to failure (a) 3D plot; (b) 2D plot.	167
Figure 5-17: Effect of slipping with increasing the contact stress.	169
Figure 5-18: Effect of impact loading under different contact pressure.	169
Figure 5-19: Modified S-N curve of the test disc material using linear and exponential approximations.	175
Figure 6-1: Comparison of five damage estimation methods under the same cyclic ratio.	181
Figure 6-2: Damage energy in a balancing energy system.....	182
Figure 6-3: Calculating an equivalent number of cycles using the area under the S-N curve.	184
Figure 6-4: Flowchart of the new damage estimation method.....	186
Figure 6-5: Characteristic curves of a 1.7 MW wind turbine (a) power curve; (b) planet speed curve.	190
Figure 6-6: S-N curve of the bearing material [238].....	191
Figure 6-7: Operating wind speed distribution using SCADA data for (a) for the first year; (b) for the second year.....	192
Figure 6-8: First-year results of damage using SCADA data (a) accumulative damage using P-M theory and the new method; (b) wind speed distribution.....	193
Figure 6-9: Second-year results of damage using SCADA data (a) accumulative damage using P-M theory and the new method; (b) wind speed distribution.....	194
Figure 6-10: Damage accumulated curves for two years using SCADA data.....	195

Figure 6-11: Accumulative damage using standard wind speed occurrence during a year (a) Damage accumulation; (b) Standard wind speed distribution.....	197
Figure 6-12: Torque fluctuation during three events in 750 kW wind turbines.	198
Figure 7-1: Sample sectioning of a test disc for surface and subsurface investigation.	203
Figure 7-2: Failed upper and lower test discs classified into four groups depending on the SR.....	204
Figure 7-3: Radial crack introduced if impact location in an incorrect position (T11 left, T13 right).....	204
Figure 7-4: Surface damage of tests without stress concentration.....	205
Figure 7-5: Damage of test disc without impact loading (T6B).	206
Figure 7-6: Comparison of surface damage feature under different SR.	206
Figure 7-7: Hardness variation of test discs before and after the test.	207
Figure 7-8: Upper and lower test discs average measured surface roughness.	208
Figure 7-9: Circumferential surface roughness of the elliptical contact test disc.....	209
Figure 7-10: Alicona scanner analyses of investigating the effect of impact on damage depth (a) T6B (no impact); (b) T6 (impact stress=435 MPa); (c) T6A (impact stress=705 MPa).	211
Figure 7-11: Subsurface damage features of two failed test discs (a) from T6A; (b) from T7.	213
Figure 7-12: Subsurface stress distributions of the test discs under contact pressure of 2400 MPa and, 6.7% and 22 % traction coefficients. Von-Mises stress (top), maximum shear (middle) and orthogonal shear (down).	213
Figure 7-13: Examples of damage features observed (a) inclusion damaged by upper separation; (b) inclusion damaged by cracking; (c) surface and subsurface microcracks.	214
Figure 7-14: Damaged and undamaged inclusions (a) damaged by cracking close to its boundaries; (b) damaged by separation; (c) and (d) undamaged inclusions.	216
Figure 7-15: (a) Damaged inclusions according to aspect ratio; (b) surface and subsurface cracks.....	216

Figure 7-16: Damaged inclusions in the five investigated test discs (a) by separation; (b) by cracking.	217
Figure 7-17: Damaged inclusions by separation (a) near the spalling area; (b) different separations at the same depth; (c) upper separation (from T6A); (d) Lower and side separation (from T7).....	219
Figure 7-18: Examples of inclusion separation damage (a), (b) and (c) from T14; (d), (e) and (f) from T6.	220
Figure 7-19: Effect of compressive load on damaged inclusion by separation (a) test T14 (compression stress=2410 MPa); (b) test T6 (compression stress=2603 MPa).	221
Figure 7-20: Examples of undamaged and damaged inclusions (a) undamaged inclusion from T6; (b), (c) and (d) damaged inclusions by separation from T6; (e) undamaged inclusion from T14; (f) damaged inclusion by separation from T14.	222
Figure 7-21: Effect of impact on separation type (a) test T6 (impact stress=407.6 MPa); (b) test T6A (impact stress=705 MPa).	223
Figure 7-22: Examples of damaged inclusions by separation under the effect of impact (a) and (c) close to contact surface (from T6); (b) and (d) lower separation appears in a deep region (from T6A).	224
Figure 7-23: Effect of increasing SR on damaged inclusion by separation (a) T7 (SR=6.71%); (b) T7A (SR=22.82%).	225
Figure 7-24: Crack and separation damage of inclusions (a) From T7; (b) from T7A.	226
Figure 7-25: Damaged inclusion (a) in the same region have different damage features in circumferential section; (b) cracked inclusion observed in the axial direction.	227
Figure 7-26: Inclusion cracking damage due to compressive loading (a) From T14 (b) from T6 (c) two inclusions with different damage features; (d); (e) and (f) inclusion cracking damage examples (from T6).	228
Figure 7-27: Comparison of cracking damage with depth due to increasing compressive load (a) test T14 (compressive stress=2410 MPa); (b) test T6 (compressive stress=2603 MPa).	229
Figure 7-28: Effect of increasing compressive load on inclusion damage by cracking (a) test T14 (compressive stress=2410 MPa); (b) test T6 (compressive stress=2603 MPa).	230
Figure 7-29: Hypothesis: Stresses and their directions may cause damage initiation.	231

Figure 7-30: Damaged inclusions by cracking due to the effect of impact loading (a) close to contact surface (from T6A); (b) defects in the axial section (from T6); (c) kinked cracks (from T6 axial); (d), (e) and (f) defects and microcracks near damaged inclusions.....	232
Figure 7-31: Subsurface microcracks connection to produce crack network (a) from T6; (b) from T6A.....	233
Figure 7-32: Effect of impact on damage by cracking (a) test T6 (impact stress=407.6 MPa); (b) test T6A (impact stress=705 MPa).....	234
Figure 7-33: Effect of impact on inclusion cracking damage (a) test T6 (impact stress= 407.6 MPa); (b) test T6A (impact stress=705 MPa).....	235
Figure 7-34: Examples of damaged inclusions by cracking (a) upper cracked (from T7); (b) internally micro-cracked (from T7); (c) internally cracked in the shallow region (from T7A); (d) Internally cracked (from T7A).....	236
Figure 7-35: Sample from T7A showing the possible initiation of microstructural alteration.	237
Figure 7-36: Effect of SR on damage by cracking (a) test T7 (SR=6.71%); (b) test T7A (SR=22.82%).....	238
Figure 7-37: Effect of SR on cracking type (a) test T7 (SR=6.71%); (b) test T7A (SR=22.82%).....	239
Figure 7-38: Damage region of T6B (without impact loading).....	240
Figure 7-39: Subsurface investigation of T6B (a) microcracks with depth; (b) damaged inclusion by separation; (c) damaged inclusion by cracking.....	241
Figure 7-40: Effect of test parameter levels on surface damage feature.....	243
Figure 7-41: Subsurface damage features from fully crowned tests (a) and (b) T1P; (c) and (d) T2P; (e) T3P; (f) T4P.....	245
Figure 7-42: Long inclusions observed in test disc material in the axial direction.	247
Figure 7-43: Defects on the inclusion borders outside the damage affected area (a) in circumferential direction; (b) in axial direction.....	247
Figure 7-44: Compression tests of the bearing and test disc materials.....	248
Figure 7-45: S-N curves of the test disc material (top) and the real bearing material (down) [238].....	249

Figure 7-46: Surface and subsurface cracks may not initiate from inclusions	250
Figure 7-47: Example of damaged inclusion analysis using EDX technique.....	250

Figures of the Appendices

Figure A. 1: Reaction forces on the planetary stage components	272
Figure C. 1: Pressure and stress distribution for a contact of two flat test discs the upper has an axial length of 8 mm and the lower is 4 mm (a) schematic of the problem; (b) effect of stress concentration at the edges; (c) orthogonal shear stress; (d) Von-Mises stress.....	278
Figure C. 2: Pressure and stress distribution for a contact of two flat test discs having the same axial length of 8 mm (a) schematic of the problem; (b) effect of stress concentration at the edges; (c) orthogonal shear stress distribution; (d) Von-Mises stress distribution.....	279
Figure C. 3: Pressure and stress distribution for contact of flat fillet upper disc on flat lower disc 8 mm (a) schematic of the problem; (b) effect of pressure and stress concentration at the edges; (c) orthogonal shear stress distributions in three dimensional view and (d) Von-Mises stress distributions in three dimensional view.....	280
Figure C. 4: Pressure and stress distribution for contact of curved upper disc on flat lower disc 8 mm (a) schematic of the problem; (b) effect of stress concentration at the edges; (c) and (d) orthogonal shear stress distribution in three-dimensional view; (e) and (f) von-Mises stress distribution in two perpendicular planes	281
Figure E- 1: Test disc material static response	283
Figure E- 2: Test disc material dynamic response. Flat discs (top) and fully crowned discs (bottom).....	284
Figure E- 3: Fully crowned test disc stiffness within the test rig assembly.....	285
Figure G. 1: Flanged groove synchronous timing pulley and belt.....	289
Figure G. 2: Modification of impact mechanism camshaft.....	289

LIST OF TABLES

Table 2-1: Typical wind turbine operating events and their effects.....	25
Table 2-2: Chemical compositions of two bearing steels [146].	31
Table 3-1 Wind turbine gearbox specifications and working hours.....	63
Table 3-2: Measured dimensions of the inner races and rollers (all dimensions in mm)....	65
Table 3-3: Chemical composition of the bearing material (AISI 52100/100Cr6) [37].	65
Table 3-4: Mechanical properties of the bearing material [37][164][146].....	65
Table 3-5: Quantitative variation of maximum subsurface stresses and locations with contact pressure and surface traction coefficient.....	71
Table 3-6: Percentages of depth and stress variations with the variation of contact pressure and traction coefficient.	71
Table 3-7: Details of grinding and polishing processes.....	81
Table 3-8: Different damage forms initiate from inclusions.....	82
Table 4-1: Bearings of the test rig and specifications (dimensions in mm).	115
Table 4-2: Chemical analysis of test disc material.	121
Table 4-3: Test disc radii and the corresponding slipping ratio.....	121
Table 4-4: Heat treatment procedure of the test disc material.....	125
Table 4-5 Mechanical properties of the test discs material [56][146].....	126
Table 4-6: Film thickness to roughness ratios under different loading conditions.....	133
Table 4-7: Dynamic test parameters.	135
Table 4-8: Parameters of the designed impact mechanism.....	138
Table 4-9: Available test ranges of the study parameters.....	142
Table 5-1: DOE analysis methods and their advantages and disadvantages.....	144
Table 5-2: Testing parameter levels and variation ranges.....	147
Table 5-3: Test parameter levels and the number of cycles to failure.	149
Table 5-4: Life estimation equations and their percentage of error.....	171
Table 5-5: Experimental and estimated test disc life and their percentage of error.....	173

Table 5-6: Disc life estimation using RMS technique and its percentage of error.....	174
Table 6-1: Stress based life prediction theories.	180
Table 6-2: Life prediction and percentage of error of the conducted tests.....	189
Table 7-1: Parameter levels of test discs used for microstructural damage investigation.	212
Table 7-2: Effect of increasing the studied factors on inclusion damage by cracking	226
Table 7-3: Effect of increasing the studied factors on inclusion damage by cracking.	239
Table 7-4: Results of applying accumulative friction energy formula for the tests.....	252
Table A-1: Useful dimensions and specifications of the wind turbine gearbox.....	284

AGREEMENT DETAILS OF FIGURES REUSED FROM OTHER PUBLISHED WORKS

Figure No.	Page No.	Reference No.	Agreement License No.	Date	Notes
Figure 1.1 a	2	6	----	June 10 th 2020	Agreement received by an email from secretariat@ren21.net
Figure 1.2	4	21	----	May 27 th 2020	Agreement received by an email from Rob.Finger@nrel.gov
Figure 1.3	7	36	----	May 27 th 2020	Agreement received by an email from Rob.Finger@nrel.gov
Figure 2.2 a	15	49	Springer 4836571109124	May 26 th 2020	
Figure 2.2 b	15	38	ASTM 4837250946795	May 27 th 2020	
Figure 2.4 b	18	21	----	May 27 th 2020	Agreement received by an email from Rob.Finger@nrel.gov
Figure 2.5	23	25	600014662	May 27 th 2020	
Figure 2.9	36	164	Springer 4836661351759	May 26 th 2020	
Figure 2.10	36	167	ASTM 4837251257165	May 27 th 2020	
Figure 2.12	44	30	----	June 29 th 2020	permission from the corresponding author Juergen.Gegner@skf.com
Figure 2.17 a	52	116	4837811506665	May 28 th 2020	
Figure 2.17 d	52	122	Elsevier 4836611462850	May 26 th 2020	
Figure 2.17 e	52	189	Elsevier 4836630519990	May 26 th 2020	
Figure 2.17 f	52	99	----		Direct agreement from the copyright website for thesis use.
Figure 4.18	128	195	39953	17 th July 2020	From PLSclear website.
Figure 4.23	132	3	----		Direct agreement from https://creativecommons.org/licenses/by-nc-nd/2.0/uk/
Figure 6.6	191	258	600015776	June 4 th 2020	

1

INTRODUCTION

Rolling Contact Fatigue (RCF) phenomena appear in different applications such as gears, railway tracks, cams and bearings. Wind Turbine Gearboxes (WTGs) consist of many bearings and the gearbox is one of the costliest components of the turbine drivetrains. However, their bearings are suffering significantly from premature failure, often much earlier than their design life of 20 to 25 years. This is by flaking of the bearing inner race (removal of material from the contact surfaces). This premature failure results in a considerable increase in the Operation and Maintenance (O&M) cost which is a considerable percentage of the Wind Energy (WE) cost. The main causes and damage initiation and propagation mechanisms of these premature failures are not fully understood despite extensive research and investigation in recent years. In this chapter, the incremental trend of the wind turbine capacities and gearbox design are presented, furthermore, operating events and the severe operating conditions occurring during these events are outlined. The chapter also provides an overview of the effective factors recently investigated, such as loading levels during normal operating conditions and the operating events, bearing material microstructure and different phenomena observed within the bearing race materials (that will be discussed with more details in [Chapter 2](#)). Impact loading during normal operation and operating events were observed in previous literature [1]–[5], however, there is a lack of information about its role on RCF life and distribution of the subsurface damage features including microcracks and damaged non-metallic inclusions in addition to microstructural alterations. The research background and objectives are outlined, and the research gaps are identified. Finally, the structure of this thesis and the key contributions are presented.

1.1 Justification of the research

The increasing demand for energy has pushed governments and companies to look for alternative energy sources. Renewable Energy (RE) sources such as solar and wind energy have more focus. In the USA RE increased from 6.7% of the total energy in 2006 to 10.4% in 2016 [6]. Wind Energy (WE) is one of the most important green energy sources to overcome the negative impact of fossil fuel on climate change and the possibility of running out the oil. The WE industry has expanded considerably during the last decade. For example, in 2016, USA wind energy increased by ~19% compared to 2015 with an average annual percentage of expansion from 1.1% to 7% within the period between 2006 and 2016 respectively [6]. Figure 1-1(a) shows the considerable growth of the WE compared with the other green energy sources. The UK focused on this energy source and it contributes 14.5 GW of the total WE produced by the top ten countries of ~410.5 GW in 2016, as illustrated in Figure 1-1 (b).

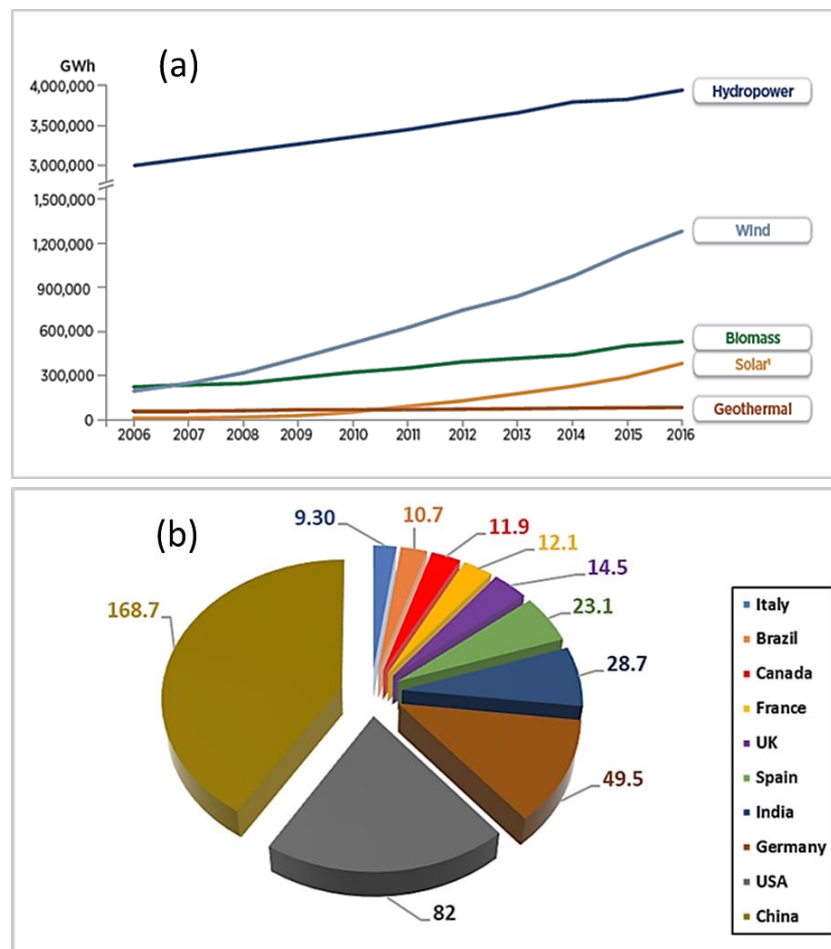


Figure 1-1: (a) Growth of global renewable electricity generation [1]; (b) the top 10 countries and their production of wind energy in GW in 2016 (reproduced from [6]).

The average Wind Turbine (WT) power capacity was 1.6 MW in 2006 and had been increased to 2.15 MW in 2016 [6][7]. This shows a noticeable trend of using high WT power capacities, i.e. multi-megawatt turbines. Increasing the turbine size also increases the complexity of the turbine design requirements, especially the gearbox, by introducing more than one planetary gear stage [8]. The planetary stage in WTGs is used due to a very high torque in the gearbox low-speed stage (at the gearbox input).

The WTGs increase the low speed in the rotor side to high speed on the generator side which should be enough to produce electricity from the turbine generator. Each gearbox consists of four main stages which are; Low-Speed Shaft (LSS), i.e. rotor side, Planetary stage which specified as Planetary Pin (PP) in [Figure 1-2](#), Medium Speed Shaft (MSS) and High-Speed Shaft (HSS). PP is a non-rotating part that carries the planetary gear on two non-rotating inner race roller bearings. The non-rotating inner races of the planetary bearings concentrate the applied load (RF) at a unique location wherever the position of the planet. This considerably increases the probability of damaging this location.

WTs are often suffering from many issues and one of the most important issues is the reliability of the turbine dynamic components, i.e. the failure of the mechanical components in the turbine drivetrain, especially the gearbox [8]. [Figure 1-2](#) also illustrates the main components of a WT and its gearbox. In this figure, the gearbox bearings are specified with crossed squares. The gearbox planetary stage and the forces acting on the planetary components are also presented. The main issue of the WTGs is in their bearings which fail unexpectedly within 5% to 20% of their designed lives [9]. Different damage features were widely reported and sometimes observed to be associated with microstructural alterations beneath the inner race contact region [9]–[11]. This type of fatigue damage is thought to be initiated in the subsurface regions [9]–[14], i.e. beneath the rolling contact surfaces, and the microstructural alterations are the cause of this premature failure, however, other research thought the alterations as a consequence of this bearing failure [15]. The premature failure of gearbox bearings has a significant impact on increasing the Operating and Maintenance (O&M) cost due to unplanned maintenance and early replacement, which influences the wind energy cost. The O&M cost is a considerable fraction of the wind energy cost and it increases with increasing the turbine size [1], [2],[16]–[18]. The gearbox maintenance also results in relatively high downtimes due to the special equipment required for the maintenance [19].

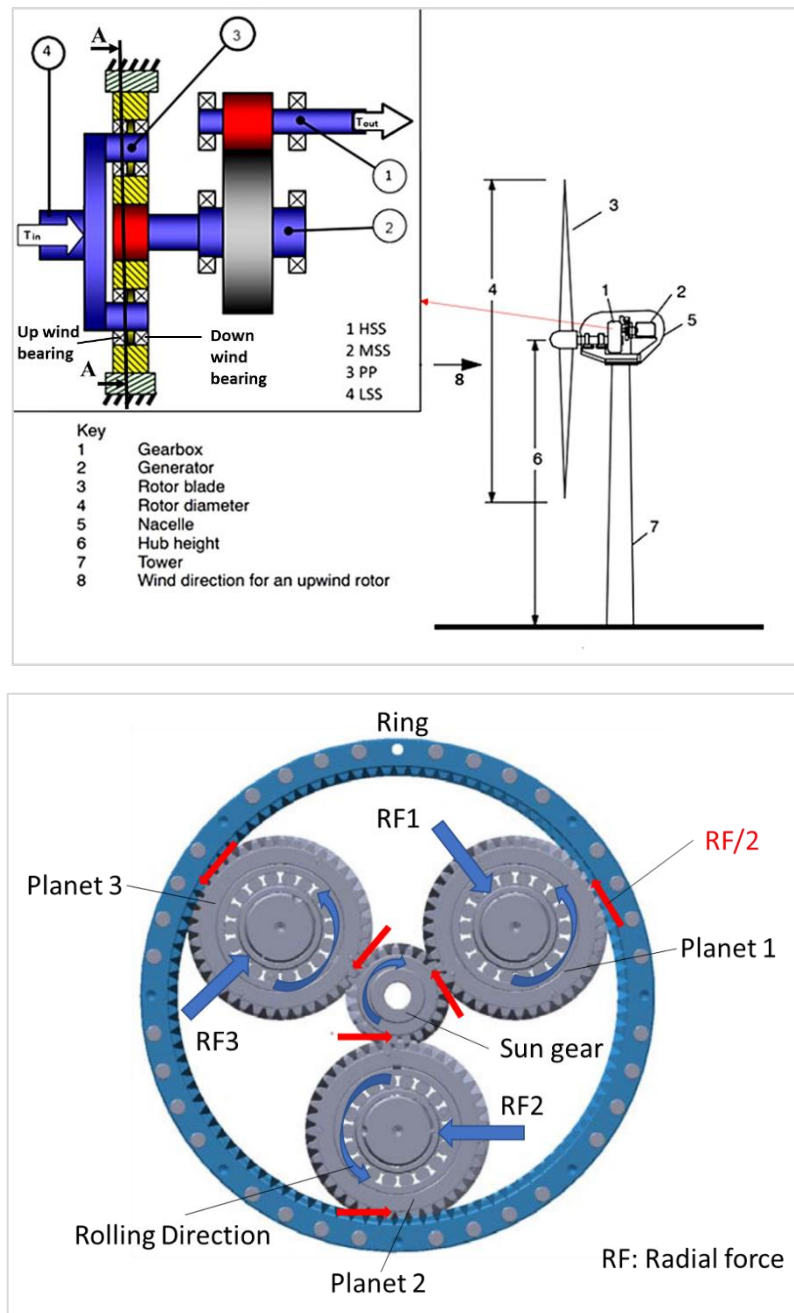


Figure 1-2: Wind turbine components showing the details of the gearbox (top) [20]; planetary stage components and their rotations and forces (down) [21].

WTGs are designed to have an anticipated lifespan of 20 to 25 years [22]–[24], however, their bearings often prematurely fail in different gearbox stages. This may cause catastrophic damage to the other gearbox components. In WTGs, three planets are normally used in the planetary stage, however, two planetary stages are sometimes used in large WT capacities (>3 MW) [8]. In the planetary stage, the high input torque from the rotor is divided into three loads (RF1, RF2 and RF3), then the

torque accumulates on the sun gear after increasing the rotational speed. Each planet gear is usually supported by two planetary bearings, one is called the UpWind (UW) bearing located in the turbine hub side and the other is called the Down Wind (DW) bearing located beside the UW one away from the turbine hub side [23]. Roller bearings have larger loading capacity than the ball bearings thus, the former type is always used in the WTGs. One of the most important issues in roller bearings is the stress concentration which is often introduced in the contact surfaces of the inner race due to misalignment, debris, roller profile, bending of the shafts carrying by the bearings and skewing of the rollers (misalignment of the roller rotating axis from the bearing rotation axis) [3]. Depending on the loading direction, two regions were identified on the bearing inner race which are: no loading and loading regions [25]. Skewing always take place at the beginning of entering the roller element to the bearing loading region and causes a transient loading, however, in the subsurface of the contact region, inclusions (impurities in the bearing material), voids and defects (casting disadvantages), also cause a subsurface stress concentration [1].

Both the UW and DW planetary bearings often experience a premature failure in their inner races by flaking. If the flaking failure is associated with microstructural alterations within the race material, it named White Structure Flaking (WSF). Different forms of microstructural alterations were observed throughout the Wind Turbine Gearbox Bearings (WTGBs) investigations, however, the most apparent features of these alterations are: Dark Etching Areas (DEAs) [26], White Etching Areas (WEAs) (sometimes called White Etching Bands (WEBs)) [27][28], White Etching Cracks (WECs) [24][29], and butterfly wings [22][25][26]. The term “white” comes from the appearance of these features under optical microscopes after etching the examined surface by nital (1% to 2 % nitric acid in ethanol). Despite the discovery of these alteration features in the 1940s [24][32], the main cause and mechanism of their initiation and propagation have not been completely understood even though there have been extensive studies about this alterations phenomenon [27][33]. The role of these alterations is also a debatable subject; some studies considered them as a cause of failure while others considered them as a damage consequence [9][15][2]. Bearings are the most susceptible components due to various loading levels produced from the stochastic wind speed and various operating events such as start-up, speed-up, generator connection/disconnection, normal and emergency stops, and grid loss [34]–[36]. Wind gust and the operating events always cause transient and severe loading levels (impact loading), that may push the bearings beyond their design limits and probably cause their premature failure [37]–[40]. Premature failure and microstructural changes were also observed in different applications subjected to a wide variety of operating

conditions such as marine propulsion systems, lifting gear drive, paper mills, crusher mill gearboxes in addition to WTGs. The unstable loading (transient) in these applications causes high impact loading on their gearbox' bearings [41].

Figure 1-3 shows the variations of the WTG torque (green lines) and speed (purple lines) in a 750 kW turbine rotor during three operating events including start-up, speed up and normal shutdown. Moments on the rotor in two perpendicular axes M_{yy} and M_{zz} that cause rotor bending are also presented. Torque reversal (changing the torque from a positive to negative value), can be observed in speed up and shutdown events. This fluctuation of loading transfers to the planetary stage and cause transient loading on its bearings [42]. These transient loading and speed variations also cause a variation in the Slipping Ratio (SR) which represents the percentage of the relative velocity between the bearing contact surfaces and their average velocity [43][44].

To study the effects of this loading variation on the bearing life, testing of real WTGBs in actual size platforms was used, however, this testing procedure is an uneconomic process due to the high cost of the bearings, the time needed for the tests and the high cost of the test platforms. Therefore, RCF tests of two contact discs are usually used to study the effect of different factors. Contact pressure throughout the RCF testing is often applied using hydraulic cylinders. However, the transient loadings would produce damage in the pressure washers of the cylinders. Furthermore, the complexity of the impact loading subject and the unknown impact levels on the WTGBs. Therefore, there are very few studies on the effect of the impact loading. Assessment of the factors affecting RCF was performed by Oila and Bull [45], they found compressive load as the most significant factor in fatigue life followed by Slipping Ratio (SR). The effect of impact due to transient loading was suggested as one of the effective factors on bearing premature failure in several studies [42][46][5]. Therefore, the effect of these parameters on fatigue life and how the variation of their levels affects the distribution of induced subsurface damage features will be investigated.

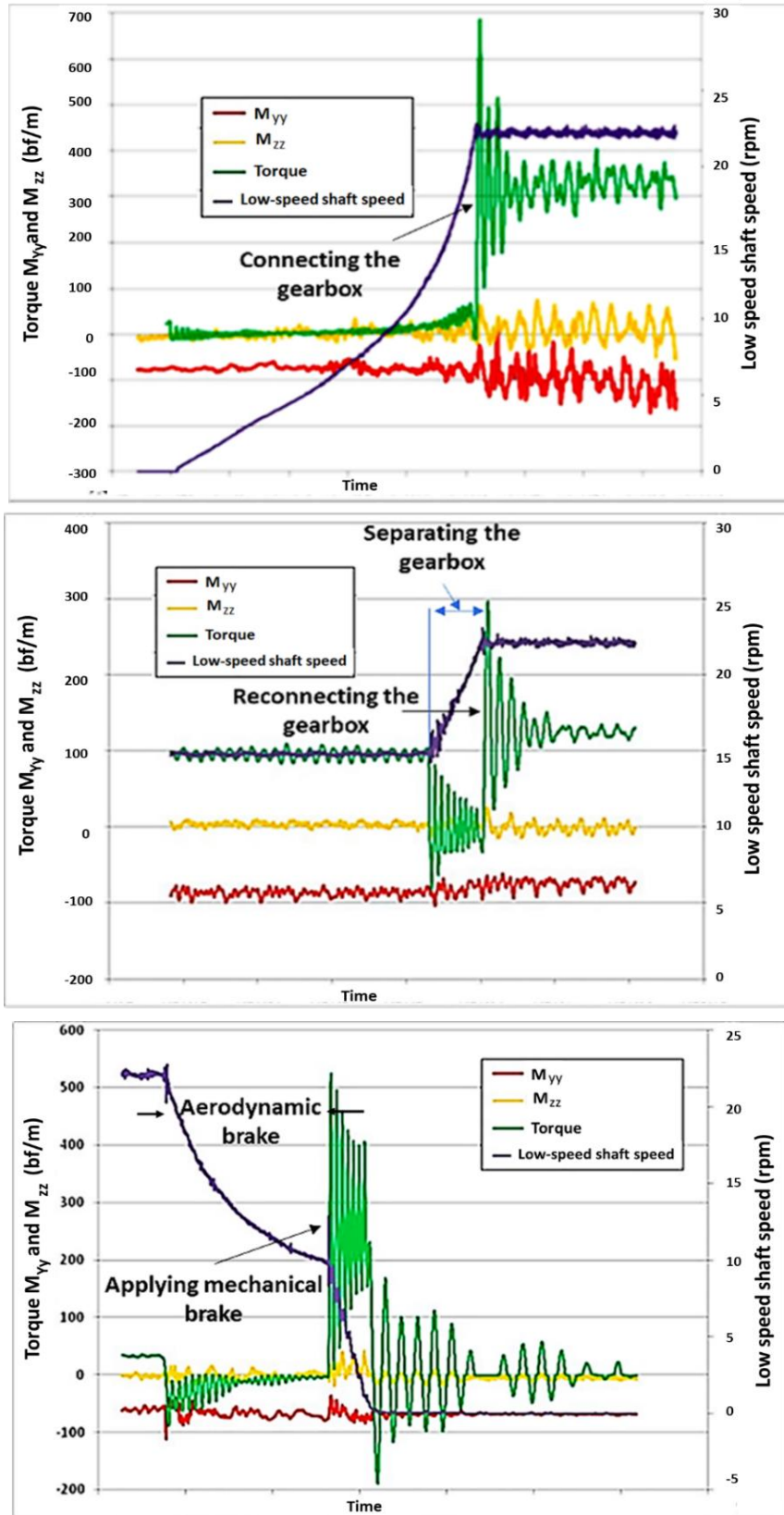


Figure 1-3: Rotor torque and speed variations with time during three operating events, start-up (upper), speed up (middle) and normal shutdown [36].

When a test factor level varies, the effect of the other factors which continuously affect the damage initiation and propagation will also vary. This effect is known as an interactive effect that may have a considerable effect on fatigue life [47]. The individual and interactive effects of three parameters impact loading, Slipping Ratio (SR), and compression loading will be investigated in this study by analyzing the variation of test disc lives with the variation of the study parameter levels. Stress concentration can be introduced to the bearing contact surfaces especially the inner race due to misalignment, the debris of the gearbox components, roller profile, bending of the shaft carried by the bearings and skewing the rollers at the beginning of transient loading. Therefore, the investigation was with and without stress concentration. Despite stress concentration due to using a flat profile of the test discs that can produce early damage, it can be used to accelerate the tests due to time facilities and to apply loading levels quite higher than the rig capacity. Four tests without stress concentration also conducted to perform a qualitative analysis for the effect of increasing the study parameter levels on the test disc life and the surface and subsurface damage features.

No test rig was found with the ability to apply impact loading in combination with the other Rolling/Sliding (R/S) test parameters. For this, a new test rig was designed to apply impact, compression and slipping in combination like the bearing operation case and under complete control levels. Despite using advanced technologies and standards in designing the WTGs and selecting their bearings, premature failure is not avoided. This is because the life prediction and damage estimation theories give unprecise results. All the damage features and S-N curves present the fatigue life in terms of contact loading level and the number of cycles under that level are unable to predict the WTGBs lives. Therefore, suggesting and testing a new life prediction methodology for WTGBs depending on both the contact stress and its number of cycles will help to manage the maintenance of WTGs.

1.2 Research aims and objectives

The aims of this study is to investigate how the three study parameters (impact loading, SR and compressive stress), affect individually and interactively the RCF life in terms of test disc number of cycles to failure and how the variation of testing parameter levels affect the subsurface damage feature distributions by designing a new test rig and conducting a systematic RCF tests with and without stress concentration. Furthermore, deriving and testing a new damage estimation and life prediction methodology and test its results using experimental and real wind

turbine operating data. The progressive steps of this study are illustrated in Figure 1-4.

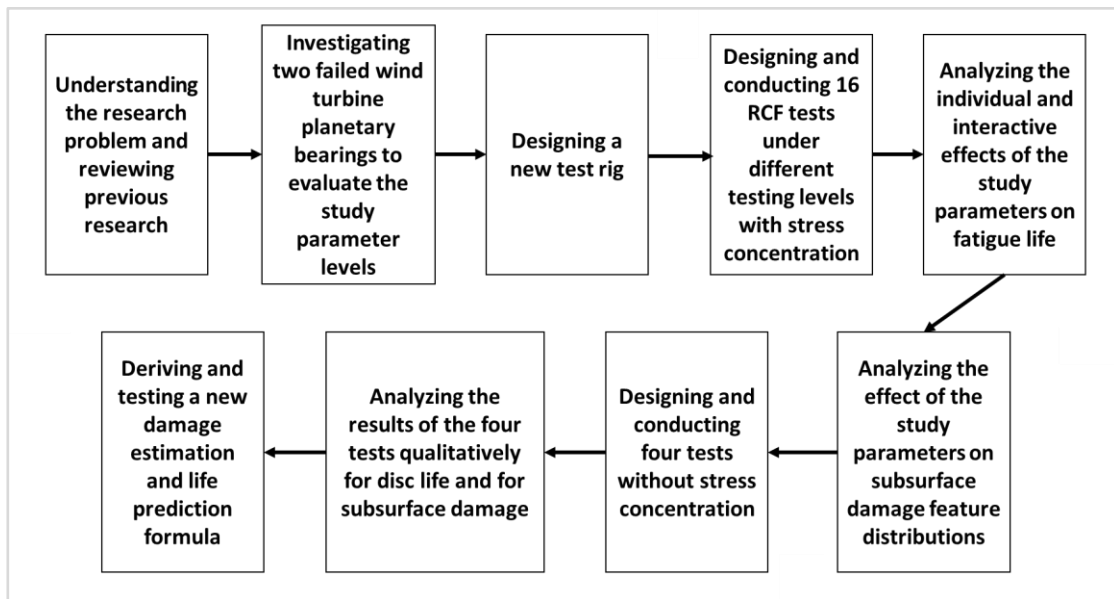


Figure 1-4: Flowchart of the study progress.

The main objectives of this study can be summaries as:

- To review and understand the previous studies in the WTGB premature failure field and the main causes and theories of justifying this phenomenon and the proposed failure initiation and propagation mechanisms that have not been completely understood.
- To investigate and analyze two multimegawatt WTG planetary bearings that failed in the service by flaking. This includes the bearing surface properties' variation of roughness and hardness and characterise the observed subsurface damages with depth to estimate the study parameter levels.
- To design a new test rig for investigating the individual and interactive effects of the study parameters (contact pressure, slipping and impact loading), on two discs in contact and count their number of cycles to failure.
- To study the individual and interactive effect of the three parameters with and without stress concentration on the test disc life and investigate the damage types which induced, especially due the impact loading.

- To compare the damage characteristics of the failed planetary bearings with those of the test discs to evaluate the capability of using the test discs and the new test rig in reproducing damage features like what observed in the WTGBs.
- To evaluate the effect of slipping and impact under different testing levels.
- To conduct additional tests to investigate the effect of stress concentration on RCF life by applying percentages of impact cycles under two levels of each parameter.
- To derive and test a new life prediction method to estimate the damage in RCF of the WTGBs and predicting their life depending on real recorded operating data.

1.3 Thesis layout

The chapters in this thesis are arranged as follows: [Chapter 2](#) presents the literature review of the premature failure of WTGBs, the postulated causes of this failure and its different associated microstructural alterations observed in the previous studies. The suggested mechanisms and theories to explain the microstructural alteration and their initiation and propagation are illustrated. The main factors affecting the RCF and the associated phenomena observed during the investigation of WTGBs are also presented. This chapter also has an overview of the previous test rigs used in investigating the RCF phenomenon.

[Chapter 3](#) describes the surface and subsurface investigations of two failed planetary bearings taken from a multimegawatt WTG. The surface investigation includes inner race surface roughness and hardness that are related to overloading, traction and slipping. This chapter also presents the results of characterizing the bearing subsurface damage features with the depth beneath the contact surface.

[Chapter 4](#) presents the development of a new test rig. Test rig details, mechanisms and components are explained. [Chapter 5](#) presents the outcome of the test runs for flat disc and fully crowned contact profiles. Qualitative and quantitative analyses are performed to specify the individual and interactive effects of the study parameters.

[Chapter 6](#) consists of details of a new damage estimation and life prediction methodology. This suggested method was tested using the test results, real operating data from SCADA for two years and by using annual average wind speed distributions. The effect of operating events on bearing life is also discussed. [Chapter 7](#) consists of the surface and subsurface damage investigations of the test

discs by following the same procedures of the cutting and sample preparation explained in [Chapter 3](#) then, correlating the results with the subsurface stress distribution to predict the main cause of each observed damage features.

[Chapter 8](#) presents the conclusions and highlights the conclusions, recommendations for future works and suggestions to improve WTGBs life.

Seven appendices are presented at the end of this thesis, to show some useful information related to this study.

1.4 Main novelty key contributions

This is the first study to investigate the combined effect of impact loading with other rolling contact parameters of compression and slipping on RCF life. Despite applying impact loading as compression, its individual effects were found to be different than Hertzian contact loading. Two main effects were observed for impact, the first in shallow regions (close to the contact surface) by introducing internally cracked non-metallic inclusions while the second is the introducing of damage in a deeper region which is similar to the effect of increasing the Hertzian contact pressure. The interactive effects of impact with slipping and compression were also found to differ from that of contact pressure. It is expected that there is a considerable role of impact on producing butterfly wings because all the observed wings throughout the investigation of the planetary bearings have internally cracked inclusions.

Development of a new test rig to investigate the individual and interactive effects of different factors on RCF life and subsurface damage features. This novel design can apply the study parameters in a combination similar to the actual case in bearings. Only three parameters have been investigated in this study (compression, slipping and impact), however, test disc material cleanliness, material mechanical properties, and microstructure should be taken on considerations in future tests to reflect the results on WTGBs.

The slipping ratio was found to have more effect on reducing fatigue life under low compressive contact loading levels and this effect is reduced with increasing the contact loading, however, impact loading effect on damage seems unaffected by the contact stress level.

Butterfly wings observed in this study have no connection with the crack networks. This may refer to a marginal role of this damage feature on the bearing flaking. This

damage feature may be produced in a late stage of damage due to severe loading conditions produced by the introduction of debris between the contact surfaces. However, subsurface microcracks, not initiated from non-metallic inclusions, but from the defects and voids associated with carbides were frequently observed and thought to have a significant role in the damage initiation and propagation.

The statistical analyses confirmed the role of Von-Mises and to a lower extent the maximum shear stress on subsurface damage initiation and propagation, however, more investigations are still required.

Deriving and testing a new life prediction formula for WTGBs using SCADA data. The percentage of error in this methodology is quite less than the method presented in the standards; however, more tests are required to show the reliability of this method.

Despite postulating over-rolling and subsurface plastic deformation in previous literature, this study provides evidence that the contact pressure in the investigated planetary WTGBs during the turbine operating not only exceeded the design stress limit but also the compression elastic limit of the bearing material. Furthermore, despite using advanced techniques to design the WTGs, bearing contact stress in the WT design standards [20][23], may require a re-evaluation (reduced). Modifying the design of the planetary stage is also very important by making the planetary pin and its bearing inner races as rotating components to reduce the probability of applying the load at the same location of the bearing inner races or improving the bearing design.

2

LITERATURE REVIEW

This chapter presents a literature review of the premature failure of Wind Turbine Gearbox Bearings (WTGBs) and the Rolling Contact Fatigue (RCF) phenomena. The postulated causes of this failure and their different damage features are presented and discussed. The suggested mechanisms and theories to explain the initiation and propagation of bearing flaking damage are illustrated with some details. This chapter also consists of an overview of some test rigs previously used in investigating the RCF failure and the associated phenomena such as hydrogen emission, carbon immigration, lubricant dissolving and microstructural alterations. None of the test rigs used before can apply impact loading in combination with the other RCF parameters. Furthermore, some life prediction and damage estimation theories are illustrated and discussed. The effect of loading levels and severe operating conditions of WTGBs can be observed as surface and subsurface damage features. The methodologies for investigating the variation of the subsurface damage features can be used to study the role of the effective factors on RCF failures are also illustrated and discussed. Finally, the research gaps are identified.

2.1 Introduction

The most common occurrences of RCF can be seen in bearings, gears and train tracks. Bearing fatigue and reliability in different applications, especially in Wind Turbines (WTs), is one of the most important engineering issues which has brought attention in recent years [41][48]. The premature failure of WTGBs is often quite below their design life of 20 to 25 years [9][24]. The WTs as a green future energy

source has undergone a considerable expansion compared with other renewable energy sources such as solar, geothermal, hydropower and biomass. However, the bearing premature failure of the turbine gearboxes is considerably increasing the cost of Wind Energy (WE), due to unplanned maintenance by using special equipment, early replacement and downtime. The increase in WE costs restricts the investment and the expansion in this field [37].

RCF is studied in terms of loading (contact stress), damage features (Microcracks, damaged nonmetallic inclusions and microstructural alterations), lubrication, surface and subsurface properties variation and fatigue life. Investigating the failed WTGBs by flaking (removal of material from the contact surfaces) showed different damage distributions on the inner race contact surfaces as can be seen in [Figure 2-1](#). In the subsurface of the flaking, different microstructural damage features were observed including damaged nonmetallic inclusions, cracks and microstructural alterations.



Figure 2-1: Examples of failed inner races of wind turbine gearbox bearings by flaking.

The alterations appear as white bands or dark regions under Light Reflection Microscopes (LRMs) when the samples are etched with nital (1-2 % of nitric acid in ethanol). Microstructural alterations such as White Etching Bands (WEBs) were firstly observed by Jones [32] in the 1940s, however, until now the main causes and mechanisms of their initiation and propagation are not fully understood despite the extensive research in this field [24]. [Figure 2-2](#) shows common types of microstructural alterations and their orientations and locations beneath the contact surface. This figure also shows the Over-rolling Direction (OD) which is thought to control the inclination angles of WEBs and the butterfly wings which is one of the alteration features [38]. These microstructural alterations are thought to have a considerable role in the bearing premature failure, however, some studies postulated these alterations are a consequence of bearing damage not a cause of

it [15]. The scientific and economic impacts of studying the premature failure phenomenon provide the study of this subject with increasing importance nowadays.

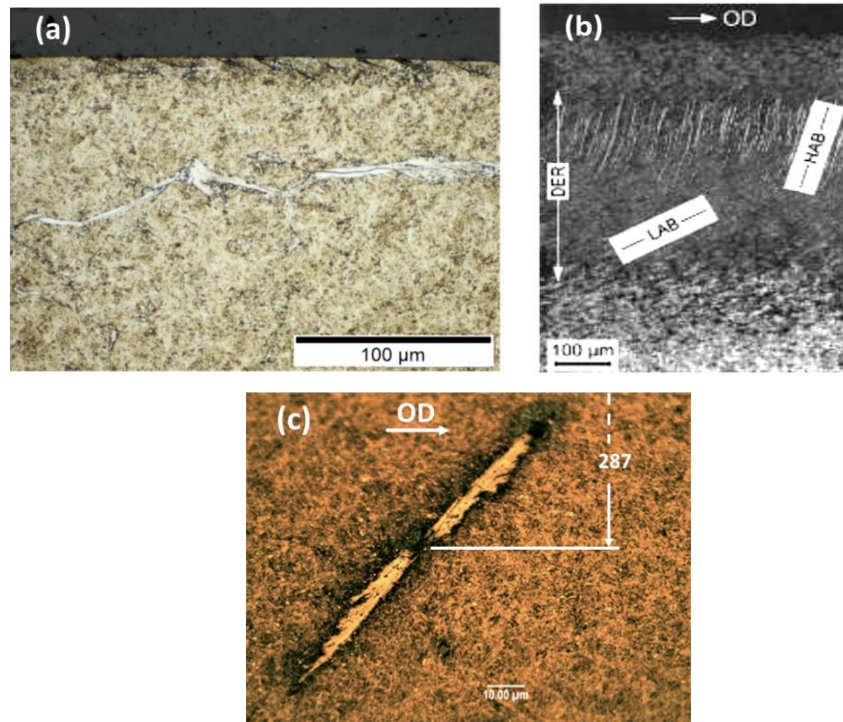


Figure 2-2: Microstructural alterations with their depth and orientations (a) WEC [49]; (b) Dark Etching Region (DER), High Angle Band (HAB) and Low Angle Band (LAB) [38]; (c) butterfly wings.

Investigating the bearing contact surfaces and subsurface regions provides significant information about the overloading and the required testing levels and may lead to a better understanding of the bearing premature failure phenomenon. The subsurface investigations had the biggest focus in the previous studies; however, the surface investigation may provide additional useful information. Different hypotheses were postulated to explain the initiation and propagation of the bearing damage and the subsurface microstructural changes. However, each one has debatable weak points and there is no agreement amongst the researchers [39]. Premature bearing failure and microstructural alterations are a very complex phenomenon due to the failure being related to different aspects such as mechanical, tribological, chemical, electrical and metallurgical aspects in addition to the environmental effects [24] as illustrated in Figure 2-3. The mechanical aspect of bearing failure deals with geometry, stresses, load variation, manufacturing accuracy and surface finishing of the bearing components, while the tribological issues deal with lubricant film thickness, surface finishing, contamination and

temperature. Chemical aspect consists of the decomposition of lubricant, hydrogen emission inside the bearing material throughout the service, carbon and chromium immigration under specific loading conditions and temperature, while the electrical aspect deals with the possible currents inducted during the WTG operation. Finally, the metallurgical aspects take the grain size, grain boundaries, material cleanliness, heat treatment and the effect of casting defects, into consideration. The wide variation of environmental conditions such as the temperature variation in the different seasons and the harmful conditions of a salty and humid environment were also reported to have a considerable effect on different components of the WTs [23]. The highlighted parameters in Figure 2-3 have been frequently reported as the main contributors of premature bearing failures. Thus, this study will investigate the effect of these factors on RCF life and different surface and subsurface damage features.

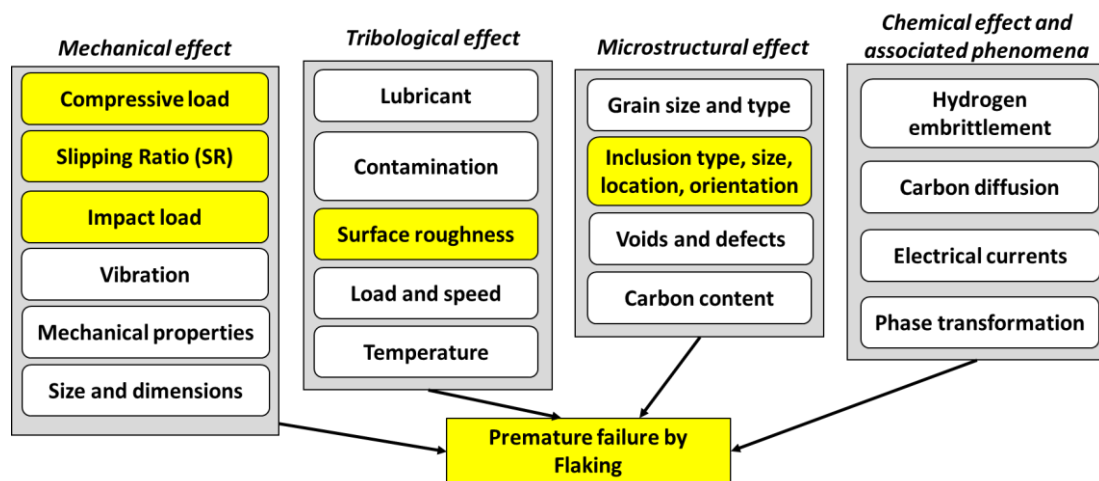


Figure 2-3: Factors affecting wind turbine premature failure.

Testing of real WTGBs is an uneconomical way to study their damage. For that reason, studying the Rolling and Sliding (R/S) damage is achieved using small scale test rigs. Different test rigs were used to reproduce the surface and subsurface damage features and to investigate the effect of the testing parameters on the damage initiation and propagation. The effect of impact loading has had insufficient investigation due to the subject complexity and the high possibility of damaging the hydraulic cylinders normally used to apply the testing contact pressure due to the transient loading. Thus, studying the effect of impact required designing a new test rig to apply all the study parameters in combination likes the real WTG operation in the field.

This review shows the importance of the study parameters (compressive loading, slipping and impact) on RCF life and the subsurface damage initiation and propagation. The aims of this literature were as follows:

- To understand how the investigated and the other bearings failed.
- Finding information to understand RCF incidence.
- To have an idea about the common rigs used to investigate and reproduce damage features.
- Identifying the weak of RCF life prediction theories.
- To identify the scientific gaps of the study and translate this into aims and objectives.

2.2 Wind turbine gearbox design and Bearings loading

Wind Turbine Gearbox (WTG) is one of the most important and costlier components of the turbine drivetrain; it costs ~13% of the total turbine cost [50]. The aim of the gearbox is increasing the low rotational speed in the input shaft (rotor-side) to a high speed which should be suitable to generate electricity on the generator side. The dynamic components in the WT drivetrain, especially the gearbox experience variable cyclical loadings due to a wide variation range of operating conditions throughout the year [24]. This probably leads to WTGB premature failure. A schematic of a typical WTG to show its stages and bearing locations can be seen in [Figure 2-4\(a\)](#). The WTG is usually subjected to various loading conditions during the turbine operating due to wind gust and operating events such as start-up, shutdown, generator engagement/disengagement, grid loss and braking. These events cause load fluctuations in the torque of the gearbox shafts in addition to the torque fluctuations during the normal operational conditions. [Figure 2-4\(b\)](#) shows an example of the torque variations on the High-Speed Shaft (HSS) of a 750 kW WTG [21]. This torque variation was recorded during two events including grid loss and braking. The torque variation during WT normal operation also can be observed which may lead to the bearing premature failure [40]. It can also be observed that there are torque fluctuations, torque reversal (changing the torque from positive to negative values) and vibrations following the occurrence of braking events for several cycles. The induced transient loadings cause impact loadings on the gearbox shafts and this transmits to the gearbox bearings [5].

According to the statistics of turbine monitoring, WTs are annually subjected to ~15000 overloading cycles throughout ~3000 operating events [51], with approximately five effective loading cycles followed each event [36]. During the

over-loading cycle, the bearing loading zone is relocated due to torque variations and reversals that changes the rotating speed and causes an additional sliding [33]. Furthermore, misalignment and impact loading occurs during sliding and can produce high stresses in the gear and bearing contact regions [40]. The transient operating conditions in WTGBs and their loading levels are random and unknown because these loading levels depend on the wind speed at which the event is taking place. Therefore, in the stage of bearing design and selection, the designers do not take these loadings into consideration [40][41].

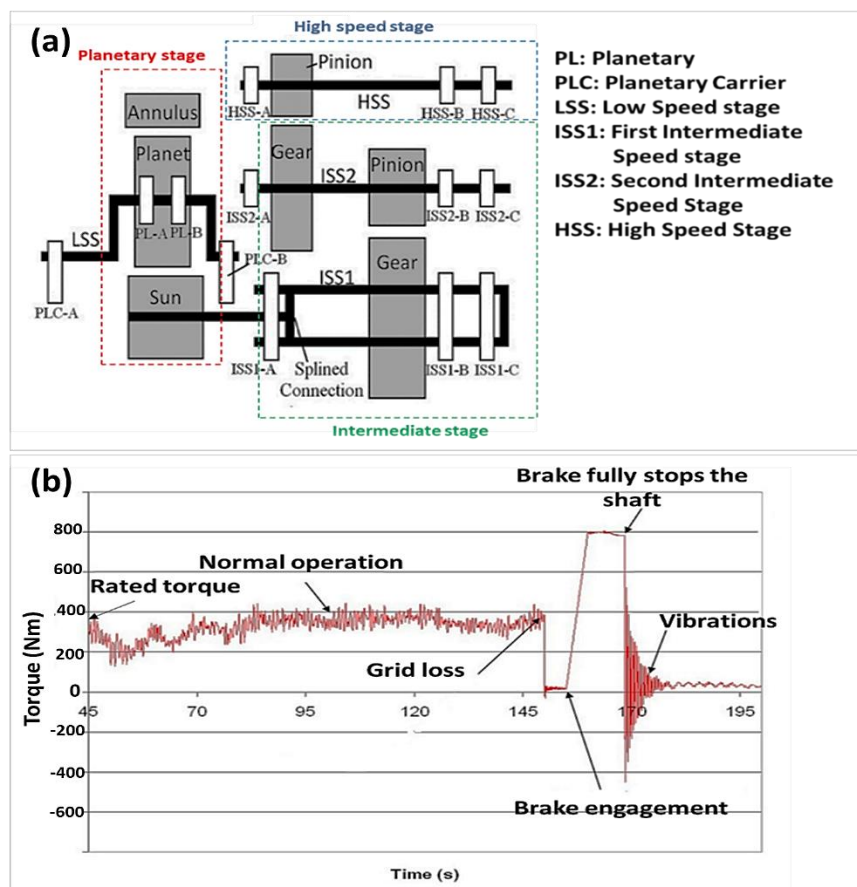


Figure 2-4: (a) Typical gearbox consists of one planetary stage showing the bearings locations (b) torque variation during grid loss and braking events [21].

AL-Hamadani et al. [52] compared the behaviour of three types of WTGs during normal operation and a shutdown event. Their findings showed that, during the shutdown event, the maximum torque was higher than the recommended level specified in the standards, while in normal operation the torque is within the acceptable range. Keller et al. [53] also studied the difference between normal stop (applying aerodynamic brake followed by mechanical brake) and emergency stop (applying the mechanical brake without aerodynamic brake), in a 2.0 MW WTG.

Their results showed extreme torque variation levels during the emergency stop compared with that in the normal stop.

Torque and load during the steady-state on WTG components depends on the turbine size, gearbox design (number of stages and their rotational speed), annual wind gusts, method of fixing the gearbox (2, 3 and 4-point fixing system) [36][54], load share factor in the epicyclic stage [55] and UW and DW load differences [42], [55]. The number of rollers and the bearing type (taper or cylindrical), number of rows and the bearing tolerances also affect the bearing loading zone and the bearing life [37]. Despite using modern techniques in designing and analyzing the WTGs, the load of the bearing in service is higher than the design load, especially during the operating events [56].

2.3 Wind turbine gearbox operating and monitoring

The wind turbine drivetrain represents the dynamic components which mainly experience fatigue failure. The drivetrain consists of the turbine hub, rotor, gearbox and generator as presented in [Figure 1-2](#). Premature failure of WTGBs occurs in the majority of WTGs [9]. According to data from the National Renewable Energy Laboratory (NREL) in 2016, WTGB faults represent ~76% of the total WTG faults [57][58].

When a WT starts rotating, the turbine generator is unconnected until the turbine reaches its steady-state speed. This case is called “no-loading” operation which was studied by Jauregui et al. [59]. They found the gravity of the drivetrain components in addition to the rotational speed at start-up and the supporting structure of the gearboxes have a considerable effect on the wind turbine dynamic loadings [54]. When the turbine generator connects with the electricity grid, a sudden loading takes place. This produces a severe loading state for several transient loading cycles (impact) [44]. After that, the turbine returns to its steady-state again. The sudden change in the drivetrain loading level is unknown because it depends on the turbine rotation and the wind speed at that time.

To prevent any catastrophic damage in the WT drivetrain components due to faults in the gearbox components, a condition monitoring methodology was used to evaluate the health of the drivetrain components and to investigating the load variation throughout the normal and transient operating [60][61]. Monitoring of WT is a high-cost process due to instrumentation costs and the huge amount of data that were recorded and have to be analyzed.

Supervisory Control And Data Acquisition (SCADA) is a traditional condition monitoring system used in some WTs [62]. The recorded data in this system calculates the averages of wind speed, rotor and generator speeds and the generator output power every ten minutes [63][64]. These data are used to predict the time of the bearing failure to arrange for the gearbox maintenance. The average time of SCADA (10 minutes), is longer than most of the operating events. Thus, the effect of these events has no effect on SCADA data. Furthermore, during most of these operating events, the generator is unconnected, i.e. the generator output power is unaffected by these events. Despite of these drawbacks, the SCADA system provides a useful source of information about the drivetrain operating and loading conditions [65]. The instrumentation of gearbox components, i.e. fixing of measuring sensors, is an alternative procedure to investigate the stress levels induced throughout these operating events [40] for a few seconds. This procedure is currently used to investigate the loading level throughout different operating events [35]. WTGBs experience several severe transient loading cycles during each of the operating events (as will be discussed in [Section 2.4](#)). The number of these cycles depends on the turbine size and the drivetrain design [42]. Furthermore, the load on the turbine drivetrain components is unsteady even during the normal operation due to wind gusts, i.e. instantaneous wind speed variations [36]. The other operating conditions such as environment, humidity, and temperature variation throughout the year, also have a significant impact on the life of the WTGBs and currently have more attention. The factors affect the operating conditions and the load of WTGBs will be discussed in more detail in the following section.

2.4 Factors affecting the premature failure of WTG bearings

Different factors were reported to have a considerable effect on WTGB premature failure that work as drivers for the final flaking such as compressive loading [32][51], slipping and traction forces [66], impact loading and operating events [47][63], induced stresses due to vibration [67], material microstructure [68], lubricant [69], lubricant contamination [70], hydrogen generated from the lubricant or water [69][71] and corrosion [72].

Oila and Bull [45] assessed the effect of seven parameters which are: load, lubricant, temperature, surface roughness, material, slipping ratio and speed. They found the load and slipping have a more significant role than the other factors. Therefore, severe compression loading and plastic deformation were postulated as important factors that affect the bearing fatigue damage. The affected region by contact is rapidly increased with increasing contact load thus, only surface and close to surface

stress distribution should be considered [25]. The second parameter (slipping) in roller bearings increases with torque reversal and transient loading due to accelerating/decelerating of the rolling elements and excessive slip is a possible trigger of bearing failure [44].

The effect of material defects and inclusions on fatigue life and damage were studied by Murakami and coworkers [73]–[75]. The frequency and size of the material inclusions can be expressed in terms of material cleanliness which can be evaluated by classifying the inclusions into groups according to their chemical compositions then evaluating the cleanliness index depending on the inclusion dimensions according to the international standard ISO 4967-2013 [76]. The effect of material cleanliness was also studied by Neishi et al. [77], Makino et al. [78], and Lewis and Tomkins [79]. The RCF life was found to considerably decrease with increasing inclusions and defect density and size. However, orientation (inclination angle of the inclusion major axis relative to the rolling surface) and location (depth beneath the contact surface), were also reported to have a considerable role in fatigue life [80].

Debris produced from bearing flaking may enter the bearing loading zone and cause localized severe loading levels which have an effective role in fatigue life. Debris is not only produced from flaking the bearing contact surfaces during the operation, but also from other sources such as from gears, seals, bearing housings, micro-cutting, and micro-pitting. The debris produced due to bearing flaking is much bigger than that formed from micropitting and micro-cutting [81] thus, they may have a more harmful role in accelerating the reach to a severe damage level. The insertion of large debris between the contact surfaces can produce vibrations and impact loadings that considerably reduce the bearing fatigue life [82]. The effect of debris and dents on the ball and roller bearings was studied by Morales-Espejel and Gabelli [83]. They investigated the bearing flaking failure which was proposed to start across the raceway surface due to these dents and then propagates in the rolling direction.

Misalignment of bearing components can produce severe loading conditions. The effects of misalignment were studied by Ahmadi et al. [84] and, Johns and Gohar [85]. They found the misalignment of a bearing roller by 0.1° leads to double the Hertzian contact stress in normal operation. However, Bruce [3] postulated the bearing contact pressure to be more than 3.1 GPa due to misalignment. The rolling element misalignment may cause a sudden loading in addition to stress concentration. That is also classified as one of the important causes of premature bearing failure [40]. Stress concentration at the roller and the test disc edges can significantly affect the stress distribution beneath the contact region, however, the contact stress level

return to be uniform after a small distance (~ 1 mm) as will be explained in the next chapters. This stress concentration can significantly reduce the bearing fatigue life [25] and considerably changes the subsurface stress distribution which pushes the damage to be initiated from the contact surface (more details can be seen in [Section 4.2.2](#)). To avoid the stress concentration on the bearing roller edges; the designers made the rollers to have curved edges shape (partially crowned edge). The stress raise at the blends of the roller with the crowned edges should be carefully examined to know whether the contact pressure causes high-stress concentration or not. [Figure 2-5](#) shows different roller types and the contact stress distribution under two loading levels and with misalignment. The effect of roller profile on the contact stress distribution is one of the factors studied by Poplawski et al. [86], Ahmadi et al. [87] and Hartnett [88]. After years of investigation; a logarithmic roller profile was designed to have a specific cut at the roller-ends and can completely avoid the stress concentration [25], however, this type of roller edge is not easy to manufacture.

When the contact surfaces are flat, stress concentration cannot be avoided even if the two contact surfaces have the same length. Therefore, fully crowned contact is the easiest way to avoid the stress concentration state [25]. Material type and cleanliness have also a considerable role in the stress concentration in the subsurface regions which may considerably decrease the bearing life [24].

The influence of the microstructural grain size, defects, and notches on fatigue damage was studied by Kerscher [89]. He suggested increasing the static strength and hardness to increase the fatigue limit and correlated this with the microstructure of the bearing steel. This effect was also studied by Yang, Zhou and Ling [90], Chan [68], and Osoviski [91].

Bearing clearance effect on the load distribution in the ball and roller bearings were discussed by Oswald et al. [92]. They observed the gradual fatigue life decrease in bearings with positive clearance, i.e. tolerance, while with negative clearance (interference), bearing-life could be rapidly decreased. Furthermore, Keller and Guo [93] compared two gearboxes planetary stages: the first has a preloaded Taper Roller Bearings (TRBs), while the second has Cylindrical Roller Bearings (CRBs). The former has no clearance and was introduced a reduction in the load share between the UW and DW bearings from $\sim 47\%$ in the latter type to $\sim 14\%$, and this increases the bearing fatigue life to be ~ 3.5 times the CRBs.

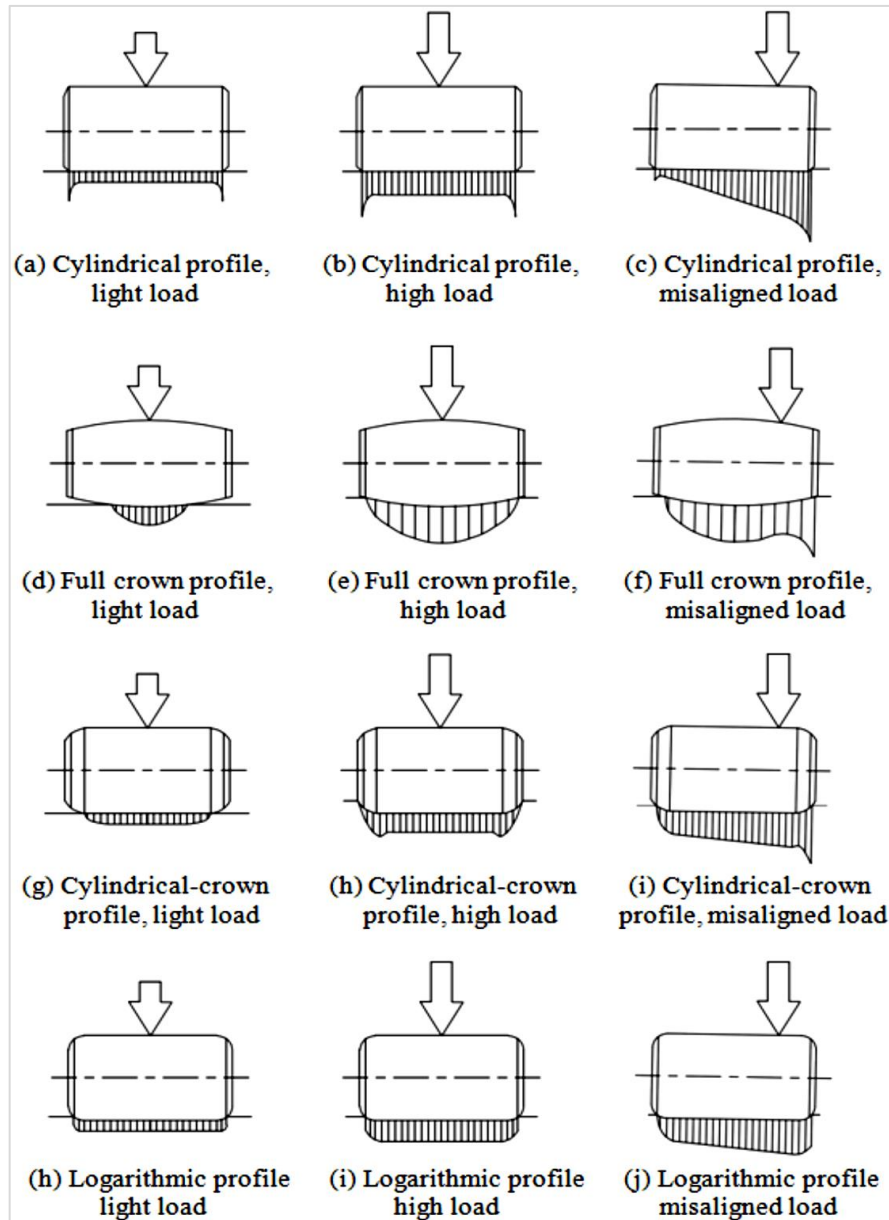


Figure 2-5: Contact stress distribution under different roller types and contact stresses [25].

The bearing damage and fatigue life also depend on the turbine size, gearbox design, bearing design, lubricant type, and the lubrication system and filtration, bearing surface finishing, rotational speed and velocity of the contact surfaces [24][94]. The accuracy of manufacturing the bearing houses and gears (especially planet gears) also affect the load share factor among the planets and cause overloading in one planet more than the others [55], and this reduces the bearing life in the planet which has higher loading level.

Electrical currents inducted throughout the bearing rotation was also cited in previous studies as a cause of the fatigue life deterioration [95][96] and this depends

on the rotational speed. For high-speed bearings, centrifugal forces and the gyroscopic moment have also a significant effect and the friction due to sliding motion tends to increase [25]. This may explain why the bearings of the High-Speed Shaft (HSS) suffer from more severe failure compared with the other WTG locations. Premature failure of WTGBs is a very complicated issue due to its reliance on different subjects such as mechanical, metallurgical, electrical, tribological and chemical issues. Thus, more investigations are still required to have a full understanding of the premature failure phenomenon. The effect of the parameters investigated in this study will be discussed in further detail in the following sections.

2.4.1 Effect of impact and transient loadings

During the turbine operating events, loads on the gearbox bearings are varying. The transient loading causes impacts on the gearbox shafts and their supporting bearings [42][97]. Premature failure of WTGBs probably has a strong relationship with the severe transient loading induced during the operating events [98]. Despite confirming the impact loading during the operating events, there is a lack of information about the impact levels and their role on the RCF life and subsurface microstructural damage features. The microstructural damage feature means any damage feature in the microscale level such as damaged inclusions, microcracks and/or microstructural alterations.

Holweger et al. [99] proposed that plastic deformation followed by impact loading disrupts the material at the microscale in the impact region. Their suggestion depends on postulating a mechanical impact wave transmitted inside the material beneath the impact region. They considered this wave as the main cause of the microstructural change initiation. The experiments of Yang et al. [81] confirmed the effect of impact loading on WEA formation. Two regions were identified during their study of wear and structural change of hard steel under impact loading. These regions were named as the White Layer (WL) and the Deformed Zone (DZ). The former was a highly deformed layer and microcracks could be observed, while the spalling occurs when the microcracks propagate to the DZ. Their findings referred to the possibility of the WL formation after a small number of severe impacts.

The effect of impact on the subsurface crack and microstructural alterations was studied by Bruce et al. [100]. They applied point impact loading (using ball impactor) then separately applied RCF by using a twin-disc machine with flat contact discs. This study confirms the role of impact on subsurface microcrack initiation from the material inclusion and the formation of WEA under contact stress

of 1.79 GPa to 3.03 GPa and 10% SR after 200,000 impact cycles. They also applied an inclined impact in 45° to investigate its effect on the formation of WEA.

Operating events produce different impact loading levels and have different effects on WTGB damage. [Table 2-1](#) illustrates some of the operating events, the procedure of their occurrence and their effects. These events currently have great attention; however, their effect is always investigated under rated torque operation.

Table 2-1: Typical wind turbine operating events and their effects.

Operating event	Procedure	Effect
Start-up	Start gearbox rotation.	Material to material contact that may produce WTGB skidding.
Generator connection	A sudden connection of the generator.	Sudden severe loading during the transient state.
Grid connection	A sudden increase in the torque loading.	Sudden severe loading during the transient state.
Speed up	Increasing the rotation speed due to increasing wind speed.	Severe transient loading due to disconnecting then, connecting the generator.
Normal shut down	Applying aerodynamic brake, disconnect the generator followed by applying the mechanical brake.	Less harm compared with emergency stop.
Emergency stop	Applying the mechanical brake directly after the disconnection of the generator.	Very harmful due to severe loadings induced.
Braking	Applying mechanical brake.	It depends on the load and drivetrain inertia.
Grid loss	Sudden unloading.	This event was found to produce ~2.3 times the normal torque[35].

2.4.2 Compressive contact loading of WTGBs

Different standards are using to specify the design requirements of WTs such as; IEC 61400-1:2005 [23], however, BS EN 61400-2:2014 [101] is for designing small wind turbines. The standard BS EN 61400-3:2009 [102] specifies the offshore turbine design requirements. These three standards indicate the importance of turbine size and location (offshore or onshore) in their design. Design requirements of the turbine gearboxes are specified in BS EN 61400-4:2013 [20] and BS ISO-

81400-4:2005 [103], however, roller bearing dynamic loadings were specified in BS ISO- 281:2007 [104]. The international standards specify the planetary roller bearing contact load to be 1700 MPa with bearing rated life of 20 to 25 years and 90% survival reliability. However, planetary bearings are often prematurely failed by flaking within 5% to 20% of their design life, i.e. within 1 to 5 years [55], [105][106]. White Structure Flaking (WSF) as a subsurface initiated damage type was observed to be produced due to RCF tests when typically investigated under high constant contact pressure in the range of 2.0 to 5.6 GPa [79][107]–[110]. These testing levels are higher than the typical WTG bearing contact load of <2.0 GPa [104]. Evans [1] postulated that the damage initiation mechanism leading to WSF may be different from that of RCF. However, the testing loading conditions and the required number of cycles for WSF initiation had a wide range of variation (2.2 GPa to 5.6 GPa and 10^9 cycles to 10^6 cycles respectively). This supports the dependence of these damage features on a considerable number of factors and this specifies the requirement for further investigation of this unclear phenomenon.

Rolling elements are instantaneously loaded when they enter the bearing loading zone and the misalignment (skewing of the roller rotation axis from the bearing rotation axis) due to this entry can produce high contact stress. For example, in a 1.5 MW gearbox, this misalignment produces contact pressure exceeding 3.1 GPa [85][104]. However, an impact loading duration of ~0.3 seconds was noticed in accelerating-decelerating testing and it was found to reduce the RCF life [111]. Transient compressive contact conditions such as impact loadings probably lead to contact stresses exceeding the yield limit.

Compressive loading and slipping in combination with impact loading increase the stresses beneath the contact region. The individual and interaction effects of these parameters on the fatigue life of test discs and real bearings will have a significant scientific value on understanding the premature failure of the WTGBs. These three parameters affect the stress distribution beneath the roller/inner race contact region, as can be seen in [Figure 2-6](#). However, introducing a traction force in the contact region increases the magnitude of the maximum shear stresses (as a main contributor of damage), and brings them towards the contact surface. This is probably the main cause of fatigue failure [43][71].

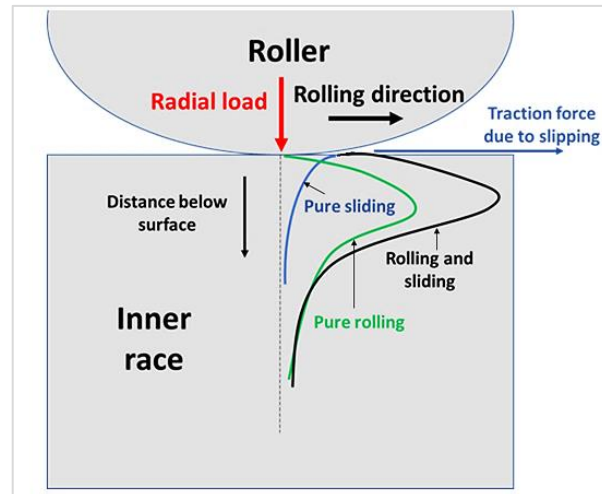


Figure 2-6: Shear stress distribution under rolling-sliding conditions [112].

WTGB loads in different gearbox stages of a 750 kW wind turbine were investigated by Guo et al. [113] using a fully flexible FE model. This investigation included operating events such as normal shut down (grid disconnection followed by aerodynamic brake and finally applying mechanical brake), start-up (connection of the electrical grid loading) and emergency stop (sudden apply of the mechanical brake). They illustrated and compared bearing loadings in rigid and flexible models. Their findings showed that the rigid model had bearing forces 20% higher than the flexible model and they pointed out the high-speed shaft bearings as that experiences the highest damage levels.

Kuhlmann-Wilsdorf [114] modified Taylor's theory of Low Energy Dislocation Structure (LEDS) which states that, in a dislocation structure which experiences plastic deformation, the instantaneous heat generation inside the deformed material is in equilibrium with the applied shear stress and slip band. He explained that the microstructural transformation was due to breaking up the microstructural grains into fine grains to keep the structure stable under very high loading levels.

The introduction of debris between the contact surfaces due to lubricant contamination with hard particles causes severe contact loading and dents. Sayles and Ioannides [82], reported a hardness change away from the dents by three times the dent size. Therefore, indentation regions on the contact surfaces must be avoided in measuring the surface hardness.

2.4.3 Slipping of contact surfaces

When there is a relative velocity between two bodies under rolling contact, this means there is a slipping. Slipping is always expressed as a Slipping Ratio (SR) or sometimes called Slip to Roll Ratio (SRR), which can be defined as the ratio of the difference between the velocities of the contact surfaces to their average velocity. This can be expressed as a percentage according to [Eqn. 2.1](#).

$$SR\% = \frac{\text{Linear velocity difference between the two bodies}}{\text{average velocity of them}} \quad 2.1$$

Slipping causes friction and increases torque loss (see Chapter 10 in Ref.- [25]). The torque loss depends on the friction due to loading and that due to lubricant viscosity. This torque loss estimation depends on an empirical formula of Palmgren who investigated the frictional torque by testing different bearing types and sizes under different shaft speeds and loading levels ranging from light to heavy loading by using different types of lubricants [25]. Slipping due to acceleration/deceleration of bearing rolling elements was proven in WTG bearings [44]. The planetary bearing inner race in WTGs is a stationary component (non-rotating) and the velocity variation of the bearing rollers throughout the turbine operating is due to wind gust and operating events in addition to load variation during torque reversal. Two types of SR have been identified [49]: a negative SR is when the traction force is in the opposite of rolling direction, while a positive SR is when both the rolling and traction have the same direction [66] as illustrated in [Figure 2-7](#). SR in bearings is affected by many factors such as contact loading, surface roughness, lubricant properties, rotational speed and direction, and contact surface velocities [3].

Vaes et al. [105] investigated the roller slide of high-speed shaft bearings in a 1.66 MW wind turbine gearbox. The speeds of the bearing cage and one of its rollers were measured during the rated operation at a rotation speed of 1440 rpm. They found the roller speed inside the bearing loading region reduced by approximately 60% than the pure rolling speed after traversing the unloaded region. They also observed that the roller speed in the entrance of the bearing loading region and that when the roller leaves the loading region has a considerable difference, this is due to a high effect of lubricant on the rollers outside the loading region and this shows a considerable effect of the loading on the rolling element slipping. They also found the roller inertia has more importance than its load.

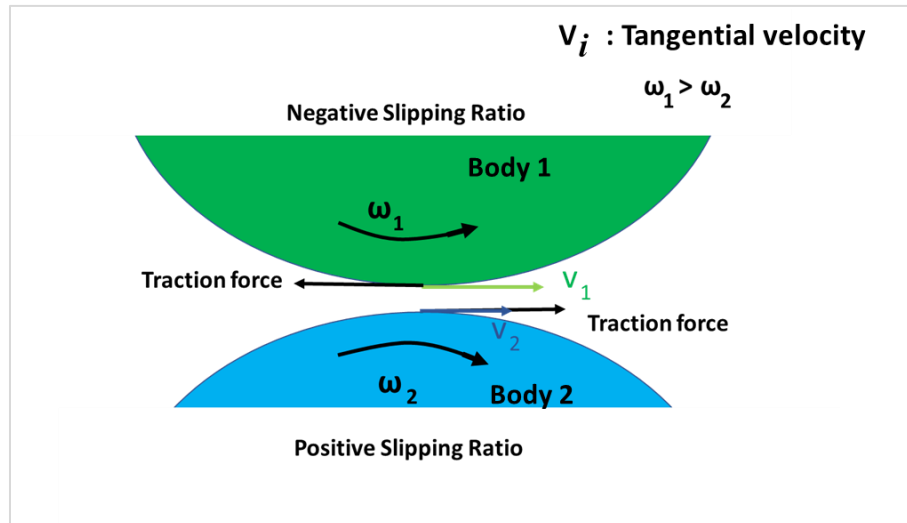


Figure 2-7: Positive and negative slipping ratio.

Danielsen et al. [115] reproduced microstructural alteration damage in the form of WECs under a constant compressive loading of ~ 2.3 GPa and negative SR of -30% after 3.6 million cycles. However, the compressive loading of WTGB is not constant. The effect of contact pressure variation on slipping in WTGBs due to a grid loss event was investigated by Helsen et al. [44] using a full-scale wind turbine nacelle and focusing on the taper roller bearings of the High-Speed Shaft (HSS). An increase in the bearing loading was observed during this event. They recognized bending and torsional deformations during this event that increased the roller slip and they pointed out this event as a possible cause of the bearing failure.

A Frictional Heat Accumulation (FHA) hypothesis was proposed by Gould and Greco [49] to predict the formation of microstructural changes depending on the velocity difference between the contact bodies and other factors. They postulated that the estimated FHA is proportional to the applied load, friction, relative velocity of the contact bodies and running time. Their findings specified that the FHA required to initiate microstructural alterations was ~ 6.26 MJ. Keller, Gould, and Greco [116] also demonstrated the loading level, Slipping Ratio (SR) and the number of cycles required to initiate WECs. They found the loading level of 1.9 GPa and over with high negative SR (-30%) in addition to at least 30 million cycles at a rolling velocity of 1 m/s are required to form this microstructural alteration and they postulated FHA to be ~ 6 MJ to produce WECs.

Gutiérrez et al. [117] successfully recreated WECs in two discs under a contact pressure of 1400 MPa and SR of -23.5%, after 28.5 million cycles, however, more than 40 million cycles failed to produce WEC under a contact pressure of 1200 MPa.

The effect of lubricant and slipping was studied by Ruellan et al. [118], they concluded that the high slippage is enhanced by transient loading. They also tested pre-charged bearings with hydrogen and their tests revealed a higher ability to produce microstructural alterations than the uncharged bearings. Surface roughness is strongly relevant to SR and can change the contact loading on the surface asperity level. The importance of the effect of surface roughness on fatigue life was also pointed out in a number of studies such as; Shuangwen et al. [34], Li [119], and Wan et al. [120].

2.4.4 Inclusions of bearing steels

Despite using advanced techniques in casting the bearing steels, inclusions in the bearing material is an unavoidable issue [121]. Removing the small inclusions from the bearing material is a high-cost process. However, the manufacturing process and heat treatment procedure may affect the inclusion's coherence with the material. Inclusion parameters were studied by a considerable number of researchers, for example, size [122], location [31][77], orientation [123] and type [31][98]. Steel cleanliness can be evaluated using the standard ISO 4967-2013 [76]. However, for the bearing inner races, it is difficult to take the required examination specimens from the recommended locations because of the race shape and dimensions. Evans et al. [98] suggested the standards of steel cleanliness as an appropriate way to describe WSF.

Different types of steels are used as bearing materials (for more details see Table 1 in Bhadeshia [124]). American Iron and Steel Institute (AISI) gave the code of 52100 for one of the most common bearing steel which has approximately the same chemical compositions of 100Cr6 steel as illustrated in Table 2-2. Therefore, these two types are sometimes considered as the same type [125]. Hashimoto et al. [126] investigated this bearing steel under accelerated test conditions with Hertzian contact stress of 5.3 GPa. They concluded that cracks are probably initiated from elongated MnS inclusion tips. Different types of inclusion damage were reported such as inclusion separation from different locations [79][3], i.e. upper separation of the inclusion boundaries from the locations towards the rolling contact surface, lower and side separations. Inclusion cracking also reported to be either internally cracked inclusions, crack propagated from the inclusion to the bulk or mixed of them [3]. Figure 2-8 Shows examples of nonmetallic inclusion damages.

Table 2-2: Chemical compositions of two bearing steel [124].

Grade	C	Mn	Si	Cr	Ni	Cu	S	P
AISI 52100	0.95-1.1	0.20-0.50	≤0.35	1.30-1.60	-	≤0.025	≤0.025	-
100 Cr6 (w)	0.90-1.05	0.25-0.45	0.15-0.35	1.40-1.65	≤0.30	≤0.30	≤0.025	0.03

Inclusion damage probably initiates when the stress level around the inclusion exceeds a critical limit, however, the inclusion also produces a stress concentration around its boundaries and the stress intensity factor around the inclusions was used to describe crack initiation and the fatigue strength in this region [127][128].

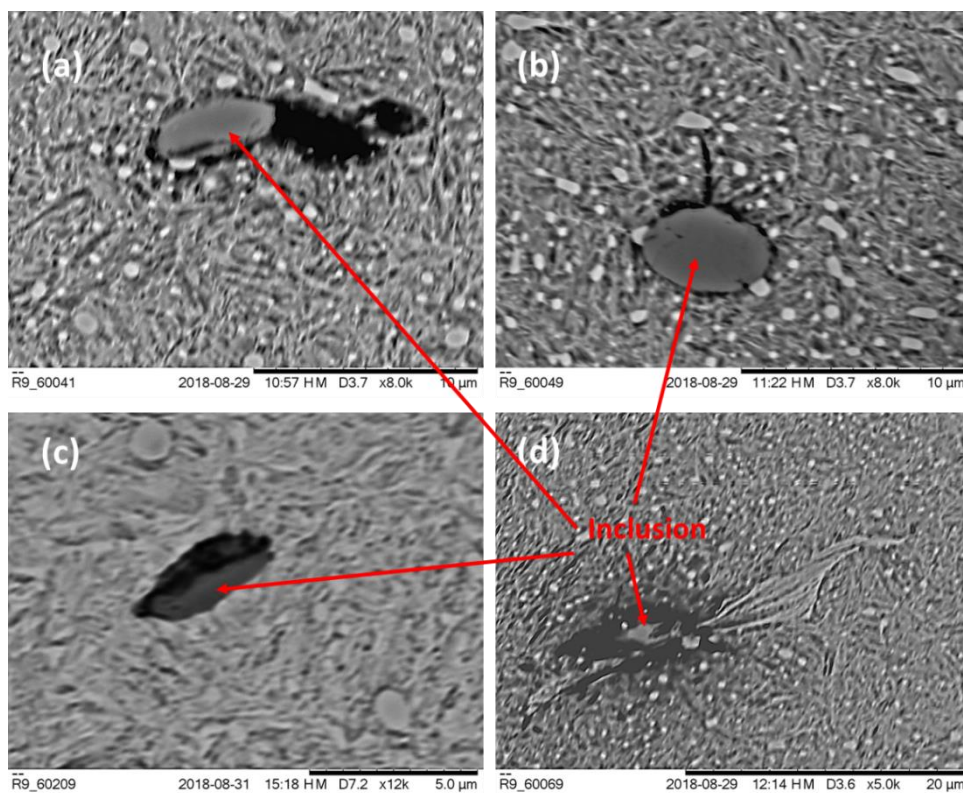


Figure 2-8: Examples of damaged inclusions (a) side separation damage; (b) crack initiated from an inclusion; (c) internally cracked inclusion; (d) inclusion associated with butterfly wing damage feature.

Murakami [73] hypothesized a geometrical parameter of inclusion to calculate the maximum stress intensity factor for fracture mechanics in RCF. This parameter depends on the square root of the inclusion or the defect area and the maximum principal stress. He also postulated that the change in subsurface crack direction is due to inducing a higher stress intensity factor than the crack currently has. However, Solvano-Alvarez et al. [84] postulated the predominance of voids around

the inclusions as the cause of de-bonding the inclusion boundaries that finally lead to bearing fatigue failure. They concluded that the linking of voids was the source of crack initiation. Furthermore, they pointed to the concentration of debonding damage is at the maximum orthogonal shear stress location. However, the depth of orthogonal shear stress is near the maximum shear stress location and the latter is larger than the orthogonal shear. Thus, the role of orthogonal shear in failure is a controversial conclusion.

Bruce et al. [5] referred to the role of inclusion in crack initiation within the maximum shear stress zone due to overloading that probably exceeded the yield limit. They also discussed the role of traction force in changing the value and direction of the induced maximum shear and this may control the direction of crack propagation and the inclination of butterfly wings. This research supports the findings of Stadler and Stubenrauch [41] and Qin et al. [112].

The inclusion type has a considerable effect on its associated damage features [129]. Calcium additives throughout the steel casting process work as deoxidizers to remove the impurities from the steel. However, these additives have detrimental effects on the RCF of bearing steels [33]. Oxide inclusions (SiO_2 , Al_2O_3 and $\text{Al}_2\text{O}_3\text{-CaO}$) were found affecting the formation of butterfly wing damage [33][130] more than the other types because of their mechanical properties, i.e. they are hard and brittle [98]. The easy de-bonding behaviour of the oxide inclusions due to an incoherent interface between the inclusion boundaries and the bulk helps to initiate the cracking [131][132]. Singh et al. [133] found the oxide and dual-phase inclusions have a more detrimental effect than MnS inclusions. They also found a considerable number of inclusions isolated from the crack network. The effect of Coefficient of Thermal Expansion (CTE) of the inclusions was also investigated. MnS inclusion has a larger CTE than Al_2O_3 thus, compressive residual stress is probably produced in the beginning of casting stage, however, tensile residual stress can be produced later during the solidification process [134]. MnS inclusions have been reported having rare butterfly initiation in the old studies [33], however, recent researches showed the ability of these inclusions to form butterfly wings [31][1][133].

2.5 Phenomena associated with WTGB premature failure

A hydrogen embrittlement phenomenon was observed in the investigated WTGBs [135]–[140] and the hydrogen was cited to be one of the most important root causes of microstructural alterations and premature failure. This phenomenon accelerates WSF by enhancing the local plasticity and increasing the grain slip

deformation that leads to increasing the crack density during the RCF [141][142]. Hydrogen can be produced from the lubricant because of severe compression conditions and/or from the lubricant contamination with water. The latter may dissolve due to an inductive current [24] which may be produced during the turbine operating. The effect of hydrogen on premature WTGB failure was reported as the trigger of WEC formation in a number of studies [28][143].

Carbon migration from the interior side of stressed grains to their boundaries is another observed phenomenon [1][144]. This makes the grain boundaries showing a brittle behavior and enhancing the crack initiation from these sites. Carbon immigration was frequently cited despite this phenomenon requiring a temperature rise of a few hundred degrees centigrade [145].

Carbides are hard particles, however, deformation or dissolving of these microstructures was also reported under severe loading conditions [144][146]. The additional phenomenon of electrical currents induction throughout the bearing rotation was also cited in previous studies [95][96][147]. These currents can be generated during the WTG operation that may lead to hydrogen generation which may cause lubricant chemical instability [96][147][148].

Bujoreanu [149] pointed out the complexity of the interacting effects of mechanical, chemical and physical phenomena on RCF. The mentioned groups of phenomena and causes increase the complexity of studying the premature failure of WTG bearings and indicate the need for intensive investigations to have a reasonable explanation for the bearing premature failure phenomenon and the associated microstructural changes.

2.6 Bearing damage features

2.6.1 Surface and subsurface microcracks

Both surface and subsurface crack initiation under rolling and sliding contact were mentioned in the previous studies. However, which type is dominant is a debatable question. Surface initiated RCF cracks were reported by Mayer et al. [150], Rycerz, Olver and Kadiric [151], Bush et al. [152] and Yang et al. [81]. In contrast, Chan [68] postulated the subsurface crack initiation from grain boundaries having intergranular embrittlement due to carbon immigration and this supported by the findings of Paladugu and Hyde [4]. Subsurface crack initiation has more supporting evidence and was reported in a considerable number of studies such as; Keer et al.

[11], Evans et al. [13], Cerullo [153], Lund [154], Al-Tameemi et al. [155] and Bomidi and Sadeghi [156]. However, some studies reported a competition of both surface and subsurface cracks [98]. The important question about the subsurface crack initiation is; what is the most prevalent site of this damage initiation? Different sites were reported, and extensive discussion was made in the previous studies. The majority of literature refers to the weak region of the inclusion-matrix interface as the main site of crack initiation [13][31][157]. On the other hand, material defects have also been reported as a crack initiator in Murakami's works [73][75][158].

The use of crack growth to describe the damage propagation had considerable importance due to its relationship with fatigue life estimation. Rycerz et al. [151] conducted experimental rolling contact tests under high contact pressure of 3.63 GPa to 4.76 GPa, they referred to contact pressure and crack size as the main parameters affecting the crack growth rate of surface-initiated cracks and there are secondary subsurface cracks which propagate towards the contact surface with an exponential related to the increasing of the contact pressure.

Warhadpande et al. [159] concluded that subsurface plasticity was the initiator of subsurface microcracks due to overloading. They built a Finite Element (FE) elastic-plastic model to confirm the subsurface crack initiation, while Kerscher et al. [145] showed the possibility of subsurface featureless crack initiation from any origin in high cleanliness steels. Nucleation of material voids as the crack initiator was reported by Solano-Alvarez et al. [84]. However, Karsch et al. [160] found the chromium carbides to be the initiator of subsurface cracking. Furthermore, Martin et al. [109] postulated the grain boundaries to be the plane of weakness and this was also supported by Evans [24].

Solano-Alvarez and Bhadeshia [161] hypothesized that the subsurface crack orientation is controlled by the shear stress and the rolling direction. They also discussed how to control the grain size and how to initiate subsurface and surface microcracks by using a Vickers hardness measuring device and heat treatment. The results of their study postulated a significant number of important notes from the metallurgical point of view. They identified the size of austenite grains, the stress transferred between martensite and austenite and the carbon content of martensite, as the effective factors on crack initiation. The pre-existence of subsurface microcracks in the materials was postulated by Campbell [121]. He hypothesized that the microcracks are produced during the casting of the bearing steel due to a "Bi-Film" phenomenon. This phenomenon of producing relatively cold faces during the pouring of molten steel within the casting process is responsible for producing microcracks and oxide defects which significantly affect the structural fatigue life.

2.6.2 Microstructural alterations

Microstructural alterations were firstly reported in the 1940s by Jones [32]. White patches were observed under a Light Reflection Microscope (LRM), in subsurface sections of a failed bearing made from 100Cr6 steel after etching the samples with nital. Different terms were used to refer to these white patches such as white phase, White Etching Areas (WEAs), White Etching Layer [162], Light Etching Areas (LEAs), White Etching Bands (WEBs) or grey lines [163]. These white etching patches are now described in different forms such as White Etching Areas (WEAs), White Etching Cracks (WECs) and butterfly wings. Later, Dark Etching Areas (DEAs) or sometimes called Dark Etching Regions (DERs), were also reported to be produced before the formation of WEAs [139]. Two types of WEAs were reported, the first inclined at $\sim 30^\circ$ to the rolling surface and called Low Angle Band (LAB), and the second type inclined at $\sim 80^\circ$ and called High Angle Bands (HABs) [164]. Other classifications for WEAs were also proposed, for example, classifying them as softer and harder WEAs depending on the comparison of their hardness with the bulk material [165]. Another classification was made by considering “deformed WEAs” due to a high loading level that causes plastic deformation, and “transformed WEAs” due to chemical interface and phase transformation of the material [166]. These microstructural alterations considered as damage features and they depend on the number of loading cycles and the magnitude of the contact stress [1]. The relationship of the number of cycles for initiating these alterations under specific loading levels was investigated by Swahn et al. [164]. They produced a chart to show the relationship between the maximum contact stress and the required number of cycles as can be seen in [Figure 2-9](#). Rolling contact under higher contact stress levels than 3720 MPa and their required number of cycles to onset of the alterations are unknown. However, it may be estimated by extending the chart lines.

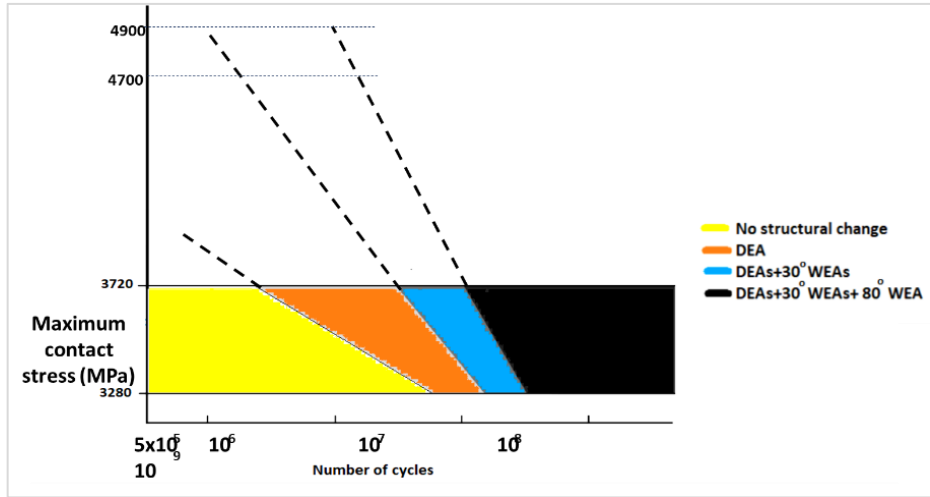


Figure 2-9: Contact stress and the number of cycles for the formation of microstructural alterations (adapted from [164]).

Zwirlein and Schlicht [167] introduced a diagram for estimating the required number of cycles for the initiation of microstructural changes depending on the contact pressure as can be seen in Figure 2-10. Contact stress levels in this diagram imply that under contact pressure less than 2500 MPa, no microstructural alterations can be introduced without billions of cycles. A considerable number of studies successfully reproduced different microstructural alterations under lower loading levels than (2500 MPa) and in several tens or hundreds of millions of cycles [117].

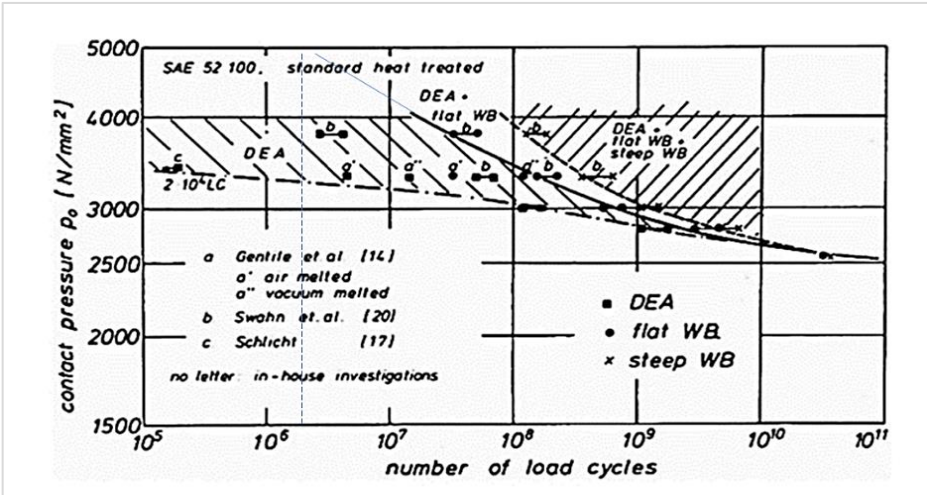


Figure 2-10: Zwirlein and Schlicht diagram of microstructural change correlation with contact pressure and the number of rotating cycles [167].

Microstructural alterations also reported as a consequence of damage not a cause of it [15]. The microstructural alteration is a very complex phenomenon and there are

a considerable number of factors proven to have a considerable role in the alteration initiation and propagation. The effect of impact loading in producing microstructural alteration as one of the damage features which can be observed in WTGBs was specified in the previous studies [100] and the microstructural alterations in the form of WEA were postulated to have a considerable role in reducing the RCF life [168]. This also studied by Yang, Zheng and Yang [81]. They reported that five high impacts due to dropping a 100 mm steel ball from a height of 3.5 m were enough to induce a microstructural change of WEA beneath the contact surface. However, they found the plastic deformation and cracks propagating are in a direction depends on the deformation lines observed in the alteration area.

Residual stresses induced during the machining and heat treatment may play a considerable role in introducing the plastic deformation and hence the microstructural changes [169]. Errichello et al. [28] compared two types of bearing heat treatments which are through hardening and carburized bearings. The carburized bearings revealed no microstructural alterations, while the second type had. They postulated that the high nickel content, high amount of retained austenite, the low carbon content of the bearing core and the greater compressive residual stress can provide a higher fatigue failure resistance. The phenomenon of alterations also observed in other applications such as rail treads [170]. These alterations considered by Voskamp [171] as a material response to RCF loading while, Swahn, Becker and Vingsbo [172] consider the alterations as carbide decay phenomenon.

The tests in this study will show if these testing levels can produce microstructural alterations or not. Different theories of the initiation mechanisms of the mentioned microstructural changes were postulated. However, more focus will be given to the butterfly wing initiation mechanism theories because this feature was observed predominately in the investigated WTGBs.

2.6.3 Theories and mechanisms of microstructural alterations

1. Dark Etching Areas (DEAs)

The first phase of microstructural alteration which starts to appear is a Dark Etching Area (DEA). These are dark regions that appear under optical microscopes in the subsurface of failed bearing inner races close to the contact surface at 100 μm to 600 μm depth [28][164]. This depth corresponds to the highest magnitude of stress. DEA consists of ferritic phase grains with a non-homogenous distribution of carbon content [117]. The main cause of the DEA initiation was postulated to be due

to microplastic deformation which found to be induced where there are a slip motion and carbon migration towards the heavily dislocated regions [76][137], [138]. Martensite decay was also reported as an important cause of DEA formation [136]. This formation was postulated to depend on the maximum contact stress level and the number of rolling cycles [139]. The required number of cycles for DEA formation was reported in AISI 52100 steel to be 5×10^6 and 5×10^7 cycles under a maximum contact pressure of 3.72 GPa and 3.28 GPa respectively [164]. This range also agreed with the results of Schlicht et al. [173] who reported the number of cycles to introduce DEA in this type of steel to be in the order of 10^6 and 10^9 cycles under maximum contact pressure of 3.5 GPa and 2.7 GPa respectively. These results identified that, under lower contact pressure (<2500 MPa), the formation of DEAs requires a very large number of cycles. Even for the same material, the required number of cycles under a specific contact pressure may vary considerably. This is probably because of the alteration dependence on the material cleanliness and mechanical properties which depends on the heat treatment procedure.

Kang et al. [174] postulated a tempering process during this phase transformation from retained austenite to martensite which occurs due to grain dislocation. On the other hand, Gegner [175] proposed that DEAs are the precursor of WEC formation. He postulated the dislocations are accommodated at the grain boundaries and the carbon migrating from the grain interiors makes the boundaries enriched with carbon. Carbon migration to the grain boundaries leads to its precipitation as lenticular carbides [109] and the dislocation causes tempering of these carbides. Increasing the number of over-rolling cycles can produce another ferritic phase of microstructural alterations called WEAs inclined at $\sim 30^\circ$ to the rolling contact surface [1].

2. *White Etching Areas (WEAs)*

White Etching Area (WEA) is a microstructural feature having a disc shape with $\sim 0.1 \mu\text{m}$ to $0.5 \mu\text{m}$ thickness and a $\sim 30^\circ$ inclination angle to the rolling contact surface, sometimes called Low Angle Bands (LABs) [24][5][146]. This feature is probably initiated under high loading levels after a high number of loading cycles. After further over-rolling cycles, WEAs inclined at $\sim 80^\circ$ to the rolling surface start to appear (called High Angle Bands (HABs)). The latter type is a fine ferritic phase, but are thicker than the 30° WEAs [1]. The initiation of 80° WEA was postulated by Polonski and Keer [39] as a response to residual stresses induced due to the formation of 30° WEAs. They also discussed the most popular theories of the microstructural change initiation and hypothesized a new theory of dislocation and

carbon diffusion to explain the WEA formation. They also studied the increase of the contact surface traction as a reason for the decreasing of the WEA angle. This increasing of the traction force was achieved by varying the raceway roughness and/or lubricant viscosity. Li et al. [146] suggested an initiation mechanism of WEA due to severe local plastic deformation which causes a carbide dissolution and carbon redistribution. They also postulated that the grain boundaries work as a carbon trap that causes a weak region and this region is the most likely site for crack initiation. Spherical carbide elongations, breaking up, deformation and dissolution were also postulated to be the possible causes of the WEA initiation in a number of studies [110][157][161][164][176][177].

Šmeļova et al. [178] postulated redistribution of carbon and chromium within the microstructural alteration region owned and suggested the diffusion of these as the main cause of WEA formation, while Voskamp et al. [179] postulated that the residual stress had a considerable role in producing WEA. High residual stress was suggested due to a local volume increase which associated with the decay of retained austenite in DER to form the WEA. In bearing steels with a typical austenite content of 12.5% [33][152], it is possible to produce compressive residual stress up to 400 MPa [33].

Solano-Alvarez and Bhadeshia [161] recommended a few methods to eliminate the WEAs from the bearing steels. They also discussed the most influential factors in their formation such as carbide intensity. They found that bearing steel with a ductile fracture failure mechanism has less ability to produce WEAs. Therefore, they suggested a new class of bearing steel with a nanostructure containing a mixture of bainitic ferrite and retained austenite. The failure region of this type of steel exhibits a ductile fracture with voids at the interference locations between the inclusion and the matrix [108]. This type of bearing material has good wear and RCF resistances with a good ability to be manufactured on a large scale.

The most debated issue about another type of WEA associated with cracks, i.e. WECs, is whether the cracking phenomenon is a consequence of this microstructural alteration or the cause of it? Some researchers concluded that WEAs associated with cracks are a consequence of the cracking and the rubbing of the crack-free surfaces is the main cause of alteration. However, many observations do not support this suggestion and cannot answer the question: Why WEAs are sometimes found without any attached crack? More details about WECs will be presented in the next section.

3. *White Etching Cracks (WECs)*

When subsurface cracks are associated with WEAs, these cracks are called White Etching Cracks (WECs). This type of cracks was observed in the investigated failed WTGBs. WECs were successfully reproduced by a number of researchers, for example, Evans et al. [98] under maximum contact pressure of 2.15 GPa. However, no DEA was observed in their tests. They concluded that the WEC formation depends on inclusion type, orientation, and location. They also found that two-thirds of the inclusions interacted with WECs were D_{Sulf} and D_{Dup} types (according to ISO-4967 [76]).

WECs were proposed to be formed due to sliding in a number of studies [44], [49][66]. Danielsen et al. [115] found the large MnS inclusions do not seem to have any relationship to the crack network, while voids and Al_2O_3 were followed by the cracking during the propagation process. Their investigation showed that no retained austenite was observed in the alteration area that supports the phase transformation during the microstructural alterations. Holweger et al. [99] investigated the root cause of WEC. They pointed to the accumulative successive structural plastic distortion as a cause of producing supersaturated carbon grains which is unrelated to non-metallic inclusions. They also postulated that the distortion in the vicinity of carbides is probably leading to carbon diffusion and then the plastic deformation is induced. This process was found to enhance the initiation of the microstructural change. Gould et al. [180] referred to multi-phase inclusions which containing Manganese, Sulphur, and Aluminum as the preferred site of WEC initiation; and they concluded that the alterations initiate from pre-existing failure locations close to the inclusion boundaries. They also concluded that the inclusions may be unrelated to WEC formation.

Five main theories have been widely discussed and proposed for WEC formation. The first refers to their initiation from surface cracks [110][175] due to a hydrogen effect produced from lubricant dissolution under high local compressive pressure inside the surface crack when the roller moves over the surface crack tip. The second theory postulated that the butterfly wings and inclusions are the main cause of the WEC formation due to stress concentration [110][154]. The third suggested mechanism is from an Adiabatic Shear Band (ASB) due to impact loading [46]. This band is a severely plastic deformed region due severe shear stress. The fourth theory hypothesized the rubbing of crack faces [161][181]. The last hypothesis referred to the dissolution of the spheroidal M_3C (Iron Chromium carbide), that can form carbon supersaturation ferritic grains to be observed later as WEAs; and the

crack may be formed later [131][182]. Crack face rubbing theory has recently had more attention [165][183]. However, this hypothesis has many drawbacks. For example, the maximum relative motion between the crack faces is in the middle of the crack; this should produce maximum alteration density around the crack midpoint, however, this has no supporting evidence. The second drawback comes from the asymmetrical shape of the alteration about the crack itself. Alterations should be symmetric due to their affecting both crack faces by the same action. The third drawback is that the small microcracks have less relative movement. However, WEAs associated with microcracks were also observed [147]. The last drawback is the formation of alterations was also observed near the crack tip where there is no relative movement and WEAs were also found sometimes without associated cracks.

Contact pressure used to generate WEA/WEC in laboratory was in a wide range of 2.0 GPa to 5.6 GPa [76][105][106][108][134][184]–[186] and 10^6 to 10^8 cycles. However, the inner races of WTGBs are typically subjected to 0.9 GPa to 2.0 GPa during normal operation. Furthermore, transient loading due to operating events could result in much higher contact pressure, i.e. over-rolling. Evans [1] expected that the number of rotating cycles and maximum contact pressure are not the only driving factors in WTGB failure by WSF.

4. *Butterfly wings*

A butterfly wing is a specific damage feature associated with central non-metallic inclusion, defects or cracks. The name of this feature came from the specific shape of wings as can be seen in [Figure 2-11\(a\)](#). Butterfly wings can be classified into two types which are single and double butterfly wings. The single-winged butterflies have subtypes which are upper and lower single-winged butterflies. Upper wing butterfly refers to one where the wing location is above the central inclusion, i.e. towards the contact surface, while the lower wing refers to the wing below the central inclusion. Wings of butterflies consist of ferritic grains with different sizes like those observed in WEAs [24]. Formation of butterfly wings has been investigated over several decades by a considerable number of studies, for example, Evans et al. [27], Brückner et al. [30] and Moghaddam et al. [31]. Different butterfly depths (below the contact surface) and sizes (distance between the two wings tips) have been reported, however, the maximum depth previously reported was 1.5 mm [56], while the butterfly size was in the range of 10 μm to 100 μm . The inclined angle of the maximum wing length axis to the rolling surface was reported to be 30° to 50° and 130° to 150° [109][177]. Thus, maximum unidirectional shear inclined at $\pm 45^\circ$ may have the main role in wing formation [1], and the traction force

between the contact surfaces maybe responsible for changing the wing inclination angle. The butterfly wing shape is identical to orthogonal shear stress distribution under a Hertzian contact pressure, thus, this shear stress is also postulated to be one of the most likely causes of wing formation.

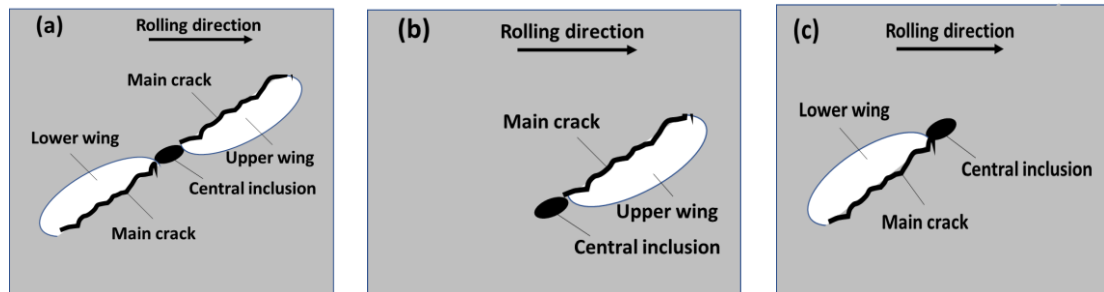


Figure 2-11: Butterfly wings feature and their types (a) double wings; (b) upper wing; (c) lower wing.

Different initiation sites of butterfly wings have been reported such as voids [107], [177], large carbides [176], microcracks [107], porosity [131] and non-metallic inclusions [1][157]. Butterfly initiation parameters also differ from one study to another. For example, the most discussed parameters are the inclusion type, size, depth, shape and the adhesion between the steel matrix and the imperfections, the Coefficient of Thermal Expansion (CTE) [134] and the difference in modulus of elasticity between the defects and the steel matrix [176][187][188].

Different ferrite grain sizes were reported inside the wings with the range of 10 nm to 100 nm diameter, and the intensity of the small grain was observed to be higher near the main crack and wing boundaries. The intensity of larger grains increases with increasing the distance from the wing boundaries towards the wing center [157][176][177].

Singh et al. [133] found the distribution of butterfly wings with depth is corresponds to the maximum orthogonal shear stress depth. MnS inclusions rarely cause butterfly initiation in previous literature[33]. However, recent research showed the ability of this type to form butterfly wings [38][1][133].

Evans [1] classified butterfly wings into two categories; those which do not propagate significantly and not causing damage, and those which propagate to a critical length and may connect to a crack network. It has been also noticed that reversing the direction of bearing rotation leads to form another pair of butterfly wings in a symmetrical orientation [13]. Martin et al. [109] postulated that the clustering of network dislocations generates sub-grains to form nano-ferrite grains

in the butterfly wings, while Guetard, Toda-Caraballo and Rivera-Díaz-del-Castillo [189] demonstrated the primary carbide as the possible cause of butterfly formation. They also postulated the length and angle of butterflies are probably controlled by the butterfly depth beneath the contact surface and increasing the contact load leads to an increase in the wing formation depth. Their investigation led to the postulation that butterflies tend to be approximately parallel to the contact surface under a relatively low loading level of ~ 3.2 GPa. However, under 4.0 to 6.1 GPa, the wings are inclined at 20° to 25° .

Obstacles such as vacancy clusters, carbide precipitation, and high dislocation density may cause a dislocation warping which was confirmed in butterfly wings [1]. However, carbide dissolution and its relationship with WEA in butterfly wings are not completely understood [27][31]. It has been suggested that the dissolution is the driver of grain refinement under high stresses in locations adjacent to inclusions or cracks, together with the plastic deformation and dislocation, causing a break-down of the grains to form nano-ferrite grains in a gradual process leading to butterfly wing formation [24].

Threshold compressive contact stress to form butterfly wings has been reported across a wide range. For example, Lund [56] made his experiments on ball bearings under a maximum contact pressure of 2.25 GPa to 4.9 GPa and he specified the threshold orthogonal shear stress of butterfly wing formation to be ~ 400 MPa. However, Takemura [190] postulated threshold contact pressure to be 1.3 GPa for “dirtier” 100Cr6 steel and 2.0 GPa for “cleaner” ones, while it was reported that the threshold contact pressure was ~ 1.4 GPa for medium and large sizes of bearings [33]. Grabulov [131] found the butterfly wings to be formed at depths corresponding to an orthogonal shear stress of ~ 450 MPa. Most of the previous studies did not report on the required number of cycles for the wing initiation since the butterfly formation cannot be precisely specified throughout the testing or the operating conditions. Evans et al. [27] successfully reproduced butterfly wings under transient loading and pointed to carbides dissolving as the main cause of their initiation.

Analysis of butterfly wings with depth beneath the contact surface in the circumferential direction of a failed test disc made from a steel powder with the composition of 100Cr6 steel was conducted by Brückner et al. [30]. They proposed a mechanism for butterfly formation by cracking the inclusion in a direction coinciding with its maximum axis length due to cyclic loading. They also postulated that the butterfly wing length is typically increased with increasing over-rolling cycles. They found $\sim 88\%$ of the inclusions exhibited butterfly wings in

circumferential sections. They found the distribution of butterflies with depth had a noticeable correlation with the orthogonal shear stress as can be seen in Figure 2-12, where 56% of the butterflies have a depth between 0.2 mm to 0.5 mm.

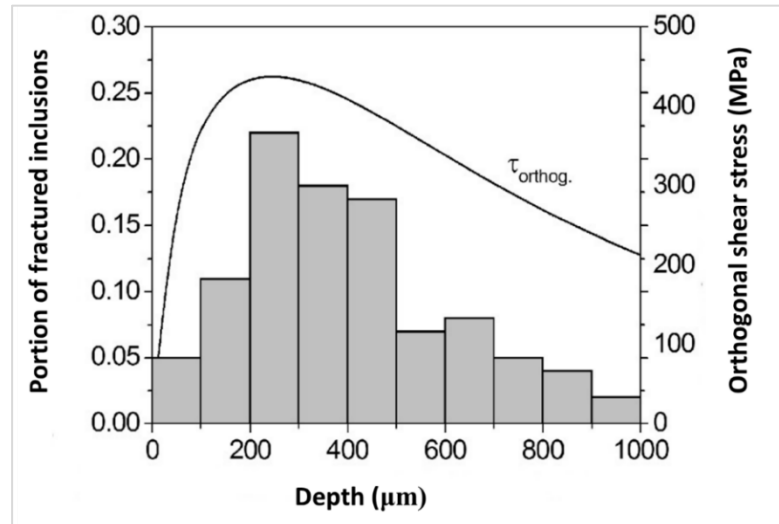


Figure 2-12: Characterization of butterfly wings with depth [30].

Reproducing microstructural alterations is a very complex process and depends on a large number of factors and a full understanding of this phenomenon and its role on bearing damage require a huge effort and massive investigations.

2.7 Rolling Contact Fatigue (RCF)

Rolling Contact Fatigue (RCF) is a type of fatigue damage consisting of a surface and/or subsurface crack initiation that is completely different from the classical fatigue type. In the latter, the material is cyclically loaded by bending or tension/compression to produce maximum stress on the outer surface of the test specimen, while in the former fatigue type, the maximum stress is beneath the contact surfaces of two bodies under rolling and sliding conditions [167][191]. In 1896, Hertz developed a theory [192][193] to solve contact problems under elastic conditions. The main assumptions considered by Hertz were; there is no traction. This theory can be used for normal elastic contacting bodies are perfectly smooth and the contact width is small relative to the dimensions of the contact bodies. The distribution of contact pressure within the small contact area which is produced due to the flattening of the material was postulated by Hertz to have an elliptical pressure distribution [193]. This theory can be applied with reasonable accuracy to bearing contact problems [25][194], where there are two contact lubricated smooth surfaces (rolling element and inner race). Contact pressure calculated using Hertz

theory is usually in the order of few gigapascals, while in microscale contact, the surface asperity contact stresses are significantly higher [49][195]. Different damage features due to this high loading levels can be observed on the bearing inner race surface [23]. The damage features observed in bearings are illustrated in the standard BS ISO 15243 : 2017 [148]. This standard also illustrates the main causes of each damage type. Examples of these bearing damage features illustrated in this standard can be seen in [Figure 2-13](#).

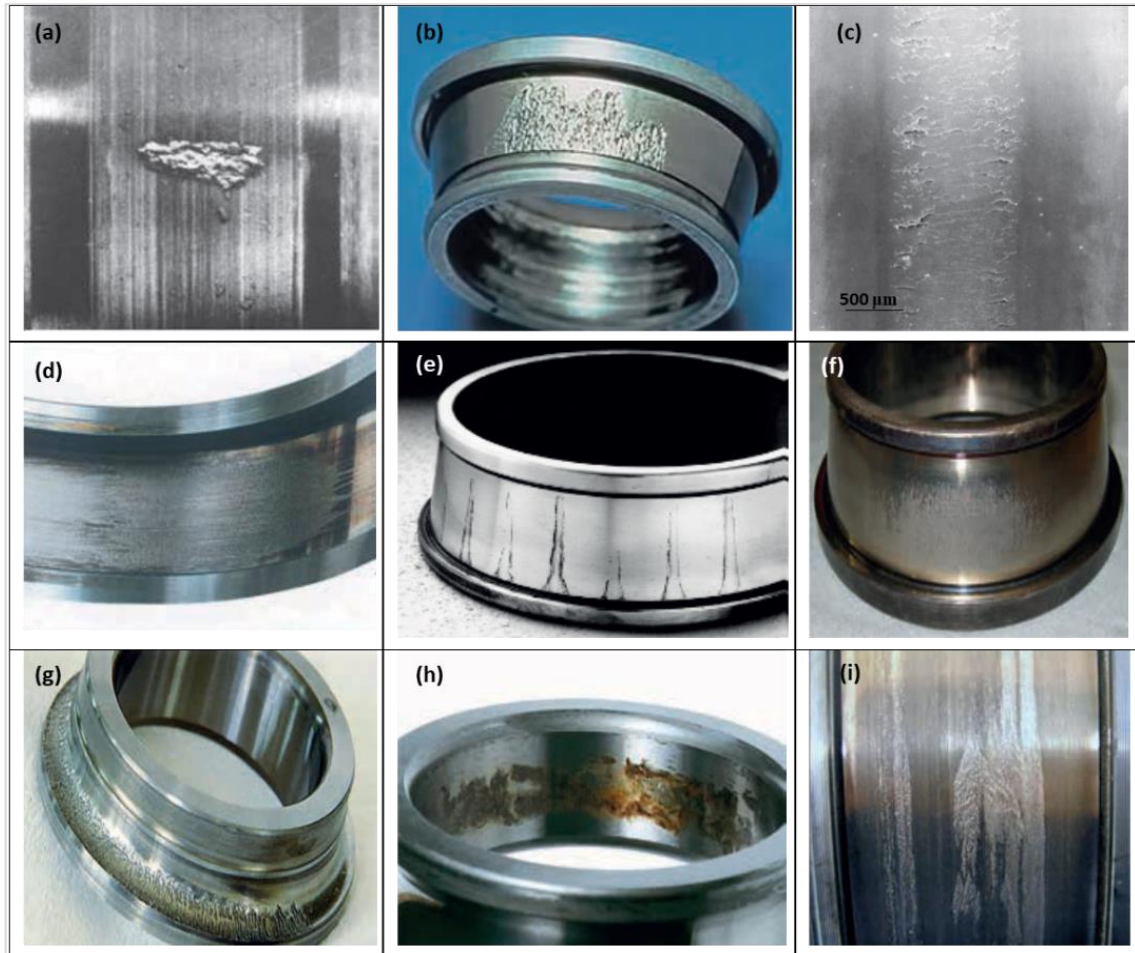


Figure 2-13: Examples of bearing inner race failures [148]. (a) Spalling in early-stage; (b) Spalling in advanced stage; (c) micro-spalls; (d) Smearing; (e) contact corrosion; (f) surface-initiated micro-spalls; (g) surface-initiated spalling; (h) fretting; (i) smearing and skidding.

Subsurface stresses distribution due to Hertzian contact, such as orthogonal shear (τ_{xy}), maximum shear (τ_{max}) (sometimes call unidirectional or principal shear), Von-Mises stress (σ_{vm}), and octahedral shear (τ_{oct}) which is proportional to Von-Mises stress [23], can be calculated using Hertz theory depending on the location of the point under consideration beneath the contact surface and its distance from the acting of the maximum contact pressure. The τ_{xy} acts in a specific direction (parallel

to the contact surface), while the τ_{max} direction inclines at $\pm 45^\circ$ with the contact surfaces [3][1]. Variation of contact pressure and introducing a traction force between the contact surfaces vary the magnitudes, directions and locations of all types of the maximum subsurface stresses [79]. However, alternative methods (superposition and FE) can be used for calculating the stress distribution under the combined action of compressive and traction forces.

In most of the previous researches, only some contact stresses were often presented in the contact region depending on which one was taken into consideration. Figure 2-14 presents the pressure distribution and magnitudes of maximum stresses of all types of surface and subsurface stresses within a contact region for a 2.0 MW planetary bearing under a Hertzian contact stress level of 2.4 GPa which is close to the elastic stress limit (yield stress) under compression for AISI 52100 steel. This type of steel is widely used as a bearing material [33].

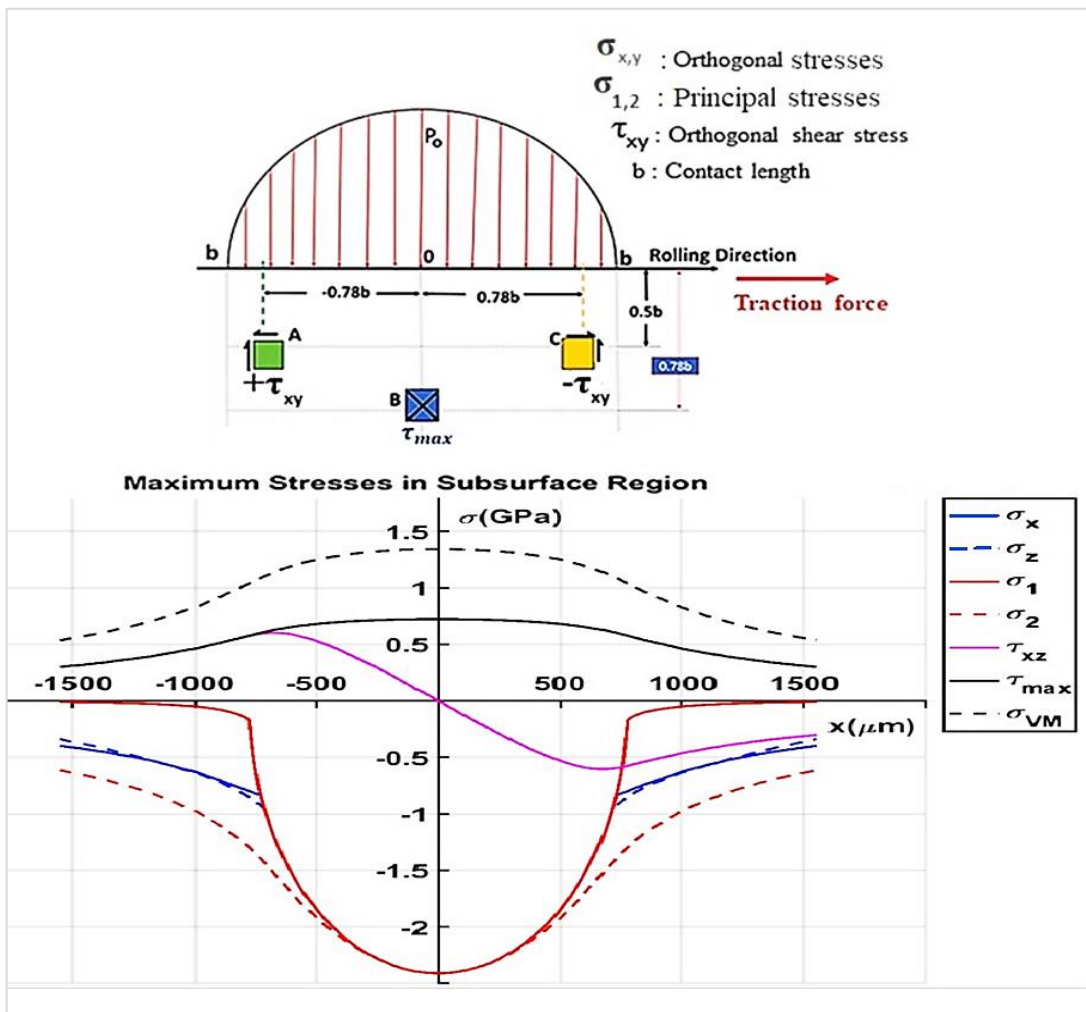


Figure 2-14: Pressure distribution and maximum stresses in the contact region under Hertzian contact pressure of 2.4 GPa on a typical 2 MW planetary bearing.

Different sites of fatigue initiation were reported in the previous studies such as nonmetallic inclusions in the bearing material which was specified to have the main role of fatigue failure initiation [1]. For that, improving the bearing material cleanliness had the main concerns [79] and provided promise improvements for the bearing life. Carbide can be introduced in bearing materials due to heat treatment. This was also thought to be the location of a fatigue failure initiation site due to their weakness [25].

In bearings, traction force between the contact surfaces depends on the rolling direction, the geometry of the contact components, surface roughness, the lubricant specifications, contact pressure and the relative velocity of the contact surfaces [25]. However, shear stresses due to this traction were thought to be responsible for the bearing damage [24][196].

2.8 Theories and mechanisms of fatigue damage

In 1924, Hencky hypothesized a maximum distortion energy criterion to describe RCF [33]. He assumed that, when the magnitude of the distortion energy which is part of the strain energy per unit volume, exceeds a critical limit, yield occurs and the distortion energy induced will be enough to change the shape of the material of the mechanical components [1].

Von-Mises and maximum shear stresses were assumed to be the main causes of RCF failure depending on von-Mises and Tresca failure criteria respectively [79][197]. The von-Mises criterion states that: failure occurs when equivalent stress reaches the yield stress limit and this equivalent stress (σ_e) depends on the three principal stresses, as shown in Eqn. 2.2 [1].

$$\sigma_e = \sqrt{\frac{(\sigma_1 - \sigma_2)^2 + (\sigma_2 - \sigma_3)^2 + (\sigma_3 - \sigma_1)^2}{2}} \quad 2.2$$

The Tresca criterion is relevant to the yield in ductile materials caused by crystal planes slippage along the direction of maximum shear stress [79][1]. It states that: failure occurs when the maximum shear stress reaches the critical value of the uniaxial tension test. Therefore, it depends only on the maximum and minimum principal stresses (σ_1) and (σ_3) respectively, to calculate the maximum shear stress using Eqn. 2.3;

$$\tau_{max} = \frac{\sigma_1 - \sigma_3}{2} \quad 2.3$$

High loading levels (overloading) were postulated as the main cause of fatigue failure [9]. The overloading either by exceeding the contact stress to the design limit or exceeding the yield stress can introduce a plastic deformation. The maximum pressure required for plastic contact deformation is ($\sim 1.67\sigma_y$) [1][195], where σ_y is the material yield stress. When any of the mentioned critical stress limits occur, plastic deformation will be induced and there is a high-possibility of introducing a subsurface cracking. Subsurface damage was observed at different depths. Therefore, damage formation due to the action of different stress types and levels can be postulated. However, the initiation and propagation mechanisms are still have lack of understanding [79][191].

Finite Element (FE) simulation models were also used to study the bearing contact of roller to inner race in hundreds of studies. For example, the model of Kabus et al. [198] showed that the bearing inner race experiences a stress level higher than that on the outer race, this postulation is logic due to the contact geometry at these two contact locations. They also studied the effect of roller misalignment and axial loading on the contact stress distribution and the bearing fatigue life. Their findings refer to the high influence of the mentioned factors on reducing the RCF life. Furthermore, the Roller profile also affects the stress distribution in the contact region due to stress concentration at the roller ends [198].

Two mechanisms were postulated for RCF damage. The first states that: the crack initiates from the contact surface and propagates inside the material then changes its direction towards the contact surface. This leads to the removal of a piece of the material from the contact surface [199][200]. Surface initiation cracks in RCF were reported by Rycerz et al. [151]. However, the second mechanism postulates a subsurface crack initiation due to shear stress [156] and this crack propagates toward the surface in different directions and when reaching the contact surface, the material will be flaked. Evans et al. [13] confirmed the subsurface initiation of bearing cracking. The subject of surface and subsurface crack initiation remains a controversial issue and the competition between these mechanisms depends on many factors such as contact stress, lubricant, surface finishing quality, material cleanliness and loading direction [191]. Different contact failure mechanisms were presented and discussed in several studies such as: Sheng, et al. [22], Harris and Motzala [25], Lewis and Tomkins [79], Link et al. [87] and Ishizaka, Lewis and Lewis [201].

When the flaking is associated with microstructural alterations in the form of WEC and/or WEA, the term White Structure Flaking (WSF) is used to describe this failure.

Both the cracks and alterations are considered as damage features. However, the question about which type is initiating first continues without a convincing answer. Richardson et al. [166], used serial sectioning to investigate which damage is initiated first in WSF. Their findings stated that subsurface cracks are a prerequisite of WEAs which is initiated from non-metallic inclusions and this supports the opinion of Ooi et al. [147]. However, in contrast, Uyama [202], postulated the initiation of WEA occurred before the crack formation due to stress concentration. The mentioned two main theories of WSF initiation are illustrated in Figure 2-15.

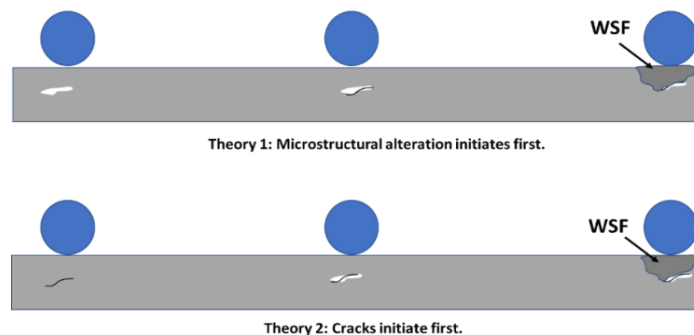


Figure 2-15: Theories of white structure flaking initiation.

Sadighi et al. [191] and Voscamp [200], identified three stages for fatigue failure which are: shakedown, steady-state elastic response and instability. Information about these stages is presented in Figure 2-16. The first stage refers to the occurrence of micro yielding (dislocation glide) which produces a considerable number of defects such as vacancies and dislocations [79]. This stage also consists of developing residual stresses, work hardening and transformation of the retained austenite to martensite, which increases the material strength in the micro-level. This stage takes place normally before 10^4 to 10^5 cycles [191]. However, the number of cycles to reach this stage also depends on the loading level. When a higher saturation level of hardening arrives, the second stage will start.

Throughout the second stage (the steady-state elastic stage), no damage is thought to occur. However, it is a temperature-sensitive stage [191]. This stage is a function of material characteristics and load. At the end of this stage, localized damage occurs and the probability of microcrack initiation is significantly increased [1].

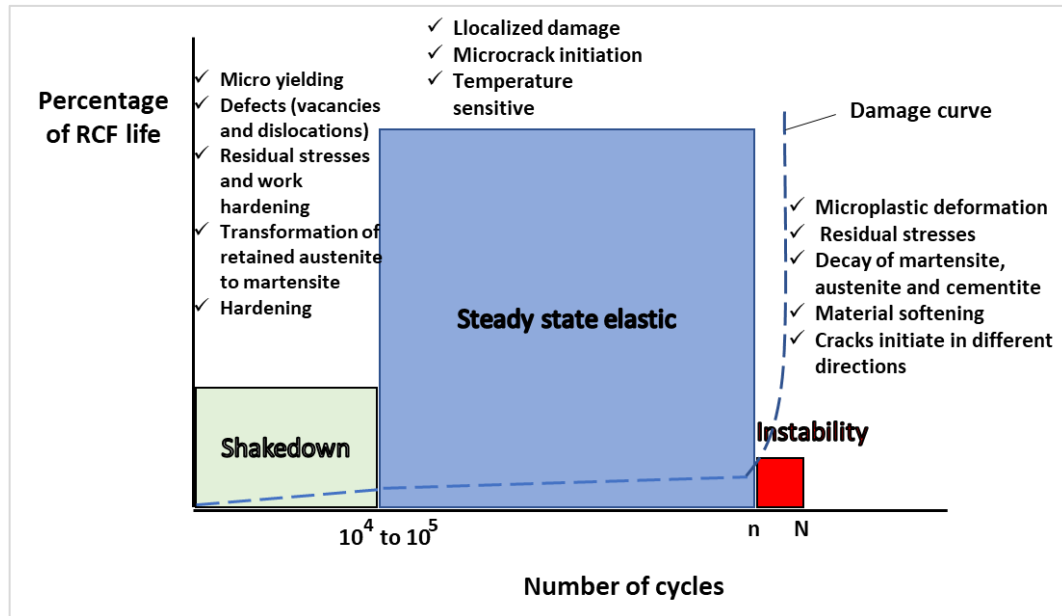


Figure 2-16: Stages of rolling contact fatigue and microstructural damage associated (adapted from [1], [191] and [200]).

Instability is the last stage where the probability of cracking considerably increases. Voskamp [200] also illustrated different material responses during this stage such as microplastic deformation starts, residual stress is built up, martensite, austenite and cementite are decayed, material softening occurs and finally, the cracks initiate in different directions. However, Sadeghi [191], noticed that, during this stage, radial tensile stress produces subsurface cracks parallel to the contact surface.

Crack growth leading to flaking was studied by Shamsaei and Fatemi [203]. Their findings showed that cracks can be initiated in the maximum shear stress plane and the crack frequency increased with increasing the contact loading. Other researchers also studied fatigue crack growth throughout the fatigue failure stages such as Ishizaka et al. [201], Rycerz et al. [151] and Fujita et al. [142].

In 1969, Lin and Ito [204] studied the fatigue crack initiation depending on the slip band theory. They postulated that the plastic shear strain is responsible for introducing a slip among the material layers and this Intrusion/Extrusion is the mechanism of fatigue surface crack initiation. Surface micro-pitting is another damage type observed in wind turbine gearboxes and high hardness materials under rolling and sliding contact such as gears [57]. This damage reduces the gear contact accuracy and escalates the probability of catastrophic damage in the other gearbox components such as bearings [105][206]. Micropitting was observed to take place in hard steels when the film thickness is thinner than the height of the contact surface asperities, i.e. it is highly dependent on lubricant properties. Thus,

the micropitting mechanism is probably associated with the severe stresses produced by asperity contact [207] which leads to breaking down the lubricant film. Despite the role of lubricant in separating the contact surfaces, the lubricating regime (boundary, mixed and Elastohydrodynamic lubrication (EHL)), also has a considerable effect [208]. In high-speed bearings, an EHL lubrication regime occurs. This lubrication regime causes a pressure spike in the oil outlet, which increases the contact pressure and induces higher contact stresses. This may affect the contact surfaces more than the other lubricating regimes [195], i.e. boundary and mixed lubricating regimes that take place in the planetary stages of the wind turbine gearboxes [209], where there are lower rotating speeds.

2.9 Test rigs used to investigate RCF

The effect of factors related to RCF and reproducing fatigue damage features and microstructural changes has been studied by using bearings [54][97], twin disc machines [3][210], ball to disc contact [122], Ball to rod contact [189][211] and using thrust bearings [99][212]. [Figure 2-17](#) illustrates six types of test rigs commonly used in investigating the RCF and microstructural alterations. The Micro Pitting Rig (MPR) shown in [Figure 2-17\(a\)](#) consists of three discs applying pressure on a small test specimen of ~1 mm contact length. This rig was used by Gould and Greco works [49][211] to investigate the conditions required for initiating WEC and was also used by Keller et al. [116], to investigate the bearing axial cracking. [Figure 2-17\(b\)](#) shows a method used to test different sizes of real bearings. This investigation methodology was used by Haward [213], to investigate the damage in real WTGBs and develop a new concept for improving the reliability of the turbine bearings.

Small test discs have also been used to investigate the RCF phenomenon and the factors affect the damage initiation and propagation. A twin-disc test rig, seen in [Figure 2-17\(c\)](#) was commonly used. This methodology was also used to investigate the surface and subsurface damage under different contact stress and SR using curved and flat contact discs by AL-Tameemi et al. [155]. In 2017, Shu-Xin et al. [214] used two flat discs with different contact lengths to investigate the microstructural evolution under RCF in bearing steel. The flat discs were also used to study the crack growth in RCF by Seo et al. [215] and to simulate the line contact by Bruce [3], Garnham and Beynon [216], Gallardo-Hernandez and Lewis [217], Arias-Cuevas et al. [218], and Santa et al. [219]. The expected stress concentration at the test disc edges was ignored in these studies. The curved contact disc profile was also used to investigate the microstructural alterations in RCF by Evans et al. [26] and to analyze

the contact fatigue in gears at a particular point along with the gear tooth profile by Meneghetti et al. [220].

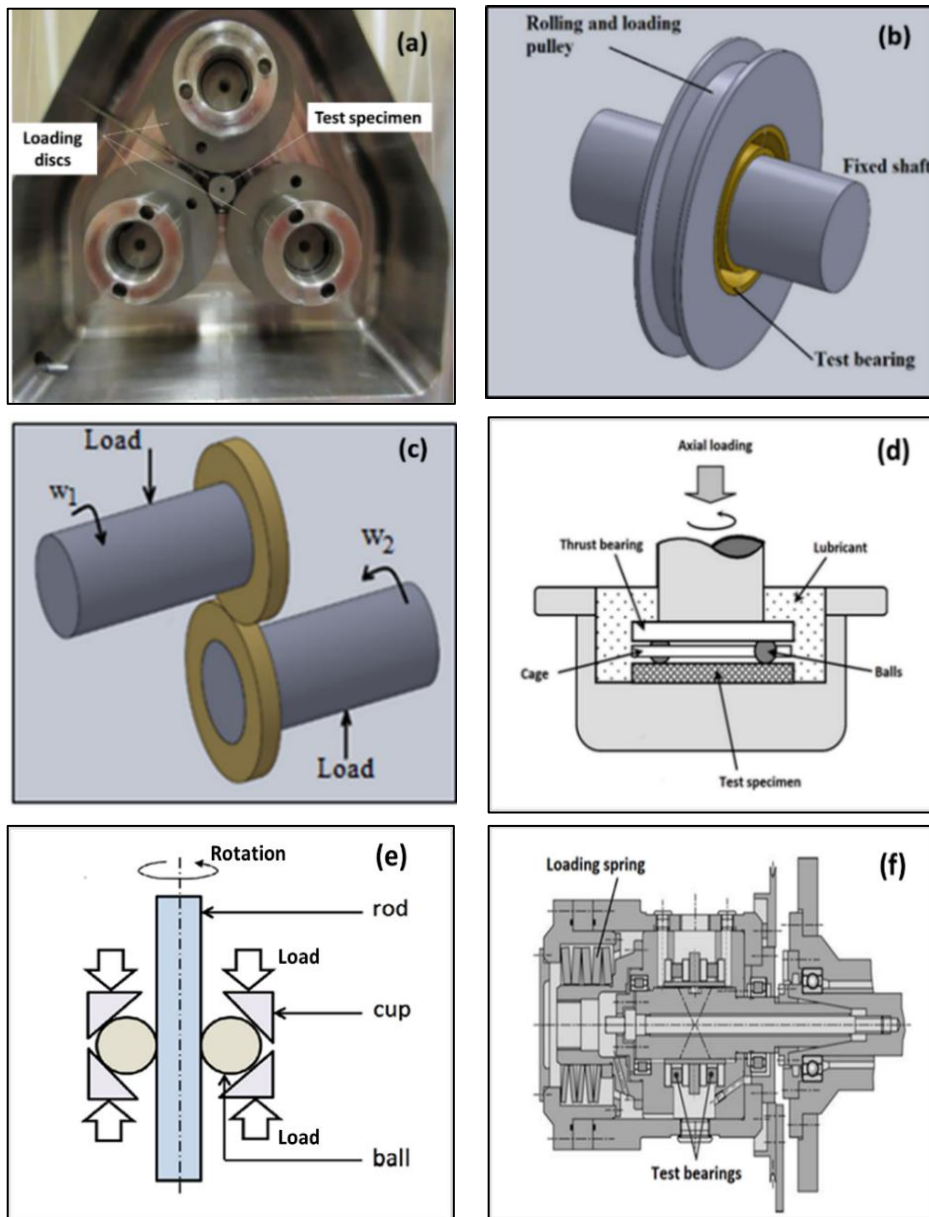


Figure 2-17: Typical test rigs used to investigate RCF failure. (a) MPR test rig [116]); (b) real bearing tester; (c) twin disc test rig; (d) thrust loading rig [122]; (e) ball against rod tester [189]; (f) thrust bearing test rig [99],[212].

The design can be shown in [Figure 2-17\(d\)](#) uses thrust loading on balls to produce high contact stress on a test specimen that will be cut to investigate the subsurface damage. This test rig was used by Hisao et al. [122] to investigate the effect of depth and size of small defects on the RCF strength. Another test rig with the details shown in [Figure 2-17\(e\)](#) uses loaded balls on a rotating rod to simulate RCF. This was used by Satya et al. [211] to analyze and draw three-dimensional characterizations of

WEBS and butterfly wings using automated serial sectioning. The last test rig includes testing of thrust bearings to produce damage by applying a compressive load through a loading spring as can be seen in [Figure 2-17\(f\)](#). This rig was used by many researchers such as Danielsen et al. [115] and Richardson et al. [166] to investigate the microstructural alterations in bearing steel and map them in a three-dimensional space using serial sectioning technique. Recently, Schwarze et al. [221] used a PWD4 test rig to apply dynamic loading and to investigate the damage modes in roller bearing inner races.

Because of the importance of wind turbine bearings, the National Renewable Energy Laboratory (NREL) built a drivetrain test platform with the real scale, of a 1.5 MW wind turbine. This test platform is used to investigate the effect of normal operating and some operating events such as shutdown and braking [113].

Instrumentation (placing of sensors and measuring instrument in WTG in the operating and testing fields) was used by Keller and Lambert [222] to have real operating data. However, rotating components of bearings are always submerged in a lubricant, and this causes problems for recording the real operating data. Studying key factors in WTGB failure using full-scale bearings is an uneconomical procedure due to requiring very large-scale test rigs which incur a huge cost.

No test rig can apply impact loading during the testing. However, the impact effect was studied separately by Bruce et al. [5]. They applied several impact cycles on a specific location on a flat test disc contact surface using ball impactor then subjected these discs to rolling and sliding contact using a twin-disc machine. It will be a more practical case study if the impact is applied in combination with the rolling and sliding which is similar to the case of real operating.

The test velocity (tangential velocity in the contact region) and rotational speed (the number of rotating cycles per unit time which is also called frequency), are very important due to their relationship with the straining rate and probably should be taken on consideration. Additives to lubricant may also have a considerable effect on WTGB failure [69]. Temperature change during the bearing operating has also significant importance due to its effect on the lubricant viscosity that changes the traction forces and SR.

Studies on the effect of impact loading are one of the rarest investigations in the previous literature due to the complexity of studying the impact subject and the high possibility of harming the hydraulic cylinders usually used for applying the

contact pressure by damaging the cylinder's pressure washers due to impact, vibration and transient loadings.

2.10 Fatigue life prediction theories

Rolling Contact Fatigue (RCF) failure is an unavoidable phenomenon even if the bearings are well mounted and lubricated, and kept free from moisture, corrosive reagents and abrasives [25]. Bearing life criteria have been selected depending on the contact stress, the bearing type and material. Lundberg and Palmgren derived a life formula presented as standard nowadays [23][104], which can be written as:

$$L_{10} = \left\{ \frac{C}{P_{eq}} \right\}^e * 10^6 \text{ cycle} \quad 2.4$$

where C is the dynamic load capacity in newtons (N), which can be defined as the load gives the bearing inner race a life of 10^6 cycles, P_{eq} is the equivalent radial load in newton (N) and e is an exponent has empirical values (3 for ball bearings and 3.333 for roller bearings) [25][104]. This formula is basically based on 90% of survival under the same loading and operating conditions. This theory has several limitations regarding the accuracy of the predicted bearing life because it depends on constant and radial loading; thus, modification factors have been added to make the formula has more reliable for different operating conditions [27][223].

Arakere [224] made a review of the life prediction for gigacycle bearing steel and pointed out the associated difficulties of getting a precise life prediction. He specified the importance of compressive mean stress, material properties change in the subsurface, the stress field and the phenomena associated with RCF in different scales (nanometers to millimeters) as the main limitations of the life prediction methods. Fracture mechanics was also used in life prediction theories by studying the crack growth rate and stress concentration around the crack tips. Warhadpande et al. [159] studied the crack propagation in a Hertzian contact model using Finite Element (FE). They used an elastic-plastic material behavior. Their results revealed that crack growth represents ~15% to 40% of the total RCF life. They also showed

that the material defects within the contact region probably lead to a considerable decrease in fatigue lives and increase the scatter in life results.

The S-N curve (Woehler curve) is the basis of any life prediction formula. However, in the majority of the engineering materials, there are two distinct zones in the S-N curves. This refers to two different behaviors of the materials depending on the loading level [104][225].

The first linear damage accumulation theory was proposed by Palmgren in the 1920s. Later, Miner expressed this theory in a mathematical formula as given in [Eqn. 2.5](#);

$$D = \sum_1^k \frac{n_k}{N_k} \tag{2.5}$$

where D is the damage, k is the number of loading levels, n_k and N_k are the number of loading cycles and the number of cycles to failure under the specific loading level respectively. Despite making this formula dependent on the number of rotating cycles only, it is still one of the most popular rules used in fatigue life prediction and damage accumulation analyses due to its simplicity and applicability. P-M theory does not take the effect of load sequence, i.e. when the loading level changes from high to low and vice versa, into consideration [226][227][228]. However, previous literature showed that High to Low (H-L) loading sequence has a lower fatigue life than that when the loading sequence applied is Low to High (L-H) [229][230]. P-M theory claims the damage to be linearly accumulated, however, in practical cases, crack size which represents the important damage indicator is changing after each cycle. Thus, damage cannot be linearly accumulative due to different damage levels caused during each loading cycle [134][231]. Marco-Starkey [232] introduced a nonlinear damage theory by considering the effect of loading sequence on a non-linear damage curve (D-r curve), in which the damage is represented by a power relation as:

$$D = \sum r_k^{x_k} \tag{2.6}$$

where x_k is a variable quantity depends on k^{th} loading level and r is the cyclic ratio used in [Eqn. 2.5](#). Owen and Howe [233] expressed the fatigue damage in a power series formula of the cyclic ratios as:

$$D = A \left(\frac{n_k}{N_k} \right) + B \left(\frac{n_k}{N_k} \right)^2 \tag{2.7}$$

where A and B are constants. This formula postulated two effects, the first is linear and depends on the fraction “ A ”, while the second is nonlinear.

Lamatre [234] estimated fatigue damage using the form,

$$D = 1 - \left(1 - \frac{n}{N}\right)^w \quad 2.8$$

where w is an exponent depends on stress amplitude, i.e. the difference between maximum and minimum stress levels during a fatigue cycle, mean stress (the average of the maximum and minimum stress levels) and fatigue limit, while Dattoma et al. [235] suggested a more complicated formula which can be expressed as:

$$D = 1 - \left(1 - \left(\frac{n}{N}\right)^{1/(1-A)}\right)^{1/(1+B)} \quad 2.9$$

where A and B are constants determined based on the material type.

Double Linear Damage Rule (DLDR) was suggested by Grover [236], He postulated that damage had two linear stages: crack initiation and crack propagation. This method depends on α which represents the life fraction factor for the initiation stage. DLDR can be expressed mathematically as:

$$N_I = \alpha N_f \quad \text{for crack initiation} \quad 2.10 \text{ (a)}$$

$$N_{II} = (1 - \alpha)N_f \quad \text{for crack propagation} \quad 2.10 \text{ (b)}$$

where N_I represents the number of cycles for crack initiation, α is a fraction of crack initiation, N_{II} the number of cycles for crack propagation and N_f is the number of cycles to failure.

Shimizu [236] proposed a life prediction model depending on Weibull life distribution slop and survival, load capacity and load-life component (e):

$$L_f - \exists = \left(\frac{C}{P_{eq}}\right)^e \left(\frac{\ln s}{\ln 0.9}\right)^{\frac{1}{m}} \quad 2.11$$

where m is the Weibull slope, \exists is the minimum life prior to failure, P_{eq} equivalent load, C the dynamic load capacity, s is the raceway survival probability and L_f is the fatigue life.

Considering the damage induced during crack propagation stage, Manson [237][238] suggested another two expressions;

$$N_I = N_f - \beta N_f^{0.6} \quad \text{for crack initiation} \quad \mathbf{2.12(a)}$$

$$N_{II} = \beta N_f^{0.6} \quad \text{for crack propagation} \quad \mathbf{2.12(b)}$$

where β is a fatigue life coefficient for the crack propagation stage. This theory was tested under two constant amplitudes with H-L loading sequence and had good results. This method depends on finding the knee point of the double curves i.e. the intersection point of the two curves.

Linear Elastic Fracture Mechanics (LEFM) expressed the crack growth per cycle (da/dN) depending on crack length, loading level and mechanical properties of the material [239]. This relation can be expressed mathematically as:

$$\frac{da}{dN} = Af(\sigma)a \quad \mathbf{2.13}$$

where A is constant, $f(\sigma)$ is a function depends on the loading and material type and a is the crack length. Huiying et al. [228] postulated another non-linear fatigue damage accumulation model based on the damage curve approach and taking the load interaction effect into consideration. This model was based on the fact: crack length is propagating from a_o to a by following the rule:

$$a = a_o + (0.18 - a_o) \left\{ \frac{n_a}{N_f} \right\}^{\left(\frac{2}{3} \right) N_f^{0.4}} \quad \mathbf{2.14}$$

where n_a is the number of cycles to propagate the crack length from a_o to a and N_f is the number of cycles to failure and the damage can be estimated by:

$$D = \frac{1}{0.18} \left[a_o + (90.18 - a_o) \left(\frac{n_a}{N_f} \right)^{\left(\frac{2}{3} \right) N_f^{0.4}} \right] \quad \mathbf{2.15}$$

This model has a noticeable drawback because it assumes that damage can occur even when the ratio $\frac{n_a}{N_f}$ is equal to zero, i.e. there is no rotation. This damage is equal to $\frac{a_o}{0.18}$ which means that a crack or defect already exist in the material and the initial crack or defect plays the main role in damage. Damage and crack propagation considered in this

model is independent of loading levels. If there is an initial crack which has a length of 0.18 unit-length, the damage will be 100%! This means that, even if there is no cyclic loading, a failure may occur. This interpretation does not present a logical base for the damage accumulation process.

A damage Curve Approach (DCA) and Double Damage Curve Approach (DDCA) were developed by Manson and co-workers [226][238]. DCA is expressed as;

$$a = a_o + (a_f - a_o)r^q \quad 2.16$$

where q is constant depends on the material, r is the cyclic ratio i.e. the ratio of rotating cycles to the number of cycles to failure, a_f , a and a_o are the final, instantaneous and initial crack length respectively. The damage in this formula is expressed as the instantaneous crack length to the final crack length i.e. $D = \frac{a}{a_f}$ and the damage function simply becomes:

$$D = r^q \quad 2.17$$

In DDCA, damage can be calculated as [239]:

$$D = [(Ar)^k + (1 - A^k)r^{kq}]^{1/k} \quad 2.18$$

where k is an exponent represents the best curve fitting to DLDA and A is constant. To overcome the drawbacks of depending P-M linear damage accumulation theory on the fraction of the number of cycles under consideration only and its independence on loading level, Kaminski [233] used both stress and number of cycles for estimating the damage as:

$$D = \frac{n}{N} \cdot \left(\frac{\sigma_a}{\sigma_{a \max}} \right)^e \quad 2.19$$

where σ_a and $\sigma_{a \max}$ are the loading and maximum stresses respectively and e is an exponent related to the material.

Wang and Brown [240] discussed two theories in detail, the first is the Bannantine-Socie method and the second is the Wang-Brown method. The former suggested that; fatigue occurs in a plane experiencing maximum damage and the local strain approach is used to identify this plane. The second method depends on short and long cracks and a

specific cycle counting technique to estimate the damage. Continuum Damage Mechanics (CDM) is used to introduce a coupling between stress-strain behavior and the damage process. Chaboche [241] inserted Damage Growth Equations (DGEs) which consisting of Creep, fatigue, ductile and brittle damage and their interaction to describe crack initiation and propagation depending on fracture mechanics.

Studying the effect of damage on material properties is an alternative method for studying the damage accumulation process. Mechanical properties such as damping, fatigue limit and modulus of elasticity are varying during fatigue failure process. This point is used by Brooks and Parry [239] to investigate the change in natural frequencies due to damage by considering the change in these properties as an indication of fatigue damage. Reduction in material modulus of elasticity under fatigue loadings also used to estimate the damage, this can be expressed as:

$$D = 1 - \frac{E_n}{E_o} \tag{2.20}$$

where E_n and E_o are the modulus of elasticity after n loading cycles and the modulus of undamaged respectively. A similar formula to Eqn. 2.20, but with using material strengths (σ_u) instead of the modulus of elasticity was also used. Henry[242] suggested that, fatigue damage lowers the endurance limits with increasing the number of cycles until they become zero at failure. A non-linear endurance limit reduction under cyclic loading is suggested and used as a damage indicator. There are many models to describe these non-linear reduction relations [242][227].

More complicated models were postulated by Loannides and Harris [243] and Arakere [224] depending on the volume stressed with levels beyond the elastic limit.

A one-parameter accumulative fatigue damage model was proposed by Rege and Pavlou [126]. This unique stress amplitude dependence parameter is $q(\sigma_i)$ which can be calculated as;

$$q_i = \left(\frac{2\sigma_i}{\sigma_s} \right)^{-0.75} \tag{2.21}$$

where σ_i is the applied stress and σ_s is the intersection of the S-N curve with the stress axis. This method depends on knowing the knee point of the S-N curve i.e. fatigue strength limit. The authors recommended more experimental results to test this method.

There are many hundreds of life prediction models in uniaxial and multiaxial loadings, however, life prediction theories can be classified into two types; stress-based theories and strain-based theories. The former type is normally used for experimental work, while the latter is used for theoretical approximations. The previous life prediction theories and models cannot predict WTGB premature failure precisely or at least with a reasonable percentage of error. Therefore, introducing a more accurate life prediction model is a big challenge that needs a solution.

2.11 Summary and research gap

Rolling Contact Fatigue (RCF) failure is a chronic issue in a considerable number of engineering applications such as; bearings, gears, cams and train tracks. One of the interesting issues of RCF can be observed in Wind Turbine Gearbox Bearings (WTGBs) which suffer from premature failure by flaking under rolling/sliding and impact operating due to various operating conditions and events. This premature failure often within 5% to 20% of the bearing design life. This failure increases the wind energy cost due to unplanned maintenance and early replacements. WTGB damage is often associated with microstructural alterations in specific locations beneath the contact surfaces, especially in the bearing inner races. A considerable number of hypotheses have been postulated to explain the microstructural alteration damage features, and to predict the main causes and mechanisms of these damage feature initiation and propagation. However, this phenomenon is not fully understood due to the considerable number of factors shown to have a significant effect on it. It is planned to conduct a number of RCF tests to investigate whether these testing conditions are able to produce the microstructural alterations.

The effect of factors on the premature failure of WTGBs can be classified into mechanical, tribological and microstructural effects in addition to the associated phenomena to this failure as illustrated in [Figure 2-3](#). Different phenomena were also observed throughout the previous investigation such as; hydrogen embrittlement, carbon, and chromium diffusion and electrical current induction. Recently, the investigation of these phenomena and their role in premature bearing failure is continuing. Material cleanliness was considered as the main factor affecting RCF life, and the inclusions are specified as the main damage initiation site.

The assessment of effective factors has specified the importance of compressive loading and slipping as the most significant factors. However, the effect of impact loading on WTGBs was also demonstrated and postulated to have a significant role in bearing life. The effect of impact has had insufficient investigation because of the complexity of this subject and the unknown impact loading levels in WTG components. Furthermore, the life of WTGBs cannot be precisely predicted because of the large number of effective factors relating to their lives.

RCF can be initiated either from the contact surface or subsurface. However, the competition between these two sites depends on the predominance of the mentioned factors in [Figure 2-3](#). The effect of loading levels causing failure can be observed as damage features and changes on and beneath the contact surfaces. The surface investigation had less attention in the previous studies. However, investigating the contact surface hardness can provide valuable information about the overloading stress level; while the loading and slipping can change the contact surface roughness which also should be investigated. Furthermore, the butterfly wings distribution within the subsurface region to predict the stress responsible for their initiation which used by Brückner et al. [30] will be used to predict the subsurface stress responsible for other subsurface damages such as damaged inclusions and cracking.

3

DAMAGE INVESTIGATION OF FAILED PLANETARY BEARINGS

In this chapter, two planetary bearings from a failed gearbox of a multi-megawatt wind turbine undergo surface analyses and destructive subsurface investigations. These analyses and investigations were to characterize the surface and subsurface damage features. This represents a trial of understanding the bearing damage initiation mechanism leading to the final bearing failure by flaking and estimating their operational loading level. The two bearings, one is an Up Wind (UW) Single-Row Cylindrical Roller (SRCR) bearing and the other is a Down Wind (DW) Double-Row Cylindrical Roller (DRCR) bearing. The analysis of operational loading levels was to look for the main factors affecting the bearing failure, which were probably incident from features on the contact surface and in the subsurface. For example, if the overloading exceeds the elastic limit, the surface will undergo a hardening and the future testing levels should be beyond the elastic limit, however, compression and slipping affect the surface roughness. The non-destructive surface investigation include both the contact surface roughness and hardness, while the subsurface investigation consisted of the distribution of the microstructural damage features (damage at a microlevel in the material structure) including the damaged inclusions, by either separation or cracking. The distributions of these damage features then correlated with the subsurface stress distributions using Hertzian contact analysis. The samples for the destructive investigation were cut from the severely damaged regions then examined in axial and circumferential directions using a Light Reflection Microscope (LRM), Scanning Electron Microscope (SEM) and Energy Dispersive X-ray analysis (EDX) technique.

3.1 Investigation of failed planetary bearings

Two damaged inner races of planetary bearings from a multimegawatt WTG were provided by a WT company. The first bearing race is an Up Wind (UW) bearing race, i.e. located towards the turbine hub side. It is a Single Row Cylindrical Roller (SRCR) bearing, while the other is a Down Wind (DW) bearing race, i.e. located away from the turbine hub, and is a Double Row Cylindrical Roller (DRCR) bearing. [Table 3-1](#) illustrates the WTG specifications from which the two bearings were taken in addition to the number of operating hours, while, the damaged inner races can be seen in [Figure 3-1](#). The contact surfaces of the inner races are classified into three zones according to the damage level. Zone 1 consists of the severely damaged regions, each one represents $\sim 3\%$ of the race circumference, while Zone 2 is the indented regions with $\sim 60\%$ of the circumference and Zone 3 is the undamaged region with $\sim 37\%$.

Table 3-1 Wind turbine gearbox specifications and working hours.

Details	Value (unit)
Nominal power	2000 (kW)
Nominal rotor input speed	16.7 (rpm)
Nominal generator output speed	1680 (rpm)
Planet relative speed	42.47 (rpm)
Generator hours with power production	64,658 (hrs)

Zone 1 in both UW and DW bearings have a maximum circumferential length of $\sim 23\text{mm}$, while their lengths in the bearing axial direction were larger than the roller strike length ($\sim 73\text{ mm}$). In the UW bearing, Zone 1 has approximately a constant maximum circumferential length of $\sim 23\text{ mm}$ while, the DW bearing has a taper shape damage region ending at $\sim 3\text{ mm}$ at the axial end of the roller strike, i.e. away from the bearing rim. Comparing the area of the two severely damaged zones, the UW bearing has a larger severely damaged area than the DW bearing which means it was subjected to a higher loading level than the DW bearing. This supports the finding of La-Cava et al. [55]. For the calculation procedure, the rolling element length has been estimated depending on the roller strike length appears on the axial direction of the bearing race because the rolling elements were not provided with the bearing races.

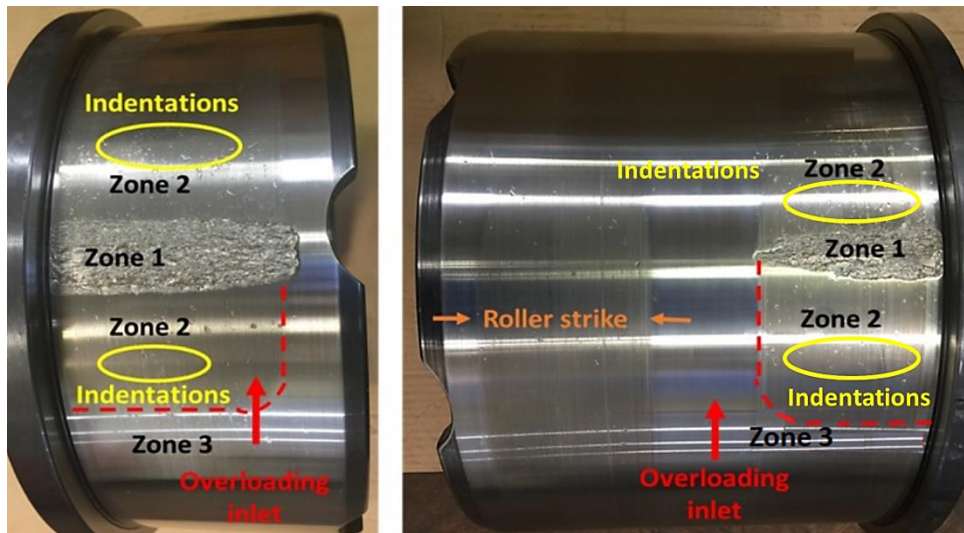


Figure 3-1: Investigated failed inner races and specimen locations (upwind on the left-hand side and downwind on the right).

Indentations can be seen on both sides of the severely damaged regions. However, the indentation frequency is lower in the load inlet zone (in the lower side of the bearings shown above). If the two bearings were taken from the same planet which did not approve by the provider company. The severely damaged regions were probably produced due to misalignment, i.e. planet pin bending and stress concentration. This expectation came from the way of contacting the spacer slots of the two races as can be seen in Figure 3-2. Misalignment can produce stress concentration and overloading as discussed in Section 2.4.

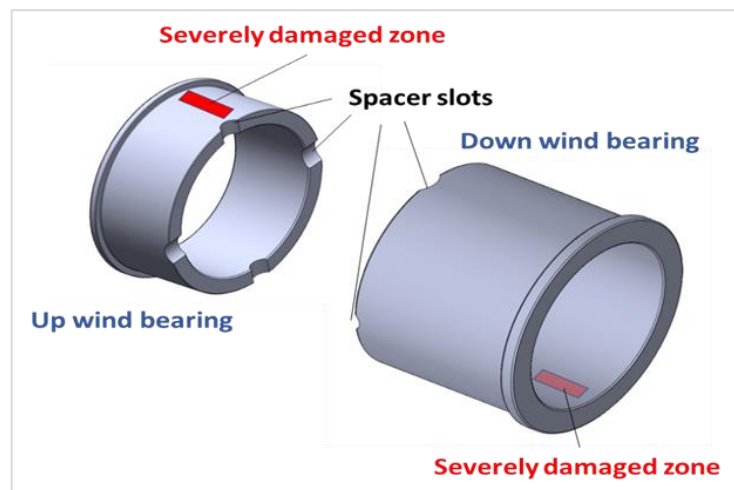


Figure 3-2: Spalling damage locations due to misalignment.

Only the failed inner races were provided from the WT company; the outer ring, roller dimensions, and the number of rollers were not provided due to the company confidential policy. Thus, the estimated dimensions illustrated in Table 3-2 (in red)

are taken from the nearest SKF bearing type having the same inner race diameter which is SKF NCF 3048 CV [244]. The number and length of rolling elements were also checked using SolidWorks software by redrawing the bearings at the real scale. These dimensions were used in a calculation procedure using Hertzian contact theory.

Table 3-2: Measured dimensions of the inner races and rollers (all dimensions in mm).

Bearing type	SRCR	DRCR
Inner race bore Dia.	240	240
Inner race Dia.	290	290
Axial length	96	210
Rim outer Dia.	310	312
Rim Thickness.	17	17
No. of roller	16	16x2
Roller Dia.	50	50
Roller length	70	70

Mechanical properties of the bearing material affect the calculation results. These properties depend on the chemical composition of the material and the heat treatment procedure which is one of the most confidential procedures of the bearing manufacturing companies. Table 3-3 illustrates the chemical composition of AISI-52100 steel normally used as a material for most of the large-scale bearings [33], [124][133], while Table 3-4 illustrates the mechanical properties of the material used in the calculation procedure [33][142].

Table 3-3: Chemical composition of the bearing material (AISI 52100/100Cr6) [33][133].

Matter	C	Mn	Si	P	S	Cr	Mg	Fe
% wt	0.98 ~1.10	0.25 ~0.45	0.15 ~0.35	0.025 max	0.025 max	1.30 ~1.60	0.00 ~0.10	Remaining

Table 3-4: Mechanical properties of the bearing material [33][142][124].

Modulus of elasticity E (MPa)	Poisson's ratio ν	Ultimate stress tensile (MPa)	Yield stress under compression (MPa)	Vickers hardness
210,000	0.3	1748	2550	745±20 HV

3.2 Stresses induced in the investigated bearings

Specifying the rated load and predicting the loading range in WTGBs depends on the turbine capacity and its gearbox design, however, the loading level will help to estimate the rated loading stresses of the future planned tests. The contact force on any WTGB can be calculated based on the generator torque from the generator output power and rotational speed using the power-law (SI system is used in these calculations);

$$P_{gen} = T * \omega_{gen} \quad 3.1$$

where P_{gen} is the generator output power, T is the torque on the generator shaft and ω_{gen} is its rotational speed. To calculate the normal contact load (F_N); transfer this power to the planetary stage, the gear ratio (G), ring and sun gear diameters (R_D and S_D respectively), the total number of roller rows of the planetary bearings (H), (for these bearings $H=3$), and the number of rollers in each row ($Z_{rol}=16$) can be used in [Eqn. 3.2](#). Three plants in the gear planetary stage are usually used. The details of this equation derivation can be seen in [Appendix A](#).

$$F_N = \frac{9.333 * G * P_{gen}}{H * \eta * (R_D + S_D) * \omega_{gen} * Z_{rol}} \quad 3.2$$

where F_N is the maximum Hertzian contact load, and η is the overall drivetrain efficiency. This efficiency can be calculated by multiplying the mechanical and electrical efficiencies of the turbine drivetrain. [Figure 3-3](#) shows the contact of a roller and an inner race in addition to pressure distribution under the Hertzian contact condition.

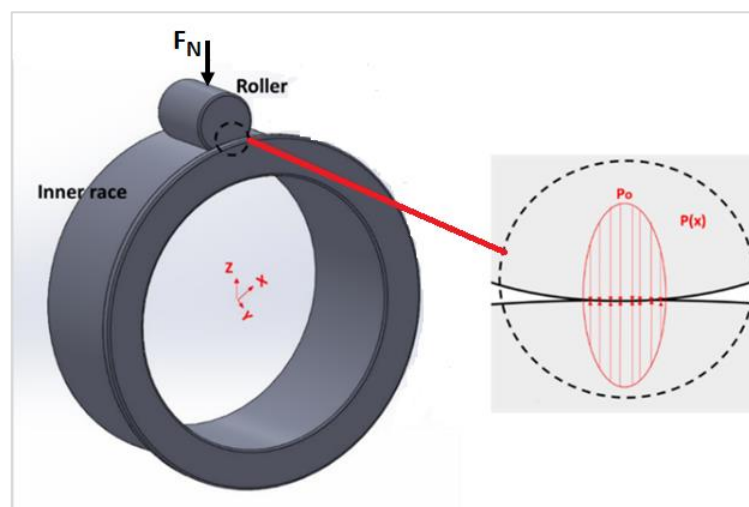


Figure 3-3: Hertzian contact of two parallel cylinders.

The UW bearings carry a load around 30% to 50% more than what the DW bearings carry [55]; therefore, the average of these percentages is used, i.e. 40% more than the DW bearing will be considered in the calculation procedure. In this calculation, it was assumed that there was an equal load share among the roller rows and the three planets. The calculated contact stress by following the calculation procedure in [Appendix A](#) was found to be **~1.8 GPa**. The procedure of calculating this contact stress was by calculating the torque on the generator shaft from its output power and rotational speed then, this torque should be transmitted to the turbine rotor after dividing the generator power by the drivetrain overall efficiency to find the rotor torque. This torque is divided into three forces at the centers of the planet pins. After that, these forces are divided by the number of planet bearings rows and the upwind bearing row considered to carry 40% more than the calculated pin force [55]. The calculated maximum contact pressure on one roller is more than the design stress recommended in the standards [23][104] which specified as 1.5 GPa to 1.7 GPa. This calculation procedure assumes an equal share factor among the planets, i.e. each planet carries the same loading level. If the share factor of the planets is not equal, the contact stress level on one planet can be higher and the bearings of this plant may fail before the others. Stress distributions beneath the contact region in circumferential plane (the rotating plane) under this loading level are shown in [Figure 3-4\(b\)](#). This represents the stress level distributions independently on whether the stress is surface or subsurface. There are stresses having small values as can be seen outside the contact region (for more information about these small stresses see Engineering Tribology book by Stachwowiak and Batchelor) [195]. These distributions are calculated by applying Hertz theory and then the super-position technique was used to add the stresses due to traction between the contact surfaces [195]. The friction coefficient of 0.05 for well-mounted bearings with sufficient lubrication was specified by Harris and Motzala [25] and used in this analysis. Over-rolling which means carrying the bearing more than its design load is expected. Therefore, subsurface stresses were also calculated for a 20% increase in the contact pressure as shown in [Figure 3-4\(c\)](#).

Applying a traction force changes the depth of the subsurface stresses and brings the maximum shear and Von-Mises stresses towards the contact surface [195][245]. It is important to point out that, there is a sudden change from positive to negative stresses in σ_2 at the end of the contact region, i.e. in the opposite side of the rolling direction. This makes this region a preferable location of surface damage initiation.

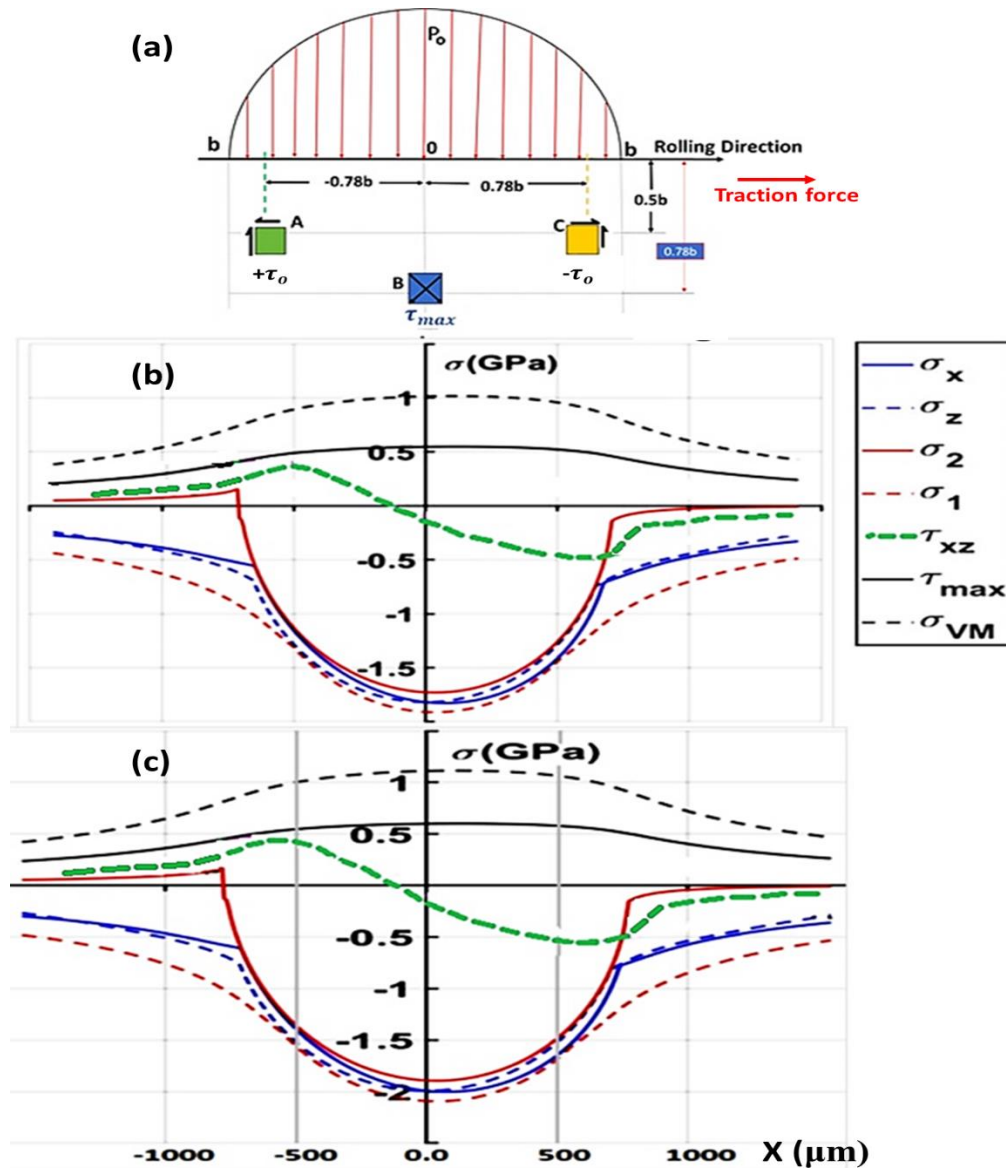


Figure 3-4: Effect of increasing contact pressure on stresses (a) contact pressure distribution and locations of maximum shear stresses; (b) stresses under 1.8 GPa contact pressure and friction ($\mu=0.05$); (c) stresses under 2.15 GPa contact pressure and friction ($\mu=0.05$).

Figure 3-5 presents three subsurface stress scenarios with the depth beneath the contact surface (z) that are commonly considered as the main causes of the subsurface damage in the previous literature which are: von-Mises, maximum shear and orthogonal shear stresses. 5% traction coefficient is used in the first analysis (on the left-hand side) then increased to 15%, to show the effect of traction and specifying the stresses maximum depths under 1.8 GPa contact stress. The main aim of this analysis is to correlate the maximum subsurface stress distributions with the maximum frequency of different damage features to predict the stress responsible for each damage type.

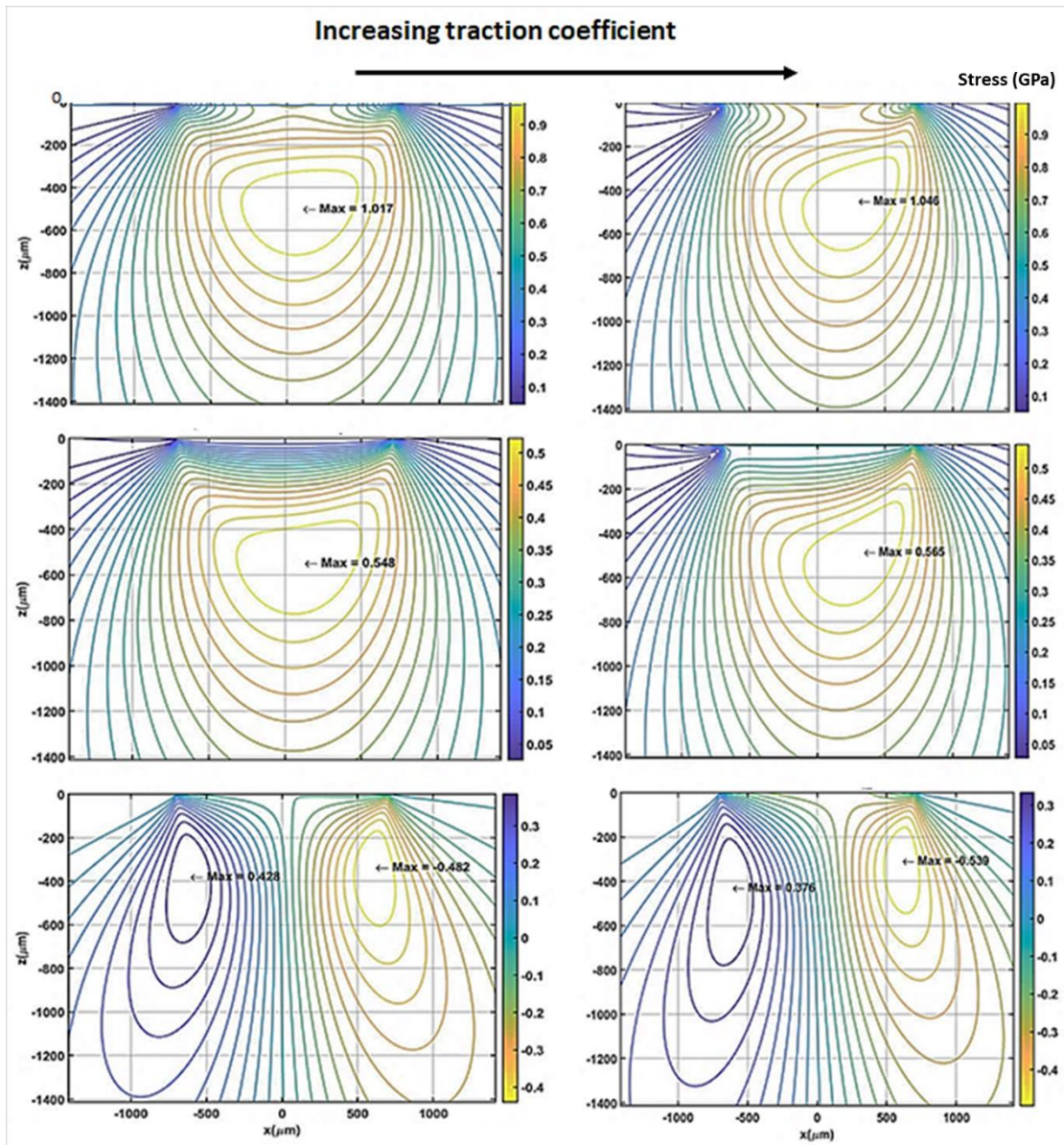


Figure 3-5: Variation of subsurface stresses von-Mises (top), maximum shear (middle) and orthogonal shear (down), with increasing friction coefficient under compression of 1.8 GPa.

Subsurface damage initiation has been confirmed by the previous studies [13][99], [112]. [Figure 3-6](#) shows the variation of the calculated three stresses with the depth corresponding to those in [Figure 3-5](#). maximum shear and Von-Mises stresses are increased and become closer to the contact surface with increasing traction force. The values of this stress affect more on the contact surface with increasing friction. This may declare the responsibility of Von-Mises stress for the surface crack initiation which is confirmed to occur under high traction levels. When the traction coefficient increases to 0.3, the calculations showed the maximum Von-Mises stress being at the contact surface [25].

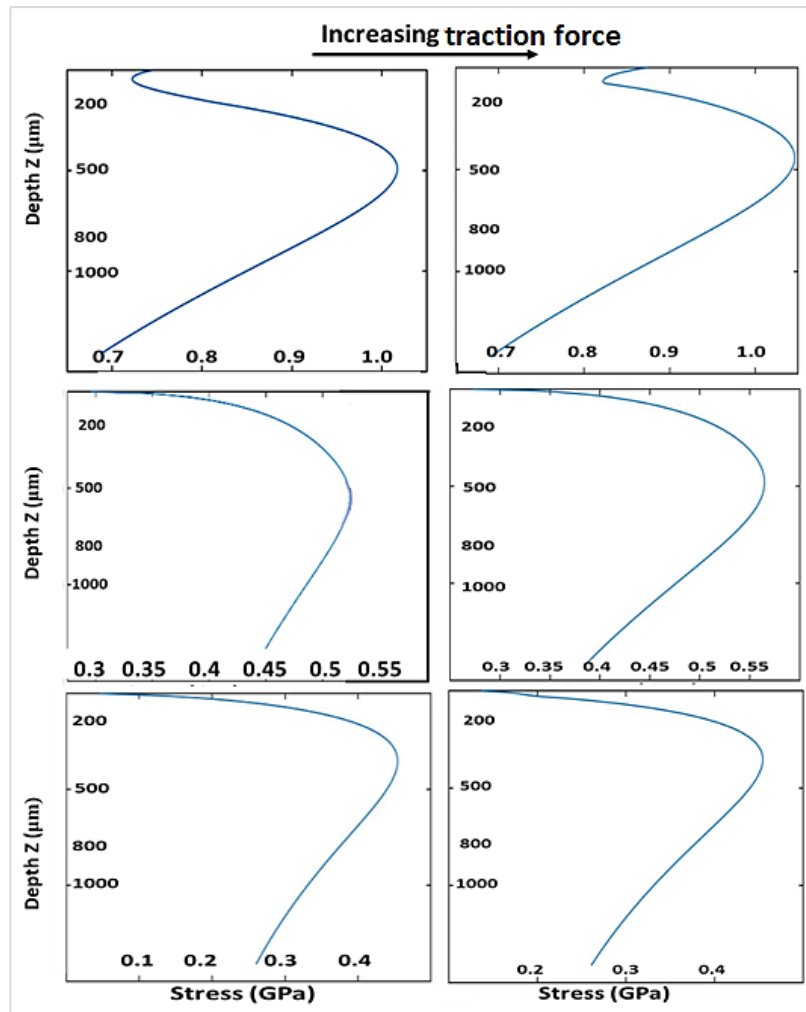


Figure 3-6: Maximum subsurface stresses distribution beneath the contact region under a compressive stress of 1.8 GPa and coefficient of friction ($\mu=0.05$ and 0.15); von-Mises (top); maximum shear (middle) and orthogonal shear (bottom).

Increasing the contact pressure and traction coefficient changes the magnitude and location of the maximum subsurface stresses as illustrated in Table 3-5. The magnitudes in this table were calculated under the same contact pressures and traction coefficients in the previous analyses. The depth of Von-Mises and maximum shear affect more than the orthogonal shear depth with increasing the traction coefficient. This may point out the responsibility of these stresses on the subsurface damages observed in different depths.

Table 3-5: Quantitative variation of maximum subsurface stresses and locations with contact pressure and surface traction coefficient.

Stress type	1.8 GPa contact pressure and 5% traction	1.8 GPa contact pressure and 15% traction	2.15 GPa contact pressure and 5% traction	2.15 GPa contact pressure and 15% traction
	Stress value (MPa)/ Depth (μm)	Stress value (MPa)/ Depth (μm)	Stress value (MPa)/ Depth (μm)	Stress value (MPa)/ Depth (μm)
τ_{xy}	482/-331.89	539/-303.64	528/-363.57	590/-332.63
τ_{max}	548/-543.73	565/-480.18	600/-595.63	619/-526.01
σ_{vM}	1017/-494.30	1047/-444.87	1114/-541.48	1146/-487.34

Quantitative analyses of varying depth and stress values with the variation of contact pressure and traction coefficient (μ) are illustrated in Table 3-6. In this analysis the traction coefficient varies from 0.05 to 0.15 while, the compression load varies between 1.8 GPa and over-loading of 20%, i.e. 2.15 GPa. Both stress values and depths are varying with the same absolute percentage of ($\sim 9.52\%$) with varying the contact pressure, however, with the variation of traction coefficient, the values of orthogonal shear stress (τ_{xy}) were affected more than the other subsurface stresses, this probably because the traction is applied in the same direction of the orthogonal shear. The depths of the maximum shear stress were affected more with increasing the traction coefficient (μ) followed by von-Mises stress and then the orthogonal shear stress. This may explain the increasing of damage frequency close to the contact surfaces due to this considerable role of traction.

Table 3-6: Percentages of depth and stress variations with the variation of contact pressure and traction coefficient.

Stress type	Increasing of μ from 0.05 to 0.15				Increasing of contact stress from 1.8 to 2.15 GPa			
	% stress variation under 1.8 GPa	% stress variation under 2.15 GPa	% depth variation under 1.8 GPa	% depth variation under 2.15 GPa	% stress Variation under 5% μ	% stress Variation under 15% μ	% depth variation under 5% μ	% depth variation under 15% μ
τ_{xy}	11.83	11.74	- 8.51	- 8.51	9.54	9.46	- 9.55	- 9.55
τ_{max}	3.10	3.17	- 11.69	- 11.69	9.49	9.56	- 9.55	- 9.54
σ_{vM}	2.95	2.87	- 10.00	- 10.00	9.54	9.46	- 9.54	- 9.55

3.3 Investigation procedure

Before conducting a destructive investigation for the bearing material microstructure, and cutting the inner races to small specimens, surface investigations were undertaken. Figure 3-7 illustrates the investigation stages of the races which include surface and subsurface investigations to get the results. This figure also illustrates the materials and machines used at each stage in addition to the details of the sample preparation processes.

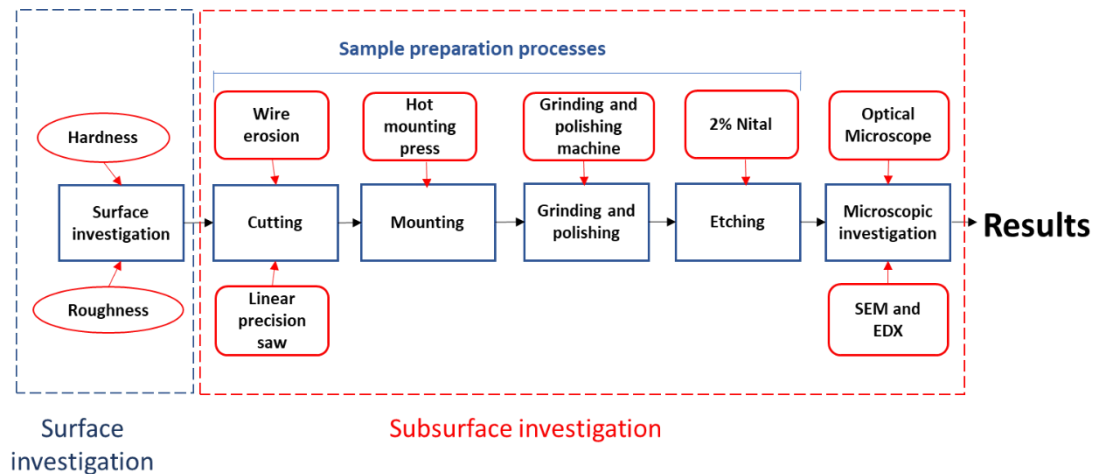


Figure 3-7: Investigation stages of the bearing inner races.

Investigating the contact surface was very helpful to direct the case study towards using the changes of the surface properties in estimating the operating level and having a general view about the future testing that should be considered in testing WTGBs or the alternative tests using discs. Despite the significant number of studies dealing with bearing failure, there is an insufficient focus on changing the properties of the contact surface such as roughness and hardness. The surface investigations were conducted in damage zone 2 including surface hardness and roughness. This zone has two individual regions separated by the severely damaged area (Zone 1). These two regions can be distinguished which are the loading inlet region and the loading outlet region depending on the rotational direction as shown in Figure 3-8. Nevertheless, the subsurface investigation was made in Zone 1. This figure shows a very interesting marking of the roller inlet strike. The inlet to the loading zone shows a non-uniform region (path) in the roller entry to the loading region. This non-uniform path confirms that the rollers skewed when they entered the loading region that may have caused overloading [3] and sometimes caused a breaking down of the roller cage [148]. The sudden inlet to the loading region (expected from the short distance of the loading inlet region), can produce vibration and misalignment that may cause bearing premature failure [3]. However, the variation of the light

reflected from the loading region due to the contact in the asperities level [25], was clearly observed.

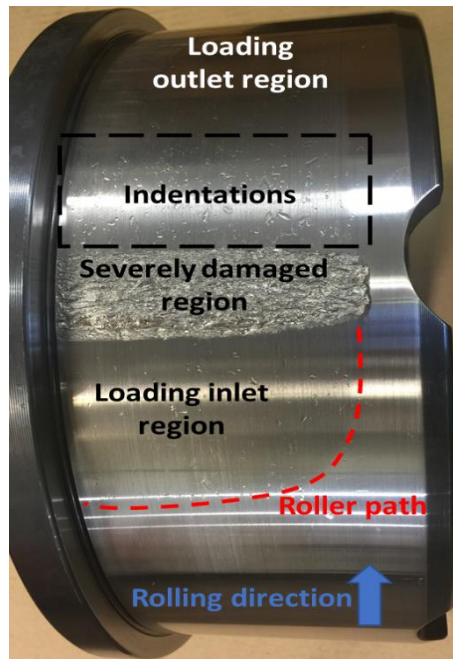


Figure 3-8: Surface damaged regions in the investigated up-wind bearing.

The inner races have a large number of noticeable indentations on their contact surfaces inside the roller path in the loading region. The surface observation of indentations and wear shows that the loading region is larger than 50% of the circumferential direction length specified by Harris and Motzala [25]. Bruce [3] specified the wear zone as $\sim 55\%$, however, in this study the loading region specified according to roller path and indentations was found to be $\sim 63\%$ of the inner-race circumference. This means there is a positive clearance (tolerance) between the bearing inner race and rollers [25]. After the surface investigation, the severely damaged bearing areas (Zone 1 of each bearing) were cut for conducting the subsurface investigation.

A *Sodick* wire erosion machine was used for the first cutting process then, the same machine was used to cut the chosen pieces to reduce their thickness to 10mm (below the contact surface); to enable fixing two specimens in each microscopic investigation sample. Small specimens were cut from Zone 1 using a linear precision saw to get the final specimen dimensions. A low cutting rate of 1.0 to 1.5 mm/min and a high cutting speed of 3500 rpm was used to reduce the determinantal effect of the cutting process on the microscopic damage features. The small specimens finally had the dimensions 23x13x10 mm. These dimensions allow for the previously investigated subsurface depth in the range of 1 mm to 1.5 mm [3], to be applied in this study.

Figure 3-9 shows a Light Reflection Microscope (LRM), and two types of SEM microscopes that were used in this study. The images from the LRM were taken using a *Nikon Eclipse LV 150* microscope. Its lenses have magnification levels between 50 to 1000. This microscope is attached to computer software to measure length, angle and scale on the investigation surface in addition to the capability of image contrast correction that can be controlled under different magnification levels. SEM has a higher magnification ability than LRM with black and white images. Energy Dispersive X-Ray (EDX) is available with the *FEI-inspect F SEM* shown in Figure 3-9(b). The accelerating voltage used was 20 kV, the spot size was 2.5 μm and Working Distance (WD) was ~ 10 mm. This microscope has well-focused images, with over X30,000 magnification. The second SEM used is a *TM3030Plus* shown in Figure 3-9(c).

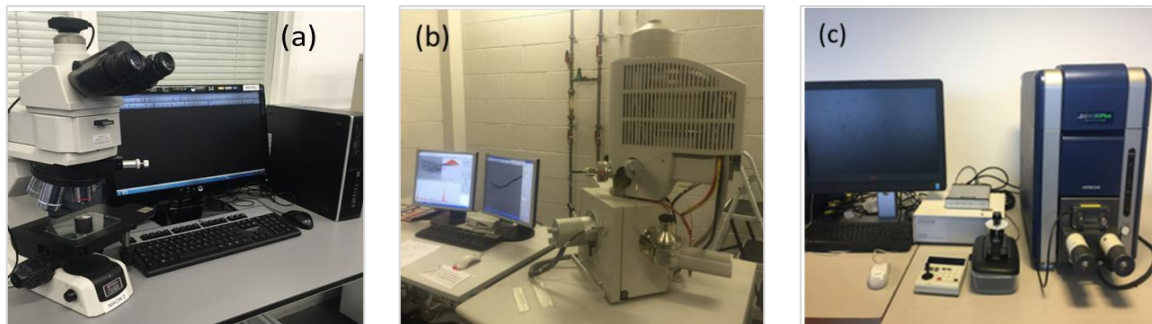


Figure 3-9: Microscopes used (a) Optical Nikon Eclipse LV 150 microscope; (b) FEI-inspect F Scanning Electron Microscope (SEM); (c) TM3030Plus SEM.

3.4 Surface investigations

Overloading and other fatigue causes are affecting the contact surface of the loading region by changing the contact surface properties and also causing damage features in the subsurface region. Investigation of bearing race surfaces included two categories; contact surface hardness and surface roughness. If the contact surface experienced overloading that exceeds the compressive yielding limit, it would be expected to find a hardening phenomenon on the contact surface, otherwise, no hardening refers to a loading level within the recommended design stress level and the future tests will be conducted below the yield contact stress. Therefore, investigating the surface hardness will help to estimate the loading level that will be considered in future tests.

Slipping and loading level affects the surface roughness due to their effect on deforming the surface asperities, therefore, it relates to two of the investigation parameters of this study.

3.4.1 Contact surface hardness

The hardness of the inner races was investigated inside and outside the contact region to specify the hardness variation and to estimate the loading level during the turbine operation. *DuraScan®Struers* digital hardness machine produced by the *Emco.test* company, which has higher accuracy than the manual Vickers hardness device was used for point measurements. To increase the reliability of the results, ten measurements were performed outside the contact region to represent the hardness before service, and the mean value was calculated in addition to fifteen hardness measurements inside the contact region. It is important to point out that, the measuring region should be away from the indentations to increase the result's accuracy and avoid the hardening effect of these indentations. Measurement of contact surface hardness should be taken away from the indentation with at least three times the indentation size according to Solano-Alvarez et al. [84]. This is to avoid the affected zone by the indentation's plastic deformation. [Figure 3-10](#) presents the hardness measurements inside and outside the contact regions. These measurements have equal spaces of 1mm in the axial direction. Because of the curved contact surface in the circumferential direction, the test piece should be rotated after each measurement. However, measuring the hardness variation in the circumferential direction will be very valuable because this will show the overloading distribution within the loading region. The mean Vickers Hardness (HV) before the bearing use, i.e. out of the loading region, was 738 (~61 HRC), while after service and failure, it was ~796 HV (~64 HRC). There is a noticeable hardness increase between the two regions, therefore it is expected that a hardening phenomenon took place inside the contact region. This phenomenon requires a contact stress level beyond the compression yield stress therefore, it is expected that; the planetary bearing loading was above the design stress specified in BSI-61400-1 [23] and ISO 281 [104].

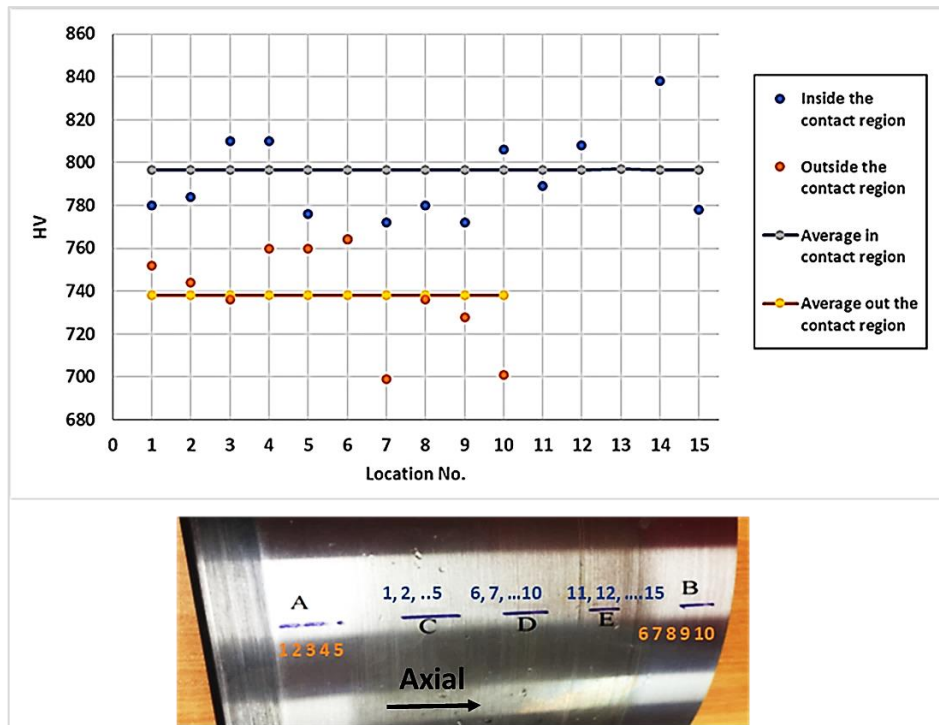


Figure 3-10: Hardness measurements of the regions within and outside the loading zone.

3.4.2 Surface roughness

The surface roughness of the contact surfaces is affected by loading level, slipping, surface hardness, lubricant, and operating temperature. The roughness of the contact surfaces of the two races was measured in the axial and circumferential directions (perpendicular to the rolling direction and parallel to it respectively), and the mean was taken. Despite the importance of the circumferential roughness to show the rolling effect, axial roughness probably plays a considerable role due to asperities contact and the bearing axial loading. Arithmetical Mean Deviation (R_a) is the mean deviation from the mean surface, i.e. the average height of asperities from a mean line, is stated in this surface investigation. The mean of at least five measurements should be taken inside and outside the contact region to increase the measurement reliability and accuracy.

In this study, *MITUTOYO®SJ.400*, *Contour GT® Veeco* and *Alicona optical scanner* devices were used in surface roughness measurements. The first is a contact profilometer which can make radius compensation to measure the roughness on curved surfaces, while the second and third, are non-contact devices with high accuracy and magnification and used for plane measurements therefore, small regions of the contact surface $\sim 466 \mu\text{m}$ in the circumferential direction were used to avoid the effect of the inner race curvature.

The bearing surface out of the roller path was considered as the before service reference while the roughness inside the contact region was considered as the after-failure condition. Inside the contact region, both axial and circumferential surface roughness measurements were reduced after service as can be shown in Figure 3-11. The bearing surface average roughness changed from $\sim 0.22 \mu\text{m}$ to $\sim 0.16 \mu\text{m}$ in the axial direction and from $\sim 0.17 \mu\text{m}$ to $\sim 0.12 \mu\text{m}$ in the circumferential direction.

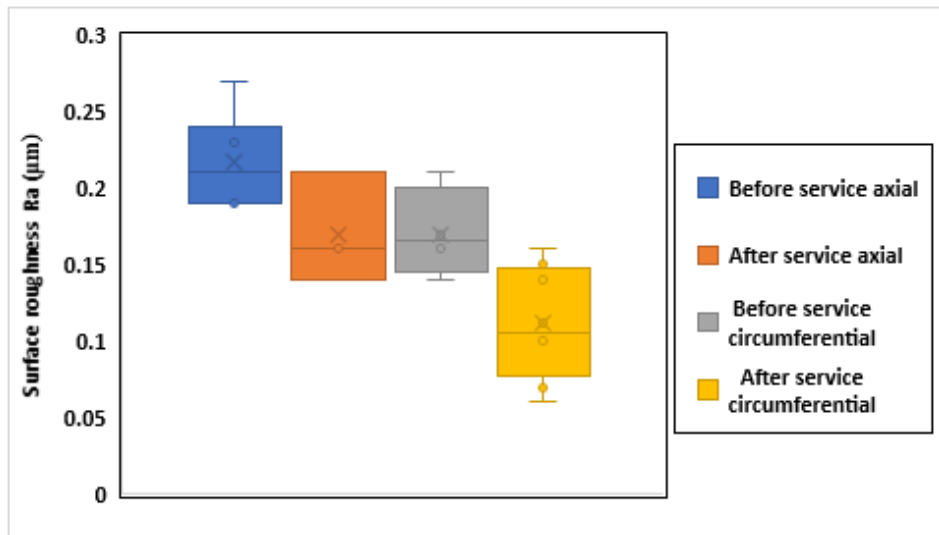


Figure 3-11: Bearing surface roughness variations before and after used in service.

The higher roughness reduction in the circumferential direction shows a considerable change due to rolling and sliding throughout the operating. Using a non-contact profilometer *Contour GT® Veeco*, the results had no noticeable differences compared with those achieved from the contact profilometer. Figure 3-12 illustrates the surface roughness of two equal areas ($621.2 \mu\text{m} \times 465.9 \mu\text{m}$), the first from outside the contact region (on the left-hand side) with R_a value $\sim 0.265 \mu\text{m}$, while the asperities have lower height inside the contact region (on the right-hand side) with an average surface roughness R_a of $\sim 0.151 \mu\text{m}$. The rolling in the circumferential direction gave the asperities a specific direction, i.e. parallel lines in the rolling direction. This specific direction can also be shown out of the contact area due to the surface finishing process. The higher surface asperities appear with a dark brown color. There are many surface elevations below the mean line, these represent micro valleys and may be responsible for surface crack initiation. Deformation of the asperities inside the loading region in the rolling direction appears clearly using the contour GT device. Comparing these two surfaces roughness measurements pointing a plastic deformation due to deforming the higher asperities. This led to postulate that improving the surface roughness of the bearing contact components (especially the races) probably has a considerable role

in reducing the deformation of the asperities and increasing the bearing life (as will be investigated in [Chapter 7](#)). The improved bearing surface roughness must be relevant to the lubricant viscosity, i.e. film thickness, which also depends on the operating temperature.

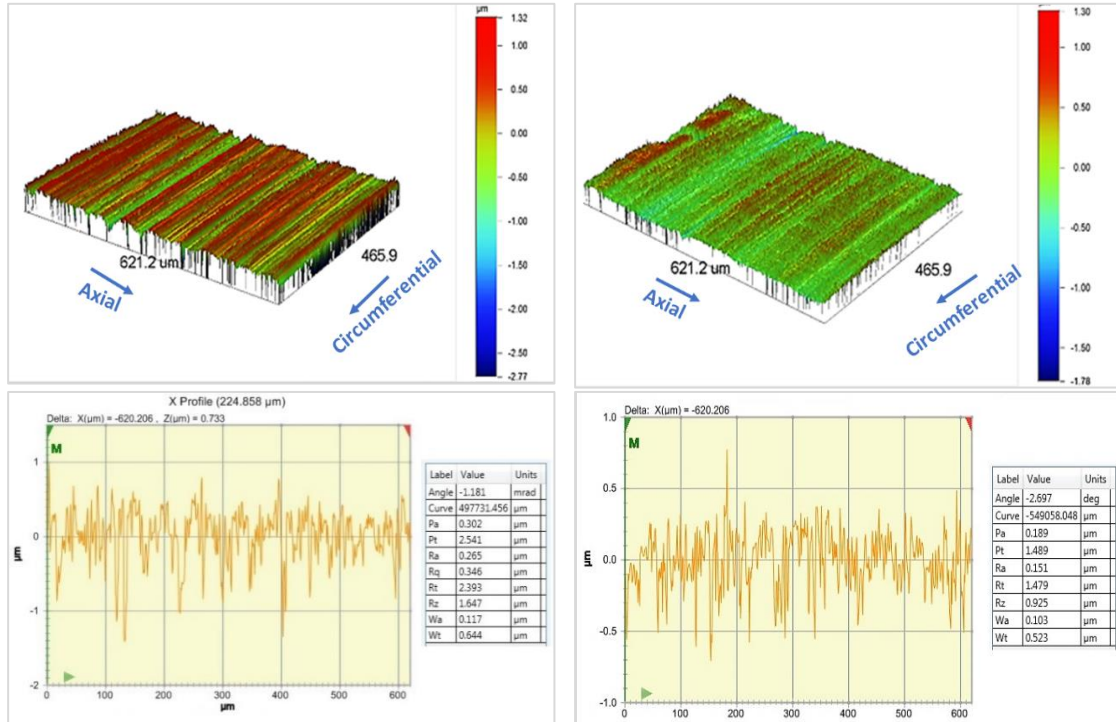


Figure 3-12: Surface roughness using non-contact contour GT: (left) out of the contact region and (right) inside the contact region.

Surface dents were also considerably observed inside the bearing loading regions (Zone 2). These dents were produced due to contamination of the lubricant with hard particles such as debris. Severe plastic deformation was observed in the indented area which may produce contact stress level quite larger than the yielding stress limit. [Figure 3-13](#) presents an example of dent located 21 mm from the severely damaged region (Zone 1) towards the loading-in region. Dent density increase towards Zone 1, with an average depth of $\sim 30 \mu\text{m}$ down the contact surface. Severe plastic eroding in the Rolling Direction (RD) was also observed.

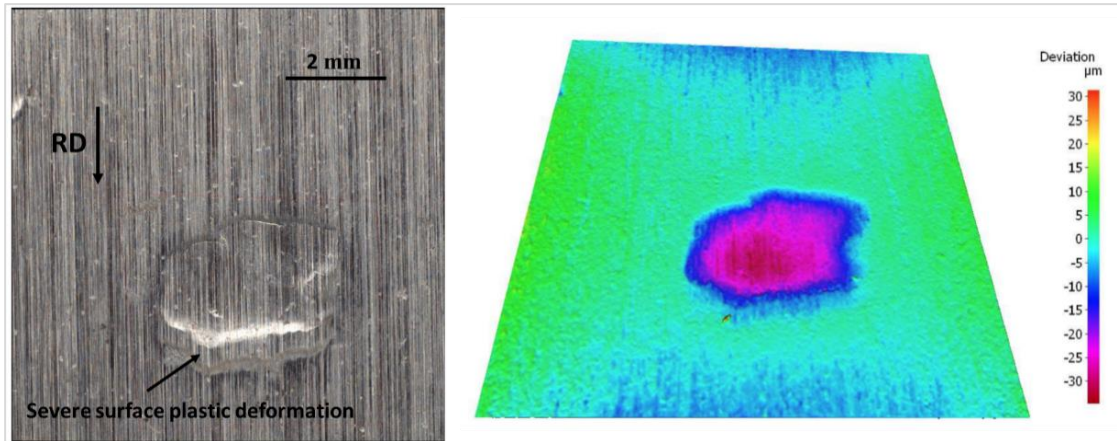


Figure 3-13: Example of analysis of a dent observed on the UW bearing inner race surface.

Investigating the subsurface of the circumferential direction of the plane passing through the end of the dent showed a small butterfly wing as can be seen in Figure 3-14. The dimension marked with "*" in this figure represents the horizontal distance towards the rolling direction from the end of the dent.

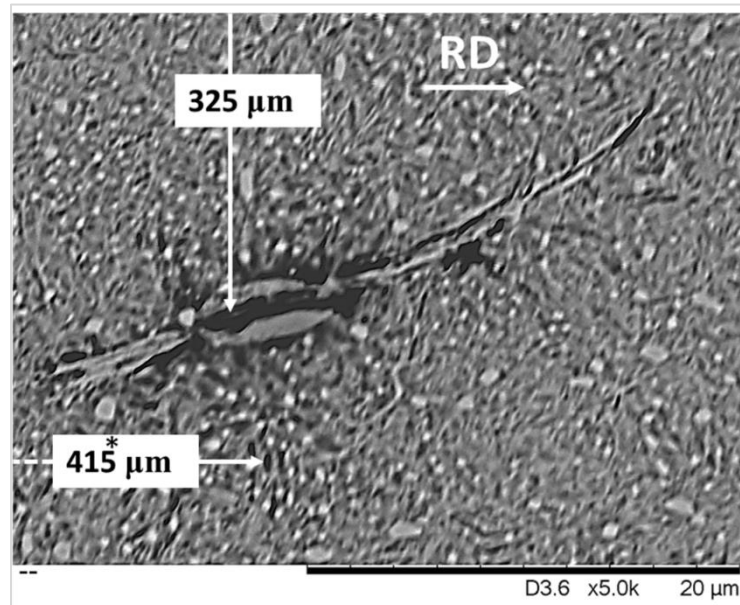


Figure 3-14: A butterfly wing observed beneath the dent in the circumferential section.

Regrinding the plane of this butterfly wing during the looking for other damage features led to disappearing the wings when the central inclusion disappeared. The regrinding continued till the indent disappear but, no other butterfly wings were observed. Studying the indentation size, depth and distribution on the inner race contact surface may supply considerable information due to the possible role of these dents on the final damage, especially at the late damage stage.

3.5 Subsurface investigations

3.5.1 Sample sectioning and mounting

From each inner race, Zone 1, samples were cut as illustrated in Figure 3-15. The mounting stage followed the cutting, consisting of fixing two specimens from one section. The first specimen was fixed to show the axial cutting plane, while the second specimen showed the circumferential plane. This cutting and mounting procedure allowed investigation along whole the bearing axial plane and six equally spaced planes in the circumferential direction. Furthermore, the other surfaces not appearing in this mounting procedure could also be examined by breaking down the sample mold and re-mounting the same specimens to show the other surfaces by rotating each specimen in the samples with 90°. In this way, all the cutting surfaces have been investigated. A *Beuller® SimpliMET® 1000* hot mounting press was used. The mounting process consisted of heating the specimens and the resin to 180 °C under a pressure of 250 bar for 150 seconds; then cooling the sample to room temperature through 240 seconds. *Beuller®Konductomet™* graphite and mineral (SiO₂) thermosetting resin was used in the mounting process due to its ability to absorb electrons during the SEM investigation.

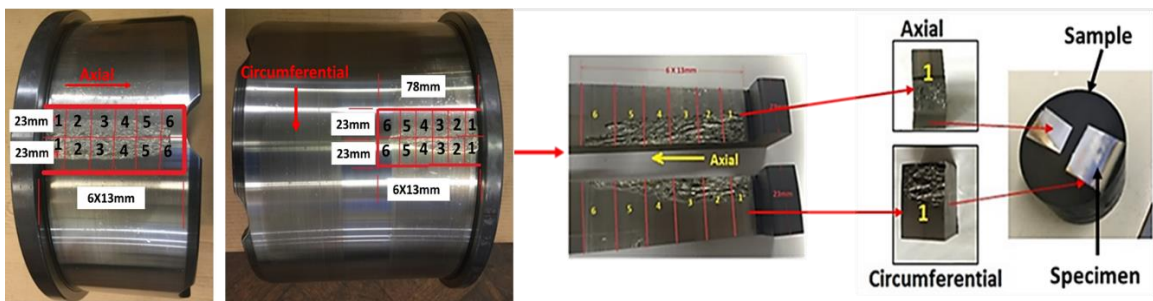


Figure 3-15: Cutting and numbering of zone 1 specimens.

3.5.2 Sample preparation

Sample preparation is one of the most important steps which precedes the etching and microscopic investigation processes. In this section, the preparation of the race specimens to characterize the subsurface damage features will be explained. After the sectioning and mounting, a grinding, polishing and etching processes were conducted to reveal the microstructural features of the specimen surfaces. Stages of sample preparation are optimized to get the clearest metallographic images. The mounted cylindrical samples were ground using sequential steps to prepare for the polishing process. The first grinding step should

remove all the noticeable cutting defects or any undesired mounting layers. This process is always conducted using low grade grinding papers. The grade of the grinding papers refers to the number of grinding particles in a square inch; the higher the grade the finer the grinding particles. Table 3-7 illustrates the details of the grinding and polishing procedures.

Five polishing steps were conducted using progressively finer diamond particles suspensions that are provided by *MetprepTM* company. The polishing stages were performed using a suitable suspension on compatible polishing discs to have a mirror-like surface that can provide high-quality images under high magnification levels.

Table 3-7: Details of grinding and polishing processes.

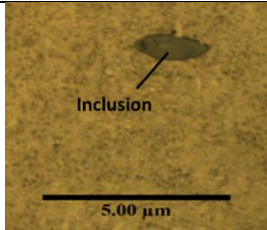
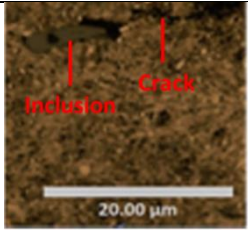
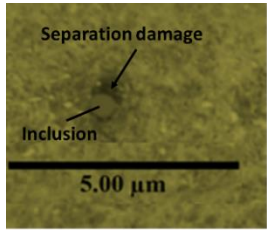
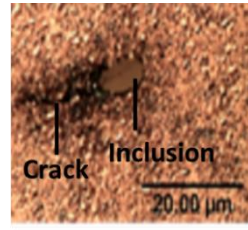
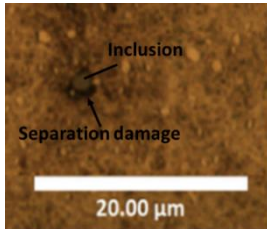
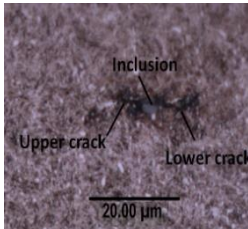
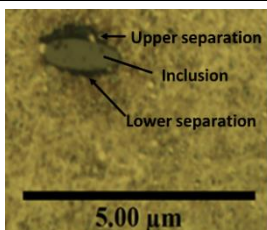
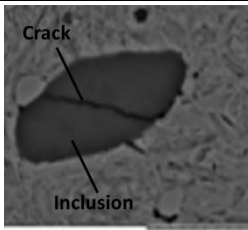
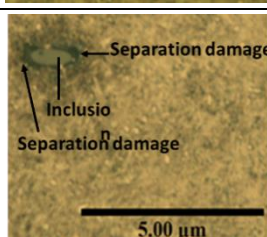
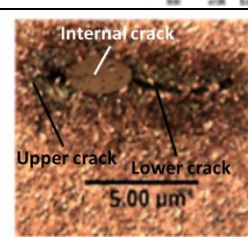
Preparation type	Step No.	Grade (par/in ²) and (μm)	Force (N)	Time (s)	Base speed (rpm)	Head speed (rpm)	Rotational direction (base/head)
Grinding	1	240	20	Until level	150	51	Same
	2	600	20	240	150	51	Same
	3	1200	20	240	150	51	Same
Polishing	1	6	20	480	150	51	Same
	2	3	20	480	150	51	Same
	3	1	20	480	150	51	Same
	4	1	15	360	150	51	Opposite
	5	0.04	10	600	200	51	Opposite

The etching process is also a very important and sensitive stage. 2% nital which consists of 2% nitric acid and 98% ethanol, was used to etch the prepared specimens. This nital concentration was identified by the previous studies [33][3],-[154][177] as an ideal concentration for revealing the grain boundaries, carbides and WEAs in AISI 52100 bearing steel. 5 to 10 seconds is the normal etching time and visual inspection by the naked eye is used to identify whether the etching process is sufficient or not. Sufficient etching shows the material surface to be slightly clouded with light various colours, however, an over-etching process was accidentally conducted, it is found to be very beneficial in identifying the subsurface microcracks and defects. Over etching makes the specimen surface being relatively dark. Different grains and other microstructural features reflect different light concentrations that add a contrast to the metallographic images taken by using the microscopes.

3.6 Subsurface microstructural observations

Damage features such as inclusions, cracks, and microstructural alterations were investigated and characterized with depth, then correlated with the subsurface stress distributions to predict the stress type responsible for each damage feature. The observed features showed different types of inclusion-related damages including inclusion separation from the matrix, inclusion associated with cracks, butterfly wings, and irregular cracks with no associated inclusions. Table 3-8 illustrates the observed damage-forms initiated from the inclusions. The contact surface in all the images is towards the image top.

Table 3-8: Different damage forms initiate from inclusions.

Separation at inclusion		Cracking at inclusion	
Damage type	Examples	Damage type	Examples
No separation		Upper cracking	
Upper separation		Lower cracking	
Lower separation		Upper and lower cracking	
Upper and lower separation		Internally cracked inclusion	
Side separations		Mixed types of cracking	

In this table, the term “Upper” refers to damage forms (separation or crack) located between the inclusion and the rolling contact surface while “Lower” refers to the location of damage away from the contact surface. Damage form characterization probably has a considerable scientific impact since it probably indicates the driving stress and its level. Only two samples from each investigated race were analyzed and each one had axial and circumferential specimens. These two samples (No. 3 and 4 in Figure 3-15) were chosen in the middle of the severely damaged zones of each bearing because the characterization is a time-consuming process. Because the majority of observed damage features in the previous studies were in the depth of few micrometers to 1.5 mm, the investigation was carried within the maximum depth of 1.0 mm. The damage features were very rare in a depth greater than 0.7 mm to 1.5 mm thus, all the observed damage features were presented in the range of $>700 \mu\text{m}$. 55 damaged inclusions from 149 investigated inclusions that represent $\sim 37\%$ were observed in the axial sections; and 94 inclusions in the circumferential sections. The distribution of the investigated inclusions can be shown in Figure 3-16. Different damage features at different depths were observed, this supports the suggestion that; different stress types under different levels may be responsible for these different damage features.

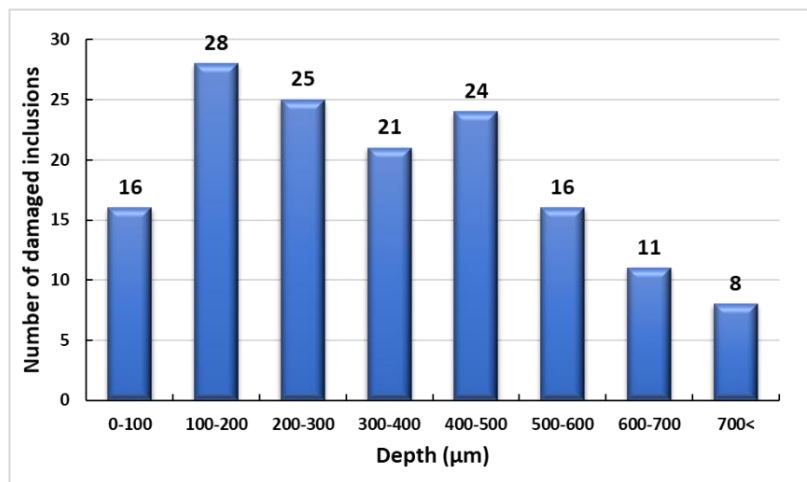


Figure 3-16: Distribution of damaged inclusions with their depth.

Classifying the damaged inclusions according to their Aspect Ratio (AR) which is the ratio of the major inclusion axis length to its minor shows that, inclusions with a low aspect ratio (1:1 to 3:1) were dominant in the circumferential direction, while inclusions with higher ARs were found in the axial direction. This may explain why most of the WTG bearings failed by axial cracking, probably due to the role of these longer inclusions which represents the weak regions to initiate axial cracks. The investigated inclusions classified according to their AR and depth are presented in Figure 3-17. Inclusions having AR of 1:1 to 2:1 are presented as 1 to 2 in this figure,

however, the damaged inclusions number and percentage are also illustrated in the pie-charts.

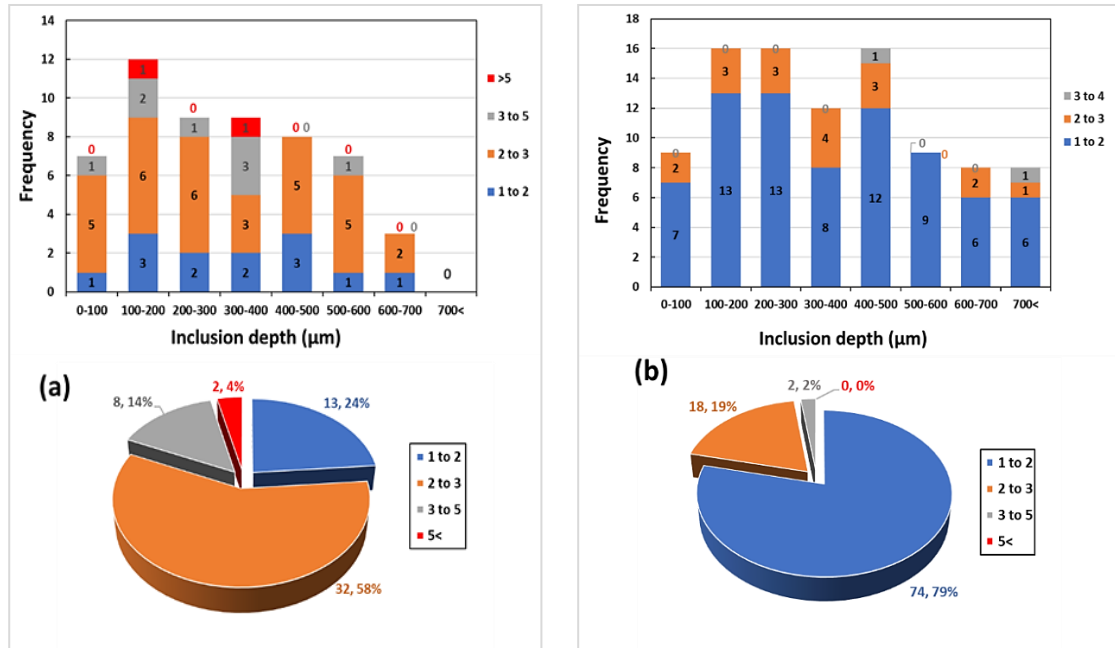


Figure 3-17: Distribution of the investigated inclusions according to inclusion aspect ratio (a) axial direction; (b) circumferential direction.

This inclusion distribution is due to the bearing steel casting and manufacturing processes and there is no evidence supporting the effect of bearing load on the inclusion shape, orientation and AR. In the circumferential section, most of the inclusions had AR 1 to 2, however, in the axial section, the inclusions tended to be longer and had an AR of 2 to 3.

The inclination angle of the inclusion major axis in the circumferential planes with respect to the rolling contact surface is very important because most the butterfly wings follow specific directions, which may correspond to the maximum shear stress direction. Classification of the investigated inclusions according to their inclination angle can be seen in Figure 3-18. It reveals that, ~85% of the inclusions are inclined with an angle between 0° to 20°. It seems that this orientation is very critical due to the high possibility of matching the inclusion major axis which represents the weak direction with the maximum shear stress direction produced due to compression and traction forces. This is thought to be one of the important causes of damage initiation. Figure 3-18(c) shows the general inclusion orientation inside the bearing material which is drawn according to the bearing axial and circumferential directions.

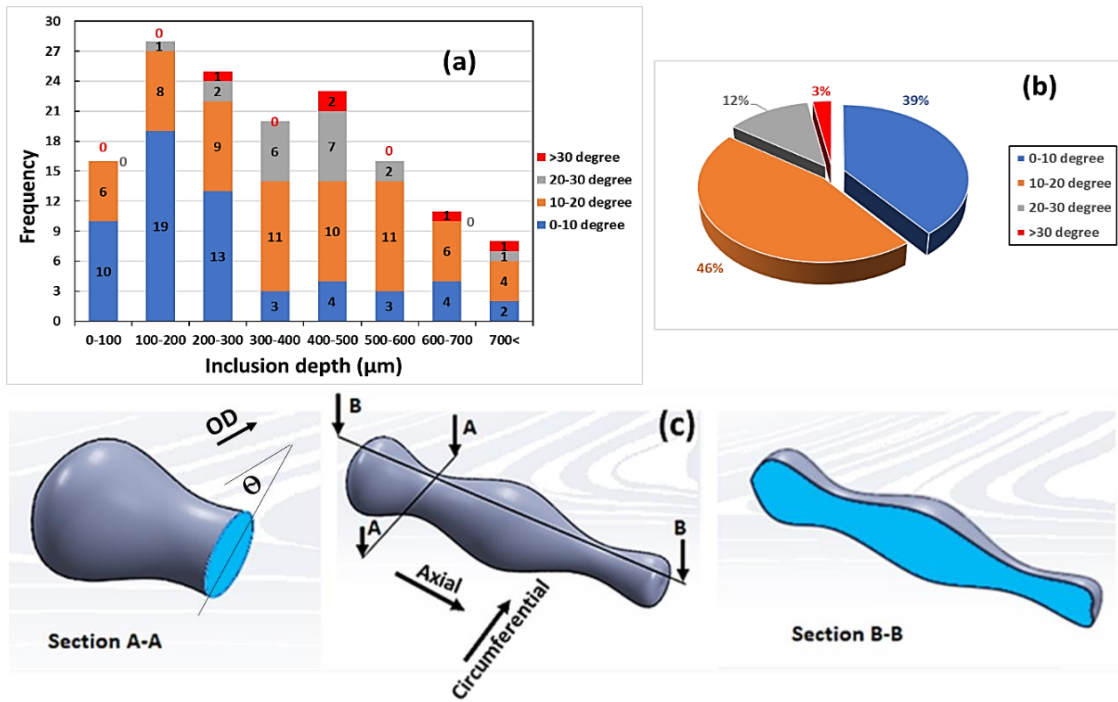


Figure 3-18: Inclination angle of damaged inclusions, (a) distribution with depth; (b) percentages (c) schematic representation of inclusion orientation inside the bearing material bulk.

Separation damage (debonding of inclusion from the bulk) was either from upper, lower, upper and lower, or side separation, while inclusion-damage by cracking includes upper cracking, lower cracking, upper and lower cracking, cracking the inclusion itself (internally cracked) or mixed types of cracking. The distribution of damaged inclusions by separation with depth can be seen in Figure 3-19. By comparing the curves in this figure with the subsurface stress distributions in Figure 3-6, the upper, upper and lower, and no separations probably occurred due to maximum shear stress, however, lower and side separation follow the von-Mises stress distribution. The maximum numbers of the separated inclusions were found in different depths. This means this separation damage was probably occurring under different loading levels and the lower separation type seems to occur under much higher loading levels compared with the other types of separation damages. Upper separation damage increased considerably near the contact surface thus, this damage may occur due to high traction force and/or due to the impact effect in shallower regions. Upper and lower separation seems to occur under normal operating contact stress level (see the depth of maximum shear under contact pressure of 1.8 GPa in Figure 3-6), this may explain why upper and lower separation damage is dominant in previous literature or, this damage occurs under higher loading levels, but with high traction force which brings the subsurface stresses towards the contact surface. The trend of no separation (only cracks without

separation) shows a different trend and it seems to increase with depth. This means the damage without separation may occur under a very severe compression level that may be due to impact loading or introducing debris between the contact surfaces. The distribution of lower and side separation damage matches the Von-Mises stress distribution; however, the maximum number of damaged inclusions was found near the contact surface. This is probably due to introducing high traction force (higher than 15% and may be higher than 30%) or due to impact effect in shallower regions.

The qualitative comparison of subsurface stresses with the variation of contact pressure and traction coefficient in Table 3-5 and Table 3-6 reveals that, the depths of Von-Mises and maximum shear stresses are close to each other so, it is difficult to separate their effect on damage, however, Von-Mises stress value is higher than the maximum shear and probably plays the main role in damage initiation and propagation.

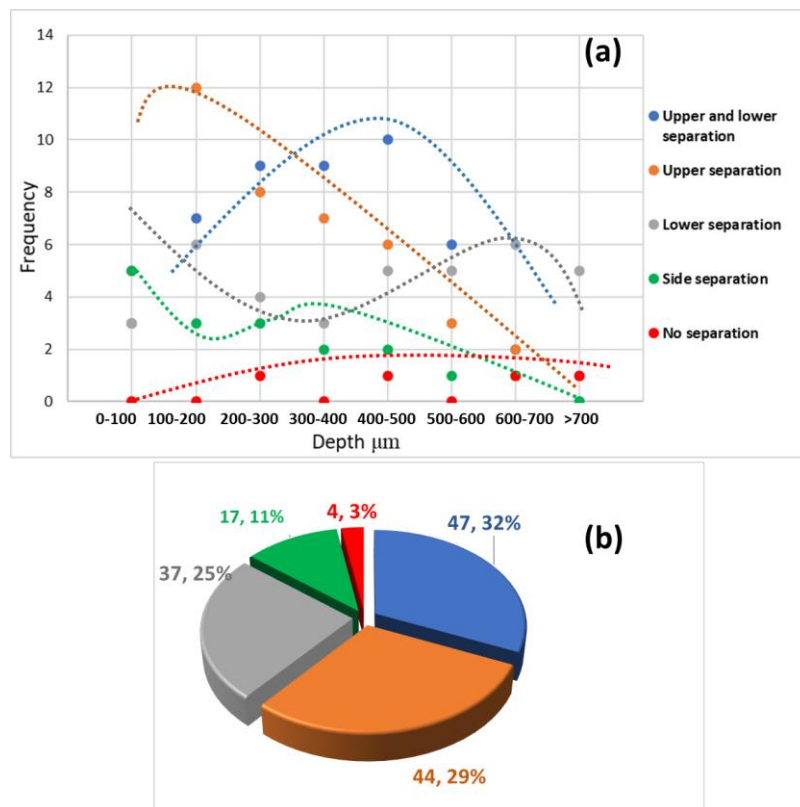


Figure 3-19: Damaged inclusions by separation, (a) in relation to subsurface depth; (b) numbers and percentages of separated inclusions.

Despite the dominance of the inclusion separation damage feature, damaged inclusions are also observed to be by cracking. Figure 3-20 shows these cracking damage forms and their percentages from the investigated inclusions. Upper, upper and lower, and internally cracked inclusions (no separation) follow the maximum

shear stress distribution with depth. Internally cracked inclusions concentrated near the contact surface thus, this damage type is either due to high traction force and/or due to an impact effect in shallower regions. However, the mixed type of cracking followed the Von-Mises stress distribution and the increase in the shallower region shows the possibility of a high traction force. Only lower cracked inclusions were observed to increase with increasing depth. This increases the probability of their formation due to Von-Mises stress under severe loading levels because its maximum values are located deeper than the normal loading level. However, if the traction effect is introduced, the locations of these stresses are being closer to the contact surface. This means a very high loading level is responsible for the damaged inclusions by lower cracking. There is a considerable percentage of double cracked inclusions, i.e. upper and lower cracking which were observed to have a maximum value at a depth identical to maximum shear stress depth under normal loading (~1.8 GPa), however, if the traction effect is introduced, higher loading levels can be expected.

Most of the damaged inclusions have separation and cracks together, except five inclusions only which had internally crack without separation, their depth was between 20- 250 μm , i.e. at shallow regions. This may be due to the effect of impact.

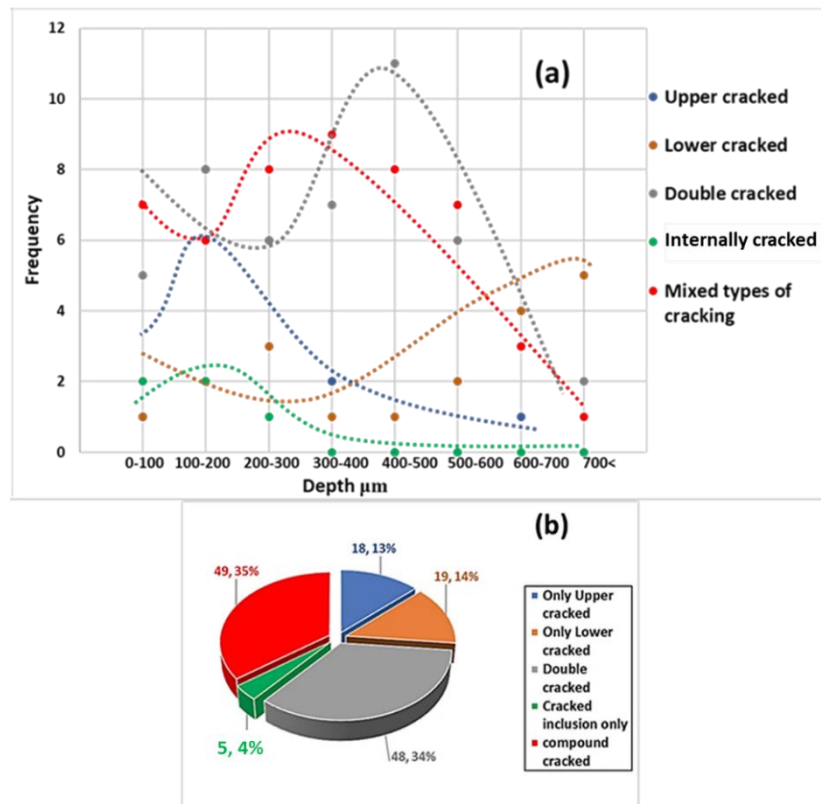


Figure 3-20: Damaged inclusions by cracking, (a) in relation to subsurface depth; (b) numbers and percentages of cracked inclusions.

Further investigation by analyzing a large number of damaged inclusions (by separation and cracking) and comparing their distribution with the subsurface stress distribution is still required to confirm the responsibility for each type of stress on inclusion damage. In this study, most of the observed microstructural alterations were found as butterfly wings thus, the investigation and analyses will focus on this type of microstructural alteration.

3.6.1 Butterfly wings

The observed butterfly wings are classified into double-winged and single-winged butterflies. The single-winged type is also classified into upper and lower single winged as illustrated in Figure 3-21. Examples of the observed butterfly wings can be seen in Figure 3-22. The depths of these butterfly wings are within the maximum shear stress depth under contact stress around the bearing material yield stress.

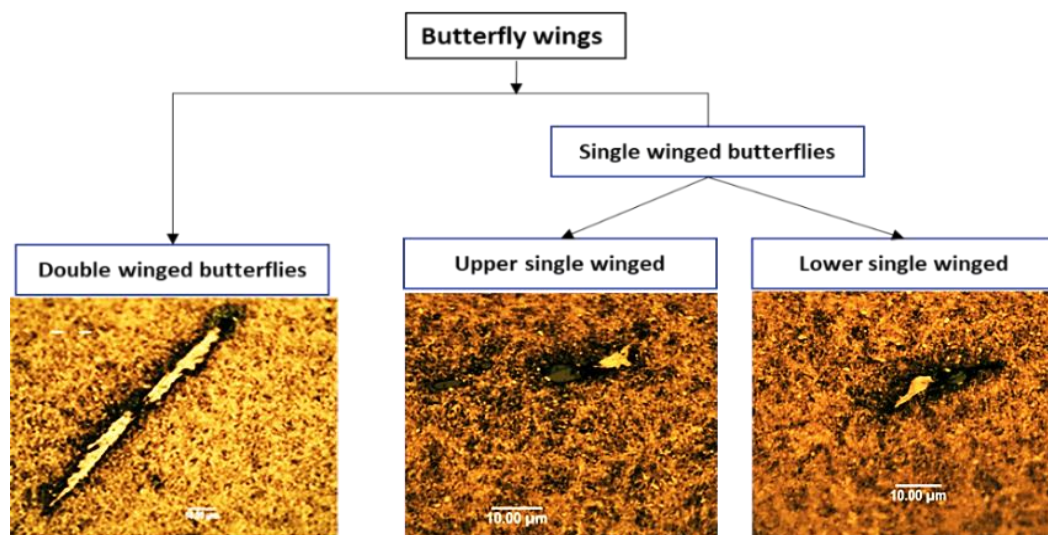


Figure 3-21: Types of investigated butterfly wings (rolling surface in the top).

The observed 49 butterfly wings were classified according to the depth of the central inclusion as presented in Figure 3-23. All these butterflies are observed in the circumferential sections. Their number was found to increase with increasing depth till reaching a depth of $\sim 600 \mu\text{m}$. Then their number starts reducing, however, no butterfly was observed in depths greater than $700 \mu\text{m}$.

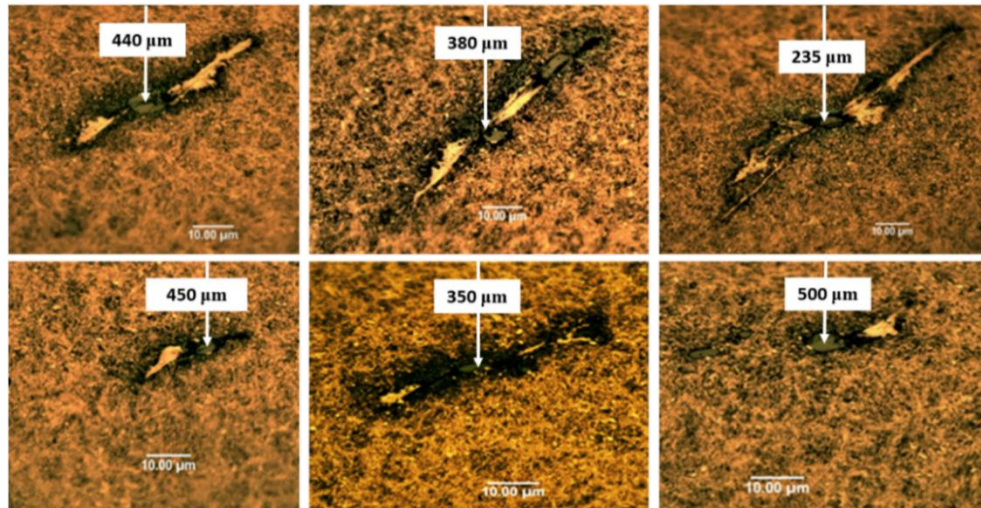


Figure 3-22: Examples of butterfly wings showing the associated cracked inclusions (rolling surface in the top and the rolling direction from left to right).

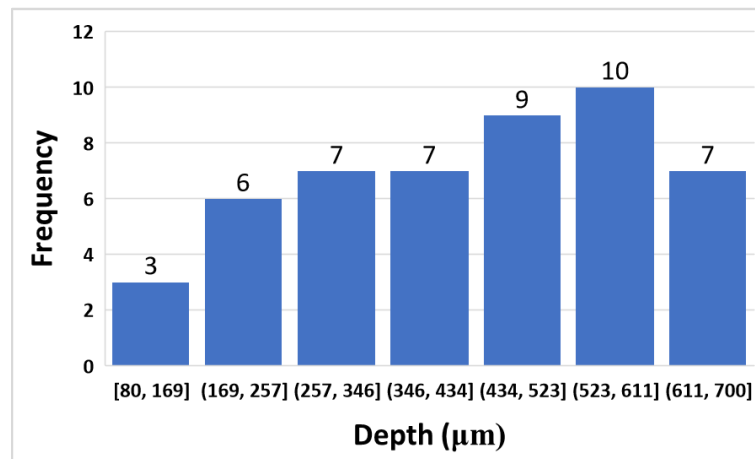


Figure 3-23: Distribution of observed butterfly wings with depth.

If the butterfly formation followed the frequency, maximum shear under higher levels than the normal operating contact stress is expected to produce the wings because the maximum depth is higher than that of maximum shear stress under a contact pressure of 1.8 GPa. Despite the butterfly wing's shape which is identical to the orthogonal shear stress distribution, the maximum shear values are higher than the orthogonal one and their maximum levels are approximately located in the same depth, however, the possibility of wing formation due to orthogonal shear is still considerable and needs further investigations. If the traction force is taken into consideration, a higher contact stress level than the 1.8 GPa is required to initiate the butterflies. If the wings with higher length are assumed to initiate first, the distribution in [Figure 3-24\(c\)](#) also correlates with the maximum shear stress

distribution. This is an additional evidence about the responsibility of maximum shear on producing this type of subsurface microstructural alteration.

Only one small butterfly wing was observed with an orientation approximately parallel to the contact surface that represents ~2% of the investigated butterflies. The highest percentages of 29% and 21% of the butterfly wings were found to be inclined with the rolling contact surface at 25° and 40° respectively as can be seen in [Figure 3-24\(b\)](#) where the inclination angle and percentage are presented. This specific inclination refers to a loading level quite higher than the yield stress (higher than 4.0-6.0 GPa) [189]. This is also supported by the hardening phenomenon observed on the contact surfaces. The distribution of the butterfly wings according to wing-length shown in [Figure 3-24\(a\)](#), indicates that most of the observed butterflies have wing lengths between ~9 to ~32 μm (~26% of the observed butterflies). This difference in the wing size points out the possibility of introducing and propagating them under different contact and traction levels.

Around 71% of the observed butterflies (34 butterflies) were double-winged, while 57% of the remaining percentage (29%) were upper single winged, and the other 43%, had a lower single wing only. Single winged butterflies have shorter lengths compared with the double-winged butterflies. This leads to the postulation that the butterfly wing probably initiates as a short single wing and the other wing appears later, after that, the two wings may propagate together under severe loading conditions.

There is no evidence supporting whether the upper or lower wing initiates first, however, it seems that the location of wing initiation depends on the location of its associated inclusion related to subsurface maximum shear stress distribution under severe loading levels. The observed butterflies were beneath the severely damaged region (Zone 1), whereas the contact surface was flaked; no butterflies were found in shallower regions (<70μm). To investigate which wing initiates first, the double-winged butterflies were classified into type A when the upper wing is longer than the lower one, and type B when the lower wing is longer. In type A, wings have longer wing lengths compared with the other type and the upper one was observed to be longer than the lower thus, the upper wings may be initiated first. On the other hand, the single winged butterflies seem to initiate close to the contact surface, this is probably due to high traction.

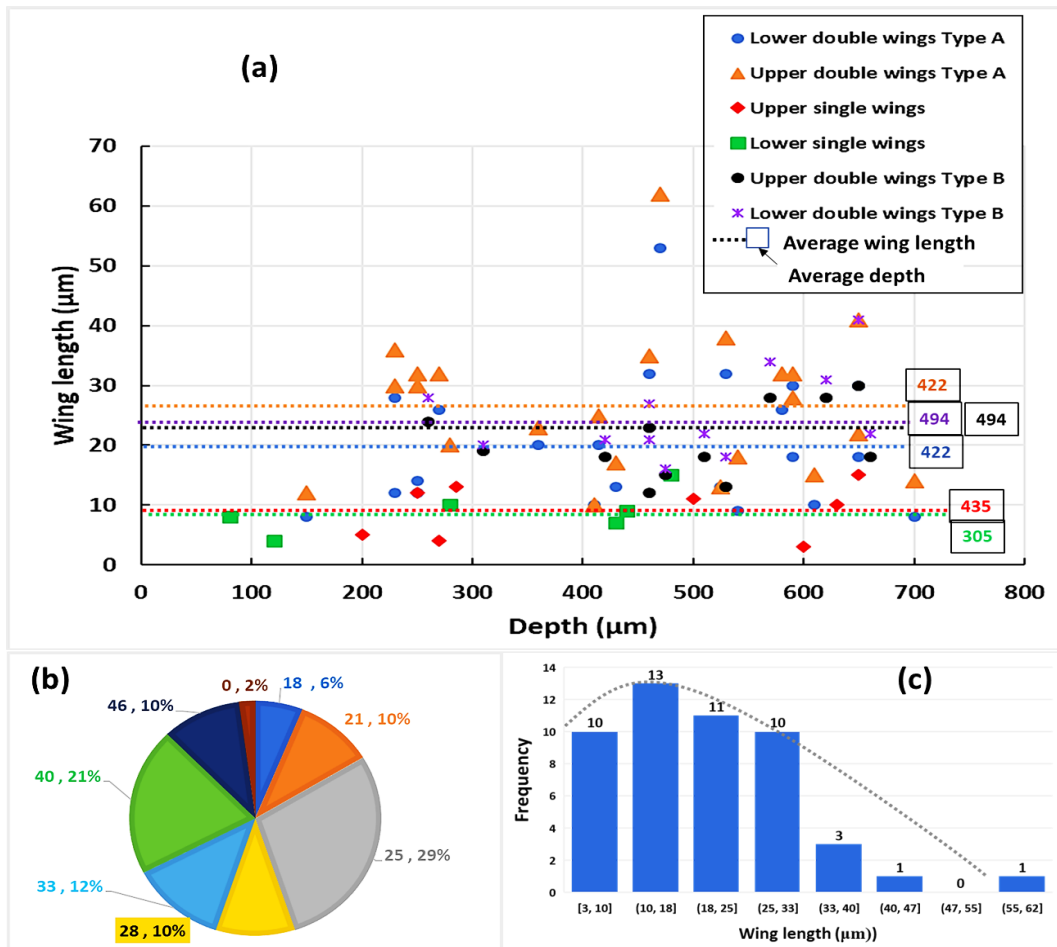


Figure 3-24: Investigated butterflies (a) distribution according to wing length and depth showing the average length and depth; (b) approximate wing angle and percentage; (c) distribution of wing frequency and length.

If the butterfly types initiated and propagated due to the same stress type, the different average depths refer to various loading levels to initiate them. Since it is postulated that the butterflies initiate as small single winged and propagate later, upper single winged seems to initiate first because it propagates more than the other types. However, studying the distribution of butterfly wing length with depth may provide more information about which wing was initiated first [30], and this needs further investigation since some controversial evidence in this study did not support this postulation. For example, [Figure 3-25\(a\)](#) presents two inclusions having approximately the same depth ($\sim 320 \mu\text{m}$). However, the first has an upper single-wing while the other has a lower single winged. [Figure 3-25\(b\)](#) shows another two butterfly wings located at a depth of $\sim 250 \mu\text{m}$ and $\sim 398 \mu\text{m}$ respectively. One has an upper single-wing while the other has a lower single wing.

This evidence leads to the postulation that the location of butterfly inclusion (depth and relative location to the contact center), orientation (inclination of the inclusion

maximum axis), the loading level in addition to traction force, and inclusion type, are probably the key factors of butterfly wing initiation and their effect cannot be separated.

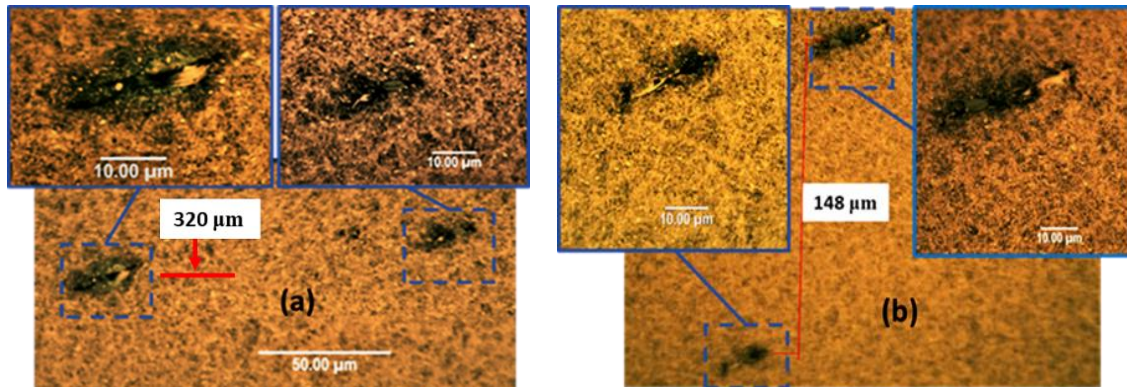


Figure 3-25: Upper and lower butterfly wing types (a) two butterfly types located at the same depth; (b) two butterfly types located at different depths (from the circumferential specimen 4 UW bearing).

Figure 3-26 shows the independence of butterfly-type (being single or double-winged), on the depth where single and double-winged butterflies can be initiated either at the same or at different depths. This also confuses the results and opens the door for further investigation.

Investigating the circumferential direction of sample No.6 of the UW bearing in Figure 3-15 shows a relatively higher number of butterflies (9 butterflies) which represents ~19% of all the observed butterflies. In this region, there is no axial loading (because the region located at the end of the roller contact region), but high shear stresses due to compressive loading, stress concentration and the shear stress due to traction. The above results lead to the suggestion that butterfly wings are probably initiated due to a high contact stress level that exceeds a critical value beyond the yield limit. The initiation of the butterfly wing may be as presented in Figure 3-27.

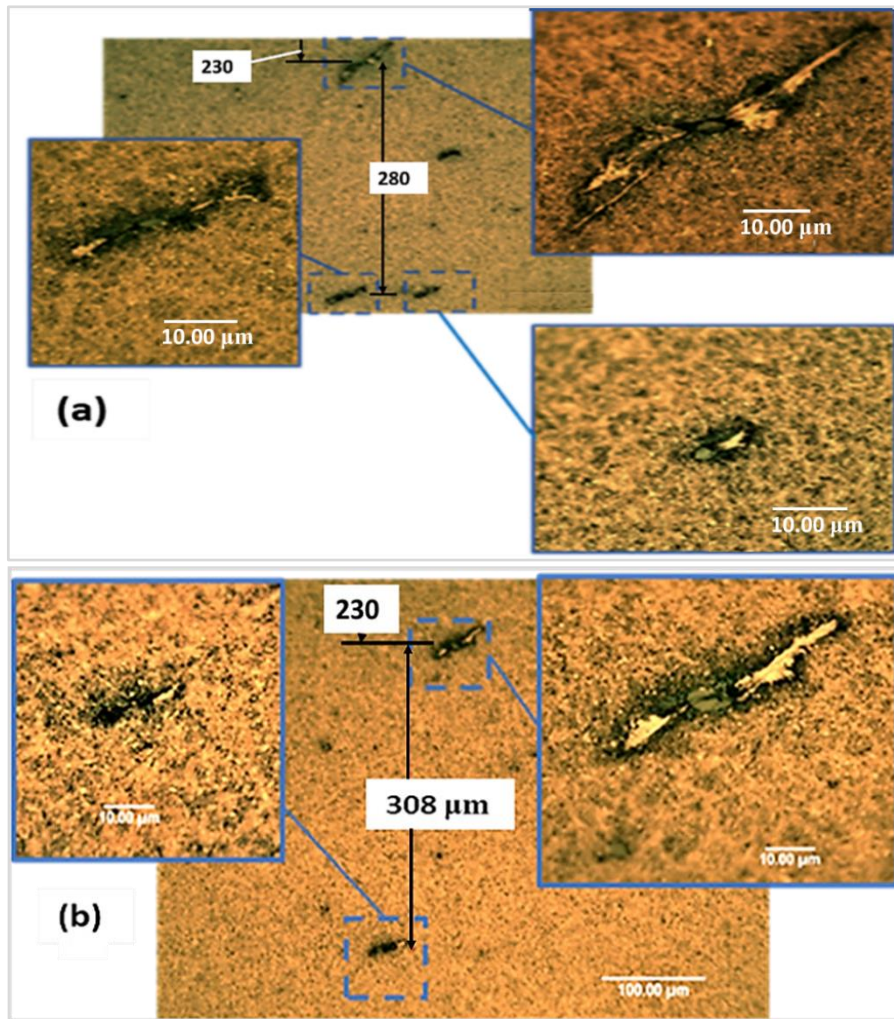


Figure 3-26: Double and single butterfly wings (a) double and upper butterfly wings depth $\sim 220\mu\text{m}$; (b) double and upper butterfly wings depth $\sim 230\mu\text{m}$ (from the circumferential specimen 6 UW bearing).

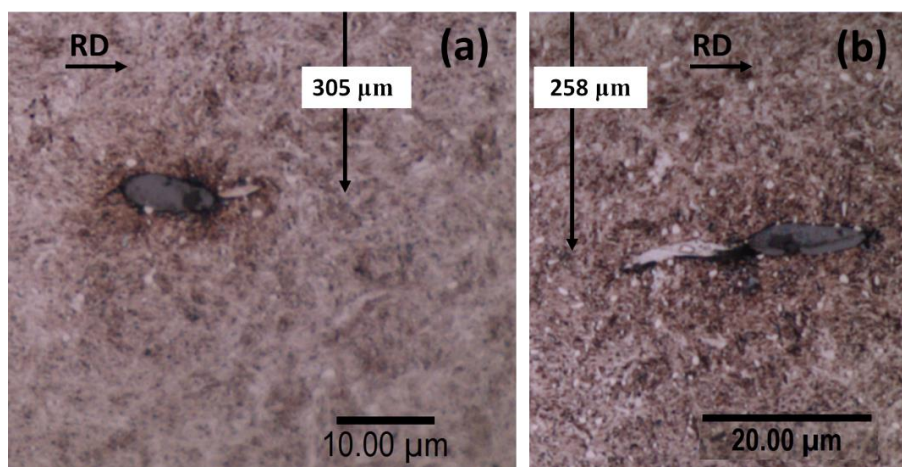


Figure 3-27: Two stages of butterfly wings (a) initiation of a baby butterfly; (b) small wing.

The largest butterfly observed in this study can be seen in [Figure 3-28\(a\)](#). It was observed in sample No. 6, i.e. at the end of the severely flaked area away from the bearing rim of the DW bearing. The central inclusion of this butterfly was located at 470 μm beneath the surface which was in the region of the maximum shear and Von-Mises stresses produced by the Hertzian contact under contact pressure of ~ 1.8 GPa (see [Figure 3-6](#)). The inclusion in the centre of the wings has a darker colour compared to the MnS inclusions which have light grey colour [76]. Energy Dispersive X-ray analysis (EDX) was used to investigate the inclusion's chemical compositions, as can be seen in [Figure 3-28\(c\)](#). The analysis shows a compound inclusion of manganese sulfide (MnS), Aluminum, and Silicon, which means that the inclusion type is D_{Dup} according to the International Standard ISO-4967:2013 [76]. Regrinding and polishing of the sample containing this largest butterfly revealed a disappearance of the butterfly and the associated cracks with the disappearance of the central inclusion. Butterfly disappearance was also noticed in most of the observed butterflies and no crack remains in the butterfly location. This may show a marginal role of butterflies on flaking; however, this does not neglect the possible role of butterfly cracks in the damage propagation but with a lower possibility in WSF. No crack associated with the wing was observed to be connected to the crack network as can be shown in [Figure 3-29](#). This also confirms the possible marginal role of these butterflies which may be initiated at late stage of bearing damage due to severe loading.

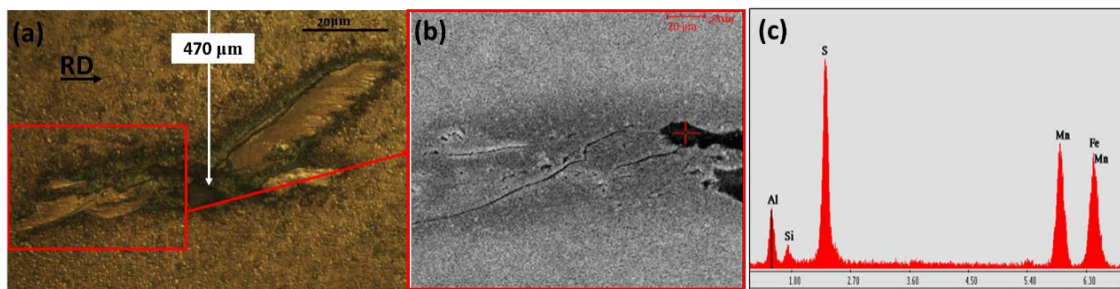


Figure 3-28: Analysis of butterfly inclusion (a) Optical image of the largest investigated butterfly; (b) SEM image of one wing; (c) EDX analysis of the central inclusion.

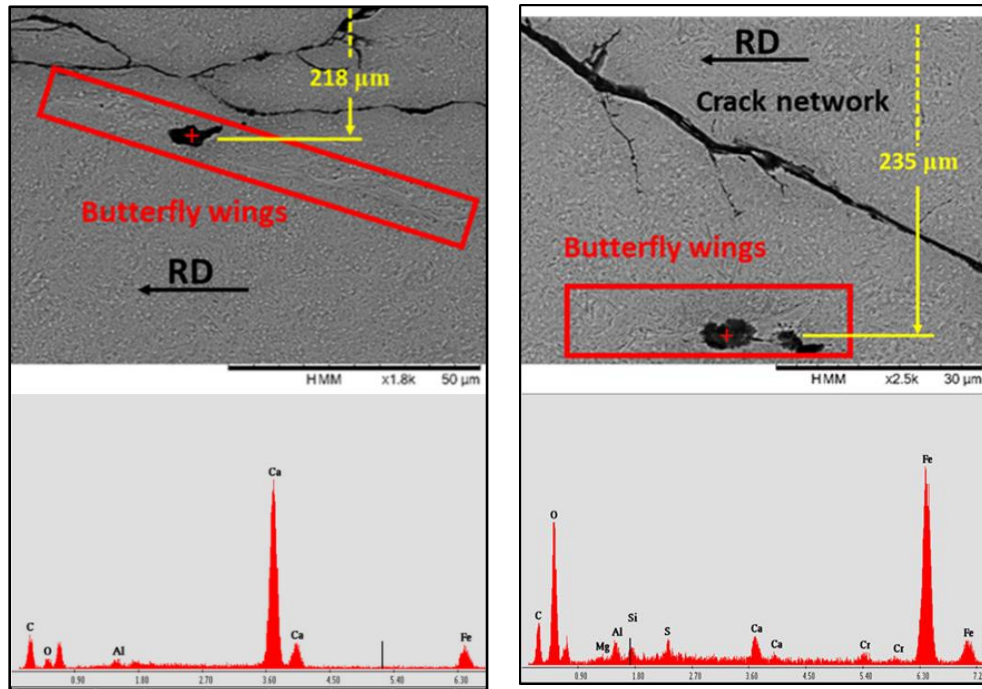


Figure 3-29: Two butterfly wings close to cracks, but not connecting with the crack network (from the circumferential specimen No. 2 UW bearing).

In this study, most of the inclusions associated with the butterfly wings were found to be broken down in a direction approximately parallel to the maximum wing length. Wings also observed to be free from carbides, and the dissolution or deformation of carbides takes a specific direction and is associated with micro-voids that may be connected to form other associated cracks, as can be seen in [Figure 3-30](#). Another inclusion attached to what was thought to be a butterfly wing in its initial stage (baby butterfly wing) was analyzed using the EDX technique as presented in [Figure 3-31](#). Small microcracks appear near the inclusion end which leads to suggest that, butterfly wings are probably initiated after the crack initiation.

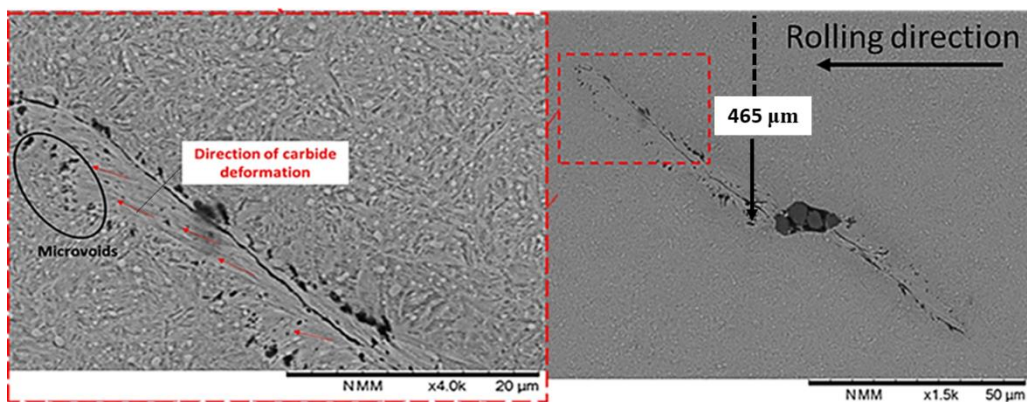


Figure 3-30: Butterfly wing and associated damage and changes (from the circumferential specimen No. 3 DW bearing).

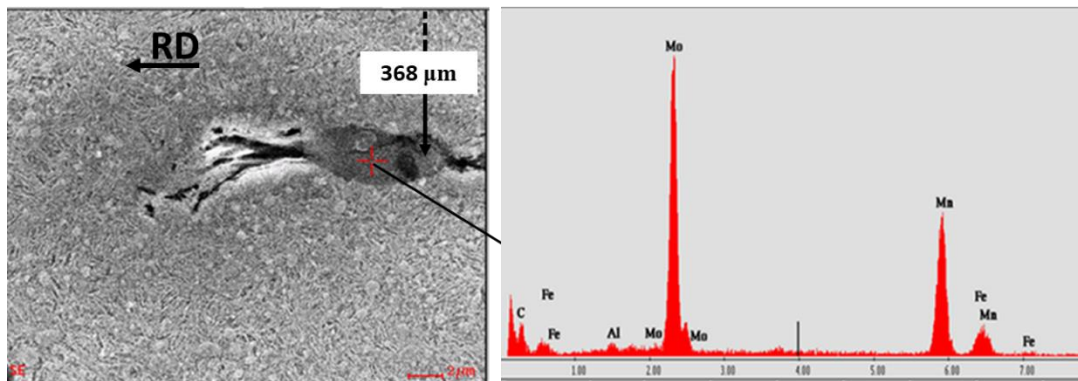


Figure 3-31: EDX analysis of the most dominant inclusion type associated with butterfly wings (from the circumferential specimen No. 4 UW bearing).

Breaking the mounting of the samples to investigate the other cutting surfaces confirms the findings of the detailed investigations of the mentioned planes in [Section 3.5](#). The observed butterfly wings in circumferential sections probably have not had any role in the crack network caused the flaking as can be seen in [Figure 3-32\(a\)](#). Interesting features of double wings on one side of the central inclusions were observed and presented in [Figure 3-32\(b\)](#) and [\(c\)](#). This may refer to initiating these wings under different loading levels. Two features presented in [Figure 3-32\(d\)](#) and [\(e\)](#) are two butterfly wings without a central inclusion that observed in this investigation. This confirms the other sites of butterfly wing initiation postulated in the previous studies such as voids [107][177], large carbides [176], microcracks [107] and/or porosity [131].

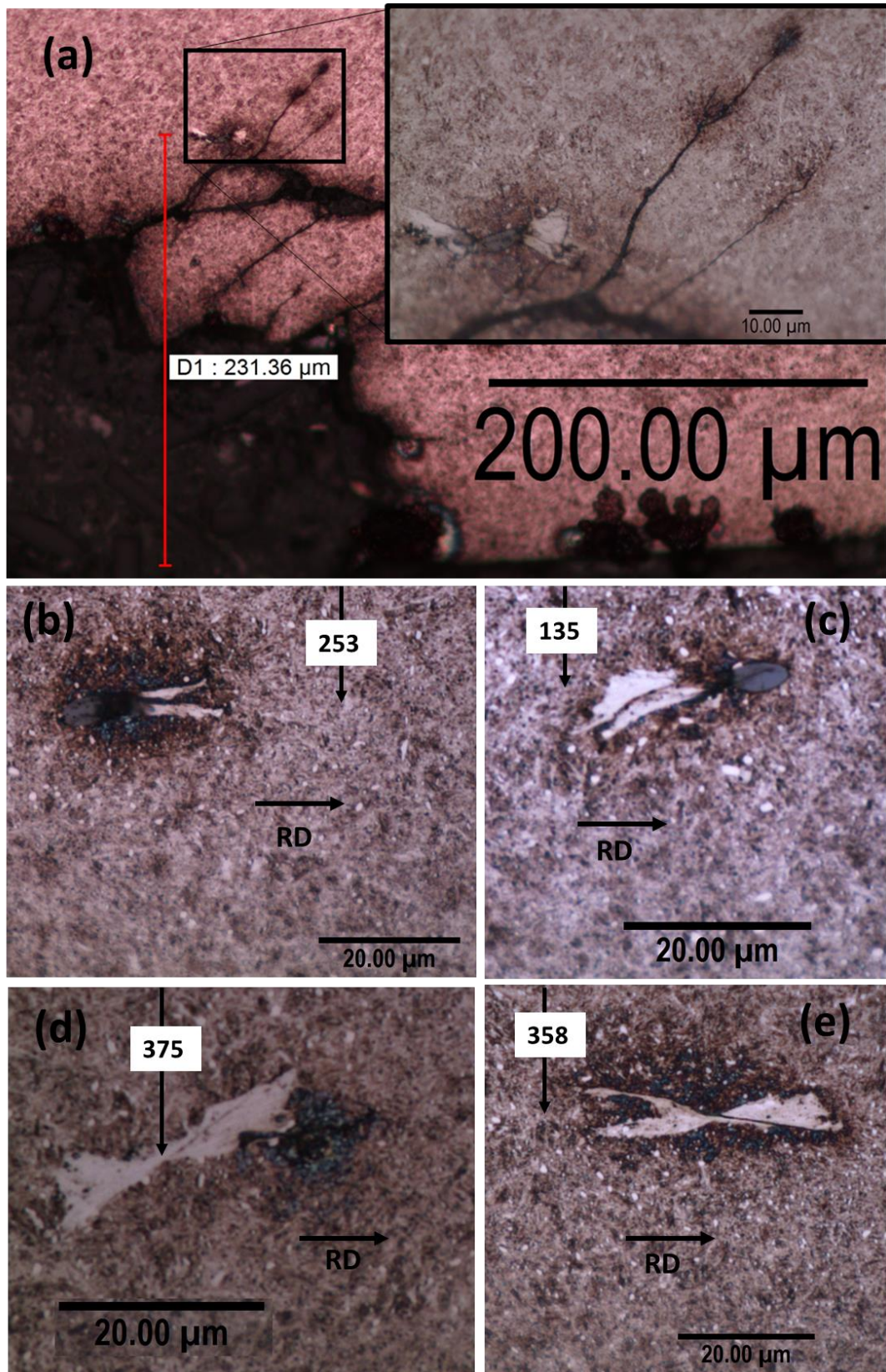


Figure 3-32: (a) butterfly wings not connected to the crack network causing flaking; (b) and (c) two features with double wings on each side; (d) and (e) two butterfly wings without central inclusion.

3.6.2 Subsurface microcracks

During the investigation, an over-etching process was accidentally carried out on one sample; and a considerable number of features, which though they may be microcracks, appeared as can be seen in [Figure 3-33](#) (marking with white arrows). Focusing on the existence of the microcracks in the other samples led to discover a considerable number of these features in both the axial and circumferential directions. By using the SEM microscope and high magnification levels, not all the marked features were really microcracks, but some of them were found to be defects in the investigated surface. Thus, subsurface microcracks must be studied under high magnification levels and by using an SEM. A considerable number of subsurface microcracks and macrocracks were observed in the previous studies without a sufficient focus on them [178][203][246]. Microcracks were observed near the macrocrack sides and the crack ends. Their number is larger than the number of inclusions; this leads to the conclusion that the inclusion is not the unique trigger for the subsurface microcrack initiation. This does not diminish the role of inclusions and their weak boundaries with the matrix in addition to the possible role of residual stress in these regions in damage initiation and propagation.

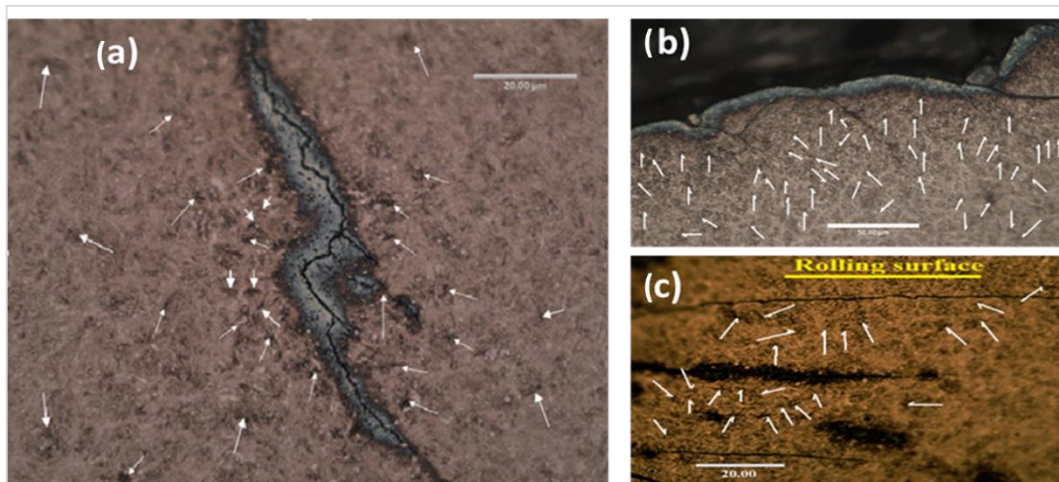


Figure 3-33: Over etched specimens showing microcracks (a) and (b) circumferential sections; (c) axial section.

[Figure 3-34](#) shows a group of subsurface micro and macro-cracks taken from different locations as examples. These subsurface microcracks were initiated from locations where there is no inclusion in the investigated surface. In these images, the rolling surface location is at the top of the images and the rolling direction from right to the left-hand side. Despite the possibility of inclusion existence behind the investigated surfaces, the number of microcracks is larger than the expected number of inclusions behind the investigation surface. Therefore, subsurface

microcracks can be initiated from inclusions, butterfly wings and probably from the defects within the bulk or maybe from the grain boundaries. Therefore, further investigations are still required.

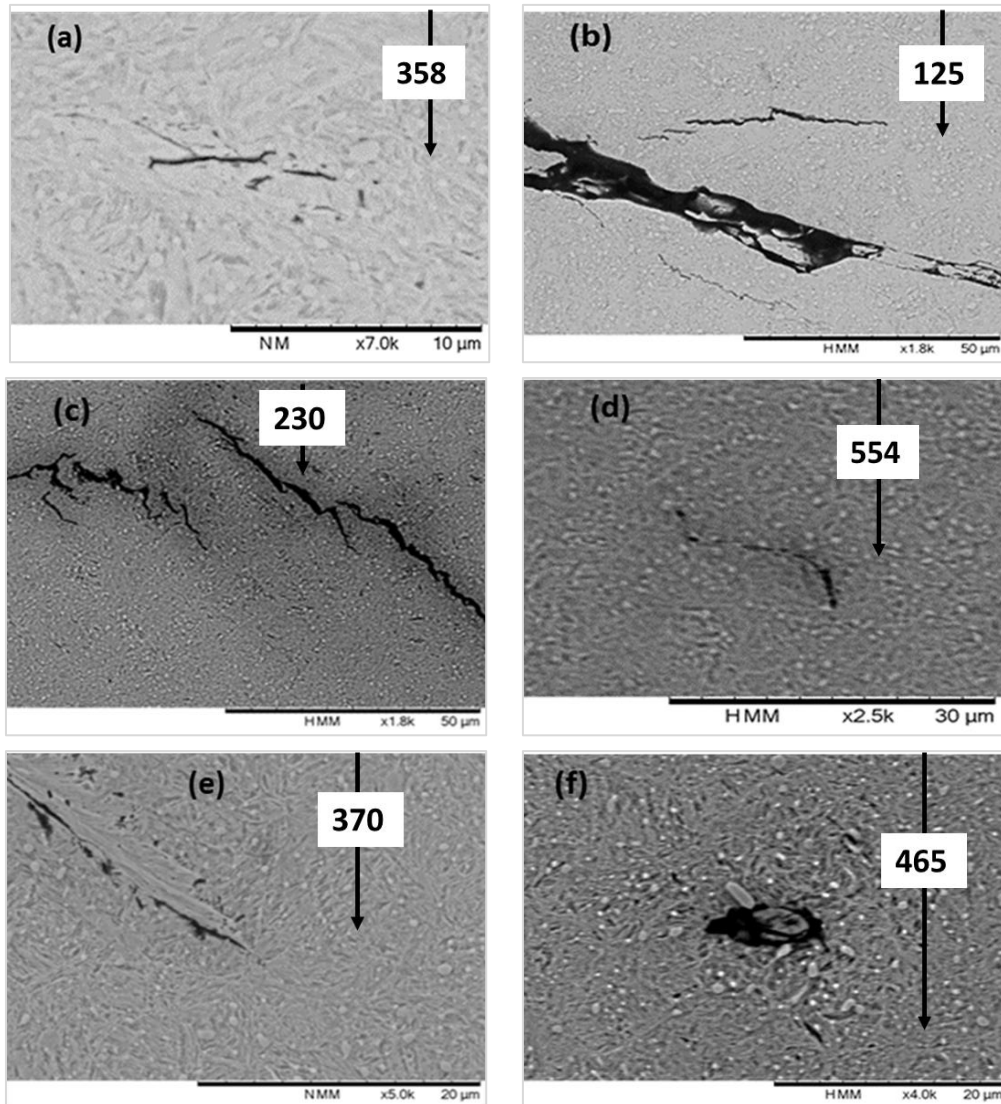


Figure 3-34: SEM images showing microcracks initiated in the subsurface region without inclusion.

The expected role of subsurface microcracks that have not initiated from inclusions is also supported by other evidence shown in the axial section presented in [Figure 3-35](#). There was a relatively large inclusion located close to the contact surface and the main crack network. There was also a large crack located beneath this inclusion and connected to the rolling surface, however, this large inclusion was not connected to the main crack network. Despite observing two inclusions connected to each other with a small crack (marked by a red oval) and there were a considerable number of subsurface microcracks in the enlarged view (marked by white arrows), this relatively large inclusion was unconnected to the crack network.

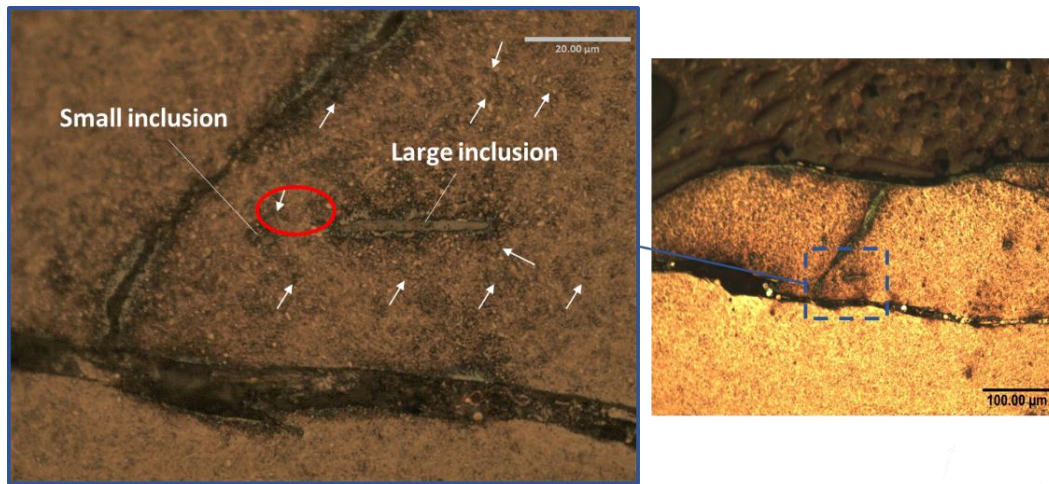


Figure 3-35: Large inclusion unconnected to the crack network in the axial direction.

Macrocracks were found to be approximately parallel to the contact surface in axial sections, while they tended to be approximately vertical in the circumferential sections as can be seen in [Figure 3-36](#), this also supports the findings of Evans's works [1][24].

The above evidence leads to the conclusion that not only the non-metallic inclusions are the unique trigger of subsurface damage initiation, but also microcracks probably play an important role in producing bearing damage by connecting to each other and forming macrocrack networks then reaching to the bearing inner race contact surface causing flaking. Subsurface microcracks and/or the cracks initiating from the separation of inclusion boundaries are probably spreading towards each other depending on the stress direction in the high-stress locations, after that, growing towards the contact surface in a 3D space and lead to surface flaking.

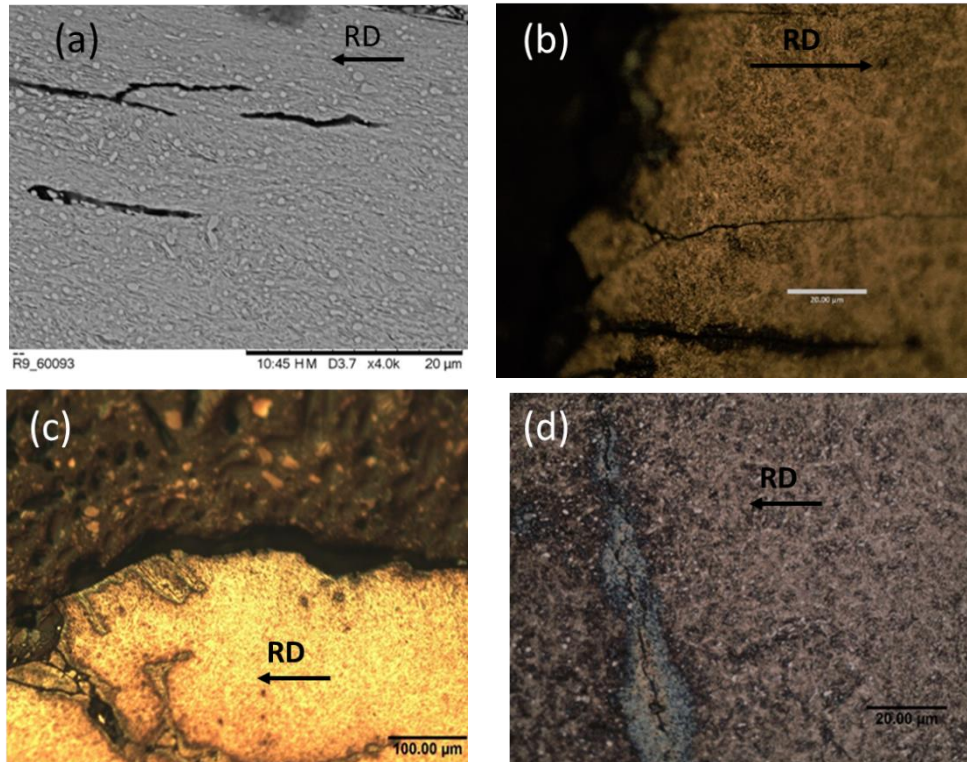


Figure 3-36: Crack orientation in axial and circumferential sections (a) and (b) axial sections; (c) and (d) circumferential sections.

3.6.3 Other observations

In this section, the term WECs was used to elucidate any crack associated with white microstructural alterations even if the cracks were not part of the crack network as defined in Section 2.6.2, while WEBs is used to describe irregular white patches observed close to the contact surface without taking a specific direction, this was used to describe microstructural changes in investigating train tracks, however, the term WEA will be used to describe the white areas having a specific direction inclined with 30° and 80° . The former will be called 30° WEA while the latter will be named 80° WEA. WEAs and WECs were very rare in the investigated bearing samples.

Figure 3-37 shows four images a, b, c and d. These features were observed in the subsurface of axial sections at depths between $270\ \mu\text{m}$ and $390\ \mu\text{m}$. Increasing the magnification of the first three images (a,b and c) showed deformation features that are different from the typical butterfly wings for that, they were classified as separated WECs. No typical WEC networks (defined in Section 2.6.2) were observed in the investigated bearings and the observed features may be parts of butterfly wings located in planes inclined with the investigation surface due to their relatively small length and not connecting to a typical WEC network. In the axial sections, there

are two irregular WEBS. These are shown in [Figure 3-37 \(e and f\)](#). Like these features usually observed in the contact of train wheel to the rail track and the interpretation for these features is probably a severe loading contact in these regions may be due to inserting debris between the contact surfaces or due to high impact level and vibration throughout some of the turbine operating events. Only one WEC appeared in the investigated specimens and presented in [Figure 3-37\(d\)](#). However, it disappeared after a regrinding process to get better images. Specifying the rolling direction, depth and number of rotating cycles of each damage and microstructural change features are very important and should be specified in each image throughout the future studies to estimate the creation conditions of these features.

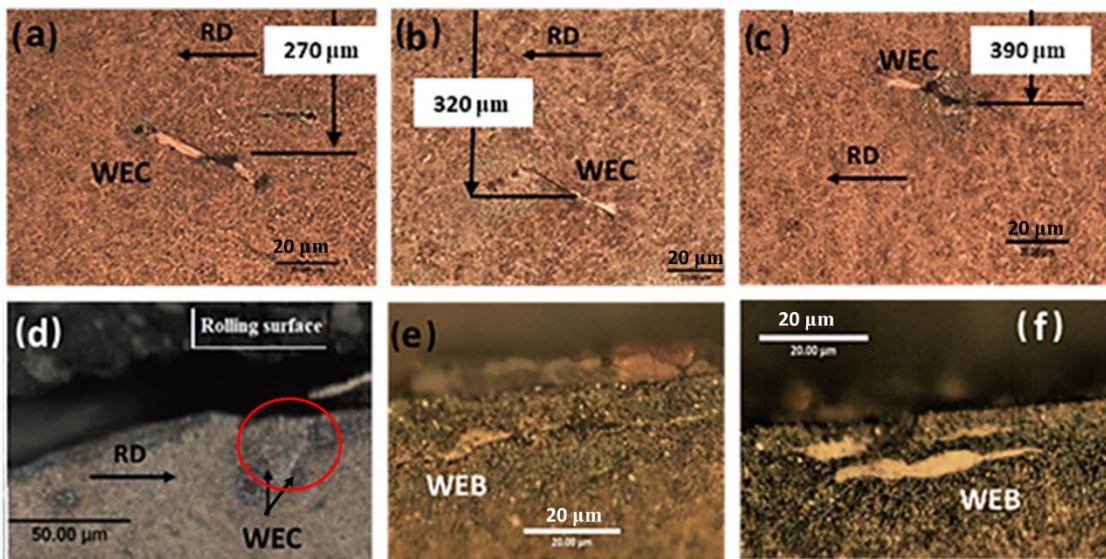


Figure 3-37: Microstructural alteration features; (a), (b) and (c) WEAs in axial section; (d) WECs in circumferential direction; (e) and (f) WEB in the axial direction.

Surface and subsurface cracks probably work together on bearing spalling and flaking, however, the dominance of one depends on the loading level and direction, lubricant and surface finishing, i.e. tribological effects. [Figure 3-38](#) shows the directions of surface cracks (marked with red arrows) and subsurface cracks (white arrows) and more investigation will be presented in [Chapter 7](#). One of the interesting points of the crack direction is that cracks often change their direction when passing through an inclusion; and the new direction probably depends on the stress level, direction and the distance to nearest defect, as shown in [Figure 3-39](#). In general, it is difficult to specify the damage initiation after bearing failure and more investigation during the damage propagation is required. Experience is required in the investigation, however. It was noticed that subsurface cracks are more dominant compared with surface cracks, and the possibility of subsurface crack initiation is

higher than the surface initiation and this supports the findings of Gould et al. [2], Gould and Greco [49] and Evans [13].

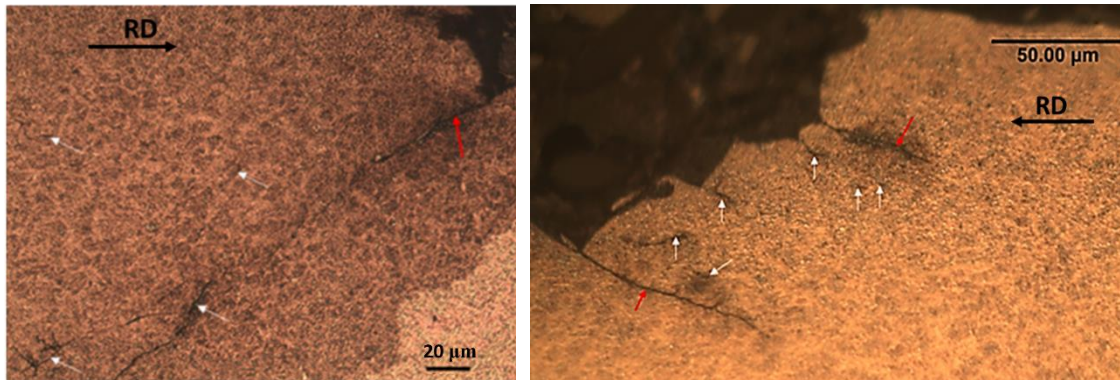


Figure 3-38: Surface and subsurface cracks' role in spalling failure initiation.

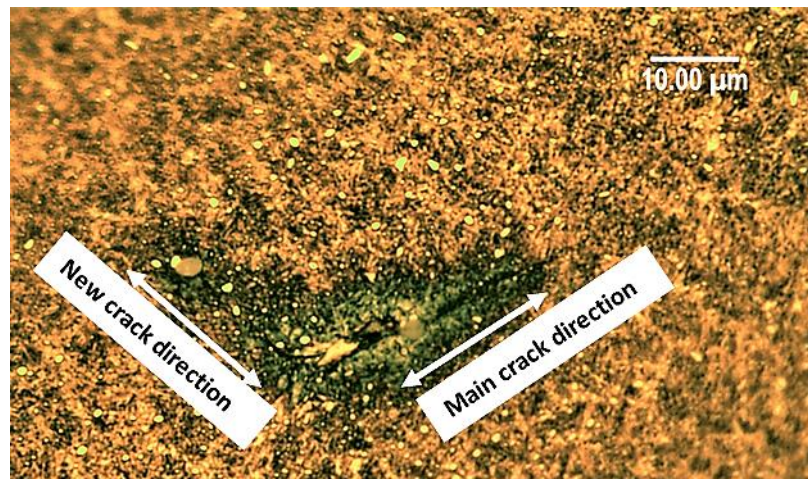


Figure 3-39: Crack direction changed towards the weak points such as voids and inclusions.

3.7 Bearing failure causes and mechanisms

Examining the severely damaged regions (Zone 1) showed a nonuniform damage distribution along the axial direction, the damage near the bearing rim had larger circumferential lengths. This was seen more clearly in the DW bearing, and the damage regions were probably located in the opposite part of each bearing (see [Figure 3-2](#)), therefore misalignment is one of the possible causes of bearing failure. The hardening phenomenon observed on the contact surfaces of the bearing races confirms the overloading to a contact stress levels beyond the compression yield limit, however, it is not clear if this overloading was due to normal operation or due to the operating events. The noticeable variation in the contact surface roughness

between the loading region and out of it leads to the consideration of the tribological causes of unsuitable inner race surface finishing, slipping, overloading and maybe the unsuitable properties of the lubricant as reasons to be nominated as the main causes of the bearing failure. Furthermore, the indentation intensity was observed to be increased towards the severely damaged regions either in the loading inlet and the loading outlet regions with fewer indentations in the loading inlet regions. Different sizes of indentations were observed, and the possible sources of these indentations are the debris from the failed races surfaces, gears, keyways and the gear housing. Indentation size, volume and depth at different locations in the circumferential direction probably provide more information about the loading level and distribution in spite of the formation of this debris at the late damage stage. The non-uniform and short contact strike in the loading inlet region identifies a roller skewing and sudden loading change that may introduce impact loadings within this region.

Overloading causes severe contact stresses beneath the contact region and the high contact stresses due to the surface asperities and/or the severely contact stresses from inserting debris between the contact surfaces, may motivate some tribo-chemical phenomena to take place, such as carbon emigration from the interior of the grains towards their boundaries that cause carbon saturation state and weaken these boundaries, this makes them a preferred site for crack initiation. Furthermore, the severe loading levels may cause dislocation and motivate the small voids associated with the carbides to extend and connect with the nearest voids to initiate microcracks. The continuous overloading and impact stresses increase the possibility of crack initiation in the grain boundaries in addition to the cracks that may initiate from the inclusion boundaries and/or from cracking the inclusion itself and that probably initiated microcracks from the voids. These types of cracks propagate towards each other to introduce macro-cracks and the crack may change its direction depending on the loading level and the nearest weak region (inclusion or void). The group of macrocracks produces a crack network that finds its way towards the inner race contact surface and causing flaking.

3.8 Discussion

The aim of investigating the bearings is achieved by confirming the overloading and the importance of contact stress and SR as very important parameters that deserve to be investigated. The effect of impact does not appear clearly on the surface apart from the length of the loading in distance on the inner race contact region but it was noticed on real turbine operation and testing platforms [247]. Furthermore, there is no previous study presenting the effect of

impact on producing surface and subsurface damage features therefore, investigating the impact loading has a considerable role in understanding the premature bearing failure and investigating this effect should be done by conducting a specific testing procedure by applying various impact loading levels using a new designed test rig as will be presented in the coming chapters. Bruce et al. [5][100] applied the impact loading separately from rolling and their damage features could not be considered as a result of impact loading because there is no evidence that the observed features were due to impact loading. The analyses of the damage distributions gave preliminary results about the stresses which probably caused each damage type. The investigations also revealed interesting damage features to be investigated with more details in the coming chapters by using a new test rig and sets of test discs. The impact loading has been proven in different operating conditions of the wind turbine gearboxes. The new test rig can apply rolling/sliding and impact loading in combination to investigate their individual and interactive effects on fatigue life and subsurface damage features can be introduced by applying the test parameter levels. The probable causes of the investigated bearing damage were also postulated and discussed; however, more investigations are still required for a better understanding of the premature bearing failure phenomenon.

The results of this chapter revealed the future testing levels and the damage features (inclusion damage by separation and cracking, and subsurface microcracks), that should be investigated in the future works. It was also noticed that surface stresses with introducing a traction force have a considerable change, especially in the departure of the rolling element to the contact region. This increases the possibility of surface crack initiation. The interpretation of this, is the opening of the surface crack at this region, i.e. mode I of crack propagation (opening mode), and maybe the crack initiation as well, while at the entrance of the rolling element to the contact region (towards the rolling direction), the possibility of subsurface crack initiation is greater than that from the surface due to high subsurface stresses (maximum shear and Von-Mises). There is also a closing of surface crack at this region that may reduce the possibility of the surface crack initiation and propagation. For that, surface and subsurface microcracks may initiate throughout the RCF damage and propagate towards each other to form a macrocrack which finally causes the damage. This will undergo further investigation within the analyses of the test discs in the coming chapters.

3.9 Conclusions

In this chapter, two planetary WTGBs undergo surface and subsurface investigation. There are several concluding thoughts presented throughout this chapter and they can be summarized in the following points:

- Severe loading levels beyond the bearing material elastic limit. This supports the previous studies which identified the over-rolling as one of the main causes of the bearing premature failure. Different causes such as misalignment, roller edge stress concentration and the wind turbine operating events may be the main causes of the bearing failure. These loading levels affect the surface properties (hardness and roughness) and can introduce subsurface damage features such as damaged inclusions by separation and cracking, in addition to subsurface microcracks.
- The race contact surface roughness experienced a considerable variation within the bearing loading region. This variation either by the severe loading levels or the high slipping (probably more than what currently thought of 5% to 10%).
- The investigated butterfly wings were found to be initiated from the compound type of inclusions by cracking them in a direction approximately parallel to the maximum wing length axis may be due to impact loading. These butterfly wings were observed unconnected to the main crack networks that found their way to the contact surface. A butterfly wing feature was observed beneath one of the dents on the contact surface of the inner race, therefore, this damage feature may be a consequence of severe damage and may be produced in a late damage stage, i.e. after producing the debris from the contact surface flaking, however, this requires more investigation .
- The investigated inner race bearings were probably exposed to a very high loading level maybe higher than 6.0 GPa throughout their operation and a high slipping according to the observed butterfly wing direction and the finding of Vaes et al. [105] and Guetard et al. [189]. This may considerably accelerate the bearing damage. More investigations are still required to estimate the contact stress level precisely.
- A considerable number of microcracks unassociated with inclusions were observed within the subsurface region, therefore, subsurface microcracks may be another damage initiation trigger in addition to those initiated from inclusions. The initiation of these microcracks probably from the voids significantly observed to be associated with the carbides. This will be investigated in further detail in the test disc investigation chapters.

- The inclusions' damage and subsurface microcracks are thought to be produced due to high von-Mises and/or maximum shear stresses. These damaged inclusions were observed close to the contact surfaces. This only takes place when the traction coefficient around 0.3. Therefore, high traction force was expected throughout the bearing operation.

3.10 Key findings forward to rig design and testing

The role of compression and slipping on RCF was confirmed and extensively investigated, however, the role of impact loading on RCF life still has a lack of information. Despite using advanced techniques in designing the turbine gearboxes, the operating contact stress of the planetary bearings is higher than the yield limit. For that, the design stress of the gearbox bearings may need a re-evaluating. However, in the planned tests, the testing contact level will be applied at the yield stress to enable applying Hertz contact theory. This will be performed by designing a new test rig to apply Rolling/ Sliding (R/S), and impact loading on cylindrical test discs made from the bearing steel (AISI 52100). The SR cannot be precisely estimated throughout the bearing rotation, however, it is more than 5% which is specified for the ideal bearing operation [25], and higher than this value is expected. A considerable number of studies were carried out with an SR of -30% to reproduce microstructural alterations. Therefore, the planned tests will be under an SR of $\pm 22.82\%$, to show whether this testing conditions and the test disc number of cycles to failure can reproduce these alterations or not. Despite confirming the impact loading throughout the normal and operating events in WTGs, the contact stresses due to impact loading are not precisely specified. Minitab software of the Design Of Experiment (DOE) will be used to design the internal testing parameter levels (between the chosen minimum and maximum testing parameter levels) by using the Taguchi method. This to investigate the individual and interactive effects of the study parameters (compression, slipping and impact) on fatigue life and the subsurface damage feature distributions. The new test rig will be designed to apply these parameters in combination in a similar way to that in the operation of real WTGB. The details of the newly designed test rig will be explained in the coming chapter.

4

TEST RIG DESIGN FACILITATING COMBINED ROLLING, SLIDING AND IMPACT LOADING

This chapter presents the development of a new test rig to investigate the individual and interactive effects of compressive loading, impact stress and the Slipping Ratio (SR) on fatigue life of two discs made of bearing steel (AISI 52100). Firstly, the design requirements of the test rig mechanisms are summarized. After that, the test rig details, and the rig components are explained. Three mechanisms were designed in order to apply a wide range of the study parameters. Furthermore, the procedure of calculating the test compression stress, impact stress with its assumptions and SR are presented. The geometry of the test discs, material, heat treatment, chemical compositions of the disc material and lubricant are briefly explained and discussed. The operational loading, slipping and impact levels were estimated depending on the results achieved from investigating the WTGBs. The test rig is designed to apply the study parameters in combination like the real bearing operational conditions.

4.1 Design concept development

A new test rig is designed as one of the objectives of this study. This rig uses two different cylindrical discs with line contact to simulate the rolling bearing contact and fully crowned discs to simulate the elliptical contact and to investigate the effect of changing the study parameters (compression, slipping and impact), on the disc RCF life and the subsurface damage features can be introduced under the testing levels. The two test discs (the upper and lower test disc), are made from

bearing steel (AISI 52100 steel) undergone a heat treatment of hardening and tempering to have approximately similar mechanical properties of the real bearings. The cost of these discs is quite less than the bearings, however, most of the contact conditions can be applied under completely controlled levels. The design functions of this rig are:

- To apply contact stress within a wide range of elastic and elastic-plastic contacts.
- Changing the Slipping Ratio (SR) can be easily achieved by changing the outer disc diameters only.
- To apply impact loading which can be varied by varying the test speed and/or increasing the impactor mass by adding additional weights.

The compressive contact load can be measured by using a load cell which should be a zero-order instrument to measure the dynamic loading within short periods (nanosecond), however, the project budget prevents this optimum choice. The SR can be calculated by using the disc diameters during the disc design, however, stress due to impact (impact stress) depends on the mass of the rig dynamic components and its rotational speed.

The new Rolling/Sliding (R/S) and impact test rig is designed to apply the study parameters simultaneously in combination under controlled levels. The rig consists of three mechanisms; each one is used to apply one of the study parameters. The main components of the designed test rig can be seen in [Figure 4-1](#). The rig is driven by a 3-phase 4.0 kW A/C electric motor (part 5), with a rotational speed of 1500 rpm. A gearbox (part 6) is attached to the motor to reduce the motor speed to a rotational level identical to that of the planetary bearings in real WTGs. The gearbox ratio (the input speed of the motor to the output speed of the gearbox output shaft), is 10:1. The output shaft of the gearbox is connected to the main shaft of the rig using a flexible coupling. The main shaft supports the lower disc and passes through two side plates (parts 13 and 19) and settling on two ball bearings.

The control panel of the test rig can be seen in [Figure 4-2](#). The motor can rotate in two directions using a directional button (part 6), and the rotational speed can be controlled using a motor speed adjuster button (part 5). A load cell digital indicator (part 1) is used to show the compressive loading applied.

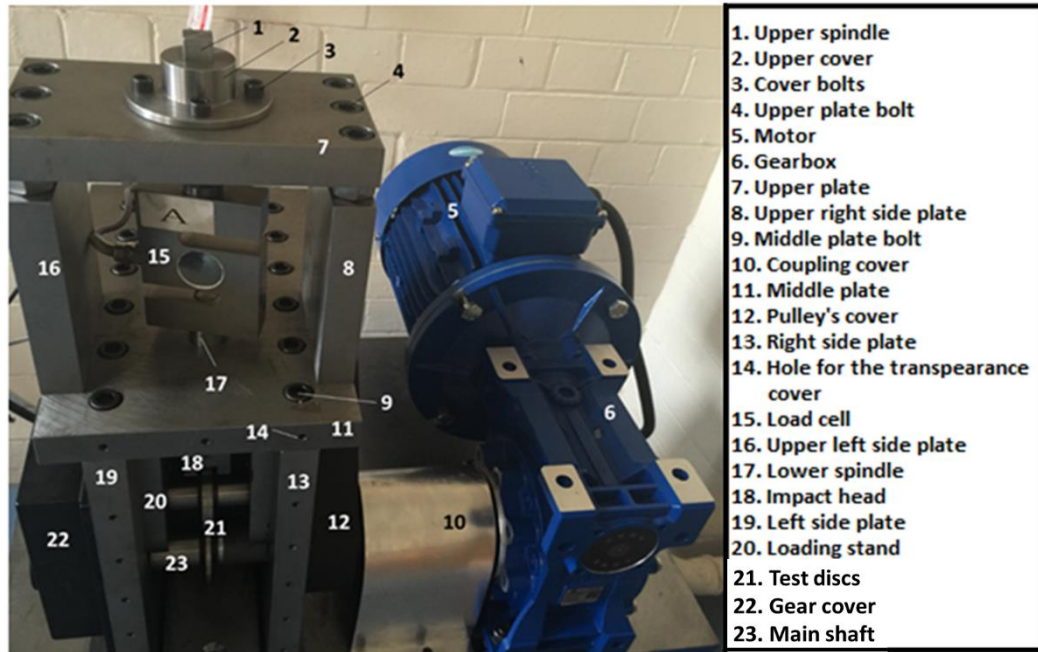


Figure 4-1: Main components of rolling/sliding and impact test rig.

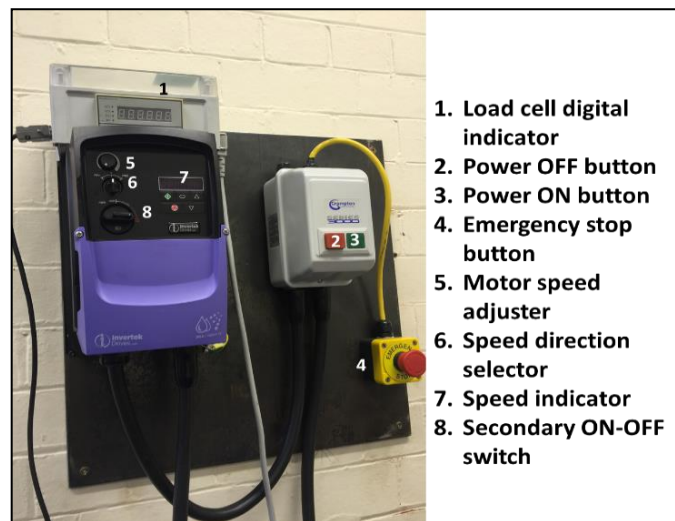


Figure 4-2: Control panel of the test rig.

There are meshed gears, with a 1:1 speed ratio, that connect to the main and loading shafts on the other side of the motor. This gear can be seen in [Figure 4-3](#). With this speed ratio, the slipping ratio can be controlled by changing the outer test disc diameters. The left bearing cover (part 7), is designed to be larger than the loading shaft bearing diameter to enable taking the loading shaft and its bearings out when replacing the test discs or carrying out rig maintenance. This bearing cover has a

vertical slot hole (part 14) to permit the loading shaft to move slightly up and down during the application of the compressive loading.

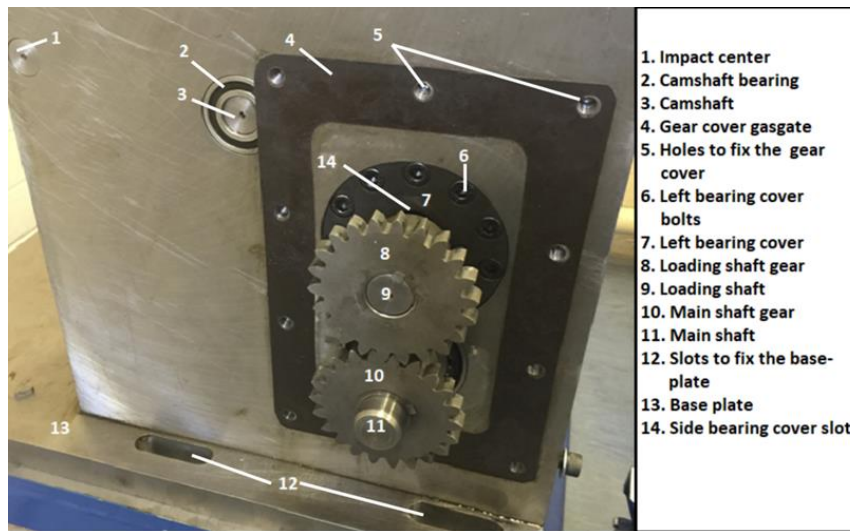


Figure 4-3: Details of the test rig gears.

A pulley is also attached to the main shaft to drive another one on the camshaft via a V-belt to produce impact loading as can be seen in [Figure 4-4](#). The camshaft rises an impact lever and when it falls off, the impact will be applied on the top of the upper test disc. The speed ratio of the pulleys is 1:1 to produce one impact event at the same location in each rotating cycle. Impact loading on the wind turbine bearings is not continuously applied in each cycle, despite the relatively small load variation due to wind gust. An additional mechanism to control the impact application has been designed to enable applying an impact loading percentage identical to that in the real operating conditions as can be seen in [Figure 4-5](#). The pulling of the red handle will raise the horizontal impact releasing component and pull the impact lever up by a steel rope. An extensometer is also introduced to measure the deflection under applying the quasi-static and dynamic loadings. The test disc deformation will be assumed to be due to the loading and the main and loading shafts were assumed to be rigid due to their large diameters and short spans. However, this will be discussed in more detail later. The extensometer has a high accuracy of $\pm 1 \mu\text{m}$ and a variable sample rate in the range of 1,000 to 51,000 reading/s.

In each test, two cylindrical test discs are used. These discs are made from commercial bearing steel (AISI 52100) and exposed to a heat treatment according to the standard hardening procedure in BS EN ISO 683-17:2014 [248]. The discs (upper and lower disc) are tested to determine the number of cycles to produce

damage in their contact surfaces. By using the test speed and the time of introducing the damage; the number of cycles to failure can be calculated.

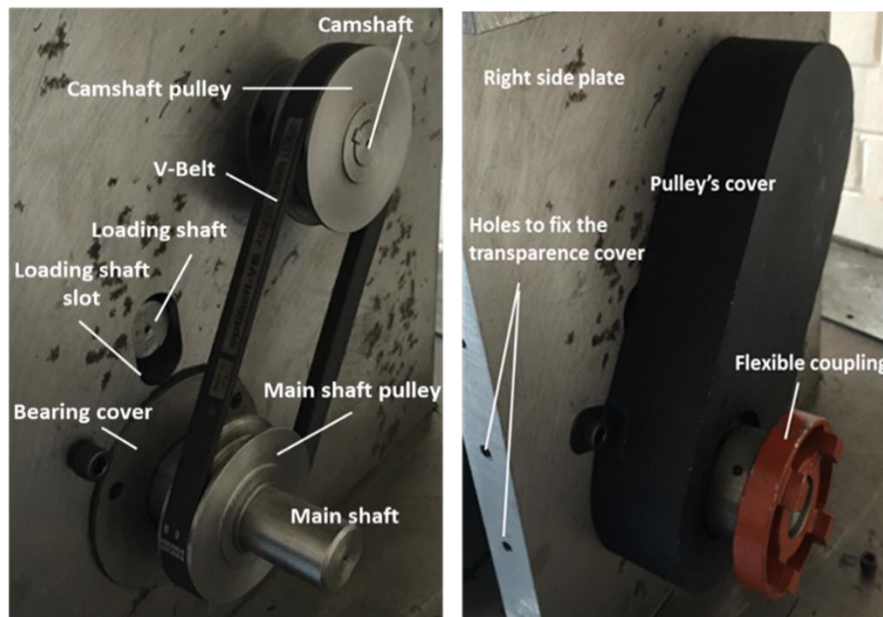


Figure 4-4: Details of the belt drive mechanism used to rotate the camshaft, without cover (left) and with cover (right).

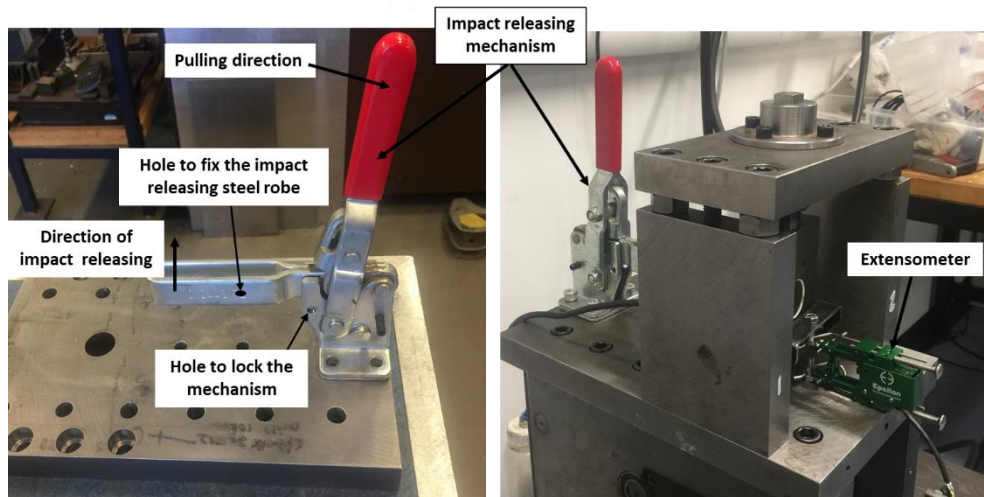


Figure 4-5: Impact releasing mechanism and extensometer.

A translucent cover is fixed at the front of the test rig to enable observation of the damage when it appears to the contact surface. The test discs have a surface roughness approximately similar to the investigated planetary bearings in [Section 3.4.2](#) of $\sim 0.23 \mu\text{m}$. Throughout the testing, the lower test disc is submerged

in *SP 320 Alpha* oil which is the same type of lubricant used in multi-megawatt wind turbine gearboxes. This eliminates the effect of lubricant type on the RCF life. Because the oil additives may affect the damage features, especially the microstructural alterations, the oil is used without any additives for wear reduction or for improving the stability of the lubricant viscosity like the real WTGs. During the test disc rotation, the lower test disc carries the lubricant to the contact region via a splash approach. A constant compressive load is applied to the test discs using a screw jack mechanism. The design of this mechanism can be seen in [Figure 4-6](#), it consists of an upper spindle (part 10), loading nut (part 11), load cell (part 7), lower spindle (part 13) and loading stand (part 3). Simultaneously, impulse loading (impact) is applied to the contact line of the two cylindrical test discs. Details of test rig mechanisms for applying the study parameters will be explained extensively in the following sections.

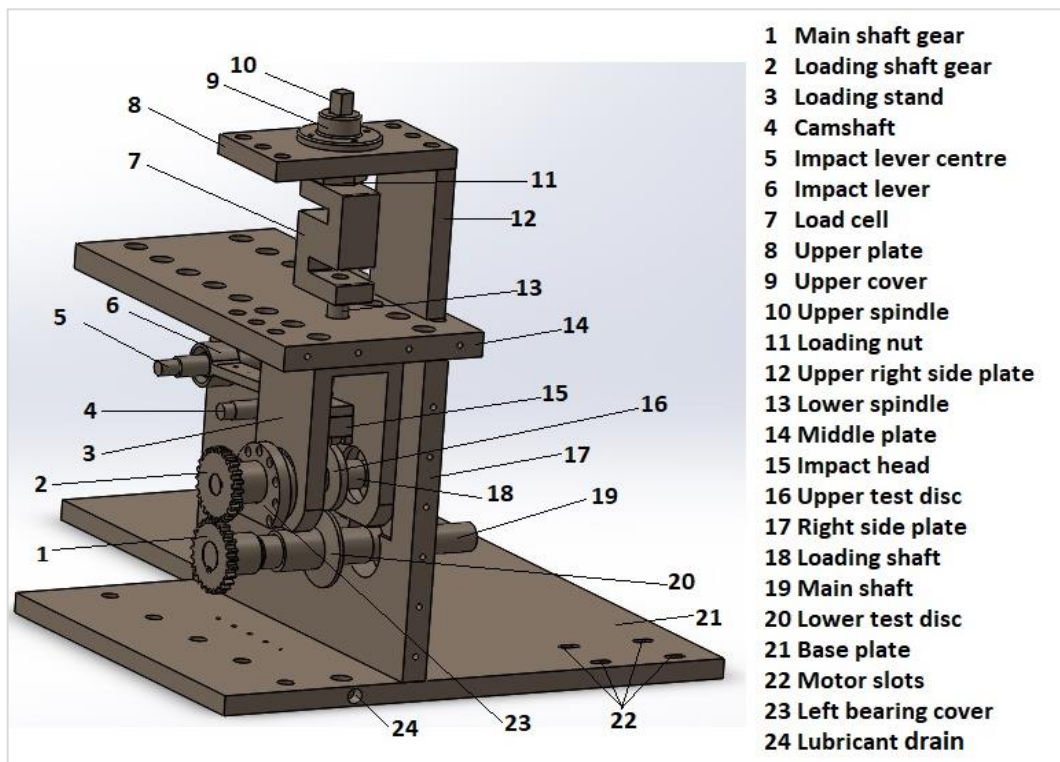


Figure 4-6: Schematic diagram showing the main parts of the designed test rig.

4.1.1 Compression mechanism

in the previous studies [49][213], compressive loading has been applied by using hydraulic cylinders. If there is a significant transient loading, the loading may damage the hydraulic cylinder pressure washers. In this study, to reduce the possibility of damaging the washers, a screw jack compression mechanism was

designed. This mechanism includes a load cell to measure the compressive force and other parts to apply and transfer the force. To allow for a slight vertical movement of the test discs during the application of the compression, two slots with vertical centrelines are made in the right-hand side plate (part 17 in Figure 4-6) and the left bearing cover (part 23) to allow for a relatively small vertical movement during application of the load, disc replacement and rig maintenance. Figure 4-7 illustrates the components of the compression mechanism. The upper spindle (part 1) has a square end penetrating the upper cover (part 2) to prevent any rotational movement throughout the application of the compressive load by turning the loading nut (part 4) in an anticlockwise direction or releasing the load by turning it in the other direction. The compressive load is transmitted from the upper spindle and nut to the load cell (part 5) and from the load cell to the lower spindle (part 17) then to the loading stand (part 8) to apply finally on the upper test disc (part 15). The upper test disc is fixed on a simply supported loading shaft (part 10) settling on a pair of Single Row Angular Contact Ball Bearings (SRACBBs) type 7305BEP SKF (see Table 4-1 which illustrates all the specifications of the bearing types used in the test rig). The rig main shaft (part 11) which carries the lower test disc is also supported by a pair of 7207BEP SKF Single Row Angular Contact Ball Bearings (SRACBBs). This pair of bearings is fixed inside bearing houses (one on each side plate). For safe operating, the dynamic capacity of each supporting bearing is higher than the combined load of compression and impact loadings.

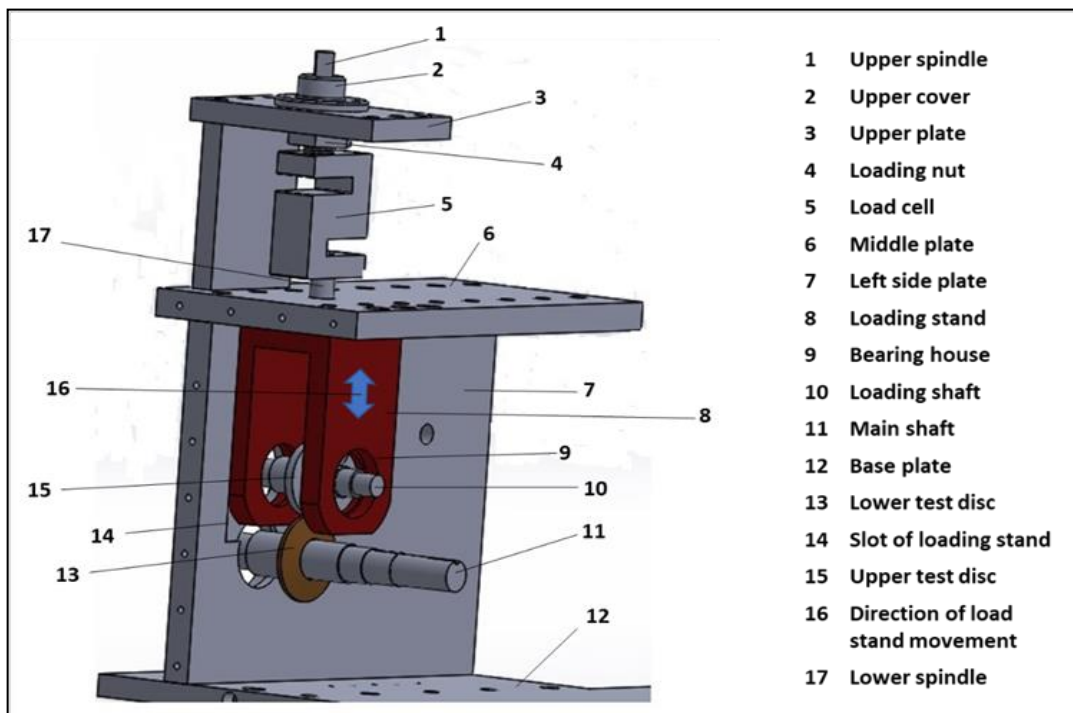


Figure 4-7: Main components of the compression mechanism.

To be able to apply the Hertzian contact theory, the vertical loading stand movement is restricted by two slots in the inner side of the two side plates (part 14 [Figure 4-7](#) and the slot shown in [Figure 4-8](#)).

Table 4-1: Bearings of the test rig and specifications (dimensions in mm).

Bearing location	Bearing model	Inner Dia.	Outer Dia.	Thickness	Static load rating (kN)	Dynamic load rating (kN)
Loading stand	7305BEP SKF	25	62	17	15.3	26.5
Main shaft	7207BEP SKF	35	72	17	20.8	31
Camshaft	6004 FAG	20	42	12	5	10

[Figure 4-8](#) shows the configuration of the test discs, bearings and impact head (part 4) which is one of the components of the impact mechanism. To increase the accuracy of the compressive loading measurement, a calibration curve for the load cell was made by applying known loads. This was compared with the load cell readings, as can be seen in [Figure 4-9](#). The maximum error in the load cell readings was 1.16% thus, there is no need for any correction factor for the load cell reading.

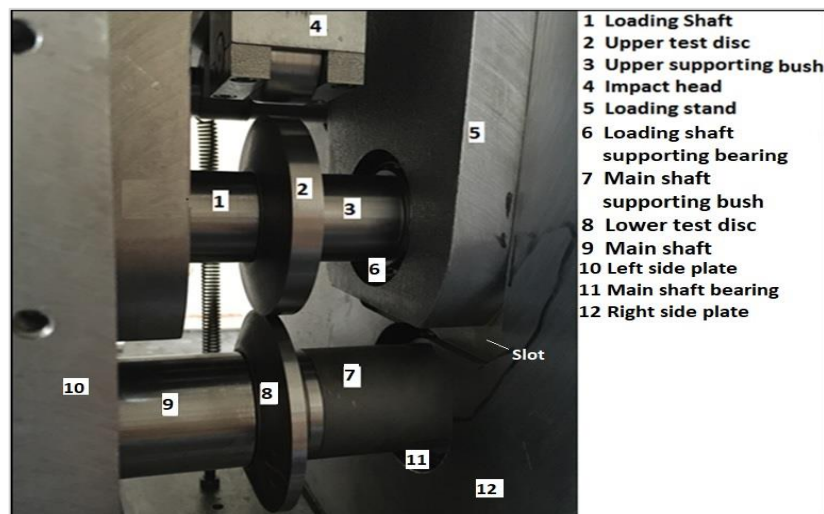


Figure 4-8: Configuration of test discs and impact head with loading shaft supporting bearing.

The central distance between the main shaft (part 9) and the loading shaft (part 1) centerlines must be equal to the summation of any two test discs radii plus an additional distance of 1.5 to 2.0 mm. This additional distance is for the test discs deformation when applying the compressive loading and having relative movement during the test disc replacement. Two slots, one on the side plate and the other in the left bearing cover, allow for this small relative movement which also has a small effect on the gear teeth mesh. For that, involute gear teeth have been chosen because

they are more suitable than the stub gear teeth type since the former has a longer tooth profile which allows for the required small relative change in the central distance between the loading shaft and the main shaft whilst applying the compressive and impact loadings.

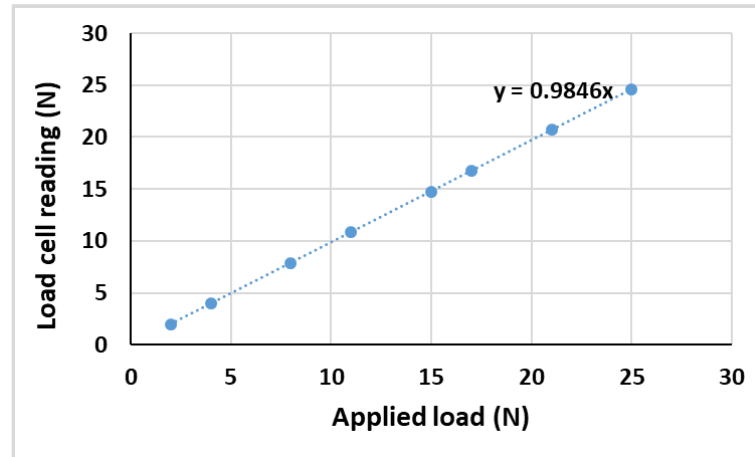


Figure 4-9: Calibration curve of the test rig load cell.

4.1.2 Slipping mechanism

During an ideal condition of ball bearing rotation, i.e. under constant loading, good mounting and sufficient lubrication, there is a small Slipping Ratio (SR) of ~5% [25]. This SR is due to the rotational motion and momentum of the rolling elements. SR results from a relative movement between the contact surfaces especially during the variation of the rotational speed. In WTGBs, SR increases with transient loading where the rotational speed and contact loading are varying due to wind gust and operating conditions [43][44][117]. There are other factors which can affect SR, for example, the roughness of the contact surfaces, lubricant viscosity and film thickness, as will be explained in Section 4.3.2. SR can be defined as the ratio of the difference between the linear contact velocities, i.e. rolling elements and race, to the average velocity of them. SR for the test discs can be calculated as:

$$SR\% = \frac{\text{Linear velocity difference between the two discs}}{\text{average velocity of the two discs}} * 100\% = \frac{2(U_{ud}-U_{ld})}{(U_{ud}+U_{ld})} * 100\% \quad 4.1$$

where U is the linear velocity in the contact region and the subscripts ud and ld refer to upper and lower discs respectively. The two test discs are rotating with the same rotational speed by the pair of the gears on the test rig left-hand side. In this test rig, SR can only be varied by changing the test disc diameters. When the lower disc velocity is greater than the upper one, i.e. $U_{ld} > U_{ud}$, SR will have a negative

value. Positive and negative SR have been found to have a considerable effect on fatigue failure [49][66]. Accordingly, positive SR takes place when the traction force produced by friction has the same direction of the linear velocity direction, i.e. it takes place on the test disc having a smaller diameter. Similarly, negative SR takes place when the traction force is in the opposite direction to the movement, i.e. on the test disc with a larger diameter as can be seen in Figure 4-10. In this test rig, there will be a positive SR on the upper test disc contact surface and negative SR on the lower disc surface.

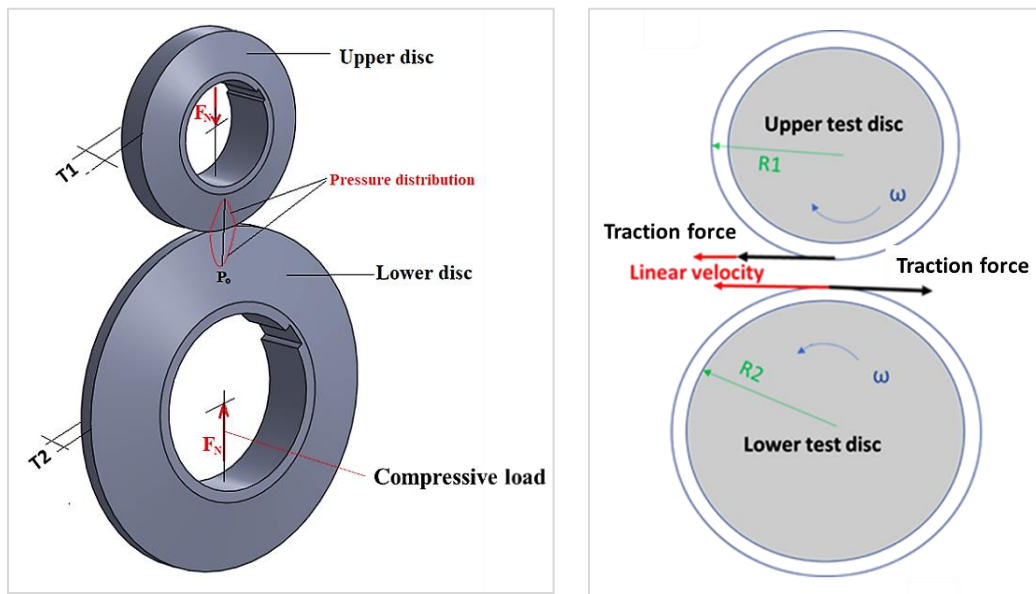


Figure 4-10: Test discs contact showing compression force and pressure distribution (left) and, velocity and traction force (right).

4.1.3 Impact mechanism

To introduce impact and compressive loadings simultaneously, an impact mechanism is designed to have an impact lever moving beneath the loading stand during the application of the compressive loading. Figure 4-11 shows the main components of the impact mechanism. The impact centre (part 5) is a non-rotating component fixed between the two side plates and the camshaft (part 7) takes its rotational speed from the main shaft through a pulley and V-belt drive presented in Figure 4-4. The impact lever (part 3) can rotate freely about the impact centre.

To prevent more than one impact hit which may result from bouncing of the impact head (part 15) which is attached to the impact lever, a spring is attached to the impact lever using threaded holes (part 6). These holes also used to fix the robe of the impact releasing mechanism. In addition, there are threaded holes in the base

plate (part 10) to fix the impact lever spring in a vertical position. The camshaft is supported by two ball bearings (one at each side), to reduce the friction and support the camshaft during the impact process. A brass bush (part 4) is located between the impact center and the rotating center of the impact lever (part 3) to reduce the friction and make the relative rotation easier.

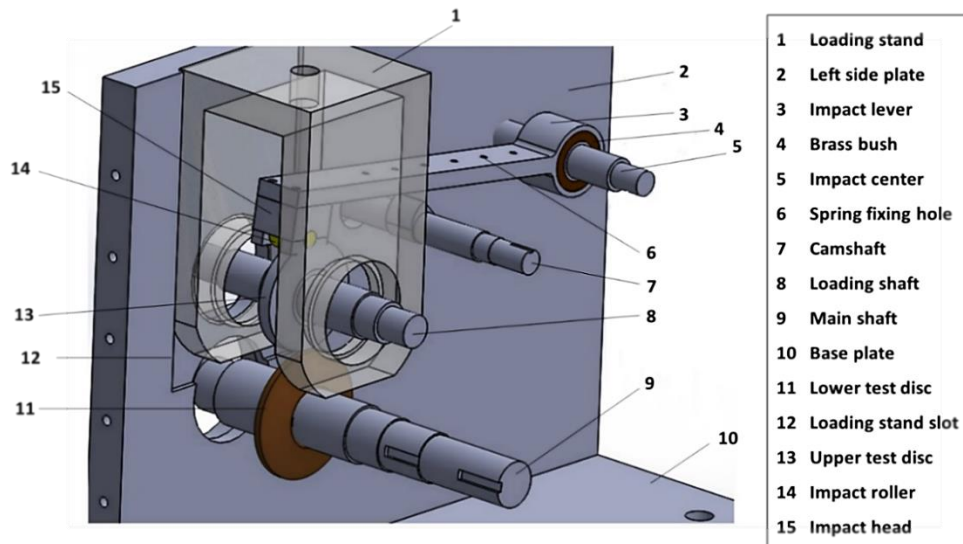


Figure 4-11: Main components of the impact mechanism.

Cam and camshaft details can be seen in [Figure 4-12](#). This special cam design does not follow any type of classical cams because the contact point of the follower (impact lever) is sometimes being above the cam center and at other times is offset either to the left or right-hand side. The maximum cam displacement of 22 mm which is the basis of designing the cam has been divided into 8 divisions and the displacement of each division was calculated (at the radius of each angle). The impact lever velocity (follower velocity) depends on the test rotational speed and it is considered as negative when the impact lever is going up and positive during the impact stroke. The cam profile was designed to give a smooth movement to the impact lever. The cam-side (cut cam profile) is designed to increase the impact velocity and to prevent the cam profile from controlling the impact lever velocity during the camshaft rotation. Characteristic curves for the cam design can be seen in [Figure 4-13](#).

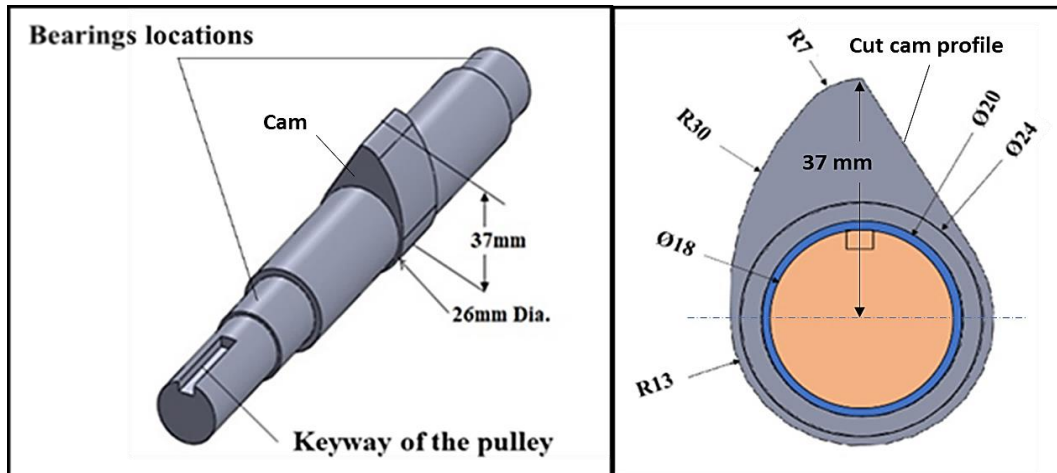


Figure 4-12: Camshaft details (left) and cam dimensions (right).

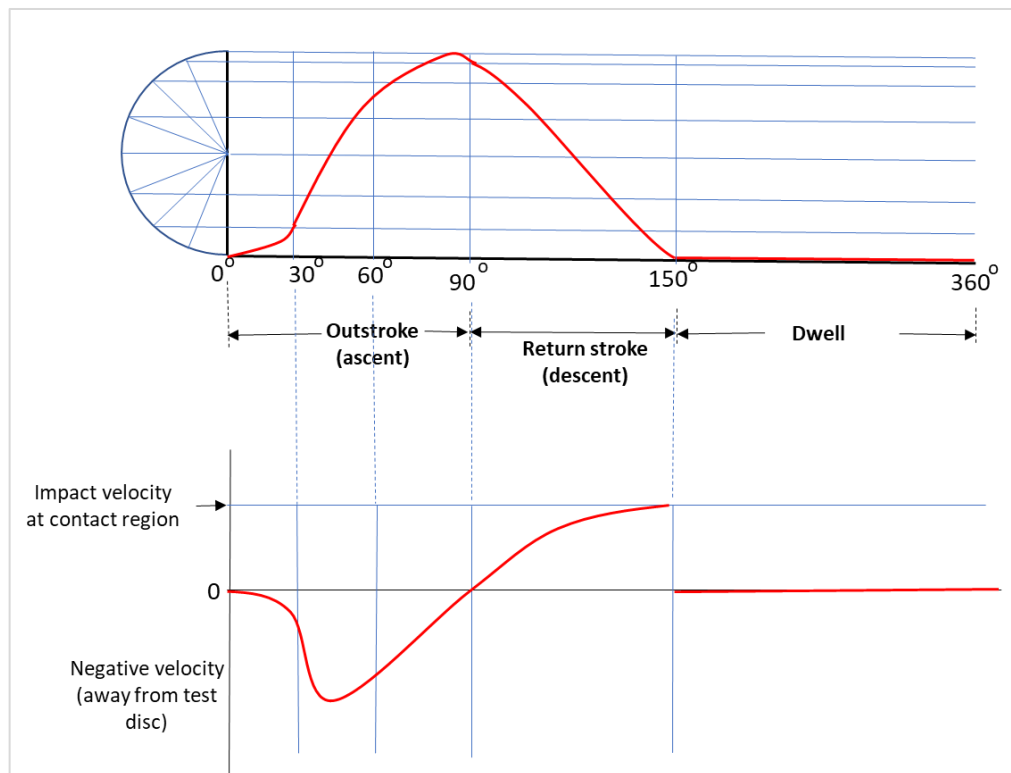


Figure 4-13: Characteristic curves of the cam, displacement curve (top) and impact roller velocity curve at the contact region (down).

Figure 4-14 illustrates the components of the impact lever which consists of three main parts; lever body (part 1), impact head body (part 2) and brass bush (part 5). The impact head body is fixed on the lever body using four M4 bolts. The impact head also consists of secondary components such as bolts, impact roller (part 4) and impact roller covers (part 3).

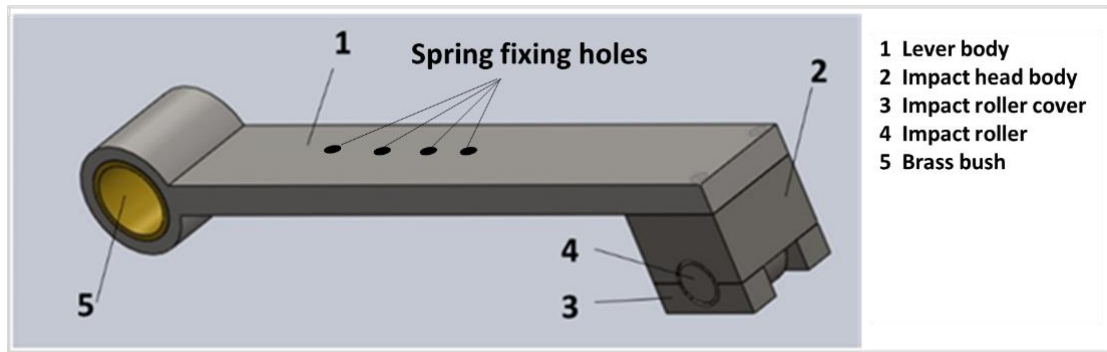


Figure 4-14: Impact lever components.

The locations of the camshaft centre and impact lever centre are chosen precisely to ensure that the impact loading is applied when the impact lever is completely horizontal to simplify the calculations, i.e. vertical impact state. This mechanism applies impact on the top of the upper test disc, however, in the contact region between the two test discs, this impact loading transfers into pulse loading due to pre-compression loading. This case is similar to apply impact loading on the planetary gears in WTGs and its transform to preloaded planetary bearings.

4.2 Test disc design

Two types of disc profiles were manufactured: a disc profile with the effect of stress concentration (flat test discs with different lengths) to simulate line contact of roller bearings and one with a fully crowned profile to avoid stress concentrations (a fully crowned upper disc on a flat lower disc) to simulate elliptical contact. The elliptical contact has a stress state of plane stress, however, for the line contact, a plane strain contact state should be used to analyze the subsurface stress distributions. Both of these two types of contact have a considerable number of engineering applications and there is slightly difference in their subsurface stress distributions.

The summation of the upper and the lower disc radii must be equal to the distance between the loading and main shafts plus 1.5 mm to 2.0 mm as mentioned in [Section 4.1.1](#). This centreline distance was designed to be where the loading shaft is located at the centres of its side-slots to provide a space for a relative vertical movement throughout the assembly, loading and maintenance processes. The lower and upper test discs are fixed on the main and loading shafts using standard 6mm and 5 mm keyway respectively, and each test disc has a maximum thickness of 15 mm in the test disc to shaft contact region. Two steel bushes are designed to be

placed beside the test discs pair, i.e. between each test disc and the supporting bearing in the right side plate, to prevent any side movement throughout the testing.

4.2.1 Material and dimensions

According to the standard ISO 683-17: 2014[248], the test disc material used was the bearing steel 100Cr6 (AISI 52100). This was concluded from the steel chemical compositions are provided by the material supplier certificate can be shown in [Appendix B](#) and re-illustrated in [Table 4-2](#).

Table 4-2: Chemical analysis of test disc material.

Cast No.	C	Si	S	P	Mn	Cr	Mo
A0865Z	0.98	0.21	0.018	0.009	0.44	1.36	0.06

Roller bearings are normally used in WTGs due to high loading levels and flat discs contact usually used to simulate this contact type, despite the slightly curved roller profile in these bearings to avoid stress concentration [25]. Misalignment of bearing components, roller profile, bending of shafts carried by bearings and the deformation of bearing houses usually introduce overloading on the roller edge due to stress concentration. For that reason, conducting tests using flat discs with edge stress concentration has a great importance because this contact state is closer to the real one in roller bearings. To avoid this stress concentration in WTGBs, the rollers usually have a specific curved profile (crowned), however, this profile work under a range of loading level and the stress concentration exists out of this loading range (see Oswald et al. [249] for more information). Test disc design and dimensions for line contact were chosen to apply the required compressive stress and SR as can be seen in [Figure 4-15](#). Outer radii can be chosen for each test depending on the required SR as illustrated in [Table 4-3](#). The upper test disc has an axial length (contact length), of 8 mm. This is to avoid the misalignment of contact in the test disc contact region, while the lower disc has an axial length of 4 mm to apply a suitable contact stress levels as will be detailed in [Section 4.3.1](#).

Table 4-3: Test disc radii and the corresponding slipping ratio.

Lower disc Dia. mm	Upper disc Dia. mm	SR%
77	72	6.71
78	71	9.4
81	68	17.45
83	66	22.82

It is important to check the axial length and the contact length due to flattening the contact bodies under the effect of compression. For flat discs, this contact is a perfect line contact with a stress concentration at the disc edges (for more details see Chapter 6 in Harris and Motzala [25]). For elliptical contact, i.e. the fully crowned test discs, the subsurface stresses are slightly different than the line contact due to different contact stress states (plane stress for fully crowned discs and plane strain for line contact). However, the elliptical contact stress can be safely used as case without stress concentration. For the importance of fully crowned test discs, the geometry and dimensions of them will be explained in the coming section.

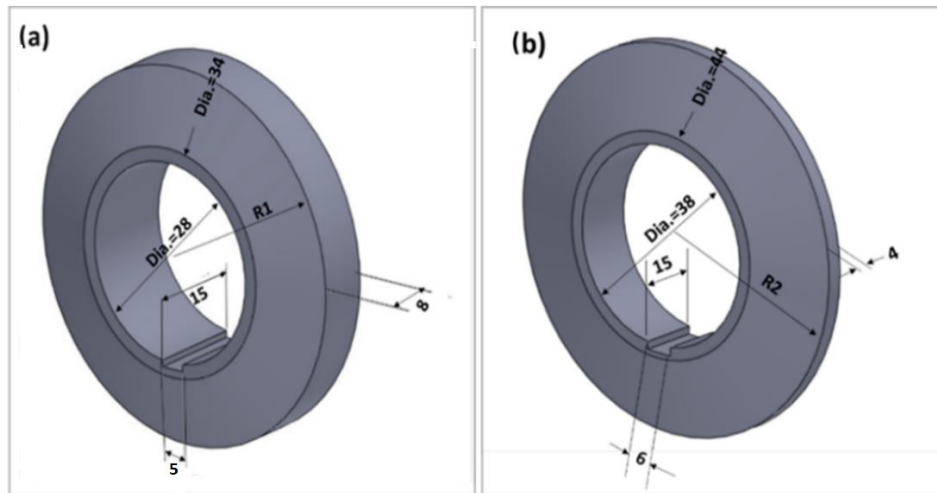


Figure 4-15: Flat test discs dimensions (a) Upper disc; (b) lower disc.

The denoted company of the investigated 2 MW WTGBs provided the number of the power productive operating hours of the gearbox, which is 64,658 hours. This means a continuous operation for 7.381 years. From Table 3-1, the nominal planetary speed is 42.47 rpm, thus, the bearings rotated 164.762 million cycles with an average annual million cycles of ~ 22.322 . The annual impact cycles due to operating events that causing impact loading are $\sim 15,000$ cycles (as mentioned in Chapter 2). This by considering 3,000 operating events/year [51]. Thus, the percentage of impact loading will be $\sim 0.067\%$, i.e. ~ 7 cycles for each 10,000 cycle. The same percentage of $\sim 0.068\%$ is also confirmed by calculating the total number of rotating cycles for 76,577 hours of productive and idling time by considering the same annual number of operating events. The impact loading will be applied in the fully crowned tests at a percentage similar to that taking place due to operating events in WTGBs, i.e. 35 impact cycle for each 50,000 rotating cycle which means 0.07% of the rotating cycles.

4.2.2 Test disc design to avoid the edge stress concentration

Designing the test discs with a different axial length (thickness) produces a stress concentration at the edges of the contact due to the test disc flat profile. However, this stress concentration is unavoidable in actual roller bearings, even by using flat contact discs of the same axial length or by filleting the disc edges according to the standards BS- ISO 7063:2018 [250] and BS ISO 3096:2018 [251]. Four three dimensional FE models to analyze the surface and subsurface contact stress distributions by using flat discs with different thickness, equal thickness, fillet test disc edges and fully crowned discs, will be discussed.

Simulating the contact problems using Finite Element (FE) analysis is an alternative way to show the surface and subsurface stress and strain distributions. Four FE models of three-dimensional test disc simulations were built up using ABAQUS-6.14.2 software and by using real test disc dimensions. This was to carry out the pressure and stress analyses within the contact region and to show the stress concentration. The analyses of these models can be seen in [Appendix C](#).

Point contact (or sometimes call circular or elliptical contact), represents ball bearing problems; however, this is widely used to simulate RCF problems. This type of contact is a plane stress problem that slightly differs from plane strain in line contact (roller bearings) [252]. Theoretical impact calculation formulas for this type of contact including impact forces and stresses are available. Furthermore, stress concentration cannot be avoided except by using this type of contact or by using a logarithmic roller profile (see [Figure 2-5](#)). For the mentioned reasons, testing the contact of the curved upper disc on a flat lower disc will be considered to avoid the stress concentration state. To accelerate the test, high slipping levels (as presented in previous studies in [Section 2.4.3](#)) can be used. The SR of 22.82% has been chosen to enable comparing the results with flat discs and confirm the effect of the study factors on test disc life and the effect of stress concentration. The geometry and dimensions of the upper and lower discs without stress concentration are presented in [Figure 4-16](#).

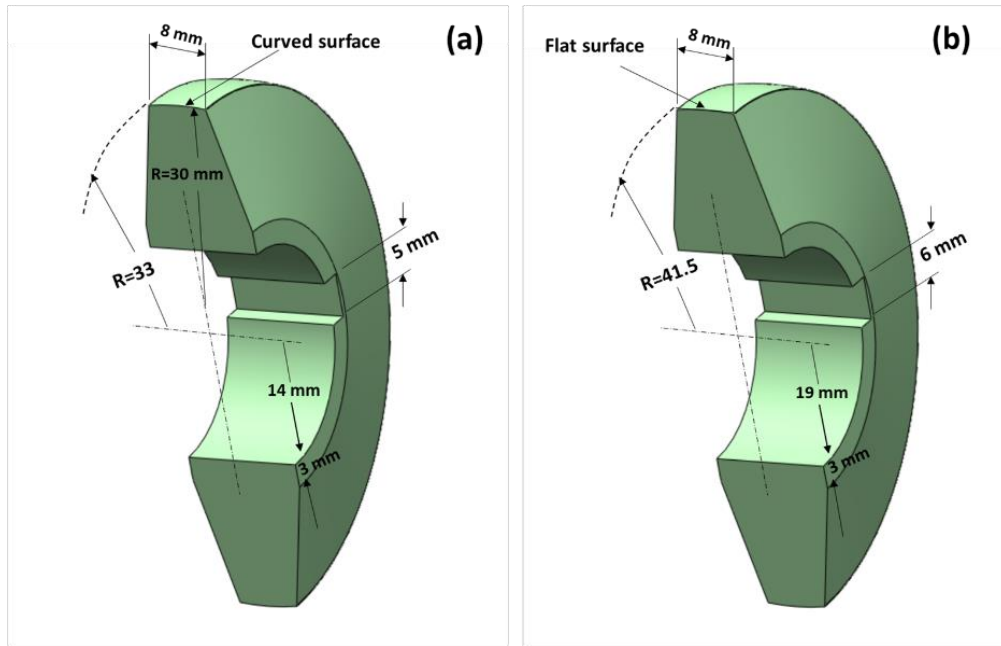


Figure 4-16: Full section and dimensions of crowned and flat test disc (a) upper test disc (b) lower test disc.

For the second group of test discs (fully crowned upper disc), it is expected that the required number of cycles to introduce surface spalling or subsurface damage (flaking), will be larger than the required number for flat discs because there is no stress concentration.

The aim of testing the fully crowned disc profile is to compare the disc life with those having a stress concentration (flat discs). If the fully crowned test discs fail before the required number of cycles under yield stress contact, due to unsuitable material cleanliness level, it is expected that no microstructural alterations will be introduced.

4.2.3 Heat treatment

Heat treatment is very important to ensure that the test discs have approximately the same mechanical properties as the investigated WTGBs. According to ISO 683-17: 2014 [248], the procedure of the heat treatment considered in this study is detailed in Table 4-4. After the heat treatment, the test disc material hardness was measured by using a microhardness instrument and applying a 1.0 kg load for 15 seconds. The hardness was found to be ~59 to ~60 HRC.

Table 4-4: Heat treatment procedure of the test disc material.

Description	Temperature / time	Cooling method
Stress relieve annealing	550 - 650°C / 120 min	Air cool
Martensitic hardening	830 - 870°C / 20 - 60 min	Oil quench
Tempering	160 - 350°C / 120 min	Air cool

4.2.4 Surface finishing

Test disc surface roughness is a very important parameter due to its effect on the traction coefficient. To eliminate the effect of surface roughness between the investigated failed bearings and the test discs; they should have the same surface roughness. The surface roughness of the test discs was checked by measuring the roughness by choosing three test disc pairs. The roughness (R_a) of the upper and lower disc of each pair was measured in the axial and circumferential directions in three locations and the average was calculated. For the upper test disc, the circumferential roughness, was $\sim 0.27 \mu\text{m}$, while axial surface roughness of the upper test discs had an average roughness of $\sim 0.37 \mu\text{m}$. However, the lower test disc roughness was ~ 0.4 in the axial direction and the circumferential roughness was ~ 0.32 . The surface roughness of the fully crowned discs could not be precisely achieved by the mentioned level because of their manufacturing process (machining cut and surface polishing). The best average roughness achieved was $0.65 \mu\text{m}$ in axial direction and ~ 0.38 in the circumferential. This probably affected the results; however, the roughness difference is considered as an undesired factor like the difference in the material inclusion distribution which cannot be controlled.

4.3 Design calculations

A vertical compressive loading should be applied within the maximum elastic limit to ensure that the calculations of stress distributions can be made according to the Hertzian contact theory. Impact loading levels are unknown in WTG bearings; therefore, the test impact loading is controlled by the test rig rotational speed, the equivalent impact mass of the impact lever and the test disc geometry and their material stiffness. Details of the calculation procedure according to the test rig mechanisms will be presented in the following sections.

4.3.1 Compressive pressure and stress calculations

Hertzian contact stress is a function of the mechanical properties, the geometry of the contact bodies and the compression force. For the designed test discs, the calculation results have a percentage error due to the effect of edge stress concentration which affects the pressure levels within the edge neighbouring regions. However, to simulate roller bearing contact, a flat disc profile with equal disc length was used in previous studies such as Bruce [3] and flat discs with different contact length were also used by Shu-Xin et al. [214] and Hertz contact theory is usually used for calculating the contact stresses for this geometry. The mechanical properties used in the calculation procedure are the modulus of elasticity of the test disc material (E) and the Poisson's ratio (ν), while for geometry, the reduced radius of curvature (R^*) is used. The reduced radius and reduced modulus of elasticity (E^*) can be calculated using Eqn. 4.2(a) and Eqn. 4.2(b) respectively [252].

$$R^* = \frac{1}{\frac{1}{R_1} + \frac{1}{R_2}} \tag{4.2(a)}$$

$$E^* = \frac{1}{\frac{1-\nu_1^2}{E_1} + \frac{1-\nu_2^2}{E_2}} \tag{4.2(b)}$$

where R is the test disc radius and the subscription 1 and 2 refer to upper and lower discs respectively. The mechanical properties of the test disc material including the disc hardness are illustrated in Table 4-5. The disc hardness after the heat treatment and the polishing process was measured by using *DuraScan*[®]*Struers* machine.

Table 4-5 Mechanical properties of the test discs material [3][124].

Young modulus (GPa)	210
Hardness (HV)/HRC	727-775/59-61
Poisson's ratio	0.3
Density (kg/m ³)	7800

Using Hertzian contact theory, pressure distribution $p(x)$, contact width (a and b) which introduced owing to the deformation of the contact region in the rolling direction and perpendicular to it respectively. and the maximum compressive contact stress (P_0) for the two types of contact (line and elliptical contact) can be calculated using Eqn 4.3. and Eqn. 4.5 respectively.

$$p(x) = P_o \sqrt{1 - \left(\frac{x}{b}\right)^2} \quad 4.3$$

$$a = 1.128 * \sqrt{\frac{F_N R^*}{T_2 E^*}} \quad \text{and} \quad P_o = \sigma_c = \frac{2F_N}{\pi a T_2} = \sqrt{\frac{F_N E^*}{\pi R^* T_2}} \quad \text{for line contact} \quad 4.4$$

$$a = \sqrt[3]{\frac{3A^2 B F_N R^*}{\pi E^*}}, \quad b = \sqrt[3]{\frac{3B F_N R^*}{\pi A E^*}} \quad \text{and} \quad P_o = \sigma_c = \frac{1.5F_N}{\pi ab} \quad \text{for elliptical contact} \quad 4.5$$

where F_N is the applied compressive force, T_2 is the contact length, A and B are constants which can be calculated using Eqn. 4.6 [252];

$$A = 1.0339 \left(\frac{R_y}{R_x}\right)^{0.636} \quad \text{and} \quad B = 1.0003 + \frac{0.5968 R_x}{R_y} \quad 4.6$$

where R_x and R_y are the reduced radius in the rolling and axial directions respectively. The procedure of calculating the contact force and stress is given in Appendix A.

Increasing the compressive loading level leads to an increase in the maximum stress levels and changing their depths, however, introducing a traction force between the contact discs, brings the maximum stresses towards the contact surface. However, all the stresses induced due to contact are increased by increasing the traction force. All contact stresses in the test disc contact region are presented in Figure 4-17. The two loading levels presented in this figure represents the increase of contact load by 10%. This distribution shows the stress levels within the contact region independently of whether the stress location on the contact surface or in subsurface.

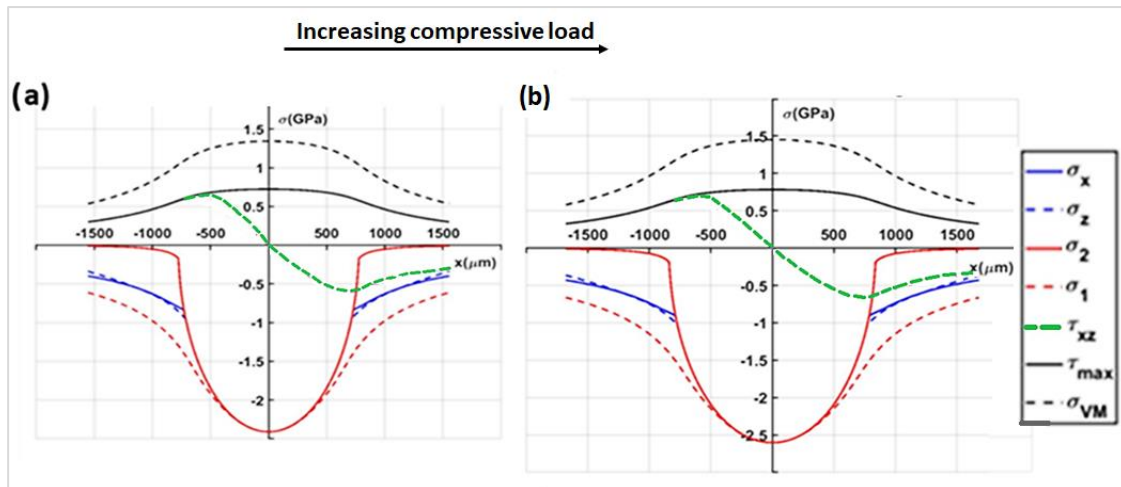


Figure 4-17: Variation of contact stresses beneath the test disc contact region (a) Hertzian contact stress of 2.40 GPa; (b) Hertzian contact stress of 2.64 GPa.

Figure 4-18 [195] presents the effect of traction force. Introducing this loading type change the contact problem to be a non-Hertzian contact problem. In the opposite direction of rolling and traction force, i.e. at the region where the roller leaves the contact region (in the left-hand side), σ_x increases to more than three times the tractive load. The elevation of the positive value of σ_x (tension), probably play a significant role in initiating and propagating the surface cracks under mode I (opening mode). However, at the entrance to the contact region σ_x also increases but its value is negative (compression) thus, the probability of surface crack initiation reduced and the subsurface crack initiation mechanism being more possible.

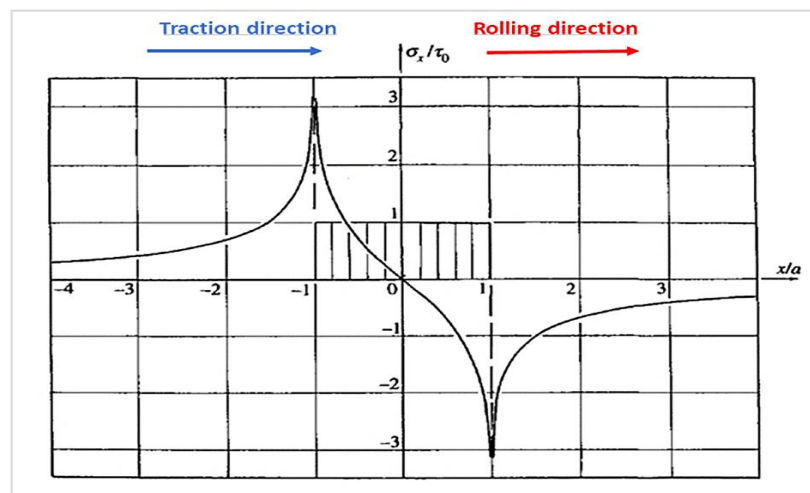


Figure 4-18: Distribution of σ_x under uniform traction load [195].

The traction force is not applied separately from the compression thus, analyses of this combination with the contact depth were carried out for the test disc geometry. Most of the previous studies postulated that the damage may initiate and propagate due to the action of maximum shear and/or Von-Mises stresses or sometimes due to orthogonal shear stress [24][249]. Thus, these three stresses under a compressive stress of 2400 MPa and ~ 2650 MPa, i.e. $\sim 10\%$ more than the disc material yield stress was carried out. Figure 4-19 presents the variation of maximum shear stress in two cases which are Hertzian contact and the superposition of Hertzian contact and 0.22 friction coefficient.

Subsurface damage initiation mechanism probably the more acceptable postulation and this is supported by more evidence in the previous literature compared with the surface initiation mechanism and the subsurface maximum shear stress probably has the main role in damage [25].

In the light of the possible role of von-Mises stress and orthogonal shear stress as subsurface stresses and to investigate the subsurface damage initiation, the subsurface distributions of Von-Mises and orthogonal shear stresses are also presented under the mentioned loading conditions in [Figure 4-20](#) and [Figure 4-21](#) respectively. The analyses presented in these figures are made in the center of the disc width where the effect of stress concentration at the disc edge was assumed to be negligible.

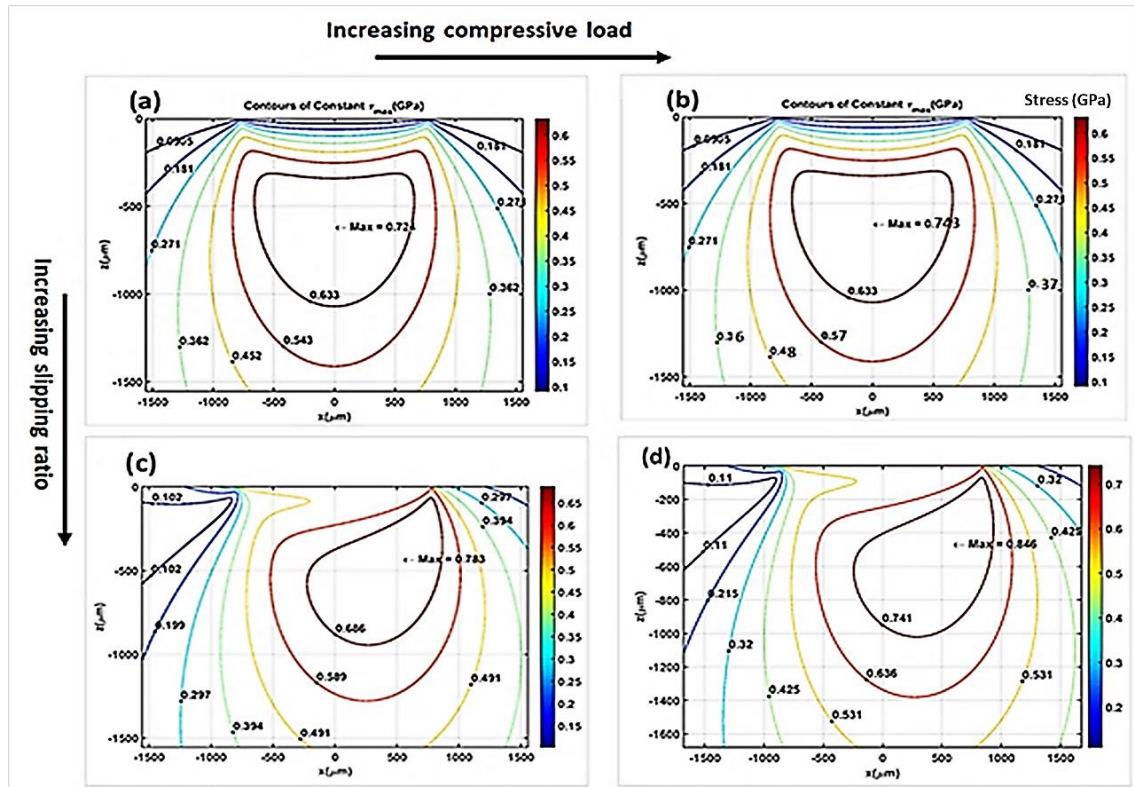


Figure 4-19: Variation of shear stress distribution with increasing load and slipping.

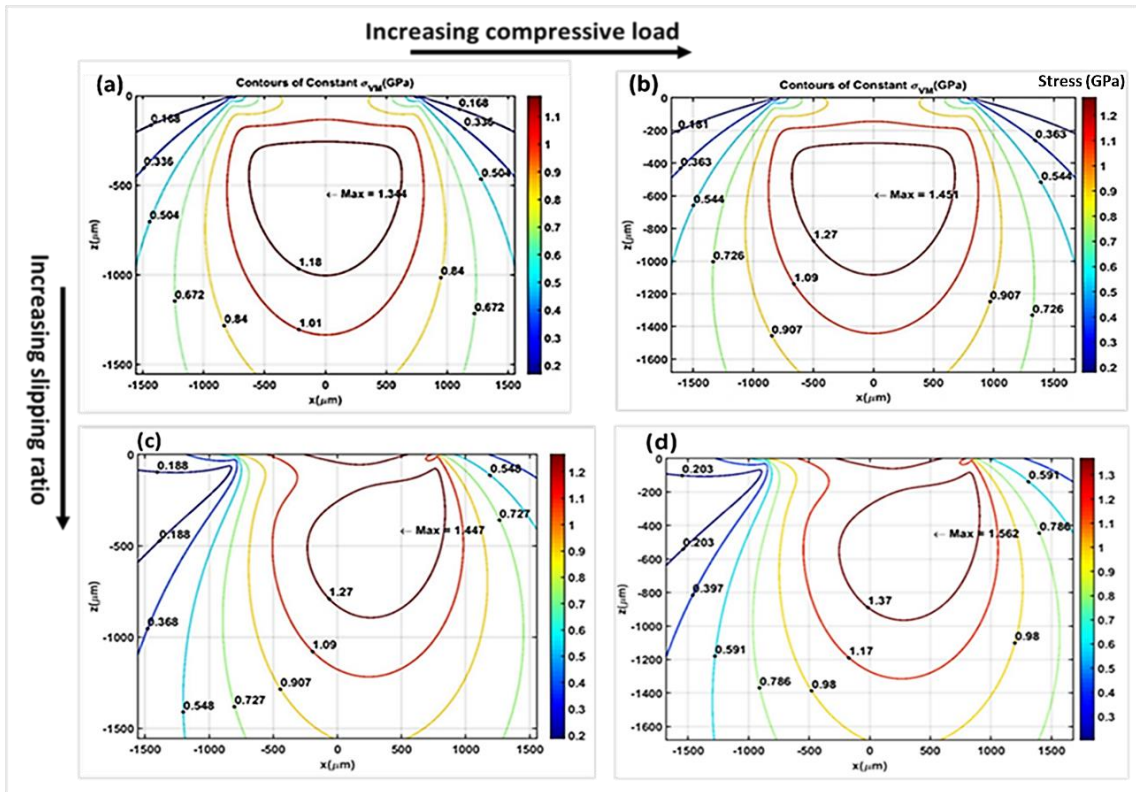


Figure 4-20: Variation of Von-Mises stress distribution with increasing load and slipping.

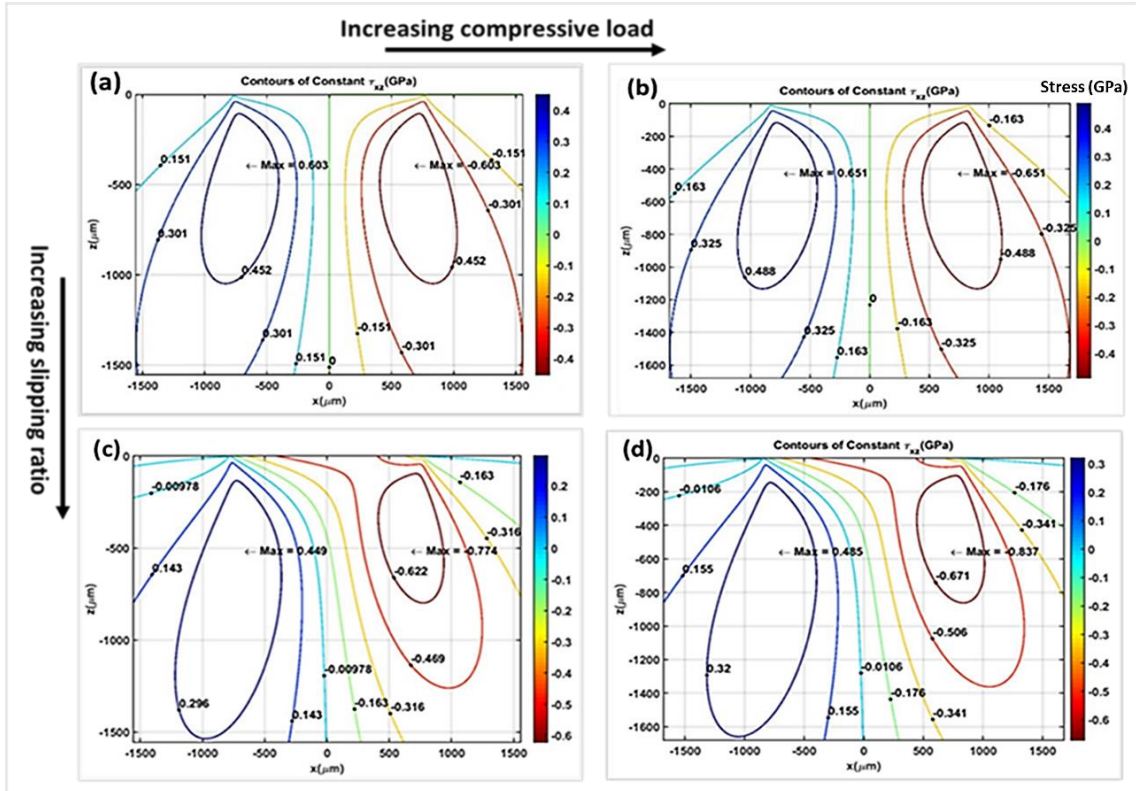


Figure 4-21: Variation of orthogonal shear stress distribution with increasing load and friction.

4.3.2 Slip Ratio and traction force calculations

Slipping Ratio (SR) is defined in Section 4.1.2 as the ratio of the difference between the linear contact velocities of the contact bodies to their average velocity. To have different SRs, test disc diameters can be varied to change their linear velocities. This will produce slight differences in the contact stress calculations when the calculations are carried out under the same compressive loading level. Figure 4-22 shows the negligible effect of varying the dimensions of the test discs (which is expressed as SR), on the contact stress calculations.

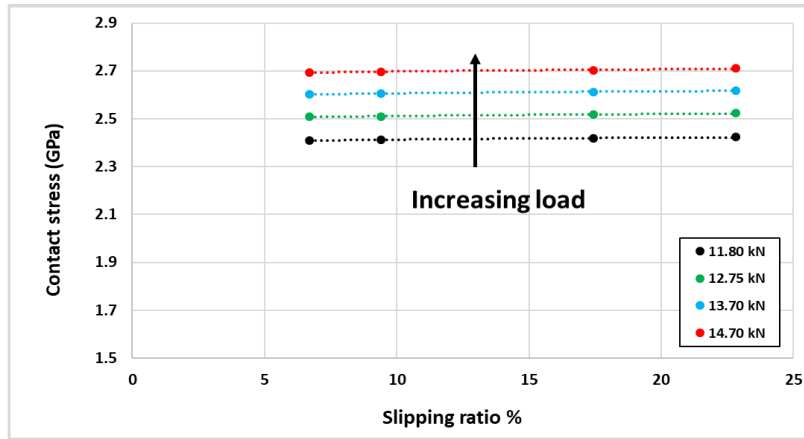


Figure 4-22: Variation of contact stress with SR under different compressive force levels.

Under the same loading and surface roughness levels, traction force F_t is proportional to SR because both of them depend on the difference between the linear velocities, and it can be calculated as [195];

$$F_t = \frac{A_c * \Delta U * \varphi}{h_f} \quad 4.7$$

where A_c is the contact area, ΔU is the difference between the linear velocities at the contact region, φ is the lubricant dynamic viscosity and h_f is the lubricant film thickness. According to Spark et al. [253], kinematic viscosity (\mathcal{K}) and lubricant density (ρ) can be expressed in terms of the dynamic viscosity (φ) as;

$$\varphi = \rho * \mathcal{K} \quad 4.8$$

The ratio between lubricant film thickness (h_f) and surface roughness (R_a) is a function of the force between the contact discs, their mechanical properties and geometry in addition to the average linear velocity (U) and the pressure-viscosity coefficient (ϑ) which can be calculated by using Eqn. 4.9 [3];

$$\vartheta = (0.6 + 0.965(\log_{10}\varphi * 10^3)) * 10^{-8} \quad 4.9$$

And the ratio of lubricant film thickness to surface roughness can be calculated using Eqn. 4.10 [3][195].

$$\frac{h_f}{R^*} = 1.714 \left(\frac{\varphi U}{R^* E^*} \right)^{0.694} (\vartheta E^*)^{0.568} \left(\frac{F_N}{R^* E^*} \right)^{-0.128} \quad 4.10$$

The friction coefficient can be calculated depending on the ratio between traction to normal forces. The friction coefficient depends on the lubrication regime which includes three types; boundary, mixed and elastohydrodynamic. Bruce [3] estimated the friction coefficient in planetary bearings to be 0.07 and the lubrication regime to be mixed. He also adapted Figure 4-23 to show the traction coefficient (μ_T) variation with SR, however, the traction coefficient is not only dependent on the slipping, but also on the contact loading and the surface roughness.

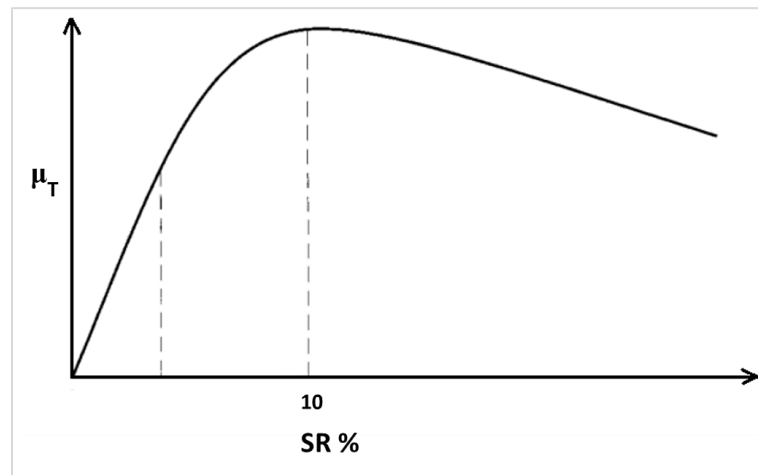


Figure 4-23: Variation of traction coefficient with the slipping ratio [3].

During the tests, the temperature of the lubricant increased from the ambient temperature to ~ 39 °C within ~ 45 minutes of starting the tests and stayed approximately constant (± 2 °C), throughout each test. Thus, the lubricant specifications at 40 °C were used in the calculation procedure (see Appendix D).

According to the calculation results of the previous equations, Table 4-6 illustrates the film thickness to roughness ratios. These results show the test lubrication is within the mixed lubrication regime because the calculated values were within the range (1-1.5). Therefore, the friction coefficient of 0.07 will be considered. Because of the high possibility of changing the WTG bearing loads during the operation and the change of the lubricant temperature, furthermore, contamination of the

lubricant with hard particles such as debris and the insertion of this debris between the contact surfaces, the friction coefficient may increase. Higher friction coefficients can be suggested for comparison purposes.

Table 4-6: Film thickness to roughness ratios under different loading conditions.

Compressive load (N)	Average velocity of the contact discs (m/s)	h_f/R^*
12753	0.355	0.995
13734	0.410	1.089
14715	0.492	1.229
15696	0.546	1.316

4.3.3 Assumptions of impact stress calculations

The calculation of impact forces and stresses induced during the impact period is very complicated due to the very short duration of impact. Impact forces of the test rig depend on the impact velocity, i.e. test rig rotational speed, the mass properties of the impact lever, geometry of the discs and their mechanical properties. A tensional spring was attached to the impact lever to increase the rotating speed of the impact lever by introducing additional torque, but the cam rotational speed and its profile prevent producing a high angular acceleration for the impact lever. Therefore, the impact velocity could be changed only by varying the camshaft rotational speed and/or by adding additional mass to the impact lever. The following assumptions for the impact forces and stresses were considered;

- The impact force is applied normal to the contact disc. This was considered during the test rig design, i.e. horizontal lever when applying the impact.
- The impact is applied at the same location, i.e. neglect the slip of the V-belt on the pulleys.
- The attached spring to the impact lever does not have any effect on the impact lever rotational speed and it is just used to keep the cam and the impact lever in continuous contact. In reality, this spring produces a small additional torque that increases the contact force, but its effect can be ignored because this effect appears when the cam leaves the impact lever contact which is the same instantaneous time of applying the impact loading.
- All the test rig and impact mechanism components will be considered as rigid; therefore, the effects of impact lever bending, and vibration will be ignored.

- 97% of the impact energy is transformed to impact force through one impact and the bouncing at the impact region will be ignored.
- The test rig components and bearings are rigid, and they have no deflection during the application of the test loadings. This may produce an error; however, the separation of their effect is out of the scope of this study.
- Hardening effect and plastic deformation are ignored. The impact region may have a hardening and the mechanical properties of the test discs in this region may change throughout the test.
- The impact region is small compared to the test disc dimensions and Hertz contact theory and its assumptions can be applied.
- Impact energy lost due to the deformation of the upper test disc and its damping is negligible.

4.3.4 Static and dynamic response of test disc material

The most critical assumptions are the considering of the test rig shafts as rigid because they may deflect under the loading, and the second is using Hertz theory to calculate the impact contact stress because the material response (deformation), may be different under the static and dynamic loading. For that, the test discs were tested using a fatigue test machine (MCSL/10) in LEA Lab at the University of Sheffield by applying static and dynamic loading at two different frequencies. The first is similar to the testing speed (2.5 Hz), while the other was 5 Hz. This to measure the disc deformation, i.e. approaching each other throughout static and dynamic loadings. The main problem in these tests is the very small values of the disc deformation. For that, a high accuracy extensometer was used ($\pm 1 \mu\text{m}$) and a high recording sample rate of 1,000 to 51,000 reading/s. The software of the extensometer appears six digits after the decimal point of its measuring in (mm). This enables measuring parts of a micrometer, however, during the tests; the last extensometer reading digit was fluctuated and had not been considered. The testing parameters can be seen in [Table 4-7](#). The static tests were conducted by increasing the contact force and recording the extensometer reading under different loading levels. After that, the response (deformation) of the discs within the test rig assembly was measured to compare the results and show the accuracy of considering the rig shafts as rigid. The test arrangement on the test machine can be seen in [Figure 4-24](#), however, the extensometer was fixed on the test rig as presented in [Figure 4-5](#).

Table 4-7: Dynamic test parameters.

Contact type	Set point force (kN)	Test amplitude (kN)	Test frequency (Hz)
Line contact	11	±5	2.5 and 5.0
Line contact	10	±4	2.5 and 5.0
Point contact	2.8	±1.8	2.5 and 5.0

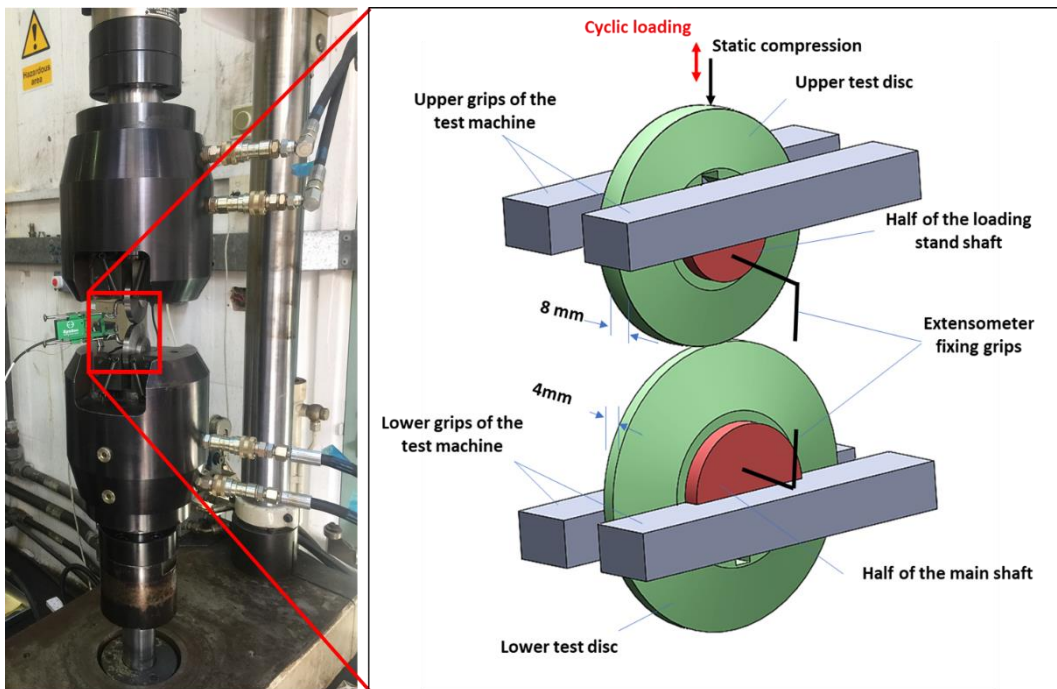


Figure 4-24: Experimental measurement of the test disc response.

The static force-displacement relation was drawn, and the slope of the curve was found which represents the material stiffness. For elliptical contact, material stiffness (k_s) can be calculated using Eqn. 4.11[254];

$$k_s = \frac{4}{3} E^* R^{0.5} \quad 4.11$$

The extensometer was arranged to be attached to the test rig to measure the total displacement variation due to impact loading to estimate the impact forces and stresses. The extensometer requires a design of an additional plate with Z shape but with perpendicular sides have supporting brackets to reduce the plate deflection throughout the testing. To place the extensometer, two pins were used, the first on

the Z-plate, while the second was on the reference point on the middle plate of the test rig (which is rigid), as can be seen in [Figure 4-25](#).

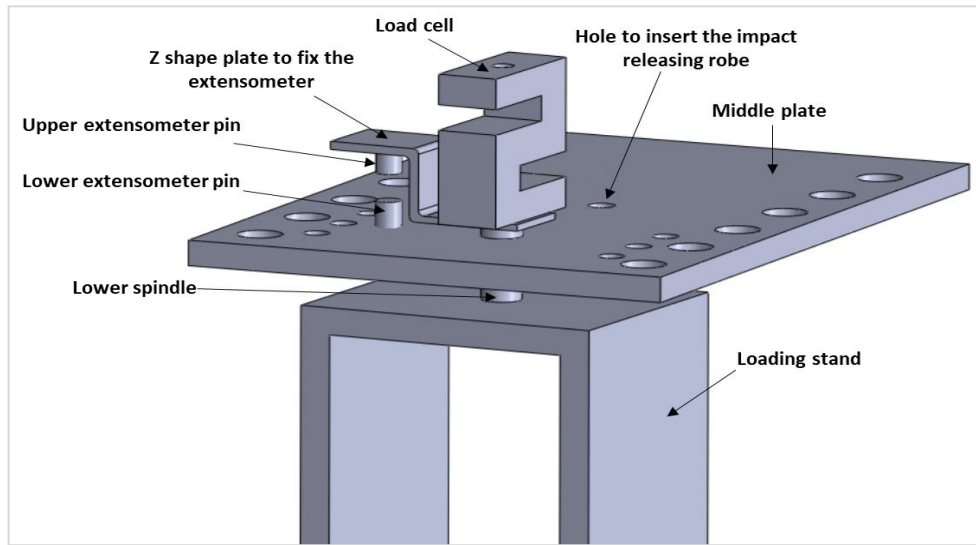


Figure 4-25: Adding of extensometer to measure the deformation due to impact.

The measured disc deflections were less than 1 μm for that, the results are out of the extensometer accuracy and presented in [Appendix E](#). The static and dynamic response of the test disc material has small differences; thus, using Hertz theory for calculating impact stresses is acceptable. Furthermore, there are small differences between the extensometer reading during the test of the disc on the test machine with that on the test rig. This means the assumption of considering the test rig shaft as rigid is acceptable.

4.3.5 Theoretical calculations of impact forces and stresses

The mass of impactor, camshaft speed and the cam profile control the impact energy. Cam tip velocity V_{cam} , can be calculated as:

$$V_{cam} = \frac{\pi N_{cam}}{30} * R_c \quad 4.12$$

where N_{cam} is the rotational speed of the camshaft in rpm and R_c is the radius of the highest point on the camshaft (Cam tip) that is separated from the impact lever instantaneously when applying the impact loading. For the chosen test rig dimensions, the velocity of the contact region of the impact lever (V_{il}) inclined at 30° with the cam tip velocity is shown in [Figure 4-26\(a\)](#). The impact lever rotational speed (ω_{il}) and the velocity at the impact location (V_{imp}) can be calculated depending on [Figure 4-26\(b\)](#). SolidWorks software was used to find the mass moment of inertia

of the impact lever and its additional components about the center of gravity. This mass moment of inertia should be transformed into the impact lever rotating centre “C” by using the parallel axes theorem. According to this theorem;

$$I_c = I_g + M * d_g^2 \quad 4.13$$

where I_c and I_g are the angular mass moment of inertia about the impact lever rotating center and about the lever centre of gravity respectively, and d_g is the distance between these two centres. As mentioned in Section 4.1.3, this cam is different from the classical cams because the location of the contact location of the follower (impact lever) and the cam is changing throughout the cam rotation, i.e. the location of the contact relative to the cam centre is changeable during the cam rotation.

Effective mass (M_{eff}) is an equivalent mass which should be assumed at the impact region and can be calculated by equating the real mass moment of inertia about the impact lever rotating centre (I_c) to that of the effective mass about the same centre, thus:

$$M_{eff} = \frac{I_c}{L^2} \quad 4.14$$

where L the distance between the impact location and the impact lever centre of rotation.

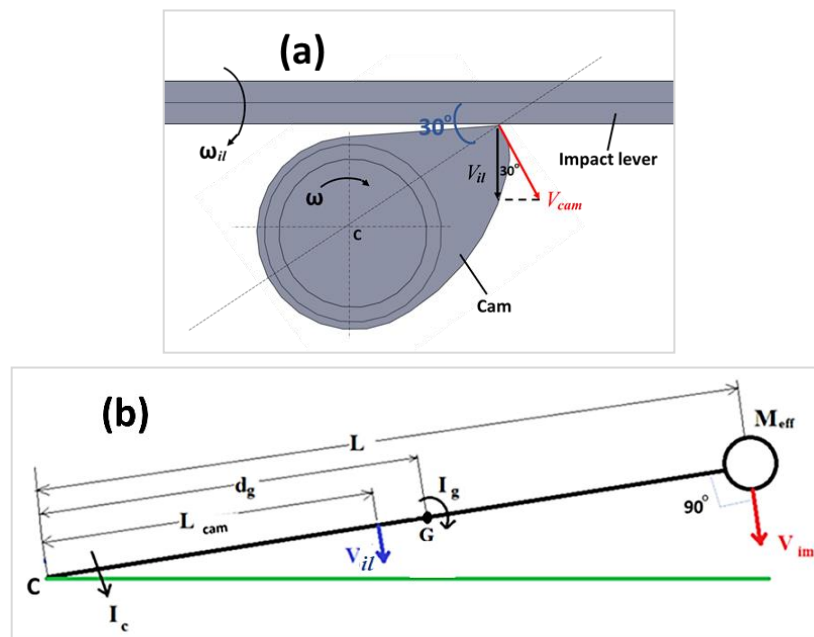


Figure 4-26: Impact mechanism details (a) cam-impact lever velocities relation (b) impact lever schematic diagram with mass, velocities and mass moment of inertia.

Table 4-8 illustrates the important dimensions of the designed impact mechanism that are useful for the calculation procedure.

Table 4-8: Parameters of the designed impact mechanism.

Description	Value
L_c : distance from the cam contact region to the impact lever centre of rotation (mm).	122
L : distance from the impact location to the impact lever rotating centre (mm).	212.4
d_g : Distance from the center of gravity to the centre of rotation (mm).	105.2
M_{total} : The total mass of the impact parts (kg).	1.24
I_g : The angular mass moment of inertia about the centre of gravity (kg.m ²)	0.00729
R_c : Cam tip radius (mm).	37.00

According to these data, the effective mass was calculated and found **0.47 kg**. The impact energy (E_{imp}) can be calculated depending on the effective mass as:

$$E_{imp} = \frac{1}{2} M_{eff} V_{imp}^2 \quad \mathbf{4.15}$$

To calculate the force due to impact for contact problems, the impact force (F_i) can be calculated depending on Stronge formula [254];

$$F_i = 1.94 * E^{*0.4} * R^{*0.2} * E_{imp}^{0.6} \quad \mathbf{4.16}$$

The impact loading is applied when there is a pre-compressive loading. This means the impact force will be distributed on the contact area due to flattening the contact region thus, the impact force and compressive loading are added to find the total force then calculating the stresses due to this combined contact force for each contact type (line and elliptical contacts) and the impact stress is the difference between the total contact stress and that of compression only.

The relation between the impact force, impact energy and rotational speed for the designed test discs can be shown in Figure 4-27. The difference in impact forces between the line and elliptical contact comes from the dependence of impact force on the geometry of the impact bodies, i.e. R^* . Despite introducing higher impact forces in line contact than the elliptical one, dividing these forces by a large contact area along the axial length produces lower impact stresses. However, impact forces in elliptical contact will produce high impact stresses. In this figure, there is a deviation of the calculated impact forces and energies from the trend curves, this

deviation is due to using a simple logarithmic equation to describe the variation which is not the real relations between the presented variables.

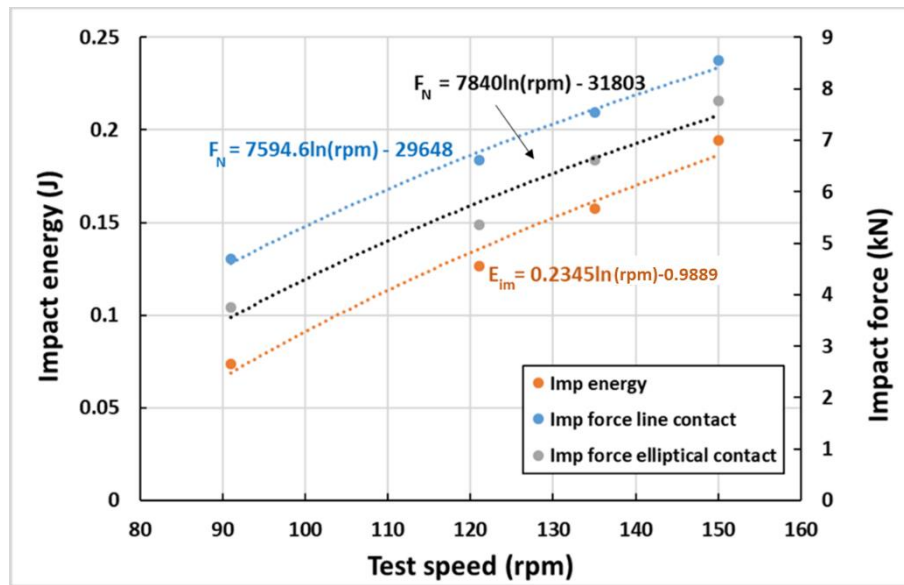


Figure 4-27: Variation of impact force and impact energy with test rig rotational speed.

To investigate the effect of impact on the number of cycles to failure, the test rig is designed to apply one impact in each test disc rotating cycle. This impact will be applied at the same location on the upper disc. In real WTGBs, low impact levels occur in normal operation. Nevertheless, high impact levels occur during the operating events discussed in Section 2.4.1. In the planetary WTGBs, impact loading applied on the planetary gear and transforms into the roller/inner race contact region which is under a pre-loading. Similarly, the impact in the test rig transforms from the impact location on the upper disc to the pre-loaded contact between the test discs. This can be considered as pulse loading, however, the increase in the pulse loading is a reflection of the impact energy by ignoring the impact energy lost due to the elastic deformation of the upper disc and the material damping (as mentioned in Section 4.3.3).

For fully crowned discs, impact loading is applied with a percentage of 0.07% (35 impact cycles for every 50,000 rotating cycles), as calculated for the investigated real bearings (see Section 4.2.2). For that, an impact releasing mechanism was added to the test rig design (see Figure 4-5) to simulate this percentage of impact loading during the tests.

Bruce and co-workers [5][3][100], applied impact loading separately by using a steel ball on flat discs then they applied the RCF test using flat discs on a twin-disc machine. In the real case, compression, slipping and impact loading were applied in

combination. This will be achieved by using the designed test rig. Combined compressive contact stress variation due to compressive and impact loading can be seen in [Figure 4-28](#). It can also be noticed that this special design of the cam differs from the standard cam-follower design. At the beginning of impact, the offset of the cam is to the right-hand side of the cam center then, the offset distance is to the left-hand side.

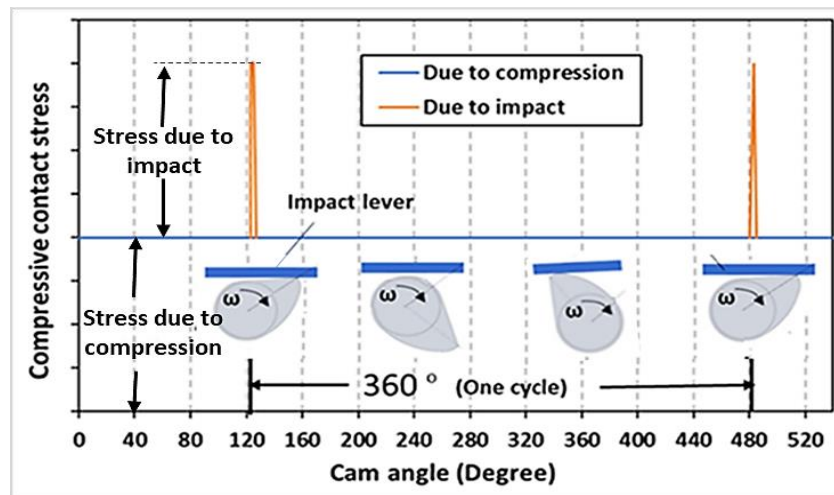


Figure 4-28: Variation of combined compressive contact stress during one test rig cycle.

4.4 Lubrication and lubricant specifications

The lubricant used in this test rig is *SP 320 Alpha* with the specifications shown in [Appendix D](#). The test rig can be filled with lubricant to a level that submerges a half of the lower test disc using a hole and plug shown in [Figure 4-29\(a\)](#). The side gearbox cover can also be used to empty the gearbox using an oil drain plug. This can be seen in [Figure 4-29\(b\)](#). [Figure 4-29\(c\)](#) shows the required lubricant level. Two covers are fitted on the front and the back sides of the test rig to prevent any lubricant leakage. The front cover is made from a transparent material to enable seeing the damage arrive to the test disc surface.

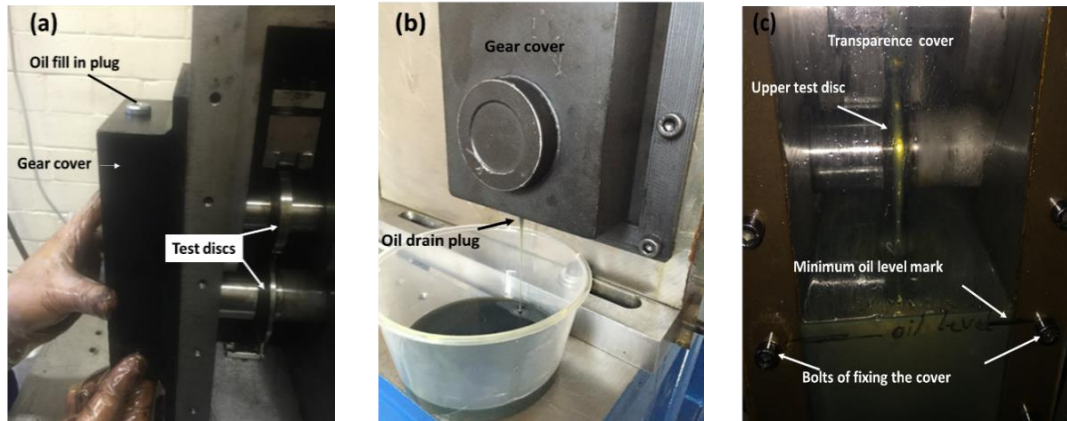


Figure 4-29: Fill in and emptying the test rig oil (a) the fill-in plug; (b) the drain plug; (c) the oil level mark.

Two holes in perpendicular positions are used as an oil drain to empty the lubricant from the space around the test discs as can be seen in Figure 4-30.

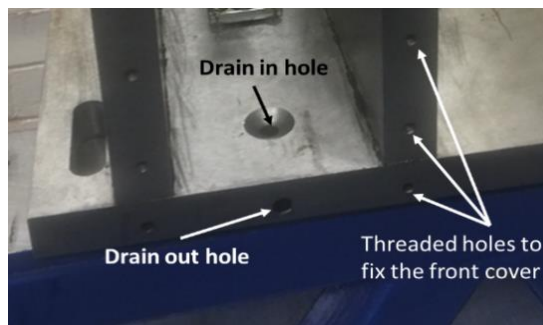


Figure 4-30: Drain holes to empty the test rig lubricant.

4.5 Test rig capabilities

The new test rig was designed to investigate the effect of different factors on the test disc lives and RCF damages instead of testing real bearings. This has an economic impact on the testing procedure. The test rig design is simple to manufacture at very low cost and it has no negative impacts on the environment. The rig is easy to be maintained and the replacement of the test discs can be done easily. The noise level of the rig was examined by the safety staff of the University of Sheffield and it was within the acceptable level, therefore, there is no need for ear protection throughout the testing. When the rig bearings are damaged, the noise increased. However, bearing replacement is recommended to be carried after three tests even if the bearings are not damaged. This is to avoid bearing damage affecting the test results. Throughout 20 tests and over 2800 operating hours, no maintenance was made except replacement of the test rig bearings.

The test rig is mainly designed to study the individual and interactive effects of a considerable number of parameters proven to have an effect on rolling/sliding fatigue with or without impact loading such as; compression, impact and traction loadings, in addition to the ability of studying the effect of lubricant type, operating temperature, rotational speed, material type and surface roughness. However, parameters out of the study scope can be implemented by introducing very simple modifications such as adding a heater in the lubricant or removing the gearbox attached to the drive motor. [Table 4-9](#) illustrates the range of the study parameters which can be applied using the designed test rig.

Table 4-9: Available test ranges of the study parameters.

Test factor	Test range available	Calculated parameter
Compressive loading (kg)	2 to 1800	Compressive stress
Rotating speed (rpm)	0.0 to 150	Impact stress
Test disc radii (mm)	33 to 45	Slipping Ratio (SR)

The test rig operating procedure is very easy and safe (see [Appendix F](#)). Despite the availability of different damage detection techniques such as ultrasound to measure the lubricant film thickness variation due to damage, the rotating components and emerging the discs in the lubricant makes the detection of surface flaking by eye as a simple way. This probably introduced a percentage of error because the damage initiates before arriving the contact surface and detecting it by eye may missed the damage initiation, however, missing the arriving of damage to the contact surface may produce a percentage of error which in the worst case cannot be more than 9,000 cycles because the test rig was checked every around one to two hours. This error if compared with the average disc life represents less than 1.5% ($9,000/612,000 \times 100\%$). arriving the damage to the contact surface is the catastrophic state where noise appears. This possible late detection of damage is similar to that in the real WTGBs where the surface bearing damage starts affecting the turbine normal operation and the transmission performance.

5

EFFECT OF TESTING PARAMETERS ON THE TEST DISC FATIGUE LIFE

This chapter presents the conducted experiments and the investigation of the effect of the study parameters on the test discs lives using the rig developed in [Chapter 4](#). The individual and interactive effects of the study parameters were investigated by designing testing levels using the Design of Experiments (DOE) technique. Minitab 17 software was used for designing the testing levels then, the software was used to analyze the output results, i.e. the individual and interactive effects of the parameters on the test disc lives in terms of the number of cycles to failure. The test disc life was determined when apparent damage can be observed in one of the test disc contact surfaces. The lower test disc always had more severe damage. This shows the importance of the interactive effect of the test parameters and the negative SR on the disc life. The analyses of the testing results confirmed the individual and interactive effects of the study parameters under stress concentration and provided a quantitative analysis for the results, however, the qualitative analysis of the fully crowned discs confirms the effect of the study parameters on disc life under plane stress state. The trend of reducing fatigue life by increasing the test parameter levels was also confirmed by the results of the tests without stress concentration. The limitations of the testing and the analysis procedures were also prescribed and discussed.

5.1 Introduction

The Design of Experiment (DOE) technique is a powerful method for designing the testing parameter levels and analyzing the experimental results. This method depends on the strong relationship between the statistical analyses (probability) of

the experimental results. This technique can be used to reduce the required tests to have approximately the same results. Analysis of fatigue life depends on the probability which also depends on many factors that naturally have a random effect, such as material structure and testing temperature. For each engineering testing system, there are two types of factors affecting the results [255]; the first is called “*controlled factors*”, i.e. parameters, which is used to vary the testing conditions and the results, however, the second is called “*uncontrolled factors*”, which are also called the noise factors. Separating the noise effect from the main effect is very difficult in experimental works and there is a considerable number of studies in this field [255]. Taguchi developed the use of statistics in engineering problems to isolate the effect of noise from the main effect. His solution requires a complete understanding of the test system and all the factors probably have a considerable effect on the testing response (output results). To analyze the results of the tests using DOE, different methods can be used depending on the required accuracy and the available time for testing. The complexity of the problem and the time required for each test are what is controlling the testing procedure and the number of output results. [Table 5-1](#) illustrates the types of DOE methods in addition to their advantages and disadvantages.

Table 5-1: DOE analysis methods and their advantages and disadvantages.

DOE method	Advantages	Disadvantages
Full factorial method	<ul style="list-style-type: none"> • Most accurate method 	<ul style="list-style-type: none"> • Needs a large number of experiments. • High time and money consumptions.
Partial factorial method	<ul style="list-style-type: none"> • Smaller experiments. • Less money and time consumption. 	<ul style="list-style-type: none"> • Less accuracy. • Requires experience to choose the testing levels.
Surface response method	<ul style="list-style-type: none"> • Excellent in finding the interaction effect. 	<ul style="list-style-type: none"> • It needs many experiments. • Accuracy depends on the number of experiments, the number of factors and the number of levels.
Taguchi method	<ul style="list-style-type: none"> • A fewer number of experiments. • Acceptable estimation for interaction and main effect. • It depends on the orthogonality of the testing matrix. • Factor levels are chosen automatically (no need for experience). 	<ul style="list-style-type: none"> • It has a few limitations in finding the interactive effect. • Considers the relation between any two sequential results as linear.

Because of the advantages of the Taguchi method and the considerable time required to complete fatigue testing; this method was chosen to be the analyzing method in this study.

In most of the engineering systems, there is at least one parameter that can significantly affect the experimental results. However, in fatigue testing, there is a considerable number of factors affecting the number of cycles to failure as discussed in [Section 2.4](#). Three types of effects can be recognized which are the main, interactive and noise effects. The effect of noise factors can be eliminated by making the testing conditions similar to in-service conditions that effectively reduce the errors on the results.

A Transfer Function (TF), describes the relationship between the input (parameter), and the output (test life results), this should be specified precisely to get a reliable result. The importance of DOE comes from its ability to reduce the required number of the output results to describe the TF. If the variation range and number of levels are known, Minitab software can suggest the internal variation levels for each test. The TF of any testing system takes the general form:

$$Resp. = N_{mean} + \beta_{input} + \varepsilon_{noise} \quad \mathbf{5.1}$$

where *Resp.* is the output (response), N_{mean} is the mean value of the output, β_{input} is the effect of the studied parameter and ε_{noise} is the error due to noise, i.e. the effect of uncontrolled factors. The percentage of noise can be calculated using [Eqn. 5.2](#) [255].

$$\% \varepsilon_{noise} = -10 \log_{10} \left(\frac{N_{mean}}{SD} \right)^2 \quad \mathbf{5.2}$$

where *SD* is the Standard Deviation (SD) of the output which can be calculated using [Eqn. 5.3](#).

$$SD = \sqrt{\frac{\sum(N - N_{mean})^2}{N_t - 1}} \quad \mathbf{5.3}$$

where *N* is the measured output (number of cycles to failure) and N_t is the total number of the conducted experiments. Increasing the number of testing levels increases the accuracy of the TF and the relation between input and output can be achieved by using the curve-fitting technique.

“Replication” is the number of repetitions of the same experiment under the same testing conditions. These can be used to increase the reliability of the results and can be considered as one of the most effective ways to eliminate the noise. The other way to eliminate noise is called a “blocking” technique. This is the process of isolating the noise from the parameters, either by specifying the optimum percentage of the noise or by introducing testing conditions identical to those that the real system experiences in service. However, some factors cannot be eliminated or blocked, such as the grain size of the material and the amount of debris produced during the operation or the test, and the variation of test speed when turning the test on or off. Such factors are unavoidable and the best way to evaluate their effect is by specifying the optimum value or the percentage of their effect on the results.

Probability Density Function (PDF) is one of the most important terms in statistics. It is a function that has a value for each test level within the parameter range. It represents the relative probability of that parameter level producing the result. The “mean value”, which is the average of the output should divide the area under the PDF curve into two equal parts. The general form of the Probability Density Factor (PDF) of failure can be written as [255]:

$$F(x) = 1 - e^{-(\beta x)^{\aleph}} \quad 5.4$$

where, β is the scale parameter and \aleph is the shape parameter of Weibull distribution (WD), which is a general distribution case that expresses all types of statistical distributions.

In the case of bearings, the question is about the survival thus, the Probability of Survival (PS) can be expressed as:

$$PS = e^{-(\beta x)^{\aleph}} \quad 5.5$$

5.2 Test parameters and variation ranges

The test rig detailed in [Chapter 4](#) is designed for applying a wide range of testing levels for the study parameters. [Table 5-2](#) shows the rig testing level ranges available and that were used in this study. These ranges were chosen to enable applying Hertz contact theory with compressive loadings approximately within the critical limit of the elastic range. However, the impact loading range is chosen according to the available impact velocity and the effective mass of the impact mechanism. The combined compressive loading (resulting from both compressive and impact loads) is chosen without exceeding the elastic stress level where the

mean pressure ($\tilde{p} < 1.1 \sigma_y$) [254], but the mean pressure is derived from $\tilde{p} = \frac{2}{3} p_o$. Thus, $p_o < 1.65 \sigma_y$, where, P_o is the maximum combined contact pressure. To recognize the effect of impact on test life and subsurface damage distribution, an additional test similar to one testing parameter levels was repeated and analyzed without impact loading. For an elliptical contact (the second row in Table 5.2), higher contact compressive contact stress can be applied due to small contact area which carries the applied load for that reason, increasing the contact area in roller bearings was used when high loading levels are applied as in WTGs. The third row in this table shows the range of changing the stress due to impact loading which achieved by changing the controlling parameter of impact speed from 0.561 to 0.924 m/s. The available range of SR (presents in the fourth row of the table), is 0.0 to 50%; however, the used testing range of 6.71% to 22.82% was achieved by changing the lower test disc diameter from 77.0 mm to 83.0 mm.

Table 5-2: Testing parameter levels and variation ranges.

Test factor	Available test range	Controlling parameter (unit)	The used test parameter range
Maximum compressive contact stress (MPa) for line contact	0.0 to 2900.0 (without stress concentration)	Contact stress (MPa)	2400 to 2700
Maximum compressive contact stress (MPa) for elliptical contact	0.0 to 7500.0	Contact stress (MPa)	2007 to 2548
Maximum impact stress (MPa)	0.0 - 727.3 for line contact 0.0 - 1188.2 for elliptical Contact	Impact speed (m/s)	0.561 to 0.924 (to get impact stress of 435.3 MPa to 727.3 MPa for line contact)
Slipping Ratio %	0.0 to ± 50	Lower test disc diameter (mm)	77.0 to 83.0 (to get SR of 6.71% to 22.82%)

Despite there are different advanced methods of damage detection such as using ultrasound detectors depending on the lubricant film thickness, the use the naked eye to detect the damage initiation by looking at the test disc contact surfaces through the transparent front cover of the test rig was used due to study budget facilities and the difficulties of fixing the sensors on a rotating components. This can

be considered as the main limitation in this rig because the delay of observing the spalling initiation may affect the results of the number of cycles to failure. However, in real bearings, the damage is always detected after the flaking reaches an advanced level and starts affecting the turbine performance. This is the easiest way to detect the surface failure initiation, however, staying beside the rig and waiting for the damage to appear is unpractical way, therefore, only the first conducted test was under the medium of the test parameter levels, that enabled a rough estimation for the test disc life under other testing levels (as will be discussed in [Chapter 7](#)). The prediction of the arrival of the damage on the disc surface being more accurate by increasing the number of tests.

5.3 The experimental results and analyses

After designing the testing levels using Minitab software. Sixteen tests were suggested by the software to study the individual and interactive effects of the three study parameters under four levels of variation. The number of four levels was chosen to have an acceptable accuracy to describe the variation trend in a curve fitting formula. After conducting the required tests, the chosen test parameter levels, and the results achieved are illustrated in [Table 5-3](#). The compressive and impact stresses were calculated by following the calculation procedures in [Section 4.3](#). Each test has been given a test code, for example, T1 is the test code of the first conducted test. The last four tests (T1P to T4P) presents the results of elliptical contact to avoid the stress concentration at the test disc edges (highlighted with orange). The test without impact loading (T6B) is highlighted in blue. In tests T1P to T4P, the effect of impact stress does not add to the combined contact stress value because the impact loading was applied in a percentage like that normally take place throughout the real wind turbine operation due to operating events which is 0.07 % of the total rotating cycles. Additional tests (T7A and T6A) were also conducted (highlighted in green in [Table 5-3](#)) to confirm the individual effect of slipping and impact loading respectively by comparing their results with that of T7 and T6 respectively.

Depending on eye detecting for the contact surface damage may introduce an error in the number of cycles to failure. Despite using a careful observing to the test discs especially close to the end of their expected fatigue life (by checking the test disc surface every one hour), the maximum possible error in the number of cycles is the number of rotating cycles throughout this one hour. The percentage of the possible error depends on the test speed and it presented in the right-hand side column in [Table 5-3](#).

Table 5-3: Test parameter levels and the number of cycles to failure.

Test code	Comp. stress (MPa)	Impact stress (MPa)	Combine d contact stress (MPa)	SR %	Total stress due to concentration and traction (MPa)	No. of cycles to failure	Possible error in disc life %
T14	2409.92	435.3	2845.27	6.71	4836.96	1,120,826	0.49
T13	2409.92	576.0	2985.97	9.39	5076.15	997,040	0.73
T12	2409.92	630.7	3040.60	17.45	5169.02	871,830	0.87
T16	2409.92	688.7	3098.60	22.82	5267.62	620,430	1.45
T1	2508.33	575.85	3084.18	6.71	5243.10	849,893	0.85
T10	2508.33	648.53	3156.85	9.39	5366.65	741,240	1.11
T15	2508.33	727.28	3235.61	17.45	5500.53	567,836	1.58
T2	2508.33	422.34	2930.67	22.82	4982.14	584,617	0.93
T6	2603.02	407.55	3010.57	6.71	5117.96	612,759	0.89
T4	2603.02	629.58	3232.60	9.39	5495.42	537,907	1.51
T8	2603.02	706.52	3309.54	17.45	5626.21	406,317	2.22
T3	2603.02	560.78	3163.80	22.82	5378.45	325,400	2.21
T7	2694.38	686.04	3380.42	6.71	5746.71	312,681	2.88
T9	2694.38	612.23	3306.61	9.39	5621.24	279,840	2.89
T11	2694.38	544.04	3238.42	17.45	5505.32	680,241	1.07
T5	2694.38	397.01	3091.39	22.82	5255.36	202,700	2.69
T7A	2694.38	688.68	3383.06	22.82	5751.19	132,300	6.8
T6A	2603.02	705.04	3308.06	6.71	5623.70	476,280	1.89
T6B	2603.02	0.00	2603.02	6.71	4425.13	1,272,750	0.707
T1P	2548.39	1188.19	2548.39	22.82	2548.39	2,837,250	0.32
T2P	2548.39	757.62	2548.39	22.82	2548.39	2,959,320	0.18
T3P	2006.96	1188.19	2006.96	22.82	2006.96	3,548,839	0.25
T4P	2548.39	1188.19	2548.39	6.71	2548.39	3,102,436	0.29

For line contact, compressive stress is a function of test disc radii which vary according to the SR, there is a negligible difference in the calculated compressive stress under the same compressive loading with different SR (as presented in Figure 4-22). Releasing the impact loading in T6B approximately doubled the test disc life. This shows the importance of this factor in fatigue life.

Plotting the results of the main 16 tests designed by Minitab software against the testing levels shows a specific trend of reducing the number of cycles to failure with increasing any of the studied parameters as shown in Figure 5-1. The numbers associated with the graph indicate the associated test code number and the compressive loading expressed in (kg) as measured by the rig load cell. The variation trend is not systematic, i.e. the equation of surface plane including all the results and the variation of the disc life with the study parameters is complex. This may be due to the noise effect, i.e. the effect of the factors which did not consider in the analysis. The noise effect causes a scattering in the test results due to possible variable interaction effect under different testing levels. Replicating the tests to

reduce the scatter and to have more reliable results is a time-consuming procedure, therefore, it will be outside the scope of this study. More details about the scatter and percentage of errors of these results will be discussed in [section 5.4](#).

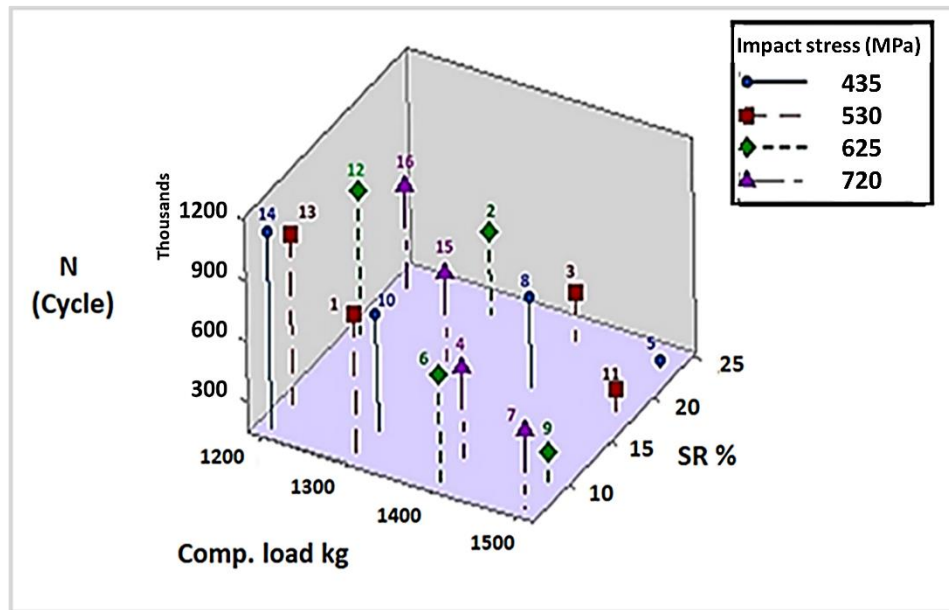


Figure 5-1: Number of cycles to failure (N) under different test factor levels.

The first important step in the analyses is testing the normality of the result distribution. Normality should be conducted before starting the analysis to show whether the results have a specific trend or not. After that, other analyses can be performed [255]. To test the normality; the results (number of cycles to failure) should be sorted from minimum to maximum then, the probability fraction $F_{(pr)}$ should be calculated, using the formula:

$$F_{(pr)} = \frac{t_n - 0.5}{N_T} \quad 5.6$$

where, t_n is the test number after sorting the results, and N_T is the total number of the conducted tests which is 16.

The test disc number of cycles to failure is calculated by multiplying the test time by the rig speed in (rpm). These results are presented in a logarithmic scale against the logarithmic value of the probability fraction using [Eqn. 5.7](#). The deviation from the straight line in [Figure 5-2](#) is normal deviation due to the scattering in the fatigue test results, however, the high value of the variance (R^2), i.e. approximately 1, shows that there is a clear trend of variation.

$$Y = \ln \left(\ln \left[\frac{1}{1-F(pr)} \right] \right)$$

5.7

The slope of this line represents the shape factor of Weibull distribution. To reduce the scatter of the results from the normality line, normalizing data can be used by dividing each test result by the mean of test discs' lives and re-plotting this line. The process of normalizing is used if the Standard Deviation (SD) has a larger value than the mean value of the results; this means the value of the mode factor, i.e. the height of the distribution peak, is relatively low [255]. However, the variance (R^2) does not change during the normalizing process and the shape modulus (Weibull mode shape) increases with normalizing to be close to ~ 3.2 . This shape modulus value means that there is an ideal symmetrical distribution below and above the mean value and the deviation from this value indicates that the results have a deviation from the ideal distribution.

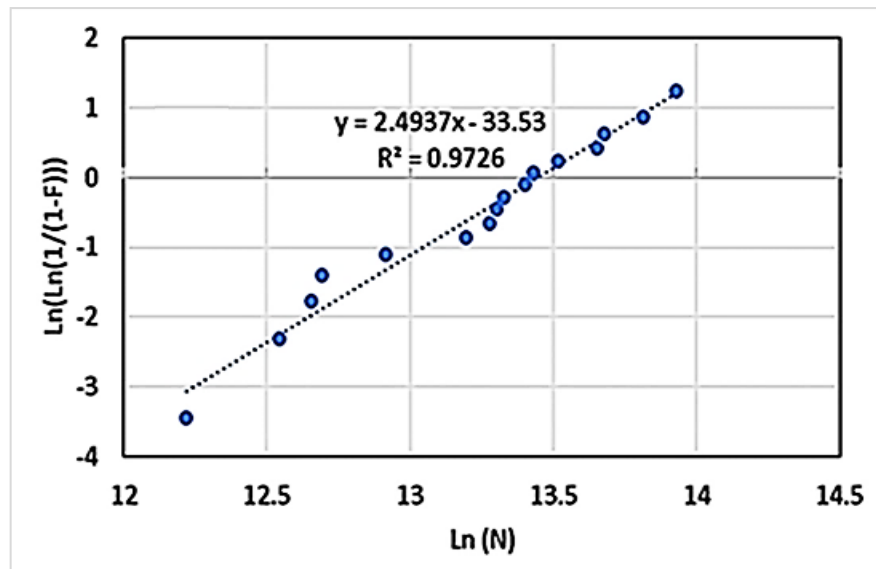


Figure 5-2: Normality test curve of the test results.

In Minitab software, the reliability of the results is automatically calculated according to two imaginary curves parallel to the ideal probability distribution line with a 5% deviation in the results.

The second method of testing the response normality is by presenting the results (test disc lives) in a box and whisker plot. If the plot is approximately symmetric about the horizontal axis passing through the mean value; the results can be considered as having a normal distribution [255], i.e. having a specific trend. [Figure 5-3](#) shows this test which indicates the accepted postulation of the results normality. This plot shows a deviation in the upper part, i.e. a longer whisker than

the lower one, which means there is a deviation in the results from the perfectly symmetrical normal distribution.

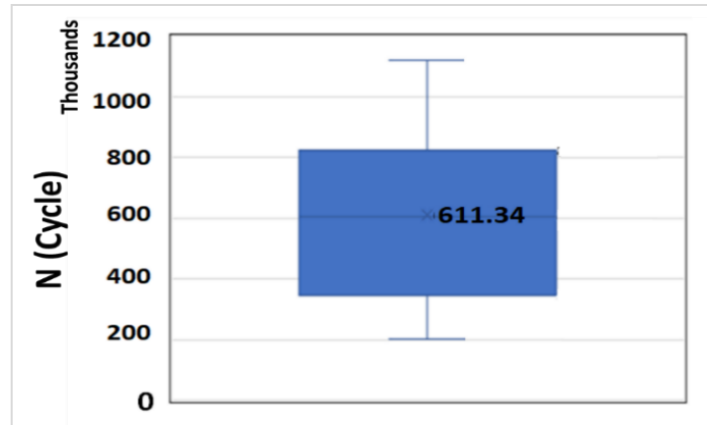


Figure 5-3: Box and whisker plot for assessing the response normality of cycles to failure.

The normality test is enough for specifying the optimum value of the results. However, if the research is about finding the trend, more analyses should be carried out. The Probability Density Function (*PDF*) of the test results is shown in Figure 5-4. This histogram can be drawn using the sorted results (from minimum to maximum) and choosing a suitable number of bins. The important issue to be considered here is that the number of bins and their ranges can considerably change the probability distribution graph. However, the frequency represents the number of results in each range.

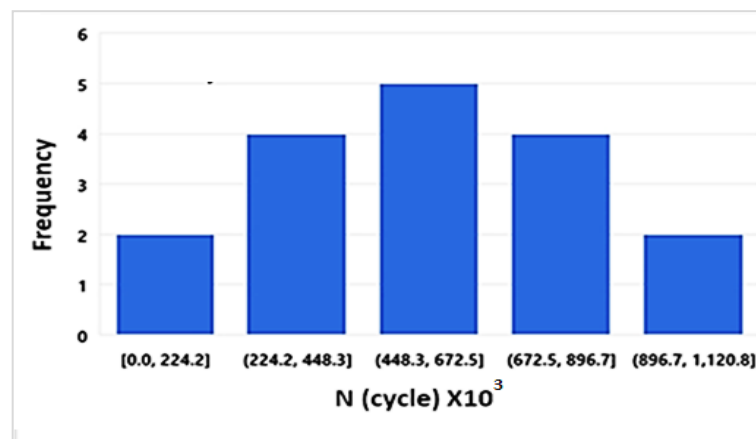


Figure 5-4: Probability distribution of the test results.

5.3.1 Individual effects of the study parameters

After conducting the designed tests and testing the distribution normality, the results were classified according to each factor with its four levels. For example, the results of tests having the same lower impact level (impact stress = ~400 MPa) were

put in a group independent of the other factor levels, then a second group consisted of the results under the second impact level (~530 MPa) and so on. The average of each group was calculated, then these averages were plotted to find the individual effect of impact stress variation [255]. The curve fitting technique was used to find the formula of the mean effect of impact loading from the averages of these groups. This procedure was also repeated for the other factors (SR and compressive loading) to specify their individual mean effects. This procedure is the basis of the analysis using Minitab software [255]. Individual mean effect analysis of the studied factors using Minitab software can be seen in [Figure 5-5](#).

Most types of steels used in the engineering applications have either an exponential or linear variation of fatigue life with the load. Thus, both exponential and linear curve fittings were used to find the trend of variation and then to evaluate which curve fitting is more suitable to describe this variation, i.e. which has less error by comparing the variance (R^2).

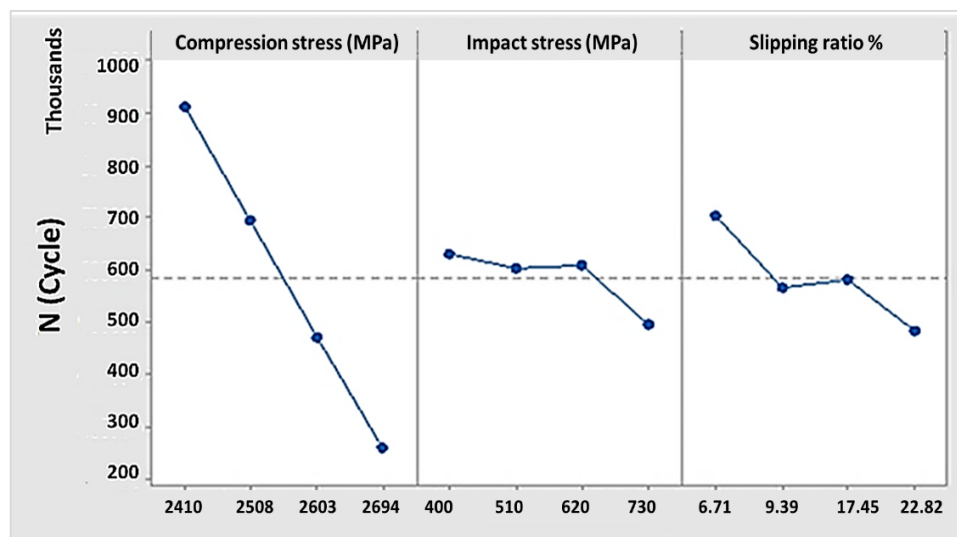


Figure 5-5: Individual mean effect of the tested factors on the line contact tests.

For the studied variation ranges of the key parameters, the test disc life is considerably affected by the variation of the compressive loading, followed by SR and finally impact stress. The mean effect of each key parameter on the test disc number of cycles to failure will be discussed in the following sections.

5.3.1.1 Effect of compression

The procedure of grouping the results according to the compressive load (*Comp.Strs*) in MPa was performed first, then plotting the average number of cycles to failure (N) of these groups against the compressive load (see [Figure 5-6\(a\)](#)). The variation trend of increasing the number of cycles to failure (test disc life), with

decreasing the loading level is the general trend. The linear and exponential variation trends of stress-number of cycles to failure (S-N curve) are usually used. For this reason, this graph consists of these two curve fitting methods. [Figure 5-6\(b\)](#) and [Figure 5-6\(c\)](#) present the individual analyses using the linear and exponential approximations respectively using Minitab software. Presenting the results in these three graphs was to show which approximation is more suitable to describe the variation trend to use it in the quantitative analyses later. Within the testing range, the average mean effect drawn in Microsoft excel shows a better correlation between the extrapolated and the experimental results with an error percentage that does not exceed 1.0% to 1.2% for the exponential and linear approximation respectively. This error estimation was according to the variance values, i.e. R^2 , however, exponential curve fitting has better coincidence with the experimental results ($R^2=0.99$), than that of the linear fitting ($R^2=0.98$). The two graphs deviate considerably from each other outside the test range. Thus, more tests under and over the testing levels are required in the future to have a reliable trend variation formula to describe the trend of disc life variation with the maximum compressive contact stress (p_o), due to compressive loading only.

[Figure 5-6\(a\)](#) was used to extend the results out of the test range using Ms office Excel. One of the disadvantages of the Minitab software is that the results can not be extended out of the test range.

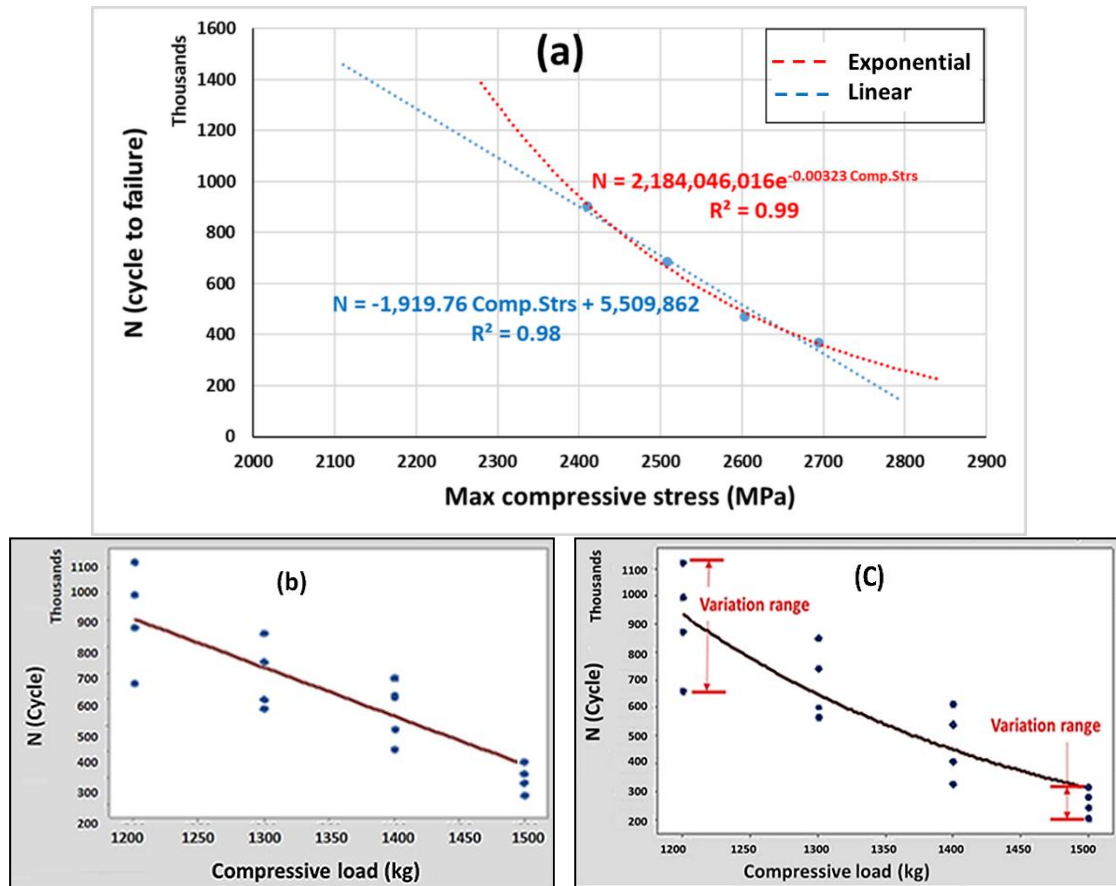


Figure 5-6: Mean effect of compressive loading without stress concentration using, (a) linear and exponential fitting curves extended out of the test range; (b) linear mean plot; (c) exponential mean and variation ranges.

The variation range of the output, i.e. the change in test disc life, under each constant compressive level varied depending on the compressive loading level as shown in Figure 5-6(C). Increasing the compressive loading level reduces the variation range of the test disc life and the difference between the maximum and minimum test disc life under the considered testing levels indicated the considerable role of this parameter on test disc life. This also supports the findings of Oila and Bull [45], despite the natural behaviour of scattering in the fatigue testing results.

In the test disc failure, the compressive loading is not applied separately, but in combination with impact loading. This results in additional compressive contact stress due to impact. It may be better to test whether the effect of individual compressive stresses of each loading level can be accurately analyzed or the combined compressive contact stress (*Cob.Strs*) due to compressive and impact loading is more accurate to describe this relationship. Figure 5-7 presents the relation of test disc life against the combined contact stress. The difference in the value of R^2 of this and the previous graphs can be considered as evidence of the interaction effect of the impact and compressive loadings.

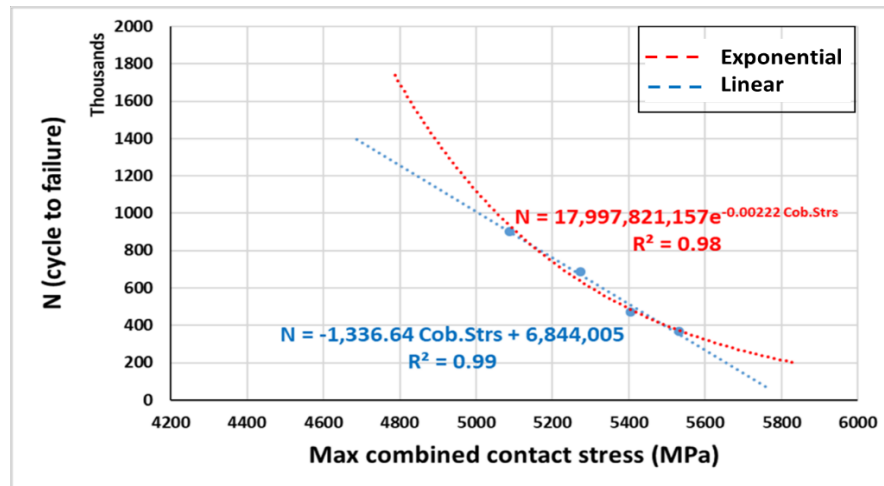


Figure 5-7: Mean effect of compressive stresses on test disc life due to combined compression of impact and compressive loading with stress concentration.

Extending the results by curve fitting for a lower and a higher loading level provides an applicable methodology for life extrapolation, but with lower reliability under the loading levels out of the test range.

5.3.1.2 Effect of impact

Effect of impact on fatigue life in combination with rolling and sliding has rarely been investigated due to technical issues in applying dynamic loading by using hydraulic cylinders usually used to apply the compressive loading when the dynamic loading is applied, and the main damage is in the cylinder pressure washers. The designed test rig uses a new design to apply compressive load, impact and SR in combination.

By following the same result grouping procedure used in investigating the mean effect of compressive load, the results of the number of cycles to failure are classified into four groups depending on the impact stress level and the mean of each impact level was determined. The average life of the four groups with impact stress and the combined compressive contact stress, i.e. stress due to the compressive and impact loadings, can be seen in [Figure 5-8](#).

The results are extended to lower and higher impact stress levels using exponential and linear curve fitting to show which one is more suitable to describe the disc life variation trend. There is a noticeable deviation between the trend of the two plots, i.e. when using impact stress alone and when combined contact stress is used. The value of the residue (R^2) by using combined maximum contact stress is greater than that of analyzing the effect of impact loading alone. However, the linear curve trend has a higher residue, i.e. shows a better correlation with the experimental results.

The values of (R^2) in presenting the effect of impact are less than that of the presented results of compression. This indicates a higher scattering in the results under dynamic loading (impact). This also indicates the importance of the interaction effect among the studied parameters and the dominant effect of compressive contact load on the impact effect, i.e. R^2 has higher value when describing the variation trend using compressive stress only. This also can be observed clearly from changing the relative locations of the points presented in Figure 5-8(b) compared with the same points presented in Figure 5-8(a) which depends on impact stress only. The variation trends of these results cannot be considered as a general case for all impact stress levels and further experimental tests under higher and lower impact levels are recommended to find and confirm an accurate variation trend formula and repeating these tests under the same testing conditions and by using the same test disc material cleanliness.

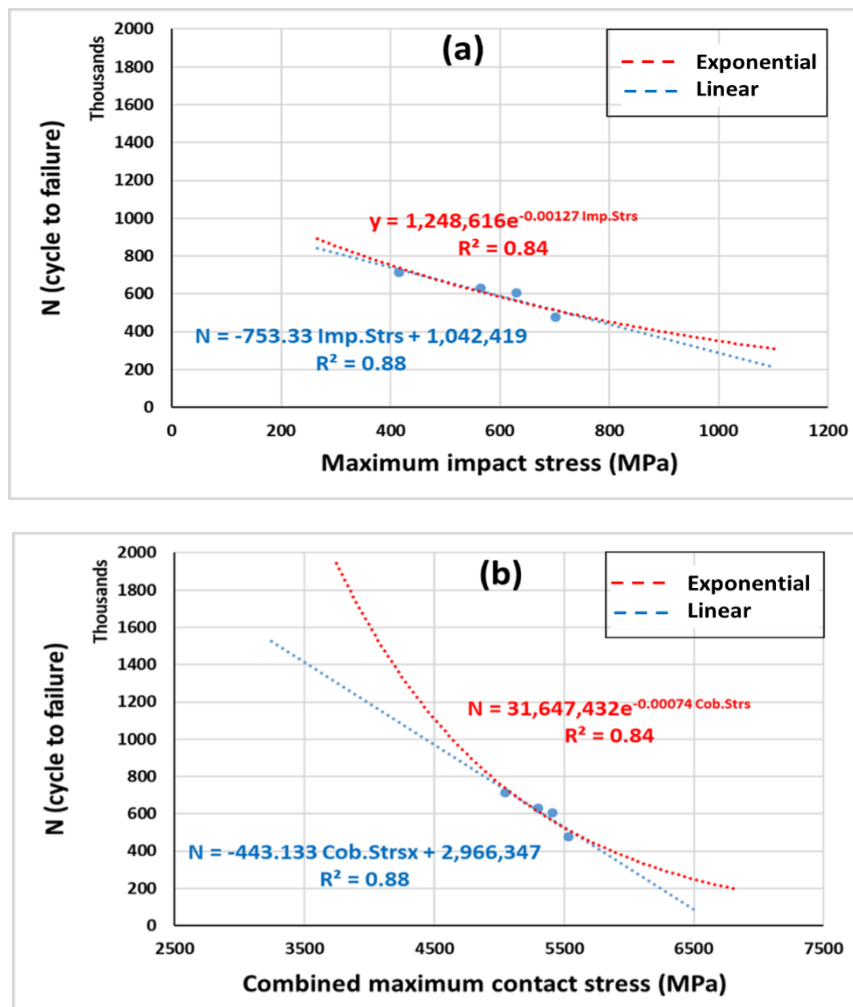


Figure 5-8: Individual mean effect of impact force on test disc life (a) impact force only without stress concentration; (b) combined force corresponding to impact with stress concentration.

The four groups created by classifying the results according to the impact stress are presented in [Figure 5-9\(a\)](#), to confirm the variation of the S-N curves for each impact level. The slopes of the curves increase with increasing impact stress. This means the test discs under higher impact levels reach their number of cycles to failure faster than those undergoing lower impact levels. The variation range of test disc life on the horizontal axis for each impact loading level was found to be decreased when with the increasing of impact stress level. The variation range appears clearly using the plot of the four groups classified according to the impact stress level in [Figure 5-9\(b\)](#). This indicates a higher sensitivity of the test discs to failure under high impact and/or maximum combined contact stress levels. Curve fitting for the test disc life shows a lower effect of impact stress than compression as it appears as an approximately horizontal curve compared with that presented in [Figure 5-6\(c\)](#).

The reliability of results outside the testing ranges and the data scattering under the same testing parameter levels are the main issues in fatigue testing. Therefore, to evaluate this effect, one of the tests (test T6) was re-conducted using the same parameter levels. This test was chosen to be re-conducted because it has the closest result to the mean test life value. In this test, the number of cycles to failure was reduced from 612,759 cycles to 575,674 cycles. The error percentage difference between these two similar tests was about -6.1%. This error is acceptable for engineering approximation, however, there is no guarantee that the other tests will vary within the same variation range and repeating all the tests is out of the scope of this study.

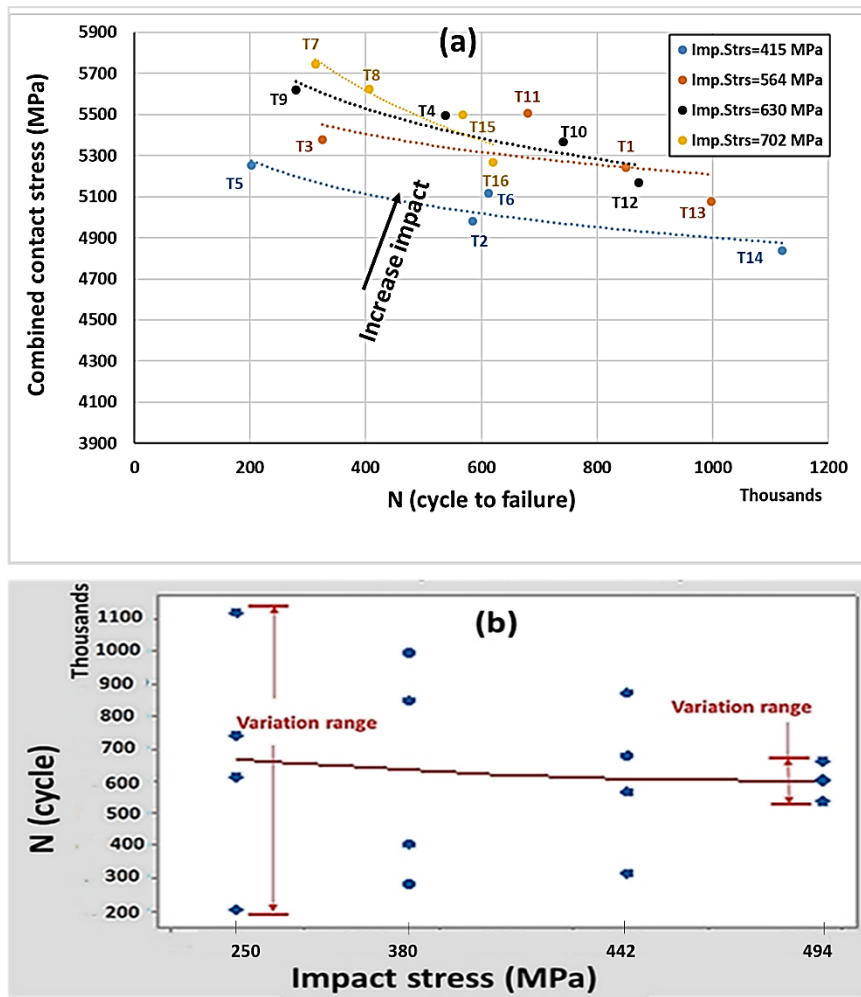


Figure 5-9: Effect of impact (a) variation trends of S-N curves under four impact levels; (b) variation range of the number of cycles to failure.

An additional test (T6A) was conducted to confirm the individual effect of impact on the number of cycles to failure under the same compressive loading level and SR of Test T6, but with higher impact stress (705.04 MPa). The reason for selecting T6 was because it has the closest number of cycles to failure to the mean value of disc life (611,340 cycles). The number of cycles to failure is reduced from 612,759 cycles to 476,280 cycles which represents a test disc life reduction of ~22%, with the increase of impact stress by ~73%, i.e. from 407.44 MPa to 705.04 MPa. This analysis of the impact effect shows the importance of stress due to the impact on fatigue failure. However, the effect of impact may depend on the pre-compressive loading level, therefore, further testing and analyses are required to have a better understanding of their interaction effect under different pre-compression levels. Another additional test (T6B) was conducted under the same testing condition of T6 but without impact loading. The same test speed used in T6 of 150 rpm was used. The results of T6, T6A and T6B can be seen in [Figure 5-10](#). It is important to repeat each test at least three times and use the average life to get more reliable results.

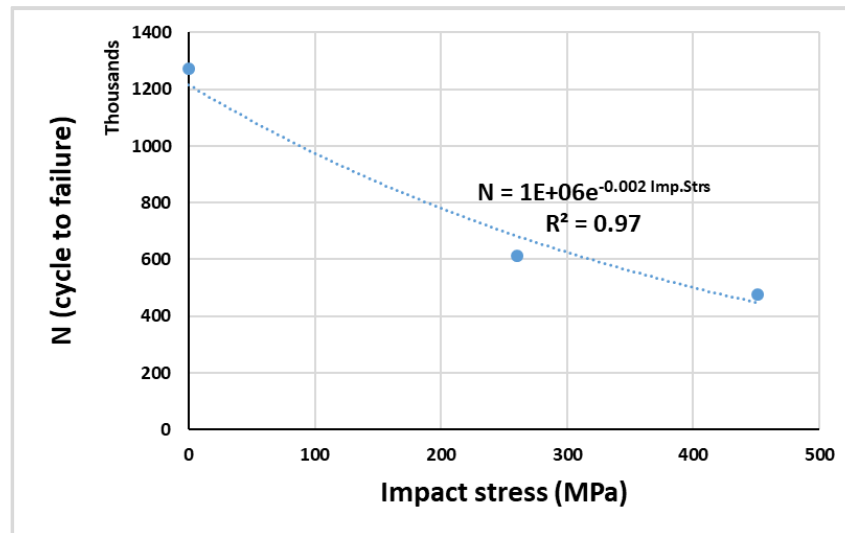


Figure 5-10: Individual effect of impact on the test disc life using flat discs.

Comparing this figure with [Figure 5-9\(b\)](#) shows a difference in the variation trend outside of the testing range. Thus, more investigation under different impact and compression loading levels, i.e. below and over the testing range is very important to investigate the accurate effect of impact. This importance came from the possibility of producing different damage initiation and propagation mechanisms under different impact and compressive loading levels.

5.3.1.3 Effect of slipping ratio

Slipping Ratio (SR) has been shown to be proportional to the traction coefficient if the other testing parameter levels were the same. The superposition technique by adding the calculated stress due to traction with that from the Hertzian contact theory can be used [195]. Grouping the results according to SR and following the same procedure mentioned before, was used to find the mean effect of SR. Linear and exponential curve fitting were again used and presented in [Figure 5-11](#). It shows that the increase of SR has a considerable effect on decreasing the test disc life. The residue (R^2) is higher for linear curve fitting which means better correlation with the experimental results.

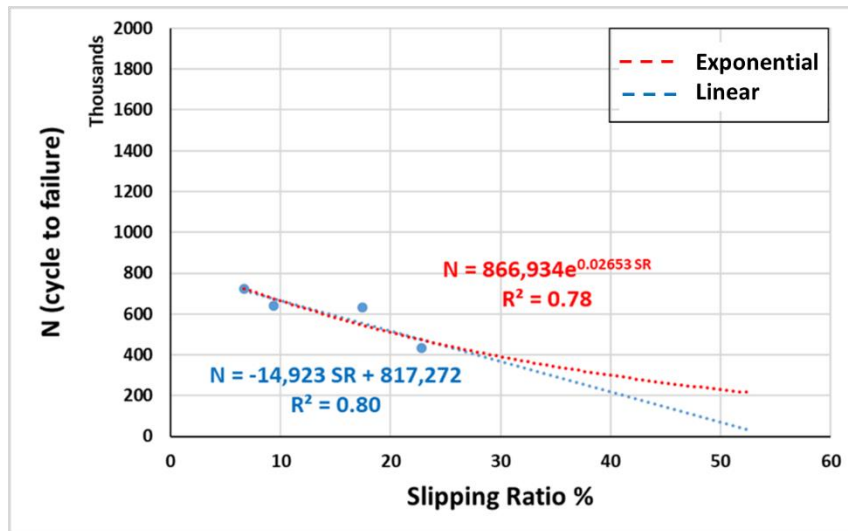


Figure 5-11: Mean effect of slipping ratio on the number of cycles to failure.

Presenting the results of the four SR groups reveals a specific trend, as shown in Figure 5-12(a). The variation ranges of the number of cycles to failure also decreased with the increasing SR. This means a shorter test time to reach fatigue failure under a higher SR compared with that of lower SR independently of the levels of the other factors. The variation ranges are presented in Figure 5-12(b) where the curve slope is higher than that presented in Figure 5-9. This means that SR in this test variation range has a higher effect than impact.

To confirm the individual effect of SR on reducing the number of cycles to failure, an additional test, T7A was conducted. This test has the same parameter levels of T7 apart from SR, i.e. SR=22.82% has been used instead of 6.71%. The test disc number of cycles to failure of T7A was found to be 132,300 cycles. This result shows a significant reduction of ~57.7% in the disc life compared with T7.

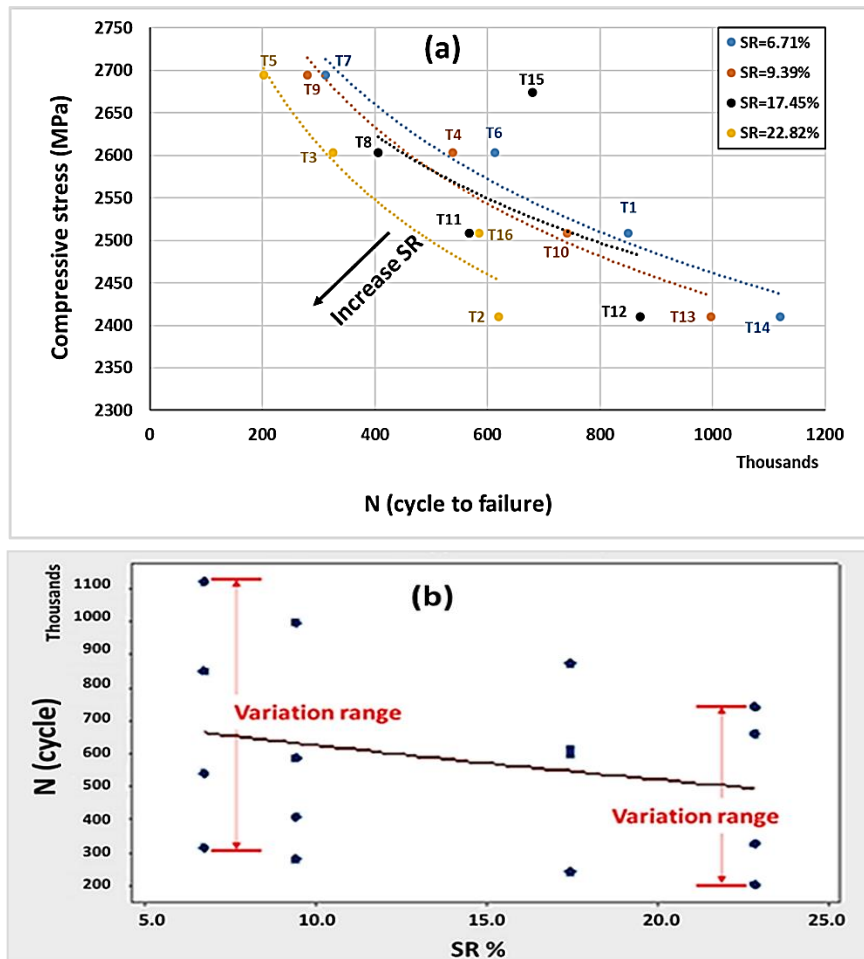


Figure 5-12: Effect of slipping (a) variation trends of S-N curves under four levels of slipping ratios; (b) variation range of the number of cycles to failure.

5.3.1.4 Analysis of fully crowned discs

Circular or elliptical contact represents a plane stress state which slightly differs from line contact of the roller bearing which represents a plane strain state. To show the individual mean effect of the study parameters, the test results are presented in Figure 5-13. Increasing the contact stresses by ~27% (from ~2000 MPa to 2500 MPa) reduced test disc life by ~25% while, increasing the impact stress by ~36% (from 757.6 MPa to 1188.2 MPa) reduced the disc life by ~4%. This small reduction probably due to applying the impact loading in a percentage of 0.07% which is the same percentage that the WTGBs are experienced due to operating events. However, increasing the SR from 6.71 to 22.1 reduces the disc life by ~9%. More investigations are still required to investigate and compare the effect of the study parameters in addition to repeating each test at least three times to increase the reliability of the results.

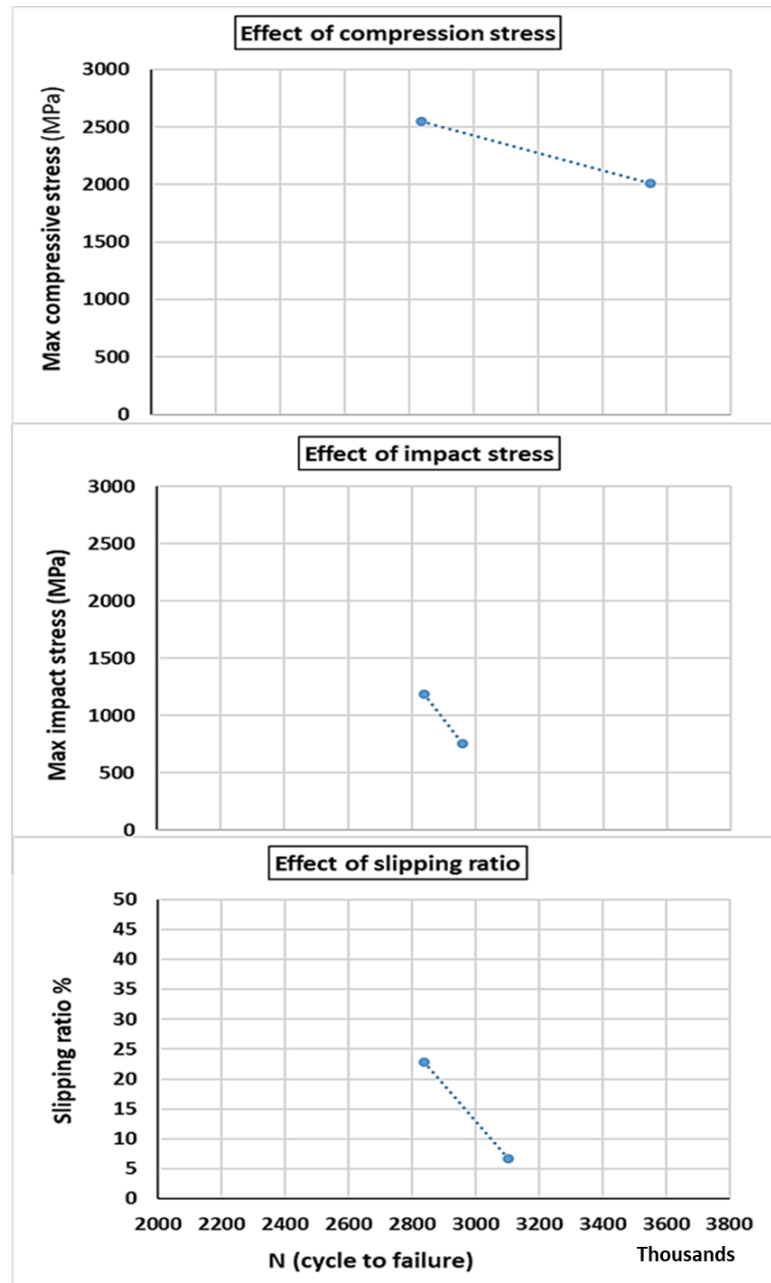


Figure 5-13: Effect of the study parameters on crowned test disc life.

The effect of compression is higher than the others following by SR and then impact loading. This also concluded for flat disc tests. Impact loading was applied by a small percentage of the rotating cycles thus, its effect probably higher than what appears in this analysis. The slope of these different trends also brings the attention; however, increasing the number of tests under different test levels will help to specify the quantitative effect of these factors, but this process requires a very long time (years). For that, these further tests are recommended for future works.

5.3.2 Interactive effect of the study parameters on disc life

The Interactive effect describes the sensitivity of one factor when other factors experience a change in their levels. Studying the interactive effect among factors has a considerable impact on predicting fatigue life and estimating the damage [228] because all the factors are applied together throughout the operating of the mechanical components. The plotting of two factors against the response (test disc life) in Minitab software provides the relation between these two factors and their interactive effect on the output, while the equation of the plane passing through the result points represents the function of the parameters quantitative effects. This equation of the plane can be derived using regression technique in Minitab software.

Figure 5-14 shows a wireframe diagram of a surface plot (plane) for compressive loading and SR against the test disc life. In this plot, the number of plot elements can be optimized to get better representation for the results which is one of the advantages of Minitab software. This can be achieved by increasing the number of elements in the presented surface but increasing the number of elements also increases the plot complexity. However, choosing a suitable number of elements can provide a clear view of the variation trend and this can be achieved by trial and error. Looking at this wireframe diagram from the right-hand side gives approximately the four plots presented in Figure 5-12 at the four SR levels. This figure shows that the test disc life is reduced with increasing SR and compressive loading. Under high compressive loading, the effect of SR is reduced. This reduction can be seen from the declined slope of the graph under high compressive loading; however, the general trend of increasing SR is still showing a decreasing of the test disc life under any compressive contact level. To give a clearer view of the effect of SR under different loading levels, ignoring the effect of scattering and find the nearest plane equation to that presenting the experimental results. However, under high SR as in the case of high compression, the number of cycles to failure is also reduced. This indicates the importance of the SR and compression load on test disc life.

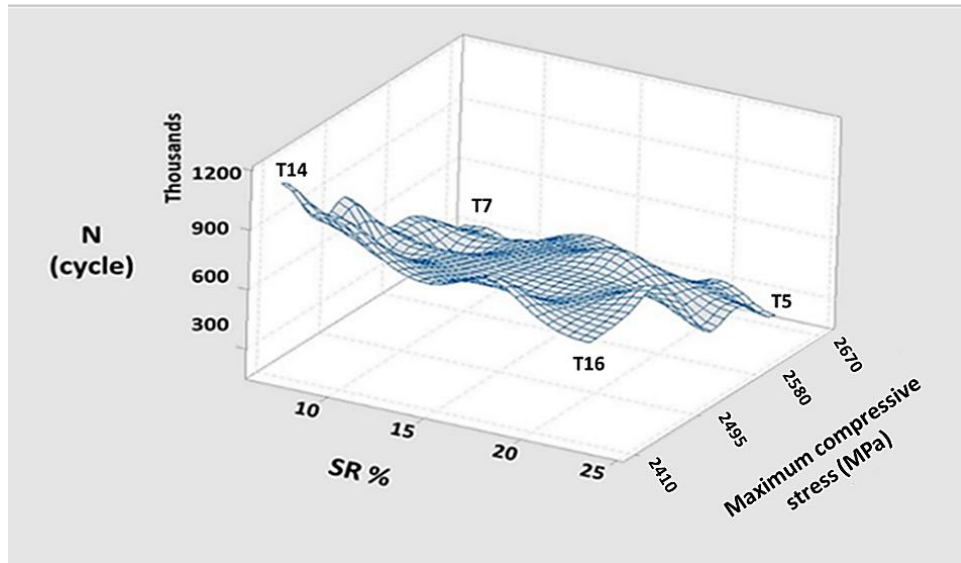


Figure 5-14: Interaction effect of slipping ratio and compressive loading on the number of cycles to failure.

The interactive effect between compressive and impact loading is presented in Figure 5-15. The variation has also a specific trend which seems to be linear, i.e. approximately a flat surface plane. Despite the same effect of compressive loading and impact on producing compressive contact stresses and using Hertz theory to calculate their contact stresses, the experimental analysis shows different trends of the compression and impact, i.e. different slopes of the plane edges. Under high compressive loading, there is not a noticeable variation in the test disc life, i.e. the plane edge T7-T5 is approximately horizontal. The effect of impact seems to be reduced under high loading levels. This is probably due to pre-compression that flattens the contact region, and this distributes the compression due to impact loading on this flattened region and reduces the effect of impact. On the other hand, under high impact loading, the effect of increasing compression is also reduced, however, under the lower impact level (the left-hand side of the plane edge T14-T7), the effect of increasing compression can be clearly seen, i.e. the edge slope has a noticeably declined.

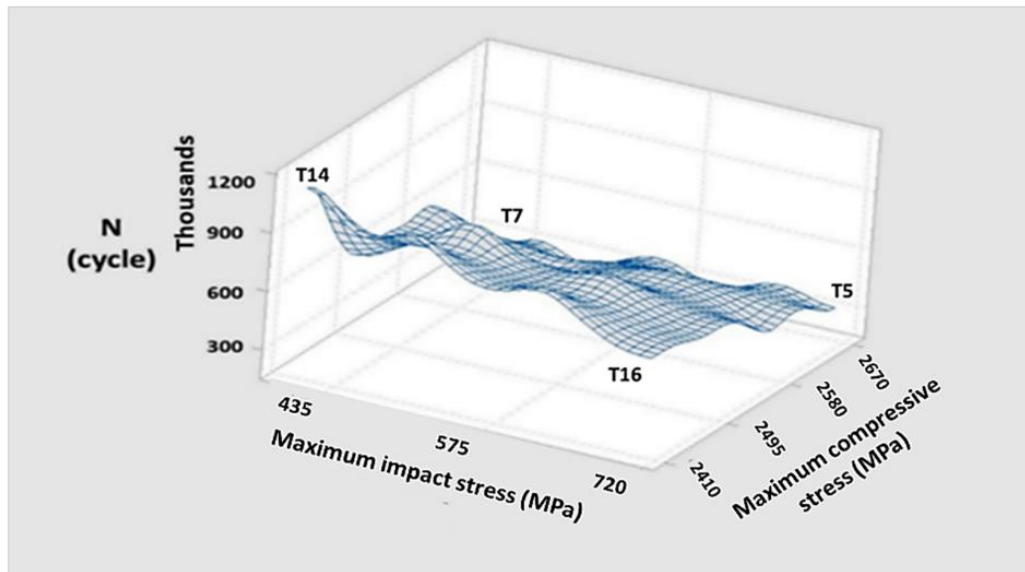


Figure 5-15: Interaction effect of impact stress and compressive loading on the number of cycles to failure.

Under high impact stress levels, the difference between maximum and minimum results is relatively small. This also confirms the lower effect of compression under high impact loading levels and vice versa. This also shows the importance of impact loading on the test disc lives. Looking at this wireframe from the right-hand side, i.e. from the maximum compressive stress-N plane, the four plots presented in [Figure 5-9](#) can be seen at the chosen four impact loading levels.

[Figure 5-16\(a\)](#) shows the interaction effect between impact stress and SR which has approximately an inversely proportional relationship with the test disc life. This figure shows unclear variation trends. For example, under high impact stress levels, there is an increasing trend in the test disc life with increasing SR (see the positive slope of the graph under the highest impact stress). On the other hand, under low impact levels, test disc life is decreased significantly with increasing SR. This also can be noticed clearly in the two-dimensional (2D) plot shown in [Figure 5-16\(b\)](#). This figure reveals that results of test disc life under the highest impact level are approximately similar, which means a lower effect of SR under this high impact level. The plot complexity may also come from the scattering nature of the fatigue testing. This complex graph indicates a strong interaction effect between impact and slipping under different testing levels; this highlights the importance of these two factors or at least the considerable effect of noise factors under these testing levels. This unsystematic variation trend needs further investigation by conducting more experiments under different SR and impact stress levels (higher and lower than the testing levels) to correlate precisely the interactive effect of impact and slipping. It can be concluded that increasing SR under low compressive levels should be

avoided to increase fatigue life. Unfortunately, this condition has a considerable occurrence during the wind turbine operation due to wind gust and the decreasing of turbine load at the beginning of some operating events on account of the disconnection of the generator and/or the electricity grid.

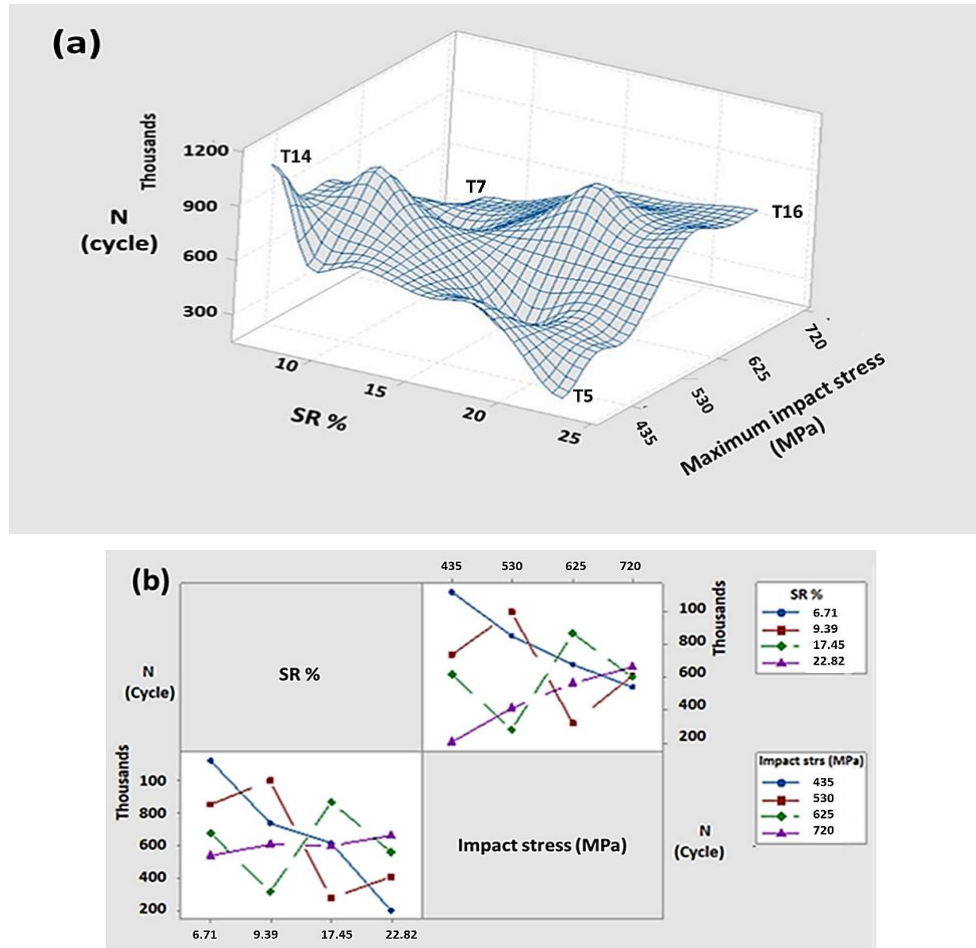


Figure 5-16: Interaction effect of slipping ratio and impact stress on the number of cycles to failure (a) 3D plot; (b) 2D plot.

Applying impact stress in combination as compressive loading produces high transient contact stresses that make the interaction effect of impact stress and SR was relatively unclear. Thus, investigation of this interaction probably will be clearer under lower impact levels. However, this investigation is a time-consuming process due to the high number of cycles required to failure under low loading levels. Despite the use of Hertz contact theory for calculating the stresses due to compressive and impact loadings, the effect of impact stress appears to be less than the compression (see the slopes of the graphs in Figure 5-15). This may be due to the pulse nature of the impact loading and the influences of mechanical wave (the wave of transforming the transient loading towards the deep of the contact region) on the failure near the impact regions only as will be investigated in Chapter 7. The

effect of impact loading probably has a complicated behavior which is still not clear despite this forward step towards understanding its effect. Nevertheless, the individual and interactive effects of impact stress on fatigue life are very important and require further investigations.

5.3.3 Effect of slipping and impact under different contact levels

To investigate the effects of slipping and impact under different compressive contact levels, the results of four tests were chosen. The first two tests having the same SR of 6.71% which are T14 and T6. These tests have different compressive loading levels and low impact loading. The second two tests are T2 and T5 which have the same SR of 22.82% and different compressive levels. The results of these four tests are presented in the upper of [Figure 5-17](#). The converging of the two plots shows that the effect of slipping on reducing the disc fatigue life is higher under low contact stresses. Despite T2 and T5 have different impact levels, the combined contact stress was considered in this plot. Tests with different impact loading may introduce a percentage of error in the results however, testing this effect under the same impact testing level will be more accurate but the required levels are not available in the tests due to designing these tests using Minitab software and this will be recommended for future work.

Four tests were chosen to confirm the effect of SR under different contact levels which are classified into two groups as mentioned above. T12 and T15 have SR of 17.45% and approximately the same impact loading but different compressive loading. The second group consists two tests T14 and T6 which presented in the lower plot. To get a clear difference, it is preferred a high contact stress difference (>300 MPa), between the chosen testing levels to investigate this effect.

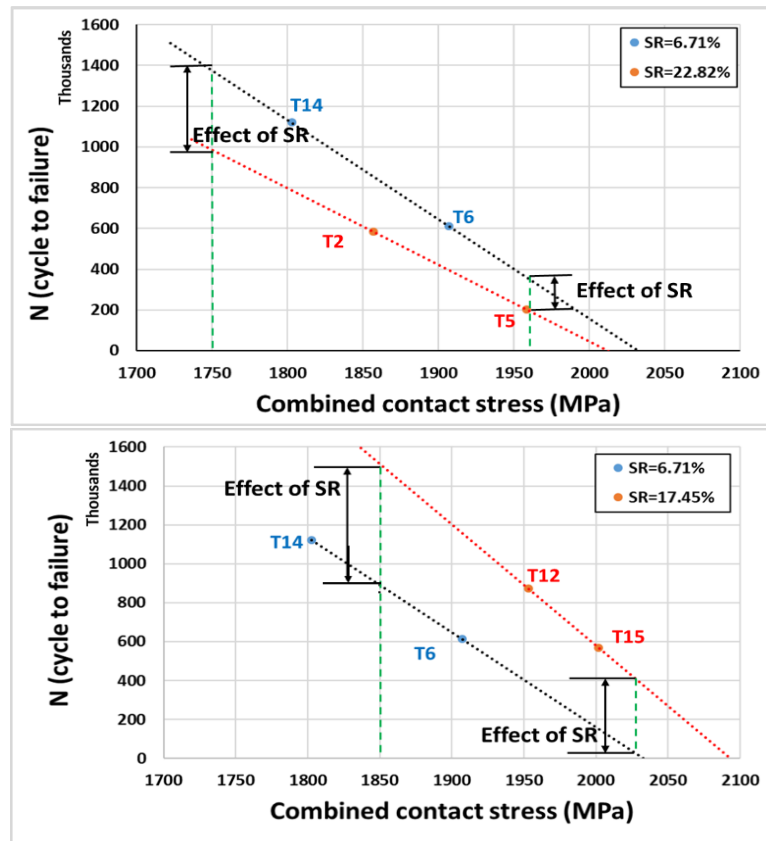


Figure 5-17: Effect of slipping with increasing the contact stress.

To investigate the effect of impact under different contact loading levels, Four test results under the same SR of 22.82% were chosen and presented in Figure 5-18. These tests are T2, T5, T16 and T7A. The former two tests were conducted under relatively low impact loading while, the other two tests under higher impact stress of ~688.7 MPa. Approximately the same effect of impact was achieved under different compressive loading levels. The two graphs are approximately parallel, this seems invariant effect of impact loading under different contact stress levels.

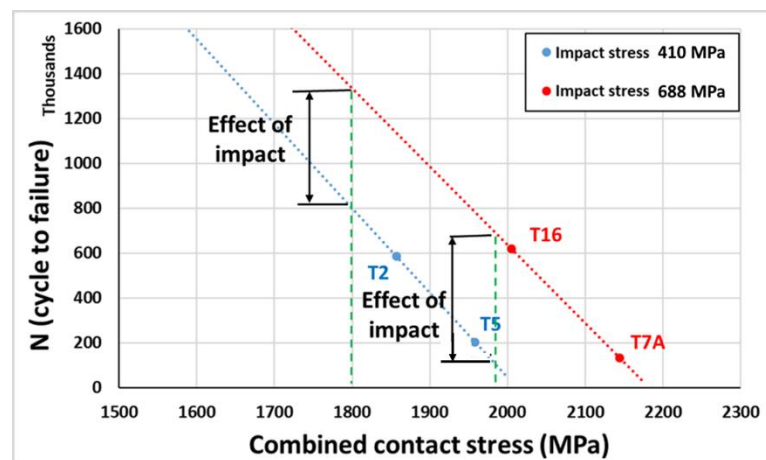


Figure 5-18: Effect of impact loading under different contact pressure.

5.3.4 Effect of surface roughness

The surface roughness of the investigated WTGBs varied considerably between the in and out contact regions, i.e. before and after service, as discussed in [Section 3.4.2](#). To investigate the effect of surface roughness on the test disc life, test T6 was repeated after improving the circumferential surface roughness (R_a) to be $\sim 0.12 \mu\text{m}$ instead of $\sim 0.27 \mu\text{m}$ in the original test. The improved surface roughness increased the test disc life from 612,759 cycles to 806,275 cycles. This represents a percentage increase of $\sim 31.6\%$. Despite the possible scatter in fatigue testing and the effect of noise factors, this considerable increase is an interesting observation and deserves to have a further investigation in the future by improving the roughness of the contact surfaces in WTGBs.

5.4 Quantitative analysis of the study parameters on test disc life

5.4.1 Individual effects

Despite the relatively small data sets achieved in this study, this data can be used to find a test disc life formula, i.e. disc fatigue life estimation, depending on one of the test parameter as independent variables, i.e. the individual effect. The reliability of this analysis can be improved when more testing data will be available from conducting additional tests under different testing parameter levels and repeating each test at least three times, as will be recommended for future work. Testing the results of life equations presented in [Section 5.3.1](#), by calculating the percentage of error between the experimental disc life and that estimated by applying the testing parameter levels in these equations. It was noticed that the percentages of error were quite high especially for the relatively low disc lives. Exponential equations to describe the trend of test disc life variation in general have less percentage of errors thus, they are present in [Table 5-4](#). The average error is the average of all the test results and the error % was calculated by using the equation:

$$\text{Error \%} = \frac{\text{life calculated by the considered fitting} - \text{Experimental life}}{\text{Experimental life}} \times 100\% \quad 5.8$$

Table 5-4: Life estimation equations and their percentage of error.

Life Equation	Error %	
	Error range	Average
$N = 2,184,046,016 * e^{-0.00323 \text{ Comp.Strs}}$	[-46.7 to 79.0]	8.6
$N = 17,997,821,157 * e^{-0.002 \text{ Cob.Strs}}$	[-47.0 to 141.9]	-13.1
$N = 1,248,616 e^{-0.00127 * \text{imp.strs}}$	[-37.0 to 282.5]	30.3
$N = 31,647,432 * e^{-0.00074 * \text{Cob.strs}}$	[-25.8 to 219.0]	22.7
$N = 866,934 * e^{-0.02653 * \text{SR}}$	[-36.0 to 133.0]	21.0

These high percentages of error show that disc life cannot be described by one factor only and the interactive effects of the fatigue factors are very important, however, using contact stress only and using combined contact stress showed less percentage of error for the individual effects. Therefore, this combined contact stress may be used to estimate the RCF life.

5.4.2 Combined and interactive effects

After investigating the variation trend due to the interactive effect of the study parameters on the disc life, it is important to evaluate this trend and calculate the percentage of error to discuss the results' reliability. To find the combined effect of the compressive loading and SR, the equation of the plane presented in [Figure 5-14](#) should be found. This can be easily by using the regression technique available in Minitab software. The plane equation was found to be as illustrated in [Eqn. 5.9](#).

$$N = 4,780,399 - 864.865 \text{ Comp.Strs} - 31061 \text{ SR} \tag{5.9}$$

The same procedure was followed to find the combined effect of compressive contact and impact stresses by finding the equation of the plane in [Figure 5-15](#). This equation is presented in [Eqn. 5.10](#);

$$N = 2,807,773 - 786.11 \text{ Comp.Strs} + 1186.62 \text{ Imp.Strs} \tag{5.10}$$

Finally, the combined effect of SR and impact presented in [Figure 5-16](#) was found to be expressed in [Eqn. 5.11](#);

$$N = 1,407,384 - 26,155 SR - 633.8 \text{ Imp. Strs} \quad 5.11$$

The basis of the test parameters analyses depends on the average effect of the factors, therefore, the average of the above three equations can be found to get:

$$N = 2,998,517 - 19072 SR + 184.27 \text{ Imp. Strs} - 550.325 \text{ Comp. Strs} \quad 5.12$$

Table 5-5 illustrates the life results achieved from the experimental and the above four estimation formulas (Eqn. 5.9 To Eqn. 5.12). Several calculated percentages of the error have high values. This probably due to the scattered nature of the fatigue tests and not repeating the tests to increase the accuracy and reliability of the results. These equations give lower percentages of error than expressing the life equations in terms of one parameter. This shows the importance of the combined effect of the study parameters on fatigue life. However, the highlighted column in green color shows less percentage of error for the tests excluding the last four tests conducted under higher contact stress level. This probably because the fatigue behavior of the material has a considerable change under severe contact levels. This also shows the importance of these two factors (compression and slipping) for fatigue life therefore, they maybe can be used to describe the test disc fatigue life.

Using combined contact stress in deriving the plane equations will cancel the effect of impact from the equations and this does not allow the individual effect of this parameter to be described. For that, individual parameter levels were used in deriving the plane equations. By comparing the coefficients in Eqn. 5.12, shows that the effect of compression approximately three times the effect of impact. This comparison is possible since both impact and compression stresses have the same unit of measurement. This also supports the result of the additional test without impact (T6B), where the disc life approximately doubled. Both the coefficient of compression and SR variables have negative values; however, the impact has a positive one. This does not mean that the impact increases the fatigue life since the plane equation has been chosen by Minitab software to give the optimum plane equation independently on the physical meaning of the study parameters. The minimum percentage of error that appeared for the impact-compression plane indicates the importance of contact stress in controlling the disc life. This means that contact stress may be used to predict the test disc fatigue life with acceptable accuracy, however, contact stress-SR plane equation also has a low percentage of error and can be used in life prediction. This will be discussed in the coming chapter by postulating a new life prediction methodology for the WTGBs and applying it to

the test results. The maximum positive and negative percentages of error are highlighted with orange and blue respectively.

Error was introduced in terms of the detection method used for the damage (human eye) and the difference between the predicted life (from the curve fitting formula) and that achieved from the tests. For this reason, apart from repeating each test under exactly the same testing conditions and using the same steel bar to manufacture the test discs to reduce errors, a proper measurement system for detecting damage should be implemented on the rig. This is strongly recommended for future works.

Table 5-5: Experimental and estimated test disc life and their percentage of error.

Test code	Experimental life (cycle)	Average planes life (cycle)	% error	SR-Impact plane life (cycle)	% Error	SR-comp. plane life (cycle)	% Error	Comp.-Impact plane life (cycle)	% Error
T14	1120826	752310	-32.9	762816	-31.9	1028739	-8	465385	-58.5
T13	997040	745273	-25.3	541119	-45.7	945495	-5	749219	-24.9
T12	871830	608666	-30.2	271450	-68.9	695141	-20	859419	-1.4
T16	620430	524419	-15.5	68503	-89.0	528343	-15	976423	57.4
T1	849893	704261	-17.1	611429	-28.1	884058	4	617311	-27.4
T10	741240	675915	-8.8	463027	-37.5	800814	8	763919	3.1
T15	567836	546865	-3.7	167366	-70.5	550460	-3	922782	62.5
T2	584617	348924	-40.3	355469	-39.2	383662	-34	307650	-47.4
T6	612759	562956	-8.1	792763	29.4	744842	22	151273	-75.3
T4	537907	581396	8.1	483437	-10.1	661598	23	599168	11.4
T8	406317	451778	11.2	189731	-53.3	411245	1	754371	85.7
T3	325400	303706	-6.7	206309	-36.6	244446	-25	460373	41.5
T7	312681	564722	80.6	492701	57.6	610516	95	590965	89.0
T9	279840	490487	75.3	502133	79.4	527272	88	442071	58.0
T11	680241	315407	-53.6	364793	-46.4	276919	-59	304519	-55.2
T5	202700	166930	-17.6	382765	88.8	110120	-46	7912	-96.1

The interactive effects can be evaluated mathematically by using the Root Mean Square (RMS) technique for the three plane equations. This also reduces the scatter of the test results and probably reduces the percentage of error in the disc life estimation formula. This RMS rule can be expressed as;

$$\tilde{N} = \sqrt{\frac{\sum_0^i \{f(N)\}^2}{i}}$$

5.13

where i is the number of equations which is 3 in this procedure. Using the three planes equations and simplify the formula; the final life estimation equation was as presented in [Eqn. 5-14](#):

$$\begin{aligned}
 N = & 674.774 [23533981 + \text{Comp. Strs}^2 + 1.325\text{Imp. Strs}^2 + \\
 & 1207.114 SR^2 + 24.272 SR * \text{Imp. Strs} + 39.333 SR * \text{Comp. Strs} - \\
 & 1.366 \text{Comp. Strs} * \text{Imp. Strs} - 268573.586 SR + 3572.226 \text{Imp. Strs} - \\
 & 9209.237 \text{Comp. Strs}]^{0.5}
 \end{aligned}
 \tag{5.14}$$

The percentages of error of this equation compared with the experimental results are presented in [Table 5-6](#). It can be seen that the percentage of error is significantly reduced; however, the maximum percentages are still associated with severe contact tests.

Table 5-6: Disc life estimation using RMS technique and its percentage of error.

Test code	Experimental life (cycle)	RMS Estimated life (cycle)	% Error
T14	1120826	760739.5	-32.1
T13	997040	738754.6	-25.9
T12	871830	636306.5	-27.0
T16	620430	626187.5	0.9
T1	849893	691128.6	-18.7
T10	741240	669738.9	-9.6
T15	567836	610700.4	7.5
T2	584617	329148.9	-43.7
T6	612759	610899.4	-0.3
T4	537907	563765.6	4.8
T8	406317	492340.8	21.2
T3	325400	309578.3	-4.9
T7	312681	545826.6	74.6
T9	279840	470726.9	68.2
T11	680241	301014.9	-55.7
T5	202700	222351	9.7

5.5 S-N curve of the disc material and disc life prediction

The test disc material S-N curve is one of the important properties of the engineering materials. By using the test disc life and contact stresses and by considering the stress concentration i.e. multiplying the maximum contact stress by a factor of 1.7. This factor has been chosen according to the FE analysis in [Appendix C](#). Adding the effect of traction (the traction coefficient of 0.07 multiplies

the contact stress); the S-N curve for the test disc material can be drawn as can be seen in Figure 5-19. Despite using the life results of line and elliptical contacts to draw this curve which probably reduced its accuracy, this curve can be used to predict the disc life. Furthermore, the effect of impact loading (applied in 0.07% of the rotating cycles) has not been added. The effect of impact could be added by multiplying the impact stresses by their number of cycles and add this to the multiplication of each test and its number of cycles to failure. This is the basis of a new life prediction method which will be discussed in Chapter 6. Adding the effect of impact for the elliptical contact shows that linear fitting describes the S-N curve more precisely. It is important to remember that this S-N curve is for the used material cleanliness level and cannot be considered for other cleanliness levels.

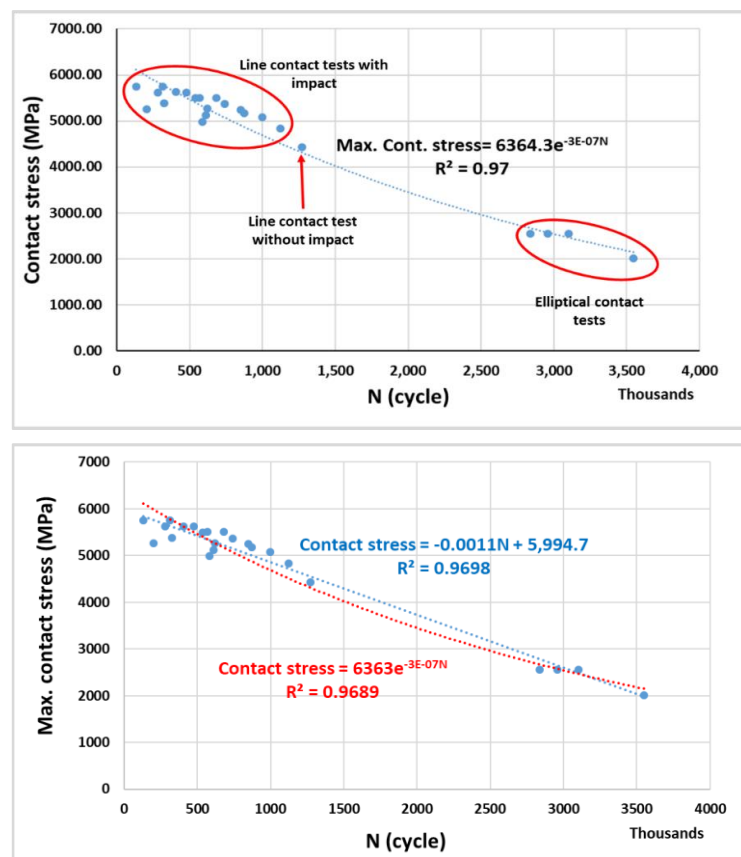


Figure 5-19: Modified S-N curve of the test disc material using linear and exponential approximations.

5.6 Discussion

The aim of the qualitative and quantitative analyses of test disc lives was presented for the line contact, i.e. the plane strain contact type. A life estimation formula for testing the discs under other testing levels was derived. The trend of disc life variation with the variation of the test parameter levels was specified and

the disc material S-N curve was drawn. The possible percentage of error in the results was also discussed. Despite applying the impact loading as compressive contact stress, its interactive effect with the other two parameters was observed to be different than that of the compressive loading. The qualitative analysis of the fully crowned discs confirms the effect of the study parameters on the second type of contact, i.e. plane stress contact. The percentage of errors was calculated for the conducted tests and the possible causes of these percentages were discussed. Describing the disc life depending on the combined contact stress is possible with a percentage of error; for that, a new simple and applicable life prediction methodology will be derived and tested in the coming chapter depending on the the average contact stress and its number of cycles to failure can be calculated from the material S-N curve.

5.7 Key findings

In this chapter, the mean individual and interactive effects of the key parameters including compressive load, impact stress and slipping ratio, on the test disc life were investigated using qualitative and quantitative procedures. The following findings can be identified:

- In the ranges of the test parameters, the compressive load has the most considerable effect on the test disc life followed by slipping ratio and then impact stress.
- Despite impact stress having an effect similar to compression in reducing the effect of SR while it increases, the individual and interactive effects of impact loading are different from those of compression.
- The interactive effect of the tested parameters has played a very important role in reducing the test disc life. The interaction between slipping ratio and compressive loading has the highest effect followed by compressive and impact loadings. This indicates the importance of slipping and friction on RCF life. However, the interactive effect between slipping ratio and impact stress fluctuates with varying impact stress levels, therefore, a clear correlation between impact and slipping could not be established, and further investigation is required.
- The slipping ratio has a higher effect at lower compressive levels. Nevertheless, this effect is reduced by increasing the compressive loading. Furthermore, the effect of impact on fatigue life seems independent on the contact stress level.

- Test disc material S-N curve was estimated, and a percentage of error is predicting in this curve due to depending on the contact stress only for elliptical and line contacts. This S-N curve represents the results for this material cleanliness level and can considerably change by changing the material cleanliness or heat treatment.
- Test disc life is considerably increased when the flat disc surface roughness improved. This probably due to initiating and propagating the damage depending on the micromechanics laws of contact. If this is correlated with the planetary bearings investigated in [Chapter 3](#), the effect of bearing surface roughness may have a considerable role in bearing failure and improving the bearing roughness may increase the bearing life significantly, however, more investigation is required.
- Under severe contact stress levels (>4400 MPa), the fatigue life trend was noticeably changed and the percentage of error in the life estimation increased.

6

A NEW FATIGUE LIFE PREDICTION METHOD

In this chapter, a new simple and applicable methodology and a calculation procedure to estimate the damage in WTGBs and predicting their life are suggested and tested by using the results of the conducted tests and real operating data of the Supervisory Control And Data Acquisition (SCADA) system for a wind turbine over two years. Furthermore, the SCADA results were reflected in the standard average annual wind speed distribution from NREL to show the ability to use this annual average wind speed in predicting the WTGB lives. The new method depends on transforming the number of rotating cycles under a specific stress level to an equivalent number of cycles under the last loading level. Bearing selection stress level and its number of cycles to failure provided by the bearing manufacturing companies after many tests can be used in this method, however, the average operating contact stress and its number of cycles to failure calculated from the bearing material S-N curve can be used instead. This method depends on the area under the S-N curve without any correction or loading factors. Further testing for this method by using real operating data is required to check its reliability.

6.1 Introduction

Different life prediction models were postulated in the last ten decades (see [Section 2.10](#)), however, none of them can precisely predict the service life of bearings especially when the bearings experience a variable loading throughout the service as in WTGBs. For that, premature and unexpected failure makes a big disturbance for the wind turbine companies due to the urgent requirements of special and high-cost equipment for the maintenance. This considerably increases the wind energy cost and reduces investment in this field.

The standard ISO/ICE 8400-4:2005 [103], presented a life prediction for gear contact in its Appendix H. The main differences between the new methodology and the standard procedure are that the standard methodology depends on calculating the damage using linear P-M theory which depends on the cyclic ratio, while the new method uses both stress and number of cycles. The second difference is that the life prediction procedure in the standard assumes the loading torque (which can be expressed as contact stress), and the number of cycles of each loading level till the failure is known, i.e. the life is predicted after the failure taking place. However, the new method can be used for unknown future loadings. The third difference is that there is no need to use the “application factor” which represents the ratio of equivalent to the nominal torques. The last difference is that the gradient of the S-N curve was used in the damage calculation procedure in the standard [103]. The slope of the material S-N curve is not used in the new method. The reason for ignoring the slope of the S-N curve is that this slope represents the variation trend at the number of cycles to failure. Therefore, using this slope with the number of cycles before the failure has no physical meaning and seems illogical. This method is tested by using operating data recorded by a SCADA system for a 1.7 MW turbine for two years. SCADA data is a data recording system widely installed in wind turbines to record and average the generator output power, its rotational speed and the wind speed every ten minutes. The annual standard wind speed distribution from National Renewable Energy Laboratories (NREL) is also used to test the new method and predicted the output turbine power depending on the averages of SCADA under each wind speed then estimating the bearing load. The effect of operating events on bearing life is also calculated and discussed. The new method has a very good correlation with the real WTGB life recorded in the previous researches. The percentage of error of predicting the bearing life using the standards often has ~400% error (premature failure) while, according to the three tests of this method, the percentage of error does not exceed 40%.

6.2 Stress-based fatigue damage theories and their issues

Before the explanation of the new suggested method, a quick review of the related issues in stress-based life prediction theories and fatigue damage tests may be beneficial. There are a large number of models and theories derived for estimating the fatigue life of mechanical components and bearings. Some of the stress-based theories to estimate fatigue damage (D) are summarized in [Table 6-1](#).

[Figure 6-1](#) shows the damage accumulation process of the first five presented methods which depend on the cyclic ratio. This figure achieved by assuming different values of cyclic ratios and suggesting the other required variables.

Starkey's nonlinear method with ($x_k=0.6$) gives the lowest fatigue life of mechanical components compared with the other methods. This method shows a gradual increase of damage and the damage rate decreases with the continuous deterioration of the component, i.e. reducing the curve slope with increasing $\frac{n}{N}$ ratio. This is in contrast with the practical case where most of the mechanical components are gradually deteriorate and then suddenly fails.

Table 6-1: Stress based life prediction theories [234].

Theory or method	Damage calculation formula
Palmgren-Miner theory [256]	$D = \sum_1^k \frac{n_k}{N_k}$
Marco-Starkey method [232]	$D = \sum r_k^{x_k}$
Owen and Howe hypothesis	$D = A \left(\frac{n_k}{N_k}\right) + B \left(\frac{n_k}{N_k}\right)^2$
Lamaitre hypothesis	$D = 1 - \left(1 - \frac{n}{N}\right)^b$
Datoma et al. theory	$D = 1 - \left(1 - \left(\frac{n}{N}\right)^{1/(1-\alpha)}\right)^{1/(1+\beta)}$
Double Linear Damage Rule (DLDR) by Grover [238]	$N_I = \alpha N_f$ for crack initiation $N_{II} = (1 - \alpha)N_f$ for crack propagation
Manson hypothesis	$N_I = N_f - PN_f^{0.6}$ for crack initiation $N_{II} = PN_f^{0.6}$ for crack propagation
Huiying et al. method	$D = \frac{1}{0.18} \left[a_o + (90.18 - a_o) \left(\frac{n_a}{N_f}\right)^{\left(\frac{2}{3}\right)N_f^{0.4}} \right]$
DCA method by Halford et al.	$D = [(pr)^k + (1 - p^k)r^{kq}]^{1/k}$
Morrow and Kaminski theory	$D = \frac{n}{N} \cdot \left(\frac{\sigma_a}{\sigma_{a\max}}\right)^\epsilon$
Reduced rigidity theory by Fitzgerald and Wang	$D = 1 - \frac{E_n}{E_o}$

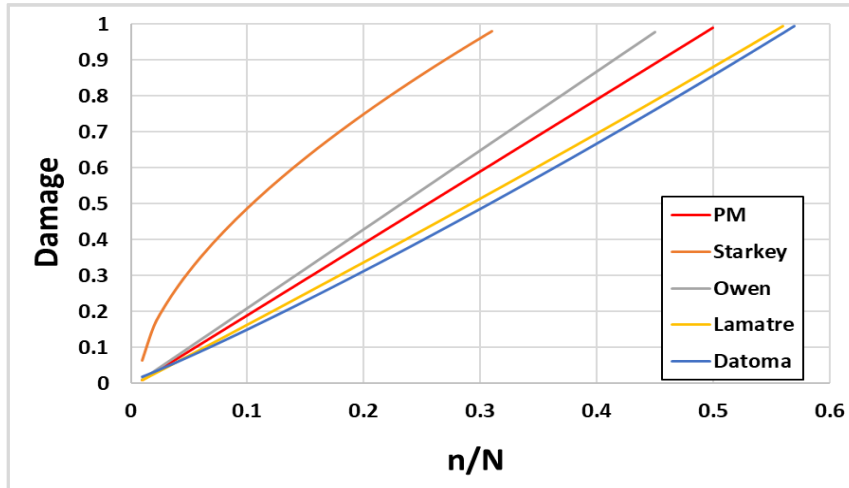


Figure 6-1: Comparison of five damage estimation methods under the same cyclic ratio.

A completely reversed bending fatigue test is widely used in postulating material S-N curves. In this type of test, maximum stress is produced at the outer surface of the test specimens which means there is no possibility of subsurface damage initiation like the RCF tests. The damage mechanism in this test is different from the failure mechanism of bearings. This is due to the stress distribution differences between these two cases. Loading direction also affects the damage mechanism, for example; tension loading produces crack openings which leads to the first mode of failure (opening mode), while compressive loading closes the crack and enforces the material to fail under the second and third failure modes, i.e. shearing modes. For the previous, testing of the engineering materials to draw their S-N curve must be made under identical loading conditions and geometries to that in service. S-N curves can be used to predict the fatigue life of mechanical components under any constant loading by applying one of the damage estimation theories such as P-M linear theory. This theory postulates a linear damage accumulation procedure under random loading levels depending only on the ratio of the rotating cycles to the number of cycles to failure, i.e. cyclic ratio. If the mechanical component does not fail after several cycles, the remaining number of cycles to failure can be estimated by subtracting the damage percentage and multiply the result by the number of cycles to failure under the stress level expected to be exerted on that mechanical component. In the new method, the area under the S-N curve will be used to describe damage accumulation instead of the direct use of the original S-N curve in predicting the damage and estimating the fatigue life. The low percentage of error of the compact plane presented in [Table 5-5](#) and that for average contact presented in [Table 5-6](#) supports the postulation of this method.

The new methodology postulated in this chapter depends on both the loading level and the number of cycles. In this method, the S-N curve is used in predicting fatigue

life by combining the loading stress spectrum (contact load-number of cycles histogram), with the S-N curve because both have the same phase, i.e. stress and the number of cycles. This method also depends on the design stress level (bearing selection stress) and its number of cycles to failure which should be provided by the bearing manufacturing companies.

6.3 New damage estimation method

A considerable difference was observed between the service and estimated bearing lives especially the bearings subjected to variable loading. For any mechanical system experiences fatigue loading, a fraction of the input energy will transform into internal energy to produce microstructural damage, plastic deformation (if the stress level is high enough), heating of lubricant or the mechanical components themselves in addition to the elastic energy absorbed by damping as illustrated in Figure 6-2. It can be assumed that a fraction of the loading energy to be transformed into damage throughout an accumulation process which is proportional to the loading stress and its number of rotating cycles in an accumulative process. Because of that, this method can be called Energy Fraction of Damage Accumulation (EFDA). This method assumes that the damage accumulates within each cycle of loading depending on the loading stress level.

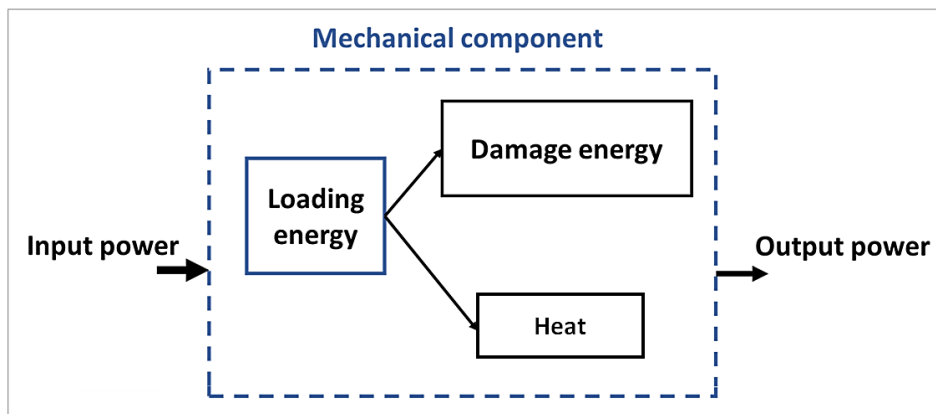


Figure 6-2: Damage energy in a balancing energy system.

If a mechanical component model having the same mechanical and microstructural properties is tested under identical operating conditions to that used in drawing its S-N curve, life achieved should be identical to that for the actual mechanical component in service and the component life can be predicted, however the material cleanliness, voids and inclusion distributions cannot be exactly symmetric for these components thus, fatigue tests have usually a scatter in their results. An Identical geometry and loading level in addition to material cleanliness are required to ensure

that the same fraction of loading energy will be transformed into damage during both the test and service. The quantity of energy absorbed to produce damage is proportional to the loading level and the number of rotating cycles. This also observed in the test results presented in [Section 5.3](#). The fraction of energy to produce damage, i.e. Damage Energy (DE) is assumed to be directly proportional to the stress level (σ) and the number of cycles (n);

$$DE \propto \sigma \cdot n \quad \mathbf{6.1}$$

Assume the fraction of energy transforms into damage during testing is (F_1) and that during service is (F_2); DE can be calculated as:

$$DE = F_1 \cdot \sigma \cdot n \quad \text{during the test} \quad \mathbf{6.2(a)}$$

$$DE = F_2 \cdot \sigma \cdot n \quad \text{during the service} \quad \mathbf{6-2(b)}$$

If the test and service conditions are identical, [Eqn. 6.2\(a\)](#) and [Eqn. 6.2\(b\)](#) are equal and $F_1=F_2$.

To explain this basic idea, suppose a mechanical component experiences a stress level σ_1 for N_1 number of cycles to failure; the area of the rectangle A1 shown in [Figure 6-3](#) can be easily calculated and this is proportional to the damage induced due to this loading case, i.e. 100% damage. This number of cycles N_1 can be transformed into an equivalent number of cycles (N_2) under another stress level σ_2 which can produce the same percentage of damage (100%). The damage mechanism may be different if the two stress levels have a high difference thus, average applied stress can be used in this calculation procedure. By dividing A1 by the new stress level, the equivalent number of cycles (N_2) can be calculated. The new method assumes that; the damage of failure produced by these two stressing levels (σ_1 and σ_2) and their number of rotating cycles is equal because both stresses produce the same percentage of damage. In the same way, any other stress level and a number of rotating cycles not producing 100% damage can be transformed into another stress level and its equivalent number of cycles by following the same procedure. The life prediction method in the standard [103], Loading Factor (LF) requires that all the loading levels and their number of cycles are known till the failure. In the case of a bearing, expecting the remaining life is required, i.e. when the loading is unknown, thus there is no need to use this factor.

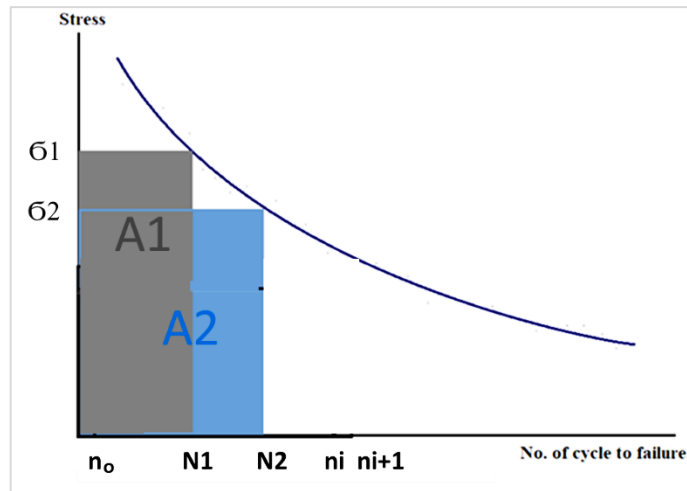


Figure 6-3: Calculating an equivalent number of cycles using the area under the S-N curve.

In the P-M theory, If the denominators and numerators are multiplied by their stress, the damage is then the ratio of the portion of the area under the S-N curve (in the numerator) to the total area under the S-N curve in the denominator.

The following example shows the step by step procedure of the suggested method to give a clearer view.

Assume a bearing experiences three loading stress levels S_1 , S_2 and S_3 and rotate for n_1 , n_2 and n_3 respectively. The following procedure can be used:

- 1 Calculate the area under the S-N curve for the first stress level, i.e. $a_1=S_1*n_1$, and the damage can be calculated by dividing this area by A_1 which is the total area under S-N curve under this stress level ($A_1=S_1*N_1$) where N_1 is the number of cycles to failure under S_1 is the stress. The damage for this loading stage is equal to that of the P-M theory, i.e. $D = \frac{S_1 n_1}{S_1 N_1} = \frac{a_1}{A_1} = \frac{n_1}{N_1}$.
- 2 When a new stress level applied (S_2), the first stress level should be transformed into an equivalent number of cycles under the second stress level because it is expected the second stress level will continue till the failure because the future loading is unknown, this can be done by dividing a_1 by the new stress level, i.e. $n_{eq.1} = \frac{a_1}{S_2}$.
- 3 The new equivalent number of rotated cycles $n_{eq.2}$ is the summation of n_2 and $n_{eq.1}$ and the damage (D) is the dividing of the new area (multiplication of S_2 by $n_{eq.2}$), by the area under S-N curve under the average stress level. However, the average stress level represents the bearing selection stress which is the stress level that the bearing manufacturing companies tested the manufactured bearing many times under that stress and the reliability of this test is very high. Thus, the

damage will be the area due to the two stresses ($n_{eq2}\sigma_2$), dividing by the total area under the S-N curve under the design stress and its number of cycles to failure.

- 4 If a new stress level S_3 and number of cycles n_3 is applied, only the second stress level will be transformed into an equivalent number of cycles, i.e. $n_{eq.3} = n_3 + \frac{S_2 * n_2}{S_3}$ and the damage is $D_3 = \frac{S_3 * n_{eq.3}}{S_d * N_d}$, where S_d and N_d are the bearing selection stress (design stress) and the number of cycles to failure under this stress respectively. The design stress and its number of cycles are provided by the bearing manufacturing companies.
- 5 The damage of each stress level and the number of rotating cycles is used twice in this procedure thus, the damage must be divided by 2.

In general, the equivalent number of cycles and damage equations can be written as;

$$n_{eqi} = \left(n_i + \frac{S_{i-1} * n_{i-1}}{S_i} \right) \quad 6.3$$

$$D_i = \left(\frac{1}{S_d * N_d} \sum 0.5 * n_{eqi} * S_i \right) \quad \text{OR} \quad 6.4$$

$$D_{i+1} = \left[\sum_i \frac{0.5 * \left(\frac{n_i S_i + n_{i+1}}{S_{i+1}} \right) S_{i+1}}{(S_d N_d)} \right]$$

where D is the damage, i the loading counter, S the stress, n the number of rotating cycles and N is the number of cycles to failure and the subscript d refers to the designed values. Bearing design stress and the design number of cycles to failure is independent on the counter i , thus, the damage equation can be rewritten as:

$$D_{i+1} = \frac{0.5}{(S_d N_d)} * \left[\sum_i \left\{ \left(\frac{n_i S_i}{S_{i+1}} + n_{i+1} \right) S_{i+1} \right\} \right] \quad 6.5$$

If the term S_{i+1} is distributed to the bracket, the damage can be expressed as the ratio of the average multiplication of the two sequential stresses by their rotating cycles to the multiplication of design stress by the designed number of cycles to failure. Thus, the calculation of the equivalent number of cycles can be avoided and there is no need to use the half and the damage can be expressed as;

$$D_i = \frac{\sum S_i * n_i}{S_d * N_d} \quad 6.6$$

The new method will be tested and compared to the results of using Eqn. 6.4 to Eqn. 6.6. The latter equation shows that the damage can be estimated by multiplying the contact stress by its number of cycles and divided by the total area under the S-N curve for the design contact stress. The bearing manufacturing company provided a reliable data of bearing design stress and its number of cycles to failure. If this data is unknown, the average applied stress during the turbine operating can be calculated from SCADA data and its number of cycles to failure can be calculated from the bearing material S-N curve. These two values can be used instead of the design stress and its number of cycles to failure. Bearing selection stress (design stress) should be close to the nominal operating stress in service to have more reliable results because the damage mechanism may change with changing the contact stress level. The flowchart of the calculation procedure for this method is presented in Figure 6-4.

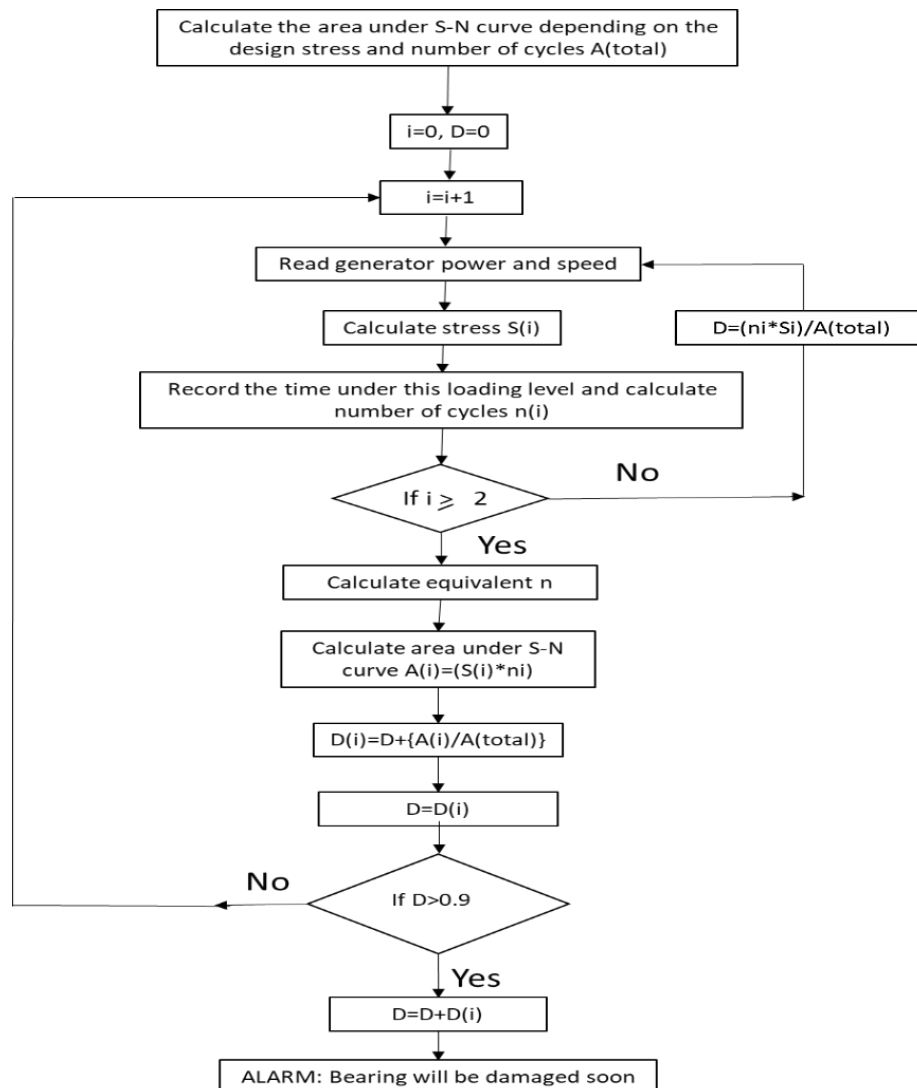


Figure 6-4: Flowchart of the new damage estimation method.

6.4 Assumptions and limitations of the model

This method was built upon some assumptions and has some limitations; it needs more tests by using real testing and operating data from SCADA to ensure its reliability and applicability. The following assumptions were considered:

- 1 The damage depends only on the contact stress level and number of cycles under each level. In reality, the damage also depends on the material microstructure, the distribution of inclusion, operating temperature and type of lubricant and lubricating regime. Depending on fatigue tests under identical conditions can reduce the effect of these factors on the fatigue life results but this cannot be completely overcome and a percentage of error is introduced throughout the life prediction calculations.
- 2 Damage is directly proportional to contact stress and number of cycles. This to some extent is right if the S-N curve of the material under fatigue loading is linear under different loading levels, however, in a considerable number of engineering materials, damage is non-linear and the S-N curve either being curved (non-Linear) or has two portions which refers to different fatigue behavior under different loading levels.
- 3 The damage process was assumed as linearly accumulated under different loading levels. In some previous methods such as the standard 81400-4: 2005 [238], damage was considered to be dependence on the S-N curve gradient, however, this gradient appears when the damage arrives its final stage (100% damage). For this reason, this gradient was neglected in this suggested method.
- 4 The damage was assumed to be as a fraction of the multiplication of the contact stress under consideration and its number of cycles to the design contact stress (sometimes the average contact stress during the operating) and its number of cycles to failure. Because of the wide range of operating contact stress and the possible change of damage initiation and propagation mechanism under different loading levels; it maybe more appropriate depending on more than one contact stress level to estimate the damage and to predict the fatigue life. This will be a part of the future work of testing and modifying this new method.
- 5 Depending on turbine operating monitoring data from SCADA is an advantage of this method, however, the confidentiality of these data required a sharing policy among the companies. This method will be tested using the testing results and SCADA data for two years in the coming sections in addition to test the method by using the average annual wind speed distrion. More tests are still required to show the reliability of this method.

6.5 Applying the new method on the conducted tests

The conducted fatigue tests in [Chapter 5](#) were under constant loadings thus, the average contact stress can be calculated using the data presented in [Table 5-3](#). There is no need to calculate the equivalent number of cycles because this procedure is used only if the contact loading is variable during the test or the service. Using the disc material S-N curve presented in [Figure 5-19](#), the number of cycles to failure under this average contact stress can be calculated. The average applied contact stress for the tests was 4810.5 and its number of cycles to failure was 1,065,243 cycles. Multiplying these two values and dividing the result by the contact stress of each testing level gives the estimated disc life of each test. After adding the friction coefficient effect, i.e. multiplying the contact stress by 1.07. The calculated values of the average contact stress and its number of cycles to failure are 5147.212 MPa and 757129 cycles respectively. By following the same procedure to estimate the test disc life, the percentage of error of the results calculated using [Eqn. 5.8](#) are illustrated in [Table 6-2](#). Adding the effect of friction reduces considerably the percentages of error. This means that the effect of friction probably reduced the error even if it was not considered throughout the drawing of the S-N curve. However, the percentages of error for several discs are still considerable, especially that having a relatively short lives (less than the average disc life of 611,340 cycles). In any engineering design, the number of cycles to failure should be as high as possible for elongating the service life. Therefore, it is expected that for practical applications, the percentage of error in this life estimation could be quite smaller than what presented in this table, i.e. more precise life estimation. The high percentages of error for several tests are probably due to the following reasons:

- 1 The reliability of the tests is low due to not repeating them for at least three times and using the average life. This was mentioned before as out of the scope of this study due to time facilities.
- 2 The S-N curve of the test discs was drawn independently on the contact type, i.e. using the results of elliptical and line contacts. These two types have slightly different stress states (plane stress and plane strain respectively).
- 3 The effect of stress concentration probably makes the damage initiation being from the contact surface however, subsurface damage initiation mechanism is probably taking place in the elliptical contact.
- 4 When the fatigue life is relatively small, the percentage of error increases significantly due to dividing the difference between the estimated and the experimental lives by a small value (See [Eqn. 5-8](#)).

Increasing the contact stress by 0.07% due to taking the effect of friction reduced considerably the percentage of error. This probably because the RCF life already affected by traction. Therefore, for the S-N curve drawn by the cyclic test, fatigue stress should take the friction force on consideration for life prediction even if the S-N curve was drawn by ignoring the friction. The percentage of error, in general, is lower for the first 16 tests than the last four. This probably because of the more dependence of drawing the S-N curve on these results. For that, testing the mechanical components under the same operating condition and geometry probably will provide more accurate results. The negative error in estimating the elliptical contact lives is an advantage because we can prepare for maintenance before the damage occurrence.

Table 6-2: Life prediction and percentage of error of the conducted tests.

Test code	Experimental No. of cycles to failure	Total contact stress due to traction and concentration (MPa)	Life prediction by EFDA method	% error of EFDA by considering the friction	% error of EFDA without friction
T14	1,120,826	5175.55	752985	-32.8	-5.5
T13	997,040	5431.48	717503	-28.0	1.2
T12	871,830	5530.85	704612	-19.2	13.7
T16	620,430	5636.36	691423	11.4	56.8
T1	849,893	5610.12	694656	-18.3	15.0
T10	741,240	5742.32	678664	-8.4	28.8
T15	567,836	5885.57	662146	16.6	64.1
T2	584,617	5330.89	731042	25.0	75.9
T6	612,759	5476.22	711641	16.1	63.4
T4	537,907	5880.10	662762	23.2	73.4
T8	406,317	6020.05	647355	59.3	124.2
T3	325,400	5754.94	677175	108.1	192.8
T7	312,681	6148.98	633781	102.7	185.2
T9	279,840	6014.72	647928	131.5	225.8
T11	680,241	5890.69	661570	-2.7	36.8
T5	202,700	5623.23	693037	241.9	381.0
T7A	132,300	6153.78	633287	378.7	573.5
T6A	476,280	6017.36	647644	36.0	91.3
T6B	1,272,750	4734.88	823062	-35.3	-9.0
T1P	2,837,250	2726.78	1429198	-49.6	-29.1
T2P	2,959,320	2726.78	1429198	-51.7	-32.1
T3P	3,548,839	2147.45	1814762	-48.9	-28.1
T4P	3,102,436	2726.78	1429198	-53.9	-35.2

For WTGBs, the friction coefficient is not precisely specified, and their life is relatively longer than the test discs. Thus, this method will be tested by using real WT operating data recorded by SCADA to find the contact stresses and their number of cycles under different wind speeds.

In some WTs, the SCADA system is installed to record and averaged the operating conditions (generator power and its rotational speed in addition to wind speed), every 10 minutes. These operating conditions can be used to calculate the bearing contact stress as presented in [Appendix A](#). Only two years of SCADA data is available due to the confidentiality of this data and the WT companies do not share it. Thus, this method will be tested by using these two years data only and then the results applied on the average annual wind speed distribution from NREL to predict the WTGBs lives to evaluate the percentage of error of each case.

6.6 Testing the new method using SCADA data

The SCADA system is widely installed in wind turbines. SCADA data for a 1.7 MW wind turbine collected over two years was used to test the suggested EFDA method and compare its results with that of the P-M theory.

The cut-in wind speed (minimum wind speed to start the turbine power generation) and cut-out wind speed (maximum wind speed of the turbine power generation) [23] are 3.0 m/s and 25 m/s respectively [257]. Therefore, excluding the wind speed values less than the cut-in and over the cut-out from the SCADA data are performed first, i.e. data filtering. The percentage of the removed data was found representing $\sim 7.56\%$ of the year. This means the WT is out of service due to cut in and cut out wind speed for ~ 27.6 days in each year. Characteristic curves for the 1.7 MW turbine using the average data of the first year are shown in [Figure 6-5](#).

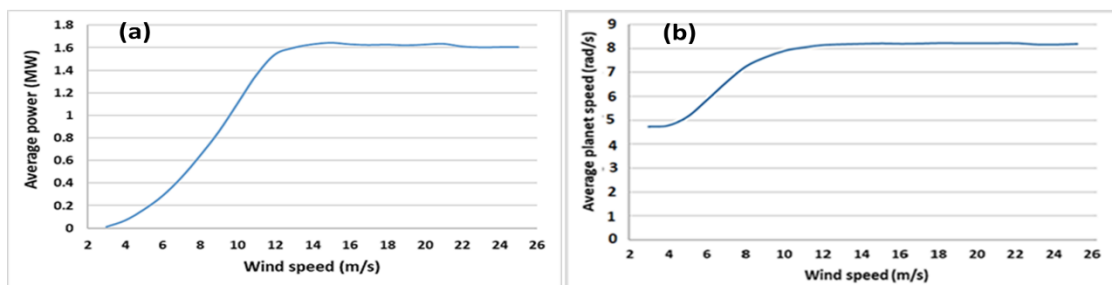


Figure 6-5: Characteristic curves of a 1.7 MW wind turbine (a) power curve; (b) planet speed curve.

The power curve in [Figure 6-5\(a\)](#) is one of the most important characteristic curves which can be used to predict the power and hence the loading level variation with

the wind speed variation. In the gear planetary stage, planet gear rotational speed with wind speed is also important since the torque and power are related to each other by speed. This variation can be seen in [Figure 6-5\(b\)](#).

Despite using the maximum contact stress to describe most the S-N curves, shear stress may be more suitable for describing the bearing material fatigue behaviour for two reasons:

1. Bearing materials probably fail under shear stress easier than their failure under other types of stresses.
2. The available S-N curve of the bearing material under consideration is drawn by using shear stress [258], as shown in [Figure 6-6](#). The S-N curve equation for this bearing material is:

$$N = \left(\frac{\tau}{2.27}\right)^{-10.34} + \left(\frac{\tau}{2.27}\right)^{-9.9} \quad 6.7$$

where the shear stress (τ) in GPa and N is the number of cycles to failure. The S-N curve of the bearing materials can be drawn by testing the bearings under different contact stress levels and count the number of cycles to failure for each testing level then, presenting the results in a diagram and using curve fitting to find the trend equation.

Hertzian contact theory (which is used in the contact stress analysis) neglects the traction force which may produce a change in the values and locations of maximum shear stresses during the operation and this may affect the results. There are no precise average values for SR and friction coefficient in WTGBs due to their change with changing the contact load. These two factors are currently investigating [105]. Therefore, using the traction force in the calculation procedure because this provides more accurate results as presented in [Table 6-2](#) and this will be recommended for future work.

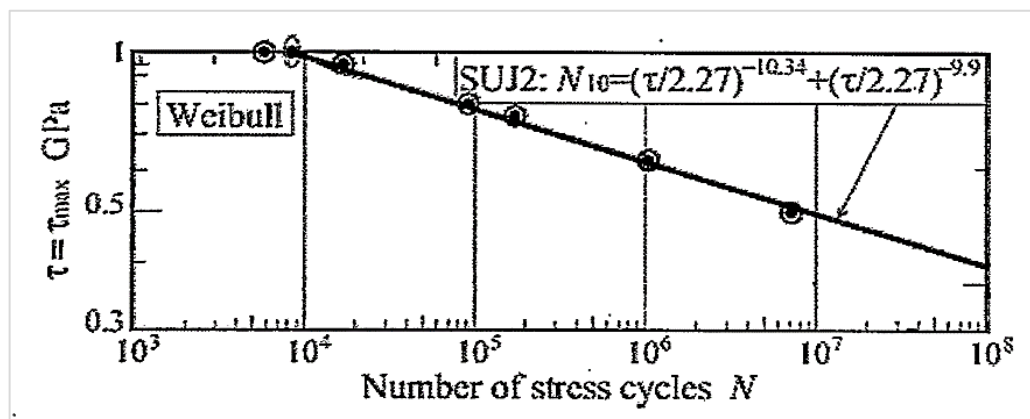


Figure 6-6: S-N curve of the bearing material [258].

6.6.1 Fatigue life prediction results

The EFDA method was used for estimating the damage and fatigue life for a 1.7 MW WTGB which is suffering from severe variable loading conditions due to wind speed variation and/or operating events. Wind speed varies randomly throughout the years. Figure 6-7 shows the wind speed distribution during two years by taking 0.1 m/s as an increment step of the wind speed variation. There are considerable differences in the number of occurrences (frequency) between the two years. For example, the maximum number of occurrences in the second year is ~425 at a wind speed of ~4.9 m/s, while in the first year, the maximum number of occurrences is ~375 at wind speed ~6.3 m/s. These wind distribution differences increase the complexity of selecting the WTGBs for specific operating conditions. Figure 6-8(b) and Figure 6-9(b) are showing the wind speed distributions for the two years by taking the wind speed increment step as 1 m/s which is the incremental step commonly used in the previous analyses [259].

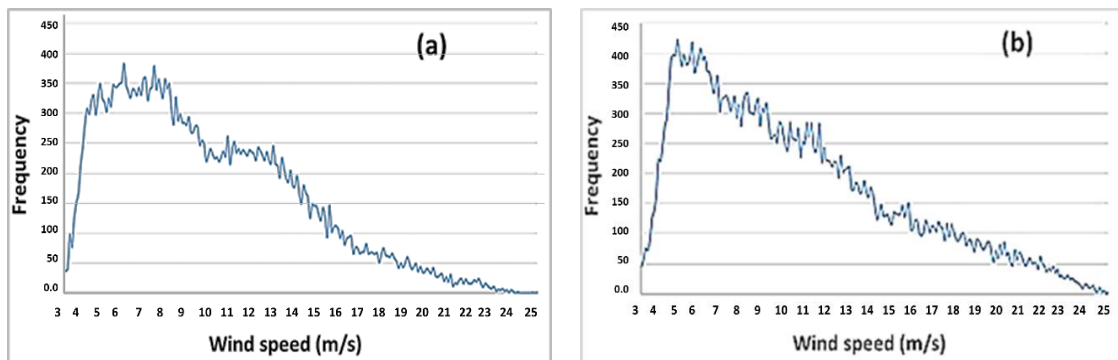


Figure 6-7: Operating wind speed distribution using SCADA data for (a) for the first year; (b) for the second year.

To calculate the damage using the EFDA method, the design shear stress of the bearing is required which is unknown. Thus, the average operating shear stress due to contact along the two years was calculated and was considered as the design stress (bearing selection shear stress). This procedure is logical since the design always performed under average stress. The number of cycles to failure for this stress level can be calculated depending on the bearing material S-N curve as presented in Figure 6-6. This average τ_{max} due to contact was found to be **433.21** MPa and the number of cycles to failure under this shear stress level is **40,630,109** cycles. Damage accumulation process throughout the first-year using the EFDA method and P-M theory can be seen in Figure 6-8(a). The calculation procedure of these data sets is by using the wind turbine output power recorded by SCADA and the generator speed to find the torque on the generator shaft. This torque

transforms into the turbine rotor depending on the gear ratio of the gearbox and the overall efficiency as presented in [Appendix A](#). Torque carried by one plant gear is then used to find the maximum contact force on one roller and to find the maximum contact pressure using Hertzian contact theory and to calculate the maximum shear stress in subsurface region. From the S-N curve presented in [Figure 6-6](#), the number of cycles to failure under each loading level can be calculated and then used in the calculation procedure of the P-M theory to compare its results with the EFDA method.

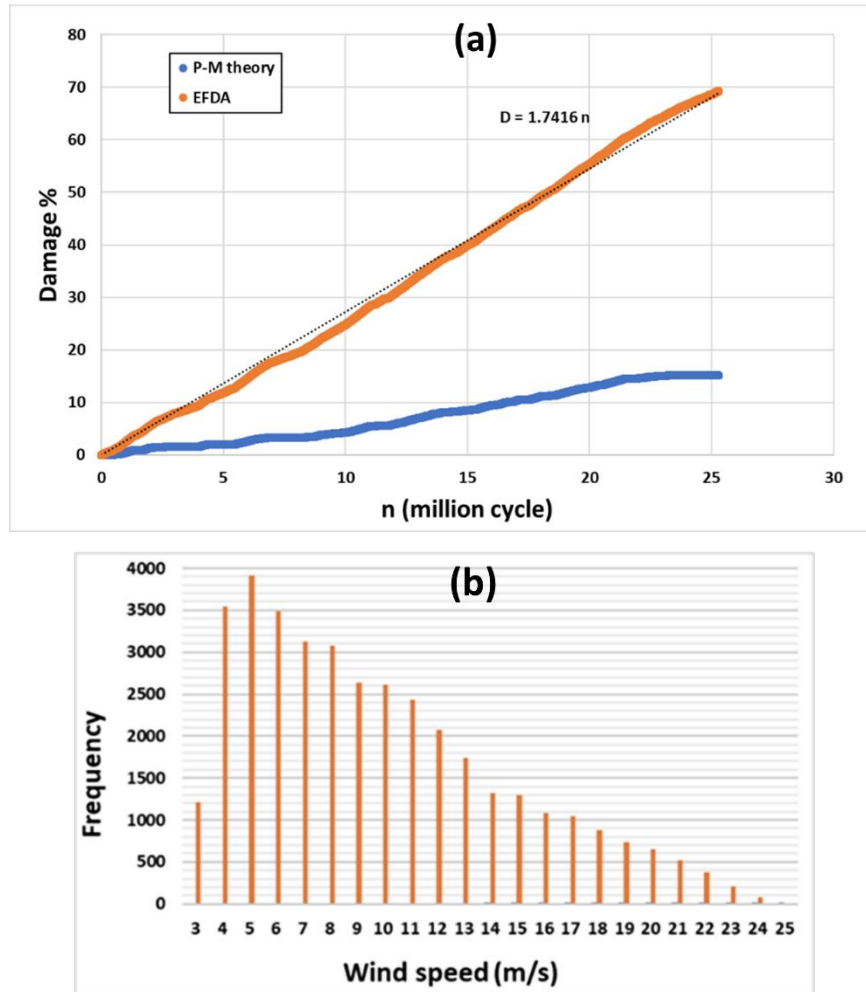


Figure 6-8: First-year results of damage using SCADA data (a) accumulative damage using P-M theory and the new method; (b) wind speed distribution.

The calculated damage in the planetary bearing at the end of the first year using the EFDA method was 69.26% compared with 15.24% using the P-M theory. If the same damage is produced throughout the next years, the life of the bearings according to the achieved results will be ~1.444 years for the suggested method compared with ~6.56 years for P-M theory. The damage accumulation results using EFDA method

are quite close to the real data of WTG bearing life in previous research which was specified to be around 2 to 5 years [33].

The results of the second-year accumulative damage using SCADA data are presented in Figure 6-9(a) which shows the damage using the same mentioned two methodologies (EFDA and P-M). During the second year, the damage estimated using the suggested method was ~55.57% compared with 7.48% using the P-M theory. If the same damage is assumed to be produced in the following years, the EFDA method gives a bearing life of ~1.80 years while the P-M theory gives 13.35 years. By introducing the traction force, axial loading and operating events, the estimated bearing life will probably be much closer to the real bearing life in service.

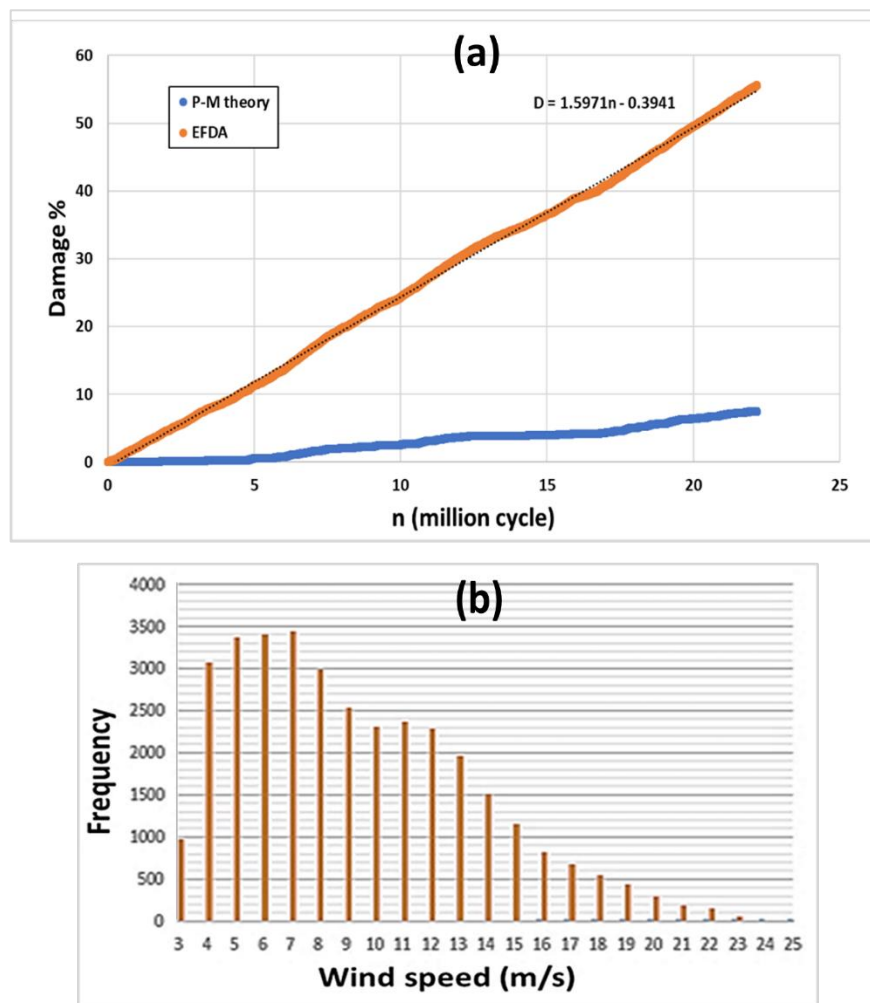


Figure 6-9: Second-year results of damage using SCADA data (a) accumulative damage using P-M theory and the new method; (b) wind speed distribution.

Damage accumulation for the two years using the EFDA method and P-M theory can be added now. The linear damage accumulation equation seems to be able to describe the damage accumulation process. It has been noticed that the damage

accumulation process is completely dependent on the stress and the number of rotating cycles which vary depending on wind speed which also varies randomly throughout the years. By adding the results of the two years, the damage using EFDA method is found to be 1.0 (100%), after 37,529,428 cycles. This means that the planetary bearing is failed after one year, six months and 25.59 days as can be seen in Figure 6-10. It is important to point out that, under the same wind speed, stress values and output power may considerably different because SCADA data gives the average data over ten minutes. Stresses in the bearing material also depend on the electrical controlling system of the turbine and the load of the electric grid which affects the turbine rotational speed and the bearing stresses.

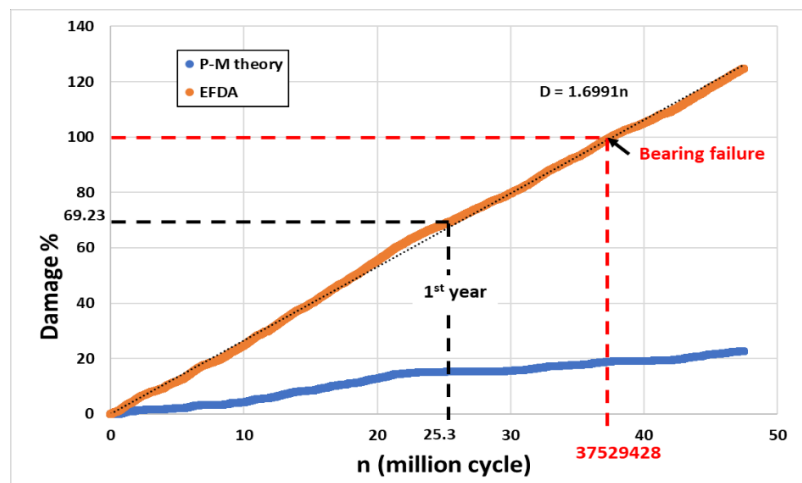


Figure 6-10: Damage accumulated curves for two years using SCADA data.

The National Renewable Energy Laboratories (NREL) averaged the wind distribution for tens of years and this average distribution was also used to check the EFDA method. The procedure of estimating the damage depends on the turbine power curve presented in Figure 6-5(a). The average power production and its corresponding contact stress can be estimated or by following the procedure:

- 1- From the number of occurrences of each wind speed and its percentage from one-year time, the number of cycles can be counted depending on the bearing rotation speed under this wind speed.
- 2- From the turbine power curve, power and bearing load (stress) can be estimated under each wind speed.
- 3- If the bearing selection stress and its number of cycles to failure are available, they can be used directly, otherwise, the average contact stress throughout the recorded data by SCADA system can be used to estimate the average stress then from the bearing material S-N curve the number of cycles to failure can be calculated.

4- The damage under each wind speed can be calculated by dividing the result of multiplying the contact stress by its number of cycles and divide this by the multiplication of the average stress and its number of cycles to failure in an accumulative procedure.

The damage estimated using P-M theory by using the standard wind speed distribution from NREL is ~11.46%. This means the bearing can be in service for ~8.72 years as can be seen in [Figure 6-11](#). On the other hand, the damage estimated by using the new method for the same standard wind speed data was ~92.38%, i.e. the bearing service life will be ~1.08 years. This result is closer to the real bearing life recorded in the WTG operating field and matches that specified in previous research to be ~5% to 20% of the design life of 20 to 25 years. The damage estimated by using average NREL wind speed data is larger than that achieved from using SCADA data by applying both the new method and P-M theory due to the differences in the operating hours of the two years data and the average wind speed distribution. For example, the turbine is in standby for ~7 days in the average wind speed distribution while for each year of SCADA data, the standby time was ~27 days.

Damage estimation in this suggested method depends on the S-N curve which strongly recommended to be achieved by testing the bearing in actual size under different stress levels and using the same stress type to be calculated from SCADA data. If the number of cycles increased with a low-stress level (below the endurance limit), the accumulated damage curve will be shifted to the right in an approximately horizontal direction, while increasing the stress would shift the damage curve up for the same number of cycles.

The same results of damage for the two years of SCADA data and the standard wind speed distribution are achieved by applying [Eqn. 6.4](#) to [Eqn. 6.6](#). However, for the suggested method. The differences in the results of these equations are negligible (< 0.2%).

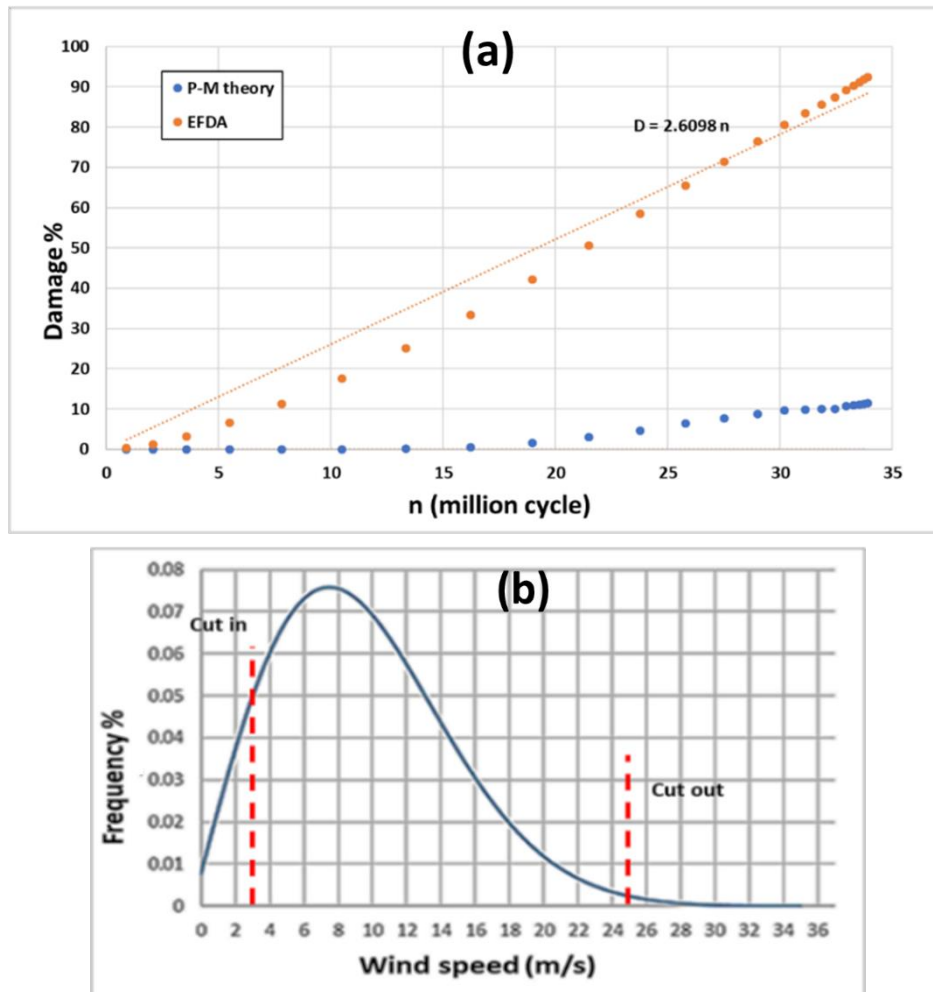


Figure 6-11: Accumulative damage using standard wind speed occurrence during a year
(a) Damage accumulation; (b) Standard wind speed distribution.

6.6.2 Effect of operating events on damage estimation

Effects of operating events such as start-up, shutdown and power shift-up on the damage process will be discussed in this section. A wind turbine with 750 kW capacity has been tested by NREL and its data will be considered for the above three events because no data is available for other wind turbine capacities due to a confidentiality issue. During startup, bearings of the turbine rotor undergo four fluctuation cycles over 4.5 s with maximum torque of 400 to 700 kNm as can be seen in Figure 6-12 (a). During a shutdown event, seven cycles of torque fluctuation in the range of 400 to 510 kNm were taking place during ~4 s while, during power shift up, the torque fluctuates for four cycles during ~5 s and the torque variation range between 200 to 325 kNm. These data were recorded by supposing the events are induced during the rated power operation. The same torque fluctuation ratios are probably transformed into the planetary gears and their supporting bearings.

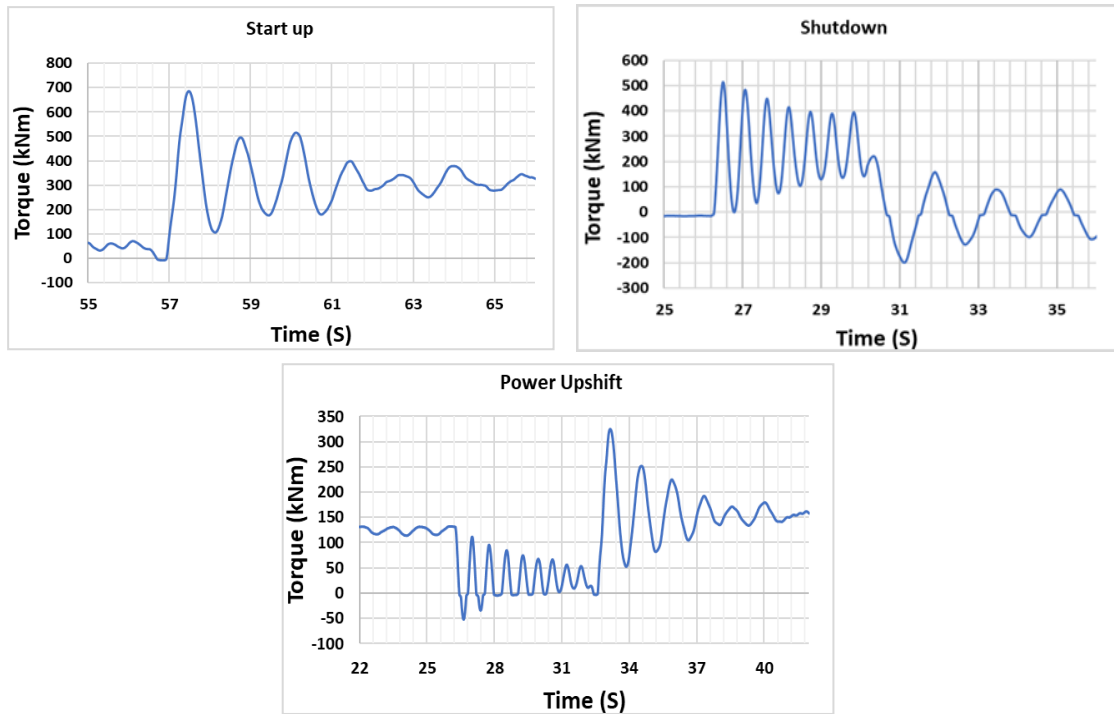


Figure 6-12: Torque fluctuation during three events in 750 kW wind turbines.

Previous research from Keller, Helsen and Guo [44] investigated the effect of a grid loss event. They found the torque ratio reaches ~ 1.5 times the rated torque during this event. Stadler and Stubenrauch [41] postulated that grid loss can lead to torque ~ 2.5 to 4 times more than the nominal torque. For the same event, the torque ratio differs from one researcher to another, however, studying the effect of operating events on damage has recently increasing importance. The emergency stop event (applying the mechanical brake without an aerodynamic brake and grid off) was studied by Kenneth et al. [40]. They indicated the damage due to an emergency stop to be more than 3 times the damage in a normal stop (applying the aerodynamic brake followed by grid off then applying the mechanical braking). It is expected that the emergency stop, start-up and grid loss cause high-torque ratios which may represent the most important factors in WTG bearing failure due to their high torque fluctuations. Most torque fluctuation data in megawatt WT classes are confidential and unavailable to all researchers, therefore, it is preferred to depend on the field measurements rather than simulation to specify the torque ratio and the number of cycles during these events. The number of torque fluctuation cycles and the torque amplitudes of 750kW turbines cannot be reflected on the other WTs due to many differences in the drivetrain design and the natural frequencies of the gearboxes. The damage produced during these events is unrelated to generator output power recorded in SCADA data because the generator is disconnected during most of these events. Thus, it is recommended to calculate the damage due to the operating events in a specific WT according to the number of occurrences using AGMA standard [51]

and measured the stress levels in addition to the number of transient cycles experimentally throughout each event.

SCADA data can be used for damage estimation with some assumptions and the results can be to some extent acceptable and logical, however, the use of averaged data over ten minutes reduces the reliability of the achieved results because of the SCADA average recorded data time is quite long compared with the time of the most operating events and the wind speed variation time.

6.7 Discussion

The aim of this chapter is suggesting and testing a new simple and applicable life prediction methodology for WTGBs. The area under the S-N curve when the bearing selection stress is applied can be used to estimate the bearing damage because this data is the most reliable data provided by the bearing manufacturing companies after many bearing tests. Instead of the bearing design data, the average stress throughout the service can be used and its number of cycles to failure which can be calculated from the material S-N curve can be used. The stress type that should be used in the calculation procedure is the same as that used in presenting the bearing material S-N curve. The percentage of error of this method is lower than that of the design standards which was ~400% for the real service life with a design life of 25 years.

The S-N curve gradient represents the case when 100% damage takes place, thus this gradient was ignored in this method. Furthermore, the application factor presented in the standard BSI ISO 81400:2005 [103], was also ignored because the bearing loading levels are unknown and depend on the wind speed which varies randomly. More investigation using SCADA data is required to show the reliability of this suggested method. The results must be applied for one contact type (either point or line contact) to get more accurate results. SR and friction are very important and should be taken into consideration when calculating the contact stress even if it was not considered during the drawing of the S-N curve.

6.8 Key findings

A new accumulation damage method was proposed and tested using field measurement data from SCADA for a 1.7 MW wind turbine over two years in addition to the standard average wind speed distribution from NREL. This method assuming a fraction of the applied loading energy which is proportional to the

applied stress and the number of loading cycles is responsible for producing damage. The following key points also can be concluded:

- The damage accumulation process cannot be described precisely using linear, exponential, logarithmic or polynomial formulas because it depends on loading condition which varies with the random wind speed variation, however linear damage accumulation may be more suitable to describe the deterioration of WTGBs.
- The stress to be used in the calculation procedure of the suggested method could be principal, shear or equivalent stress depending on the stress type used in drawing the bearing material S-N curve or that provided by the bearing manufacturing companies. It is strongly recommended to draw the S-N curve by testing real WTGBs in loading levels close to the average service contact stress. This increases the reliability of the results and the damage estimation being more accurate.
- The WTGBs are often subject to random operating conditions. Therefore, the equivalent number of cycles should be calculated depending on the last stress level by assuming the last stress level will continue until the bearing failure because the future loadings are unknown.
- The results of damage using the suggested method gave a bearing life prediction quite close to that recorded in the wind turbine operating field and that pointed out in the previous studies.
- The new method (EFDA) is simple and applicable. Furthermore, there is no need for any factor or exponent to estimate the damage, however, more tests are required to show its reliability. It is maybe improved in the future to have less percentage of error.
- The S-N curve of the bearing material is used for comparing the results with P-M theory, however, in the suggested method, there is no need to know the bearing material behavior under different loading conditions, i.e. S-N curve is not important if the design stress and its number of cycles to failure are known. The required is only the contact stress level and the number of cycles to failure under this level. The other operating conditions and their number of cycles to failure are to be divided by the multiplication of design stress and its number of cycles to failure in an accumulation procedure.
- If the SCADA data are recording in a higher sample rate, i.e. recording the operating conditions (wind speed, generator power and generator speed) after any change in the output power and directly used in calculating the damage without averaging the data every ten minutes, the result probably being more accurate.

- Standard wind speed distribution gives damage results higher than that of the real operating data recorded by the SCADA system thus, it would be safer to be used in estimating the bearing damage in the design stage.
- The damage due to operating events such as start-up, shut-down, emergency shutdown, braking and the connection/disconnection of the electrical grid and generator should be calculated separately because the effect of these events does not affect the SCADA data.

7

MICROSTRUCTURAL DAMAGE ANALYSIS OF TEST DISCS

Surface and subsurface damage investigations of chosen test discs are described in this chapter. The surface analysis included surface roughness and hardness, while subsurface analysis included correlating the distributions of damage features with the subsurface stress distributions. The term “microstructural damage” used represents any subsurface damage at the micro-level within the microstructure of the test disc material. The results of characterizing the test discs subsurface damage features (damaged inclusions and cracks) are compared with those obtained from the investigated WTG planetary bearings to confirm the predicted stresses that caused different observed damage features. The investigated samples were prepared using the same procedure used for bearing samples to avoid any differences due to the cutting and sample preparation procedure. The investigations were carried out by using optical and SEM microscopes in addition to the EDX technique and Alicona surface scanner. The results support the main role of maximum shear and Von-Mises stresses as being responsible for different subsurface damage initiation and propagation. The subsurface microcracks serving as a damage-initiation trigger, which was suggested in the investigated WTG bearing has been confirmed in this chapter. The variation of damage distributions due to varying the test parameter levels are also presented and discussed.

7.1 Test disc damage investigation

Test disc surface roughness and hardness were the key parameters assessed during the bearing and disc surface investigations. These two parameters are measured in axial and circumferential directions before and after the testing to assess their variations. The investigation of changes in the surface properties was made in order to postulate recommendations to reduce the effect of these parameters and to increase the WTGB lives. Figure 7-1 illustrates the details of surface investigation directions in addition to the cutting process of the test disc specimens for subsurface investigations. Damaged test discs were classified according to SR and presented in Figure 7-2. Despite the images were taken after the damage propagation, the test disc lives were recorded when the damage appeared on the contact surface.

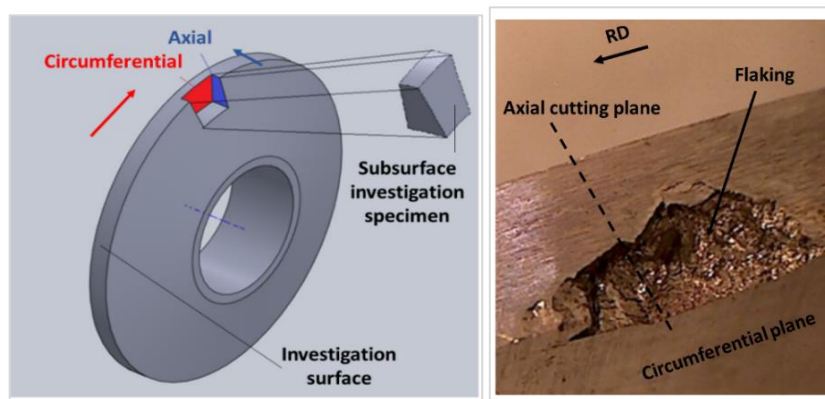


Figure 7-1: Sample sectioning of a test disc for surface and subsurface investigation.

For line contact tests, the lower test disc had a smaller axial length (4 mm) than the upper disc (8 mm). This produces stress concentration at the disc edges and accelerates the disc damage.

The lower test discs revealed more severe damage forms compared with the upper discs, however, the spalling areas have different shapes and dimensions. Increasing of SR and/or impact makes the damaged area propagate in the circumferential direction more than in the axial as can be seen in T2, T16, and T1.

Some tests were kept under rolling contact after the appearance of surface damage to investigate the damage propagation and enable comparison with the real bearings which continue in service after the damage arriving at their contact surfaces due to late detection of damage. When the tests continued after the appearance of surface damage, two tests (T11 and T13) had a radial crack from the contact surface towards the keyway as can be seen in Figure 7-3. The test time was

recorded when the damage can be noticed on the contact surface and before the appearance of these large radial cracks, however, the reasons of these radial cracks are due to stress concentration at the keyway corners, vibration, impact, and overloading after the surface damage initiation. Thus, in future tests, impact location should be away from the keyways to prevent this situation.

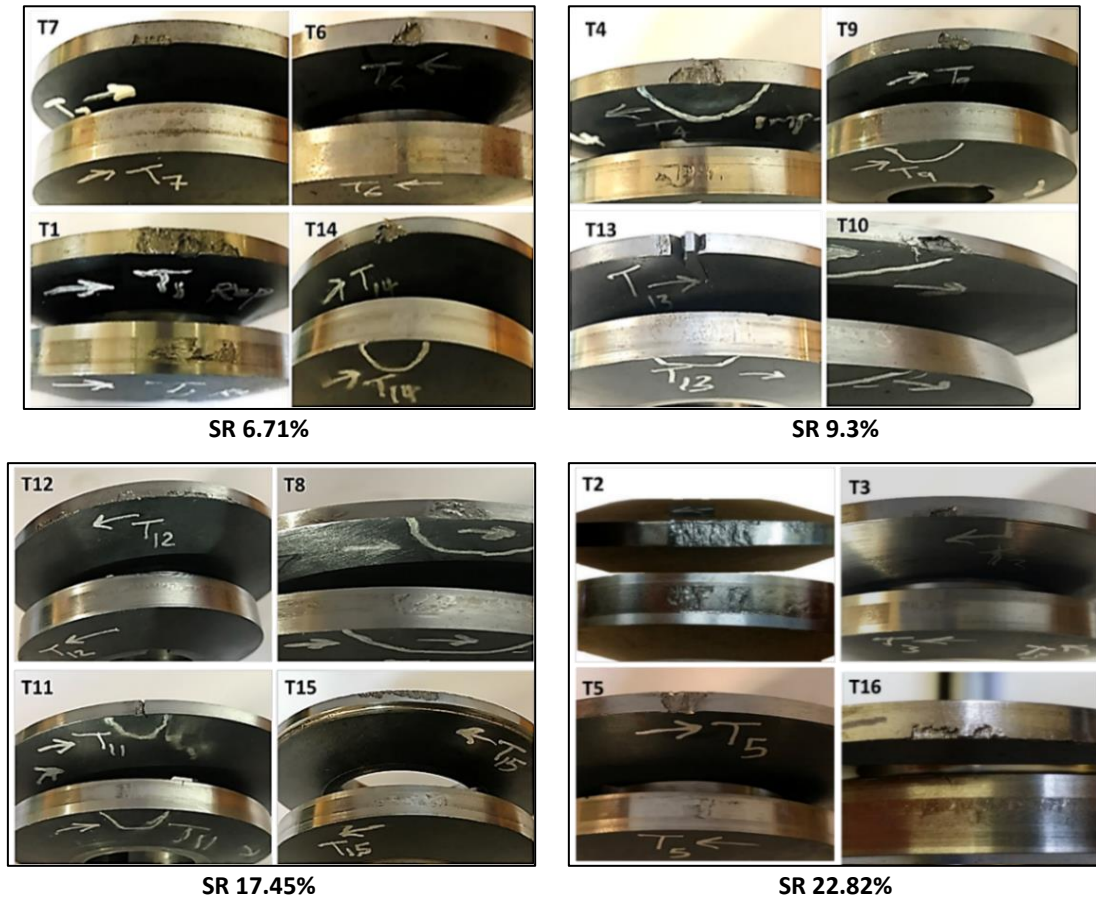


Figure 7-2: Failed upper and lower test discs classified into four groups depending on the SR.

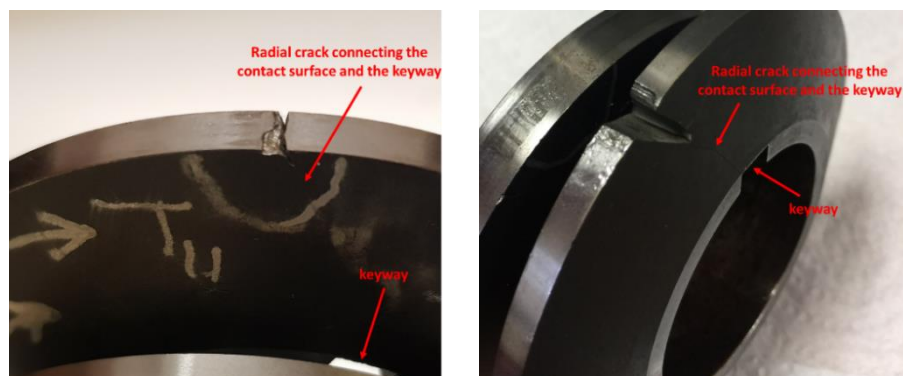


Figure 7-3: Radial crack introduced if impact location in an incorrect position (T11 left, T13 right).

For fully crowned contact discs (T1P, T2P, T3P and T4P), contact disc damage can be seen in [Figure 7-4](#). The more severe testing conditions (T1P) showed more damage in the contact region, i.e. at the center of the crowned discs. Despite applying the impact in a percentage of 0.07%, reducing the impact level showed a noticeable difference in the surface damage feature of T2P compared with T1P. Decreasing of contact stress in T3P, makes the damage depth shallower than that in T1P while, reducing the SR has approximately the same of the latter effect.

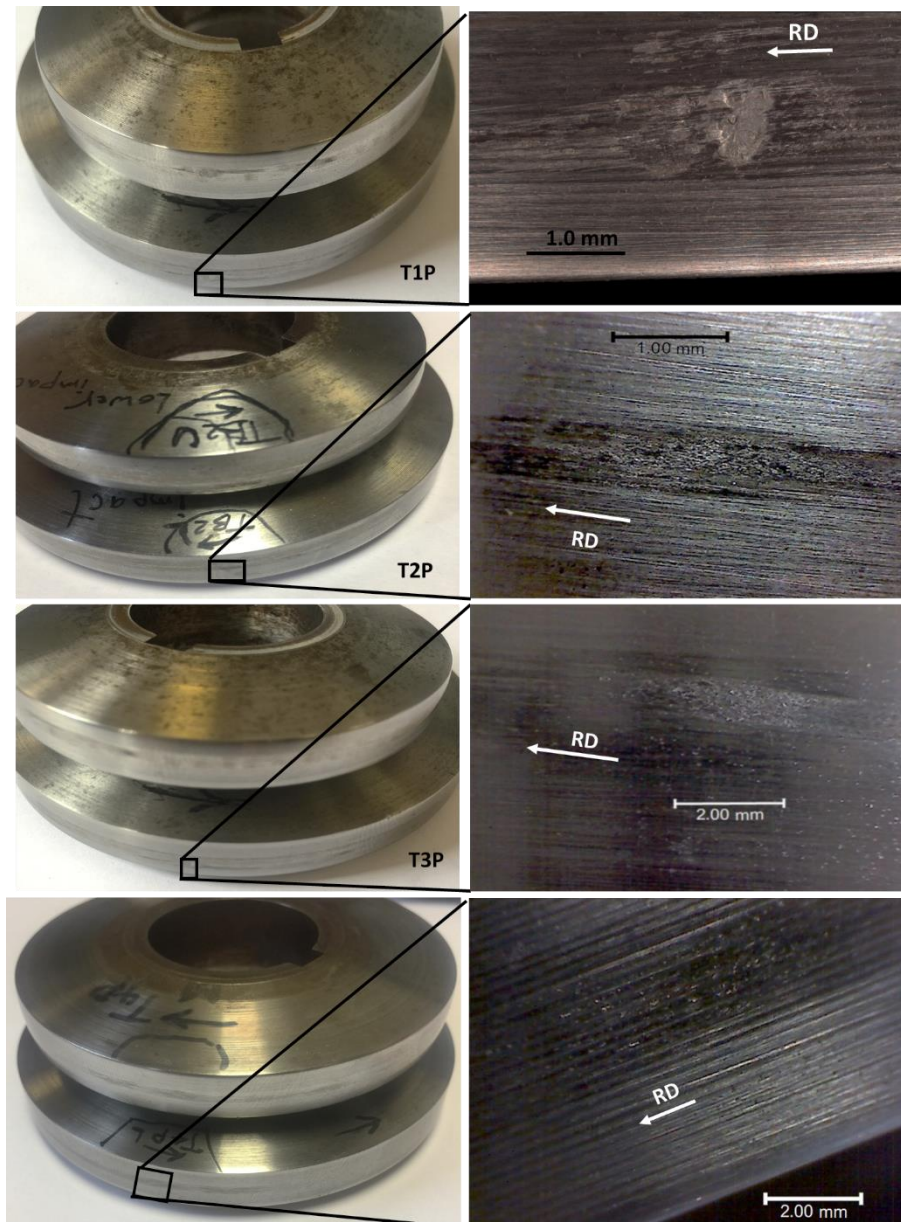


Figure 7-4: Surface damage of tests without stress concentration.

The additional test without impact (T6B) showed the spreading of surface damage approximately uniform in the circumferential direction and along the axial direction as can be seen in [Figure 7-5](#).

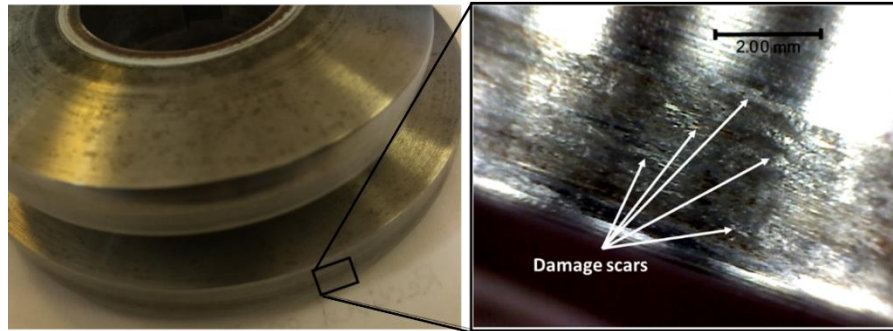


Figure 7-5: Damage of test disc without impact loading (T6B).

T7 and T7A have the same testing levels apart from SR which has 6.71% and 22.82% respectively. These two tests were continued in rotation even when the damage appeared on the contact surfaces for 3,000 cycles. The damage was propagated differently in the axial and circumferential directions as can be seen in Figure 7-6. This noticeable difference, especially in the circumferential direction shows the important effect of SR on damage propagation.

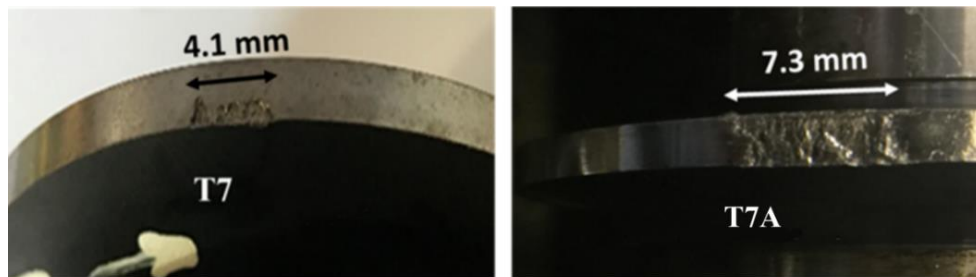


Figure 7-6: Comparison of surface damage feature under different SR.

In all the conducted tests, spalling and/or flaking took place in the contact region between the test discs, but it does not appear in the upper test disc where the impact is directly applied. Despite losing a fraction of the impact energy due to damping inside the upper disc body due to elastic deformation, the observed disc damage location was still on the lower test disc. This may be because of the effect of negative slipping on the lower disc which specified to have a considerable role (see Section 2.4.3). The location of the applied impact on the upper test disc is exposed to compression, impact and slipping when it passes in the contact discs region, however, it is separately exposed to these parameters at the top of the upper disc (the impact loading region). This location of damage confirms the importance of the interaction effects among the studied parameters and probably the studying of each parameter separately is not an efficient way to describe the RCF damage.

7.1.1 Surface hardness

Vickers hardness (HV) was used in measuring the contact surface hardness of the test discs. The hardness of the lower and upper test discs was measured in the axial direction before and after the testing using a group of three lower test discs and three upper test discs and taking the average. Because of the effect of the hardness indenter on the test disc life [122], the test discs used to measure the hardness before the tests were not used in the fatigue testing. Before testing, both the lower and upper test discs had approximately the same HV hardness of 703 ± 20 (~ 59 HRC), while the surface hardness was considerably increased after testing to $\sim 753 \pm 20$ (~ 61 HRC) as can be seen in Figure 7-7. Most of these hardness measurements were taken from the test discs of (T4) and (T15) which experienced moderate contact stresses compared with the other testing levels. These measurements were taken from regions close to the severely damaged areas to be closer to the hardness of the damaged regions. The investigated bearing hardness in Section 3.4.1 had HV ~ 740 out of the loading region which is harder than the test discs. This probably due to using advance and special technologies in increasing the WTGB surface hardness. However, both the bearing and test discs hardness increased which supports the postulation of plastic deformation within the contact region. For the elliptical contact discs, the hardness of the curved surface is not easy to measure, therefore, it was not measured, however, the lower disc has non-uniform pressure distribution on the lower disc; therefore, the hardness variation of the lower disc cannot be precisely compared.

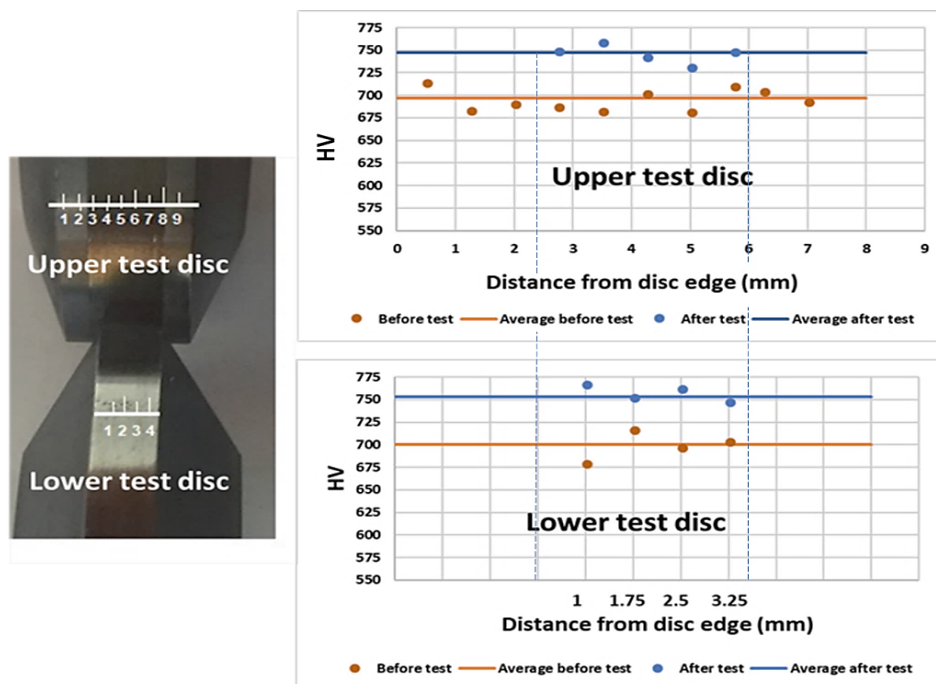


Figure 7-7: Hardness variation of test discs before and after the test.

7.1.2 Surface roughness

The test disc surface roughness (Ra) was measured in the axial and circumferential directions then averaged for both the upper and lower discs and for flat and fully crowned discs. For line contact (flat discs), this process was performed for three pairs of upper and lower test discs with five different locations on the disc surfaces. Test disc roughness cannot be controlled precisely throughout the test disc manufacturing process, however, both circumferential and axial roughness measurements showed a noticeable reduction in roughness after the testing (named as used), as can be seen in Figure 7-8. For the upper test disc, the circumferential roughness (Ra) before the testing (named as unused), was $\sim 0.27 \mu\text{m}$ and reduced to $\sim 0.21 \mu\text{m}$ after the testing while, the axial surface roughness of the upper test discs had an average reduction from $\sim 0.34 \mu\text{m}$ to $\sim 0.27 \mu\text{m}$ during the tests. However, the lower test disc axial roughness reduced from $\sim 0.4 \mu\text{m}$ (before the test (unused)) to ~ 0.37 (after the test(used)) while, the circumferential roughness reduced from $\sim 0.32 \mu\text{m}$ to $\sim 0.24 \mu\text{m}$. The higher axial roughness was because of the direction of the cutting and surface finishing processes throughout the disc manufacturing. The reduction of roughness shows the importance of asperity contact and deformation during RCF testing. This reduction of surface roughness was also observed in the investigated planetary bearings in Section 3.4.2. Surface roughness is considerably changed from location to location within the same component and it gradually changes throughout the testing. This can be seen by the noticeable differences in the axial and circumferential roughness of the upper and lower test discs. The roughness is considerably change within the severely damage region that restricts comparing it with the situation before the damage. For this, test disc roughness was measured excluding the severely damage region of the lower disc and avoiding the contact region of the upper one that in contact with the severe damage region of the lower disc to exclude the effect of its contact with the severely damaged region.

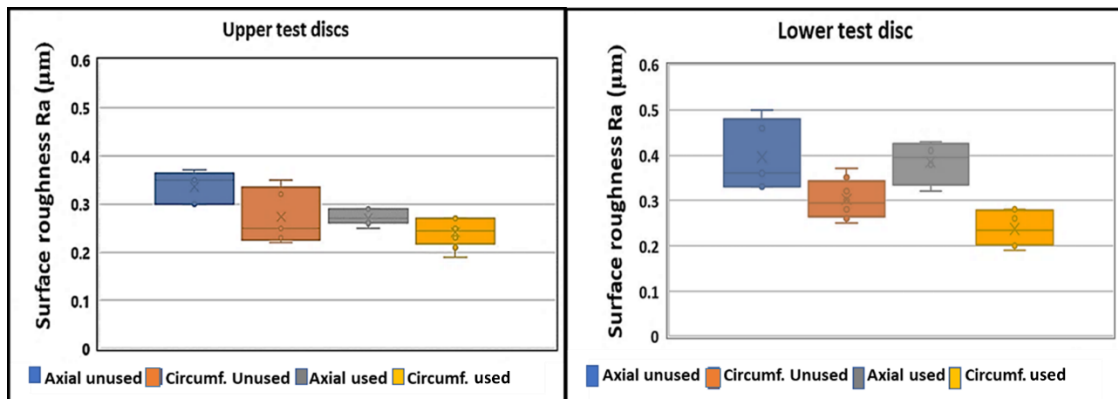


Figure 7-8: Upper and lower test discs average measured surface roughness.

For elliptical contact (fully crowned upper disc on flat disc), the contact profilometer could not be used due to considerable height change a few micrometres away from the maximum contact plane. For that, surface roughness out of the contact region and within it was measured by using the Alicona surface scanner. There is a noticeable difference in circumferential roughness when moving a few hundreds of micrometres from the maximum contact plane as can be seen in Figure 7-9.

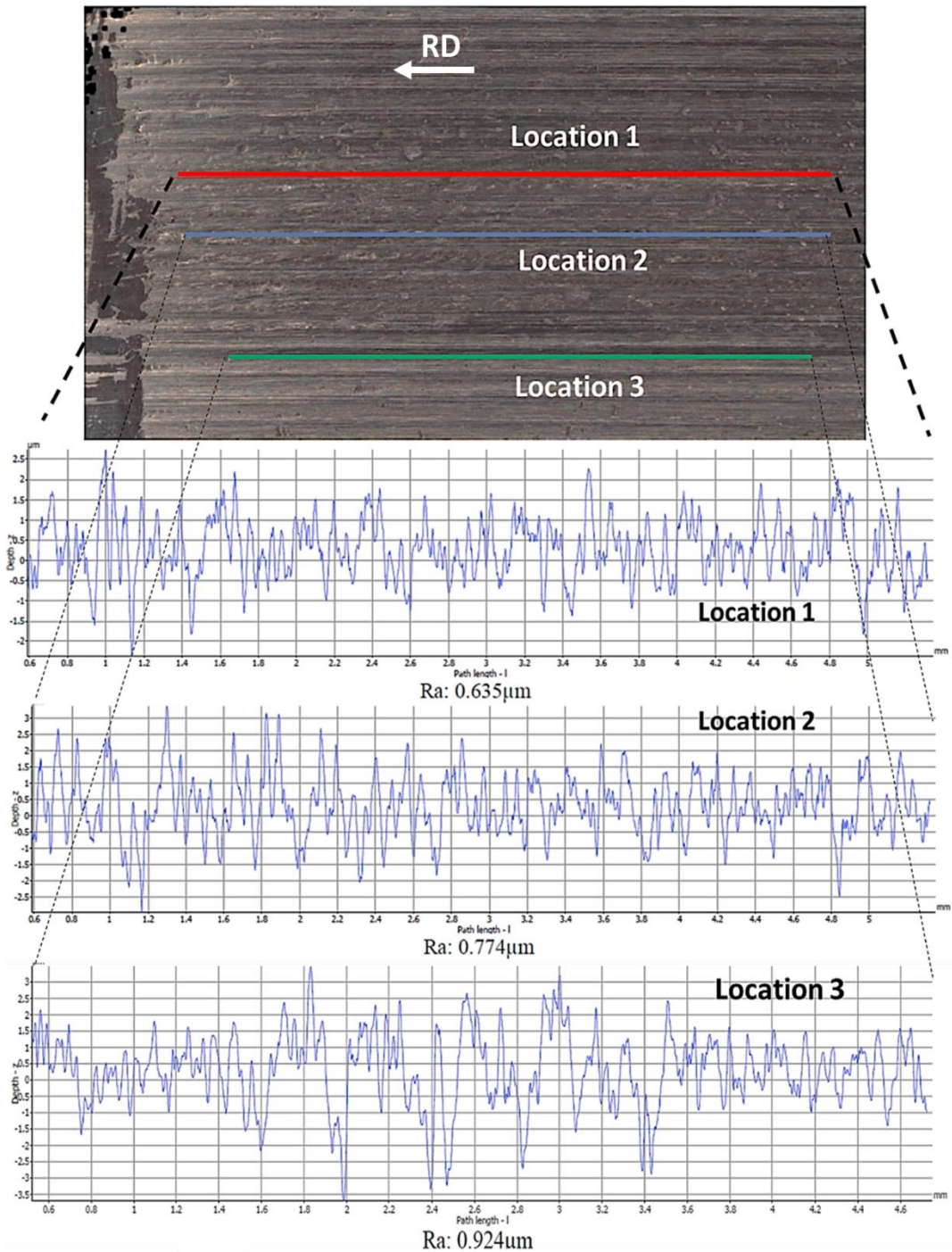


Figure 7-9: Variation of circumferential surface roughness of an elliptical contact fatigue test (from test T2P).

These measurements were performed more than three times and the average was presented. Fore axial direction, i.e. perpendicular to the three directions specified, the roughness out of contact region was higher (in the range of 0.94 μm to 1.42 μm), however, within the maximum contact region it was around 0.79 μm . These measurements were taken from the region close to the severe loading area of test T2P.

7.1.3 Effect of impact loading on damage propagation

The severe surface damage of the test without impact (T6B), which reveals approximately uniform surface damage is presented in [Figure 7-10\(a\)](#), while increasing the impact loading and SR showed a considerable increase in the damage depth beneath the impact location as can be seen in [Figure 7-10\(b\)](#) and [\(c\)](#). These damaged areas were investigated using Alicona scanner. The RCF test without impact showed low damage depth while the other tests under different impact and SR levels showed damage depths of ~ 0.25 mm to ~ 0.65 mm. This increase in damage depth is probably because of increasing the impact loading since the compression loadings are equal in the chosen tests. Despite the fact the damage was just started in T6B, the other two tests (T6 and T6A) rotated 3,000 cycles after the damage observation to investigate damage propagation in different tests, it seems that impact loading may have a considerable role in increasing the damage propagation with depth.

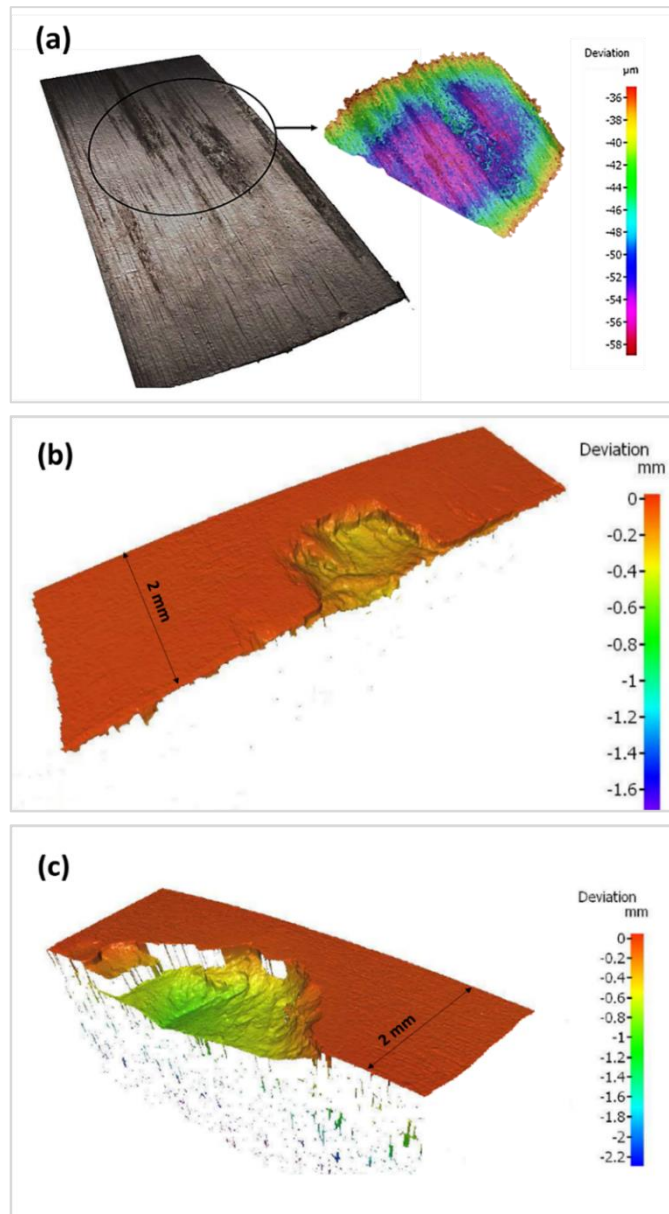


Figure 7-10: Alicona scanner analyses of investigating the effect of impact on damage depth
 (a) T6B (no impact); (b) T6 (impact stress=435 MPa); (c) T6A (impact stress=705 MPa).

7.2 Preparing for subsurface investigations

To investigate the effect of the three parameters (compression, impact and SR) on the subsurface damage, two lower test discs were used to investigate the effect of each parameter. Three pairs of test discs were chosen to be microscopically investigated in the circumferential and axial directions. Table 7-1 illustrates the details of the chosen test discs and their testing parameter levels. To investigate the effect of compression, two lower test discs of T6 and T14 were used. These discs were failed under the lower impact stress and the same SR, but different compressive loading levels. The second two discs used to investigate the effect of

impact loading were T6 and T6A which had the same SR and compressive loading, but different impact stresses. The last two discs of T7 and T7A were used to investigate the effect of SR because their compressive and impact loadings were the same, however, their SR was different. The samples have been prepared by following the same procedure used for the investigated bearings in [Section 3.5.2](#). The chosen discs were cut in circumferential and axial directions using a linear precision saw with the same cutting rate and rotating speed used in cutting the WTGBs of (1.5 mm/min and 3500 rpm respectively). This was to produce approximately the same extra damage due to the cutting and sample preparation processes in both the investigated bearings and the test disc specimens. The discs were microscopically investigated using optical and SEM microscopes in addition to the EDX technique to compare the distribution of their damage features (damaged inclusion and subsurface crack).

Table 7-1: Parameter levels of test discs used for microstructural damage investigation.

Test code	Investigation parameter	Compression stress (MPa)	Impact stress (MPa)	SR %
T14	Compressive Load	2410	435.30	6.71
T6		2603	407.55	6.71
T6	Impact stress	2603	407.55	6.71
T6A		2603	705.04	6.71
T7	SR	2694.4	686.04	6.71%
T7A		2694.4	688.68	22.81%

[Figure 7-11](#) shows two damage patterns of the test disc material taken from the circumferential sections of the lower test discs T6A and T7, where a considerable number of non-metallic inclusions and defects have been observed and marked with red arrows, while the subsurface microcracks are marked with black arrows. [Figure 7-11\(b\)](#) shows a high magnification view from T7, where subsurface microcracks, M_3C carbides (the white patches) and inclusion can be seen. Material defects such as voids and/or casting defects (marked with white arrows) also observed at this high magnification level.

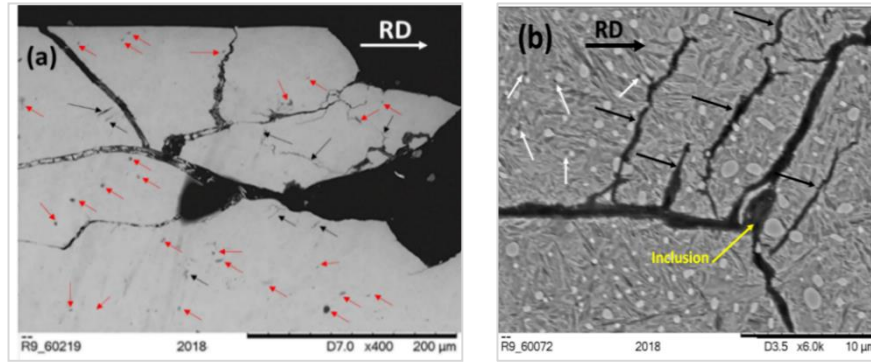


Figure 7-11: Subsurface damage features of two failed test discs (a) from T6A; (b) from T7.

Damaged inclusions by separation and cracking in addition to subsurface microcracks were characterized to be correlated with the subsurface stress distributions to investigate which type of stress is responsible for the initiation and propagation of each damage feature. Analyses of the test disc subsurface stress distributions can be seen in Figure 7-12. This is for correlating the maximum stress depths with the maximum subsurface damage depth.

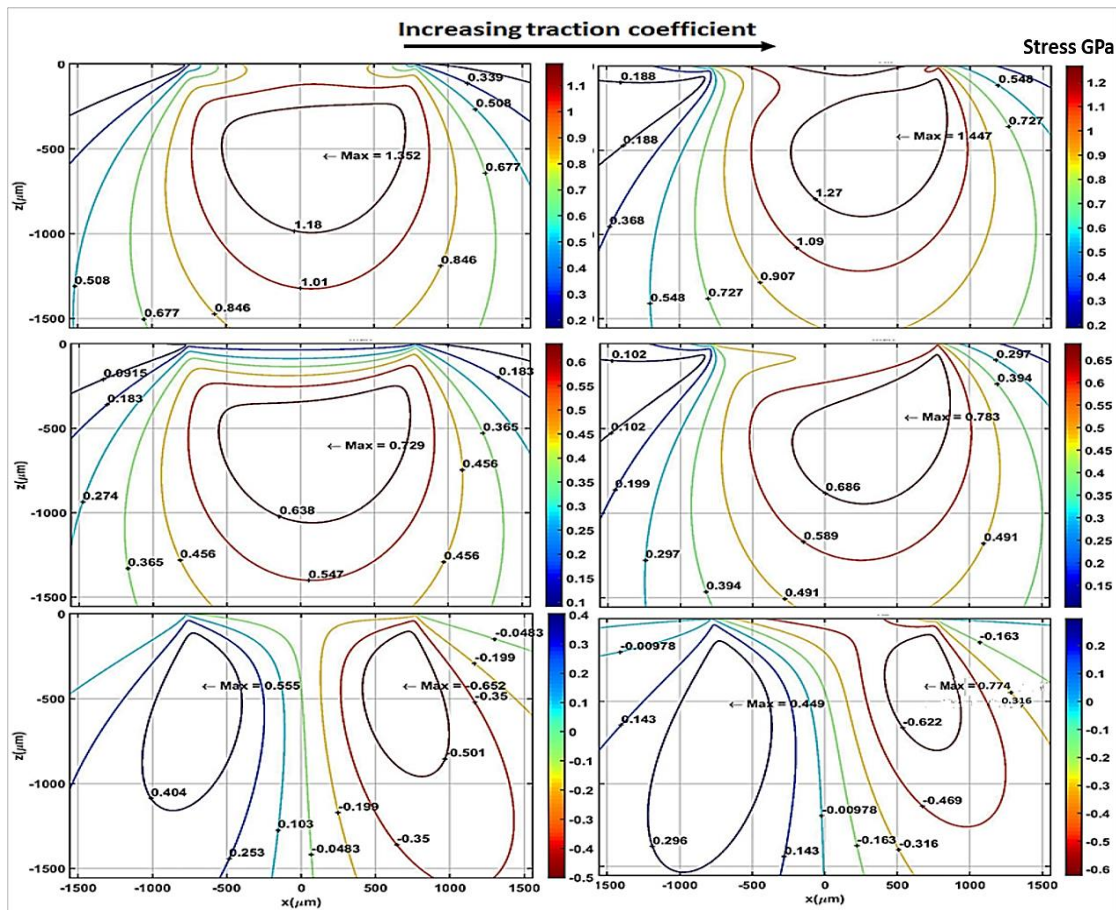


Figure 7-12: Subsurface stress distributions of the test discs under contact pressure of 2400 MPa and, 6.7% and 22 % traction coefficients. Von-Mises stress (top), maximum shear (middle) and orthogonal shear (down).

Traction coefficient is different than slipping ratio despite they both depend on the velocity difference between the contact bodies, however, traction coefficient can vary in a wide range depending on the contact stress, surface roughness and the relative movement velocity of the contact bodies. In Hertz contact, slipping cannot be presented but the additional force due to traction can be calculated [195].

There is no considerable difference in the subsurface stress distributions shown in the analysis of the WTGBs presented in Figure 3-5, except the values of stresses and their depths due to using different compressive forces and traction coefficients. Applying impact forces increases the contact stresses values and depths in a way similar to that presented in Figure 3-4 and Table 3-5.

Details of the investigated damage features are illustrated in Figure 7-13. The investigation will be carried out by characterizing the depths, lengths, inclusion aspect ratios and the type of inclusion damage, i.e. inclusion damage by separation or by cracking (as the WTG bearings were investigated). The locations of the inclusion separation and cracking can be from the upper, lower or the sides of the inclusions. Throughout the investigation, rolling direction, depth of the centre of damage and the damage type will be specified in each metallographic image which taken within the severely damaged regions.

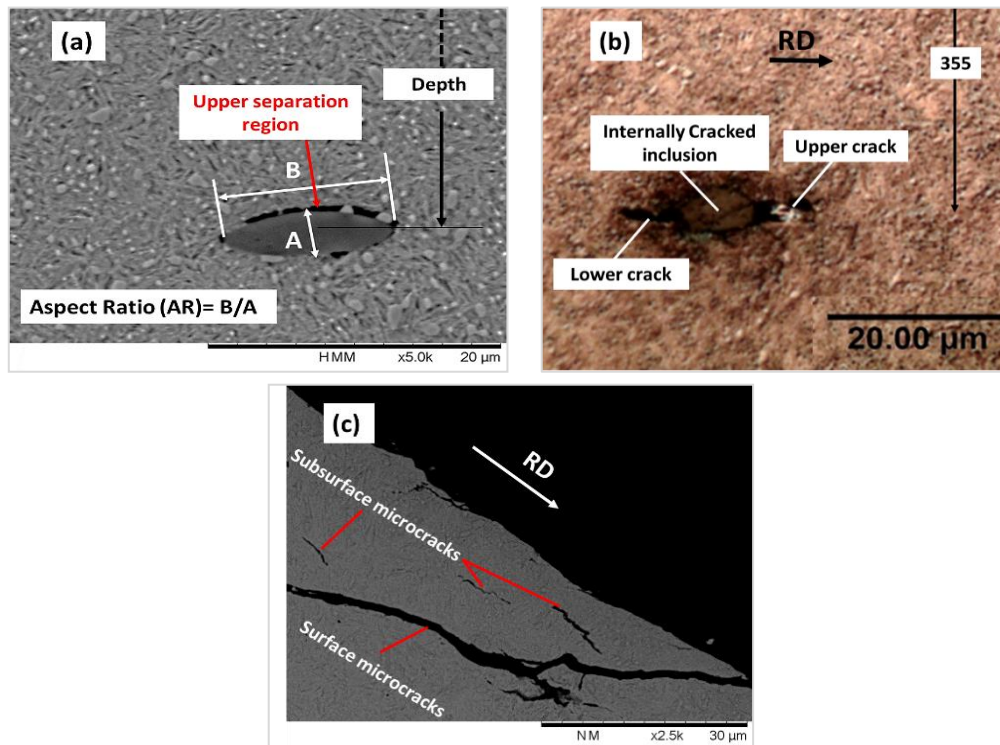


Figure 7-13: Examples of damage features observed (a) inclusion damaged by upper separation (observed in T4); (b) inclusion damaged by cracking (observed in T6); (c) surface and subsurface microcracks (observed in T5).

7.3 Damaged inclusions and microcracks

There is a considerable difference in the number of inclusions among the chosen investigated discs despite manufacturing them from the same steel rod. Test disc analyses were carried out by focusing on the circumferential sections for the lower test discs, due to the observing more severe damages compared with that in the upper one. Most of the inclusions observed throughout the investigation were group A (sulfide type), due to their grey color and rounded ends [76] in addition to the EDX analysis which will be discussed later. However, some black spots were observed sometimes inside the inclusion. These were analyzed by Bruce [3], who found them to be oxides. Some damaged inclusions are not easily can be considered as damaged by separation from the bulk or cracked without a high magnification level as can be seen in [Figure 7-14\(a\)](#). Thus, SEM microscopy is preferred for investigating the damage features and their characterization. Under high magnification, a considerable number of defects were observed that will be discussed in more detail in the coming sections. Because of disc spalling, the material was released from the severe damage regions. This increases the complexity of studying the damage distribution in these removed areas. For that, the damage regions were investigated with 0.5 mm to the side of the spalled area to present the damage distribution in these regions. Subsurface microcracks considered in the coming analyses were only the small microcracks (<100 μm length) which can be recognized as unrelated to the surface crack network or when the comparing of the Crack Opening Distance (COD) of the microcrack under consideration. The surface crack pointing that the majority of cracks are initiated from the subsurface region and not a branch from the main network. [Figure 7-14\(b\)](#) shows a damaged inclusion by separation, where carbides seem to have a stronger bonding with the inclusion body (the locations marked with yellow arrows), than the other locations where there are no carbides in contact with the inclusion body. The investigated inclusions are either damaged by separation, by cracking or by a combination of both. One of the most interesting observations is that separation of inclusion boundary is not uniform and there are locations that are not completely separated from the bulk.

The majority of the investigated inclusions have an Aspect Ratio (AR) between 1:1 to 2:1. This will be expressed as AR 1-2 in the legend of [Figure 7-15\(a\)](#). This figure presents the general analysis of the damaged inclusion according to their AR in the chosen test discs. Surface and subsurface microcracks are also characterized and presented in [Figure 7-15\(b\)](#). The number of subsurface microcracks is larger than the number of surface cracks. This evidence supports the subsurface damage initiation mechanism postulated in the previous literature [29][180]. However,

Increasing the testing parameter levels increases both surface and subsurface cracks despite the difference in the number of inclusions in each investigated sample.

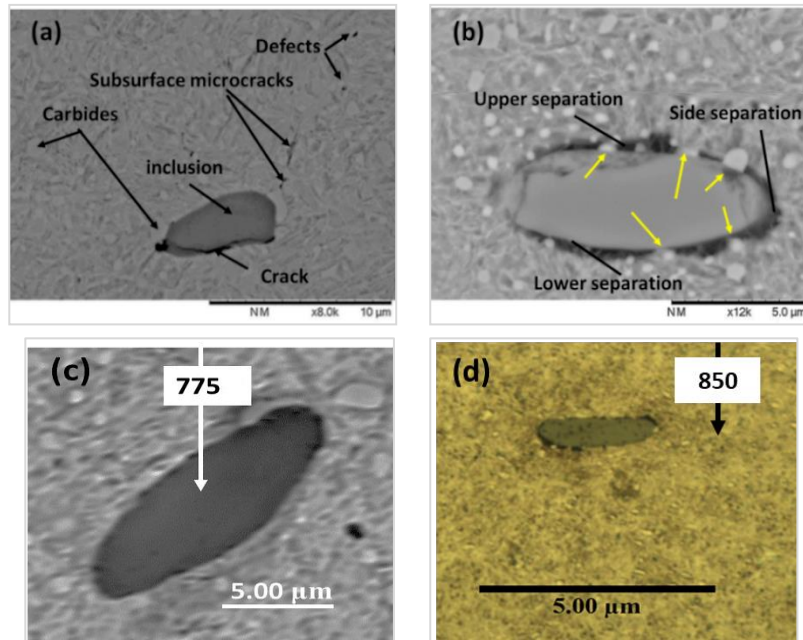


Figure 7-14: Damaged and undamaged inclusions (a) damaged by cracking close to its boundaries; (b) damaged by separation; (c) and (d) undamaged inclusions.

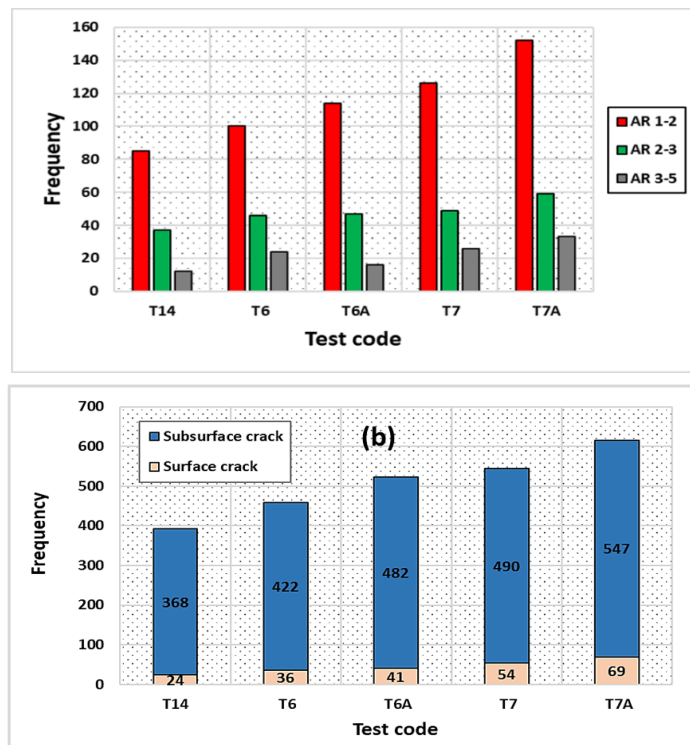


Figure 7-15: (a) Damaged inclusions according to aspect ratio; (b) surface and subsurface cracks.

Figure 7-16 shows the analysis of 932 damaged inclusions by separation and cracking that observed throughout the test disc investigation. Comparing separation damage in test T14 and test T6 shows that, increasing the compressive loading increases considerably the lower and side separation with a noticeable increase in mixed separation damage. However, the number of internally cracked inclusions has no noticeable change and the upper separation has a little reduction. This may be the effect of compression which tries to reduce the separation in the locations towards the contact surface. Figure 7-16(b) presents the effect of the studied parameters on inclusion damage by cracking. By increasing all the studied parameter levels, the number of upper, internally and combined cracking damages were increased. It can be recognized that the number of damaged inclusions by lower cracking is affected more (increased) by increasing the compression loading level more than increasing the other parameters.

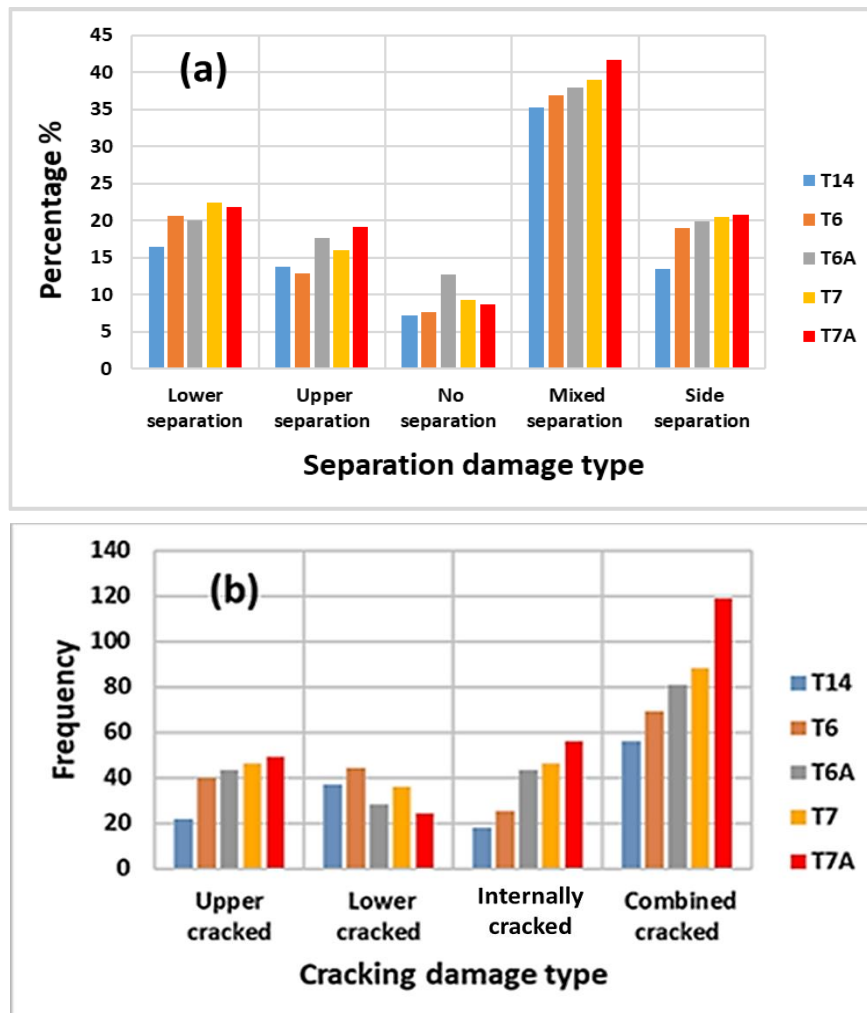


Figure 7-16: Damaged inclusions in the five investigated test discs (a) by separation; (b) by cracking.

A comparison of the separation damage features in T6 and T6A (brown and grey bars respectively in [Figure 7-16](#)) can be performed to show the effect of impact loading. The percentage of upper separation and internally cracked damaged inclusions increases with an increase in the impact loading level. This probably indicates the role of impact in producing internally cracked inclusions. The number of damaged inclusions without separation was also increased. This may refer to the effect of impact in producing cracking damage more than introducing separation damage.

The effect of increasing the SR can be seen by comparing test T7 and T7A ([Figure 7-16](#) yellow and red bars respectively). Increasing of SR increases considerably the combined and internally cracked inclusion damage, in addition to a considerable increase in the number of combined cracked inclusions. The comparison of the frequency of damaged inclusions by cracking shows an increasing trend with an increase in all the testing parameter levels apart from the lower cracking damage which decreases with increasing impact and SR. Despite making the test disc analysis in an advanced stage of test disc spalling, i.e. when the failure reaches the test disc contact surface, the damage feature characterization may be useful to be correlated with the subsurface stress distributions to predict the cause of each damage type. This will be discussed in further detail in the next sections.

7.3.1 Inclusion damage by separation

In the investigated wind turbine bearings, separation damage in the samples was observed beneath the severely damaged regions. Inclusion damage by separation was dealt with independently from inclusion damage by cracking, i.e. when a damaged inclusion has both separation and cracking damage, the inclusion was considered in each category of damage separately. This is because these two damage features were considered as two different separated damage depending on the observations of the investigated bearings. The damage features of the severely damaged area were investigated and characterized within 1mm beneath the contact surface because, in more depth, no damage features were observed. A considerable number of inclusions outside the severely damaged area had separation damage without cracks. This can be seen in [Figure 7-17\(a\)](#). Damaged inclusions beneath the severely damaged regions were observed sometimes had different separation types (upper, lower, side or mixed separations) at approximately the same depth, as can be seen in [Figure 7-17\(b\)](#), [\(c\)](#) and [\(d\)](#). Within the investigation plane, a considerable number of black spots (voids) were observed to be associated with the carbide boundaries. These may be the initiation site of subsurface cracks not relevant to

inclusions (see the black spots in [Figure 7-17\(c\)](#) and [\(d\)](#)). Further investigation and discussion will be presented in the next sections.

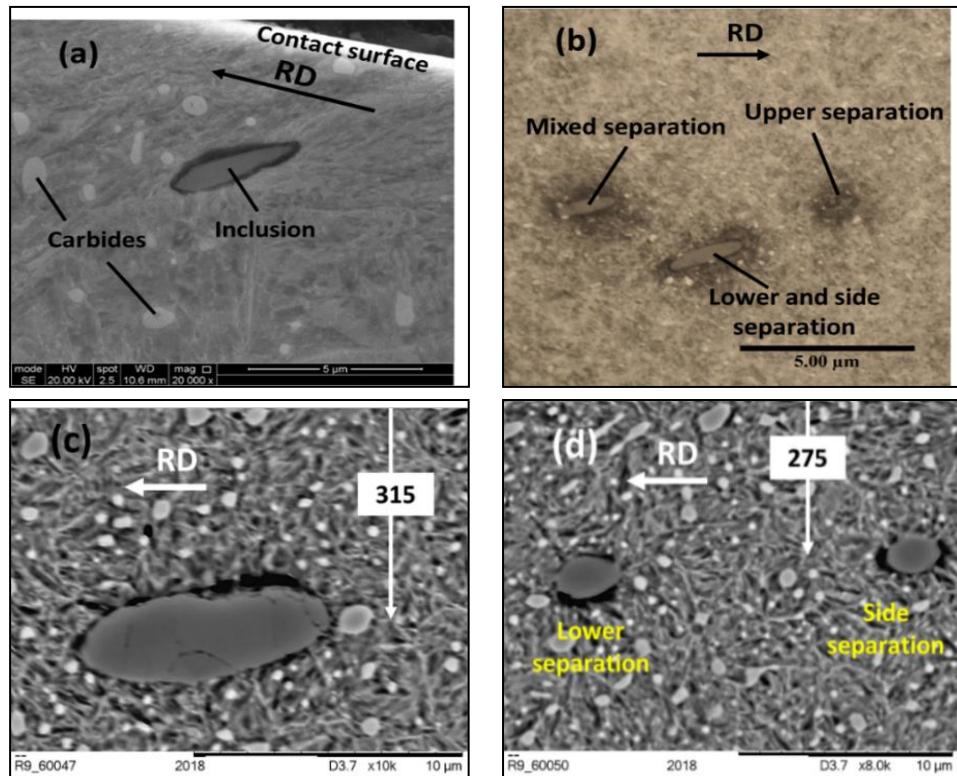


Figure 7-17: Damaged inclusions by separation (a) near the spalling area (front T1); (b) different separations at the same depth (from T4); (c) upper separation (from T6A); (d) Lower and side separation (from T7).

To analyze the individual effects of the three key parameters (compressive loading, impact loading and slipping), two samples having minimum and maximum level of each parameter were analyzed, i.e. six figures for concluding the individual effects of the key parameters as will be presented in the following sections.

7.3.1.1 Effect of compressive loading

An investigation of the effect of compressive loading on the damaged inclusions by separation was carried out by analyzing this damage type in T14 and T6. These two tests have the same testing conditions apart from the compressive loading level. Thus, the difference in the distribution of damaged inclusion can be considered as the effect of compressive loading. Examples of separation damage beneath the severely damaged regions in these two tests can be seen in [Figure 7-18](#).

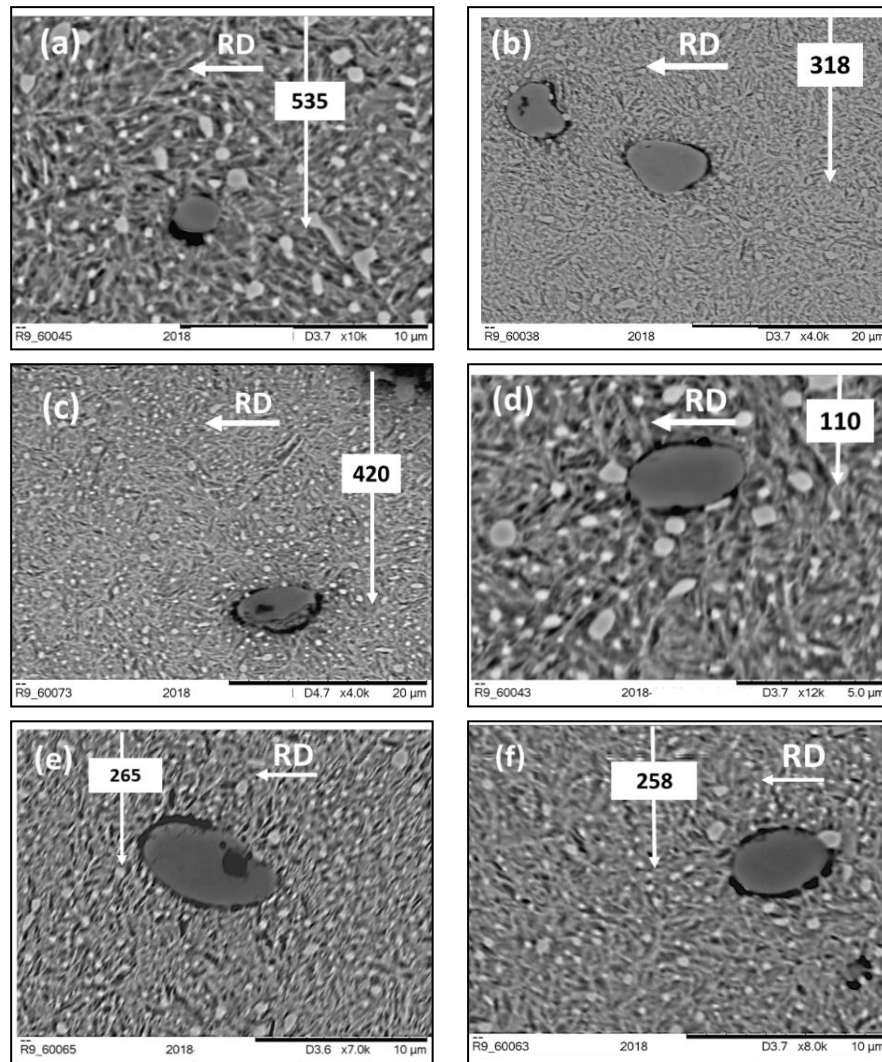


Figure 7-18: Examples of inclusion separation damage (a), (b) and (c) from T14; (d), (e) and (f) from T6.

Increasing the compressive contact load reveals, in general, a large separation distance between the inclusion body and the bulk. This separation distance was observed to be reduced with increasing depth. The damaged inclusions by separation were illustrated in a database system with their depths and the type of separation; then they were sorted and classified into groups according to their depth then presented in [Figure 7-19](#). The Moving Average method was first used to approximate the variation trend and according to this approximation, the best average trend has been drawn. If the Moving Average graph had two peaks or the number of separation damage close to the contact surface was slightly higher than other depths, the best average approximation used was correlated with the von-Mises stress distribution. All the analysis of separation damage shows trends identical to a Von-Mises stress distribution with the depth presented in [Figure 3-6](#).

This encourages the consideration that Von-Mises stress is probably the main cause of separation damage.

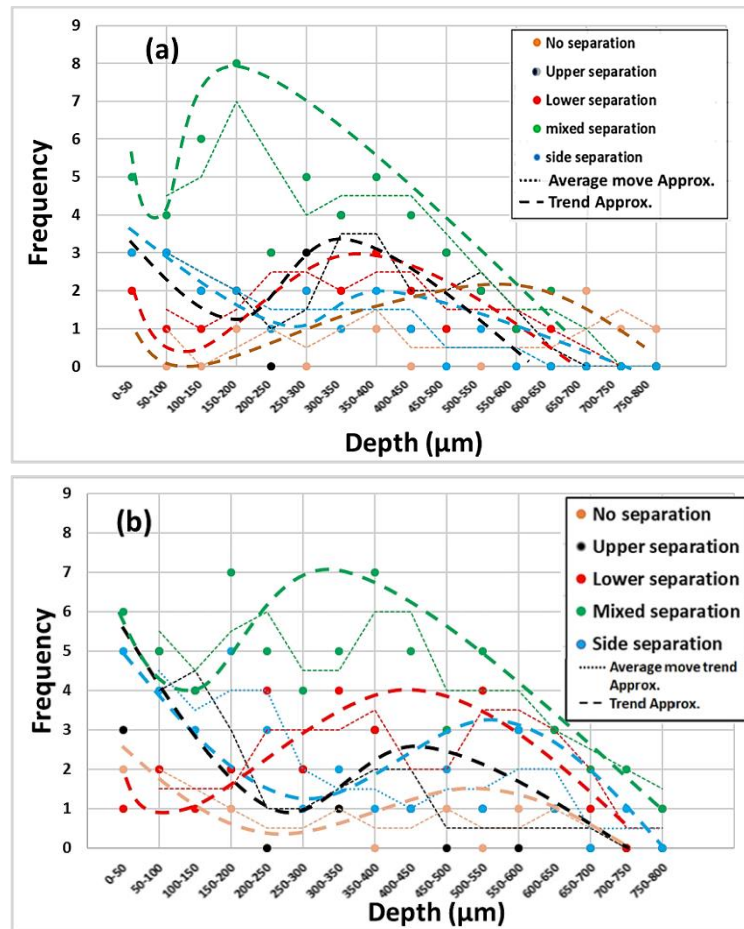


Figure 7-19: Effect of compressive load on damaged inclusion by separation (a) test T14 (compression stress=2410 MPa); (b) test T6 (compression stress=2603 MPa).

This figure shows a noticeable increase in the number of separation damage inclusions with increasing compression loading, especially in the shallower regions. This increment can also be observed at different depths, and the peaks of damage distribution tend to be deeper with increasing contact pressure. However, the difference in impact loading between these two tests also affects the separation damage. In general, the well-known compressive effect of increasing the depth of maximum stresses was confirmed in these analyses. All the maximum subsurface stresses in Figure 7-12 were located within a depth of 400 μm to 600 μm beneath the contact surface and the peaks of separation damaged inclusions sat within this range. Comparing the separation damage distribution of these tests with that of the real bearings in Figure 3-19, Von-Mises stress seems to have an effective role in introducing the separation damage in RCF, however, the possible role of maximum shear stress cannot be neglected.

Comparing the damaged inclusions in [Figure 7-20](#) confirms the increasing of separation distance with increasing compressive loading and the reduction of it with increasing depth. The black spots associated with carbides mentioned in [Figure 7-17](#) were also observed in [Figure 7-20\(b\)](#).

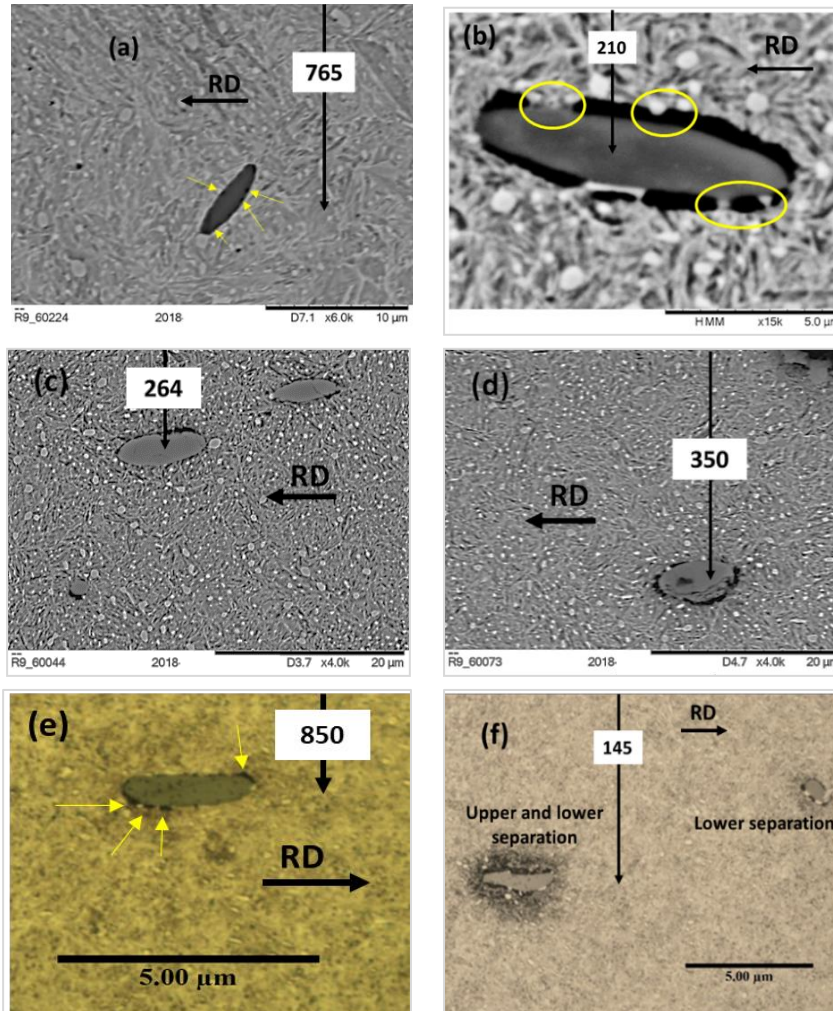


Figure 7-20: Examples of undamaged and damaged inclusions (a) undamaged inclusion from T6; (b), (c) and (d) damaged inclusions by separation from T6; (e) undamaged inclusion from T14; (f) damaged inclusion by separation from T14.

The locations marked with yellow ovals in this figure reveal a connection of the inclusion matter with the carbides. This shows that other regions are weaker regions and these locations are their preferred locations for the separation damage initiation. Inclusions at depths greater than 0.8 mm revealed undamaged features by separation but microvoids can be noticed as black spots on the inclusion boundaries as can be seen in [Figure 7-20\(e\)](#). The black spots of oxide inside the inclusion body also can be observed. It has been noticed that separation damage may be pre-existing throughout the manufacturing and heat treatment processes or it may be introduced throughout the sample preparation process. This can be seen

as dark spots (marked with yellow arrows) in Figure 7-20(a) and (e) and the loading exited these separations to propagate.

7.3.1.2 Effect of the impact stress

The characterization of damaged inclusions by separation in test T6 and T6A is presented in Figure 7-21. These two tests had the same testing parameter levels apart from the magnitude of impact stress. Increasing the impact loading increases the frequency of damaged inclusions at shallower depths (close to the contact surface) for different types of separation damages. The peaks of all separation damage distributions tend in general to be deeper with increasing impact stress. This supports the effect of impact as compression. Despite the low level of SR (6.71%) used in the two tests under consideration, the damage distribution frequency close to the contact surfaces is higher than that at deeper depths. However, separation damage close to the contact surface probably increased due to the effect of impact mechanical wave produced during the transient loadings. This can be considered as additional evidence to support the fact that impact has different effects from those of the compressive loading that discussed in Section 5.3.2.

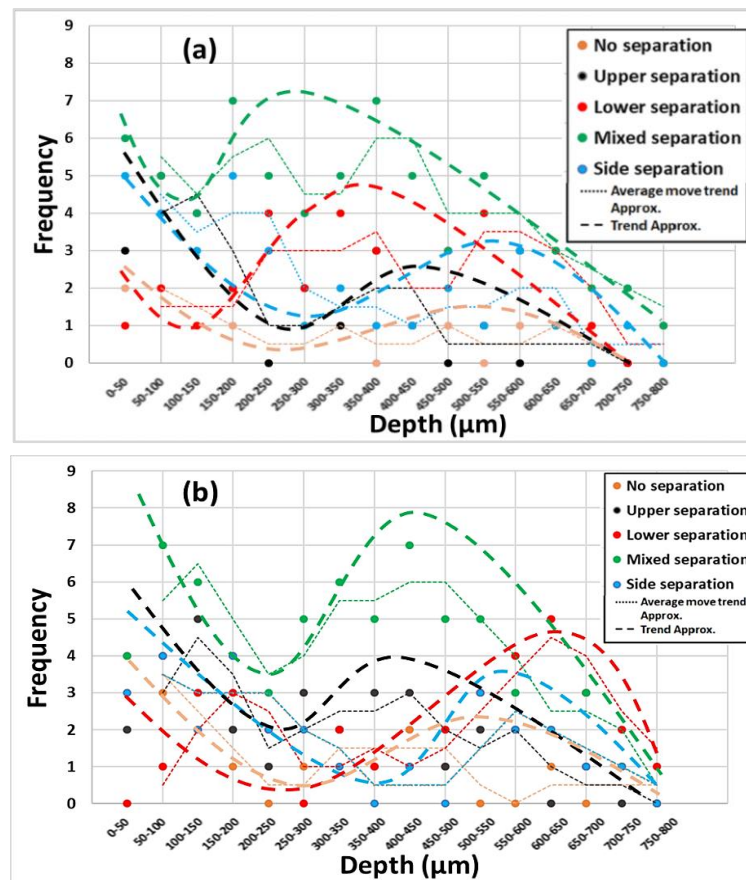


Figure 7-21: Effect of impact on separation type (a) test T6 (impact stress=407.6 MPa); (b) test T6A (impact stress=705 MPa).

Figure 7-22 shows examples of separation damaged inclusions taken from T6 and T6A. Increasing the depth to more than 500 μm reveals a considerable decrease in separation damage. However, no separation damage was observed at a depth of ($>0.8\text{mm}$).

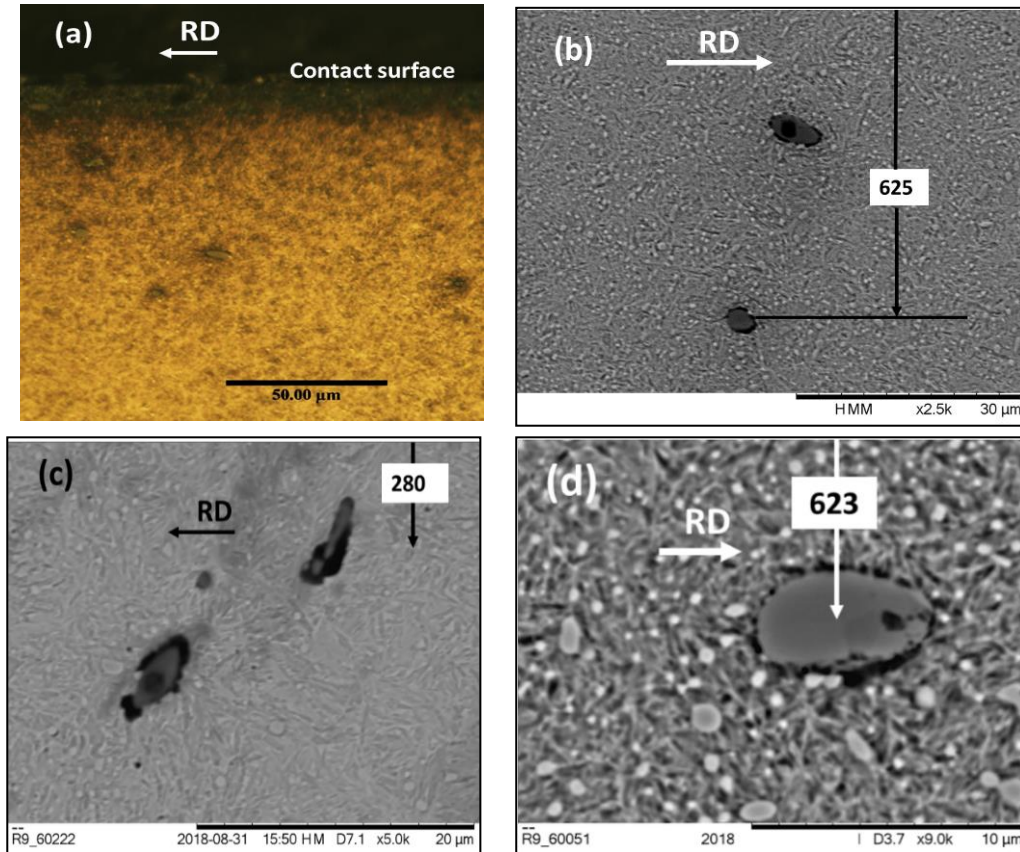


Figure 7-22: Examples of damaged inclusions by separation under the effect of impact (a) and (c) close to contact surface (from T6); (b) and (d) lower separation appears in a deep region (from T6A).

7.3.1.3 Effect of Slipping Ratio (SR)

Despite SR and traction coefficient are dependent on the relative speed between the contact surfaces, the traction coefficient also depends on other parameters such as compressive loading, surface roughness and the specifications of the lubricant used. Test T7 and T7A were chosen because they had the same testing parameter levels apart from the magnitude of the SR. The high impact loading levels of these tests probably affect the results; however, these tests were designed to accelerate the tests due to time facilities, and the non-accelerated tests will be recommended for future work. Increasing the SR increases the number of damaged inclusions by different types of separation located close to the contact surface. As can be seen in Figure 7-23(a) and (b), damaged inclusions by separation

have a distribution clearly correlated with the von-Mises stress distribution with depth.

Increasing the traction coefficient moves the maximum subsurface stresses towards the contact surface as presented in Figure 4-19 to Figure 4-21. This can be proved by examining the movement of the peaks of the subsurface separation damage towards the contact surface with increasing SR. The increase in the SR to 22.82% cannot bring the maximum Von-Mises stress on the contact surface. Therefore, some of the damaged inclusions very close to the contact surface were observed probably because of a high impact level. Under higher SR (T7A), the number of damaged inclusions by mixed separation is considerably increased, especially in the shallower regions. These results show the importance of SR on separation damage that requires further investigation.

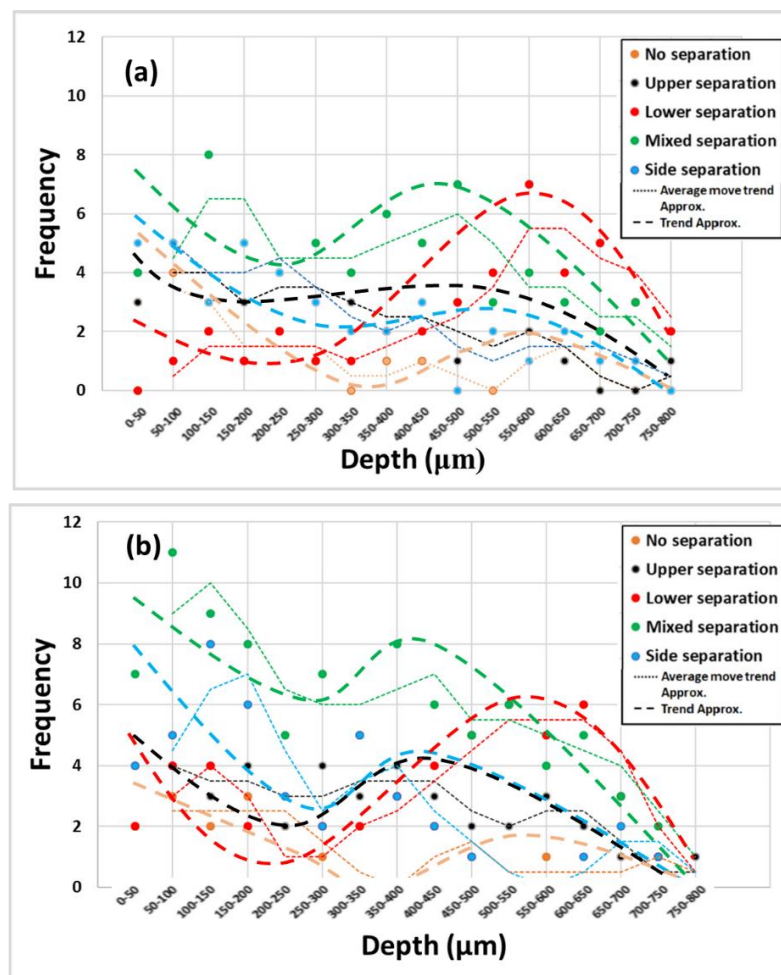


Figure 7-23: Effect of increasing SR on damaged inclusion by separation (a) T7 (SR=6.71%); (b) T7A (SR=22.82%).

Figure 7-24 shows damaged inclusions from the chosen two tests affected by increasing the SR. There are a considerable number of defects (voids) appearing as

black spots associated with carbides. Severely damaged inclusions were observed in shallower regions as can be seen in Figure 7-24(b), where both separation and cracking damage can be observed.

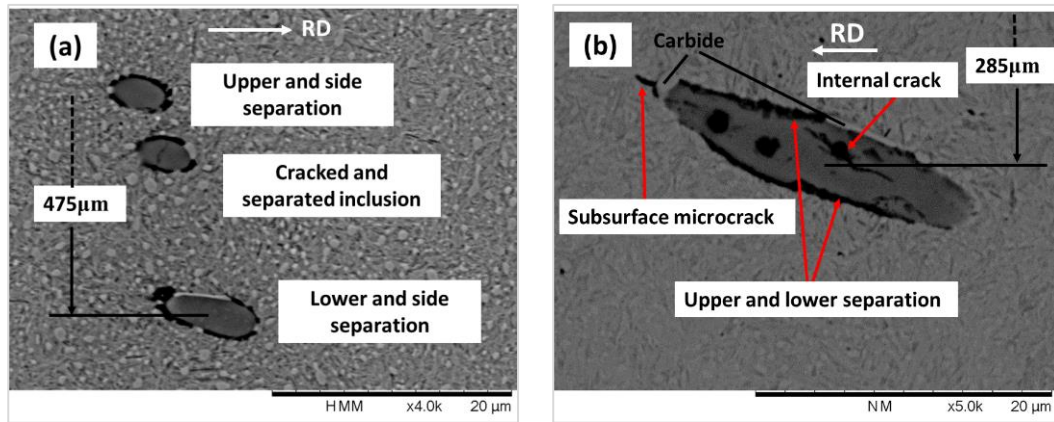


Figure 7-24: Crack and separation damage of inclusions (a) From T7; (b) from T7A.

Table 7-2 outlines the key effect of the study parameters on each type of inclusion damage by separation. The number of “+” signs refers to an increase in the damage by increasing the test parameter levels, while the “-” sign refers to a reduction in damage with increasing the parameter levels. However, the dotted line refers to approximately no effect.

Table 7-2: Effect of increasing the studied factors on inclusion damage by cracking

Study factor to be increased	Separation damage type			
	Lower separation	Upper separation	Side separation	Mixed separation
Load	+++	-	+++	+
SR	...	+++	+	+++
Impact	+++	+	+

7.3.2 Subsurface cracking damage

Damage by cracking is the second type of inclusion damage that will be investigated. Cracking is the break-down or tearing of the material at the weakest locations such as inclusions, voids, and carbides. Sometimes, inclusions at approximately the same depth show different cracking features and/or separation damage as shown in Figure 7-25(a). These different damage types observed in the circumferential direction lead to the postulation that inclusions may experience more severe damage when their inclination and location coincide with the direction and magnitude of maximum shear stress and/or maximum Von-Mises stress. When

the magnitude of these stresses exceeds a critical limit, combined damage (separation and cracking) may be initiated in the inclusions located in the maximum stress area. In addition to damaged inclusions by cracking, a considerable number of subsurface microcracks not relevant to inclusions were also observed.

Figure 7-25(b) shows an example of a damaged inclusion in an axial section beneath the severely damaged region of the lower test disc from T14. In the coming sections, both subsurface microcracks initiated from inclusions and other sites will be analyzed to predict the main stress responsible for their initiation.

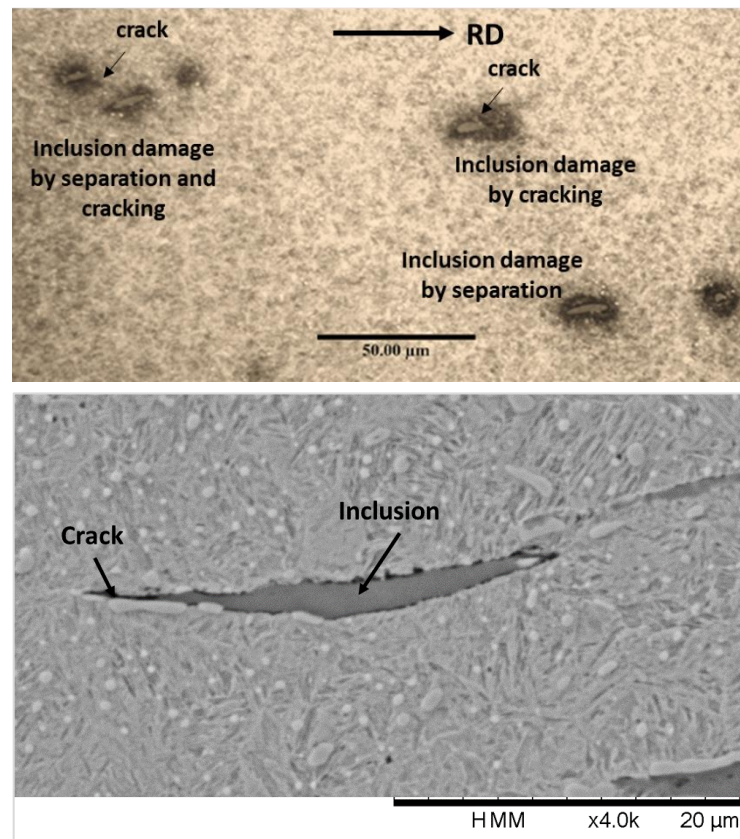


Figure 7-25: Damaged inclusion (a) in the same region have different damage features in circumferential section; (b) cracked inclusion observed in the axial direction.

7.3.2.1 Effect of compressive loading

Tests T14 and T6 were used to investigate the effect of compressive loading on cracking damage that is relevant and irrelevant to inclusions. Figure 7-26 shows examples of the damaged inclusions by cracking in the chosen two tests. Investigating the circumferential planes showed that, inclusions in shallower regions (<0.5 mm) reveal in general upper, lower, internally cracked and/or combined cracking. However, with a slight increase in depth, the number of

damaged inclusions by cracking is considerably decreased. Small inclusions show in general more severe damage. However, inclusion dimensions have been reported to have a considerable effect on damage initiation [79] rather than their depth and loading level.

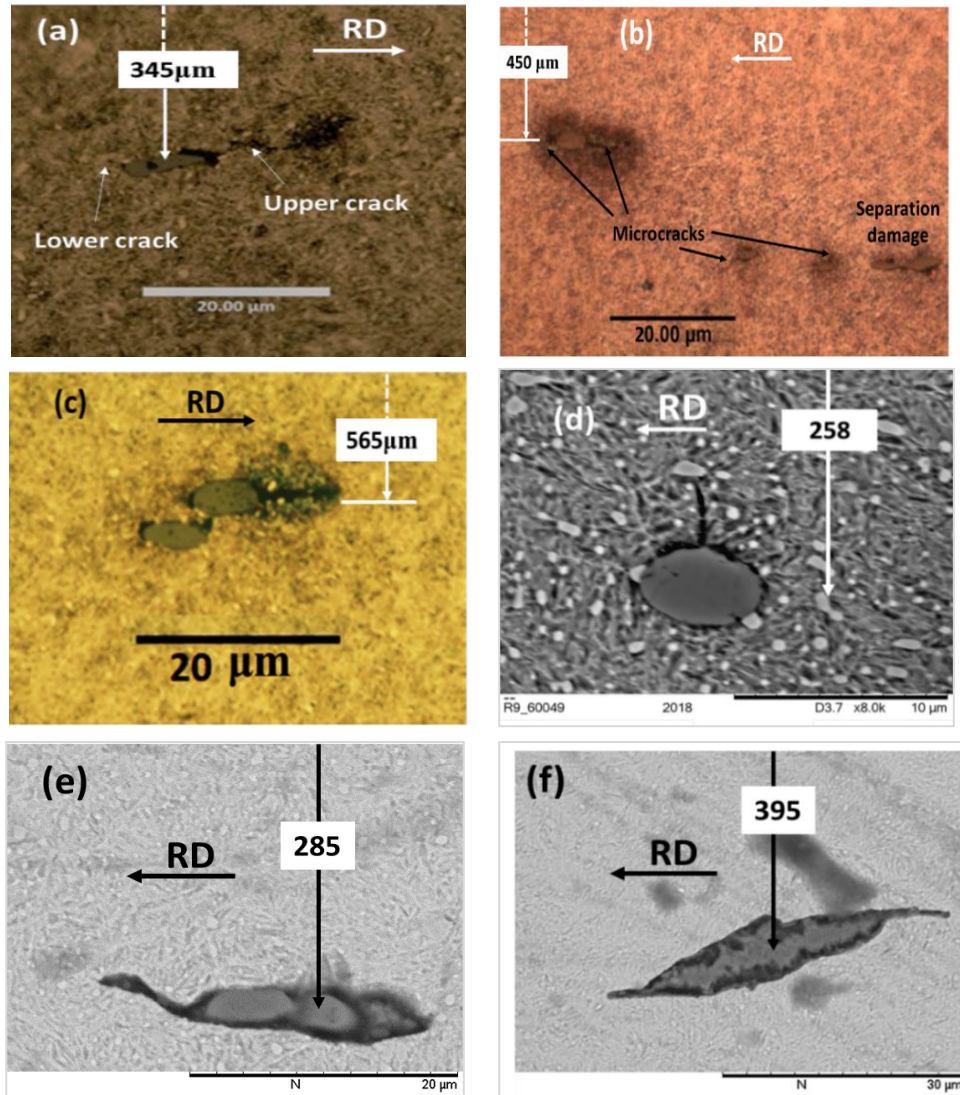


Figure 7-26: Inclusion cracking damage due to compressive loading (a) From T14 (b) from T6 (c) two inclusions with different damage features; (d); (e) and (f) inclusion cracking damage examples (from T6).

Inclusion damage features sometimes have an unsystematic trend, for example, [Figure 7-26\(c\)](#) shows two inclusions located close to each other, one of them has an upper crack, while the other has not, despite their having an approximately similar size. The above observations lead to the conclusion that; not only the loading levels, dimensions and depths of inclusions are what controlled the damage initiation but may other factors such as, the distribution of voids around the inclusions.

The measured length of subsurface microcracks irrelevant to inclusions observed in these two discs is presented against their depth in Figure 7-27. In this characterization, the crack depth was approximately considered as the crack midpoint. The number of microcracks increased with increasing the compressive loading in the shallower regions, i.e. depth < 100 μm . Microcracks were also observed to be increased in deeper regions, i.e. at depth 500 μm to 800 μm with increasing the compressive load. If the crack initiation depends on the number of cracks; Von-Mises stress is probably responsible for cracking damage because the distribution of the number of cracks with depth is identical to subsurface Von-Mises stress distribution. If the maximum average crack length may be initiated first, the maximum shear stress is probably responsible for cracking damage initiation because the distribution of the average crack length is identical to the maximum shear stress distribution.

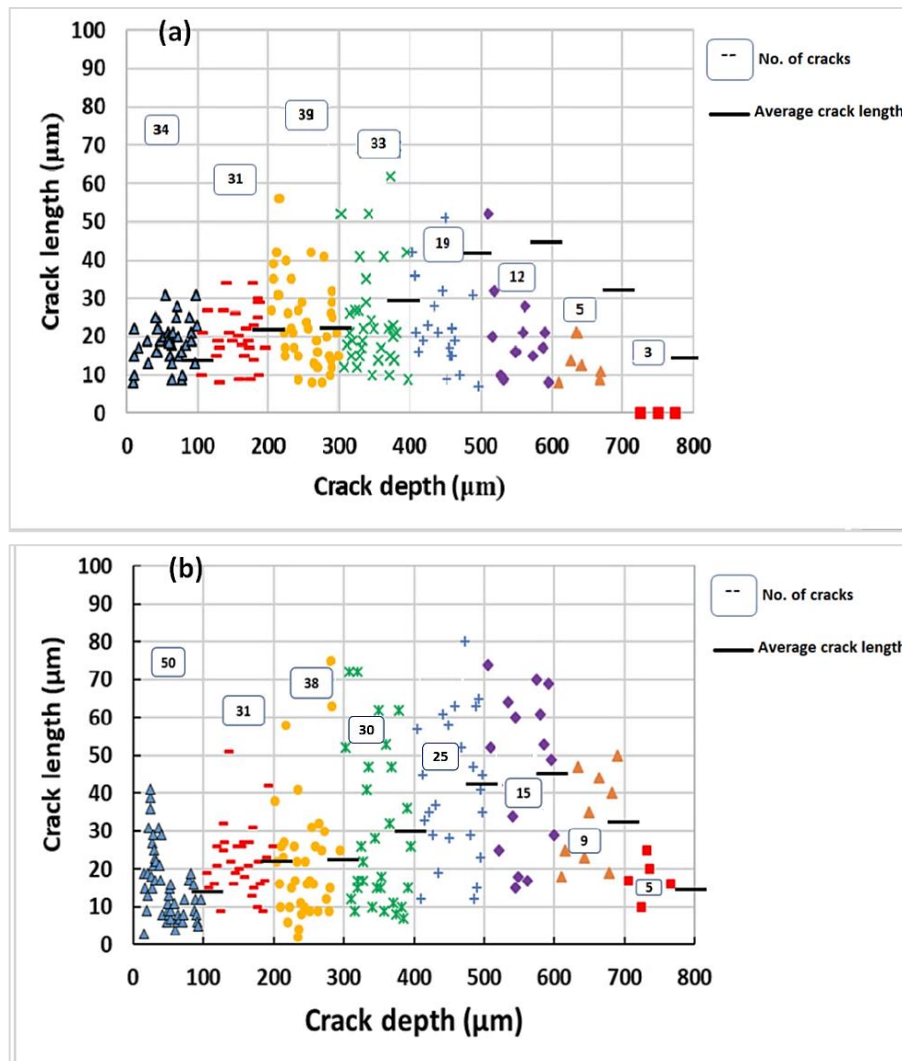


Figure 7-27: Comparison of cracking damage with depth due to increasing compressive load (a) test T14 (compressive stress=2410 MPa); (b) test T6 (compressive stress=2603 MPa).

Increasing the compressive loading not only increases the frequency of cracks but also the average crack length and this supports the role of compression in crack initiation and propagation. Comparing Figure 7-27(a) and Figure 7-27(b) shows that, crack length in deeper regions ($>400 \mu\text{m}$) was increased by increasing the compressive loading level. This supports the role of maximum shear and Von-Mises stresses to be responsible for cracking damage.

An analysis of cracking damaged inclusions was carried out. Increasing the frequency of combined cracking damaged inclusions at different depths with increasing compression can be seen in Figure 7-28. The most important observation is that the distribution of all cracked inclusions with depth is clearly correlated with the subsurface Von-Mises stress distribution. This shows the possible role of this stress in the initiation of this damage type.

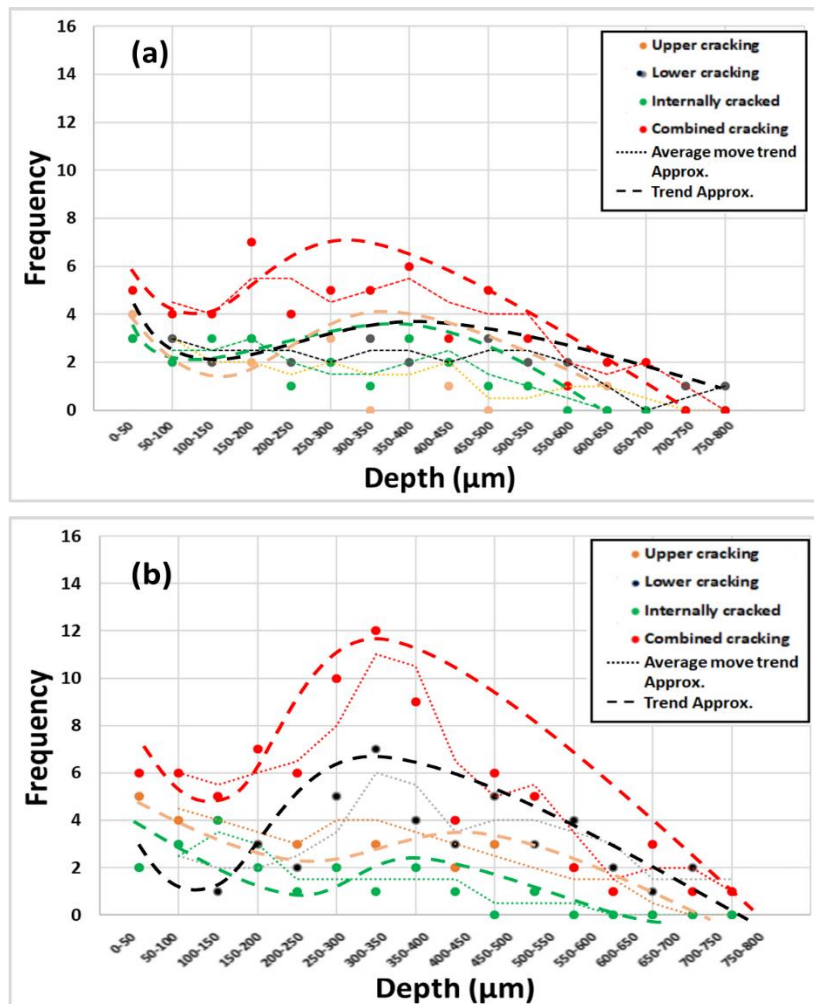


Figure 7-28: Effect of increasing compressive load on inclusion damage by cracking (a) test T14 (compressive stress=2410 MPa); (b) test T6 (compressive stress=2603 MPa).

Following the distribution of the damaged inclusions by cracking to Von-Mises stress distribution does not ignore the possible role of maximum shear in this

damage initiation and more investigation is still required. A higher magnification image shown in Figure 7-29 presents a hypothesis of crack initiation depending on Crack Opening Distance (COD) in addition to that cracks may initiate due to maximum shear.

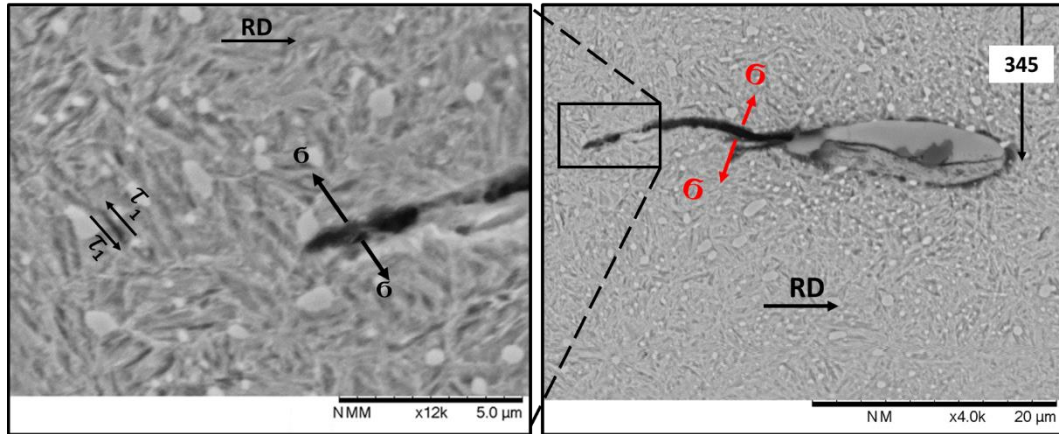


Figure 7-29: Hypothesis: Stresses and their directions may cause damage initiation.

7.3.2.2 Effect of impact loading

The same procedure used in analyzing the effect of compressive loading was also used here to analyze the effect of impact. A microscopic investigation of cracked inclusions and subsurface microcracks in samples taken from test T6 and T6A were carried out. Inclusions were observed to be severely damaged under high impact loading level especially when the inclusion location was close to the contact surface (less than the contact width), as shown in Figure 7-30(a) to (d). There are a considerable number of damaged inclusions located at depths <0.35 mm. The number of the inclusions having internal cracking damage, i.e. cracking the inclusion itself, was increased with increasing the impact loading level.

The number of material defects associated in general with carbides (marked with red arrows), that were mentioned before as black spots, is significantly higher than that observed in the investigated WTGBs. Cracks sometimes change their directions for no recognizable reason. However, it is thought that defects (marked with a yellow oval in Figure 7-30(c)) and the inclusion weak boundaries located in the direction of maximum stress (Von-Mises and/or maximum shear), may have a considerable role in changing the crack direction in addition to the role of grain boundaries specified in Chapter 2. Subsurface microcracks are also observed and marked with white arrows. Distribution of carbides in the microstructure and the associated defects maybe work as a subsurface microcrack trigger as can be seen in Figure 7-30(d), (e) and (f).

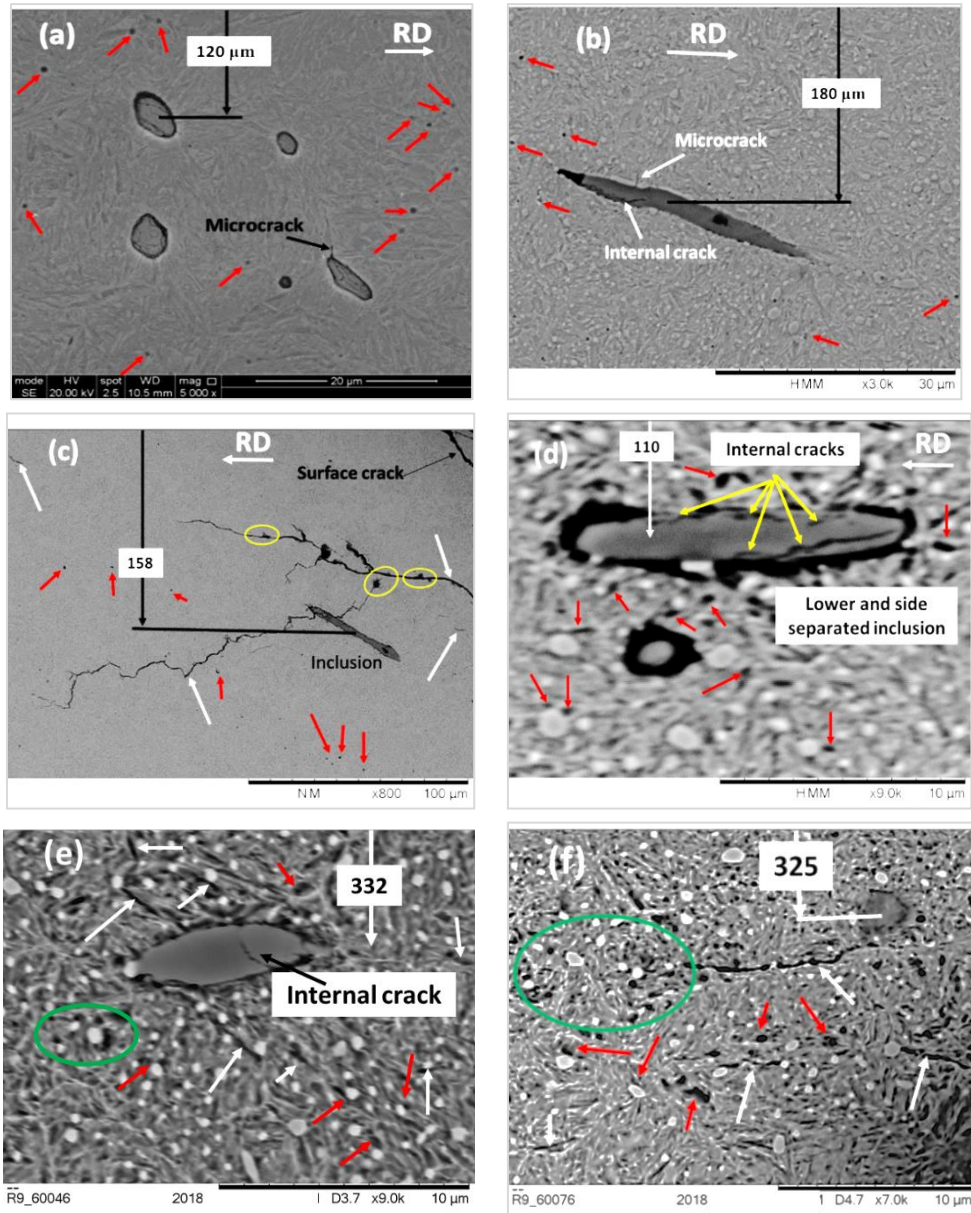


Figure 7-30: Damaged inclusions by cracking due to the effect of impact loading (a) close to contact surface (from T6A); (b) defects in the axial section (from T6); (c) kinked cracks (from T6 axial); (d), (e) and (f) defects and microcracks near damaged inclusions.

Images with high magnifications revealed a considerable number of material defects. These are marked with red arrows and some defects close to each other are marked with green ovals. These defects are probably initiated microcracks first by connecting with each other, after that, these microcracks propagate towards the nearest defect and/or connect to another subsurface microcrack or inclusion to form a larger crack. This can be seen in [Figure 7-30\(e\)](#) and [\(f\)](#), to produce a subsurface crack-network which finds its way to the contact surface and finally causes flaking. This mechanism also supported by the evidence in [Figure 7-31](#). Branching of the cracks probably also has a significant role (see the green ovals)

however, the cause of branching the crack also important to understand the damage propagation. Despite there are three inclusions close to the subsurface cracks, only one inclusion has a connection to the microcracks, it is unlikely that the cracks initiated from this inclusion. However, in the green oval, the crack seems to change its direction due to unknown reasons. Thus, more investigation is still required to confirm this mechanism and the possible role of impact in its initiation.

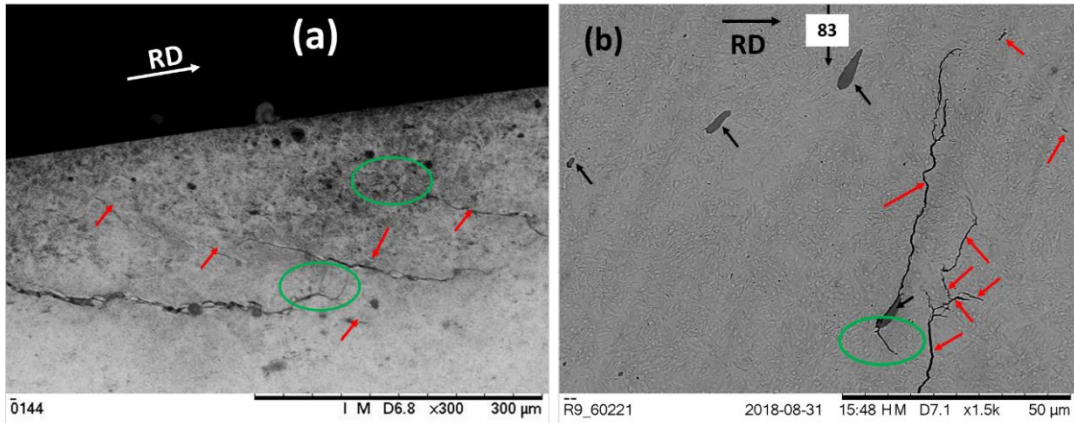


Figure 7-31: Subsurface microcracks connection to produce crack network (a) from T6; (b) from T6A.

The distribution of subsurface crack length with depth can be seen in [Figure 7-32\(a\)](#), the distribution of crack frequencies (specified in a rectangle for each depth), correlates with the subsurface Von-Mises stress distribution. However, the average crack length was observed to be reduced despite the increase in crack frequency, with increasing impact. This supports the role of impact on crack initiation more than the crack propagation. The variation of average crack length with depth can be correlated to the subsurface maximum shear stress distribution. This may be pointing to the role of this stress in crack propagation while von-Mises stress may responsible for crack initiation.

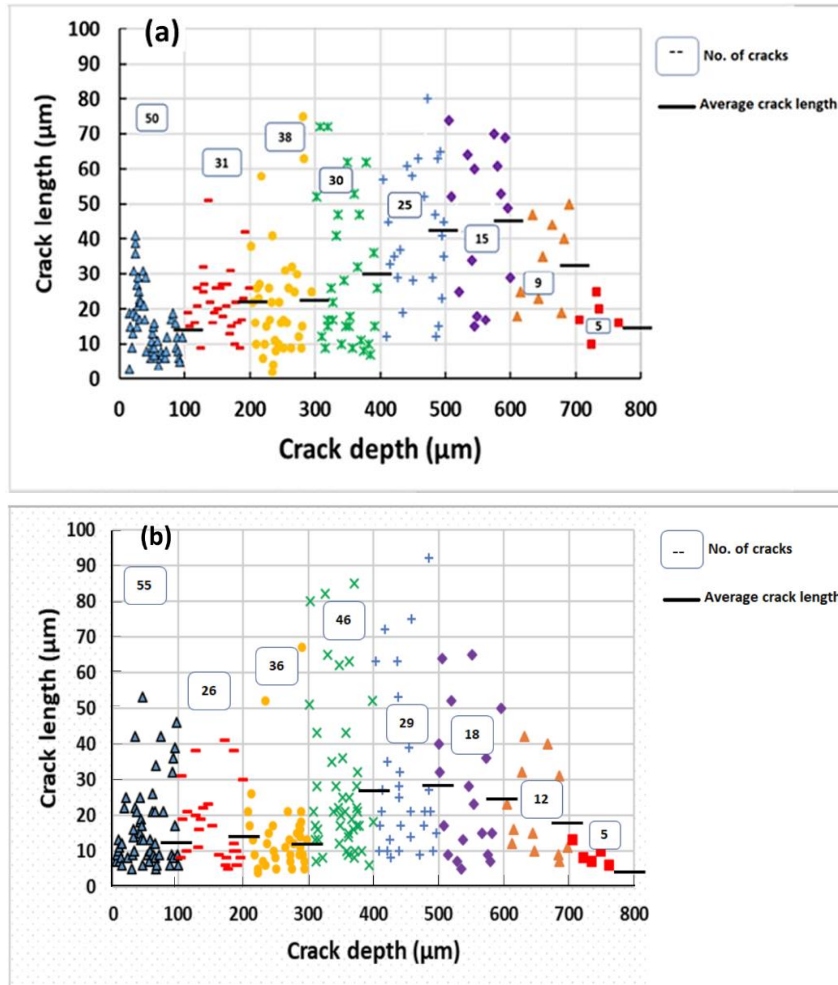


Figure 7-32: Effect of impact on damage by cracking (a) test T6 (impact stress=407.6 MPa); (b) test T6A (impact stress=705 MPa).

The frequency of different types of damaged inclusions by cracking can be seen in [Figure 7-33](#). In shallower regions (<300 μm), the number of internally cracked inclusions is considerably increased with increasing impact loading, however, in deeper regions, peaks of maximum cracked inclusions tend in general to be deeper. This shows the impact role in this type of inclusion damage and its effect as a compression. Despite this effect, impact loading has also another effect in the shallower region.

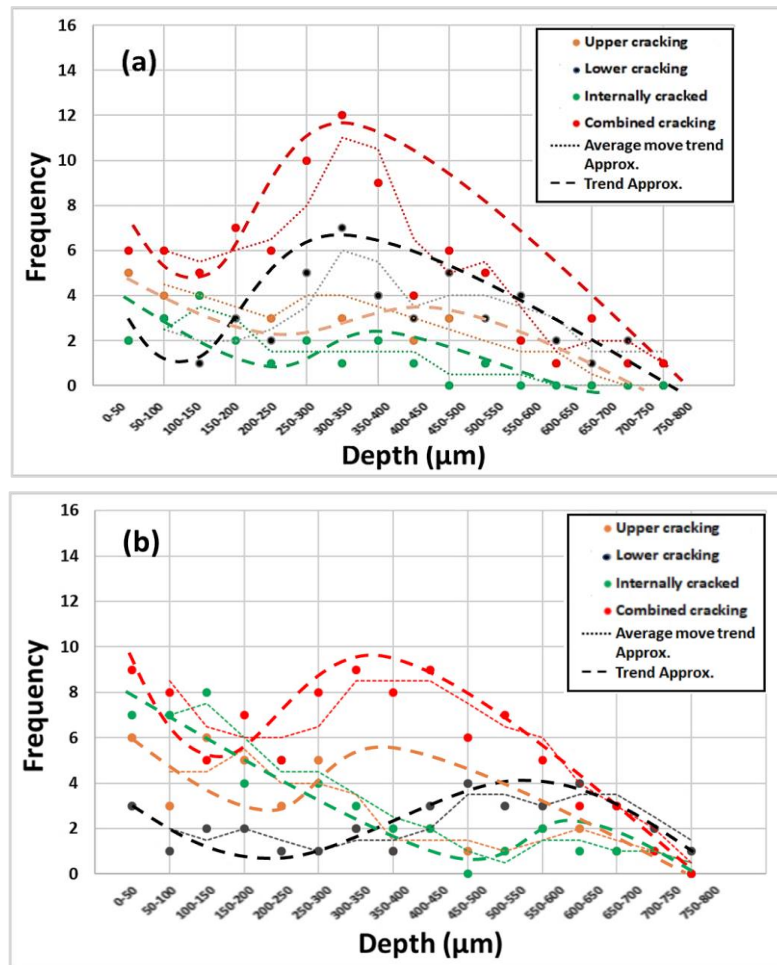


Figure 7-33: Effect of impact on inclusion cracking damage (a) test T6 (impact stress= 407.6 MPa); (b) test T6A (impact stress=705 MPa).

Both subsurface microcracks and damaged inclusions by cracking observed in deeper regions with increasing impact loading shows the effect of impact loading as compression and the role of impact on these damage features. On the other hand, the considerable increase of these damage features in the shallower regions is probably due to the impact mechanical wave introduced. These analyses show that impact has an effect as compression, and it has an additional effect on shallower regions by introducing internally cracked inclusions.

7.3.2.3 Effect of Slipping Ratio (SR)

Analysis of subsurface microcracks (associated with inclusions and irrelevant to them) under two different SR (6.7% and 22.8%) was carried out to investigate the subsurface damage distribution by cracking in T7 and T7A, and correlating the distribution with the subsurface stress distribution to predict the main cause of each cracking damage type. Figure 7-34 shows examples of damaged inclusions by cracking from the examined lower test discs of the two chosen tests. A considerable

number of material defects can be seen in a green oval in Figure 7-34(a) (dark spots). The cluster of defects has a larger opportunity to initiate a subsurface crack than largely spaced defects. When the subsurface depth increases, cracks of internally cracked inclusions become finer as can be seen in Figure 7-34(b). These cracks start to disappear with increasing depth. Increasing the slipping is identical to increasing the traction coefficient because the two tests have the same compressive and impact loading levels. This makes the maximum subsurface stresses move towards the contact surface (as mentioned in Figure 3-5, Figure 3-6, Table 3-5 and Table 3-6). Damaged inclusions in shallower regions (<300 μm) showed several inclusions with internal microcracks as shown in Figure 7-34(c) and Figure 7-34(d). This probably due to the effect of impact loading.

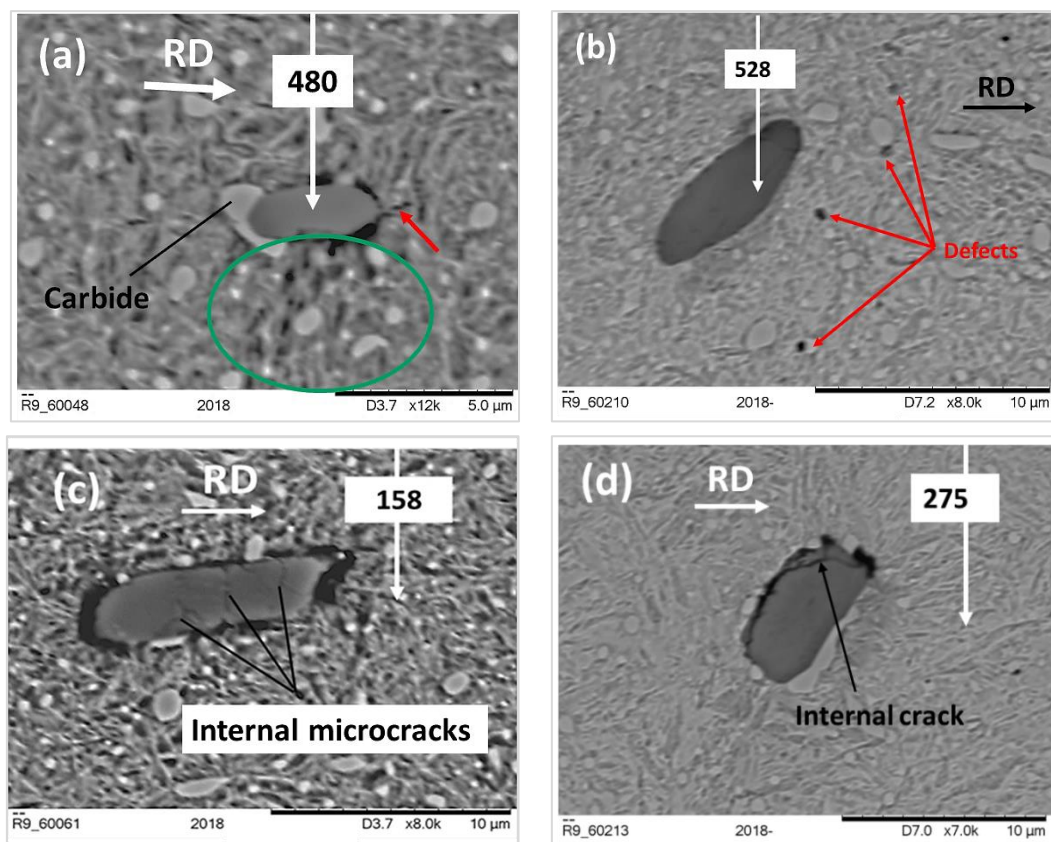


Figure 7-34: Examples of damaged inclusions by cracking (a) upper cracked (from T7); (b) internally micro-cracked (from T7); (c) internally cracked in the shallow region (from T7A); (d) Internally cracked (from T7A).

Test T7A experienced the most severe testing conditions among all the tests. One of the interesting damage features is what is thought to be an initiation of microstructural alteration which may be in the form of butterfly wings as can be seen in Figure 7-35. Although microstructural change regions are always free from carbides; a small deformed or dissolving carbide can be observed. EDX analysis of

the inclusion dark patch shows aluminum and calcium as the main composition of the analyzed location. This supports the postulation of the role of the chemical composition of the nonmetallic inclusion on microstructural change initiation. A series of defects are also observed (marked with white arrows) which are thought to be a butterfly crack, and this supports the postulated role of defects in subsurface microcrack initiation. It is thought that close defects in the material may produce a high-stress concentration and the connection of these defects with each-other may form the associated crack to butterfly wings, while the possible carbon immigration and carbide dissolution under high microstructural dislocation are thought to have a considerable role in forming microstructural changes. Furthermore, this feature which thought to be a butterfly baby has an identical shape to that observed during the bearing investigation which presented in [Figure 3-27](#).

The relatively small number of loading cycles of the test disc lives may be insufficient for the formation of microstructural changes. The short disc lives are probably because of the long non-metallic inclusions (sometimes $>50\ \mu\text{m}$), observed in the axial sections of the test disc material.

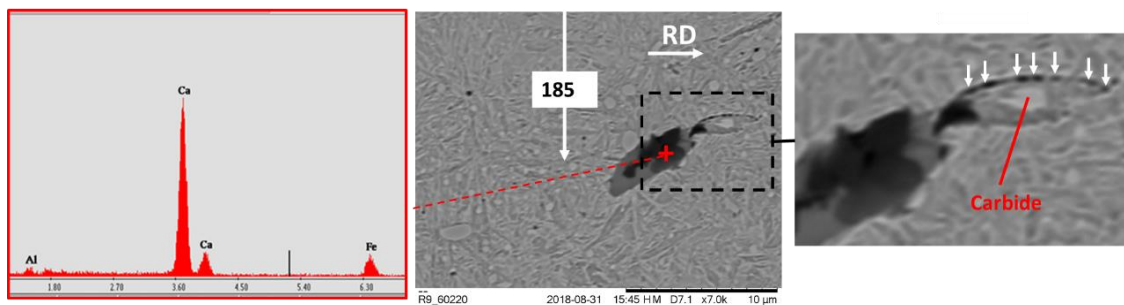


Figure 7-35: Sample from T7A showing the possible initiation of microstructural alteration.

The relatively large number of microcracks irrelevant to inclusions presented in [Figure 7-36\(a\)](#) under the low SR of T7, were probably initiated due to the effect of impact loading which applied at the highest possible level in this test ($\sim 687.0\ \text{MPa}$). The longer test disc life of T7 may permit initiating more subsurface cracks compared with T7A which has a shorter life. However, the effect of slipping can be noticed from the considerable increase in subsurface damaged inclusions by cracking at depths $<500\ \mu\text{m}$ and the reduction in this damage in deeper regions ($> 600\ \mu\text{m}$). This matches the role of traction in raising the maximum subsurface stresses towards the contact surfaces, however, the additional impact role in introducing shallower damage cannot be ignored. This also supports the findings of [Chapter 5](#) which shows the effect of slipping is more than the effect of impact, i.e. despite increasing the impact loading in T7A, the effect of slipping in reducing the damage depth appeared dominantly.

The crack propagation is an accumulative process throughout the RCF. The subsurface cracks irrelevant to inclusions showed a noticeable increase in the crack frequency and length with increasing SR especially at the depth <500 μm . This evidence supports the role of slipping in subsurface crack initiation and propagation. Despite the high levels of impact and compression used in T7 and T7A, the role of slipping appeared clearly. However, further investigation under lower contact loading and impact levels are still required to confirm this role under different loading levels.

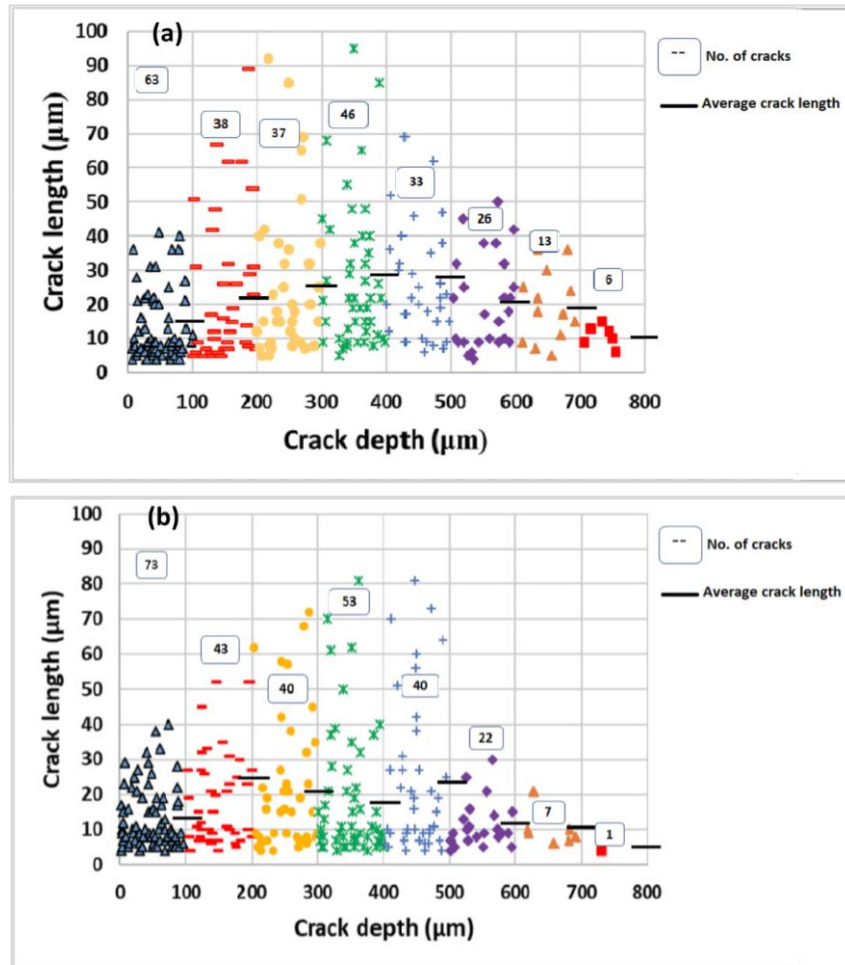


Figure 7-36: Effect of SR on damage by cracking (a) test T7 (SR=6.71%); (b) test T7A (SR=22.82%).

The frequency of damaged inclusions by different types of cracking with depth is presented in Figure 7-37, for T7 and T7A. The number of damaged inclusions in T7, especially in the regions close to the contact surface, is probably due to the high impact loading used in this accelerated test. SR was low (6.71%); if the effect of the compression level of the two tests is considered constant, it is expected that; the interactive effect of different loading parameter levels has a different effect on damage initiation and propagation. However increasing the SR increases the

number of internally cracked inclusions and combined cracking damage, especially in the shallower regions of T7A. Comparing Figure 7-37(a) and (b) shows that, the peaks of the frequency of damaged inclusions by cracking in deeper depths (>300 μm), move slightly towards the contact surface. This also supports the findings of a smaller SR effect under high compressive levels presented in Figure 5-17.

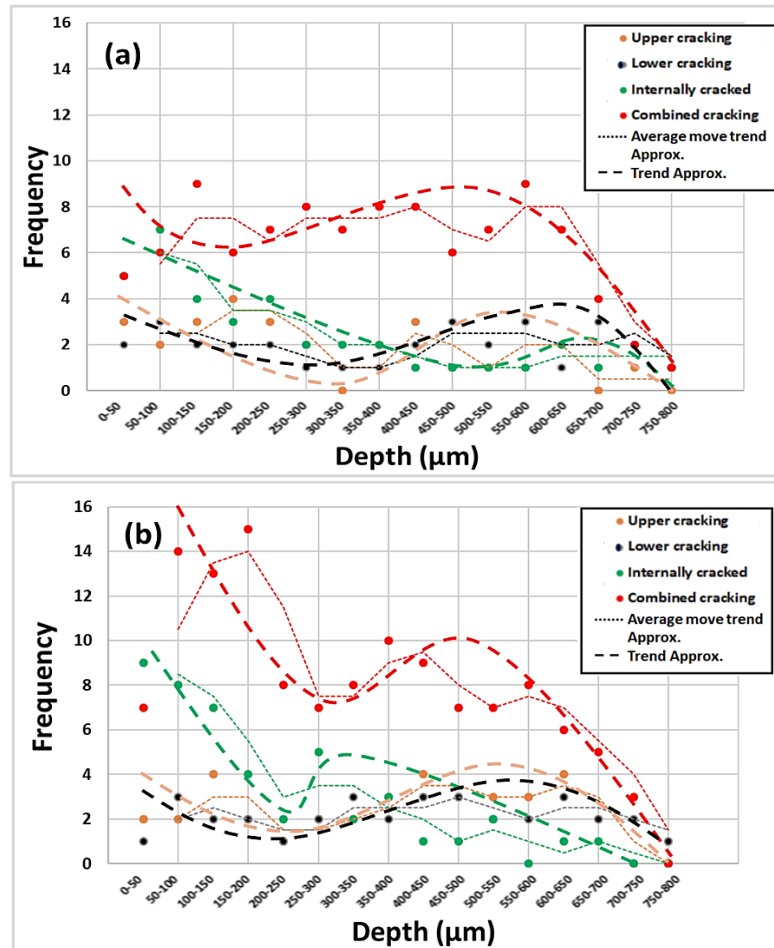


Figure 7-37: Effect of SR on cracking type (a) test T7 (SR=6.71%); (b) test T7A (SR=22.82%).

The effect of the studied parameters on damaged inclusions by cracking can be summarized in Table 7-3.

Table 7-3: Effect of increasing the studied factors on inclusion damage by cracking.

Study factor to be increased	Cracking damage type			
	Upper cracked	Lower cracked	Internally cracked	Combined cracked
Compressive load	++	++	+	++
SR	+	++	+++
Impact stress	+	+++	+

7.4 Investigation of the test without impact loading

The effect of impact on RCF life and subsurface damage features currently starts having more attention due to the impact occurrence throughout the WT operation. The test T6B has the same testing conditions as T6 and the same geometry but, without impact loading. [Figure 7-38](#) shows the surface damage scars of this test. Despite damage scars at the contact edges, there is also damage scar at approximately the middle of the contact length.

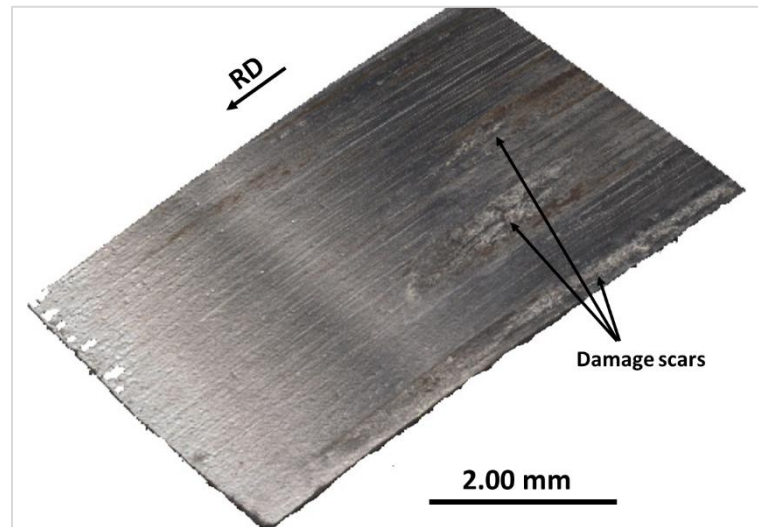


Figure 7-38: Damage region of T6B (without impact loading).

The subsurface microcracks unrelated to inclusions, the inclusions damaged by separation and that damaged by cracking were analyzed by the same procedure in [Section 7.3](#) and presented in [Figure 7-39](#). There are no noticeable two peaks in this figure therefore, maximum shear is probably the possible cause of this damage under stable loading, i.e. without impact loading. The disc life approximately doubled without impact loading (as mentioned in [Section 5.3.1.2](#)), however, the number and average length of the subsurface microcracks are considerably decreased at all depths. The number of damaged inclusions by separation and cracking also considerably decreased in this test. This shows the importance of impact loading in damage initiation and propagation.

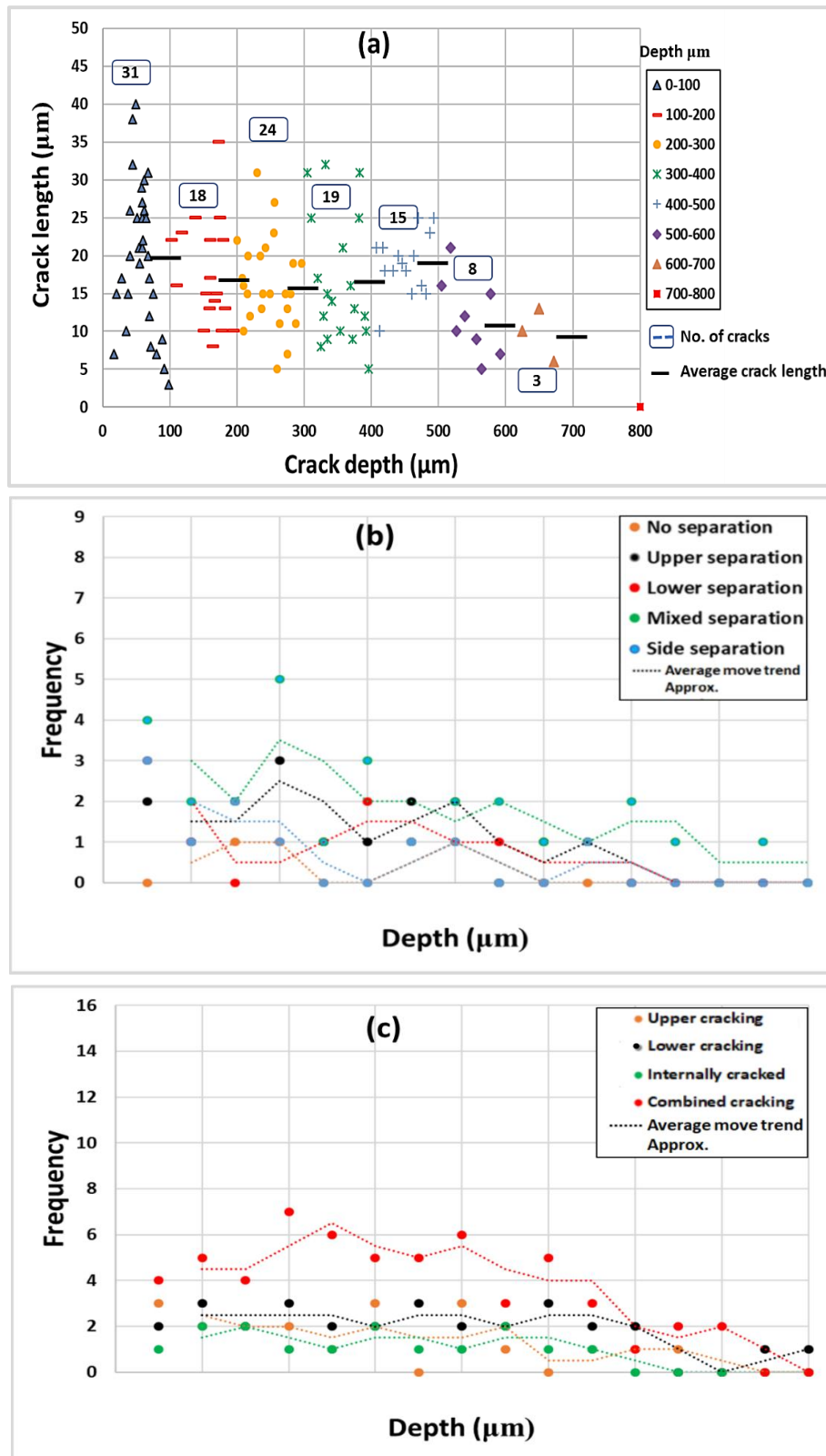


Figure 7-39: Subsurface investigation of T6B (a) microcracks with depth; (b) damaged inclusion by separation; (c) damaged inclusion by cracking.

Von-Mises and maximum shear stress are still the main possible cause of subsurface damage. Investigating and analyzing damage distribution in one plane, i.e. the

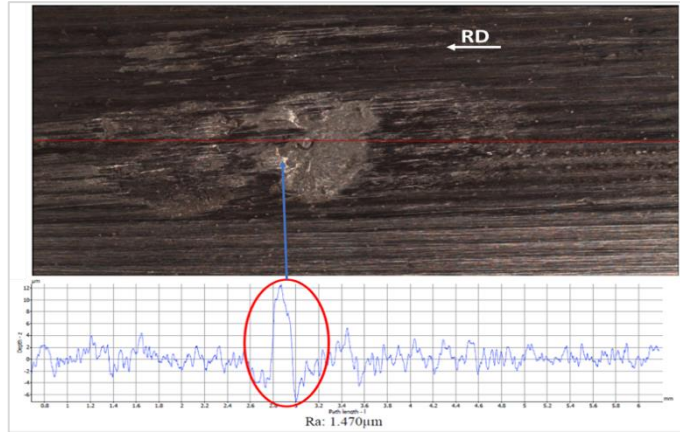
cutting plane where the characteristics were performed is not the perfect way to investigate the role of each stress type in damage because the missing of few damaged inclusions may considerably affect the results, and the investigation under high magnification levels is a time-consuming process. Therefore, serial sectioning for a chosen damage region and classifying each damage type with depth in each section and adding the results will give a better estimation for each damage cause. This will be recommended for future works due to time facilities. This recommended procedure probably more beneficial for elliptical and point contact since the missing of the severely damaged plane with several microns will considerably affect the results.

7.5 Investigation of fully crowned test discs

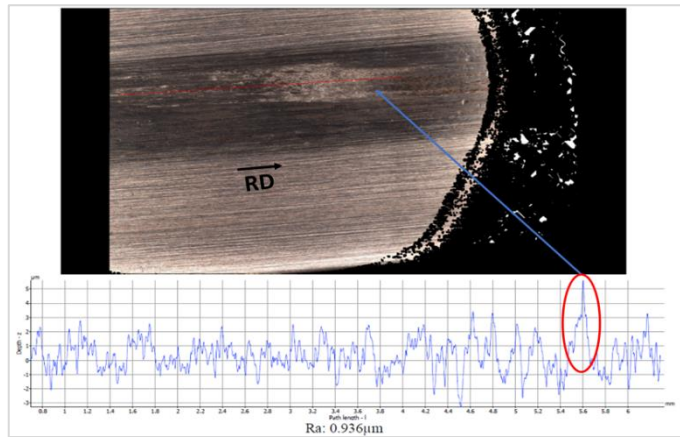
7.5.1 Surface analyses

Analyzing the surface damage feature topography provides useful information about the possible causes and mechanisms of damage initiation and propagation. [Figure 7-40](#) presents the analyses of the four elliptical contact tests topography using an Alicona scanner along lines passing through the severe damage regions in the circumferential direction and, the rolling direction was specified in this figure. It has been noticed that recognizable peaks appear in front of the impact region (marked with red ovals). These peaks pointed to a metal flow (plastic deformation) that increases the surface roughness and makes these peaks subject to a higher contact loading than the other locations. Not only the peaks were observed, but there is also a high possibility of forming valleys within the severely loaded regions. The high contact stress at the peaks and the stress concentration at the valleys may work together to initiate surface cracking at these valleys. With increasing the number of cycles, severe peaks load may be exited the surface crack to propagate and finally produce spalling of the contact surfaces. The height of the formed peaks increases with increasing the test parameters; however, it seems to be affected by impact loading more than SR and compression. Thus, future work will be recommended to investigate this effect. This finding supports the Intrusion/Extrusion theory of the fatigue failure mechanism proposed by Lin and Ito [204] and checked by a dislocation model by Tanaka and Mura [260]. The postulated causes of the investigated WTGB (see [Section 3.7](#)) point out the possible surface and subsurface initiation of the damage. The surface damage may initiate by this mechanism.

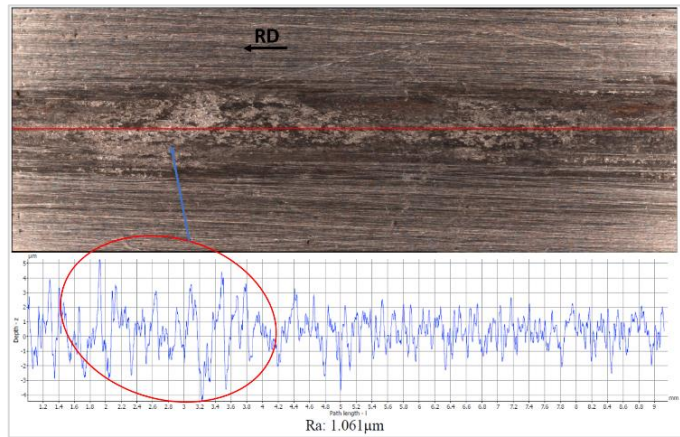
Test disc T1P
 (Comp. stress= 2548.39 MPa,
 Imp. Stress= 1188.19 MPa,
 SR=22.82%)



Test disc T2P
 (Comp. stress= 2548.39,
 Imp. Stress= 757.62 MPa,
 SR=22.82%)



Test disc T3P
 (Comp. stress= 2006.96,
 Imp. Stress= 1188.19 MPa,
 SR=22.82%)



Test disc T4P
 (Comp. stress= 2548.39,
 Imp. Stress= 1188.19 MPa,
 SR=6.71%)

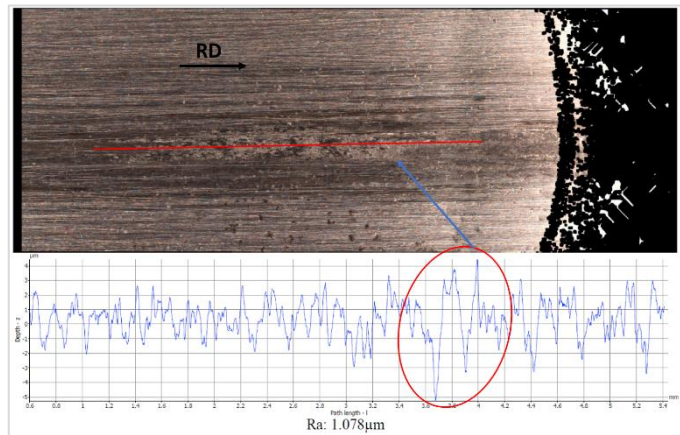


Figure 7-40: Effect of test parameter levels on surface damage feature.

7.5.2 Subsurface analyses

The fully crowned four tests were not analyzed by characterizing the subsurface damage feature distributions (subsurface microcracks, damaged inclusions by separation and cracking) for the following reasons:

1. The results represent plane stress contact that slightly different than the plane strain of line contact and the comparison of damage distributions is inapplicable. The main reason for studying this case is evaluating the stress concentration role in accelerating the damage. Furthermore, this contact type is widely used in engineering applications of RCF.
2. It is not easy to cut the damaged discs from the severely damaged region (maximum contact plane), due to the cutting accuracy of the equipment used in this study (linear precision saw). The cutting accuracy of the saw is ~ 1.0 mm, however, missing the required plane with this distance requires ~ 200 serial sectionings (each of ~ 5 μm which is the average inclusion length) to get the required plane furthermore, each section must be characterized then comparing these sections to find the severely damaged one because missing the required section without characterization will make the sample investigation useless.
3. The time available for this study prevents performing this investigation by serial sectioning, therefore, only the interesting observed damage features will be presented and discussed.

Despite these technical issues in investigating the most severe damage plane, investigating the subsurface of the damaged discs in circumferential planes confirms the previous findings as can be seen in [Figure 7-41](#). The subsurface cracks are marked by red arrows while the surface cracks marked with black, however, the direction of metal plastic flow is marked with white arrows. To investigate the peaks mentioned in [Section 7.5.1](#), T1P, which had the most severe damage pattern, was cut approximately in the maximum contact circumferential plane. The failure mechanism explained in [Section 3.7](#) which postulated the role of surface and subsurface cracks is confirmed. [Figure 7-41\(a\)](#) shows the subsurface damage ahead of the severely damaged region. The surface and subsurface cracks appear clearly. In this figure, despite there is a large number of inclusions, the crack network seems unrelated to them. In [Figure 7-41\(b\)](#), the metal flow within the border of the impact region can be observed. The surface crack (marked with a green oval) seems to be initiated from the valley beside the peak. A considerable number of subsurface microcracks are also observed, which likely will propagate and connect to the surface crack then find their way to the contact surface. The metal flow around the

impact region showed featureless grains seem to be move in a specific direction (specified in white arrows) probably depending on the normal applied load and friction. This needs more investigations in higher magnification levels to understand the direction of this deformation and the role of impact on it.

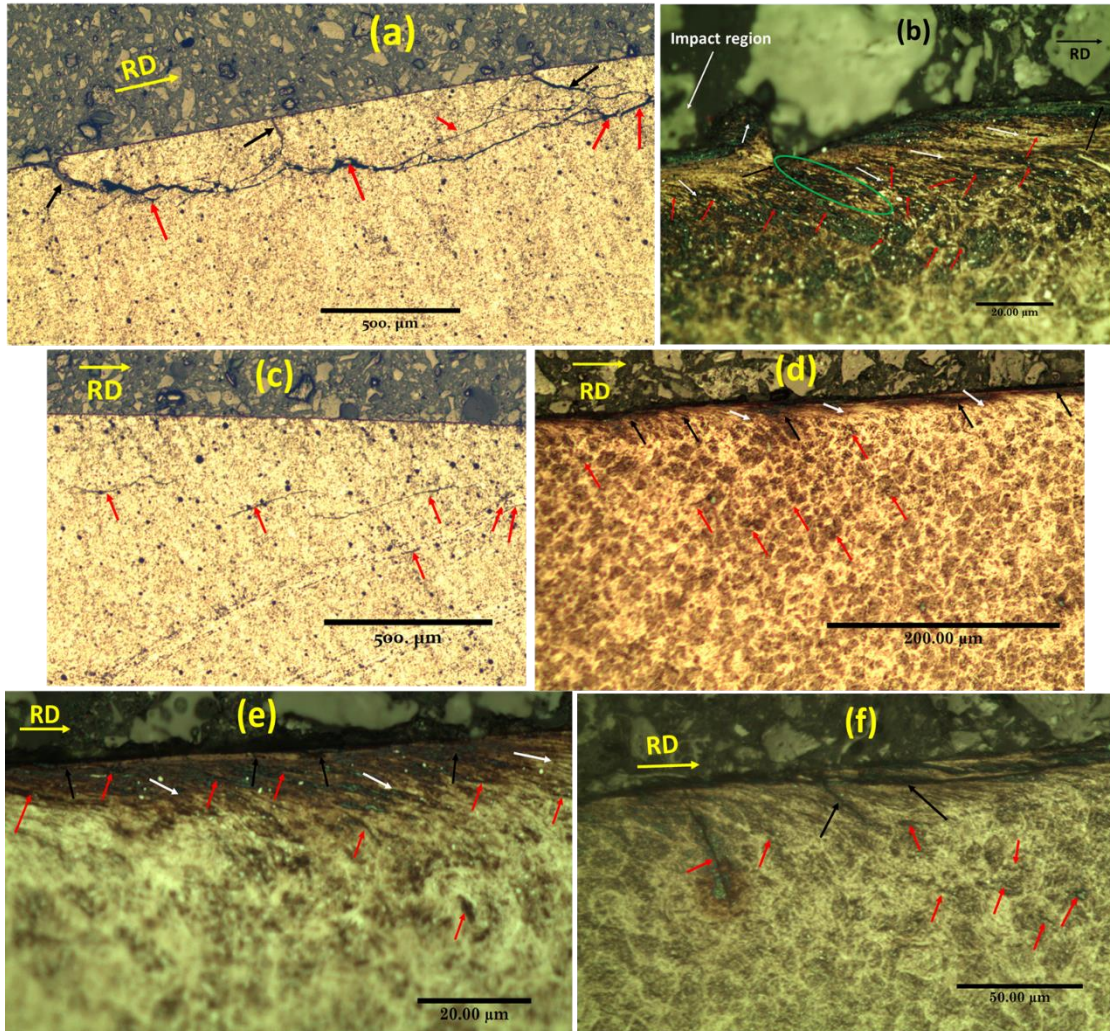


Figure 7-41: Subsurface damage features from fully crowned tests (a) and (b) T1P; (c) and (d) T2P; (e) T3P; (f) T4P.

Despite T2P showing less surface damage with decreasing impact loading, there are many subsurface cracks as can be seen in [Figure 7-41\(c\)](#). By increasing the magnification, surface cracks also observed (see [Figure 7-41\(d\)](#)), however, the metal flow was less than what observed in T1P. Decreasing the contact stress in T3P showed less surface and subsurface microcracks, however, the metal flow is still observed (see [Figure 7-41\(e\)](#)). In the last test (T4P) which has less slipping, the surface and subsurface cracks were more than T3P, however, the metal flow was less. These results point out the considerable role of the study parameter on RCF

damage and life and confirm the role of surface and subsurface cracks in damage that postulated in [Section 3.7](#) and presented in [Figure 7-15](#).

7.6 Justification of not producing microstructural alterations

Microstructural alterations as a type of damage features have been investigated in a considerable number of studies [24]. However, the formation of these alterations requires in general, a high contact loading level and a high number of cycles in the order of ~ 3.2 GPa and $\sim 10^7$ cycles respectively, which has not been achieved in the tests of this study. A considerable number of the previous studies successfully reproduced different types of microstructural alterations such as WEAs, WECs and butterfly wings by applying in general high contact stresses >2.5 GPa under several millions of loading cycles and -30% SR (as presented in [Section 2.6.2](#)).

Looking for microstructural changes, the test disc edges where a predictable high-stress concentration is investigated, i.e. introducing cutting planes in the contact edges of the upper and lower test discs. Unfortunately, no microstructural alterations in any form (DEA, WEA, WEC or butterfly wings), were observed at the investigated locations of the tests. This is probably due to relatively short test disc lives which probably relevant to the material cleanliness grade.

7.7 Comparison of test disc and bearing materials

Comparing the microstructure of the investigated planetary bearings and test discs materials showed considerable differences in inclusion number and size and the number of defects and damage features. It will be recommended to use test disc material made from the same bearing material and having approximately the same cleanliness level to have more reliable correlations with the bearings. The test disc material provided by the supplier company was ASIS 52100 steel [248]. Microscopic examination of the test disc microstructure showed relatively long inclusions, especially in the axial direction as shown in [Figure 7-42](#), compared with that in the investigated WTGB material, however, inclusion size in the circumferential sections was also relatively larger compared with the bearings.

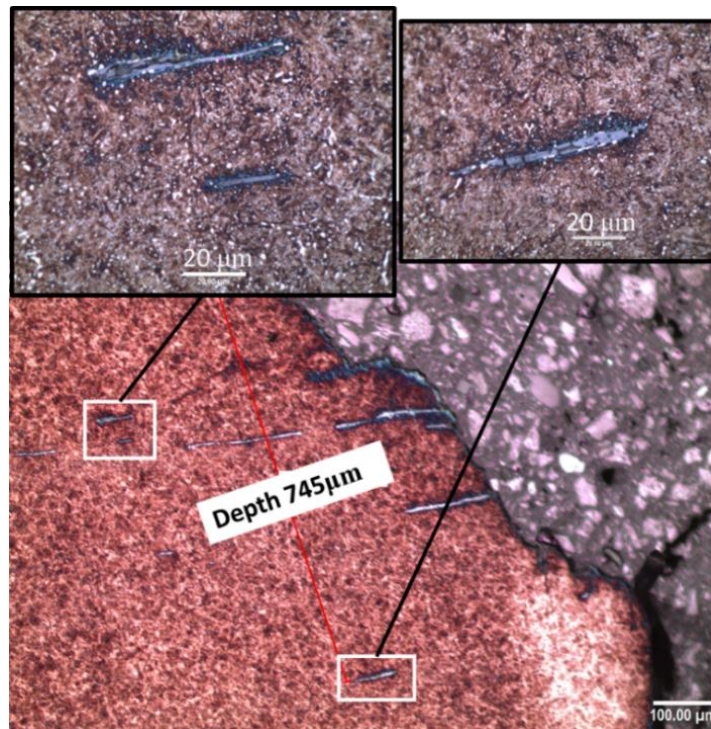


Figure 7-42: Long inclusions observed in test disc material in the axial direction.

Examples of the subsurface defects in the investigated test disc sections can be seen in Figure 7-43 at two different magnification levels. The preferred locations of the defects (marked with red arrows) seem to be at the boundaries of the inclusions and carbides. Defects represent the weak regions in the inclusion boundary, in contrast, carbides have a stronger bond with the inclusion body as shown in Figure 7-11, Figure 7-13, Figure 7-14, Figure 7-17, Figure 7-20, and Figure 7-30. Based on these observations and the evidence mentioned in this chapter, subsurface microcracks are thought to be initiated from the small defects associated with carbide boundaries in addition to those associated with the material inclusions.

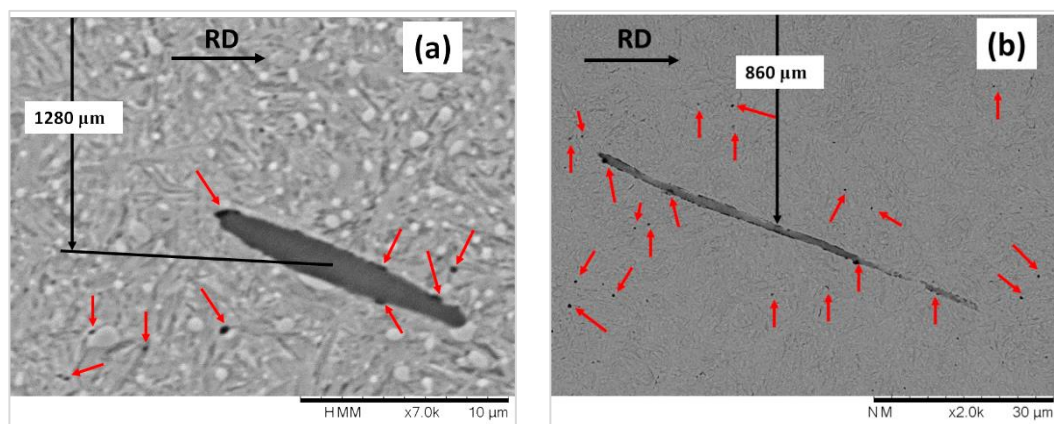


Figure 7-43: Defects on the inclusion borders outside the damage affected area (a) in circumferential direction; (b) in axial direction.

The materials of the investigated bearings and test discs have been compressively tested to compare their failure features. The compression test samples were taken from the locations shown in [Figure 7-44](#). The test disc material undergoes a heat treatment procedure as illustrated in [Table 4-4](#) before the test. It has been noticed that the real bearing material was hard (as mentioned in [Section 3.4.1](#)) and ductile. The bearing material before the service has an HV hardness of ~740 while the test disc material was HV ~700 (see [Section 7.1.1](#)). The difference between the material hardness may produce different failure features and different fatigue failure mechanisms may be introduced. Therefore, it is recommended to use the same material cleanliness level for the testing and the real components.

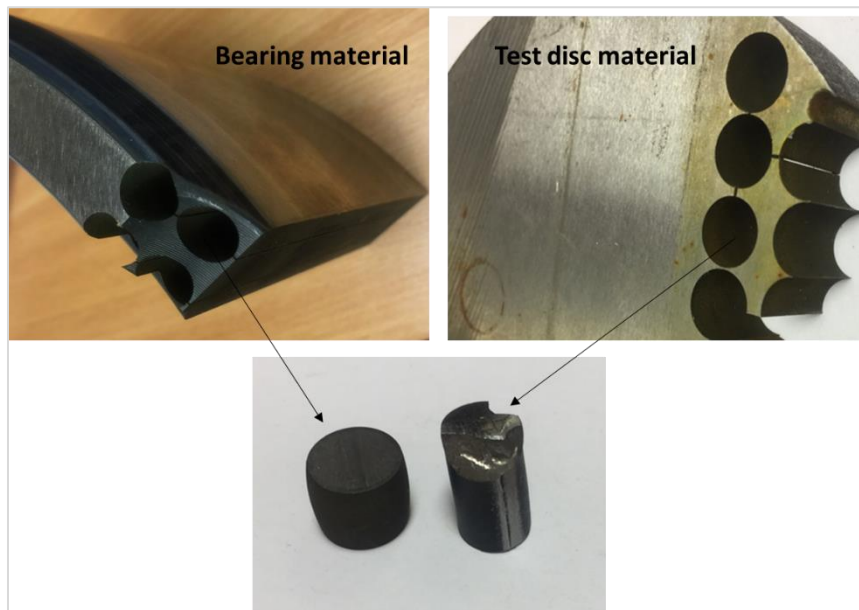


Figure 7-44: Compression tests of the bearing and test disc materials.

The sixteen tests with stress concentration and the four tests without stress concentration are presented in [Section 5.3](#). The equation of the test disc material S-N curve by using curve fitting was:

$$N = 5,161,223 - 855.6 * cob.Strs \quad 7.1$$

where *Cob.Strs* is the combined contact stress in (MPa). This S-N curve is different than that of the real bearing material presented in [Figure 7-45](#).

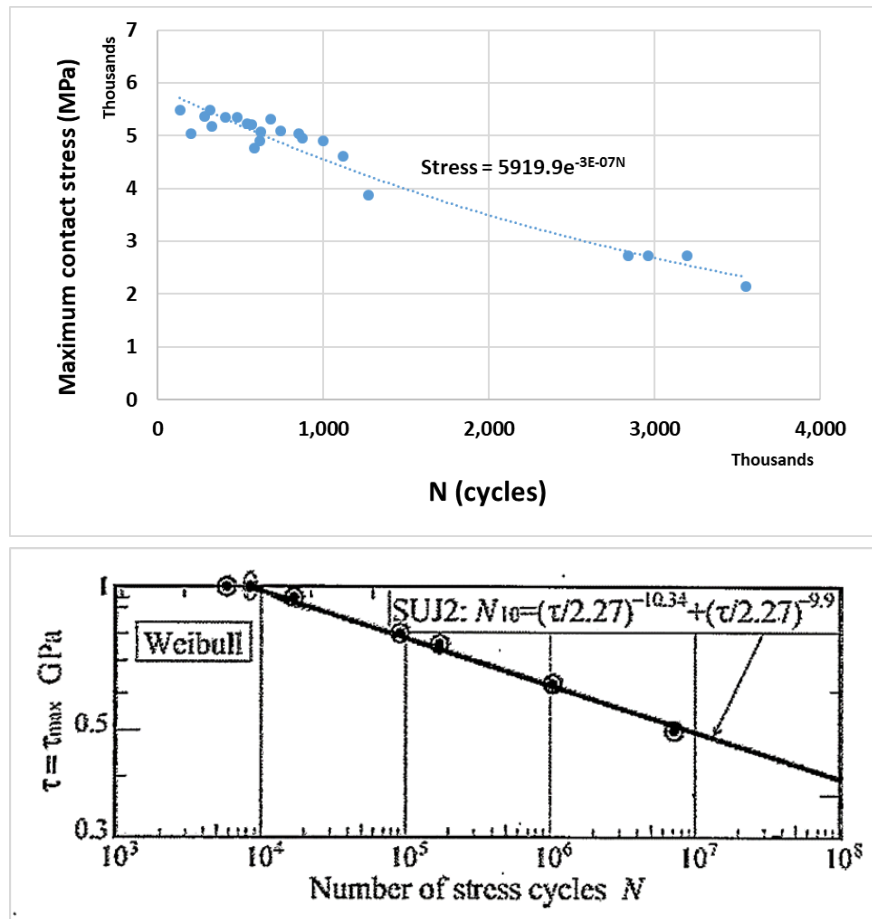


Figure 7-45: S-N curves of the test disc material (top) and the real bearing material (down) [258].

Furthermore, the inclusion types in the test disc microstructure are different from that in the real bearing material from the size, chemical compositions and orientations especially the axial direction which it is thought the crack probably initiates from.

7.7.1 Surface and subsurface microcracks as damage initiation sites

Surface and subsurface crack initiation was observed during the investigation of the test discs and the bearings. Figure 7-46 shows two examples of these cracks. Despite the existence of cracked inclusions and some defects, surface and subsurface microcracks are often not relevant to these inclusions, however, the possibility of defects and/or inclusions outside of the investigation plane as a crack initiation site is still possible and this requires more investigations by using serial sectioning technique to investigate the crack formation site in a direction perpendicular to the investigation surfaces. Furthermore, investigating the number of defects and inclusions within the crack path may be useful.

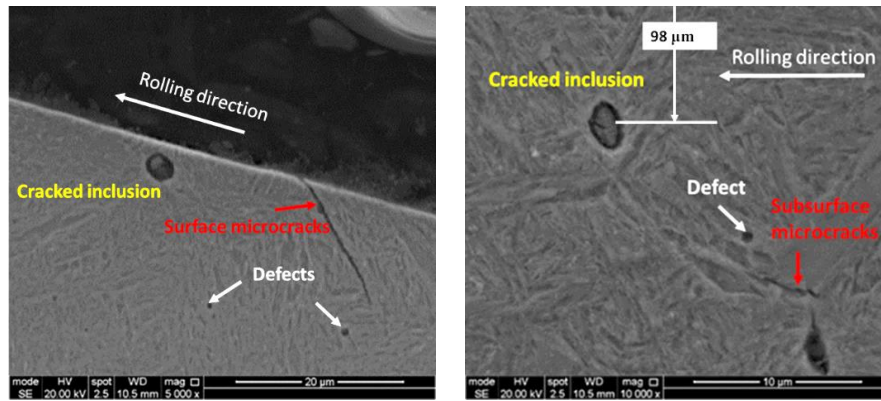


Figure 7-46: Surface and subsurface cracks may not initiate from inclusions.

The majority of the investigated inclusions of the test disc material were MnS inclusions with a small amount of oxide and silicon as analyzed by using the EDX technique (see Figure 7-47). However, silicon may come from the sample preparation suspensions used in the polishing stages. Further investigation is still required to correlate the inclusion type with the damage features.

For elliptical contact test discs investigated in Section 7.5.2, There was a noticeable variation in the properties of the contact surface, however, the damage by subsurface cracks was predominant. Furthermore, a considerable number of surface cracks were observed and presented in Figure 7-15(b). This points out a high possibility of a symbiotic role of both surface and subsurface cracks in introducing the final damage feature, however, which one has more effect in damage probably depends on the operating and loading conditions. This still requires more investigation to have a better understanding of this ambiguous phenomenon due to the considerable number of factors affecting it and the individual and interactive effects of most of these factors are not fully understood.

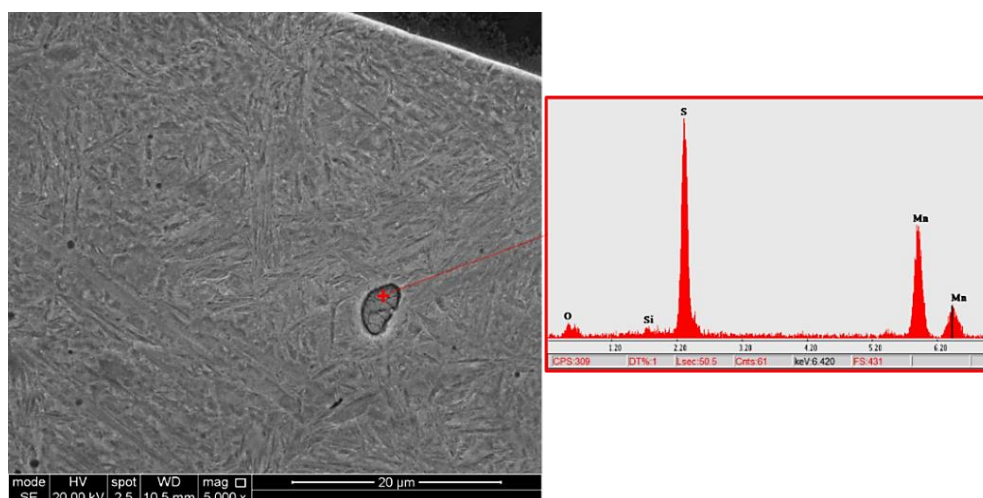


Figure 7-47: Example of damaged inclusion analysis using EDX technique.

7.7.2 Testing of accumulative frictional energy hypothesis

WEA, WEC and butterfly wings are not observed in the test disc investigation sections. There is a hypothesis about the initiation of WEA postulated by Gould and Greco [49]. They suggested an accumulative frictional energy formula to predict the initiation of microstructural alterations. This formula states that rolling/sliding fatigue will consist of microstructural alterations when the accumulative frictional energy is over ~ 8.0 MJ. This formula depends on the slipping velocity (ΔV), friction coefficient (μ), time of operating (t) and the applied load (F_N) as:

$$\text{Energy to produce WEA} = \frac{1}{2} \Delta V \mu F_N t \quad 7.2$$

The coefficient 0.5 came from the assumption of equally distributing the generated frictional heat on the two contact surfaces, and the slipping velocity (ΔV) can be calculated using [Eqn.7.3](#).

$$\Delta V = \omega(R_1 - R_2) \quad 7.3$$

where ω is the test disc rotating speed in rad/s and, R_1 and R_2 are the upper and lower test disc radii respectively. The friction coefficient was estimated in [Section 4.3.2](#) as 0.07 and used in this equation. By applying this formula to the conducted tests; [Table 7-4](#) can be introduced. According to this formula, the highlighted results should contain WEAs and WECs, but none of the damaged areas of the test discs had any microstructural changes after more than 4 sets of regrinding, polishing and etching processes. Nevertheless, these results support the hypothesis of microstructural alterations initiation under specific conditions such as a large number of loading cycles and a high level of contact stress suggested by Swahn et al. [164] and Zwirlein and Schlicht [167], in addition to high SR ($\sim 30\%$).

Table 7-4: Results of applying accumulative friction energy formula for the tests.

Test code	R1 (mm)	R2 (mm)	ω (rad/s)	Load (N)	ΔV (m/s)	Test time (s)	E (MJ)
T14	38.5	36	9.53	11772	0.0239	739006	6.218
T13	39	35.5	11.1	11772	0.03885	657389	9.020
T12	40.5	34	13.19	11772	0.08574	574833	17.405
T16	41.5	33	14.14	11772	0.12019	409075	17.364
T1	38.5	36	11.1	12753	0.02775	560369	5.949
T10	39	35.5	13.19	12753	0.04617	488730	8.632
T15	40.5	34	14.14	12753	0.09191	374397	13.165
T2	41.5	33	9.53	12753	0.08101	385462	11.946
T6	38.5	36	9.53	13734	0.02383	404017	3.966
T4	39	35.5	13.19	13734	0.04617	354664	6.746
T8	40.5	34	14.14	13734	0.09191	267901	10.145
T3	41.5	33	11.1	13734	0.09435	214549	8.340
T7	38.5	36	14.14	14715	0.03535	206163	3.217
T9	39	35.5	13.19	14715	0.04617	184510	3.760
T11	40.5	34	11.1	14715	0.07215	448511	14.285
T5	41.5	33	9.53	14715	0.08101	133648	4.779
T7A	41.5	33	14.14	14715	0.12019	87231	4.628
T6A	41.5	33	14.14	13734	0.12019	314031	15.551

7.8 Key findings

Analyzing the contact surface with respect to hardness and roughness variation and subsurface damage in the form of damaged inclusions by separation and cracking in addition to subsurface microcracks irrelevant to inclusions leads to the following key findings:

- Contact surface roughness and hardness had noticeable changes after conducting the tests. This change was also observed throughout the investigation of the WTG planetary bearings. This proves the importance of surface roughness in damage initiation and the overloading was beyond the elastic limit.
- Maximum shear stress seems to be responsible for subsurface microcrack propagation more than initiation because the average subsurface crack length distribution correlates to the subsurface distribution of this stress.
- Impact loadings have two different effects, the first is like compression and produces an increase in the damage feature frequencies in deeper regions, while the second effect appears close to the contact surface and leads to an

increase in the frequency of different damage features especially the internally cracked inclusions.

- The depth of flaking was observed to be increased by increasing the study parameters, especially impact loading. The subsurface crack paths were observed to follow the microstructural defects and voids more than following the nonmetallic inclusions.
- Carbides were found having a stronger bonding with the inclusion bodies than the other microstructure but, the carbides often associated with defects. Furthermore, the possible role of surface cracks also cannot be ignored.
- The proposed mechanism of defect damage initiation is supported by the observations of this chapter. This mechanism hypothesizes that defects and voids close to each other are probably connected to form the subsurface microcracks under high loading levels. These microcracks are connected to each other forming a macrocrack then spreads toward the surface and/or connects to other macrocracks to cause surface flaking damage.
- There are considerable differences in the material microstructure between the investigated bearings and the test discs in both circumferential and axial sections. The inclusion size, frequency and orientation, the number of defects, their size and number of carbides and the mechanical properties are thought to be the main parameters controlling the subsurface damage initiation and propagation. Further testing should be carried out using the same material cleanliness and heat treatment under lower impact loading to get more reliable results.
- The observations and the results of this chapter support the hypothesis of microstructural alterations proposed by Swahn et al. [164] and that of Zwirlein and Schlicht [167]. However, the accumulative frictional heat energy hypothesized by Gould and Greco [49] cannot be validated by the fatigue tests conducted in this study probably due to transient loadings due to impact and its role in accelerating the damage. Further testing and investigations for the RCF in combination with impact loading are still required.

8

CONCLUSIONS AND FUTURE WORK

The key conclusions and the future work recommendations of this study are presented in this chapter. The conclusions are classified into two parts, that obtained from the planetary bearing investigation and those attained from the experimental tests. Repetition of fatigue tests will significantly increase the reliability of the test results; however, long test time represents the main challenge of reconducting the tests. Other limitations of this study are also summarized throughout the study such as using the observation to indicate the arriving of spalling to the contact surfaces and the use of rotational speed variation to vary the impact stresses. These two limitations can be avoided in future work by following the recommendations for improving this first version of the developed test rig. Microstructural differences including material cleanliness, inclusion type, size, orientation and distribution, and heat treatment procedure can produce significant differences in the test results compared with the real bearings.

8.1 Conclusions

The main aim of surface analyses of the wind turbine planetary bearings was to estimate the operating contact stress level and slipping by investigating the hardness and roughness. However, effect of impact loading on damage features cannot be investigated separately due to applying all damage factors in combination and the lack of information about the damage features caused by impact. Brückner et al. [30] methodology of estimating the stress type responsible for butterfly wing formation was used to predict the main cause of the observed damage features. A new test rig has been designed and manufactured to apply impact loading in combination with rolling/sliding tests to investigate the individual and interactive effects of the study parameters on fatigue life then investigating the change in

separation and cracking damage feature distributions by the variation of the testing parameter levels. The tests were run by applying operating and loading levels estimated from the investigation of two failed multimegawatt wind turbine gearbox bearings. These levels are expected causing premature bearing failures and influencing the contact surface, subsurface damage and bearing life. The investigation was to get a better understanding of the main causes of bearing premature failure especially the effect of impact loading. Impact loading investigation showed two effects; the first is by increasing the depth of damaged nonmetallic inclusions while the second by introducing internally cracked inclusions which showed an interesting role in introducing butterfly wings. Applying these parameters in combination like the real case in bearing service helped to evaluate the importance of their interactive effects. Similar material cleanliness and heat treatment of the WTGBs are recommended to be used in future tests to increase the reliability of the results. The quantitative analysis of the fatigue tests shows the trend of the individual and interactive effects of the study parameters followed an exponential trend in reducing the fatigue test life. Two effects of impact loading were observed in subsurface damage features including microcracking and damaged inclusions by separation and cracking were investigated. Furthermore, the postulated number of cycles to initiate microstructural alterations by Swahn et al. [164] and Zwirlein and Schlicht [167] were confirmed, while the accumulative frictional energy method by Gould et al. [49] did not. The analyses of disc lives showed the high dependence of damage on the contact stress and the number of cycles. For this reason, a new damage estimation methodology was suggested depending on both the contact stress and number of loading cycled. This method was tested using real operating data from SCADA. The initial results were promising, however, more tests are still required to show the reliability of this new method.

The following sections illustrate detailed conclusions of the most important observations and analyses throughout this study that classified into two categories, the first concluded from the investigated bearings while the second from the test disc investigations.

8.1.1 Investigation of the failed planetary bearings

The main points concluded from the investigation of the real multimegawatt WTGBs presented in [Chapter 3](#) can be summarized as follows:

- Surface investigations including, contact surface hardness and roughness can provide very useful information about the operating conditions. The

investigation showed a hardening phenomenon on the bearing inner race contact surface which confirm the overloading operation to a level beyond the bearing material elastic limit. The overloading produced by misalignment can be considered as one of the most important causes of WTGB failure. Despite using advanced techniques in designing the turbine gearboxes and selecting their bearings, over rolling beyond the elastic limit was confirmed and supported by the orientations of the observed butterfly wings. For that, the design stress in the wind turbine standards may require a re-evaluation, i.e. reduced.

- A considerable number of subsurface microcracks unassociated with inclusions were observed throughout the microstructural investigation. These microcracks are probably initiated from defects, voids associated with carbides and/or the grain boundaries which led to consider these locations as another site of subsurface damage initiation rather than the non-metallic inclusions which specified in the previous studies. These voids probably initiate during the manufacturing and/or the bearing component heat treatment.
- Von-Mises stress was found to be responsible for different nonmetallic inclusion damages such as separation and cracking damage in addition to the subsurface microcrack damage una with the inclusions.
- Over slipping to a level greater than what currently investigating is expected. This confirmed by the butterfly wing inclination angle and the considerable change in the inner race surface roughness.
- The investigation of the microstructural alterations showed that the butterfly wings are often initiated from compound inclusion type D_{Dub} when the inclusion cracked in a direction approximately parallel to the maximum wing length axis in circumferential sections. However, impact loading was found to be responsible for these internally cracked inclusions therefore, impact loading probably plays a considerable role in butterfly wings initiation. The majority of the investigated butterfly wings was observed unassociated with crack network; this refers to a marginal role of this damage features in the bearing failure. The wings may introduced due to severe loading levels in a late stage from inserting debris between the contact surfaces.

8.1.2 Investigated parameters and test discs

Sixteen main tests were conducted for flat test discs (line contact with stress concentration) after designing the testing parameter levels by using Minitab software of the Design of Experiment (DOE). In addition to two tests to confirm the individual effect of the studied parameters (impact and slipping ratio) on the test disc life and one test to investigate the effect of surface roughness. Furthermore, four tests were also designed and conducted to evaluate qualitatively the effect of the study parameters on test disc fatigue life without test disc stress concentration. The following can be concluded:

- The test disc life was reduced with increasing all the studied parameters in approximately an exponential trend and increasing the impact loading is considerably reduced the RCF life of the test discs.
- The interactive effect between impact loading with slipping and that of compressive loading with slipping were found to be completely different despite applying the impact loading as compression. However, the interactive effect of impact with slipping was found to be considerably fluctuated with varying the test parameter levels and did not show a clear trend of reducing the test disc life. This led to conclude that, the effect of impact had an effect differs from that of compression. More investigations for the role of impact loading on fatigue damage features are still required.
- The characterization of the number of damage features (damaged inclusions by separation and cracking, and microcracks) and the size of them with depth showed that the distributions followed generally, the Von-Mises subsurface stress distribution and to a lower extent the maximum shear stress distribution. This led to postulate the Von-Mises stress as responsible for damage initiation and propagation in RCF and the impact loading had an apparent role in producing the nonmetallic internally cracked damage feature. The metallographic investigation of the test discs supported the postulated trigger of subsurface microcracks from voids associated with carbide as a damage source rather than that initiated from the nonmetallic inclusions which considerably reported in the previous studies.
- Despite the high-stress level due to stress concentration at the test disc edges investigated in [Chapter 5](#), this stress concentration can be helpful to accelerate the tests and it is useful to represent the real bearing contact conditions. However, accelerating the tests may produce damage features differ than that of real operating loading levels, for that, attention should be taken on the stress concentration whether the flat test discs have equal or

different contact lengths, or having fillet edges, furthermore, the same geometry of the real components will be more accurate in the future tests. Finite Element (FE) method is helpful to estimate the stress level at the disc edges before manufacturing the test discs and this is strongly recommended.

- Compression load is the main effective parameter on fatigue failure, this was concluded from that; increasing the test contact load was considerably increased all the surface and subsurface stresses and hence all types of damage features. Furthermore, life estimation formulas driven from the quantitative test result analyses showed less percentage of error when presented in terms of combined contact stress. Impact loading affects as compression in addition to its effect as an impact mechanical wave in shallower regions were specified, however, the slipping effect appeared more than the impact loading within their testing ranges. This study can be considered as the first study to investigate the effect of impact on RCF life under the joint effect of compression and slipping, therefore, more investigation for these parameters in a combination will help to get a better understanding of the damage initiation and propagation and RCF life.
- The damage depth was observed to be increased with increasing the study parameters and the damage cracks follow the defects and voids more than following the nonmetallic inclusions.
- The investigation of nonmetallic inclusion damage at their boundaries showed a stronger bonding of carbides with inclusion body than the other disc material structure. This may explain the associating of microstructural alterations with the inclusions that specified in the previous studies.
- The investigation of the test disc material structure showed that the parameters of inclusion, carbide and voids including size frequency, orientation and mechanical properties have the most important role in fatigue damage initiation. Further testing is required to specify the interactive effects of these parameters with the study loading parameters.
- The microstructural investigation of the tests of this study confirms the hypothesis of damage initiation mechanism which consists of connecting the close voids and defects to form microcracks which then connect to other microcracks to produce macrocrack then propagate towards the contact surface and causing flaking.
- The test lives and microstructural investigation confirms the findings of Swahn et al. [164] and Zwirlein and Schlicht [167] about the required loading levels and number of cycles for the initiation of microstructural alteration.

8.1.3 The new bearing damage estimation and life prediction method (EFDA)

In this study, a new life prediction and damage estimation methodology for wind turbine gearbox bearings is derived and tested depending on the damage accumulation process. This method assumes that the damage energy is directly proportional to the contact stress and number of loading cycles under each contact stress. This damage energy is a fraction of the turbine input energy; for this reason it named Energy Fraction of Damage Accumulation (EFDA). This method can use the operating monitoring data of SCADA to predict the bearing fatigue life. The initial testing of this method gave promising results by using real operating data of a 1.7 MW wind turbine throughout two years and by using the average annual wind speed distribution from NREL. The percentages of error in the bearing life predictions were lower than the bearing selection standard. More testing using real operating data of SCADA for real wind turbine operating is still required to prove the reliability of this new method.

8.2 Recommendations for future work

The main part of this study is the results achieved from the conducted experiments using a new test rig. This test rig is the first version that designed and manufactured to apply Rolling/Sliding (R/S) and impact in a combination similar to that in real bearing operation. Some recommendations to improve the rig design and testing levels are presented in the following sections. The recommendations of this study will be listed in three categories:

1. Future testing.
2. Improving the new test rig.
3. Improving the design of WTG.

8.2.1 Future testing

The test disc material quality, test disc geometry, and testing levels will be discussed to conclude recommendations for future testing. This can be summarized as:

- To investigate the premature phenomenon in WTG planetary bearings, stress testing levels should be beyond the bearing material elastic limit which represents the actual operating contact level or by mixing the contact levels of the design stress and stress beyond the elastic limit.

- Material cleanliness level, surface roughness, mechanical properties, and heat treatment should be the same for the test discs and the investigated components. Furthermore, operating conditions such as loading level and direction, and the lubricant used should also be the same. This enables applying the testing results of the test discs on the real components instead of testing the real components.
- Investigating the effect of impact should be started with a test under lower impact loading levels than the conducted tests and preferred to be under a specific contact stress level (design stress), then increasing the impact loading under the same contact stress level. This procedure is important to evaluate the individual effect of impact loading before investigating its interactive effects.
- Simulation of the testing problem using the FE technique can provide significant information such as stress distribution, stress concentration, and the suitable contact loading level before the manufacturing of the test discs.
- Stress concentration should be used carefully to introduce high contact stress levels because increasing the concentration to a high level may affect the subsurface stress distribution and the maximum stress may be on the contact surface. This probably presents a spalling damage (surface initiation) mechanism which differs from the flaking mechanism (subsurface initiation). It is preferred to use the same edge geometry throughout the testing to produce identical stress concentration levels to that of real components in the service life.
- The four tests without stress concentration using a fully crowned test disc profile (plane stress contact), were conducted to introduce a qualitative analysis for the test disc life. The relatively quick failure of test discs after a number of cycles insufficient to produce a microstructural alteration. These tests were only conducted to avoid the stress concentration.
- The reliability of the experimental results can be increased by repeating the same tests at least three times and calculating the average life for each same testing group. However, fatigue testing is a time-consuming process, that prevents conducting the required repetition due to time limitations.
- The dependence on observing the damage for detecting the surface damage initiation is one of the test rig limitations. Using a sensor (ultra-sound damage detector), to specify the damage of the contact surface is strongly recommended for future tests. The dependence on observing the damage increases the percentage of error in analyzing the results because when the surface flaking initiation missed, the surface damage can produce a

percentage of error in the life analyses. However, this error was calculated and discussed and was found within the acceptable ranges.

- When a test is prepared on this test rig, the location of impact loading is preferred to be away from the test disc keyway to avoid introducing radial cracks connecting the keyway and the contact surface, especially after arriving the damage to an advanced level at the contact surfaces. This can be achieved by rotating the test rig gears (presented in [Figure 4-3](#)) separately before meshing them together.
- The tests of investigating the effect of SR should be performed under lower contact stresses and impact loading to confirm the finding of its effect under different contact stress levels presented in [Section 5.3.3](#).
- Surface roughness investigation within the damage region is important and should be conducted using the Alicona surface scanner to show whether the intrusion/extrusion mechanism is suitable to describe the RCF damage initiation. This does not mean the damage is a surface-initiated phenomenon because the investigation showed a competition between the surface and subsurface damage initiation and both of them may propagate towards each other and produce the final damage.
- Serial sectioning to characterize the subsurface damage distribution within whole the damage region probably will give a clearer view about the main stress which causes each damage feature type by correlating the damage distributions with the stress distributions. This because missing some damage features will have less effect on the results than investigating one surface.

8.2.2 Improving the test rig

This test rig was designed as one of the objectives to investigate the individual and interactive effects of rolling/sliding and impact on RCF life and subsurface damage features. In this rig, the compressive load is measured by a load cell and the value appears on a digital indicator. The time delay of the load cell sensor is relatively large compared with the impact loading time. Thus, the digital indicator was incapable to reveal the variation in the contact pressure within the impact loading period. For that, to improve the accuracy of impact loading measurement, a load cell with high sensitivity, i.e. has high accuracy and being a zero-order sensor with a high sample recording rate, with computer software to specify accurately the stress variation throughout the impact duration. This will increase the measurement accuracy of impact loading and compare the measured values with that achieved from theoretical impact formulas and there is no need to use the extensometer.

Introducing an acoustic sensor to sense the damage initiation on the contact surfaces will reduce the error in disc lives which previously depends on observing this damage on the contact surfaces. Improving the cam profile will make the impact force independent of the test rig rotational speed. This eliminates the effect of the rotational speed on the test disc life. The impact force after this improvement will depend on the spring stiffness attached to the impact lever (see [Appendix G](#)) and the equivalent mass of the impact lever.

Two flanged groove pulleys with speed ratio 1:1 and a timing belt can be used to transfer the power to the rig camshaft. This will reduce the possibility of slipping in the V-belt mechanism, furthermore, it will reduce the load on the camshaft bearings and hence the maintenance required. Details of this improvement can be seen in [Appendix G](#).

8.2.3 Improving the WTG design

Depending on the results of this study, the following recommendations to improve the design of wind turbine gearbox were specified.

- Improving the bearing race surface roughness. Despite this increases the bearing cost, this probably increases the bearing life by a significant percentage. The additional bearing life with the additional cost should be evaluated to decide whether this improvement is economical.
- Improving the design of the planetary pin by making it as a rotating part and supporting the pin ends by bearings then supporting the planetary discs from other locations rather than the pins. This will reduce the bending in these pins and reduce the probability of applying the contact load at a unique location.
- Re-evaluating the bearing design stresses. Despite using advanced techniques in calculating the bearing stress during the gearbox design, the service operating contact stress is higher than the yield limit of the bearing material. For that, the design stress of the WTGBs must be re-evaluated (reduced).
- Improving the lubricating and filtering systems to reduce the possibility of introducing hard particles between the contact surfaces. This to prevent excessive slipping and severe loading contact stress levels due to the lubricant contamination.
- Developing and/or improving the current new life prediction formulas to estimate the bearing life and managing the maintenance process. This will reduce the Operating and Maintenance (O&M) costs which will reduce the total cost of the wind energy.

- Because of the rigid connection of the rotor and the generator with the turbine gearbox, the transient loading directly transforms into the gearbox. This produces a high contact loading level, especially at the beginning of the grid connection and applying the mechanical brake. These high loading levels can be reduced by introducing two flexible couplings between the rotor and the gearbox and between the gearbox and the generator to absorb a significant fraction of these sudden loading changes.

REFERENCES

- [1] M. H. Evans, "White Structure Flaking Failure In Bearings Under Rolling Contact Fatigue," Ph.D. Thesis, University of Southampton (UK), 2013.
- [2] B. Gould, A. Greco, K. Stadler, and X. Xiao, "An Analysis of Premature Cracking Associated with Microstructural Alterations in an AISI 52100 Failed Wind Turbine Bearing Using X-Ray Tomography," *Materials and Design*, vol. 117, pp. 417–429, 2017.
- [3] T. Bruce, "Analysis of the Premature Failure of Wind Turbine Gearbox Bearings," Ph.D. thesis, The university of Sheffield (UK), 2016.
- [4] M. Paladugu and R. S. Hyde, "White Etching Matter Promoted by Intergranular Embrittlement," *Scripta Materialia*, vol. 130, pp. 219–222, 2017.
- [5] T. Bruce, H. Long, T. Slatter and R. Dwyer-Joyce, "Formation of White Etching Cracks at Manganese Sulfide (Mns) Inclusions in Bearing Steel due to Hammering Impact Loading," *Wind Energy*, Vol. 19, pp. 1903–1915, 2016.
- [6] D. Arent, S. Cohen, J. Davis, E. Degeorge, J. Deitchel, D. Feldman, H. Johnston, R. Leland, A. Livecchi, J. Logan, D. Mooney, R. Newmark, G. Perro, C. Stewart, B. Thresher and K. Wipke, *2016 Renewable Energy Data Book*. USA: US Department Of Energy (DOE), 2016.
- [7] W. Musial, P. Beiter, P. Schwabe, T. Tian, T. Stehly, and P. Spitsen, "2016 Offshore Wind Technologies Market Report," *U.S. Department of Energy*, USA, 2016.
- [8] J. Peeters, D. Vandepitte, and P. Sas, "Analysis of Internal Drive Train Dynamics in a Wind Turbine," *Wind Energy*, vol. 9, no. 1–2, pp. 141–161, 2006.
- [9] K. Stadler, and J. Baum, "Premature White Etching Crack Bearing Failures in Wind Gearboxes," *2014 STLE Annual Meeting & Exhibition*, Florida (USA), 2014.
- [10] K. Stadler and A. Stubenrauch, "Premature Bearing Failures in Wind Gearboxes and White Etching Cracks," *Power Transmission Engineering*. October, pp. 34–40, 2014.
- [11] L. Keer, M. Bryant, and G. Haritos, "Subsurface And Surface Cracking due to Hertzian Contact," *J. Lubr. Technol.*, vol. 104, no. 3, p. 347, 1982.
- [12] A. Bhattacharyya, G. Subhash, and N. Arakere, "Evolution of Subsurface Plastic Zone due to Rolling Contact Fatigue ff M-50 Nil Case Hardened Bearing Steel," *Int. J. Fatigue*, vol. 59, pp. 102–113, 2014.
- [13] M. Evans, A. Richardson, L. Wang, R. Wood, and W. Anderson, "Confirming Subsurface Initiation at Non-Metallic Inclusions as One Mechanism for White Etching Crack (WEC) Formation," *Trib. Int.*, vol. 75, pp. 87–97, 2014.
- [14] J. H. Kang, R. H. Vegter, and P. E. J. Rivera-Díaz-del-Castillo, "Rolling Contact Fatigue in Martensitic 100Cr6: Subsurface Hardening and Crack Formation," *Mater. Sci. Eng. A*, vol. 607, pp. 328–333, 2014.
- [15] K. Stadler, E. Vegter, M. Ersson and D. Vaes, "White Etching Cracks- A Consequence, Not a Root Cause of Bearing Failure," *SKF Evolution (2018)*, January (21-29), 2018.

- [16] L. Fingersh, M. Hand, A. Laxson, "Wind Turbine Design Cost and Scaling Model," *Technical Report, NREL/TP-500-40566*, December 2006.
- [17] P. J. Tavner, "Offshore Wind Turbine Reliability," *Supergen Wind Training*; Manchester, UK, 2011.
- [18] P. Tavner, J. Xiang, and F. Spinato, "Reliability Analysis for Wind Turbines," *Wind Energy*, vol. 10, no. 1, pp. 1–18, 2007.
- [19] W. Yang, P. J. Tavner, C. J. Crabtree, Y. Feng, and Y. Qiu, "Wind turbine condition monitoring : technical and commercial challenges," *Wind Energy*, vol. 17, pp. 673–693, 2014.
- [20] BS EN 61400-4:2013, "Wind turbines — Part 4 Design requirements for wind turbine gearboxes," *BSI Standard* publication, 2013.
- [21] F. Oyague, "Gearbox Modeling and Load Simulation of a Baseline 750-kW Wind Turbine Using State-of-the-Art Simulation Codes," *Technical Report, NREL/TP-500-41160*, February 2009 Colorado, USA, 2009.
- [22] S. Sheng, M. Mcdade, and R. Errichello, "Wind Turbine Gearbox Failure Modes – A Brief Gearbox Reliability Gearbox Failure Database, ASME/STLE," *International Joint Tribology Conference*, October, 2011, California (USA). 2011.
- [23] IEC 61400-1:2005, Wind turbines Part 1: Design requirements. *International standard*, Third edition, 2005.
- [24] M. H. Evans, "An Updated Review: White Etching Cracks (Weacs) and Axial Cracks in Wind Turbine Gearbox Bearings," *Mater. Sci. Technol.*, vol. 32, no. 11, pp. 1133–1169, 2016.
- [25] T. A. Harris and M.J. Motzala, "Rolling Bearing Analysis-Essential Concepts of Bearing Technology," Fifth Edition, Taylor & Francis Group, LLC., Boca Raton, USA, 2007.
- [26] M. Evans, L. Wang, H. Jones, and R. Wood, "White Etching Crack (WEC) Investigation by Serial Sectioning, Focused Ion Beam and 3-D Crack Modelling," *Tribology Int.*, vol. 65, pp. 146–160, 2013.
- [27] M. Evans, J. Walker, C. Ma, L. Wang, and R. Wood, "A FIB/TEM Study of Butterfly Crack Formation and White Etching Area (WEA) Microstructural Changes Under Rolling Contact Fatigue in 100Cr6 Bearing Steel," *Mater. Sci. Eng. A*, vol. A 570, pp. 127–134, 2013.
- [28] R. Errichello, R. Budny, and E. Rainer, "Investigations of Bearing Failures Associated with White Etching Areas (Weas) in Wind Turbine Gearboxes," *Tribo. Trans.*, vol. 56, no. 6, pp. 1069–1076, 2013.
- [29] M. Evans, A. Richardson, L. Wang, and R. Wood, Investigations of white etching crack (WEC) formation under rolling contact fatigue, Student poster Abstract. 2014, available on: <https://scholar.google.com/scholar?cites=307492037>.
- [30] M. Brückner, J. Gegner, A. Grabulov, W. Nierlich, and J. Slycke, "Butterfly Formation Mechanisms in Rolling Contact Fatigue," *Dtsch. Verband für Mater. und -prüfung e.V.*, pp. 101–106, 2011.

- [31] S. Mobasher, F. Sadeghi, K. Paulson, N. Weinzapfel, M. Correns, V. Bakolas and M. Dinkel, "Effect of Non-Metallic Inclusions on Butterfly Wing Initiation, Crack Formation, and Spall Geometry in Bearing Steels," *Int. J. Fatigue*, vol. 80, pp. 203–215, 2015.
- [32] A. Jones, "Effect of Structural Changes in Steel on Fatigue Life of Bearings," *Steel*, vol. 119, pp. 68-70, 1946.
- [33] M. Evans, "White structure flaking (WSF) in wind turbine gearbox bearings: effects of 'butterflies' and white etching cracks (WECs)," *Material Science and Technology*, vol.28 no.1, pp. 3-22, 2012.
- [34] S. Sheng, W. LaCava, P. S. Veers, and J. Keller, "Wind Turbine Drivetrain Condition Monitoring During GRC Phase 1 and Phase 2 Testing," *Technical Report, NREL/TP-5000-52748*, October 2011.
- [35] J. Rosinski, *1.3 MW Wind Turbine Measurement campaign Results and Analysis*, Transmission Dynamics, *Technical Report No. TD-08-2068*, 2008.
- [36] H. Link, J. Keller, Y. Guo, and B. McNiff, "Gearbox Reliability Collaborative Phase 3 Gearbox 2 Test Plan," *Technical Report, NREL/TP-5000-58190*, April 2013.
- [37] F. Oyague, "Gearbox Reliability Collaborative (GRC) Description and Loading," *Technical Report, NREL/TP-5000-47773*, November 2011.
- [38] K. Stadler, J. Lai, and R. Vegter, "A Review : The Dilemma with Premature White Etching Crack (WEC) Bearing Failures," *STP 1580*, pp. 487–508, available online at [www.astm.org / doi: 10.1520/STP158020140046](http://www.astm.org/doi/10.1520/STP158020140046), 2015.
- [39] I. Polonsky and L. Keer, "On White Etching Band Formation in Rolling Bearings," *J. Mech. Phys. Solids*, vol. 43, no. 4, pp. 637–669, 1995.
- [40] S. Kenneth , D. Infield, N. Barltrop, J. Coultate and A. Shahaj "Effect of Extreme Transient Loads on Wind Turbine Drive Train," *50th AIAA Aerosp. Sci. Meet. Incl. New Horizons Forum Aerosp. 2012*, p. 1-24, 2012.
- [41] K. Stadler, and Stubenrauch, "Premature Bearing Failures in Industrial Gearboxes," *Antriebstechnisches Kolloquium (ATK)*, SKF GmbH, no. 1, pp. 1–21, 2013.
- [42] T. Bruce, H. Long, and R. Dwyer-Joyce, "Dynamic Modelling of Wind Turbine Gearbox Bearing Loading During Transient Events," *IET Renew. Power Gener.*, vol. 9, no. 7, pp. 821–830, 2015.
- [43] Y. Kang, R. Evans, and G. Doll, "Roller-Raceway Slip Simulations of Wind Turbine Gearbox Bearings Using Dynamic Bearing Model," *Proc. STLE/ASME 2010 Int. Jt. Tribology Conf.*, pp. 1–3, 2010.
- [44] J. Helsen, Y. Guo, J. Keller and P. Guillaume, "Experimental Investigation of Bearing Slip in a Wind Turbine Gearbox During a Transient Grid Loss Event," *Wind Energy*, no. 19, pp. 2255–2269, 2016.
- [45] A. Oila and S. Bull, "Assessment of the Factors Influencing Micropitting In Rolling / Sliding Contacts," *Wear*, vol. 258, pp. 1510–1524, 2005.

- [46] J. Luyckx, "Hammering Wear Impact Fatigue Hypothesis WEC/irWEA Failure Mode on Roller Bearings," *Wind Turbine Tribology Semin.* Renaiss, (USA), 2011. Available on http://www.nrel.gov/wind/pdfs/day2_s.
- [47] J. Hoo, Rolling Contact Fatigue Testing of Bearing Steels, *ASTM SPECIAL TECHNICAL PUBLICATION 771, ASTM STP 771*, Philadelphia, (USA), 1985.
- [48] J. Ribrant and L. Bertling, "Survey of Failures in Wind Power Systems With Focus on Swedish Wind Power Plants During 1997-2005," *IEEE Trans. Energy Convers.*, vol. 22, no. 1, pp. 167–173, Mar. 2007.
- [49] B. Gould and A. Greco, "Investigating the Process of White Etching Crack Initiation in Bearing Steel," *Tribology Lett.*, vol. 62, pp. 1–14, 2016.
- [50] U. Zafar, "Literature Review of Wind Turbines," *ResearchGate*, 2018. Available on: <https://www.researchgate.net/publication/329680977>
- [51] Germanischer Lloyd Industrial Services GmbH, "Guideline for the Certification of Wind Turbines Safety System , Protective and Monitoring Devices," Germanischer Lloyd Industrial Services (Germany), p. 1–384, 2010.
- [52] H. Al-hamadani, T. An, M. King, and H. Long, "System Dynamic Modelling of Three Different Wind Turbine Gearbox Designs Under Transient Loading Conditions," *International Journal of Precision Engineering And Manufacturing*, vol. 18, no. 11, pp. 1659–1668, 2017.
- [53] J. Keller, "Drivetrain Reliability Collaborative Workshop and Current Events," *Wind Turbine Tribology Seminar*, NREL/PR-5000-67443, Illinois (USA), 2016. Available at: <https://www.nrel.gov/docs/fy17osti/67443.pdf>
- [54] J. Keller and R. Wallen, "Gearbox Reliability Collaborative Phase 3 Gearbox 3 Test," *Technical Report, NREL/TP-5000-67612*, February, 2017. Available at: <https://www.nrel.gov/docs/fy15osti/63693.pdf>
- [55] W. LaCava, Y. Guo, C. Marks, Y. Xing, and T. Moan, "Three-Dimensional Bearing Load Share Behaviour in the Planetary Stage of a Wind Turbine Gearbox," *IET Renew. Power Gener.*, vol. 7, no. 4, pp. 359–369, 2013.
- [56] T. Lund, "Subsurface Initiated Rolling Contact Fatigue - Influence of Non-Metallic Inclusions, Processing Conditions and Operating Conditions," *J. ASTM Int.*, vol. 7, no. 5, pp. 1–12, 2010.
- [57] S. Sheng, "Wind Turbine Gearbox Reliability Database , Condition Monitoring , and Operation and Maintenance Research Update," *Drivetrain Reliability Collaborative Workshop*, Colorado (USA), February 16–17, 2016.
- [58] J. Keller, S. Sheng, J. Cotrell and A. Greco, "Wind Turbine Drivetrain Reliability: Tribology Collaborative," *Wind and Water Power Program, US Department of Energy*, Colorado (USA), 2016.
- [59] J. C. Jauregui, I. Torres, R. Garcia, and A. Leon, "Housing Stiffness Influence on Gearbox Dynamics Loading for Wind Turbine Applications," *Proc. ASME Turbo Expo 2012 GT 2012*, 2012.

- [60] S. Shanbr, F. Elasha, M. Elforjani, and J. A. Teixeira, "Bearing Fault Detection within Wind Turbine Gearbox," *Proc. - 2017 Int. Conf. Sensing, Diagnostics, Progn. Control. SDPC 2017*, December, 2017.
- [61] J. Yoon and D. He, "Planetary Gearbox Fault Diagnostic Method Using Acoustic Emission Sensors," *IET Sci. Meas. Technol.*, vol. 9, no. 8, pp. 936–944, 2015.
- [62] F. Oswald, E. Zaretsky, and J. Poplawski, "Interference-Fit Life Factors for Roller Bearings," *Tribology. Trans.*, vol. 52, no. 4, pp. 415–426, 2009.
- [63] S. Sheng and P. Veers, "Wind Turbine Drivetrain Condition Monitoring - An Overview," *Mach. Fail. Prev. Technol. Appl. Syst. Heal. Manag. Conf. 2011*, October, 2011.
- [64] J. Tautz-weinert, S. Watson, "Using SCADA Data for Wind Turbine Condition Monitoring – A Review," *EIT Journals, The Institute of Engineering and Technology, IET Renewable Power Generation*, pp. 1–13, 2016.
- [65] H. Long, J. Wu, and P. J. Tavner, "Analysis of Statistical Loading Conditions of Wind Turbine Gearboxes Based on SCADA Data," *Eur. Wind Energy Conf.*, 2012.
- [66] B. Gould and A. Greco, "The Influence of Sliding and Contact Severity on the Generation of White Etching Cracks," *Tribology. Lett.*, vol. 60, no. 2, 2015.
- [67] L. Niu, H. Cao, Z. He, and Y. Li, "Dynamic Modeling and Vibration Response Simulation for High Speed Rolling Ball Bearings With Localized Surface Defects in Raceways," *Journal of Manufacturing Science and Engineering*, vol. 136, 2014.
- [68] K. Chan, "Roles of Microstructure in Fatigue Crack Initiation," *Int. J of Fatigue*, vol. 32, pp. 1428–1447, 2010.
- [69] M. Kohara, T. Kawamura, and M. Egami, "Study on Mechanism of Hydrogen Generation from Lubricants," *Tribology Trans.*, vol. 49, no. 1, pp. 53–60, 2006.
- [70] M. N. Kotzalas and G. L. Doll, "Tribological advancements for reliable wind turbine performance," *Philos. Trans. R. Soc.*, vol. 368, pp. 4829–4850, 2010.
- [71] J. Lord and R. Larsson, "Effects of Slide-Roll Ratio and Lubricant Properties on Elastohydrodynamic Lubrication Film Thickness and Traction," *Proc. Instn. Mech. Engrs. Part J J. Eng. Tribology.*, vol. 215, no. 3, pp. 301–308, 2001.
- [72] W. Nierlich and J. Genger, "Frictional Surface Crack Initiation and Corrosion Fatigue Driven Crack Growth," *Wind Turbine Tribology Semin.*, NREL Workshop, Broomfield, 2011.
- [73] Y. Murakami, "Effects of Small Defects and Nonmetallic Inclusions on the Fatigue Strength of Metals," *JSME Int. J.*, vol. 32, no. 2, pp. 167–180, 1989.
- [74] Y. Murakami and M. Endo, "Effects of Defects, Inclusions and Inhomogeneities on Fatigue Strength," *Fatigue*, vol. 16, no. 3, pp. 163–182, 1994.
- [75] Y. Murakami and S. Beretta, "Small Defects and Inhomogeneities in Fatigue Strength: Experiments, Models and Statistical Implications," *Extremes*, Vol. 2, pp. 123–147, 1999. Available on: <https://doi.org/10.1023/A:1009976418553>.

- [76] ISO 4967-2013(E), Steel — Determination of content of nonmetallic inclusions — Micrographic method using standard diagrams. *International Standard*, Third edition, 2013.
- [77] Y. Neishi, T. Makino, N. Matsui, H. Matsumoto, M. Higashida and H. Ambai, "Influence of the Inclusion Shape on the Rolling Contact Fatigue Life of Carburized Steels," *Metallurgical and Materials Transactions A*, vol. 44A, pp. 2131–2140, 2013.
- [78] T. Makino, Y. Neishi, D. Shiozawa, Y. Fukuda, K. Kajiwara, and Y. Nakai, "Evaluation of rolling contact fatigue crack path in high strength steel with artificial defects," *Int. J. Fatigue*, vol. 68, pp. 168–177, 2014.
- [79] M. Lewis and B. Tomkins, "A Fracture Mechanics Interpretation of Rolling Bearing Fatigue," *Proc. Inst. Mech. Eng. Part J J. Eng. Tribology*, vol. 226, no. 5, pp. 389–405, 2012.
- [80] B. Jalalahmadi, F. Sadeghi, and V. Bakolas, "Material Inclusion Factors for Lundberg-Palmgren – Based RCF Life Equations," *Tribology Trans.*, vol. 54, pp. 457–469, 2011.
- [81] Y. Yang, Y. Zheng, and Z. Yang, "The Failure Models Induced by White Layers During Impact Wear," *Wear*, vol. 185, pp. 17–22, 1995.
- [82] R. Sayles and E. Ioannides, "Debris Damage in Rolling Bearings and Its Effects on Fatigue Life," *J. Tribology*, vol. 110, p. 26-31, 1988.
- [83] G. Morales-Espejel and A. Gabelli, "The Progression of Surface Rolling Contact Fatigue Damage of Rolling Bearings With Artificial Dents," *Tribology Trans.*, vol. 58, no. 3, pp. 418–431, 2015.
- [84] W. Solano-alvarez, E. Pickering, and H. Bhadeshia, "Degradation of Nanostructured Bainitic Steel Under Rolling Contact Fatigue," *Materials Science & Engineering A*, vol. 617, pp. 156–164, 2014.
- [85] P. Johns and R. Gohar, "Roller Bearings Under Radial and Eccentric Loads," *Tribology Int.*, pp. 131–136, 1981.
- [86] J. V Poplawski, S. Peters and E. Zaretsky, "Effect Of Roller Profile on Cylindrical Roller Bearing Life Prediction — Part I : Comparison of Bearing Life Theories," *Tribology Trans.*, vol. 44, pp 329-350, 2001.
- [87] N. Ahmadi, L. Keer and T. Mura, "Non-Hertzian Contact Stress Analysis for an Elastic Half Space-Normal and Sliding Contact.," *Int. J. solid Struct.*, vol. 19, no. 4, pp. 357–373, 1983.
- [88] M. J. Hartnett, "The Analysis of Contact Stresses in Rolling Element Bearings," *J. Lubr. Technol.*, vol. 101, no. 1, pp. 105–109, 1979.
- [89] E. Kerscher, "Influence of Microstructure and Micro Notches on the Fatigue Limit," *Procedia Eng.*, vol. 74, pp. 210–217, 2014.
- [90] X. Yang, J. Zhou, and X. Ling, "Influences of Surface Grain Size and Gradient Variation Along Depth on Fatigue Life of Metallic Materials," *Mater. Des.*, vol. 43, pp. 454–459, 2013.

- [91] S. Osovski, D. Rittel, and A. Venkert, "The Respective Influence of Microstructural and Thermal Softening on Adiabatic Shear Localization," *Mech. Mater.*, vol. 56, pp. 11–22, 2013.
- [92] F. Oswald, E. Zaretsky, and J. Poplawski, "Effect of Internal Clearance on Load Distribution and Life of Radially Loaded Ball and Roller Bearings," *Tribology Trans.*, vol. 55, no. 2, pp. 245–265, 2012.
- [93] Y. Guo, J. Keller, Z. Zhang, and D. Lucas, "Planetary Load Sharing in Three Point Mounted Wind Turbine Gearboxes: A Design and Test Comparison," 3rd Conference for Wind Power Drives, Aachen, Germany, March 8, 2017, 2017.
- [94] N. Garabedian, B. Gould, G. Doll, and D. Burris, "The Cause of Premature Wind Turbine Bearing Failures: Overloading or Underloading?," *Tribology Trans.*, vol. 2004, pp. 1–10, 2018.
- [95] J. Loos, I. Bergmann, and M. Goss, "Influence of Currents from Electrostatic Charges on WEC Formation in Rolling Bearings," *Tribology Trans.*, vol. 59, no. 5, pp. 865–875, 2016.
- [96] M. Ščepanskis, B. Gould, and A. Greco, "Empirical Investigation of Electricity Self-Generation in a Lubricated Sliding–Rolling Contact," *Tribology Lett.*, vol. 65, no. 109, p. 1–10, 2017.
- [97] N. Maharjan, W. Zhou, and Y. Zhou, "Microstructural Study of Bearing Material Failure due to Rolling Contact Fatigue In Wind Turbine Gearbox," *Proc. Int. Symp. Curr. Res. Hydraul. Turbines*, 2016.
- [98] M. Evans, A. D. Richardson, L. Wang, and R. Wood, "Serial Sectioning Investigation of Butterfly and White Etching Crack (WEC) Formation In Wind Turbine Gearbox Bearings," *Wear*, vol. 302, pp. 1573–1582, 2013.
- [99] W. Holweger, M. Wolf, D. Merk, T. Blass, M. Goss, J. Loos, S. Barteldes and A. Jakovics, "White Etching Crack Root Cause Investigations," *Tribology Trans.*, vol. 58, no. 1, pp. 59–69, 2015.
- [100] T. Bruce, H. Long, and R. S. Dwyer-Joyce, "Threshold Maps for Inclusion-Initiated Micro-Cracks and White Etching Areas in Bearing Steel: The Role of Impact Loading and Surface Sliding," *Tribology Lett.*, vol. 66, no. 111, pp. 1–18, 2018.
- [101] BS EN 61400-2:2014, Standards Publication Wind turbines — Part 2: Small wind turbines, *BSI Standard Publication*, 2014.
- [102] BS EN 61400-3:2009, Standards Publication Wind turbines — part 3 Design requirements for offshore wind turbines, *BSI Standard Publication*, 2009.
- [103] BS ISO 81400-4:2005, Wind turbines Part 4 : Design and specification of gearboxes, *British Standard*, 2005.
- [104] ISO 281:2007, Method of Calculating Dynamics Load Ratings and Rating Life of Rolling Bearings, *ISO Standard Publication*, 2007.

- [105] D. Vaes, Y. Guo, P. Tesini and J. Keller, "Investigation of Roller Sliding in Wind Turbine Gearbox High-Speed-Shaft Bearings," *Technical Report, NREL/TP-5000-73286*, May, 2019.
- [106] B. Gould and D. Burris, "Effects of Wind Shear on Wind Turbine Rotor Loads and Planetary Bearing Reliability," *Wind Energy*, Vo. 19, pp. 1011–1021, 2016.
- [107] K. Hiraoka, M. Nagao, and T. Isomoto, "Study on Flaking Process in Bearings by White Etching Area Generation," *J. ASTM Int.*, vol. 3, no. 5, pp. 1–7, 2006.
- [108] H. Harada, T. Mikami, M. Shibata, D. Sokai, A. Yamamoto, and H. Tsubakino, "Microstructural Changes and Crack Initiation with White Etching Area Formation under Rolling/Sliding Contact in Bearing Steel," *ISIJ Int.*, vol. 45, no. 12, pp. 1897–1902, 2005.
- [109] A. Martin, S. Borgese, and A. Eberhardt, "Microstructural Alterations of Rolling — Bearing Steel Undergoing Cyclic Stressing," *J. Basic Eng. Eng. ASME*, no. 65, pp. 555–565, 1966.
- [110] H. Uyama, H. Yamada, H. Hidaka, and N. Mitamura, "The Effects of Hydrogen on Microstructural Change and Surface Originated Flaking in Rolling Contact Fatigue," *Tribology Online*, vol. 6, no. 2, pp. 123–132, 2011.
- [111] Y. Murakami, M. Naka, A. Iwamoto, and G. Chatell, "Long Life Bearings for Automotive Alternator Applications," *SAE Tech. Pap. Ser.*, no. 950944, pp. 1–14, 1995.
- [112] X. Qin, D. Le Sun, and L. Xie, "Analysis of Critical Stress for Subsurface Rolling Contact Fatigue Damage Assessment Under Roll/Slide Contact," *J. Fail. Anal. Prev.*, vol. 14, pp. 61–67, 2014.
- [113] Y. Guo, J. Keller, T. Moan, and Y. Xing, "Model Fidelity Study of Dynamic Transient Loads in a Wind Turbine Gearbox," *Wind. Conf. Am. Wind Energy Assoc.*, NREL/CP-5000-58414, presented at the 2013 WINDPOWER Conference Chicago (USA), 2013.
- [114] D. Kuhlmann-Wilsdorf, "The Theory of Dislocation-Based Crystal Plasticity," *Philos. Mag. Phys.*, vol. 79, no. 4, pp. 955–1008, 1999.
- [115] H. K. Danielsen, F. Guzman, K. Dahl, Y. Li, J. Wu, G. Jacobs, G. Burghardt, S. Faester, H. Alimadadi, S. Goto, D. Raabe, and R. Petrov, "Multiscale characterization of White Etching Cracks (WEC) in a 100Cr6 bearing from a thrust bearing test rig," *Wear*, vol. 370, pp. 73–82, 2017.
- [116] J. Keller, B. Gould, and A. Greco, "Investigation of Bearing Axial Cracking : Benchtop and Full-Scale Test Results," *Technical Report, NREL/TP-5000-67523*, August 2017.
- [117] F. Guzmán, M. Oezel, G. Jacobs, G. Burghardt, C. Broeckmann, and T. Janitzky, "Influence of Slip and Lubrication Regime on the Formation of White Etching Cracks on a Two-Disc Test Rig," *Lubricants*, vol. 6, pp. 1-8, 2018.
- [118] A. Ruellan, F. Ville, X. Kleber, A. Arnaudon, and D. Girodin, "Understanding White Etching Cracks in Rolling Element Bearings: The Effect of Hydrogen Charging on the Formation Mechanisms," *J. of Eng. Tribology Proc. Inst. Mech. Eng.*, vol. 228, no. 11, pp. 1252–1265, 2014.

- [119] S. Li, "A Computational Study on the Influence of Surface Roughness Lay Directionality on Micropitting of Lubricated Point Contacts," *J. of Tribology*, vol. 137, pp. 1–10, 2015.
- [120] G. Wan, H. Lankamp, A. Vries, and E. Ioannides, "The effect of Extreme Pressure (EP) Lubricants on Life of Rolling Element Bearings," *J. of Eng. Tribology*, vol. 208, pp. 247–252, 1994.
- [121] J. Campbell, *Complete Casting Hand Book Metal Casting Processes, Metallurgy, Techniques and Design*, 2nd Edition, Elsevier, 2011.
- [122] H. Matsunaga, H. Komata, and J. Yamabe, Y. Fukushima, S. Matsuoka, "Effect of Size and Depth of Small Defect on the Rolling Contact Fatigue Strength of Bearing Steel JIS-SUJ2," *Procedia Material Science*, vol. 3, pp. 1663–1668, 2014.
- [123] K. Koumi, T. Chaise, and D. Nelias, "Rolling Contact of a Rigid Sphere/Sliding of a Spherical Indenter Upon a Viscoelastic Half-Space Containing an Ellipsoidal Inhomogeneity," *J. Mech. Phys. Solids*, vol. 80, pp. 1–25, 2015.
- [124] H. K. Bhadeshia, "Steels for Bearings," *Prog. in Mat. Sci.*, vol. 57, pp. 268–435, 2012.
- [125] J. Šmeļova, A. Schwedt, L. Wang, W. Holweger, T. Harvey, and J. Mayer, "A Study of Microstructure Alteration in AISI 52100 Bearings due to Classic Rolling Contact Fatigue and White Ething Crack," 2016 STLE Annual Meeting & Exhibition, Nevada (USA), 2016.
- [126] K. Rege and D. Pavlou, "A One-Parameter Nonlinear Fatigue Damage Accumulation Model," *International Journal of Fatigue*, vol. 98, pp. 234–246, 2017.
- [127] J. Guan, L. Wang, and C. Zhang, and X. Ma "Effects of Non-Metallic Inclusions on the Crack Propagation in Bearing Steel," *Tribology Int.*, vol. 106, pp. 123–131, 2017.
- [128] U. Zerbst, M. Madia, and H. T. Beier, "A Model for Fracture Mechanics Based Prediction of the Fatigue Strength : Further Validation and Limitations," *Eng. Fract. Mech.*, vol. 130, pp. 65–74, 2014.
- [129] A. Karrigan, J. Kuijpers, A. Gabelli, and E. Ioannides, "Cleanliness of Bearing Steels and Fatigue Life of Rolling Contacts," *J. of ASTM Inter.*, vol. 3, no. 6, pp. 101–106, 2006.
- [130] K. Hashimoto, T. Fujimatsu, N. Tsunekage, K. Hiraoka, K. Kida, and E. Santos, "Study of Rolling Contact Fatigue of Bearing Steels In Relation to Various Oxide Inclusions," *Mater. & Design*, vol. 32, pp. 1605–1611, 2011.
- [131] A. Grabulov, *Fundamentals of Rolling Contact Fatigue*, Ph.D. Thesis, University of Belgrade, Serbia, 2010.
- [132] H. Mayer, W. Haydn, R. Schuller, S. Issler, and M. Bacher-Höchst, "Very High Cycle Fatigue Properties of Bainitic High Carbon-Chromium Steel Under Variable Amplitude Conditions," *Int. J. Fatigue*, vol. 31, pp. 1300–1308, 2009.
- [133] H. Singh, R. V. Pulikollu, W. Hawkins, and G. Smith, "Investigation of Microstructural Alterations in Low- and High-Speed Intermediate-Stage Wind Turbine Gearbox Bearings," *Tribology Lett.*, vol. 65, No. 81, pp. 1–13, 2017.

- [134] P. Zerres, and M. Vormwald, "Review of Fatigue Crack Growth Under Non-Proportional Mixed-Mode Loading," *Int. J. Fatigue*, vol. 58, no. 0, pp. 1–14, 2014.
- [135] R. Vegter, and J. Slycke, "The Role of Hydrogen on Rolling Contact Fatigue Response of Rolling Element Bearings," *J. ASTM Int.*, vol. 7, No. 2, p. 1-12, 2009.
- [136] J. Hirth, "Effects of Hydrogen on the Properties of Iron and Steel," *Metall. Trans. A*, vol. 11A, no. 6, pp. 861–890, 1980.
- [137] B. Szost, R. Vegter, and P. Rivera-Díaz-del-Castillo, "Developing Bearing Steels Combining Hydrogen Resistance and Improved Hardness," *Mater. & Design*, vol. 43, pp. 499–506, 2013.
- [138] H. Lü, M. Li, T. Zhang, and W. Chu, "Hydrogen-Enhanced Dislocation Emission, Motion and Nucleation of Hydrogen-Induced Cracking for Steel," *Sci. in China Ser. E, Technol. Sci.*, vol. 40, no. 5, pp. 530–538, 1997.
- [139] M. Stopher, and P. Rivera-diaz-del-castillo, "Hydrogen Embrittlement in Bearing Steels," *Material Science and Technology*, vol. 32, No. 11, pp. 1184-1193, 2016.
- [140] B. Szost and P. Rivera-Díaz-Del-Castillo, "Unveiling the Nature of Hydrogen Embrittlement in Bearing Steels Employing: A New Technique," *Scr. Mater.*, vol. 68, No. 7, pp. 467–470, 2013.
- [141] K. Takai, H. Shoda, H. Suzuki, and M. Nagumo, "Lattice defects dominating hydrogen-related failure of metals," *Acta Mater.*, vol. 56, pp. 5158–5167, 2008.
- [142] S. Fujita, S. Matsuoka, Y. Murakami, and G. Marquis, "Effect of Hydrogen on Mode II Fatigue Crack Behavior of Tempered Bearing Steel and Microstructural Changes," *Int. J. Fatigue*, vol. 32, No. 6, pp. 943–951, 2010.
- [143] R. Oriani, "Hydrogen - the Versatile Embrittler," *Corrosion-NACE*, vol. 43, No. 7, pp. 390–397, 1987.
- [144] J. Kang and P. E. Rivera-diaz-del-castillo, "Carbide Dissolution in Bearing Steels," *Comput. Mater. Sci.*, vol. 67, pp. 364–372, 2013.
- [145] E. Kerscher, K. Lang, and D. Löhe, "Boundaries for Increasing The Fatigue Limit of the Bearing Steel SAE 52100 by Thermomechanical Treatments," *Procedia Eng.*, vol. 10, pp. 1985–1990, 2011.
- [146] Y. J. Li, M. Herbig, S. Goto, and D. Raabe, "Atomic Scale Characterization of White Etching Area and Its Adjacent Matrix in a Martensitic 100Cr6 Bearing Steel," *Materials Characterization.*, vol. 123, pp. 349–353, 2017.
- [147] S. Ooi, A. Gola, R. Vegter, P. Yan, and K. Stadler, "Evolution of White-Etching Cracks and Associated Microstructural Alterations During Bearing Tests," *Mater. Sci. Technol. (United Kingdom)*, vol. 33, no. 14, pp. 1657–1666, 2017.
- [148] BS ISO 15243 : 2017, Rolling bearings — Damage and failures - Terms, characteristics and causes, *BSI Standards Publication*, 2017.

- [149] C. Bujoreanu, and S. Cretu "Temperature Influence on Bearing Scuffing Failure," *Tribology in industry*, vol. 26, no. 3, pp. 39–43, 2004.
- [150] B. Pyttel, D. Schwerdt, and C. Berger, "Very High Cycle Fatigue - is There a Fatigue Limit?," *Int. J. Fatigue*, vol. 33, no. 1, pp. 49–58, 2011.
- [151] P. Rycerz, A. Olver, and A. Kadiric, "Propagation of Surface Initiated Rolling Contact Fatigue Cracks in Bearing Steel," *Int. J. Fatigue*, vol. 97, pp. 29–38, 2016.
- [152] J. Bush, W. Grube, and G. Robinson, "Microstructural and Residual Stress Changes in Hardened Steel due to Rolling Contact," *Proc. General Motors Symp. Rolling Contact Phenomena, Detroit 1960, Elsevier*, 1960.
- [153] M. Cerullo, "Sub-Surface Fatigue Crack Growth at Alumina Inclusions in AISI 52100 Roller Bearings," *Procedia Eng.*, vol. 74, pp. 333–338, 2014.
- [154] T. Lund, "Sub-Surface Initiated Rolling Contact Fatigue — Influence of Non-Metallic Inclusions , Processing History , and Operating Conditions," *J. ASTM Int.*, vol. 7, No. 5, pp. 1–12, 2010.
- [155] H. Al-Tameemi, H. Long, and R. Dwyer-Joyce, "Initiation of Sub-Surface Micro-Cracks and White Etching Areas From Debonding at Non-Metallic Inclusions in Wind Turbine Gearbox Bearing," *Wear*, vol. 406–407, pp. 22–32, 2018.
- [156] J. A. Bomidi and F. Sadeghi, "Three-Dimensional Finite Element Elastic–Plastic Model for Subsurface Initiated Spalling in Rolling Contacts," *J. Tribology*, vol. 136 / 011402-1, 2013.
- [157] A. Grabulov, R. Petrov, and H. Zandbergen, "EBSD Investigation of the Crack Initiation and TEM/FIB Analyses of the Microstructural Changes Around The Cracks Formed Under Rolling Contact Fatigue (RCF)," *Int. J. Fatigue*, vol. 32, pp. 576–583, 2010.
- [158] Y. Murakami, *Metal Fatigue: Effect of Small Defects and Non-Metallic Inclusions. Elsevier Science Ltd.*, 2002.
- [159] A. Warhadpande, F. Sadeghi, M. Kotzalas, and G. Doll, "Effects of Plasticity on Subsurface Initiated Spalling in Rolling Contact Fatigue," *Int. J. Fatigue*, vol. 36, no. 1, pp. 80–95, 2012.
- [160] T. Karsch, H. Bomas, H. Zoch, and S. Mändl, "Influence of Hydrogen Content and Microstructure on the Fatigue Behaviour of Steel SAE 52100 in the VHCF Regime," *Int. J. Fatigue*, vol. 60, pp. 74–89, 2013.
- [161] W. Solano-Alvarez and H. Bhadeshia, "White-Etching Matter in Bearing Steel. Part 2: Distinguishing Cause and Effect in Bearing Steel Failure," *Metall. Mater. Trans. A*, vol. 45, pp. 4907–4915, 2014.
- [162] J. Barry and G. Byrne, "TEM Study on the Surface White Layer in Two Turned Hardened Steels," *Mater. Sci. Eng.*, vol. A 325, no. 31, pp. 356–364, 2002.
- [163] A. Warhadpande, F. Sadeghi, and R. Evans, "Microstructural Alterations in Bearing Steels Under Rolling Contact Fatigue Part 1-Historical Overview," *Tribology Trans.*, vol. 56, no. 3, pp. 349–358, 2012.

- [164] H. Swahn, P. Becker, and O. Vingsbo, "Martensite Decay During Rolling Contact Fatigue in Ball Bearings," *Metall. Trans. A*, vol. 7A, pp. 1099–1110, 1976.
- [165] W. Solano-alvarez, E. Pickering, M. Peet, K. Moore, J. Jaiswal, and A. Bevan, "Soft Novel Form of White-Etching Matter And Ductile Failure of Carbide- Free Bainitic Steels Under Rolling Contact Stresses," *Acta Materialia*, vol. 121, pp. 215–226, 2016.
- [166] A. Richardson, M. Evans, L. Wang, R. Wood, M. Ingram, and B. Meuth, "The Evolution of White Etching Cracks (WECs) in Rolling Contact Fatigue-Tested 100Cr6 Steel," *Tribology Lett.*, vol. 66, no. 1, pp. 1–23, 2018.
- [167] O. Zwirlein and H. Shlicht, "Rolling Contact Fatigue Mechanisms - Accelerated Testing versus Field performance," *ASTM Inter.*, vol. 771, pp. 358–379, 1982.
- [168] D. Schwach and Y. Guo, "A Fundamental Study on the Impact of Surface Integrity by Hard Turning on Rolling Contact Fatigue," *Int. J. Fatigue*, vol. 28, pp. 1838–1844, 2006.
- [169] A. Ramesh, S. Melkote, L. Allard, L. Riestler, and T. Watkins, "Analysis of White Layers Formed in Hard Turning of AISI 52100 Steel," *Mater. Sci. Eng. A*, vol. 390, pp. 88–97, 2005.
- [170] G. Baumann, H. Fecht, and S. Liebelt, "Formation of White-Etching Layers on Rail Treads," *Wear*, vol. 191, pp. 133–140, 1996.
- [171] A. Voskamp, "Material Response to Rolling Contact Loading," *J. Tribology, (Transaction of the ASME)*, vol. 107, no. 3, p. 359-364, 1985.
- [172] H. Swahn, P. Becker, and O. Vingsbo, "Electron-Microscope Studies of Carbide Decay During Contact Fatigue in Ball Bearings," *Metal. Sci.*, vol. 10, no. 1, pp. 35–39, 1976.
- [173] H. Schlicht, E. Schreiber, and O. Zwirlein, "Effect of Material Properties on Bearing Steel Fatigue Strength," *ASTM Int.*, pp. 81–101, 1988.
- [174] J. Kang, B. Hosseinkhani, R. Vegter, and P. Rivera-Díaz-Del-Castillo, "Modelling Dislocation Assisted Tempering During Rolling Contact Fatigue in Bearing Steels," *Int. J. Fatigue*, vol. 75, pp. 115–125, 2015.
- [175] J. Gegner, "Tribological Aspects of Rolling Bearing Failures," *Tribology Lubricants and Lubrication*, pp. 33–94, 2011.
- [176] P. Becker, "Microstructural Changes Around Non-Metallic Inclusions Caused by Rolling-Contact Fatigue of Ball-Bearing Steels," *Metals Technology*, vol. 8, no. 1, pp. 234–243, 1981.
- [177] A. Grabulov, U. Ziese, and H. Zandbergen, "TEM/SEM Investigation of Microstructural Changes Within the White Etching Area Under Rolling Contact Fatigue and 3-D Crack Reconstruction by Focused Ion Beam," *Scripta. Materialia*, vol. 57, No. 7, pp. 635–638, 2007.
- [178] V. Šmejlova, A. Schwedt, L. Wang, W. Holweger, and J. Mayer, "Electron Microscopy Investigations of Microstructural Alterations due to Classical Rolling Contact Fatigue (RCF) in Martensitic AISI 52100 Bearing Steel," *Int. J. Fatigue*, vol. 98, pp. 142–154, 2017.

- [179] A. Voskamp, R. Österlund, P. Becker, and O. Vingsbo, "Gradual Changes in Residual Stress and Microstructure During Contact Fatigue in Ball Bearings," *Metals Technology*, vol. 7, no. 1, pp. 14–21, 1980.
- [180] B. Gould, A. Greco, K. Stadler, E. Vegter, and X. Xiao, "Using Advanced Tomography Techniques to Investigate the Development of White Etching Cracks in a Prematurely Failed Field Bearing," *Tribology Int.*, vol. 116, pp. 362–370, 2017.
- [181] Y. Kadin and M. Sherif, "Energy Dissipation at Rubbing Crack Faces in Rolling Contact Fatigue as the Mechanism of White Etching Area Formation," *Int. J. Fatigue*, vol. 96, pp. 114–126, 2017.
- [182] W. Šmeļova, A. Schwedt, L. Wang, W. Holweger, T. Harvey, and J. Mayer, "A Study of Microstructure Alteration In AISI Bearings due to Classic Rolling Contact Fatigue and White Etching Crack," *2016 STLE Annual Meeting & Exhibition*, vol. L. Vegas (USA), 2016.
- [183] W. Solano-Alvarez, J. Duff, M. Smith, and H. Bhadeshia, "Elucidating White-Etching Matter Through High-Strain Rate Tensile Testing," *Mater. Sci. Technol. (United Kingdom)*, vol. 33, pp. 307–310, 2016.
- [184] K. Iso, A. Yokouchi, and H. Takemura, "Research Work for Clarifying the Mechanism of White Structure Flaking and Extending the Life of Bearings," *SAE Tech. Pap. Series*, SAE International, pp. 1–12, 2005.
- [185] Y. Imai, T. Endo, D. Dong, and Y. Yamamoto, "Study on Rolling Contact Fatigue in Hydrogen Environment at a Contact Pressure Below Basic Static Load Capacity," *Tribology Trans.*, vol. 53, pp. 764–770, 2010.
- [186] N. Kino and K. Otani, "The Influence of Hydrogen on Rolling Contact Fatigue Life and Its Improvement," *JSAE Rev.*, vol. 24, no. 3, pp. 289–294, 2003.
- [187] A. Vincent, G. Lormand, P. Lamagnere, L. Gosset, D. Girodin, G. Dudragne and R. Fougères, "From White Etching Areas Formed Around Inclusions to Crack Nucleation in Bearing Steels Under Rolling Contact Fatigue," *ASTM International*, pp. 109–123, 1998.
- [188] O. Umezawa and K. Nagai, "Effects of Test Temperature on Internal Fatigue Crack Generation Associated with Nonmetallic Particles in Austenitic Steels," *Metall. Mater. Trans.*, vol. 29A, pp. 3017–3028, 1998.
- [189] G. Guetard, I. Toda-Caraballo, and P. Rivera-Diaz-del-Castillo, "Damage Evolution Around Primary Carbides Under Rolling Contact Fatigue in VIM – VAR M50," *Int. J. Fatigue*, vol. 91, pp. 59–67, 2016.
- [190] H. Takemura, Y. Matsumoto, and Y. Murakami, "Development of a New Life Equation for Ball and Roller Bearings," *SAE Technical Paper Series*, pp. 1-9, 2000.
- [191] F. Sadeghi, B. Jalalahmadi, T. S. Slack, N. Raje, and N. K. Arakere, "A Review of Rolling Contact Fatigue," *J. Tribology*, vol. 131, no. 4, p. 1-15, 2009.
- [192] H. H. Hertz, "Hertz's miscellaneous papers", *MacMillan, London (UK)*, 1896.
- [193] A. Fischer-Cripps, *Introduction to Contact Mechanics*. Springer-Verlag, New York (USA), 2000.

- [194] A. Olver, "The Mechanism of Rolling Contact Fatigue: An Update," *Proc. Inst. IMechE. Part J: J. Eng. Tribology*, vol. 219, pp. 313–330, 2005.
- [195] G. Stachwowiak and A. Batchelor, *Engineering Tribology*, 3rd ed. Oxford, (UK), Elsevier, 2006.
- [196] T. Harris, and W. Yu, "Lundberg-Palmgren Fatigue Theory : Considerations of Failure Stress and Stressed Volume," *J. of Tribology*, vol. 121, pp. 85-89, 1999.
- [197] T. Harris and R. Barnsby, "Life Ratings for Ball and Roller Bearings," *Proc. Instn. Mech. Engrs.*, vol. 215, *Part J*, pp. 577–596, 2001.
- [198] S. Kabus, M. Hansen, and O. Mouritsen, "A New Quasi-Static Cylindrical Roller Bearing Model to Accurately Consider Non-Hertzian Contact Pressure in Time Domain Simulations," *J. of Tribology*, vol. 134, pp. 1–10, 2012.
- [199] V. Šmejova, A. Schwedt, L. Wang, W. Holweger, and J. Mayer, "Microstructural Changes in White Etching Cracks (WECs) and Their Relationship with Those in Dark Etching Region (DER) and White Etching Bands (WEBs) due to Rolling Contact Fatigue (RCF)," *Int. J. Fatigue*, vol. 100, pp. 148–158, 2017.
- [200] A. Voscamp, "Fatigue and Material Response in Rolling Contact," *ASTM International, Bearing steel: Intro. to 21 Century*, pp. 152–166, 1998.
- [201] K. Ishizaka, S. Lewis, and R. Lewis, "The Low Adhesion Problem Due to Leaf Contamination in the Wheel / Rail Contact : Bonding and Low Adhesion Mechanisms," *Wear*, vol. 379, pp. 183–197, 2017.
- [202] H. Uyama, , "The Mechanism of White Structure Flaking in Rolling Bearings," *2011 Wind Turbine Tribology Seminar*, NREL (USA), 2011.
- [203] N. Shamsaei and A. Fatemi, "Small Fatigue Crack Growth Under Multiaxial Stresses," *Int. J. Fatigue*, vol. 58, pp. 126–135, 2014.
- [204] T. Lin and Y. Ito, "Mechanics of a Fatigue Crack Nucleation Mechanism," *J. Mech. Phys. Solids*, vol. 17, pp. 511–523, 1969.
- [205] W. Musial, S. Butterfield, and B. McNiff, "Improving Wind Turbine Gearbox Reliability," *Eur. Wind Energy Conf. 2007*, pp. 1–13, 2007.
- [206] C. Walford, "Wind Turbine Reliability :Understanding and Minimizing Wind Turbine Operation and Maintenance Costs," *Sandia Report, Sand2006-1100*, Unlimited Release 2006, California (USA), 2006.
- [207] H. Ghonem, and J. W. Provan, "Micromechanics Theory of Fatigue Crack Initiation and Propagation," *Eng. Fract. Mech.*, vol. 13, pp. 963-977, 1980.
- [208] D. Nuruzzaman and M. Sheikh, "EHL Oil Film Thickness Under Rolling-Sliding Contact," *J. Mech. Eng.*, vol. ME38, pp. 58–60, 2008.
- [209] R. Evans, T. Barr, L. Houpert, and S. Boyd, "Prevention of Smearing Damage in Cylindrical Roller Bearings," *Tribology Trans.*, vol. 56, no. 5, pp. 703–716, 2013.

- [210] T. Ahlroos, H. Ronkainen, A. Helle, R. Parikka, J. Virta, and S. Varjus, "Twin Disc Micropitting Tests," *Tribology Int.*, vol. 42, pp. 1460–1466, 2009.
- [211] S. Ganti, B. Turner, M. Kirsch, D. Anthony, B. McCoy, and H. Trivedi, "Three-Dimensional (3D) Analysis of White Etching Bands (WEBS) in AISI M50 Bearing Steel Using Automated Serial Sectioning," *Materials Characterization*, vol. 138, pp. 11–18, 2018.
- [212] W. Kruhöffer and J. Loos, "WEC Formation in Rolling Bearings Under Mixed Friction : Influences and ' Friction Energy Accumulation ' as Indicator," *Tribology Transaction*, vol. 60, No.3, pp. 516-529, 2017.
- [213] T. Haward, "Development of a Novel Bearing Concept for Improved Wind Turbine Gearbox Reliability," Ph.D. Thesis, The University of Sheffield (UK), 2016.
- [214] S. Li, Y. Su, X. Shu, and J. Chen, "Microstructural Evolution in Bearing Steel Under Rolling Contact Fatigue," *Wear*, vol. 380-381, pp. 146–153, 2017.
- [215] J. Seo, S. Kwon, D. Lee, and H. Choi, "Analysis of Contact Fatigue Crack Growth Using Twin-Disc Tests And Numerical Evaluations," *Inter. J. of Fatigue*, vol. 55, pp. 54–63, 2013.
- [216] J. Garnham and J. Beynon, "The Early Detection of Rolling-Sliding Contact Fatigue Cracks," *Wear*, vol. 144, pp. 103–116, 1991.
- [217] E. Gallardo-hernández, and R. Lewis, "Twin Disc Assessment of Wheel / Rail Adhesion," *Wear*, vol. 265, pp. 1309–1316, 2008.
- [218] O. Arias-cuevas, Z. Li, R. Lewis, and E. Gallardo-hernández, "Rolling – Sliding Laboratory Tests of Friction Modifiers in Dry and Wet Wheel – Rail Contacts," *Wear*, vol. 268, pp. 543–551, 2010.
- [219] J. Santa, P. Cuervo, M. Harmon, A. Beagles, A. Toro and R. Lewis, "Twin Disc Assessment of Wear Regime Transitions and Rolling Contact Fatigue in R400HT – E8 Pairs," *Wear*, vol. 432-433, pp. 1-8, 2019.
- [220] G. Meneghetti, A. Terrin and S. Giacometti, "A Twin Disc Test Rig for Contact Fatigue Characterization of Gear Materials Modeling a High Blade of an Giacometti Turbine Airplane Gas Turbine Engine," *Procedia Structural Integrity 2 (2016)*, 21st European Conference on Fracture, ECF21, 20-24 June 2016, Catania, Italy, pp. 3185–3193, 2016.
- [221] S. Harris, T. Bruce, J. Loos, B. Tarfan and K. Willson, "WEC failure on the inner rings of roller bearings under dynamic conditions," *Bearing World 2*, (2018).
- [222] J. Keller and S. Lambert, "Gearbox Instrumentation for the Investigation of Bearing Axial Cracking," *Technical Report, NREL/TP-5000-70639*, March 2018.
- [223] B. C. Li, C. Jiang, X. Han, and Y. Li, "A New Approach of Fatigue Life Prediction for Metallic Materials Under Multiaxial Loading," *Int. J. Fatigue*, vol. 78, pp. 1–10, 2015.
- [224] N. Arakere, "Gigacycle Rolling Contact Fatigue of Bearing Steels: A review," *Int. J. Fatigue*, vol. 93, pp. 238–249, 2016.
- [225] E. Zaretsky, J. Poplawski, and C. Miller, "Rolling Bearing Life Prediction — Past , Present , and Future," *NASA/TM-2000-210529*, November, 2000.

- [226] A. Fatimi and L. Yang, "Cumulative fatigue damage and life prediction theories: a survey of the state of the art for homogeneous materials," *Int. J. Fatigue*, Vol. 20, pp. 9-34, 1998.
- [227] C. H. Wang and M. W. Brown, "Life Prediction Techniques for Variable Amplitude Multiaxial Fatigue – Part 2: Comparison with Experimental results," *J. of Engineering Materials and Technology*, Vol 118, pp. 371-374, 1996.
- [228] H. Gao, H. Z. Huang, S. P. Zhu, Y. F. Li, and R. Yuan, "A Modified Nonlinear Damage Accumulation Model for Fatigue Life Prediction Considering Load Interaction Effects," *Sci. World J.*, 2014.
- [229] C. M. Sonsino, "Principles of Variable Amplitude Fatigue Design and Testing," *ASTM Spec. Tech. Publ.*, vol. 1, no. 10, pp. 3–23, 2004.
- [230] M. Gladyski and A. Fatemi, "Notched Fatigue Behavior Including Load Sequence Effects Under Axial and Torsional Loadings," *Int. J. Fatigue*, vol. 55, pp. 43–53, 2013.
- [231] L. Molent, M. McDonald, S. Barter and R. Jones, "Evaluation of Spectrum Fatigue Crack Growth Using Variable Amplitude Data," *Int. J. Fatigue*, vol. 30, pp. 119–137, 2008.
- [232] S. M. Marco, and W. L. Starkey, "A Concept of Fatigue Damage," *Trans. ASME*, vol. 76, no. 4, pp. 627–632, 1954.
- [233] M. Kamiński, "On Probabilistic Fatigue Models for Composite Materials," *Int. J. Fatigue*, vol. 24, pp. 477–495, 2002.
- [234] C. J. Lamaitre J, *Mechanics of Solid Materials.*: Cambridge University Press, Cambridge, UK, 1990.
- [235] V. Dattoma, S. Giancane, R. Nobile, and F. W. Panella, "Fatigue Life Prediction Under Variable Loading Based on a New Non-Linear Continuum Damage Mechanics Model," *Int. J. Fatigue*, vol. 28, pp. 89–95, 2006.
- [236] H. J. Grover, "An Observation Concerning the Cycle Ratio in Cumulative Damage," *symposium on fatigue of aircraft structures*, pp. 120–124, 1960.
- [237] S. S. Manson, "Interfaces Between Fatigue, Creep, and Fracture," *Int. J. Fract. Mech.*, vol. 2, no. 1, pp. 327–328, 1966.
- [238] S. S. Manson, J. C. Freche, and C. R. Ensign, "Application of a Double Linear Damage Rule to Cumulative Fatigue," *Fatigue Crack Propagation, ASTM STP 415. Am. Soc. Test. Mats.*, pp. 384–412, 1967.
- [239] R. H. Brook and J. S. C. Parry, "Cumulative Damage in Fatigue : a Step Towards its Understanding," *J. Mech. Eng. Sci.*, vol. 11, no. 3, pp. 243–255, 1969.

- [240] C. H. Wang and M. W. Brown, "Life Prediction Techniques for Variable Amplitude Multiaxial Fatigue—Part 1: Theories," *J. Eng. Mater. Technol.*, vol. 118, pp. 367–370, 1996.
- [241] J. L. Chaboche, "Continuum Damage Mechanics: Part II -- Damage Growth, Crack Initiation, and Crack Growth," *J. Applied Mechanics*, vol. 55, pp. 65--72, 1988.
- [242] D. L. Henry, "A Theory of Fatigue Damage Accumulation in Steel," 1953.CHECK
- [243] E. Ioannides and T. A. Harris, "A New Fatigue Life Model for Rolling Bearings," *J. Tribology*, vol. 107, no. 3, pp. 367–378, 1985.
- [244] SKF Product, <http://www.skf.com/uk/products/bearings-units-housings/roller-bearings/cylindrical-roller-bearings/single-row-full-complement-cylindrical-roller-bearings/single-row-full-complement/index.html?highlightid=NCF%203048%20CV>.
- [245] M. Harmon, and R. Lewis, "Review of Top of Rail Friction Modifier Tribology," *Tribology-Materials, Surfaces & Interfaces*, vol. 10, no. 3, pp. 150-162, 2017.
- [246] J. Lai and K. Stadler, "Investigation on the Mechanisms of White Etching Crack (WEC) Formation in Rolling Contact Fatigue And Identification of a Root Cause for Bearing Premature Failure," *Wear*, vol. 365, pp. 244–256, 2016.
- [247] Y. Guo and J. Keller, "Investigation of high-speed shaft bearing loads in wind turbine gearboxes through dynamometer testing," *Wind Energy*, pp. 1–12, 2017.
- [248] ISO EN 683-17:2014, Heat-treated steels, alloy steels and free-cutting steels - Part 17: Ball and roller bearing steels, *BSI Standards Publication*, 2014.
- [249] E. Zaretsky, "Rolling Bearing Life Prediction , Theory , and Application," *NASA STI Program, NASA/TP—2013-215305*, March, 2013.
- [250] BS ISO 7063:2018, BSI Standards Publication Rolling bearings — Needle roller bearing track rollers — Boundary dimensions , geometrical product specifications (GPS) and tolerance values, *BSI Standards Publication*, 2018.
- [251] BS ISO 3096 : 2018 Rolling bearings — Needle rollers — Boundary dimensions , geometrical product specifications (GPS) and tolerance values, *BSI Standards Publication*, 2018.
- [252] V. Popov, M. Heb and E. Willert, METHOD OF DIMENSIONALITY REDUCTION IN CONTACT MECHANICS: User's Manual, *Technische Universität Berlin (Germany)*, 2018.
- [253] D. Sparks, R. Smith, V. Cruz, N. Tran, A. Chimbayo, D. Riley and N. Najafi, "Dynamic and Kinematic Viscosity Measurements with a Resonating Microtube," *Sensors and Actuators A: Physical*, vol. 149, pp. 38–41, 2009.
- [254] W. J. Stronge, Impact Mechanics, *Cambridge university press (UK)*, 2000.

References

- [255] P. Mathews, *Design of Experiments with Minitab*, American Society for Quality, Quality Press, Milwaukee 53203, USA, 2006.
- [256] Z. V. I. Hashin, "A Reinterpretation of the Palmgren-Miner Rule for Fatigue Life Prediction," Office of NAVAL Research, *Naval Air Systems Command*, (USA), 1979.
- [257] W. Dong, Y. Xing, T. Moan, and Z. Gao, "Time Domain-Based Gear Contact Fatigue Analysis of a Wind Turbine Drivetrain Under Dynamic Conditions," *Int. J. Fatigue*, vol. 48, pp. 133–146, 2013.
- [258] H. Fuchs and R. Stephens, *Metal Fatigue in Engineering*, John Wiley and Sons (USA), 1980.
- [259] Germanscher Lloyd, Regulation of the Certification of Offshore Wind Energy Conversion Systems, Rules and Regulations IV, *Germanischer Lloyd WindEnergie GmbH* (Germany), 2005.
- [260] K. Tanaka and T. Mura, "A Dislocation Model for Fatigue Crack Initiation," *Journal of Applied Mechanics*, vol. 48, pp. 97–103, 2015.
- [261] Bauer and Lucas, "No Titlecotècnia ECO 80/1670 - 1,67 MW - Wind turbine," *En.wind-turbine-models.com [online]*., 2017. Available on:
<https://en.wind-turbine-models.com/turbines/787-ecotcniacotècnia-ECO-80-1670-MW>

Appendix A

Stresses calculation procedure of planetary WTGBs

Torque on the turbine High-Speed Shaft (HSS) can be calculated depending on the generator output power using the power-law;

$$P = T * \omega \tag{A.1}$$

where P is the output power in Watt, T is the torque on the generator shaft in Nm and ω is its rotational speed in rad/s. The speed ratio of the gears can be used to calculate the torque at any gear stage and the load on bearings can be calculated. The overall efficiency of the drivetrain is important due to the losses after each transmission stage between the meshed gears in addition to the generator electric efficiency. The torque on the rotor, i.e. Low-Speed Shaft (LSS) of the gearbox can be calculated as:

$$T_{rot} = \frac{GT_{gen}}{\eta} = \frac{GP}{\eta\omega_{gen}} \tag{A.2}$$

where G is the overall wind turbine gearbox speed ratio $\left(\frac{\omega_{gen}}{\omega_{rot}}\right)$, η is the overall drivetrain efficiency and the subscripts rot and gen refer to the rotor and the generator respectively.

The planetary stage contains three planets and it can be assumed that the planets have equal load share; the force on each planet is one-third of the force induces due to the rotor torque. Planet centerline location on the planet carrier is the average of the sun and ring radii. Assume the sun and ring diameters to be S and R respectively. The force at the center of each planet F_p can be calculated depending on [Figure A.1](#) and [Eqn. \(A.2\)](#) as;

$$F_p = \frac{T_{rot}}{3 * \left\{ \frac{R+S}{2} \right\}} = \frac{4T_{rot}}{3(R+s)} = \frac{4GP}{3\eta\omega_{gen}(R+s)} \tag{A.3}$$

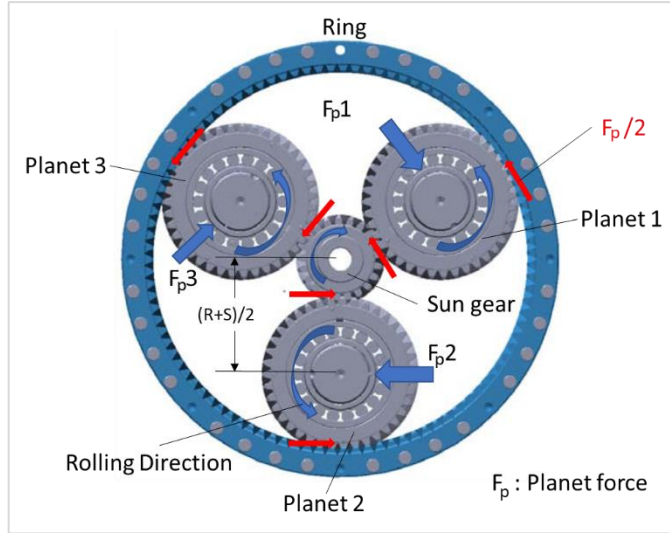


Figure A. 1: Reaction forces on the planetary stage components (modified from [21]).

The force on the center of the planet always carried by two bearings; assume the number of rows for the planetary bearings is H which is equal to 3, i.e. a single and double roller bearings then substituting in Eqn. (A.4). There are a significant number of researchers pointed out that, UpWind (UW) planetary bearing carried between 30% to 50% more than the Down Wind (DW) bearing [55][3]. Suppose the UW planetary bearing carried an average of 40% more than the DW bearing. This loading difference pointing an axial force in addition to that produced from misalignment of the planet pin during the loading process. Axial forces on planetary bearings also can be produced from the planet helical gear angle (20° in 2MW turbines) [55]. The total radial force on the UW planetary bearing row (F_{pluw}) can be expressed as;

$$F_{pluw} = \frac{0.6222 * G * T_{gen}}{\eta(R+S)} \tag{A.4}$$

For cylindrical Roller Bearing (CRB), the maximum force on one rolling element F_N can be calculated using the Stribeck formula [25];

$$F_N = \frac{5F_{pluw}}{Z_{rol}} \tag{A.5}$$

Calling Eqn. (A.4) to get:

$$F_N = \frac{3.111 * G * T_{gen}}{\eta(R+S)Z_{rol}} \quad (\text{A.6})$$

where Z_{rol} is the number of the rolling elements of one row of the bearing. By substituting Eqn. (A.2) in Eqn. (A.6), the maximum contact force on one rolling element of the planetary bearing can be calculated as:

$$F_N = \frac{3.111 * P_{gen}}{\eta(R+S)\omega_{rot} * Z_{rol}} \quad (\text{A.7})$$

The dimensions of the planetary stage used in the calculation procedure are illustrated in Table A.1 [261].

Table A.1: Useful dimensions and specifications of the wind turbine gearbox.

Rated generator speed (ω_{gen})	1800 rpm
Rated rotor speed (ω_{rot})	19 rpm
Overall drivetrain efficiency	0.933
Ring gear diameter	1.244 m
Sun gear diameter	0.24 m

Stress distribution within the contact region can be calculated by applying Hertz theory and the cartesian stresses in the contact area can be calculated as [193];

$$\sigma_x = -\frac{2z}{\pi} \int_{-b}^b \frac{p(s)(x-s)^2 ds}{((x-s)^2+z^2)^2} \quad (\text{A.8})$$

$$\sigma_z = -\frac{2z^3}{\pi} \int_{-b}^b \frac{p(s) ds}{((x-s)^2+z^2)^2} \quad (\text{A.9})$$

$$\tau_{xz} = -\frac{2z^2}{\pi} \int_{-b}^b \frac{p(s)(x-s) ds}{((x-s)^2+z^2)^2} \quad (\text{A.10})$$

The approximated solution of these equations can be achieved by calculating the notations m and n using Eqns. (A.11) and Eqn. (A.12) respectively [195].

$$m^2 = \frac{1}{2} [\{(b^2 - x^2 + z^2)^2 + 4x^2z^2\}^{0.5} + (b^2 - x^2 + z^2)] \quad (\text{A.11})$$

$$n^2 = \frac{1}{2} [\{(b^2 - x^2 + z^2)^2 + 4x^2z^2\}^{0.5} - (b^2 - x^2 + z^2)] \quad (\text{A.12})$$

And the cartesian stresses beneath the contact region at any depth z can be calculated using [Eqns. \(A.13 to A.15\)](#).

$$\sigma_x = -\frac{p_o}{b} \left\{ m \left(1 + \frac{z^2+n^2}{m^2+n^2} \right) - 2z \right\} \quad (\text{A.13})$$

$$\sigma_z = -\frac{p_o m}{b} \left(1 - \frac{z^2+n^2}{m^2+n^2} \right) \quad (\text{A.14})$$

$$\tau_{xz} = -\frac{p_o n}{b} \left(\frac{m^2-z^2}{m^2+n^2} \right) \quad (\text{A.15})$$

Stresses due to friction

Introducing a traction force in the contact region makes Hertzian contact invalid and should be replaced by a non-Hertzian contact. To overcome this issue of the complicated procedure of non-Hertzian contact, superposition can be used to find the resultant stress. Friction coefficient μ is defined as the ratio between traction and compressive forces; the traction stresses due to traction force can be calculated as [193];

$$\mu = \frac{q(s)}{p(s)} = \frac{q_o(s)}{p_o(s)} \quad (\text{A.16})$$

$$q(x) = \pm \mu p_o \sqrt{1 - \frac{x^2}{b^2}} \quad (\text{A.17})$$

$$(\sigma_z)_q = -\frac{q_o}{b} n \left(\frac{m^2-z^2}{m^2+n^2} \right) \quad (\text{A.18})$$

$$(\sigma_x)_q = \frac{q_o}{b} \left[n \left(2 - \frac{z^2-m^2}{m^2+n^2} \right) - 2x \right] \quad (\text{A.19})$$

$$(\tau_{xz})_q = -\frac{q_0}{b} \left[m \left(1 + \frac{z^2+n^2}{m^2+n^2} \right) - 2z \right] \quad (\text{A.20})$$

Principal and Von-Mises stresses can be calculated using [Eqn. \(A. 21\)](#) to [Eqn. \(A.23\)](#) respectively.

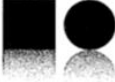
$$\sigma_{1,2} = \frac{\sigma_x + \sigma_z}{2} \pm \sqrt{\left(\frac{\sigma_x - \sigma_z}{2} \right)^2 + \tau_{xz}^2} \quad (\text{A. 21})$$

$$\tau_1 = \sqrt{\left(\frac{\sigma_x - \sigma_z}{2} \right)^2 + \tau_{xz}^2} = \frac{1}{2} |\sigma_1 - \sigma_2| \quad (\text{A. 22})$$

$$\sigma_{VM} = \sqrt{\frac{(\sigma_1 - \sigma_2)^2 + (\sigma_2 - \sigma_3)^2 + (\sigma_3 - \sigma_1)^2}{2}} = \sqrt{\frac{(\sigma_x - \sigma_y)^2 + (\sigma_y - \sigma_z)^2 + (\sigma_z - \sigma_x)^2 + 6(\tau_{xy}^2 + \tau_{yz}^2 + \tau_{zx}^2)}{2}} \quad (\text{A. 23})$$

Appendix B

The chemical composition of the test disc material



West Yorkshire Steel

West Yorkshire Steel Co Ltd
 Sandbeck Works
 Sandbeck Industrial Estate
 Wetherby, Leeds
 LS22 7DN
 Tel : 01937 584440
 Fax No : 01937 580128
 Email : sales@westyorkssteel.com

Material Certificate

University of Sheffield
 Department of Finance
 Firth Court
 Western Bank
 Sheffield
 S10 2TN

Certificate No	32314
Date	08/11/2017
Your Order Ref	XJO/4500883038
WYS Ref	4339


Qty	Size	Specification	
1.00	105mm dia x 1000mm	Grade 52100	Cast No A0865Z

Chemical Analysis									
Cast No.	C.	Si.	S.	P.	Mn.	Ni.	Cr.	Mo.	
Cast No A0865Z	0.980	0.210	0.018	0.009	0.440	-	1.360	0.060	

The above material is released in accordance with the approvals indicated below:

Deliver To :
 University of Sheffield
 Civ/Mech Eng Goods Inwards
 Pam Liversidge Building
 off Newcastle Street
 Sheffield
 S10 2TN

Signed



Quality Manager

We certify that the confirmed data, showing the physical and chemical properties of the material, are in full compliance with those stated in the mills certificate according to EN10204 3.1

VAT Reg No: 172 0259 84

Company Reg No 1229647

www.westyorkssteel.com

Appendix C

Finite Element analyses to design test discs without stress concentration

To simulate the test disc contact problem using ABAQUS software of FE, the same element type (Hexagonal diamond) with a sweep, advance front, and size (approximating the global size of 0.5) and by ticking the curvature control, were used in these models. The same boundary conditions (as can be seen in [Figure C.1](#)) were used. The first model for an upper flat disc with an 8.0 mm axial length in contact with a flat disc with 4 mm while, the second model consists of two flat discs with equal axial contact lengths of 8 mm. The third model of an upper disc with fillet edges according to the standard BS ISO 7063:2018 [250] and BS ISO 3096:-2018 [251], being in contact with a flat disc having an axial length of 8 mm. These three models were used to evaluate the stress concentration at the contact edges. The fourth model consists of a curved upper test disc with crowned contact region ($R=30$ mm), being in contact with a flat lower disc of axial length 8 mm. The use of this radius of curvature which is close to the disc radius was to make the contact approximately similar to that of circular contact. This enables using the available impact formulas to calculate the impact forces and stresses.

The first model (two flat discs with different lengths), shows that the contact pressure at the disc edges around 1.7 times that at the middle of the axial length. This value was found by presenting the pressure along a node-path which chosen with the contact line along the contact width at a sectional plane passes through the discs rotating centerlines. This value also in contact with that presented by Harris and Motzala (Chapter 6) [25]. [Figure C.1\(b\)](#), [\(c\)](#) and [\(d\)](#) present the results of the first model.

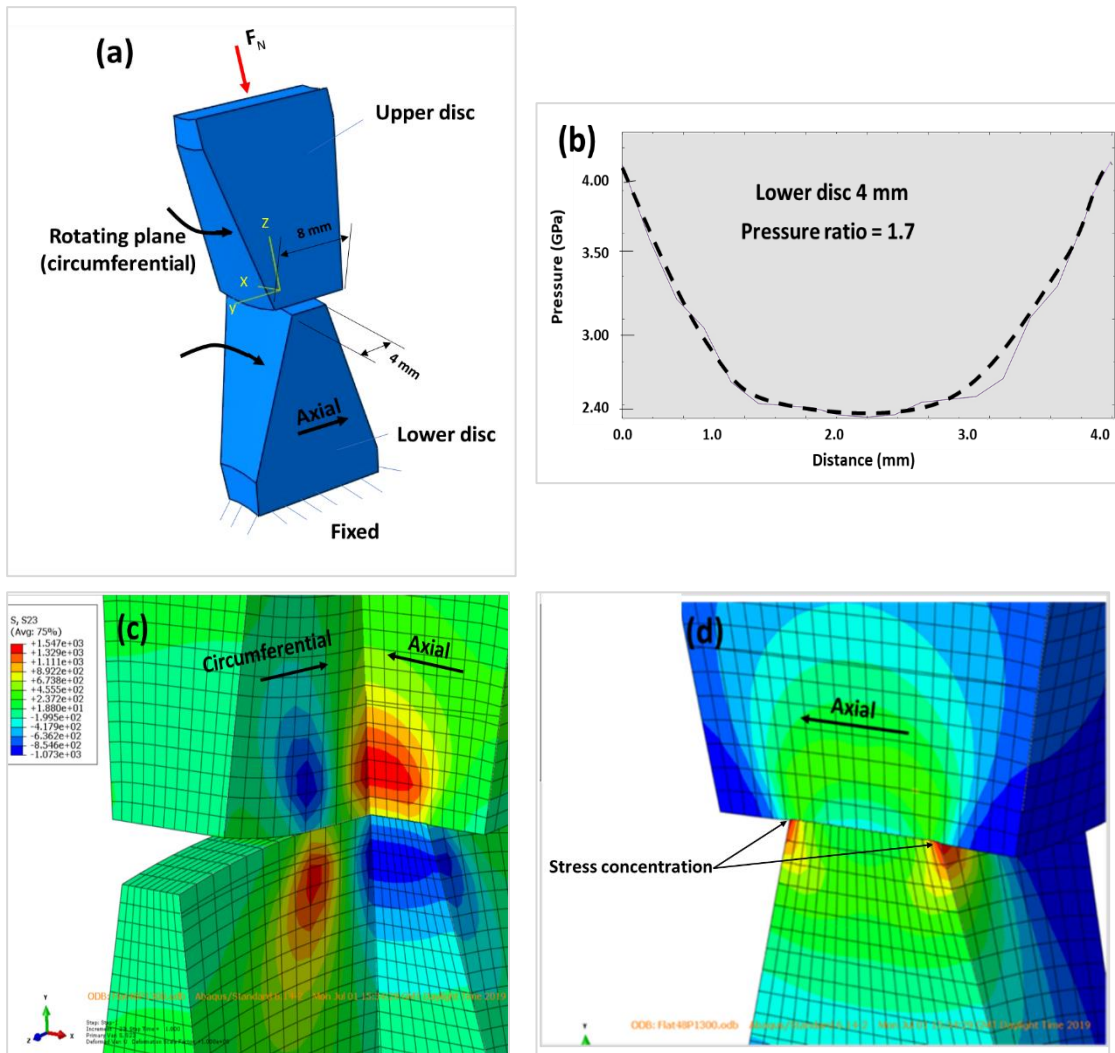


Figure C.1: Pressure and stress distribution for a contact of two flat test discs the upper has an axial length of 8 mm and the lower is 4 mm (a) schematic of the problem; (b) effect of stress concentration at the edges; (c) orthogonal shear stress; (d) Von-Mises stress.

Using a contact length of 8.0 mm for the two contact discs in the second model reduces the stress and pressure ratio which is the ratio of the pressure at the concentration region to that in the middle of the disc. This reduction probably because these ratios depend on the loading level due to a larger contact length in the axial direction as can be seen in [Figure C.2](#). This analysis also confirms the stress concentration in this model.

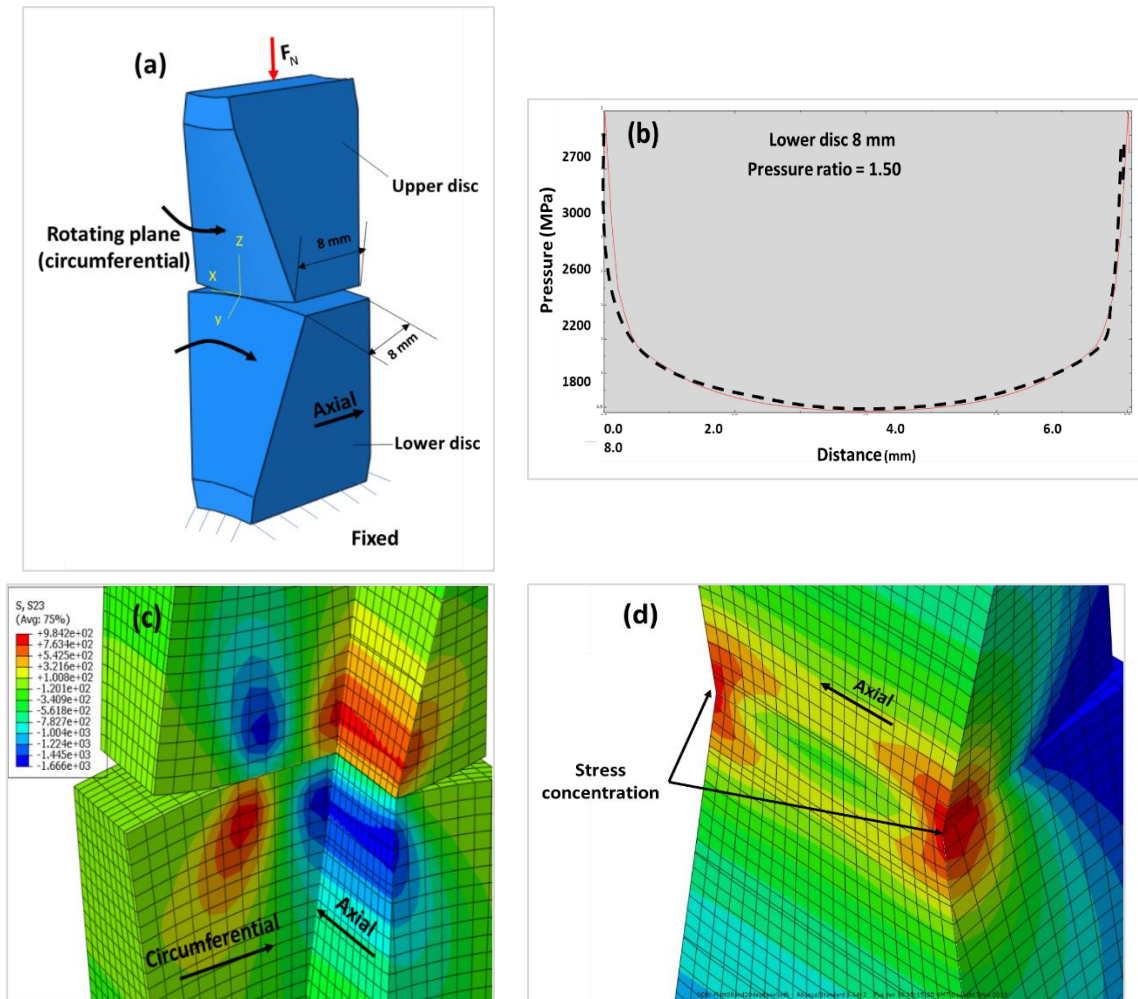


Figure C. 2: Pressure and stress distribution for a contact of two flat test discs having the same axial length of 8 mm (a) schematic of the problem; (b) effect of stress concentration at the edges; (c) orthogonal shear stress distribution; (d) Von-Mises stress distribution.

For the third model, the upper disc has a fillet at the contact edges. The fillet radius is 1 mm according to BSi ISO 3096-2018 [251]. The analysis of this model can be seen in [Figure C.3](#). There is a noticeable stress concentration at the beginning of the fillet. Despite the pressure ratio was reduced, the stress concentration by machining the roller edges can be reduced but not completely avoid.

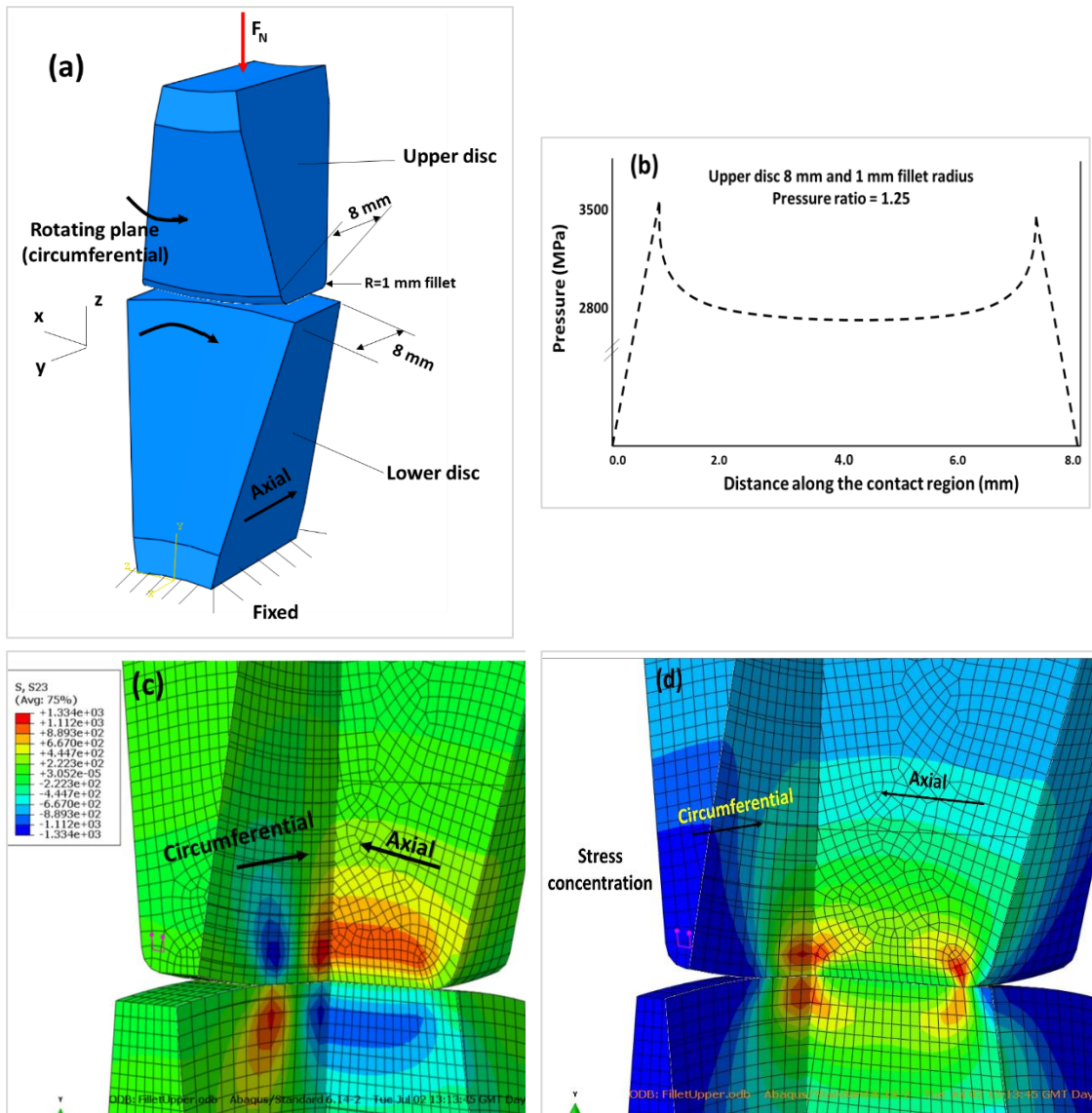


Figure C. 3: Pressure and stress distribution for contact of flat fillet upper disc on flat lower disc 8 mm (a) schematic of the problem; (b) effect of pressure and stress concentration at the edges; (c) orthogonal shear stress distributions in three-dimensional view; (d) Von-Mises stress distributions in three-dimensional view.

The fourth model was for a fully crowned upper test disc ($R=30$ mm) in contact with a flat lower test disc as can be seen in [Figure C.4\(a\)](#). There is no stress or pressure concentration in this model. The pressure distribution can be seen in [Figure C.4\(b\)](#) which shows the maximum contact pressure at the center of contact according to Hertz theory. The subsurface orthogonal shear stress distribution in a plane perpendicular to the rotating plane (the crowned plane), is presented in [Figure C.4\(c\)](#). The same orthogonal shear distribution in two sections parallel and perpendicular to the rotating plane can be seen in [Figure C.4\(d\)](#). Von-Mises stress distribution in the crowned plane and two perpendicular sections also presented in [Figure C.4\(e\)](#) and [Figure C.4\(f\)](#) respectively. The aim of introducing this model is to

confirm the validity of these models, however, Hertz's theory will be used for analyzing this contact. Using the same loading of the previous models shows a considerable increase in the contact stresses, thus low compressive loading will be enough to introduce the yield stress which is the level of testing for the planned tests. This reduces the reaction on the test rig bearings.

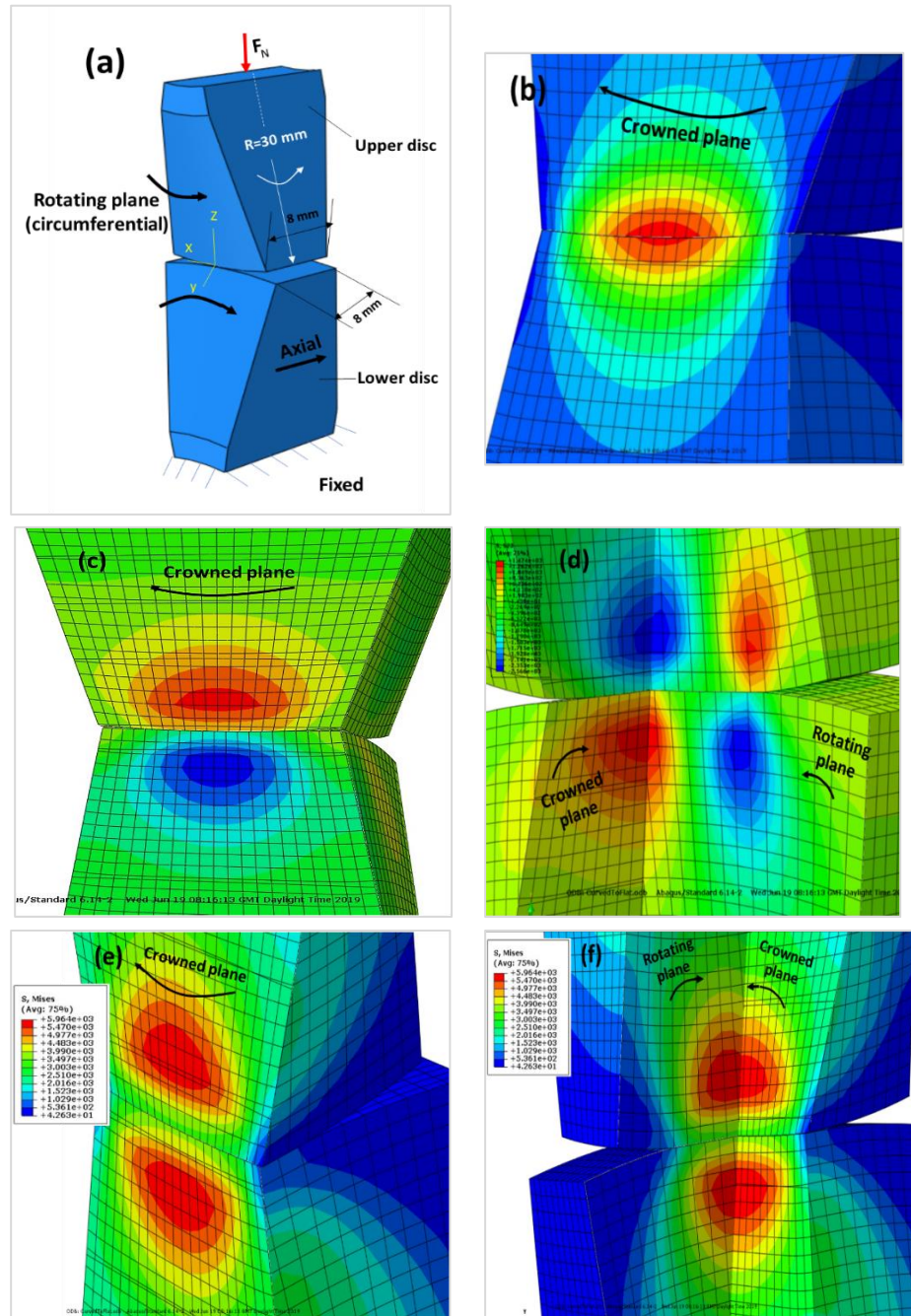


Figure C. 4: Pressure and stress distribution for contact of curved upper disc on flat lower disc 8 mm (a) schematic of the problem; (b) effect of stress concentration at the edges; (c) and (d) orthogonal shear stress distribution in three-dimensional view; (e) and (f) von-Mises stress distribution in two perpendicular planes.

Appendix D

Alpha SP 320 lubricant specifications



TYPICAL PHYSICAL CHARACTERISTICS

Castrol Alpha SP Range	Alpha SP68	Alpha SP100	Alpha SP150	Alpha SP220	Alpha SP320	Alpha SP460	Alpha SP680	Alpha SP1000
ISO Viscosity Grade	68	100	150	220	320	460	680	1000
Kinematic Viscosity								
@ 40°C, cSt	68	100	150	220	320	460	680	1000
@ 100°C, cSt	8.53	11.1	14.5	18.7	24.0	30.5	37.3	43.6
Viscosity Index	95	95	95	95	95	95	90	80
David Brown Designation	2EP	3EP	4EP	5EP	6EP	7EP	9EP	-
Relative Density @ 20°C	0.885	0.885	0.890	0.895	0.900	0.900	0.920	0.925
Pour Point, °C	-21	-21	-21	-21	-21	-6	-6	-3
Open Flash Point, °C	240	249	249	249	255	255	264	264
Demulsibility N°	240	800	210	270	330	360	600	1200
FZG Gear Test Failure Load Stage Pass	12+	12+	12+	12+	12+	12+	12+	12+
Timken OK Load, lbs	60	60	60	60	60	60	60	60
Load Carrying Capacity according to Brugger (N/mm ²)	51	51	51	51	51	51	51	51

Appendix E

Experimental check of the static and dynamic response of the test discs

The static and dynamic response of the test discs for the used geometries and dimensions are checked. This by applying an external load and measuring the deflection, i.e. approaching the discs towards each other under the action of compression. The test arrangements presented in [Section 4.3.4](#), were used. For elliptical contact, the theoretical disc stiffness using the formula by Stronge presented in [Eqn. 5.8](#) [254], was 16.486 GN/m and 16.190 GN/m for the SR of 6.71% and 22.82% respectively. However, for the same contact, the measured force/deflection relation can be seen in [Figure E. 1](#) The disc stiffness is the slope of the graph which found ~ 28.161 GN/m. According to Stronge assumptions [254], only the compressed ball is deformed, however, the flat surface which supports the ball does not, i.e. the deformation surface in the contact region is a straight line. However, in this test, it is expected that both the discs were deformed thus, the measured stiffness approximately twice the theoretical one. The deviation from being exactly twice the theoretical value is that the flat and the fully crowned discs have different deformation, i.e. flat disc deformed less than that of the crowned. This difference probably will be considerably reduced by using two flat discs that have the same SR, i.e. the same outer radii. Two flat discs with the same geometry used in the previous tests also tested to measure their response for loading (stiffness). The test results also presented in this figure (black graph). The force-deflection relation is non-linear according to Stronge [254]. This can be observed from the deviation of the test results from the fitted line, however, fitting the results to linear makes calculating the slope easier because the slope of non-linear relation is variable and depends on the loading level. However, curve fitting uses the average path among the presented points and the use of this fitting for all tests can show the differences.

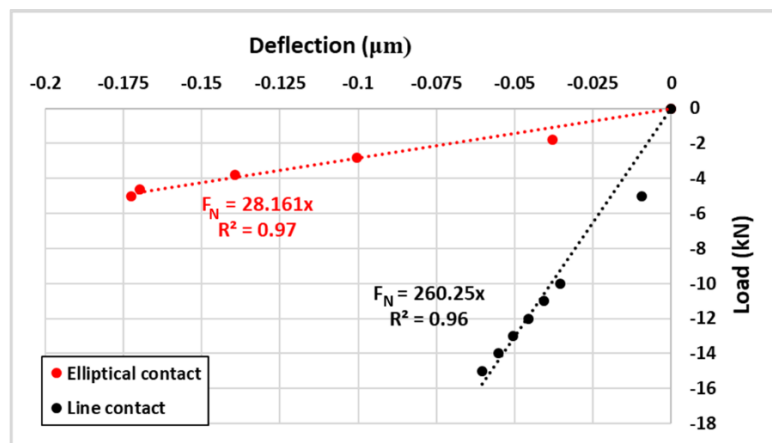


Figure E. 1: Test disc material static response.

The same pairs of test discs also tested under dynamic loading but changing the contact location to avoid the possibility of introducing a plastic contact. The results of the dynamic test can be seen in Figure E. 2. The applied dynamic loading has a sinusoidal variation because the majority consider the load variation during the impact as sine wave [254]. The test frequency in Hz that presented in the legend seems having no effect on the average disc response (stiffness). This helps to show the material response throughout the unloading period and the average slope was taken.

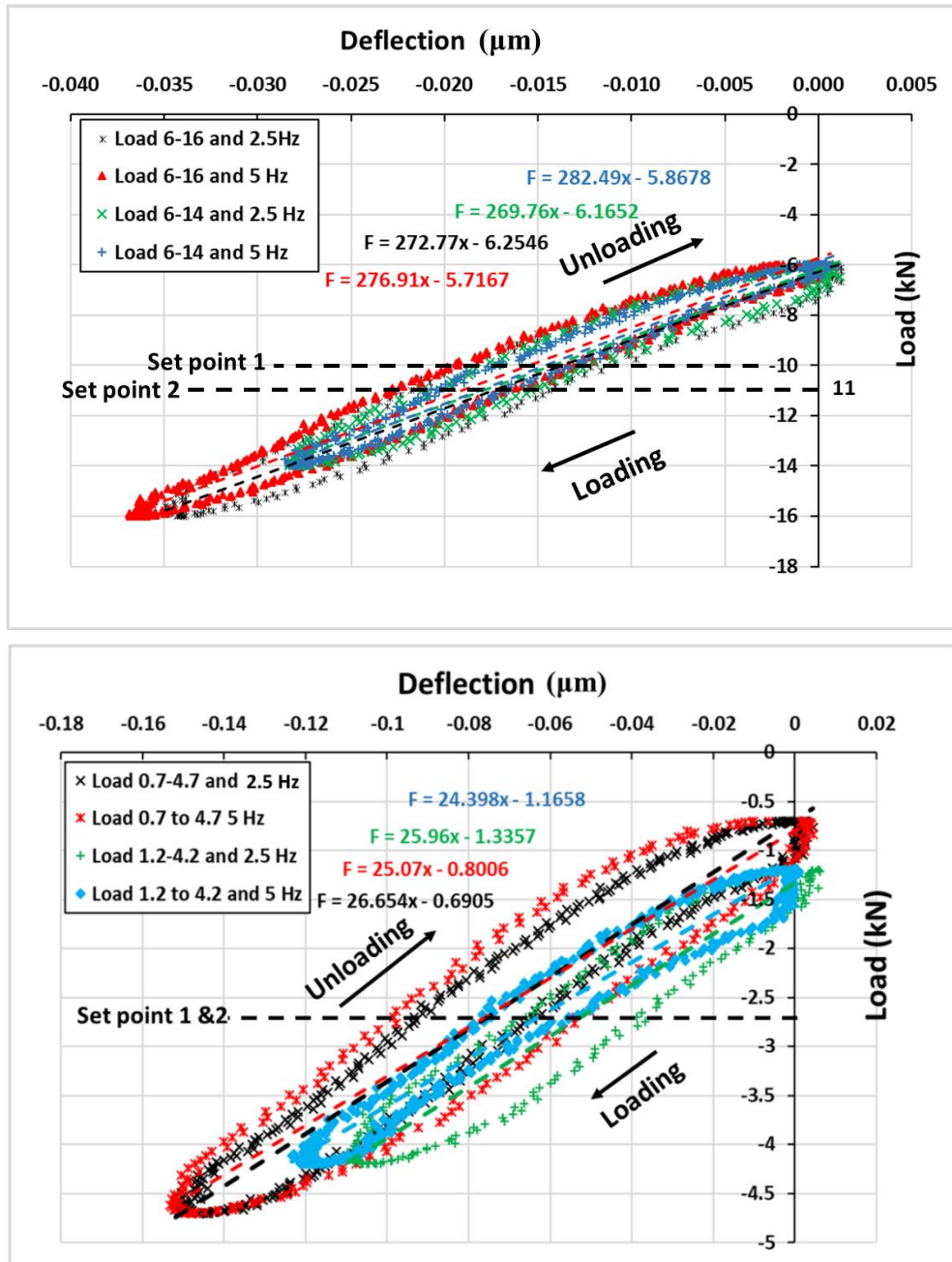


Figure E. 2: Test disc material dynamic response. Flat discs (top) and fully crowned discs (bottom).

The setpoint represents the datum point that the load applied is below and over it (this also called load the amplitude). The amplitude can be calculated from the loading range presented in the legend of Figure E. 2 by dividing the range by 2. One loading cycle was chosen randomly from the test cycles then analyzed under different loading amplitudes and frequencies. The test disc response (stiffness) shows a small effect due to testing loading but it is more than the effect of the testing frequency. However, the difference in stiffness between the static and dynamic loading shows that the impact force calculated by impact formula can be used to calculate the impact contact stress using Hertz theory. This widely used; however, it is checked by these tests. Furthermore, measurements within the microlevel can produce errors despite the high measurement accuracy.

To investigate whether the assumption of considering the test rig shafts as rigid is valid, the fully crowned test disc deformations (deflections), when the discs fixed on the test rig shafts also statically tested three times and presented in Figure E. 3. There are small differences in the results. This probably due to the deflection of the test rig shafts and their supporting bearings. These small differences prove that the assumption of considering the test rig shafts as rigid is acceptable.

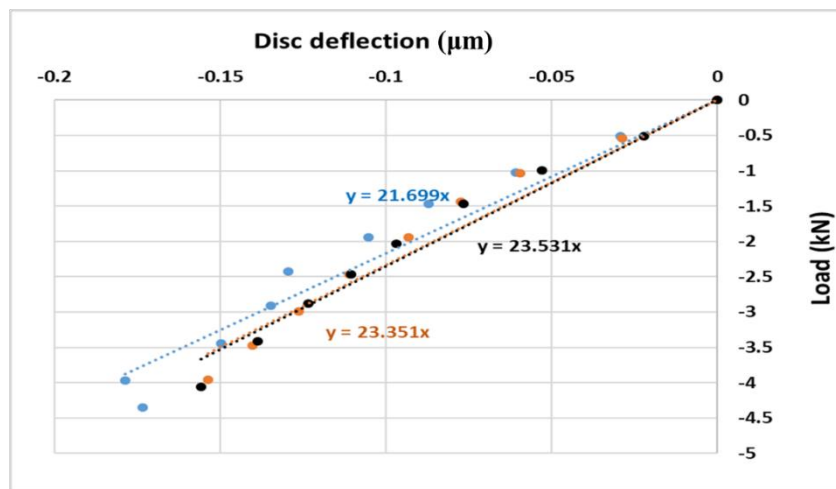


Figure E. 3: Fully crowned test disc stiffness within the test rig assembly.

Appendix F

Safety Operation Guide for Rolling, Sliding, and Impact (RSI) Test Rig

1. *Startup steps:*

- 1) **Check** the lubricant level using the marker on the front transparency cover. If the lubricant is lower than the required, add lubricant using the upper knob on the gearbox cover in the left-hand side of the rig.
- 2) **Turn ON** the single phase 220 V power switch for the loadcell.
- 3) **Turn ON** the red switch on the side of the load cell digital indicator.
- 4) Use the attached spanner to turn the loading nut anticlockwise to apply the level of the compression load required. The indicator will show the contact force in a unit of kg.
- 5) After applying the required force, **Turn Off** the red switch on the side of the digital load indicator and the single-phase switch.
- 6) **Connect** the 3-phase plug to the electricity socket.
- 7) **Turn ON** the main 3-phase electrical switch.
- 8) **Turn ON** the middle switch (conductor switch) by pressing the green button.
- 9) **Turn ON** the lower controller switch.
- 10) **Choose the direction of rotation** (forward or reversed) using the middle switch in the controller, low noise will be heard.
- 11) Choose a suitable speed using the upper knob in the controller. The range of digital speed indicator has a limited range (0.0 to 50). The output speed from the motor gearbox is 140 rpm. The test speed (X) is related to the test rig setting number in the controller. It can be calculated as:

$$\frac{X}{140} = \frac{\textit{The setting number}}{50}$$
- 12) **The lubricant** used is SP 320. Read carefully the COSHH form attached.
- 13) To replace the lubricant, ensure all electrical plugs are taken off from the electricity sockets. Take off the large front bolt and put a suitable container

to take the used oil. Empty the oil on the left side of the gearbox by releasing its lower knob and using a suitable container for taking the oil.

- 14) In the case of emergency, press the “Emergency stop” button on the control panel behind the test rig. To release the emergency ‘stop, turn the emergency stop button in the clockwise direction.

2. Turn off steps:

- 1) **Turn the speed direction position to number 0**, this will stop the motor rotation.
- 2) **Return** the upper knob in the speed controller to number zero position.
- 3) **Turn off** the lower switch of the controller.
- 4) **Turn off** the middle switch by pressing the red button.
- 5) **Turn off** the 3-phase main switch.
- 6) **Take the 3-phase plug out** of the electrical power socket.

3. Disc replacement operation:

3.1 Used Discs disassembly

- 1) Release all the electrical plugs from their sockets.
- 2) Empty the lubricant from the rig following instructions of Section 1 No.13.
- 3) Release the guard of the main shaft by removing its three bolts.
- 4) Remove the motor-gearbox combination by removing the four bolts fastening the electric motor with the base plate.
- 5) Ensure there is no compression force applied by the loading nut, this can be done using the load cell digital indicator.
- 6) Remove the flexible coupling on the main shaft on the side of the rig.
- 7) Remove the belt and pulleys cover (black cover in the right-hand side of the rig) by releasing the two bolts.
- 8) Remove the two pulleys (on the main shaft and camshaft) and their belt using puller attached with the rig.

- 9) Remove the test rig left-hand side gear cover by releasing the ten bolts of the cover.
- 10) Using rubber hammer, hit the main shaft from the motor side, it will slip to the left leaving the right main bearing. The lower test disc and the bush will fall between the two side plates.
- 11) Remove the nine bolts fixing the bearing cover on the left side plate.
- 12) Using the small shaft attached to release the upper shaft (Loading shaft) by hitting it from the right-hand side slot.

3.2 New disc assembly

- 1) Insert the upper shaft in its location then insert the new upper test disc and its bush in the inner space of the loading stand.
- 2) The test disc keyway should be in contact with the seal. Keep the loading stand at a suitable level to permit the shaft entry (Loading stand can move freely up and down).
- 3) Loading stand bearing house and the loading shaft bearing centers should be kept approximately centered before using the rubber hammer to hit the left side of the shaft to take its final position.
- 4) Fix the bearing cover using its 8-bolts.
- 5) Insert the main shaft from the left side and fix the lower test disc and its bush in between the side plates.
- 6) Tied up the left-hand side gear cover.
- 7) Fix the two pulleys in the right-hand side with their belt in their position by putting the lower and upper pulleys in the belt then insert the lower pulley to a small portion in the main shaft until reaching approximately the right-hand end of the camshaft, then insert the upper pulley. Move the two pulleys in parallel until reaching their final position.
- 8) Fix the pulleys and belt cover using its two bolts.
- 9) Fix the left part of the flexible coupling on the rig main shaft.
- 10) Fix the motor-gearbox combination using the four bolts.

- 11) Tied up the coupling guard.
- 12) Fix the front transparency cover.
- 13) Fill the lubricant using the upper knob on the top of the left-hand side gear cover.
- 14) Connect the 3-phase plug, and the single-phase load cell indicator plug, in their sockets. The rig now ready to be turned on.

Appendix G

Recommendations to improve the developed test rig

Using two grooved flange pulleys with speed ratio 1:1 and a timing belt as shown in [Figure G- 1](#), will improve the test rig camshaft-driving mechanism by preventing any slipping in addition to reduce the load on the camshaft bearings.



Figure G- 1: Flanged groove synchronous timing pulley and belt.

Because of the possible effect of the rotational speed on damage initiation, modifying the camshaft mechanism to be as a half-circle cam with eccentric of centers and introducing a follower as can be seen in [Figure G- 2](#), will enable applying different impact forces by changing the stiffness of the impact spring that attached to the impact lever without changing the rotational speed.

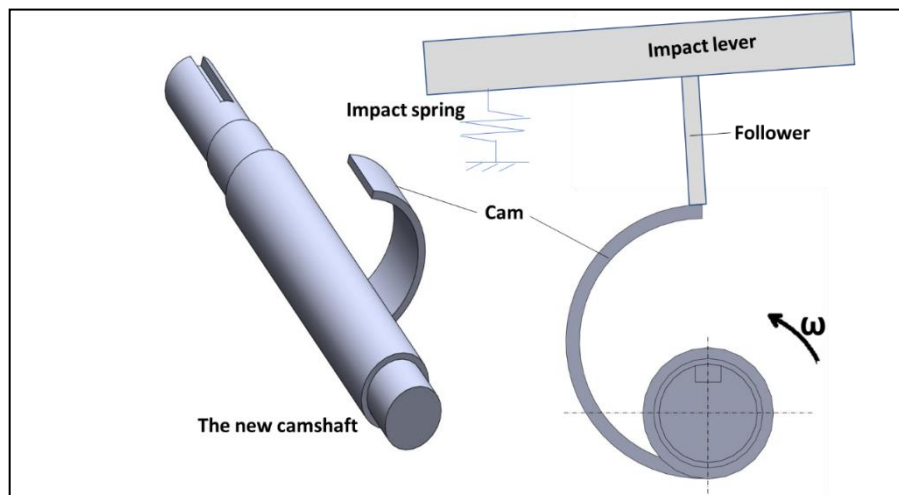


Figure G- 2: Modification of impact mechanism camshaft.

Despite the test rig working for a good testing period, replacing the test rig angular contact bearings with roller bearing type will increase the test rig reliability and reduce its maintenance.